



Fast-ion diagnostic in fusion plasmas by velocity-space tomography

Salewski, Mirko

Publication date:
2019

Document Version
Publisher's PDF, also known as Version of record

[Link back to DTU Orbit](#)

Citation (APA):
Salewski, M. (2019). *Fast-ion diagnostic in fusion plasmas by velocity-space tomography*. Technical University of Denmark.

General rights

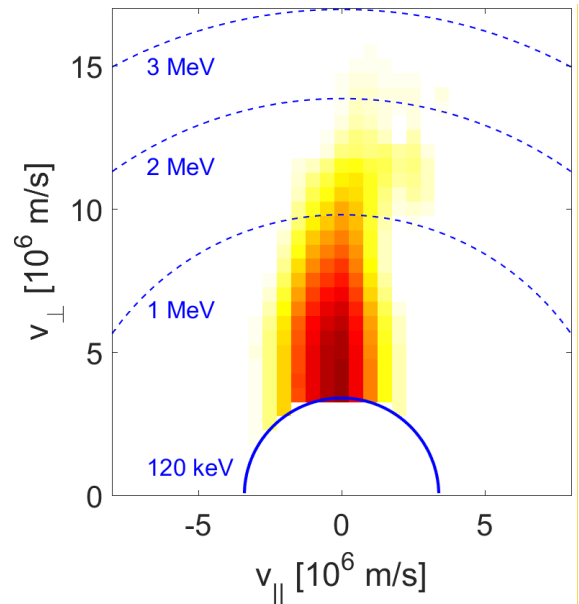
Copyright and moral rights for the publications made accessible in the public portal are retained by the authors and/or other copyright owners and it is a condition of accessing publications that users recognise and abide by the legal requirements associated with these rights.

- Users may download and print one copy of any publication from the public portal for the purpose of private study or research.
- You may not further distribute the material or use it for any profit-making activity or commercial gain
- You may freely distribute the URL identifying the publication in the public portal

If you believe that this document breaches copyright please contact us providing details, and we will remove access to the work immediately and investigate your claim.

Fast-ion diagnostic in fusion plasmas by velocity-space tomography

Dr. techn. thesis



Mirko Salewski,
January 2020

Fast-ion diagnostic in fusion plasmas by velocity-space tomography

Mirko Salewski

Department of Physics,
Technical University of Denmark

Dr.techn. thesis



Kongens Lyngby, March 2019

Technical University of Denmark
Department of Physics
Fysikvej, building 311,
2800 Kongens Lyngby, Denmark
Phone +45 4525 3344
info@fysik.dtu.dk
www.fysik.dtu.dk



Denne afhandling er af Danmarks Tekniske Universitet antaget til forsvar for den tekniske doktorgrad. Antagelsen er sket efter bedømmelse af den foreliggende afhandling.

Kgs. Lyngby, den 29. november 2019

A handwritten signature in black ink, appearing to read 'A. Bjarklev'.

Anders O. Bjarklev

Rektor

A handwritten signature in black ink, appearing to read 'Rasmus Larsen'.

Rasmus Larsen

Prorektor

This thesis has been accepted by the Technical University of Denmark for public defence in fulfilment of the requirements for the degree of Doctor Technices. The acceptance is based on an evaluation of the present dissertation.

Kgs. Lyngby, 29. november 2019

A handwritten signature in black ink, appearing to read 'A. Bjarklev'.

Anders O. Bjarklev

President

A handwritten signature in black ink, appearing to read 'Rasmus Larsen'.

Rasmus Larsen

Provost

"We have already obtained energy from uranium; we can also get energy from hydrogen, but at present only in an explosive and dangerous condition. If it can be controlled in thermonuclear reactions, it turns out that the energy that can be obtained from 10 quarts of water per second is equal to all of the electrical power generated in the United States. With 150 gallons of running water a minute, you have enough fuel to supply all the energy which is used in the United States today! Therefore it is up to the physicist to figure out how to liberate us from the need for having energy. It can be done."

R.P. Feynman, 'The Feynman Lectures on Physics', 1963

BBC: *"What world-changing idea, small or big, would you like to see implemented by humanity?"*

Hawking: *"This is easy. I would like to see the development of fusion power to give an unlimited supply of clean energy, and a switch to electric cars. Nuclear fusion would become a practical power source and would provide us with an inexhaustible supply of energy, without pollution or global warming."*

S.W. Hawking in an interview with BBC Future, 2016. Printed in 'Brief Answers to the Big Questions', 2018.

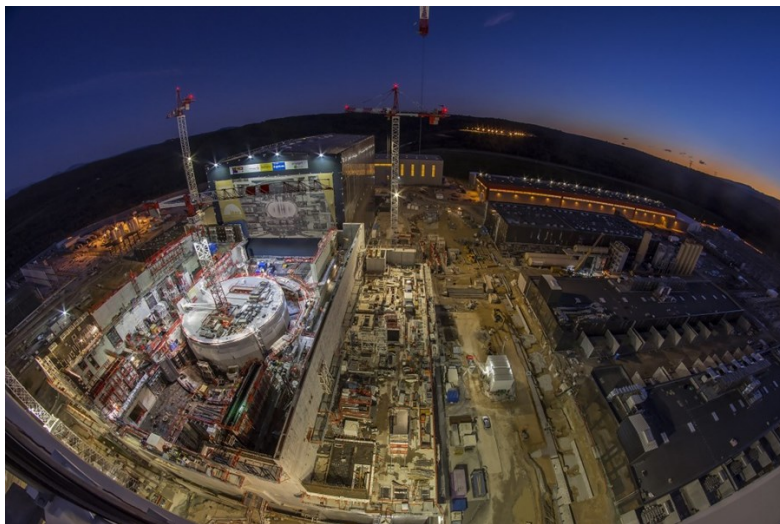


Figure 1: ITER construction site on 6 December 2018.

Summary

Velocity distribution functions of ions in high-performance fusion plasmas can deviate substantially from simple Maxwellian distributions. They can be strongly anisotropic or have local maxima at velocities larger than the thermal velocities. The distribution functions of the fast ions in the plasma are often the key to understanding heating, current drive, and various plasma instabilities. However, the distribution functions are unfortunately not always predictable for plasmas with instabilities. These often cause fast-ion transport that is not fully understood. The measurement of fast-ion velocity distribution functions is therefore crucial to operate high-performance plasmas for eventually harvesting energy. However, until now this measurement could not be done. The velocity-space tomography approach put forward in this thesis allows this measurement, providing a new meeting ground between theory and observation. This allows studies of the behavior of fast ions in fusion plasmas at an unprecedented level of detail.

Traditionally fast-ion measurements are presented in terms of spectra of a measured quantity that is particular to each diagnostic, e.g. the power density of radiation, photon or particle count rates, or the times-of-flight in a detector. These spectra in diagnostic measurables are then compared with synthetic spectra based on numerical simulations. The results of such comparisons are often hard to interpret since it is not immediately clear how to attribute any discrepancies between measurements and predic-

tions to the fast-ion distributions. To exploit the rich information about fast ions contained in the spectra by traditional procedures, we need to consider hundreds of measurements, keeping in mind nuisance parameters and the complicated relationships between the measurements and velocity space. Borrowing from usual position-space tomography, velocity-space tomography provides a way to process this wealth of information at once. It provides a 2D image that is straightforward to interpret, is the best useful fit to hundreds of simultaneous measurements, combines data from different diagnostics, shows the fundamental quantity of interest rather than quantities of secondary interest, and accounts for nuisance parameters.

Until today measurements by the diagnostics fast-ion D_α spectroscopy, collective Thomson scattering, neutron emission spectrometry, γ -ray spectroscopy, and fast-ion loss detectors installed at the tokamaks ASDEX Upgrade, JET, MAST, DIII-D, and EAST have been interpreted using velocity-space tomography. We have measured strongly non-Maxwellian fast-ion velocity distribution functions in plasmas heated by neutral beam injection and by electromagnetic wave heating in the ion cyclotron range of frequencies. The interaction of energetic particles with plasma instabilities has revealed strong selectivity in velocity space. This has filled gaps in our yet incomplete understanding of the physics of the redistribution of fast ions due sawteeth, neoclassical tearing modes, and Alfvén eigenmodes. Fast-ion densities have been measured for the first time, and first movies following the time evolution of the fast-ion velocity distribution function in plasmas with instabilities have been presented. Velocity-space tomography based on the foreseen set of fast-ion diagnostics at the next-step fusion device ITER has revealed that co-passing and counter-passing particles, which are two out of three major classes of particles in tokamaks, cannot be told apart. An additional detector is now proposed that would allow this distinction.

Velocity-space tomography has also revealed the density, drift velocity, and anisotropic temperatures of the thermal ions, has deblurred measurements with fast-ion loss detectors, and has provided a new approach to interpret γ -ray measurements of runaway electrons. This thesis describes the development of velocity-space tomography and demonstrates its utility for the interpretation of fast-ion measurements.

Resumé (Danish summary)

Ioners hastighedsfordelingsfunktioner i fusionsplasmaer kan afvige væsentligt fra simple Maxwellfordelinger. De kan være stærkt anisotropiske eller have lokale maksima og minima ved store hastigheder. De hurtige ioners fordelingsfunktioner er ofte nøglen til forståelsen af opvarmning, plasmastrømgenerering og forskellige ustabiliteter i plasmaet. Desværre er ionernes fordelingsfunktioner ikke altid forudsigelige, især i plasmaer med ustabiliteter. Ustabiliteter forårsager ofte anomal transport af de hurtige ioner. Målingen af de hurtige ioners hastighedsfordeling er derfor afgørende for at drive højtydende plasmaer, som i sidste ende skal bruges til at producere energi. Hastighedsfordelingsfunktioner i fusionsplasmaer har hidtil ikke kunne måles. Hastighedsrumtomografi, som denne afhandling beskriver, tillader netop denne måling. Dette skaber en ny måde at sammenholde teori og observationer og gør det muligt at undersøge de hurtige ioners fysik i fusionsplasmaer med en hidtil uset detaljeringsgrad.

Traditionelt præsenteres målinger af hurtige ioner i form af spektre, f.eks. spektre af strålingseffekt, foton- eller partikeltal eller flyvetid i en detektor. Disse spektre sammenlignes med syntetiske spektre baseret på numeriske simuleringer. Resultaterne af sådanne sammenligninger er ofte vanskelige at fortolke, da det ikke umiddelbart er klart, hvordan man kan relatere de hurtige ioners hastighedsfordeling til eventuelle uoverensstemmelser mellem målinger og forudsigelse. I traditionelle analyseprocedurer skal hundredvis af målinger betragtes samtidigt, og der skal tages højde

for ukendte parametre og de komplicerede relationer mellem målingerne og hastighedsfordelingerne. Som i tomografi i det sædvanlige positionsrum giver tomografi i hastighedsrum en måde, hvorpå alle informationer behandles på en gang. Resultatet er et 2D billede, som er let at fortolke og er den bedste, brugbare tilnærmelse til hundredvis af simultane målinger, kombinerer data fra forskellige diagnostikker og viser den fundamentale fordeling i stedet for størrelser af sekundær interesse.

Indtil nu har vi brugt hastighedsrumtomografi til at fortolke målinger fra D_α -spektroskopi, kollektiv Thomson spredning, neutronemissionsspektrometri, gammastrålespektroskopi og detektorer af ikke indesluttede hurtige ioner, som er installeret på flere tokamakker: ASDEX Upgrade, JET, MAST, DIII-D og EAST. Vi har målt stærkt anisotrope hastighedsfordelingsfunktioner i plasmaer, som er opvarmet ved neutralpartikelinjektion og ved elektromagnetisk opvarmning ved ioncyklotronfrekvenser. Vi fandt, at vekselvirkningen mellem hurtige partikler med ustabiliteter i plasmaet er stærkt selektiv i hastighedsrummet. Dette har bidraget til vores forståelse af fysikken bag omfordeling af hurtige ioner på grund af ustabiliteter, som savtænder, neoklassiske tearing modes og Alfvén egenmodes. Tætheder af hurtige ioner er blevet målt for første gang. De første film af tidsudviklingen af hastighedsfordelingsfunktionen i plasmaer med ustabiliteter er blevet produceret. Hastighedsrumtomografi baseret på ITER diagnostikker har vist, at medgående og modgående partikler, som er to ud af tre hovedklasser af partikler i en tokamak, ikke kan skelnes. Vi har nu foreslået en yderligere detektor, der muliggør dette.

Hastighedsrumtomografi har også målt de termiske ioners tæthed, drift-hastighed og anisotropiske temperaturer, har skærpet målinger af ion detektorer og har givet en ny metode til at fortolke målinger af gammastråler forårsaget af runaway elektroner. Denne afhandling beskriver udviklingen af hastighedsrumtomografi og demonstrerer anvendeligheden til fortolkning af målinger af hurtige ioner.

Preface

In this thesis I review my research on measurements of fast-ion velocity distribution functions in fusion plasmas by velocity-space tomography, which was done at the Technical University of Denmark from 2009 to 2019. The thesis consists of two parts: 1) A brief overview of the development of velocity-space tomography in the context of nuclear fusion research and society. 2) A collection of my published papers listed after this Preface. They are reprinted as appendices and are cited as references [1–15] in the bibliography of this brief overview. Papers [1, 3–5, 10] have been included in the annual selection of the best papers published in *Nuclear Fusion*, the *Nuclear Fusion Highlights*. Figure 12 from paper [10] was on the cover page of *Nuclear Fusion* in the April 2016 issue.

Papers by my former and present PhD students Asger Schou Jacobsen and Birgitte Madsen on velocity-space tomography are their own work and are not reprinted here. But as these papers present important elements of velocity-space tomography, I will include them in my overview on an equal footing (references [16–23]). Additionally, I have contributed or advised in velocity-space analysis to papers written by collaborators [24–38]. Finally, recent tutorial and review papers on velocity distribution functions and fast-ion diagnostics provide further technical details [39, 40].



Mirko Salewski
Lyngby, 14-March-2019

Included papers

[1]. M Salewski et al. (2010) *Nuclear Fusion* **50** 035012. Comparison of fast ion collective Thomson scattering measurements at ASDEX Upgrade with numerical simulations

[2]. M Salewski et al. (2011) *Nuclear Fusion* **51** 083014. On velocity space interrogation regions of fast-ion collective Thomson scattering at ITER

[3]. M Salewski et al. (2012) *Nuclear Fusion* **52** 103008. Tomography of fast-ion velocity-space distributions from synthetic CTS and FIDA measurements

[4]. M Salewski et al. (2013) *Nuclear Fusion* **53** 063019. Combination of fast-ion diagnostics in velocity-space tomographies

[5]. M Salewski et al. (2014) *Nuclear Fusion* **54** 023005. Measurement of a 2D fast-ion velocity distribution function by tomographic inversion of fast-ion D-alpha spectra

[6]. M Salewski et al. (2014) *Plasma Physics and Controlled Fusion* **56** 105005. On velocity-space sensitivity of fast-ion D-alpha spectroscopy

[7]. M Salewski et al. (2015) *Plasma Physics and Controlled Fusion* **57** 014021. Doppler tomography in fusion plasmas and astrophysics

[8]. M Salewski et al. (2015) *Nuclear Fusion* **55** 093029. Velocity-space observation regions of high-resolution two-step reaction gamma-ray

spectroscopy

[9]. M Salewski et al. (2016) *Nuclear Fusion* **56** 046009. Fast-ion energy resolution by one-step reaction gamma-ray spectrometry

[10]. M Salewski et al. (2016) *Nuclear Fusion* **56** 106024. High-definition velocity-space tomography of fast-ion dynamics

[11]. M Salewski et al. (2017) *Nuclear Fusion* **57** 056001. MeV-range velocity-space tomography from gamma-ray and neutron emission spectrometry measurements at JET

[12]. M Salewski et al. (2018) *Nuclear Fusion* **58** 036017. Deuterium temperature, drift velocity, and density measurements in non-Maxwellian plasmas at ASDEX Upgrade

[13]. M Salewski et al. (2018) *Fusion Science and Technology* **74**(1-2) 23-36. Bayesian integrated data analysis of fast-ion measurements by velocity-space tomography

[14]. M Salewski et al. (2018) *Nuclear Fusion* **58** 096019. Alpha-particle velocity-space diagnostic in ITER

[15]. M Salewski et al. (2019) *Journal of Instrumentation* **14** C05019. Diagnostic of fast-ion energy spectra and densities in magnetized plasmas

Acknowledgements

I thank my collaborators and colleagues for their help over the past 10 years:

Ivana Abramovic, Frederico Binda, Henrik Bindslev, Carlo Cazzaniga, Amel Durakovic, Göran Ericsson, Jacob Eriksson, Michael Fitzgerald, Vedran Furtula, Joaquin Galdon-Quiroga, Manolo García-Muñoz, Ben Geiger, Nikolaj Gorelenkov, Giuseppe Gorini, Per Christian Hansen, Bill Heidbrink, Carl Hellesen, Anders Hjalmarsson, Juan Huang, Asger Schou Jacobsen, Thomas Jensen, Owen Jones, Vasili Kiptily, Esben Klinkby, Søren Bang Korsholm, Tuomas Koskela, Taina Kurki-Suonio, Axel Larsen, Frank Leipold († 17. October 2018), Birgitte Madsen, Jens Madsen, Rachael McDermott, Ken McClements, Fernando Meo, Poul Kerff Michelsen, Dima Moseev, Volker Naulin, Anders Henry Nielsen, Stefan Kragh Nielsen, Massimo Nocente, Tomas Odstrčil, Simon Pinches, Jens Juul Rasmussen, Jesper Rasmussen, Marike Rebai, Bo Simmendefeldt Schmidt, Mireille Schneider, Phillip Schneider, Sergei Sharapov, Alexander Shevelev, Seppo Sipilä, Don Spong, Luke Stagner, Danny Steeghs, Morten Stejner, Giovanni Tardini, Marco Tardocchi, Alexander Simon Thrysoe, Markus Weiland, the ASDEX Upgrade Team, the JET Contributors, the MAST Team, the DIII-D Team, the EAST Team, the EUROfusion MST1 Team, and the ITPA Topical Group on Energetic Particles.

Contents

Summary	iii
Resumé (Danish summary)	v
Preface	vii
Included papers	ix
Acknowledgements	xi
1 Introduction	1
1.1 The energy problem, combustion products and global warming	1
1.2 Nuclear fusion and the Lawson triple product	7
1.3 Magnetic plasma confinement	10
1.4 Plasma heating by energetic particles	12
1.5 Fast-ion velocity distribution functions	13
1.6 This thesis	16
2 Energetic particle diagnostics	19
2.1 Neutron emission spectroscopy	21
2.2 γ -ray spectroscopy	24
2.2.1 One-step reactions	24
2.2.2 Two-step reactions	25
2.3 Fast-ion D_α spectroscopy	28
2.4 Collective Thomson scattering	29

2.5	Fast-ion loss detectors	32
2.6	Synthetic diagnostics	32
3	The forward problem: velocity-space sensitivity	35
3.1	Weight functions	35
3.2	Weight functions for FIDA, CTS, NES, GRS, NPAs and FILDs	37
3.3	Observable velocity space for a given line-of-sight velocity	43
3.4	Observable velocity space for a given detected energy . . .	44
3.5	The forward problem as a matrix equation	48
4	The inverse problem: velocity-space tomography	49
4.1	The inverse problem	49
4.2	Tikhonov regularization	51
4.3	Prior information	52
4.4	Inference of isotropic functions	56
4.5	Uncertainties and regularization strength	57
4.6	Tikhonov regularization in the Bayesian perspective . . .	61
5	Discussion, conclusions, and outlook	63
	Bibliography	67
	Reference [1]	79
	Reference [2]	91
	Reference [3]	103
	Reference [4]	115
	Reference [5]	127
	Reference [6]	135
	Reference [7]	151
	Reference [8]	163
	Reference [9]	179

CONTENTS

xv

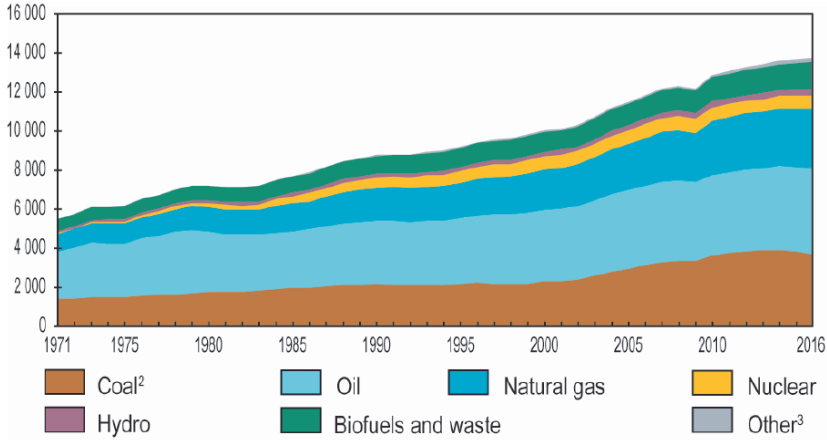
Reference [10]	191
Reference [11]	207
Reference [12]	219
Reference [13]	233
Reference [14]	249
Reference [15]	267

Introduction

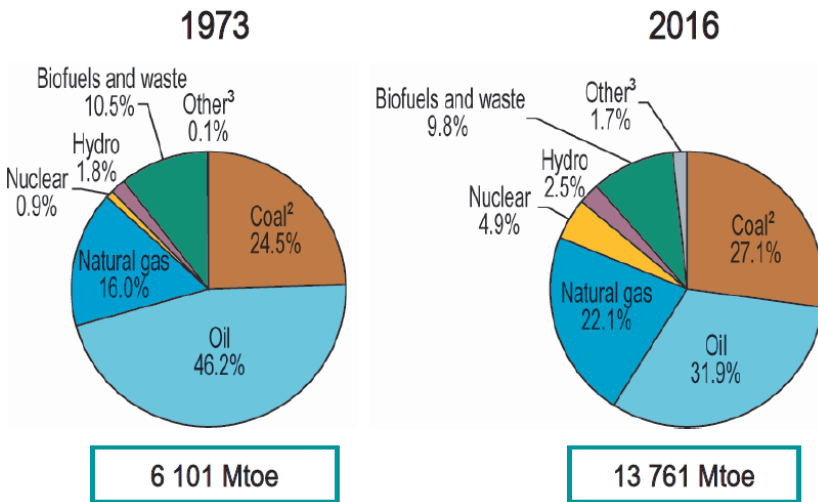
1.1 The energy problem, combustion products and global warming

One of the most urgent responsibilities of our generation is to end the era of fossil fuels. The main reason is that the combustion of fossil fuels releases carbon dioxide (CO_2) causing global warming. The annual worldwide primary energy supply best highlights our dependence on fossil fuels. Our worldwide primary energy supply from 1973 to 2016 appears in fig. 1.1 [41]. Transport, heating, and electricity generation each consume about 20% to 40% of this energy [42]. Oil is mainly used for transport, whilst coal and natural gas are mainly used for heating and electricity generation [41].

Currently fossil fuels supply more than 80% of our worldwide primary energy. Combustion of oil supplied 32% in 2016, coal 27%, and natural gas 22%. Combustion of biofuels and waste supplied another 10%. Whereas combustion of fossil fuels increases the atmospheric CO_2 concentration, combustion of biofuels does not. Biofuels are therefore regarded as a



(a)



(b)

Figure 1.1: Total worldwide annual primary energy supply in million tonnes of oil equivalent (Mtoe) by energy sources [41]. (a) Development from 1971 to 2016. (b) Comparison between 1973 and 2016.

1.1 The energy problem, combustion products and global warming 3

sustainable energy source. However, combustion always releases harmful combustion products other than CO_2 . Nuclear fission (5%) does not release CO_2 and thus mitigates global warming. However, nuclear fission is usually not considered a sustainable energy source due to the risk of nuclear accidents and the radioactive waste. Hydro energy is the largest emission-free sustainable energy source (2.5%). In 2016, other emission-free sustainable energy sources such as wind, geothermal, wave, tidal, and solar energy supplied in total 1.7% of the worldwide primary energy.

The share of fossil fuels has decreased by about 5 percent points from 1973 to 2016, but in the same time the annual worldwide primary energy supply has more than doubled, from 6.1 Mtoe to 13.8 Mtoe (million tonnes of oil equivalent). Most likely the annual worldwide primary energy supply will not decrease enough to stop global warming up to 2040, even in optimistic scenarios (New Policies Scenarios: 12.5 Mtoe; Sustainable Development Scenario: 10.2 Mtoe [41]).

CO_2 is an unavoidable product of fossil fuel combustion. CO_2 is a greenhouse gas which traps heat in analogy to glass in a greenhouse. An increase of the atmospheric concentration of greenhouse gases leads to global warming which has several severe consequences for humans as listed by the Intergovernmental Panel on Climate Change (IPCC) [43]:

- a number decrease of extremely cold temperature events,
- a number increase of extremely hot temperature events,
- a number increase of extreme rain, hail or snow events,
- a number increase of extreme sea level events,
- a decrease of food and water security and human health,
- ocean acidification,
- a substantial sea level rise,
- and extinction of many species.

Fig. 1.2 illustrates globally averaged temperature and sea level changes as well as greenhouse gas concentration levels from 1850, just before the industrial revolution, until now. The globally averaged combined land and ocean surface temperature has increased by almost 1°C since 1850 (figure 1.2(a)). The thermal expansion of water and the melting of ice on

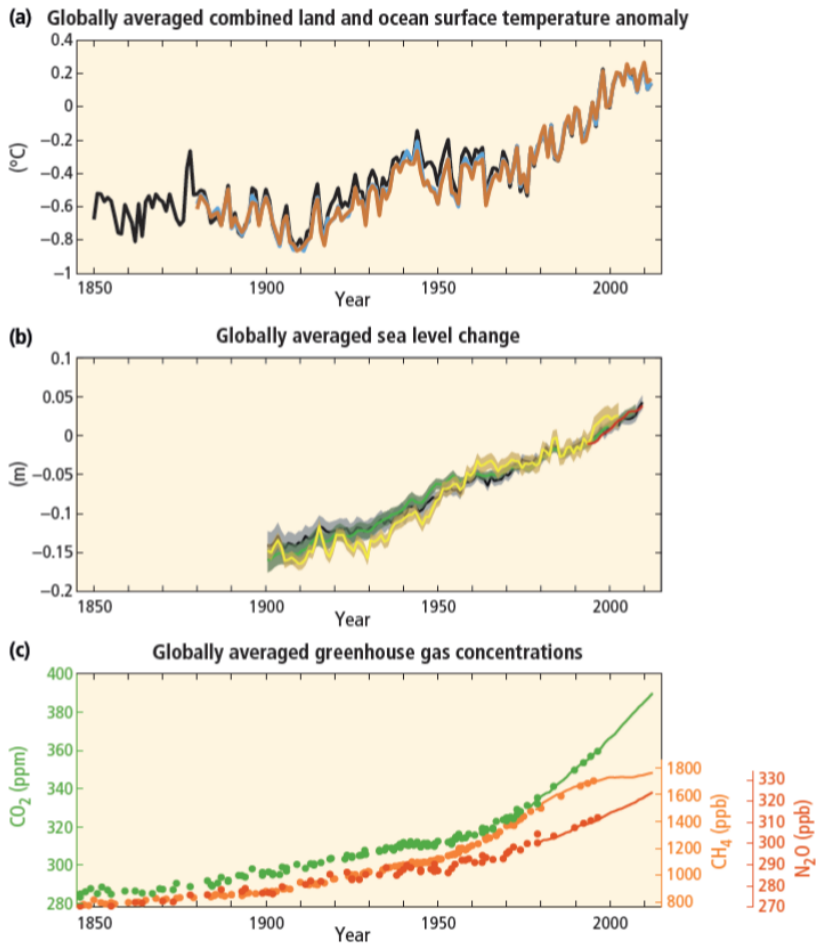


Figure 1.2: Global parameters characterizing the greenhouse effect from 1850, just before the industrial revolution, until now. (a) Globally averaged combined land and ocean temperature changes from various data sets. (b) Globally averaged sea level change from various data sets. (c) Globally averaged greenhouse gas concentrations [43].

1.1 The energy problem, combustion products and global warming 5

land has led to a globally averaged sea level rise of about 20 cm since 1900, currently at a rate of about 3-4 mm/year (fig. 1.2(b)). In the same period (since 1850), the concentration levels of greenhouse gases have increased substantially (fig. 1.2(c)).

In addition to CO_2 , other main greenhouse gases are methane (CH_4), nitrous oxide (N_2O), and water vapour. Humans are not thought to influence the atmospheric water vapour content directly due to the large natural sources and sinks. The concentration of CO_2 is 2–3 orders of magnitude higher than the concentrations of CH_4 and N_2O (fig. 1.2(c)), but CO_2 molecules are less efficient in trapping thermal radiation than CH_4 and N_2O molecules. To estimate the relative impact of anthropogenic CO_2 , CH_4 , and N_2O emission on global warming, the annual emissions of these greenhouse gases are given in terms of CO_2 emission that would cause the same global warming in fig. 1.3 (gigatonnes of CO_2 -equivalent). The dominant source of anthropogenic greenhouse gas emissions is combustion of fossil fuels accounting for about 60% of the anthropogenic global warming effect. Industrial processes, most importantly the production of cement from limestone, account for about 5%. The global warming due to anthropogenic greenhouse gas emissions by far exceeds global warming due to natural causes (fig. 1.4). Figs. 1.3 and 1.4 suggest that ending the era of fossil fuels would efficiently mitigate global warming.

As mentioned, fossil fuel and biofuel combustion processes release several harmful combustion products other than CO_2 . A breakdown of estimated harmful emissions by fuel appears in fig. 1.5 for NO_x , SO_2 , and fine particulate matter [42]. Nitrogen oxides (NO_x) cause acid rain, depletion of the ozone layer, and photochemical smog. N_2O causes global warming. Sulfur dioxide (SO_2) causes acid rain. Fine particulate matter is dangerous if inhaled, and it can cause severe disease or even death [44]. Biofuel combustion is a major source of fine particulate matter. Additionally, unburned and partially burned hydrocarbons are also toxic. These toxic emissions further support that we should avoid combustion in our future energy mix.

This section discussed the energy problem which arises from the contradicting needs to have a sustained or even increasing energy supply on the

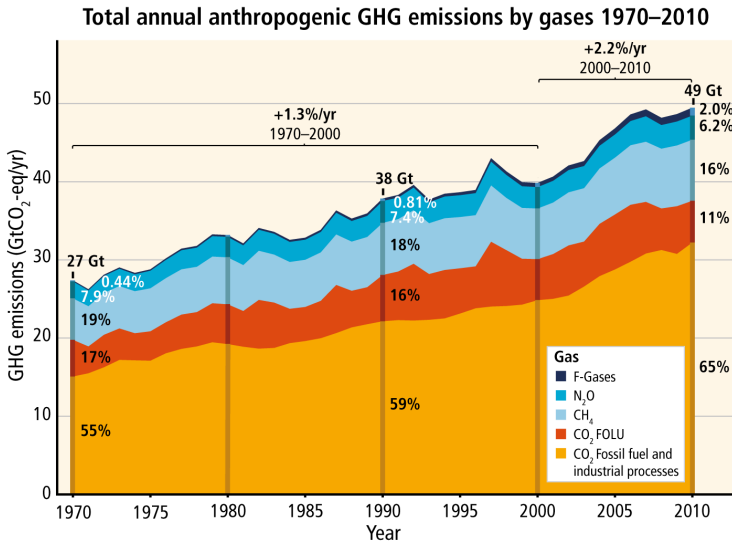


Figure 1.3: Annual worldwide anthropogenic greenhouse gas emissions in gigatonnes of CO₂-equivalent per year [43]. FOLU: Forest and land use. The CO₂ emission due to industrial processes is about ten times smaller than that due to fossil fuels.

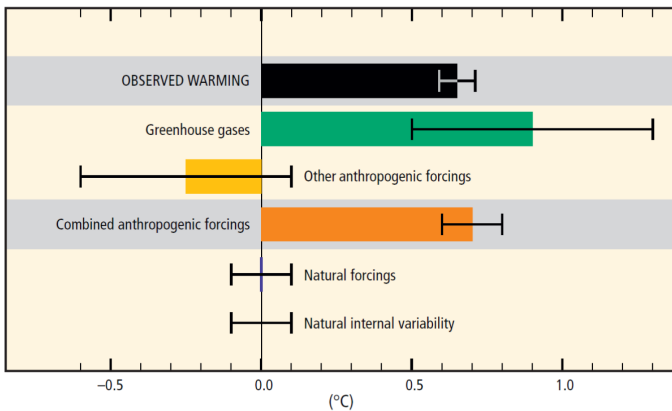


Figure 1.4: Estimated contributions to the observed temperature increase from 1951 to 2010 [43]. Anthropogenic effects by far exceed natural effects. The dominant anthropogenic effect is the emission of greenhouse gases.

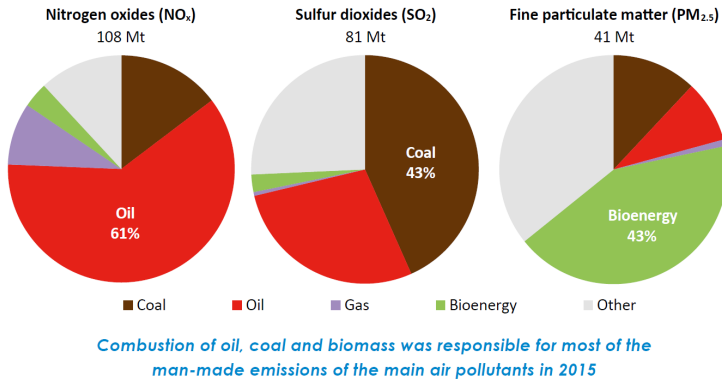
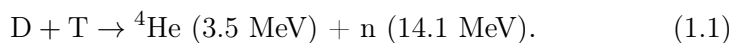


Figure 1.5: Estimated toxic gas emissions from combustion in 2015: Nitrogen oxides, sulfur dioxide, fine particulate matter [42].

one hand and a substantial reduction of fossil fuel combustion on the other hand. The inevitable conclusion is that the energy from fossil fuels must be replaced by energy from emission-free sources. Such sources include biofuels, hydro energy, wind energy, solar energy, tidal energy, geothermal energy, nuclear fission energy, and, on the horizon, fusion energy. To have a chance to stop global warming, we must make a fast, resolute, and sustained effort to substantially develop all these options. By the end of this century, we can hope to have developed fusion power well enough to supply a substantial fraction of our primary energy. If we succeed, nuclear fusion power plants can deliver steady baseload power. It has a practically unlimited fuel supply, is inherently safe, is environmentally benign, and especially does not cause global warming. This ambitious goal is believed to provide a sustainable solution to the energy problem.

1.2 Nuclear fusion and the Lawson triple product

Energy can be obtained from fusion of light elements such as the hydrogen isotopes deuterium (D) and tritium (T). The first generation of power plants will rely on the DT fusion process $T(D,n)^4\text{He}$ which is shorthand for



This reaction releases energy because the deuterium and the tritium ions are slightly heavier than the helium ion (α -particle) and the neutron. This mass deficit is released as kinetic energy of the reaction products according to Einstein's relation $E = \Delta mc^2$. One fifth of the fusion energy $E_{\text{fusion}} = 17.6$ MeV is released as kinetic energy of the α -particle and four fifth as kinetic energy of the neutron due to energy and momentum conservation.

In magnetic fusion power plants, the energetic α -particles heat the deuterium and tritium fuels to about ten times the solar core temperature at which matter is in the plasma state. The ions in the plasma are confined by a magnetic field whereas the neutrons leave the plasma. Deuterium is readily available in ocean water with an abundance of about 1/6420 of the hydrogen atoms. Tritium, however, is rare because it is radioactive and decays with a half-life of only 12.3 years. It must therefore be bred on-site from lithium placed close to the fusion plasma such that there is no need to transport radioactive fuel. Lithium is effectively the second fuel of the overall process. Future generations of fusion power plants could alternatively gain energy from the DD fusion process to avoid the need to breed tritium, but this is technologically more challenging.

The goal of fusion energy research is perhaps best summarized by the Lawson triple product which comes about by considering the energy balance in a power plant [45]. The energy sources in the plasma are the α -particle heating $P_\alpha = P_{\text{fusion}}/5$ and the auxiliary heating P_{aux} . The energy sink from the plasma is P_{loss} . In terms of power densities [W/m³], they are:

$$P_{\text{fusion}} = \frac{1}{4}n_e^2\langle\sigma v\rangle E_{\text{fusion}}, \quad (1.2)$$

$$P_\alpha = P_{\text{fusion}}/5 = \frac{1}{4}n_e^2\langle\sigma v\rangle E_\alpha, \quad (1.3)$$

$$P_{\text{aux}} = P_{\text{fusion}}/Q, \quad (1.4)$$

$$P_{\text{loss}} = \frac{3n_e T}{\tau_E}. \quad (1.5)$$

The fusion power density P_{fusion} in a DT plasma is the energy per reaction E_{fusion} times the reaction rate $n_D n_T \langle\sigma v\rangle$ where n_D is the deuteron density, n_T is the tritium density, σ is the fusion reaction cross section, v the relative velocity between the reactants, and $\langle \rangle$ denotes averaging over ve-

locities. We further assume ideal conditions with $n_D = n_T = n_e/2$, where n_e is the electron density. The auxiliary heating P_{aux} is characterized by the so-called fusion energy gain factor Q :

$$Q = \frac{P_{\text{fusion}}}{P_{\text{aux}}} = \frac{5P_\alpha}{P_{\text{aux}}}. \quad (1.6)$$

$Q = 1$ is called break-even: All produced fusion power is needed to maintain the plasma by auxiliary heating. If the conversion efficiency from fusion power to auxiliary heating power is η , then $Q = 1/\eta$ is needed to have engineering break-even. At ignition ($Q = \infty$) the plasma is entirely self-heated. At $Q = 5$ the α -particle power equals the auxiliary heating power. The goal for the next-step device ITER is $Q = 10$ which means that the fusion power is ten times the auxiliary heating power (and the α -particle heating power is twice the auxiliary heating power, such that the plasma is predominantly self-heated) [46]. Economically acceptable fusion power plants should have $Q \sim 20 - 100$ [47–49]. The energy loss from the plasma is modelled using the energy confinement time τ_E and the energy stored in the plasma, $3n_e T$.

The condition $P_{\text{loss}} < P_\alpha + P_{\text{aux}}$ must be met for a sustained fusion burn. It can be written in terms of the triple product of particle density, temperature, and the energy confinement time:

$$n_e T \tau_E > \frac{12}{E_\alpha(1 + 5/Q)} \frac{T^2}{\langle \sigma v \rangle}. \quad (1.7)$$

This is the Lawson triple product which must be above a certain value for a sustained fusion burn. Lawson originally derived an ignition condition for $n_e \tau_E$ [45]. Fig. 1.6 illustrates the Lawson triple product vs. temperature for different values of Q . Break-even and ignition conditions are easiest to access at about 15 – 30 keV ($\sim 170 - 350$ million °C) where $T^2/\langle \sigma v \rangle$ and hence the Lawson triple product threshold are minimized. For ignition it is about $n_e T \tau_E \sim 3 \times 10^{21}$ keVs/m³ or $p \tau_E \sim 9$ atm·s. Near the minimum of the Lawson triple product threshold, we have $\langle \sigma v \rangle \propto T^2$. Hence we find from equation 1.2 that the fusion power density scales as the square of the pressure: $P_{\text{fusion}} \propto p^2$. Economic power plants require large fusion power densities and therefore large pressures. The Lawson triple product can be achieved for example by $n_e = 10^{20}$ m⁻³, $T=15$ keV and $\tau_E = 2$ s. The pressure is in this case about 5 atm. Practically, there is little room for trade-offs among these parameters.

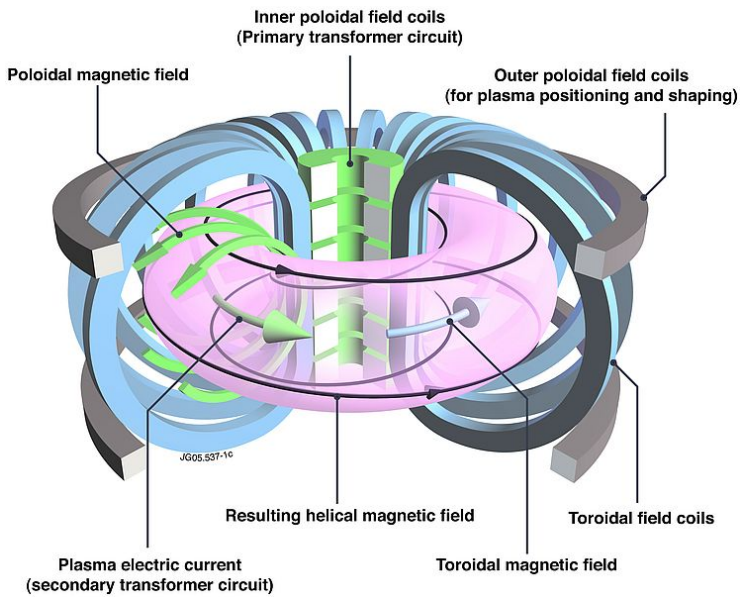


Figure 1.7: Tokamak principle: Magnetic coils and field configuration in a schematic tokamak [50].

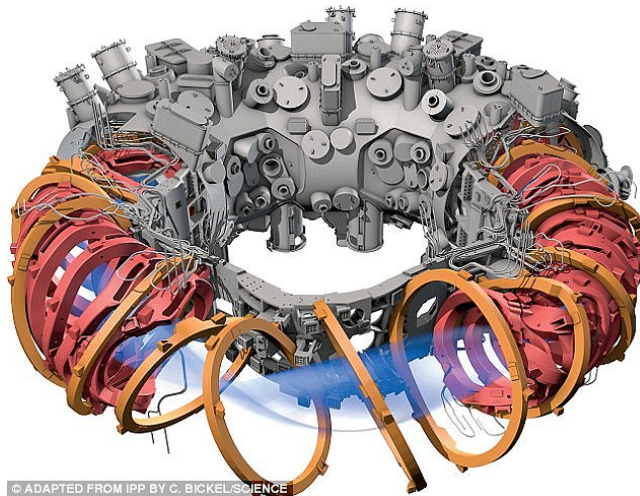


Figure 1.8: Plasma shape, magnetic coils and vacuum vessel of the stellarator Wendelstein 7-X [51].

The magnetic field in a stellarator is a complex 3D field generated by a set of coils as illustrated in fig. 1.8. A major advantage of this configuration is that it is not necessary to drive a current in the plasma. It is still not clear which magnetic configuration will give the most efficient power plants. The next-step fusion device ITER will be a tokamak.

1.4 Plasma heating by energetic particles

The Lawson triple product shows that temperatures in the range of 15 – 30 keV ($\sim 170 - 350$ million $^{\circ}\text{C}$) are most favourable in a fusion power plant. Plasmas can be heated to such temperatures by several methods (fig. 1.9). Any current in the plasma provides some Ohmic heating. But as the plasma resistivity drops with temperature ($\rho \propto T^{-3/2}$), Ohmic heating is efficient up to temperatures of only a few keV. Auxiliary heating methods comprise electromagnetic wave heating in the electron or ion cyclotron range of frequencies (ECRF, ICRF) or neutral beam injection (NBI). The dominant heating method in steady-state plasmas in future power plants will be heating by α -particles generated in fusion reactions.

Fast ions generated by NBI, ICRF, and fusion reactions heat the plasma by collisions. Present NBI heating systems inject neutral particles with energies of 20 – 400 keV. The neutral particles ionize and form a population of fast ions. ICRF heating systems accelerate ions in the plasma to energies in the MeV-range. ITER will have a total auxiliary heating power of 73 MW: 33 MW NBI, 20 MW ICRF, and 20 MW ECRF [52]. Lastly, fusion α -particles are born with an energy of 3.5 MeV. To date, substantial populations of α -particles have been generated in JET and TFTR in DT campaigns in the 1990ies. The record fusion power was achieved in JET: 16 MW at $Q = 0.64$ [53]. A second DT campaign at JET is currently being prepared [54, 55]. The main goal of ITER is to achieve a fusion power of 500 MW with simultaneous auxiliary heating of 50 MW ($Q = 10$) [52].

The fast ions from NBI, ICRF, and fusion reactions must be confined in the plasma. If too many energetic particles were lost to the wall, the power plant efficiency would be poor, and the high-energy ions may

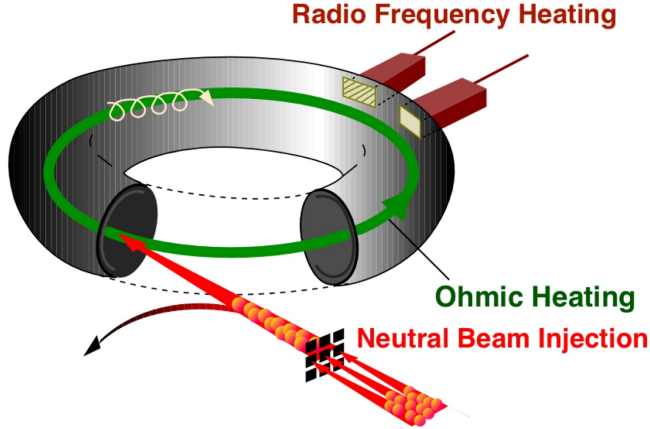


Figure 1.9: Plasma heating systems: NBI heating, radiofrequency heating (ICRF or ECRF), and Ohmic heating [50].

damage the first wall of the device. Various plasma instabilities can lead to enhanced energetic particle transport and losses which are not fully understood [56–67]. This makes the measurement of α -particle velocity distribution functions crucial. Energetic particle physics is considered a critical area for the success of the ITER mission, and it is therefore treated by the Topical Group for Energetic Particle Physics under the International Tokamak Physics Activity (ITPA).

1.5 Fast-ion velocity distribution functions

Velocity distribution functions in fusion plasmas are often complicated functions with strong anisotropy or local maxima at velocities typical for the most energetic ions in the plasma. Generally, particle distribution functions are six-dimensional and can be described by three position-space coordinates and three velocity-space coordinates. The phase-space distribution $f^{6D}(\mathbf{x}, \mathbf{v})$ specifies the number of particles dN in an infinitesimal phase-space volume $(d\mathbf{x}, d\mathbf{v})$:

$$dN = f^{6D}(\mathbf{x}, \mathbf{v})d\mathbf{x}d\mathbf{v}. \quad (1.8)$$

Tokamaks are toroidally approximately axisymmetric, disregarding the magnetic field ripple due to the toroidal field coils. Furthermore, charged particles in magnetized plasmas gyrate quickly about the magnetic field vector, such that velocity distribution functions are axisymmetric about \mathbf{B} to a good approximation. A tokamak plasma can therefore be described by a 4D distribution function, i.e. a collection of 2D velocity distribution functions at every point in a poloidal plane of the tokamak.¹ In this thesis we consider such local 2D velocity distribution functions. Dividing both sides of equation 1.8 by $d\mathbf{x}$ introduces the density dn in the velocity-space volume $d\mathbf{v}$:

$$dn = f^{3D}(\mathbf{v})d\mathbf{v}. \quad (1.9)$$

The units of f^{3D} are $[\text{s}^3/\text{m}^6]$. Various representations of distribution functions are commonly used in the plasma physics literature [40]. In Cartesian coordinates, we align one of the coordinate axes with the magnetic field vector. This axis is called v_{\parallel} . $v_{\perp 1}$ and $v_{\perp 2}$ are then the velocity components perpendicular to the magnetic field. Equation 1.9 becomes

$$dn = f_{\text{Car}}^{3D}(v_{\parallel}, v_{\perp 1}, v_{\perp 2})dv_{\parallel}dv_{\perp 1}dv_{\perp 2}. \quad (1.10)$$

Axisymmetric functions do not depend on the gyrophase Γ . Hence it is advantageous to introduce the cylindrical coordinates $(v_{\parallel}, v_{\perp}, \Gamma)$ such that $v_{\perp 1} = v_{\perp} \cos \Gamma$ and $v_{\perp 2} = v_{\perp} \sin \Gamma$ where v_{\perp} is the perpendicular velocity. Substitution of $v_{\perp 1}$ and $v_{\perp 2}$ gives a representation of 3D axisymmetric functions in two coordinates, $f_{\text{Car}}^{3D}(v_{\parallel}, v_{\perp})$, since the ignorable gyrophase Γ drops out. For a full transformation to cylindrical coordinates we also need to express the velocity-space volume element in cylindrical coordinates. The Jacobian of the transformation from Cartesian to cylindrical coordinates is v_{\perp} . Integration over the ignorable gyrophase Γ reduces the number of dimensions. The density is then given by

$$dn = 2\pi v_{\perp} f_{\text{Car}}^{3D}(v_{\parallel}, v_{\perp})dv_{\parallel}dv_{\perp}. \quad (1.11)$$

In the plasma physics literature we frequently encounter the 2D velocity distribution function defined by

$$f_{\text{Car}}^{2D}(v_{\parallel}, v_{\perp}) = 2\pi v_{\perp} f_{\text{Car}}^{3D}(v_{\parallel}, v_{\perp}) \quad (1.12)$$

¹We note that the particle phase-space distribution function in a tokamak can also be described by three constants of motion of a particle: the energy, the magnetic moment and the canonical toroidal angular momentum (plus a binary parameter labelling if a passing particle proceeds along or against the plasma current). This 3D distribution function can also be measured using a new method termed orbit tomography [68, 69].

which is also used in this thesis. Another popular coordinate system is based on (E, p) -coordinates. Here, E is the energy, and p is the pitch:

$$E = \frac{1}{2}m(v_{\parallel}^2 + v_{\perp}^2), \quad p = \frac{v_{\parallel}}{\sqrt{v_{\parallel}^2 + v_{\perp}^2}}, \quad (1.13)$$

where m is the particle mass. The pitch is the cosine of the so-called pitch angle. The density in the infinitesimal area $dEdp$ is

$$dn = 2\pi \sqrt{\frac{2E}{m^3}} f_{\text{Car}}^{3\text{D}} \left(p \sqrt{\frac{2E}{m}}, \sqrt{1-p^2} \sqrt{\frac{2E}{m}} \right) dEdp. \quad (1.14)$$

The 2D velocity distribution function in (E, p) -coordinates is

$$f^{2\text{D}}(E, p) = 2\pi \sqrt{\frac{2E}{m^3}} f_{\text{Car}}^{3\text{D}} \left(p \sqrt{\frac{2E}{m}}, \sqrt{1-p^2} \sqrt{\frac{2E}{m}} \right). \quad (1.15)$$

This coordinate system is the most widespread among experimentalists working with velocity distribution functions. Distribution functions computed with the TRANSP/NUBEAM code [70], which is implemented at most tokamaks, are usually presented in these coordinates, and we also use them here.

A standard equilibrium distribution has a Maxwellian energetic particle tail of the form $\exp(-v^2/v_{\text{th}}^2)$ where v_{th} is the thermal velocity. Fast-ion velocity distribution functions are always highly non-Maxwellian. For example, the so-called classical slowing-down distribution, which is an approximate model for isotropically distributed energetic particles (e.g., fusion α -particles), has a tail of the form $1/(v^3 + v_c^3)$, where v_c is the so-called crossover speed, up to the particle birth speed. NBI and ICRF distribution functions are even highly anisotropic in velocity space. A recent tutorial paper on analytic models for velocity distribution functions (bi-Maxwellian, ring, and isotropic and anisotropic slowing-down distributions) in the most common coordinate system provides further technical details [40]. Magnetohydrodynamically active plasmas can have anomalous velocity distribution functions due to enhanced transport which can be selective in velocity space. As we need to understand the anomalous transport, measurements of velocity distribution functions are essential.

1.6 This thesis

This thesis deals with measurements of 2D velocity distribution functions in fusion plasmas in a small measurement volume. To do this, we solve an inverse problem illustrated in fig. 1.10. The forward problem, to compute synthetic measurements S from a distribution function F , has previously been solved for all diagnostics we consider. This thesis solves the inverse problem, which is to compute F from S . As F is a 2D function, we can use methods of tomography. Examples of 2D images computed using velocity-space tomography appear in figs. 1.11 and 1.12 along with corresponding numerical simulations. Fig. 1.11 shows the fast-ion distribution generated in an experiment with ICRF heating at the third harmonic at JET [11]. Fig. 1.12 shows the fast-ion distribution generated in an experiment with NBI heating at ASDEX Upgrade [10]. In these cases the agreement between measurements and simulations is remarkable.

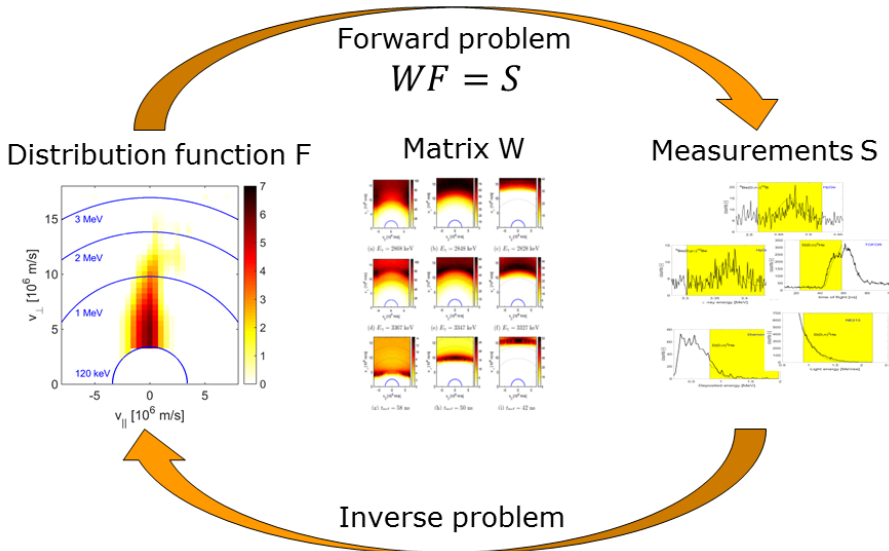


Figure 1.10: Synthetic diagnostics solve the forward problem of fast-ion diagnostics, to compute synthetic measurements S given a velocity distribution function F . Velocity-space tomography solves the inverse problem, to compute F given S .

In this overview we present a concise exposition of the most essential

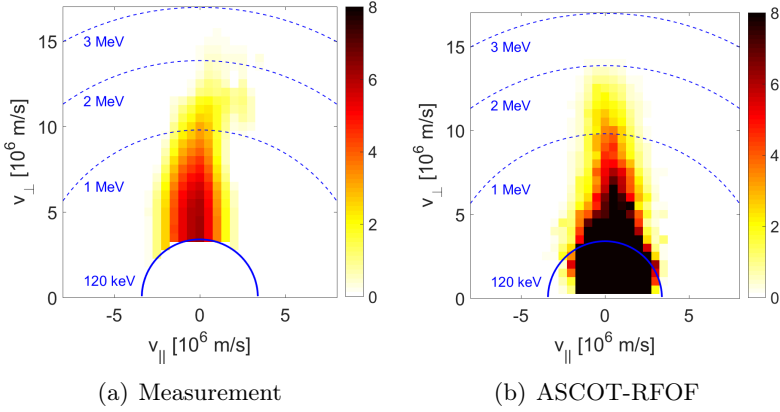


Figure 1.11: (a) Measurement and (b) simulation of a MeV-range ion velocity distribution function for third harmonic ICRF heating at JET [11].

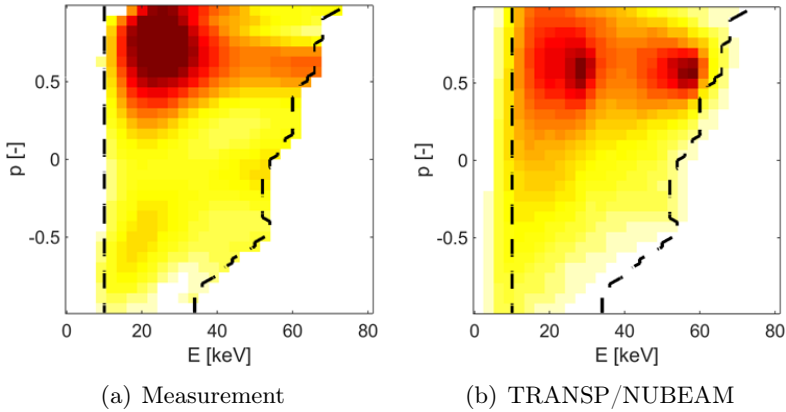


Figure 1.12: (a) Measurement and (b) simulation of a keV-range ion velocity distribution function for NBI heating at ASDEX Upgrade [10].

elements and tools required for measurements of 2D images as illustrated in figures 1.11 and 1.12. Comprehensive descriptions are found in the chronologically ordered references [1-15] reprinted with this overview.

Chapter 2 describes the fast-ion diagnostics used for velocity-space tomography and how fast-ion measurements are traditionally analyzed. Reference [1] is an example of such a conventional analysis using the collective Thomson scattering diagnostic developed at DTU [1, 31, 71, 72]. Conventionally, measured spectra of diagnostic variables are compared with synthetic spectra based on forward models. We will illustrate that the relationships of the spectra to fast-ion velocities are not obvious.

Chapter 3 examines the velocity-space sensitivity of the major fast-ion diagnostics which is quantified by so-called weight functions [73]. Weight functions were developed for the different fast-ion diagnostics in references [2, 6, 8, 9, 16–18, 21, 36]. The most exact computations of weight functions account for the same physics as the corresponding forward models. Here we use energy and momentum conservation as a common framework that explains the large-scale features of the weight functions for each diagnostic. Lastly, we reformulate the forward model encoded in the synthetic diagnostic codes as a linear matrix equation based on weight functions [3]. This allows the rapid computation of synthetic measurements from a given velocity-distribution function and constitutes the forward problem to be inverted.

Chapter 4 outlines the inverse problem: the inference of a 2D velocity distribution function from the measurements using the linear matrix equation from chapter 3. Basic principles of velocity-space tomography are reviewed as demonstrated in references [2–5, 7, 10–15, 19, 20, 22, 23]. Tikhonov regularization and various forms of prior information used in velocity-space tomography are the main focus. The computation of uncertainties is discussed. Tikhonov regularization is described from a Bayesian perspective since it is popular in the fusion plasma physics community.

Finally, chapter 5 presents a brief discussion of the main fast-ion physics results achieved by velocity-space tomography, conclusions, and an outlook on further developments of velocity-space tomography and related inverse problems.

Energetic particle diagnostics

This chapter reviews the basic principles of the diagnostics used in velocity-space tomography. The required measurement technologies are of secondary interest in this thesis and are described in a recent comprehensive review of energetic particle diagnostics [39]. Energetic ions can be divided into two basic groups: those *confined* in the plasma by the magnetic field and those *lost* from the plasma. Energetic ions confined in the plasma can be diagnosed by neutron emission spectroscopy (NES) or the simpler neutron counters, γ -ray spectroscopy (GRS), fast-ion D_α spectroscopy (FIDA), neutral particle analyzers (NPAs), and collective Thomson scattering (CTS). Lost energetic ions can be diagnosed by fast-ion loss detectors (FILD). Ion cyclotron emission (ICE) can diagnose confined and lost fast ions, but until now only qualitatively.

Confined-ion diagnostics can be categorized into *active* or *passive* diagnostics. In active diagnostics a beam of particles or radiation is injected into the plasma, and one measures a signal that is sensitive to parameters of the plasma and of this injected beam. Active diagnostics can either perturb the plasma or not. CTS is active and non-perturbative. FIDA

and active NPAs are active and perturbative (though the perturbation can be minimized). Passive diagnostics measure radiation or particles naturally emitted by the plasma and are hence never perturbative. NES, neutron counters, GRS, and passive NPA are passive diagnostics.

Active fast-ion diagnostics usually have a better spatial resolution than passive diagnostics. The probe beam and field-of-view of the detector intersect and define a small measurement volume. The diameters of the probe beam and the field-of-view as well as their intersection angle largely determine the spatial resolution. Passive diagnostics receive detectable particles or photons born along their entire lines-of-sight. However, fusion products are mostly formed in the plasma center, such that GRS and NES measurements are heavily biased towards the plasma center. Passive NPAs sometimes have, depending on conditions, a bias towards the plasma edge or to the core.

In the following, we will apply energy and momentum conservation to study the kinematics of the underlying physical process for each diagnostic. This analogous treatment gives a basic understanding of the velocity-space sensitivities of the diagnostics (chapter 3). When energy and momentum conservation are combined, the special role of the velocity of the ions projected onto the line-of-sight becomes clear. This line-of-sight velocity component u is crucial for the spectrum formation and is the key to studies in velocity space. Additional physics at play for individual diagnostics are dealt with in the comprehensive papers [2, 6, 8, 9, 16, 17, 21, 36].

The line-of-sight velocity u is related to $(v_{\parallel}, v_{\perp})$ by

$$u = v_{\parallel} \cos \phi + v_{\perp} \sin \phi \cos \Gamma \quad (2.1)$$

where ϕ is the observation angle between the line-of-sight and the magnetic field vector and Γ is the gyrophase [2]. Equation 2.1 is illustrated in fig. 2.1. The possible projected velocities of an ion with velocity $(v_{\parallel}, v_{\perp})$ observed at an angle ϕ are in the interval $u \in [v_{\parallel} \cos \phi \pm v_{\perp} \sin \phi]$. The spectrum of u is bimodal as expected for a histogram of a cosine (fig. 2.2). This spectrum in u and energy and momentum conservation set the energy range of the detected particles or photons for each diagnostic [15].

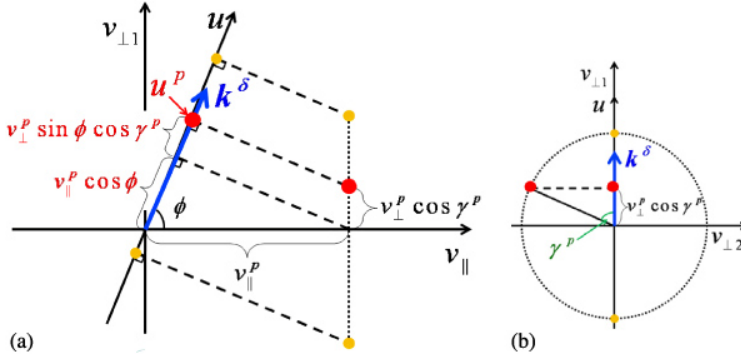


Figure 2.1: Projected velocity u^p of an ion with velocity $(v_{||}^p, v_{\perp}^p, \gamma^p)$ onto a line-of-sight described by the vector \mathbf{k}^{δ} [2].

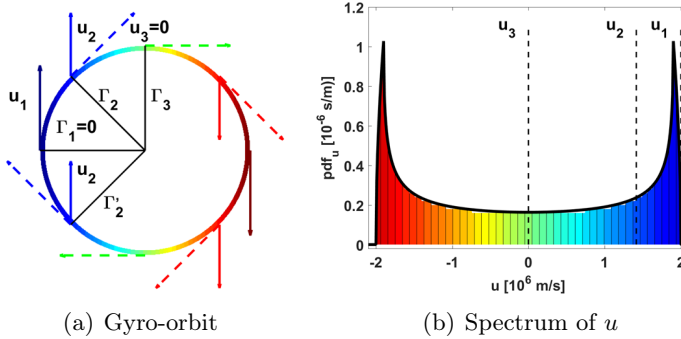


Figure 2.2: Spectrum formation for a ring distribution which is a single point in 2D velocity space [7].

2.1 Neutron emission spectroscopy

Neutrons are produced in nuclear reactions. The geometry of three NES detectors at JET is illustrated in fig. 2.3. Of particular interest are neutrons produced in the $D(D,n)^3\text{He}$ and $T(D,n)^4\text{He}$ reactions [38, 39]. The DD neutrons have an energy of 2.45 MeV in the center-of-mass frame of the reaction, whereas DT neutrons have 14.1 MeV. Neutrons at energies much larger than these center-of-mass energies can only be generated if at least one reactant is energetic. In a so-called beam-target reaction, one

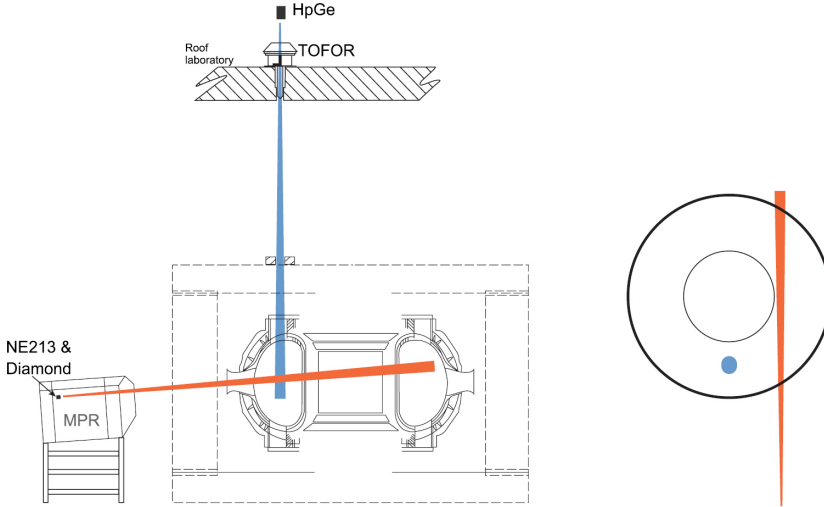


Figure 2.3: Cutaway of the JET tokamak showing the locations and lines-of-sight (red, blue) of the NES (TOFOR, NE213, Diamond) and GRS (HpGe) diagnostics [11, 26].

particle is energetic (beam) and one particle is thermal (target). Often this type of reaction is far more frequent than beam-beam reactions as the density of energetic particles is much lower than the density of thermal ions. The formation of detectable neutrons in a beam-target reaction is illustrated in fig. 2.4(a).

Consider a generic one-step fusion reaction between a fast particle (f) and a reactant thermal particle (r) to form a reaction product (pr) releasing a detectable neutron (n): $f + r \rightarrow \text{pr} + n$. The non-relativistic energy and momentum conservation equations for particles with mass m , velocity \mathbf{v} and $v = |\mathbf{v}|$ in the lab frame are, respectively,

$$\frac{1}{2}m_f v_f^2 + \frac{1}{2}m_r v_r^2 + Q = \frac{1}{2}m_{\text{pr}} v_{\text{pr}}^2 + E_n, \quad (2.2)$$

$$m_f \mathbf{v}_f + m_r \mathbf{v}_r = m_{\text{pr}} \mathbf{v}_{\text{pr}} + \mathbf{p}_n. \quad (2.3)$$

Here Q is the released energy, and E_n and \mathbf{p}_n are the energy and momentum of the emitted detected neutron, respectively. Since $v_r \ll v_f$ in a beam-target reaction, we neglect the energy and momentum of the reactant. Physically allowed neutron energies are found by eliminating v_{pr}

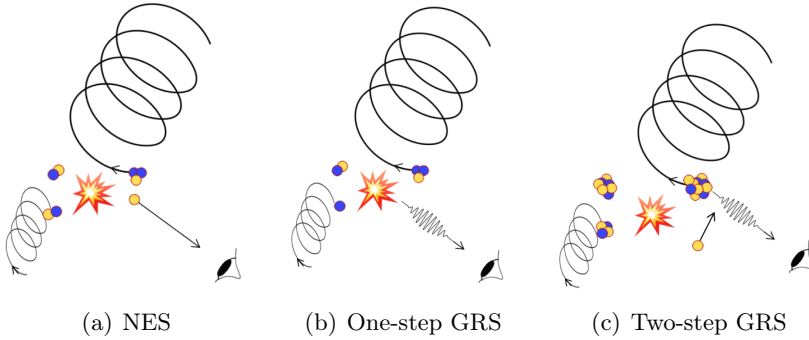


Figure 2.4: Schematic beam-target fusion reactions producing detectable neutrons or γ -rays. a) $D(D,n)^3\text{He}$. b) $D(p,\gamma)^3\text{He}$ with fast proton. c) ${}^9\text{Be}(\alpha,n\gamma){}^{12}\text{C}$.

from the energy equation using the momentum equation [15, 17]:

$$E_n = \frac{m_{\text{pr}}}{m_{\text{pr}} + m_n} Q + \frac{m_{\text{pr}} - m_f}{m_{\text{pr}} + m_n} E_f + \frac{m_f m_n}{m_{\text{pr}} + m_n} uv_n \quad (2.4)$$

where u is the velocity component of the fast ion along the line-of-sight towards the detector and v_n is the speed of the detectable neutron. Equation 2.4 could be written as an explicit expression for E_n but for our purpose this implicit form containing v_n is easier.

The first term is often largest. For example, for the DT reaction with $Q_{DT} = 17.6$ MeV, this term gives 14.1 MeV (section 1.2). The second term contributes a fraction of the fast-ion energy (for DT with fast deuterium and slow tritium $2/5$) and thus produces a spectrum of energies towards larger neutron energies. The last term is proportional to the ion velocity projected onto the line-of-sight of the detector as only neutrons moving along the line-of-sight are detected ($\mathbf{v}_f \cdot \mathbf{v}_n = uv_n$). The largest neutron energies are produced by energetic ions moving towards the detector ($u > 0$) at the time of the reaction since the dot product is then positive. The lowest neutron energies are produced by ions moving away from the detector. Due to this term also neutrons below the nominal restframe energy are emitted towards the detector. However, the low-energy tail of the spectrum is not experimentally useful as it is dominated by scattered neutrons. The detailed neutron energy spectrum

depends on the distribution functions, the gyromotion, and the reaction cross sections. It can be calculated using Monte Carlo codes such as GENESIS [74] or DRESS [75].

An additional complication is that NES instruments do not actually measure neutron energies but rather other quantities that depend on neutron energies, unfortunately not in a one-to-one correspondence [16, 21]. The time-of-flight spectrometer TOFOR measures the time-of-flight of a neutron between two detectors [76]. Liquid scintillator detectors measure the light flash emitted when a neutron hits the detector [77]. Single-crystal diamond detectors measure the energy deposited by the neutron in the diamond [78–80]. Results are usually presented in terms of spectra of these measured quantities. The relationships between these measured quantities and neutron energies are summarized in so-called response matrices as illustrated in [21].

2.2 γ -ray spectroscopy

GRS measures energy spectra of γ -rays produced in fusion reactions. Such reactions can occur in one step or in two steps [39, 81, 82]. In one-step or direct reactions, the γ -ray is a primary reaction product. In two-step or capture reactions, the γ -ray is emitted from an excited reaction product.

The geometry of the line-of-sight of the High-purity Germanium (HpGe) detector at JET is illustrated in fig. 2.3. The formation of detectable γ -rays in beam-target reactions in one or two steps is illustrated in fig. 2.4(b) and (c). As for NES, exact GRS spectra are computed using Monte Carlo codes such as GENESIS [74]. Here we again focus on the spectral range allowed by energy and momentum conservation under idealized conditions.

2.2.1 One-step reactions

One-step reactions emitting γ -rays are analogous to those emitting neutrons ($f + r \rightarrow pr + \gamma$). However, γ -rays have no rest mass such that the

energy and the momentum of the γ -ray are related by $E_\gamma = p_\gamma c$ where c is the speed of light. The energy and momentum equations for one-step reactions releasing γ -rays are

$$\frac{1}{2}m_f v_f^2 + \frac{1}{2}m_r v_r^2 + Q = \frac{1}{2}m_{\text{pr}} v_{\text{pr}}^2 + E_\gamma, \quad (2.5)$$

$$m_f \mathbf{v}_f + m_r \mathbf{v}_r = m_{\text{pr}} \mathbf{v}_{\text{pr}} + \mathbf{p}_\gamma. \quad (2.6)$$

An approximate expression for E_γ in a beam-target reaction is obtained by eliminating v_{pr} and a Taylor expansion in the small parameter $2(Q + E_f)/m_{\text{pr}}c^2$ to first order [10]:

$$E_\gamma = \frac{Q + \left(1 - \frac{m_f}{m_{\text{pr}}}\right)E_f}{1 - \frac{m_f u}{m_{\text{pr}} c}}. \quad (2.7)$$

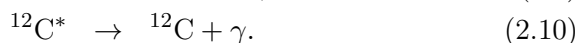
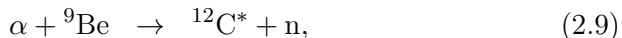
After another Taylor expansion in $m_f u/m_{\text{pr}}c$ (u/c is typically on the order of 1%), we get to first order:

$$E_\gamma = \left(1 + \frac{m_f u}{m_{\text{pr}} c}\right) \left(Q + \left(1 - \frac{m_f}{m_{\text{pr}}}\right)E_f\right). \quad (2.8)$$

As for NES, a spectrum is formed since the fast-ion energy E_f and the projected velocity u are described by distribution functions in fusion plasmas. Ions moving towards the detector ($u > 0$) always lead to blue-shifted γ -rays whereas ions moving away from the detector ($u < 0$) mostly lead to red-shifted γ -rays unless they move close to perpendicular to the line-of-sight. In contrast to NES, in GRS both the low-energy (redshifted) and the high-energy (blueshifted) tails are experimentally accessible.

2.2.2 Two-step reactions

In two-step reactions, first an excited nucleus is formed in a fusion reaction. Then the excited nucleus decays emitting a γ -ray after a very short time. The most important reaction for GRS at ITER will be ${}^9\text{Be}(\alpha, n\gamma){}^{12}\text{C}$ [83, 84] which is shorthand for



The energy release of the reaction is $Q = 5.70$ MeV of which $E_{\gamma 0} = 4.44$ MeV is required to populate the excited state $^{12}\text{C}^*$. This is also the restframe energy of the γ -ray that is emitted when $^{12}\text{C}^*$ decays to the ground state. The remaining $Q^* = 1.26$ MeV and the initial kinetic energies of the fast α -particle and the thermal ^9Be become kinetic energy of the reaction products $^{12}\text{C}^*$ and the neutron.

The γ -rays are Doppler-shifted due to the velocity component u_{pr} of the excited reaction product $^{12}\text{C}^*$ along the line-of-sight of the detector. The energy E_γ of the detected γ -ray can be found from equation 2.8 by setting $m_f = m_{\text{pr}}$ and $Q = E_{\gamma 0}$ [8]:

$$E_\gamma = E_{\gamma 0} \left(1 + \frac{u_{\text{pr}}}{c} \right) \quad (2.11)$$

which is the usual Doppler-shift formula. Energy and momentum conservation over the first step of the reaction imply a relation between u_{pr} and u [8]:

$$\begin{aligned} u_{\text{pr}} &= \frac{m_f}{m_{\text{pr}} + m_n} \cos \beta \left(u \cos \beta + \sqrt{v_f^2 - u^2} \sin \beta \cos \zeta \right) \\ &\pm \sqrt{\cos^2 \beta \left(\frac{m_f^2}{(m_{\text{pr}} + m_n)^2} \left(u \cos \beta + \sin \beta \cos \zeta \sqrt{v_f^2 - u^2} \right)^2 \right.} \\ &\quad \left. + \frac{2m_n}{m_{\text{pr}}(m_{\text{pr}} + m_n)} Q^* - \frac{m_f(m_f - m_n)}{m_{\text{pr}}(m_{\text{pr}} + m_n)} v_f^2 \right)}. \end{aligned} \quad (2.12)$$

Here the angles β and ζ appear since the reaction kinematics in two-step reaction GRS is less constrained than in one-step reaction GRS or NES. For one-step reactions we know the energy as well as the momentum of one of the reaction products (the neutrons or γ -rays) since only particles moving along the line-of-sight towards the detector are measured. In two-step reaction GRS measurements, we also know the energy and momentum of the γ -ray, but we neither know the energy nor the momentum of the nucleus produced in the first step of the reaction. We only know its velocity component u_{pr} along the line-of-sight of the γ -ray detector according to equation 2.11. The other two directions are described by the unknown angles β and ζ . These angles and the velocities and line-of-sight

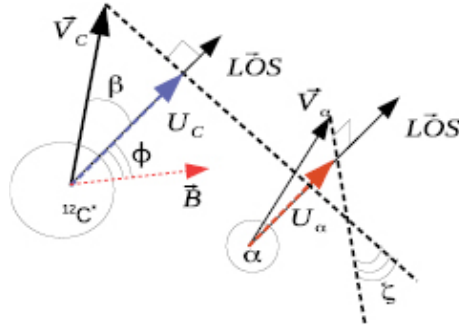


Figure 2.5: Geometry of two-step reactions with respect to the line-of-sight [8].

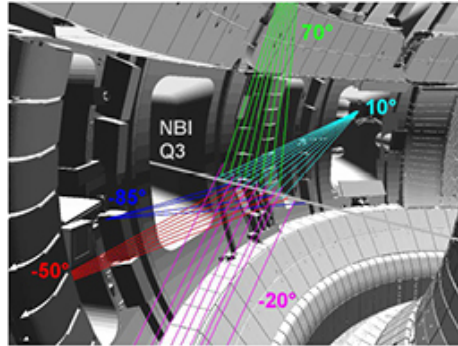


Figure 2.6: FIDA diagnostic setup at ASDEX Upgrade [27]. Five sets of lines-of-sight with different projection angles ϕ intersect the NBI path.

velocities of the two product nuclei relative to the line-of-sight and the local magnetic field are sketched in fig. 2.5 for an α -particle and $^{12}\text{C}^*$. The incomplete information about the motion of the excited nucleus makes it more difficult to draw conclusions about the fast-ion velocity compared with the other diagnostics. For example, a fast ion moving towards the detector can cause the emission of either a redshifted or a blueshifted γ -ray. Nevertheless, blueshift is more probable in this case.

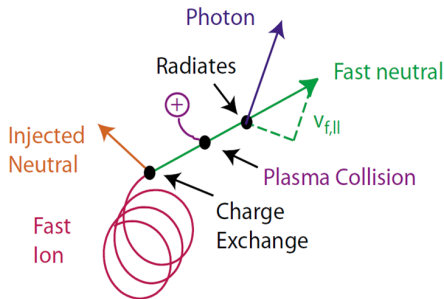


Figure 2.7: Schematic FIDA emission [85].

2.3 Fast-ion D_α spectroscopy

In FIDA spectroscopy one measures Doppler-shifted Balmer- α light emitted by neutralized deuterium after a charge-exchange reaction [39, 73, 85, 86]. The generated neutral inherits the momentum of the fast ion just before the charge-exchange reaction to a very good approximation due to the large proton-to-electron mass ratio of $m_p/m_e = 1836$. A typical geometry of a FIDA setup at ASDEX Upgrade is shown in fig. 2.6. Balmer- α light is emitted when the deuterium atom decays from the third to the second excited state. A photon emitted by deuterium has a restframe wavelength of $\lambda_0 = 656.1$ nm. A spectrum is formed by the Doppler shift due to the distribution of velocities of the excited deuterium atoms projected onto the line-of-sight. The FIDA process is illustrated in fig. 2.7. Stark splitting further changes the wavelength of the emitted photons. Reaction cross sections also influence the spectral content of the measured light, and one has to account for an instrumental function (see [6]).

Exact spectra are computed with the FIDASIM code [87]. In analogy to the treatment of NES and GRS, we invoke energy and momentum conservation rather than the Doppler shift, which is usually the starting point. Fermi pointed out that energy and momentum conservation imply the Doppler shift [88]. In the restframe of the excited atom, the energy of the released photon is the difference between the energy levels U and U' before and after the emission: $Q = U - U' = hf_0$. Here, h is Planck's constant and $f_0 = c/\lambda_0$ is the frequency. Primes ($'$) denote quantities after the reaction. In the lab frame the total energy is the sum of the kinetic

energy and the energy level U . Energy and momentum conservation of the D_α -emission process in the lab frame are [88]

$$\frac{1}{2}m_f v_f^2 + U = \frac{1}{2}m_f v_f'^2 + U' + E_{D_\alpha}, \quad (2.13)$$

$$m_f \mathbf{v}_f = m_f \mathbf{v}_f' + \mathbf{p}_{D_\alpha} \quad (2.14)$$

where E_{D_α} and \mathbf{p}_{D_α} are the energy and momentum of the D_α -photon. After eliminating v_f' in the energy equation using the momentum equation and neglecting a term containing the small factor $hf/m_f c^2$, we get the energy of the detected D_α -photons to first order in u/c ,

$$E_{D_\alpha} = hf = hf_0 \left(1 + \frac{u}{c}\right). \quad (2.15)$$

This is the same equation as for one-step reaction GRS for $m_f = m_{pr}$ as the mass of the emitting ion is the same before and after the reaction. Usually this relation is written as

$$\frac{\Delta\lambda}{\lambda_0} = \frac{u}{c} \quad (2.16)$$

where $\Delta\lambda$ is the Doppler shift. (The sign of u depends on the direction of the unit vector $\hat{\mathbf{u}}$, i.e. if it points towards or away from the detector.)

2.4 Collective Thomson scattering

Whereas Thomson scattering (TS) is sensitive to the distribution of electrons in the plasma, CTS is sensitive to the distribution of ions. A typical geometry of a CTS measurement is illustrated in fig. 2.8. A beam of probe radiation is injected into the plasma. The acceptance cone of a receiver forms a second beam. The measured scattered radiation originates from the small measurement volume where the two beams overlap.

Scattering off ions is negligible compared with scattering off electrons due to the large proton-to-electron mass ratio. The dressed particle model is well-suited to highlight the differences between CTS and TS as well as the analogy of CTS and the other fast-ion diagnostics. CTS in the dressed particle model is illustrated in fig. 2.9. A test charge in a plasma is

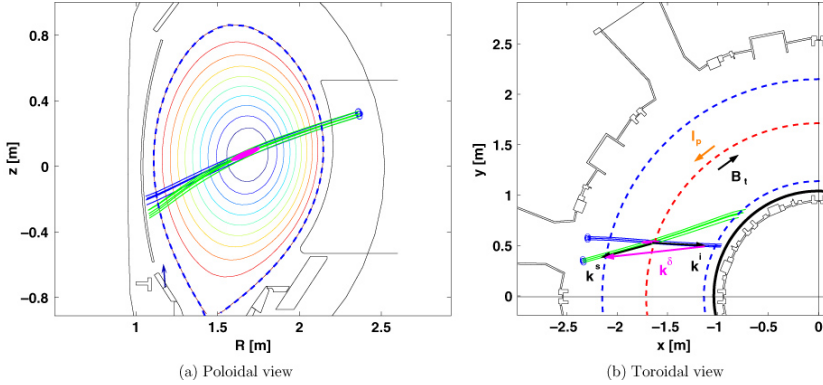


Figure 2.8: Example of a CTS diagnostic setup at ASDEX Upgrade [1] showing the probe and receiver beams in a poloidal and toroidal view. Magnetic flux surfaces indicate the position of the plasma.

surrounded by other charges that screen the potential of the test charge. This is termed Debye screening. The size of this screening cloud is on the order of the Debye length λ_D . A dressed particle is a test particle together with its screening cloud. For example, the screening cloud of an ion is composed of (a surplus of) electrons and (a lack of) ions. We consider very fast ions so that thermal ions are too slow to participate strongly in the screening, and hence the screening cloud consists mostly of electrons.

In the measurement volume, the angular frequency and wavenumber of the incident and scattered radiation are (ω^i, \mathbf{k}^i) and (ω^s, \mathbf{k}^s) , respectively. First consider CTS and TS as a three-wave mixing processes in which the ions or electrons induce a fluctuation $(\omega^\delta, \mathbf{k}^\delta)$. The matching conditions for energy and momentum are

$$\omega^\delta = \omega^s - \omega^i, \quad (2.17)$$

$$\mathbf{k}^\delta = \mathbf{k}^s - \mathbf{k}^i. \quad (2.18)$$

In incoherent Thomson scattering, the wavelength of the fluctuation wave field, $\lambda^\delta = 2\pi/k^\delta$ with $k^\delta = |\mathbf{k}^\delta|$, is much smaller than the Debye length ($\lambda^\delta \ll \lambda_D$), such that the waves are scattered off electrons incoherently at random phases of the fluctuation field. The scattering power due to

Hence the diagnostic line-of-sight is described by the wave vector \mathbf{k}^δ for TS and CTS. Introducing ω^δ , we recover the Doppler-shift relation for TS and CTS,

$$\omega^\delta = \mathbf{v}_f \cdot \mathbf{k}^\delta = uk^\delta, \quad (2.22)$$

which describes two Doppler shifts. The probe radiation has a Doppler-shifted frequency in the restframe of the particle, and the emitted radiation from the moving particle has yet another Doppler-shifted frequency in the lab frame. The measured Doppler shift of the scattered radiation can also be written as $f^\delta = u/\lambda^\delta$ which is the frequency at which an ion moving with speed u with respect to a wave with wavelength λ^δ encounters the same phase.

2.5 Fast-ion loss detectors

FILDs measure the flux of charged particles lost from the plasma impinging on a collector as illustrated in fig. 2.10. The lost ions enter the detector through a pinhole and are then dispersed in the magnetic field. The energy and pitch of a detected ion can be obtained from its strike point on the scintillator plate, such that FILD detectors measure a 2D velocity distribution function of lost ions. Velocity-space tomography here plays a different role than for the other diagnostics. One can determine the 2D velocity distribution function in the pinhole, given the measurement on the scintillator plate. This 2D image is similar but sharper than the measurement on the scintillator plate. Velocity-space tomography effectively has the task to deblur the measured image [36]. Another advantage is that we obtain the velocity distribution at the pinhole where the measured results can be easily compared with velocity distribution functions computed using standard codes.

2.6 Synthetic diagnostics

Conventionally, the fast-ion measurements are compared with numerical simulations to judge if a measurement is consistent with a theoretical

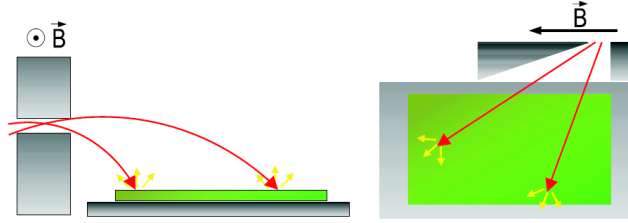


Figure 2.10: Schematic FILD detector [89]. Lost ions pass the aperture and hit the scintillator plate.

model or not. This is done by means of synthetic diagnostics in which an expectation for the measurement is computed on the basis of a simulation of the fast-ion distribution function. If the actual measurements agree with the synthetic measurements, it is usually concluded that the fast-ion distribution function in the experiment corresponds to the simulation and that the fast-ion behavior is therefore understood, at least in the restricted part of velocity space interrogated by the diagnostic. However, if they disagree, it is unclear how the experimental and theoretical distribution functions are different and how to proceed.

Examples of such traditional comparisons between measurements and simulations for the different diagnostics appear in fig. 2.11. The fast-ion diagnostics do not measure the distribution function directly, but rather quantities of indirect interest such as a spectrum of light or mm-wave radiation, γ -ray count rates, deposited energies, energies of electrons causing the same light flash, or times-of-flight. These spectra depend on the fundamental velocity distribution function in complicated ways, and additionally they depend on nuisance parameters impeding the interpretation. Further, the measurements present only an incomplete picture of the distribution function as each diagnostic interrogates a restricted part of velocity space. The approach presented in the following two chapters seeks to make up for these shortcomings.

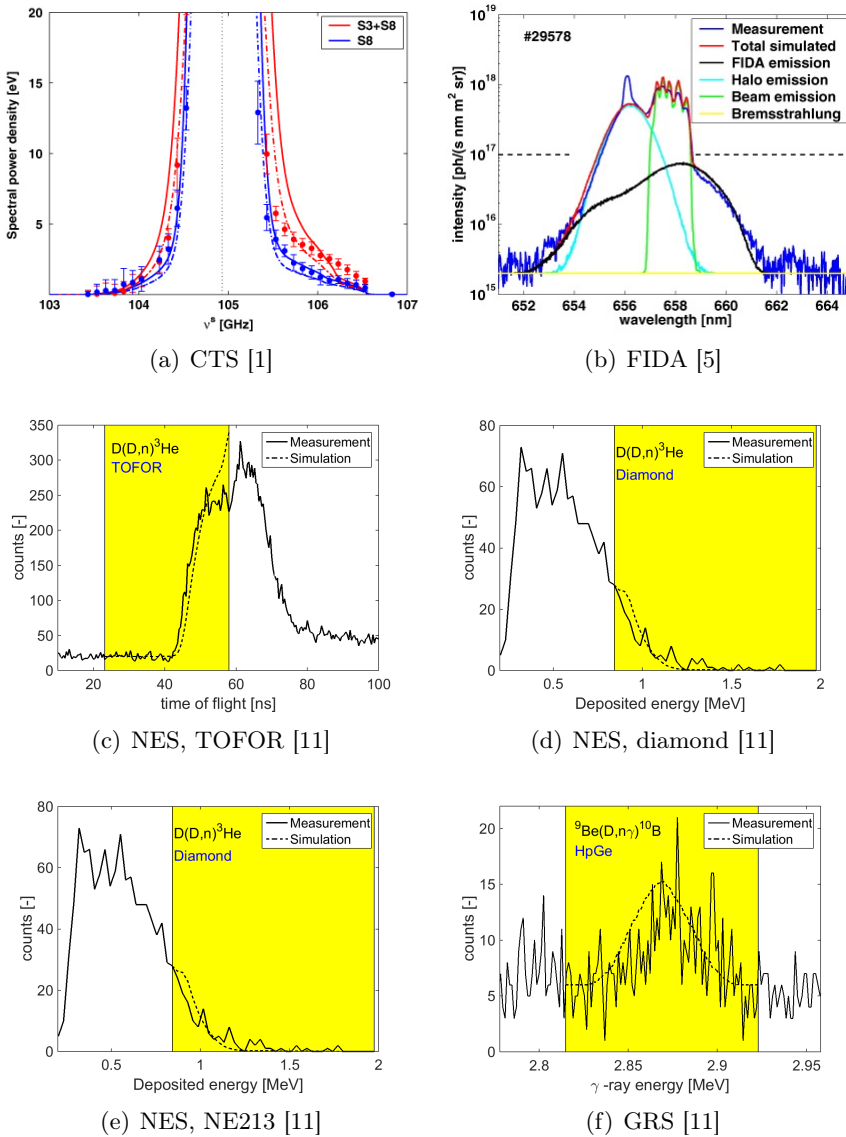


Figure 2.11: Typical comparisons of energetic particle measurements and numerical simulations for the various diagnostics. Each diagnostic measures spectra in units particular to the diagnostics.

The forward problem: velocity-space sensitivity

3.1 Weight functions

Weight functions quantify the velocity-space sensitivity of the various fast-ion diagnostics. This idea was developed as a qualitative analysis tool to understand a puzzling observation in an experiment at DIII-D [73]. The FIDA measurements and the neutron count measurements behaved in a similar way whereas the NPA measurements behaved qualitatively differently. This was at the time surprising because the NPA and FIDA measurements involve neutrals generated in the same charge-exchange reaction. FIDA measures the D_α -light emitted by the neutrals, and NPA the neutrals that do not re-ionize on the path to the detector. Therefore the NPA signal was mistakenly expected to behave in a qualitatively similar way as the FIDA signal. However, whereas the velocity-space observation regions of FIDA and the neutron count measurements are broad and fairly similar regions in velocity space, the NPA observes only a tiny part of velocity space. This was illustrated by so-called weight functions. This new understanding of the velocity-space

observation regions resolved this then puzzling observation. Since then weight functions have been developed for all major fast-ion diagnostics: FIDA [5, 73], NPAs [13, 73], CTS [2], GRS [8, 9], NES [16, 17, 21] and FILDs [36]. Weight functions have often been used to study the velocity space, e.g. in references [14, 24, 26–28, 30, 32–34, 73, 87, 90–110].

In a general definition, weight functions w^{6D} relate measurements s to 6D fast-ion distribution functions f^{6D} by the integral equation

$$s(E_{d,1}, E_{d,2}, \phi) = \int_{\mathbf{v}} \int_{\mathbf{x}} w^{6D}(E_{d,1}, E_{d,2}, \phi, \mathbf{x}, \mathbf{v}) f^{6D}(\mathbf{x}, \mathbf{v}) d\mathbf{x} d\mathbf{v}. \quad (3.1)$$

$s(E_{d,1}, E_{d,2}, \phi)$ is the detected signal in the energy range of the detected particles or photons $E_{d,1} < E_d < E_{d,2}$ with a viewing angle ϕ between the line-of-sight of the diagnostic and the magnetic field (see chapter 2). We can reduce the number of dimensions to two by integrating equation 3.1 over the small measurement volume and the ignorable gyrophase:

$$s(E_{d,1}, E_{d,2}, \phi) = \int_0^\infty \int_{-\infty}^\infty w(E_{d,1}, E_{d,2}, \phi, v_{\parallel}, v_{\perp}) f(v_{\parallel}, v_{\perp}) dv_{\parallel} dv_{\perp}. \quad (3.2)$$

This definition of 2D weight functions can equally well be given in (E, p) -space. Equations are often simpler in $(v_{\parallel}, v_{\perp})$ -space, but we plot examples in the widespread (E, p) -space.

Weight functions can be factored into a detection rate function R and a probability function [6, 8, 9, 17]:

$$\begin{aligned} w(E_{d,1}, E_{d,2}, \phi, v_{\parallel}, v_{\perp}) & \quad (3.3) \\ = R(v_{\parallel}, v_{\perp}, \phi) \times \text{prob}(E_{d,1} < E_d < E_{d,2} | \phi, v_{\parallel}, v_{\perp}). \end{aligned}$$

$R(v_{\parallel}, v_{\perp}, \phi)$ has the same units as the weight functions whereas the probabilities are dimensionless numbers in the interval $[0, 1]$. Energy and momentum conservation determine the boundaries of the probability functions $\text{prob}(E_{d,1} < E_d < E_{d,2} | \phi, v_{\parallel}, v_{\perp})$ in $(v_{\parallel}, v_{\perp})$ -space and hence ultimately the boundaries of the weight functions. These boundaries separate the observable from unobservable regions [15].

Weight functions are often found numerically by using a forward model that predicts the measured signal for an arbitrary fast-ion distribution

3.2 Weight functions for FIDA, CTS, NES, GRS, NPAs and FIELDS37

function [73]. In this numerical approach, the signal s due to a density of n_f fast ions is calculated for a grid of velocities in $(v_{\parallel}, v_{\perp})$ or (E, p) covering the target velocity-space region. The velocity distribution function of the fast ions at phase-space position $(v_{\parallel 0}, v_{\perp 0})$ is

$$f(v_{\parallel}, v_{\perp}) = n_f \delta(v_{\parallel} - v_{\parallel 0}) \delta(v_{\perp} - v_{\perp 0}). \quad (3.4)$$

Substitution into equation 3.2 and integration shows that the amplitudes of weight functions at phase-space position $(v_{\parallel 0}, v_{\perp 0})$ are readily computed from [8, 9, 17]

$$w(E_{d,1}, E_{d,2}, \phi, v_{\parallel 0}, v_{\perp 0}) = \frac{s(E_{d,1}, E_{d,2}, \phi)}{n_f}. \quad (3.5)$$

Weight functions hence show the integrated signal between two spectral points per ion density at phase-space position $(v_{\parallel 0}, v_{\perp 0})$. The computation of the signal by weight functions neglects spatial effects and makes the approximation of a small measurement volume. It is usually fairly accurate for the plasma center where profiles are flat.

3.2 Weight functions for FIDA, CTS, NES, GRS, NPAs and FIELDS

Examples of weight functions for the major fast-ion diagnostics are illustrated in figures 3.1 to 3.7 discussed in the following. The FIDA weight functions in fig. 3.1 illustrate the velocity space observed by the five-view FIDA diagnostic installed at ASDEX Upgrade. The grey regions are observable whereas the white regions are unobservable. Each FIDA view individually misses a portion of velocity space, but integrated data analysis of all five detectors together provides excellent coverage of the 2D velocity space. However, the velocity-space sensitivity of FIDA drops above the beam injection energy because the charge-exchange probabilities drop for increasing particle energy. Therefore, the measurements of the high-energy velocity space could likely be improved by supplementing the FIDA measurements by CTS or NES.

Fig. 3.2 illustrates typical CTS weight functions for observations perpendicular to the magnetic field [2]. If the geometry of CTS experiments is

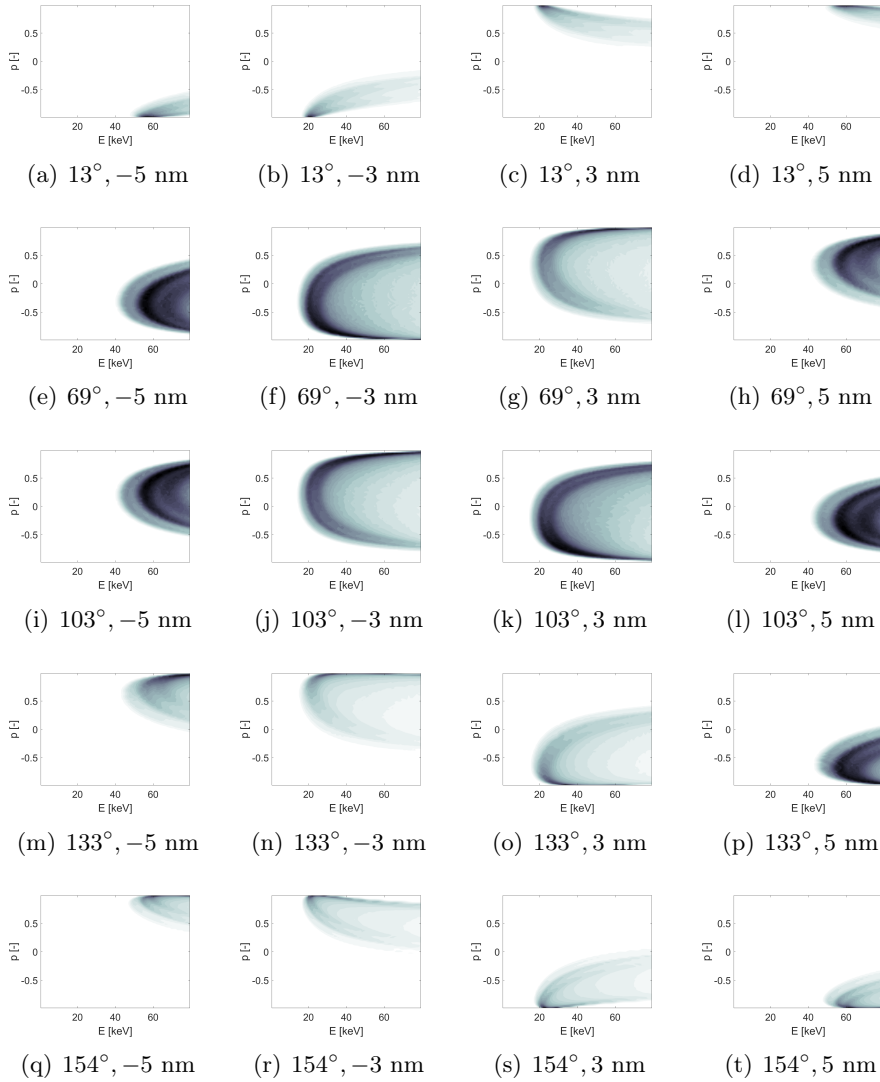


Figure 3.1: Typical weight functions [a.u.] for the five FIDA spectra for five different viewing angles for strong and moderate blueshifts (first and second columns) and redshifts (third and fourth columns). The angles describe the angle between the line-of-sight of the view and the local magnetic field. The wavelengths are relative to the unshifted D_α light wavelength of 656.1 nm [13].

3.2 Weight functions for FIDA, CTS, NES, GRS, NPAs and FILDs39

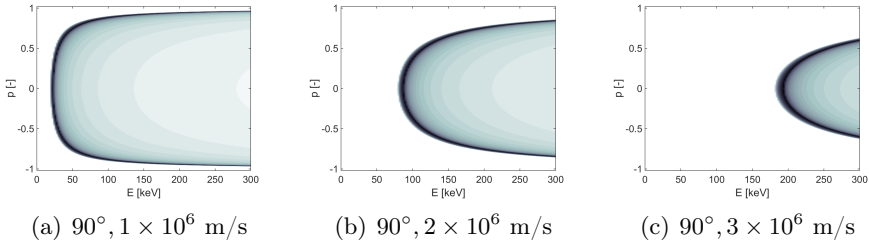


Figure 3.2: Typical CTS weight functions [a.u.] for a viewing angle of 90° for three projected velocities [13].

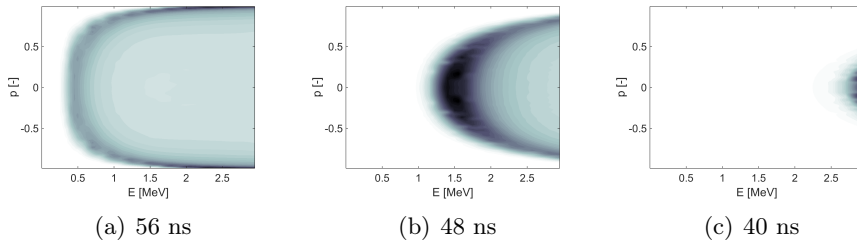


Figure 3.3: Typical TOFOR weight functions [a.u.] for three different times-of-flight [13].

flexible, the weight functions can have very different shapes. The overall shapes of CTS weight functions are similar to those of FIDA weight functions because both are largely determined by the Doppler shift.

Fig. 3.3 illustrates typical weight functions for the time-of-flight neutron emission spectrometer TOFOR at JET [17, 21]. The line-of-sight of TOFOR is approximately perpendicular to the central magnetic field at JET [76]. The weight functions are calculated for the $D(D,n)^3\text{He}$ reaction. MeV-range ions are well-diagnosed by TOFOR or other NES instruments.

Fig. 3.4 shows typical weight functions for two-step reaction GRS with a HpGe detector [7], here for the $^9\text{Be}(D,n\gamma)^{10}\text{B}$ reaction. GRS is most sensitive to fast ions in the MeV range due to the reaction cross sections. An interesting feature is that at low Doppler shifts the HpGe detector

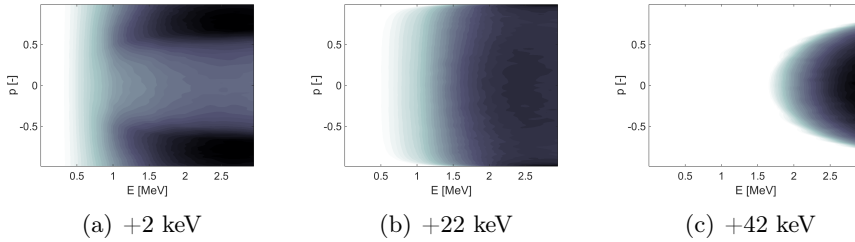


Figure 3.4: Typical two-step reaction GRS weight functions [a.u.] for ${}^9\text{Be}(\text{D},n\gamma){}^{10}\text{B}$. The shifts are relative to the nominal peak energy of 2868 keV [13].

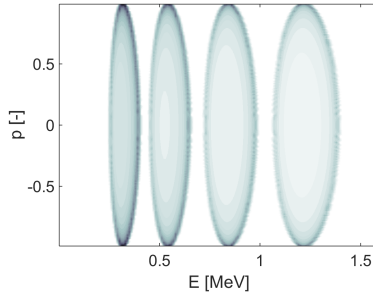


Figure 3.5: Typical one-step reaction GRS weight functions [a.u.] for $\text{D}(\text{p},\gamma){}^3\text{He}$. From left to right relative to the nominal peak energy of 5500 keV: +200 keV, +350 keV, +550 keV, +800 keV [13].

is most sensitive to high-energy ions with pitches close to ± 1 . However, at high Doppler shifts these regions do not contribute any signal whereas the ions with pitches close to zero contribute most to the signal.

Fig. 3.5 illustrates typical weight functions for one-step reaction GRS, here for the $\text{D}(\text{p},\gamma){}^3\text{He}$ reaction [10,111]. The ITER measurement requirements entail resolution of the energy spectra and densities of α -particles and other fast ions [112]. Figure 3.5 illustrates that one-step reaction GRS could in principle provide direct energy resolution of the fast ions without the need for tomographic inversion [10]. One-step reaction GRS has not yet been used in velocity-space tomography.

3.2 Weight functions for FIDA, CTS, NES, GRS, NPAs and FILDs41

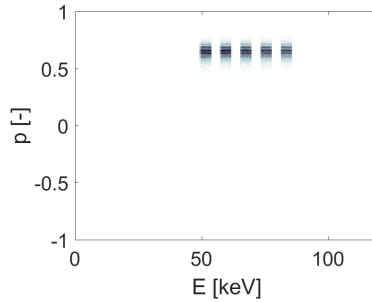


Figure 3.6: Typical NPA weight functions [a.u.] for the NPA at ASDEX Upgrade for five different energy ranges of the observed neutrals which are identical to the energy ranges of the fast ions: 50-54 keV, 58-62 keV, 66-70 keV, 74-78 keV, 82-86 keV [13].

Fig. 3.6 shows weight functions for the NPA at ASDEX Upgrade. NPAs measure the energies of fast neutrals generated in charge-exchange reactions between fast ions and neutrals. The measured energy of the neutral in the detector is the same as that of the fast ion in the plasma. Ions in very small pitch and gyrophase ranges can generate a detectable neutral which is reflected in the narrow pitch range of the weight function. The width of the energy interval is the same as the chosen energy bin width in the measurement. As one-step GRS, NPAs can provide direct energy resolution, but in a restricted pitch range. NPAs have not yet been used in velocity-space tomography, either.

Fig. 3.7 illustrates weight functions of one of the FILD detectors at ASDEX Upgrade. The weight functions relate the 2D velocity distribution function in the pinhole of the FILD detector to the measurement on the scintillator plate. The 2D velocity distribution function is here parameterized in terms of the Larmor radius and the pitch angle. A point in 2D velocity space in the pinhole maps onto a distribution of strike points on the scintillator (fig. 3.7(a)). Conversely, a strike point on the scintillator plate can originate from a region in 2D velocity space in the pinhole (fig. 3.7(b)). This instrumental blurring comes from two variable parameters: the different possible entry positions in the pinhole and a small allowed range in the gyrophase. The 2D velocity distribution function in the pinhole tends to be sharper compared with the measured, comparatively blurred 2D image.

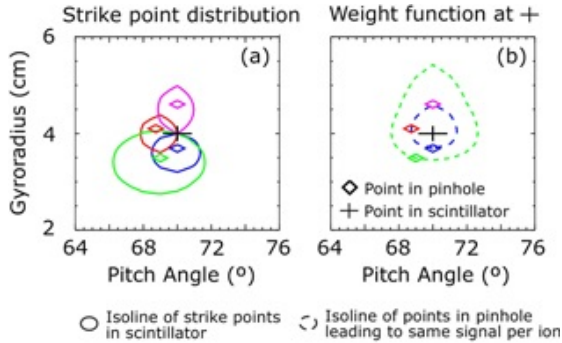


Figure 3.7: Typical FILD weight function for one of the FILD detectors at ASDEX Upgrade [36]. (a) Strike point distribution on the scintillator plate for a given 2D velocity-space point at the pinhole. (b) Weight function for $\rho_L = 4$ cm and a pitch angle of 70° .

The understanding of velocity-space sensitivities encoded in weight functions allows five types of data analysis. First, the observable and the unobservable velocity space can be told apart. Second, given a 2D fast-ion velocity distribution function, the velocity distribution of the ions generating a given measurement can be calculated. Third, given the absence of a measurement signal, the corresponding empty region of velocity space can be identified. Fourth, synthetic measurements can be calculated rapidly. Fifth, we can infer 2D fast-ion velocity distribution functions by velocity-space tomography (chapter 4).

A measure of the gross velocity-space sensitivity of a diagnostic set on a tokamak is obtained by computing normalized weight functions covering the entire accessible spectral range. Figure 3.8 illustrates such gross sensitivities for the combined CTS and GRS diagnostics for α -particles on ITER. Salient features from the individual diagnostics can be recognized in figure 3.8. α -particles at energies below ~ 0.3 MeV and co- and counter-going α -particles at extreme pitches ($|p| \gtrsim 0.9$) and energies up to ~ 1.7 MeV can hardly be diagnosed by CTS or GRS. The gross velocity-space sensitivity increases substantially from about 1.7 MeV upwards and becomes excellent around the 2 MeV resonance of the 4.44 MeV γ -ray peak. For energies close to this resonance and upwards, the gross velocity-space coverage of the combined diagnostic set at ITER is good.

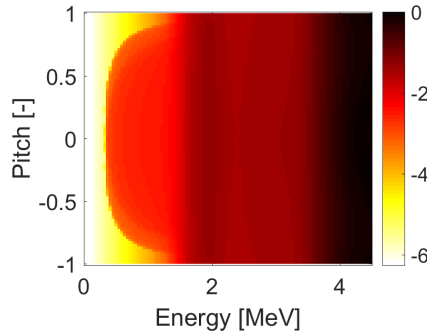


Figure 3.8: Gross velocity-space sensitivity to measure α -particles with the combined CTS and GRS diagnostics at ITER (log scale). White and yellow regions are practically not observable.

However, CTS is practically the only diagnostic detecting α -particles below ~ 1.7 MeV, covering the pitch range of $|p| \lesssim 0.8 - 0.9$. This causes the protrusion below the 2 MeV resonance of the 4.44 MeV γ -ray peak.

3.3 Observable velocity space for a given line-of-sight velocity

Equation 3.5 does not provide any insight into the peculiar shapes of the weight functions for each diagnostic (figs. 3.1 to 3.7). The basic shapes of the weight functions are explained for each diagnostic by considering the underlying physical processes [2, 6, 7, 9, 17, 21].

Chapter 2 showed that the line-of-sight velocity u is related to $(v_{\parallel}, v_{\perp}, \Gamma)$ according to equation 2.1 [2] and to the energy E_d of the detectable particle or photons by energy and momentum conservation for each diagnostic. Hence we obtain insight into the observable velocity space of each diagnostic by finding the probability density function of u or, to account for finite spectral resolution of the instruments, a histogram of u .

Given u , ϕ and $(v_{\parallel}, v_{\perp})$, the corresponding gyrophases can be computed:

$$\Gamma = \arccos \frac{u - v_{\parallel} \cos \phi}{v_{\perp} \sin \phi} \quad (3.6)$$

and $\Gamma' = 2\pi - \Gamma$. The distribution of gyrophases is uniform: $\text{pdf}_{\Gamma} = 1/2\pi$. A gyrating ion with given $(v_{\parallel}, v_{\perp})$ and projection angle ϕ hence has a distribution of projected velocities u along the line-of-sight:

$$\text{pdf}(u|\phi, v_{\parallel}, v_{\perp}) = 2 \text{pdf}_{\Gamma} \left| \frac{d\Gamma}{du} \right| = \frac{1}{\pi v_{\perp} \sin \phi \sqrt{1 - \left(\frac{u - v_{\parallel} \cos \phi}{v_{\perp} \sin \phi} \right)^2}}. \quad (3.7)$$

The factor two appears due to the two possible gyrophases Γ and Γ' for a given u . The observable velocity space has a positive radicand. While this relation is useful for the projection of 2D velocity distribution functions onto a given direction [12, 40], it is not suitable to analyze measurements. The reason is the finite spectral resolution of fast-ion measurements which implies a finite resolution in the projected velocity. Hence we integrate equation 3.7 over a small range $[u_1, u_2]$ in u :

$$\begin{aligned} \text{prob}(u_1 < u < u_2|\phi, v_{\parallel}, v_{\perp}) &= \int_{u_1}^{u_2} \text{pdf}(u|\phi, v_{\parallel}, v_{\perp}) du \\ &= \frac{\Gamma_1 - \Gamma_2}{2\pi} + \frac{\Gamma'_2 - \Gamma'_1}{2\pi} = \frac{\Gamma_1 - \Gamma_2}{\pi} \\ &= \frac{1}{\pi} \left(\arccos \frac{u_1 - v_{\parallel} \cos \phi}{v_{\perp} \sin \phi} - \arccos \frac{u_2 - v_{\parallel} \cos \phi}{v_{\perp} \sin \phi} \right). \end{aligned} \quad (3.8)$$

The unobserved velocity space corresponds to a probability of zero such that no gyrophase exists allowing a detection in the interval $[u_1, u_2]$. The observed velocity space corresponds to non-zero probabilities. In this case a detection in the interval $[u_1, u_2]$ is possible on some parts of the gyro-orbit (for $\text{prob} = 1$ on the full orbit). An example appears in fig. 3.9(a).

3.4 Observable velocity space for a given detected energy

Energy and momentum conservation determine to which velocity-space regions fast-ion diagnostics are sensitive. These conservation principles

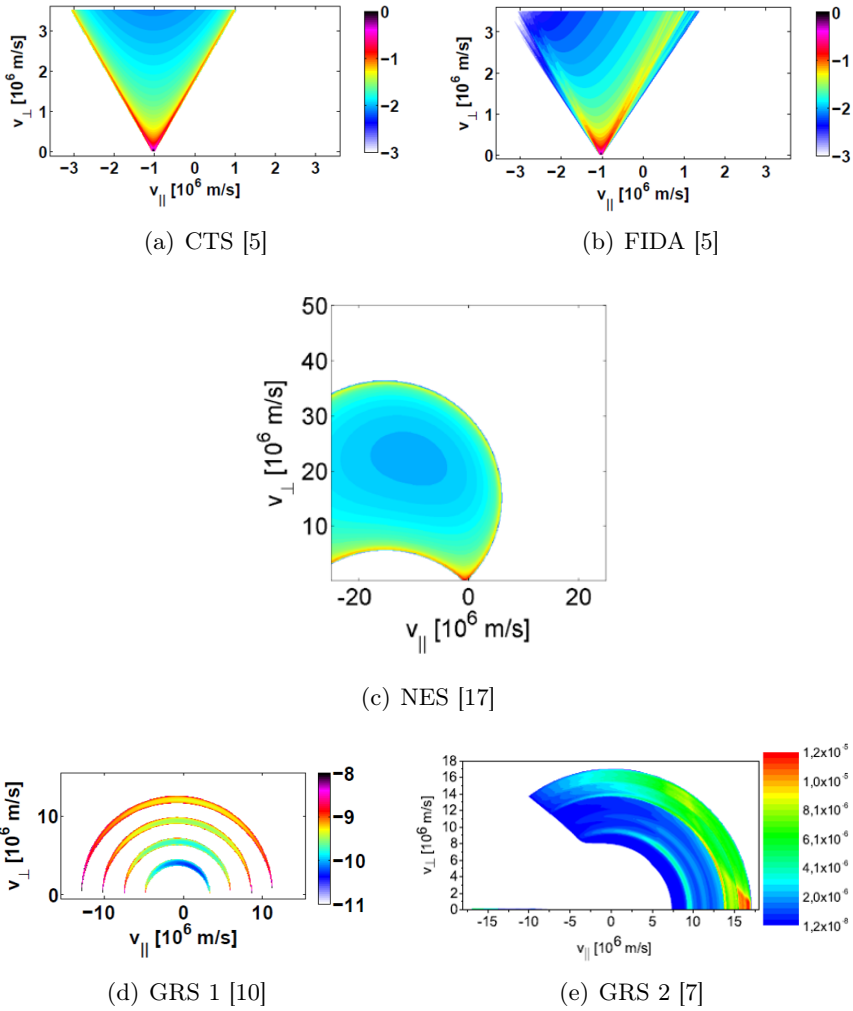


Figure 3.9: Examples of probability functions of CTS, FIDA, NES, and one-step and two-step reaction GRS.

relate the energy and momentum of the energetic particle in the plasma to the energy and momentum of the detectable particle or photon, as discussed in chapter 2. To focus on the large-scale shapes of the observable velocity-space regions, we here neglect effects leading to small changes in the observable velocity space for the various diagnostics, such as non-zero plasma temperatures, Stark splitting or instrumental broadening [6, 8, 9, 17]. Similarly, we do not consider any reaction probabilities since they do not influence the boundaries of the observable velocity space.

The resulting probability that the detected particle has an energy in the interval $[E_{d,1}, E_{d,2}]$ can be related to the probability that the fast ion has a line-of-sight velocity in the interval $[u_1, u_2]$ and to the corresponding fraction of the gyro-orbit [5]:

$$\begin{aligned} \text{prob}(E_{d,1} < E_d < E_{d,2} | \phi, v_{\parallel}, v_{\perp}) &= \text{prob}(u_1 < u < u_2 | \phi, v_{\parallel}, v_{\perp}) \\ &= \frac{\Gamma_1 - \Gamma_2}{\pi} = \frac{1}{\pi} \left(\arccos \frac{u_1 - v_{\parallel} \cos \phi}{v_{\perp} \sin \phi} - \arccos \frac{u_2 - v_{\parallel} \cos \phi}{v_{\perp} \sin \phi} \right). \end{aligned} \quad (3.9)$$

Equation 3.9 shows how to find the observable velocity space from the line-of-sight velocity u for the diagnostics that we consider. The observable velocity space according to energy and momentum conservation is revealed by solving the equations of the energies of the detected particles for the projected velocity u :

$$u_{\text{FIDA}} = c \left(\frac{E_{\text{D}\alpha} - E_{\text{D}\alpha 0}}{E_{\text{D}\alpha}} \right) = c \frac{\Delta \lambda}{\lambda_0}, \quad (3.10)$$

$$u_{\text{CTS}} = \frac{E^s - E^i}{\hbar k^{\delta}} = \frac{\omega^{\delta}}{k^{\delta}} \quad (3.11)$$

$$u_{\text{NES}} = \frac{m_{\text{f}} - m_{\text{pr}}}{2\sqrt{2m_{\text{n}}E_{\text{n}}}} v_{\text{f}}^2 + \frac{m_{\text{pr}}}{m_{\text{f}}} \frac{E_{\text{n}} - Q}{\sqrt{2m_{\text{n}}E_{\text{n}}}} + \frac{\sqrt{2m_{\text{n}}E_{\text{n}}}}{2m_{\text{f}}}, \quad (3.12)$$

$$u_{\text{GRS1}} = c \left(\frac{m_{\text{f}} - m_{\text{pr}}}{2E_{\gamma}} v_{\text{f}}^2 + \frac{m_{\text{pr}}}{m_{\text{f}}} \frac{E_{\gamma} - Q}{E_{\gamma}} \right), \quad (3.13)$$

$$u_{\text{GRS2}} = \frac{-M \pm w \sqrt{v_{\text{f}}^2 u_{\text{pr}}^2 (1 + w^2) - M^2}}{u_{\text{pr}} (1 + w^2)} \quad (3.14)$$

$$\text{with } \begin{cases} u_{\text{pr}} = c \frac{E_\gamma - E_{\gamma 0}}{E_{\gamma 0}} \\ w = \tan \beta \cos \xi \\ M = \frac{1}{2} \left(\frac{m_n}{m_{\text{pr}}} - \frac{m_f}{m_{\text{pr}}} \right) v_{\text{f}}^2 + \frac{m_n}{m_{\text{f}} m_{\text{pr}}} Q^* - \frac{1}{2} \left(\frac{m_n}{m_{\text{f}}} + \frac{m_{\text{pr}}}{m_{\text{f}}} \right) \frac{u_{\text{pr}}^2}{\cos^2 \beta}. \end{cases}$$

The observable velocity-space for the measurement is found by substitution of the corresponding equation for the projected velocity into equation 3.9. The shapes of the functions are simplest in $(v_{\parallel}, v_{\perp})$ -space (fig. 3.9). The boundaries of the probability functions and hence the weight functions for CTS and FIDA are found by substituting $\gamma = 0^\circ$ and $\gamma = 180^\circ$:

$$v_{\perp} = \pm \frac{u - v_{\parallel} \cos \phi}{\sin \phi}. \quad (3.15)$$

FIDA and CTS observe triangular regions. The two boundary lines intersect the v_{\parallel} -axis at $v_{\parallel} = u / \cos \phi$ and have the slopes $\pm v_{\parallel} / \tan \phi$. Their closest distance to the origin is u . The opening angle of the triangular region is 2ϕ . Points below these lines cannot map onto u . For FIDA, small corrections due to Stark splitting are discussed in reference [6].

Assuming that the energy and momentum of the target particle are negligible, NES and one-step reaction GRS observe regions bounded by circular arcs of the form [9, 17]

$$(v_{\parallel} - v_{\parallel 0})^2 + (v_{\perp} - v_{\perp 0})^2 = r_{\text{v}}^2. \quad (3.16)$$

For NES, we have

$$v_{\parallel 0} = -\frac{m_n v_n}{m_{\text{pr}} - m_f} \cos \phi, \quad (3.17)$$

$$v_{\perp 0} = \pm \frac{m_n v_n}{m_{\text{pr}} - m_f} \sin \phi \quad (3.18)$$

$$r_{\text{v}} = \sqrt{\frac{2m_{\text{pr}}}{m_f(m_{\text{pr}} - m_f)} \left(\left(1 - \frac{m_n}{m_{\text{pr}} - m_f} \right) E_n - Q \right)}. \quad (3.19)$$

For one-step GRS, we have

$$v_{\parallel,0} = -\frac{E_\gamma/c}{m_{pr} - m_f} \cos \phi, \quad (3.20)$$

$$v_{\perp,0} = \pm \frac{E_\gamma/c}{m_{pr} - m_f} \sin \phi, \quad (3.21)$$

$$r_v = \sqrt{\frac{m_{pr}}{m_f} \left(\frac{E_\gamma^2}{(m_{pr} - m_f)^2 c^2} + \frac{2(E_\gamma - Q)}{m_{pr} - m_f} \right)}. \quad (3.22)$$

3.5 The forward problem as a matrix equation

To interpret fast-ion measurements, forward models of all fast-ion diagnostics are being developed. These usually take the form of a code, such as FIDASIM [113], GENESIS [74], or DRESS [75], that can compute a synthetic spectrum, given a velocity distribution function. To make the forward models of fast-ion diagnostics amenable to inversion with standard position-space tomography tools, we write the forward model in the form of a matrix equation [2, 3]. Given the matrix and a fast-ion velocity distribution function, a synthetic fast-ion measurement is computed according to [3]

$$\tilde{S} = \tilde{W}F \quad (3.23)$$

where F is the fast-ion velocity distribution function written as a vector, \tilde{S} contains the measurements written as another vector, and \tilde{W} is a matrix holding the forward model. Equation 3.23 is a discretization of equation 3.1. Weight functions enter as the rows of the matrix \tilde{W} in equation 3.23 and are analogous to lines-of-sight in standard position-space tomography. They quantify how much signal per ion is measured and are hence a convenient formulation of the forward model for velocity-space tomography.

The inverse problem: velocity-space tomography

4.1 The inverse problem

Given the 2D velocity distribution function F , we can compute the synthetic measurements \tilde{S} using the linear matrix equation 3.23. The computation of \tilde{W} was discussed in chapter 3. The inverse problem is to find a stable and useful solution in F , given \tilde{W} and the measurements \tilde{S} . As F represents a 2D image, this inverse problem constitutes a tomography problem. Equation 3.23 has no solution in F due to noise in the measurements, which makes the rows of the matrix equation inconsistent. Hence we instead seek a best estimate. To take the measurement uncertainty $\tilde{\sigma}_S$ into account, each entry in \tilde{S} is divided by its associated uncertainty, as is the corresponding line in \tilde{W} [4]. Hence we obtain the matrix equation

$$S = WF \tag{4.1}$$

in the normalized quantities S and W . As the signal-to-noise ratio S is on the same order of magnitude for most diagnostics, whereas the

measured signal \tilde{S} can differ by orders of magnitude, the normalization by $\tilde{\sigma}_s$ substantially improves the conditioning of the matrix and ensures that measurements from different diagnostics are treated on an equal footing [4]. The least-squares solution is given by the normal equation

$$F = (W^T W)^{-1} W^T S. \quad (4.2)$$

However, as in most tomography problems, it turns out that the computation of F , given W and S , is ill-posed. This means that small changes in S result in large changes in F in a standard least-squares fit. The measurement noise, which is usually fairly large in fast-ion measurements, therefore generates random noise in the 2D image F , and no stable inversion, which continuously depends on the data, can be found.

This noise amplification is typical for inversions of integral equations in tomography problems. Equation 3.1 expresses that the measurements S are obtained from F by integration over velocity space. Such an integration has a smoothing property as any small noisy wiggles in F are integrated over velocity space. The signal S is therefore usually smooth even if F is wiggly. The inverse operation (to compute the F from S) consequently amplifies noise.

As in standard methods of position-space tomography, we can use regularization to prevent the propagation of noise into the 2D image. Early work on velocity-space tomography was done by McWilliams and Koslover [114] in the $(v_{\perp 1}, v_{\perp 2})$ -plane for a linear plasma device. This velocity-space tomography problem is analogous to the astrophysical Doppler tomography problem introduced by Marsh and Horne to provide 2D images of accretion disks [7, 115–122]. Egedal and Bindslev [123] first studied reconstructions in the $(v_{\parallel}, v_{\perp})$ -plane from 1D projections. To date velocity-space tomography has relied on standard regularization methods: algebraic iterative methods [2], truncated singular value decomposition [3–5, 7, 10, 18, 25, 69, 123], the maximum entropy method [7, 18, 20, 69], and a few variants of Tikhonov regularization [10–15, 18, 20, 27, 33, 69, 108].

4.2 Tikhonov regularization

Tikhonov regularization is one of the most widespread regularization methods in tomography. It is very intuitive, and it is well suited to incorporate prior information about the solution to improve the results (see next section) [10]. In Tikhonov regularization, the solution F_λ is commonly written as the solution to the minimization problem

$$\underset{F}{\text{minimize}} \left(\left\| WF - S \right\|_2^2 + \lambda^2 \left\| LF \right\|_2^2 \right). \quad (4.3)$$

The first term minimizes the two-norm of the residual of equation 4.1. The second term minimizes the two-norm of LF . L is a matrix operating on F such that LF quantifies an undesired property of the solution. If L is the identity matrix, LF minimizes the two-norm of F and will strongly (quadratically) penalize large spikes. This is the so-called zeroth-order Tikhonov regularization. If L is a numerical gradient operator, LF minimizes gradients and hence selects for smooth solutions (first-order Tikhonov). Second-order Tikhonov penalizes large curvature which is also commonly used in position-space tomography, but not yet in velocity-space tomography. The choice of L is motivated by prior information. As velocity distribution functions are smooth due to collisions, the first-order Tikhonov regularization is often a good choice. The regularization parameter λ balances the goodness-of-fit and the regularization requirement and must be found as part of the solution (see section 4.5). The dependence of the solution F_λ on the regularization parameter λ is indicated by the index.

We prefer the equivalent and computationally more convenient and stable form [124]

$$\underset{F}{\text{minimize}} \left\| \begin{pmatrix} W \\ \lambda L \end{pmatrix} F - \begin{pmatrix} S \\ 0 \end{pmatrix} \right\|_2 \quad (4.4)$$

which also reveals clearly that we are dealing with a linear least-square problem. It can be solved by the normal equation

$$F_\lambda = (W^T W + \lambda^2 L^T L)^{-1} W^T S. \quad (4.5)$$

However, F_λ computed with the normal equation usually becomes negative in some velocity-space region, which is unphysical. This is avoided by constraining the solution to be non-negative [10] as we discuss in the next section.

4.3 Prior information

Compared with many medical tomography applications, the amount of measured fast-ion diagnostic data is small due to the limited access to the plasma and the often comparatively low signal-to-noise ratio. Therefore, inversions often have so-called artifacts which are spurious features of the inversion. Artifacts can be reduced by installing additional fast-ion diagnostics [3, 27] and by optimizing the discharges for signal-to-noise ratio. For example, FIDA works very well in L-mode plasmas with low density and few impurities [5, 20, 25, 27].

High-definition tomography techniques make use of prior information in addition to the regularization encoded in equation 4.4 to remedy artifacts and to improve the inversions [10]. Additional prior information is in particular needed if velocity-space regions are observed by only one or two detectors [13, 14, 22, 23]. In actual fast-ion diagnostics implemented on tokamaks, some regions in velocity space may be well diagnosed by several detectors whereas other regions in velocity space may be observed by a single detector only or even not at all [13, 14, 22]. In such cases we know before the inversion that F in the region with only one or no observing detectors cannot be reliably inferred, and artifacts will form in such regions.

Besides the usual demand on smoothness, we can demand non-negativity of the solution and solve a least-square problem with non-negativity constraint [10]:

$$\underset{F}{\text{minimize}} \left\| \begin{pmatrix} W \\ \lambda L \end{pmatrix} F - \begin{pmatrix} S \\ 0 \end{pmatrix} \right\|_2 \quad \text{subject to } F \geq 0. \quad (4.6)$$

Since we are sure that the distribution function is never negative, this prior information is safe to use. The non-negative least-squares algorithm

in reference [125] is well-suited for this problem. We regard Tikhonov regularization with non-negativity constraint as our baseline method which can be supported by additional prior information. Alternatively, one may penalize negative values and hence force them to become small [27].

In the following we discuss the implementation of additional prior information for various plasma scenarios. One option is to modify the penalty function to become dependent on the velocity-space coordinates. Another option is to add further constraints in addition to non-negativity: isotropy, monotonicity, or restrictions on the target velocity space to be reconstructed. Lastly, we can also use a numerical simulation as prior information and penalize any deviation from the simulation. These types of prior information should only be used when appropriate. Additionally, we recommend the computation of solutions to the baseline equation 4.6 as reference cases. Wrong prior information will deteriorate the solution, and one risks to miss new physical phenomena.

We first discuss the constraints mentioned above except for isotropy for which we can derive a 1D inversion problem (section 4.4). A minimization problem with non-negativity, restricted velocity space, and monotonicity constraint in energy can be written as

$$\underset{F}{\text{minimize}} \left\| \begin{pmatrix} W \\ \lambda L \end{pmatrix} F - \begin{pmatrix} S \\ 0 \end{pmatrix} \right\|_2 \quad \text{subject to} \begin{cases} F \geq 0, \\ F(E_0, p_0) = 0, \\ L_{1,E} F(E_m, p_m) \leq 0. \end{cases} \quad (4.7)$$

$F(E_0, p_0) = 0$ is the velocity-space region with negligible fast-ion densities according to null-measurements, as identified by weight functions [10]. A null-measurement in the measured signal S is the measured absence of evidence for fast ions. Null-measurements are often found for plasma scenarios with NBI heating at large Doppler shifts. An example of an experimentally determined null-measurement velocity space at ASDEX Upgrade is illustrated in fig. 4.1(a). It is advantageous to use null-measurements to restrict the velocity space before the inversion to reduce the number of unknowns. This prevents the appearance of artifacts in regions where we know from measurements that the velocity-space densities are very small, at least below the detection limit of the diagnostic [10].

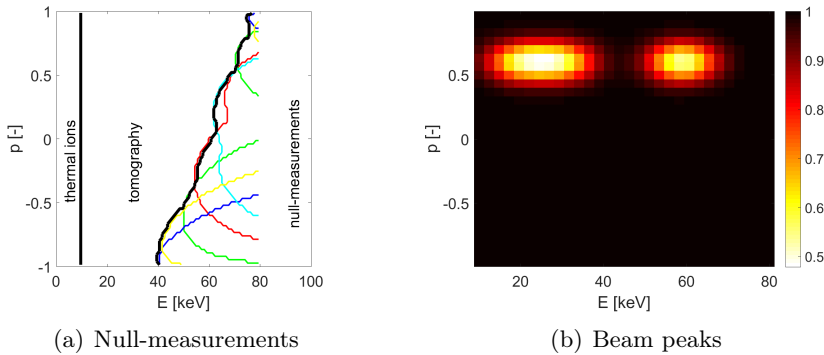


Figure 4.1: Prior information for velocity-space tomography [10]. (a) Measured absence of evidence for fast ions (null-measurements). (b) $\kappa_1(E, p)$ encodes the NBI injection energies and pitch.

The monotonicity constraint in equation 4.7 selects for monotonically decreasing functions in energy in the velocity-space region (E_m, p_m) [23]. This could be a good constraint for α -particle velocity distribution functions or for the fast-ion tail generated by ICRF heating (fig. 1.11). NBI and ICRF distribution functions may also sometimes be assumed to be monotonic in pitch in some velocity-space region [23]. The ICRF distribution in fig. 1.11 forms a ridge for $v_{\parallel} \approx 0$ and decreases in positive and negative v_{\parallel} directions. The NBI distribution function in fig. 1.12 could be constrained to be monotonically decreasing in pitch for $p \in [-1; 0.5]$ which would remove the two small regions with higher densities in the negative pitch half-plane. However, there is a risk that such small bumps originate from physics.

Another option to reflect prior information in the problem formulation is a modification of the regularization term by a function $\kappa(E, p)$ [10, 23]. The minimization problem with a mix of zeroth- and first-order Tikhonov terms is written as:

$$\underset{F}{\text{minimize}} \left\| \begin{pmatrix} W \\ \lambda_1 \kappa_1(E, p) L_1 \\ \lambda_0 \kappa_0(E, p) L_0 \end{pmatrix} F - \begin{pmatrix} S \\ 0 \\ 0 \end{pmatrix} \right\|_2 \quad \text{subject to } F \geq 0. \quad (4.8)$$

For example, $\kappa_1(E, p)$ used with the first-order Tikhonov penalty term

$\lambda_1 L_1$ can encode the velocity-space positions of the particle sources of the NBI at the well-known full-, half- and one-third NBI injection energies as illustrated in fig. 4.1(b). Gradients in the vicinity of the particle sources in velocity space are penalized less than elsewhere [10]. Alternatively, one could encode a known position of a peak in a function $\kappa_0(v_{\parallel}, v_{\perp})$ used with the zeroth-order Tikhonov penalty term $\lambda_0 L_0$. This function could be similar to $\kappa_1(E, p)$ shown in fig. 4.1(b). However, penalizing gradients is less restrictive than penalizing amplitudes as the gradients can go either way (peak or depression).

The null-measurement constraint discussed above can produce jumps at the boundary between the target velocity space and the null-measurement velocity space. Instead of a formulation as a hard constraint, we can introduce a zeroth-order Tikhonov penalty in the null-measurement velocity space [22]. Instead of setting the distribution function in the velocity space interrogated by null-measurements to zero, one may instead use a penalty term $\lambda_0 \kappa_0(E, p) L_0$ [22]. An example of the function κ_0 for a velocity-space tomography problem at the MAST tokamak is illustrated in fig. 4.2.

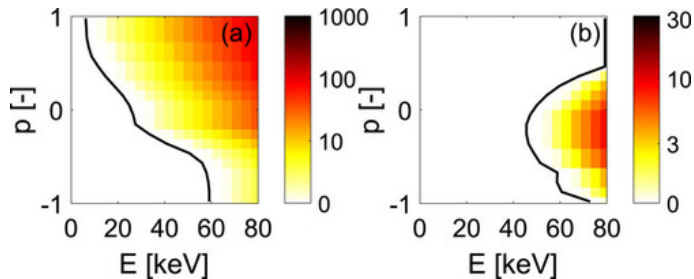


Figure 4.2: Prior information of unlikely velocity space for velocity-space tomography at MAST according to (a) TRANSP/NUBEAM and (b) null-measurements [22]. The exponentially growing $\kappa_0(E, p)$ towards higher energies expresses our increasing doubt to find ions.

The increasing penalty with energy expresses our increasing doubt to find ions at large energies [22]. This way of penalizing densities in the null-measurement velocity space does not produce a jump at the boundary between target velocity space and null-measurement velocity space. If not enough measurements are available to find a boundary between the

null-measurement velocity space and the target velocity space, one may use a numerical simulation, e.g. from TRANSP/NUBEAM, to restrict the velocity-space region considered for the inversion [22]. Here the assumption is that there is no acceleration of a significant number of fast ions to higher energies than energies achievable according to neoclassical transport.

Lastly, if inversions based on the measurements and the above prior information do not produce reasonable results, a numerical simulation F_{sim} can be used as prior information on the velocity distribution function [10]. In this case we solve the problem

$$\underset{F}{\text{minimize}} \left\| \begin{pmatrix} W \\ \lambda L \end{pmatrix} F - \begin{pmatrix} S \\ \lambda L F_{\text{sim}} \end{pmatrix} \right\|_2 \quad \text{subject to } F \geq 0. \quad (4.9)$$

In this technique a penalty is given on $\|L(F - F_{\text{sim}})\|_2$ which is the deviation from the prior distribution in the operator L , e.g., the gradient. This technique works well even if only two detectors are available. However, we do not obtain an inversion based on measurements alone, but rather identify regions in velocity space where the measurements suggest deviations from F_{sim} .

4.4 Inference of isotropic functions

If the velocity-distribution function is close to isotropic, we may seek to infer a 1D energy spectrum instead of the full 2D velocity distribution function. For example, the velocity distribution of α -particles in ITER is expected to be close to isotropic with deviations of up to about 10% [14]. The measurement of the energy spectrum of α -particles is an ITER measurement requirement [112]. For an isotropic function $f(E)$, the integral equation connecting the 2D velocity distribution function to the measurement can be simplified by integration over the pitch. We then obtain the 1D weight function $w_E(m_1, m_2, \phi, E)$. The integral equation connecting the 1D energy spectrum $f_E^{\text{1D}}(E)$ to the measurement s is

$$s(m_1, m_2, \phi) = \int_0^\infty w_E(m_1, m_2, \phi, E) f_E^{\text{1D}}(E) dE. \quad (4.10)$$

Here the dependence on the projection angle ϕ is retained, as the 1D weight function can still depend on ϕ , e.g. due to anisotropic cross sections or anisotropy or drift of the thermal ions. The integral of equation 3.7 over pitch does not depend on ϕ . Hence we find a simplified relation between the projected velocity distribution function $g(u)$ and the energy spectrum for isotropic fast-ion velocity distribution functions:

$$g(u) = \int_{E_u}^{\infty} \frac{1}{2\sqrt{2E/m}} f_E^{1D}(E) dE \quad (4.11)$$

where $1/2\sqrt{2E/m}$ is a 1D weight function obtained by integration of the 2D weight function over pitch. The lower integration limit is $E_u = \frac{1}{2}mu^2$. Inversion of equation 4.11 allows the determination of energy spectra from projected isotropic velocity distribution functions, which is a 1D analog of velocity-space tomography. Conveniently we can also consider the integral equation connecting the speed spectrum to $g(u)$, which is advantageous as u and v have the same units:

$$g(u) = \int_u^{\infty} 2\pi v f_v^{1D}(v) dv. \quad (4.12)$$

These 1D inversion techniques will prove useful to determine the energy spectrum of α -particles at ITER below 2 MeV where GRS is not sensitive and CTS will be the only diagnostic [14].

As a softer alternative compared with the isotropy constraint, which reduces the tomography problem to a 1D inversion problem, near-isotropy can be encoded by penalizing gradients in pitch direction more strongly than gradients in energy direction. This method can still allow some anisotropy which may be advantageous compared with a full constraint [14]:

$$\underset{F}{\text{minimize}} \left\| \begin{pmatrix} W \\ \lambda_{1,E} L_{1,E} \\ \lambda_{1,p} L_{1,p} \end{pmatrix} F - \begin{pmatrix} S \\ 0 \\ 0 \end{pmatrix} \right\|_2 \quad \text{subject to} \quad \begin{cases} F \geq 0, \\ \lambda_{1,p} \gg \lambda_{1,E}. \end{cases} \quad (4.13)$$

4.5 Uncertainties and regularization strength

The uncertainties in velocity-space tomography are conceptually the same as in standard position-space tomography. Calculating them is unfortu-

nately not straightforward. We may divide the uncertainties into three categories:

- uncertainties in the fast-ion measurements S [4],
- uncertainties in the weight matrix W due to uncertainties in nuisance parameters [20],
- bias uncertainties due to the regularization [20].

The nature of the uncertainties in the fast-ion measurements depends on the diagnostic as discussed in [39]. Usually apparently random fluctuations in the measured signals, which are called measurement noise, are one contribution to the uncertainty. There can also be systematic uncertainties. An example is the passive FIDA light originating from the plasma edge rather than from the measurement volume. The passive FIDA light can be subtracted by beam modulation or passive lines-of-sight, but usually some systematic error is to be expected since the active and passive signals change over time [86]. Whereas uncertainties due to measurement noise are controlled to be small in tomography, any systematic measurement error such as in the background subtraction will propagate into the inversion.

In the end of this section we will discuss the computation of uncertainties by sampling. Some insight can be gained for Tikhonov regularization without constraint. In this case the errors in the measurements can be propagated into the inversion using the regularized inverse

$$W_\lambda^\dagger = (W^T W + \lambda^2 L^T L)^{-1} W^T \quad (4.14)$$

introduced in equation 4.4. The covariance matrix $C_{F\lambda}$ of the inversion can be calculated from the covariance matrix C_S of the measurements according to standard error propagation:

$$C_{F\lambda} = W_\lambda^\dagger C_S (W_\lambda^\dagger)^T. \quad (4.15)$$

The diagonal elements $\sigma_{F\lambda}$ of $C_{F\lambda}$ are for uncorrelated noise given by

$$\sigma_{F\lambda,n}^2 = \sum_m (W_{\lambda,mn}^\dagger)^2 \sigma_{S,m}^2. \quad (4.16)$$

Uncertainties in the nuisance parameters are the uncertainties in parameters which are needed in the forward models but are of secondary interest. For example, often the densities and temperatures of ions or electrons influence the amplitude of the measured fast-ion signals. Such parameters and their uncertainties are usually measured by other diagnostics, and such measurements can be used as prior information.

Lastly, the bias uncertainties cover systematic errors introduced by the regularization which is needed to obtain stable solutions to the tomography problem. Bias uncertainties make it impossible to reconstruct the true distribution function even with perfect, noise-free measurements. The quantification of bias uncertainties is an open problem because we would need to know the true distribution function. If it was known, we could compute ideal, noise-free measurements

$$S_{\text{ideal}} = W F_{\text{true}} \quad (4.17)$$

and find the inversion of these according to

$$F_{\lambda} = W_{\lambda}^{\dagger} W F_{\text{true}}. \quad (4.18)$$

$W_{\lambda}^{\dagger} W$ is called the resolution matrix which should deviate as little as possible from the identity matrix. The regularization bias could then be found according to

$$\delta F_{\lambda, \text{bias}} = F_{\lambda} - F_{\text{true}} = (W_{\lambda}^{\dagger} W - I) F_{\text{true}}. \quad (4.19)$$

Equation 4.19 shows that we would need to know the true solution to estimate the bias uncertainty. To get a rough idea, we may use a numerical simulation or the tomographic inversion to estimate the bias uncertainty [20].

In the Tikhonov problem, equation 4.6 shows that the solution F_{λ} depends on the regularization parameter λ , and so do the uncertainties. For very small λ , the lower part of equation 4.6 becomes negligible, and one approaches the original least-squares problem. Even though the fit to the measurement data is very good, the solution is unstable and is completely dominated by measurement noise. The bias due to the regularization is in this case small. For very large λ , the upper part of equation 4.6 becomes negligible, and one approaches a very smooth function, but the

fit to the measurement data is poor. In this case the uncertainty due to measurement noise is small, but the bias due to regularization is large. A trade-off must be made in the choice of λ to balance the propagation of measurement noise into the inversion against systematic bias introduced by the regularization itself.

Various strategies to choose λ automatically exist [124], such as the L-curve, generalized cross-validation (GCV) or the discrepancy principle or the normalized cumulative periodogram (NCP) method. Most algorithms will pick λ such that it is as small as possible but still prevents the propagation of noise into the 2D image. The value of λ obtained by these and other methods can vary, and a given method may have a tendency to systematically produce oversmoothed or undersmoothed solutions. For example, the L-curve method tends to produce oversmoothed solutions in velocity-space tomography, and the GCV sometimes tends to produce noisy solutions. Since the different methods produce different λ s, a good strategy is to compute solutions for a reasonable range in λ . One then obtains a progression of solutions F_λ from undersmooth to oversmooth, such that no phenomena are missed due to oversmoothing or undersmoothing.

Assuming that we have chosen λ or choose it automatically, we can quantify the uncertainties in the inversion due to uncertainties in the fast-ion measurements and due to uncertainties in the nuisance parameters. We sample the fast-ion measurements and nuisance parameters from their probability distributions and compute a population of N inversions, $F_{\lambda,i}$. The mean of the N inversions is the best estimate of the velocity-distribution function, and the uncertainty is the corresponding standard deviation which accounts for uncertainties in the signal and the nuisance parameters:

$$\langle F_\lambda \rangle = \frac{1}{N} \sum_i F_{\lambda,i}, \quad (4.20)$$

$$\delta F_\lambda = \sqrt{\frac{1}{N-1} \sum_i (F_{\lambda,i} - \langle F_\lambda \rangle)^2}. \quad (4.21)$$

Each pixel in the inversion has its own uncertainty, such that we can assess which parts of velocity space can be reliably inferred [19, 20, 24]. If required, we can assess the individual contributions of the measurement noise and the nuisance parameter uncertainty by fixing the other values.

4.6 Tikhonov regularization in the Bayesian perspective

In the plasma physics community, Bayesian inference is a popular approach to solve inverse problems. It is hence of interest to justify Tikhonov regularization in velocity-space tomography from the Bayesian perspective in which regularization is encoded in the so-called prior distribution function [13]. Bayes' theorem relates the posterior distribution function with the likelihood function and the prior distribution function:

$$\text{prob}(F|S) = \frac{\text{prob}(S|F) \times \text{prob}(F)}{\text{prob}(S)}. \quad (4.22)$$

Here the posterior $\text{prob}(F|S)$ is the probability of the pixel values describing the distribution function, given the data. The prior $\text{prob}(F)$ is the probability of the distribution function before considering the data. The likelihood function $\text{prob}(S|F)$ is the probability of the data, given the distribution function. Lastly, $\text{prob}(S)$ is the probability of the data, often called the evidence. Using the forward model, we can assign probabilities to the likelihood function:

$$\text{prob}(\tilde{S}|F) \propto \exp\left(-\frac{1}{2}(\tilde{W}F - \tilde{S})^T \tilde{C}_S^{-1}(\tilde{W}F - \tilde{S})\right) \quad (4.23)$$

where \tilde{C}_S is the covariance matrix for the data \tilde{S} . Assuming the noise to be independent and normally distributed, the likelihood function reduces to

$$\text{prob}(S|F) \propto \exp\left(-\frac{1}{2}\|WF - S\|_2^2\right). \quad (4.24)$$

Recall that W and S are normalized by the uncertainties. We further assume the prior distribution to be a multivariate Gaussian:

$$\text{prob}(F) \propto \exp\left(-\frac{1}{2}(F - F_0)^T C^{-1}(F - F_0)\right) \quad (4.25)$$

where C is the covariance matrix for F_0 . F_0 is the estimate of the velocity distribution function before considering the data. If a numerical simulation F_{sim} is available, we may set $F_0 = F_{\text{sim}}$. Since the covariance matrix

is positive semidefinite, so is its inverse C^{-1} . Hence we can introduce the symmetric decomposition

$$C^{-1} = \lambda^2 L^T L \quad (4.26)$$

where λ^2 is a positive free parameter setting a width-scaling for the multivariate Gaussian. Equation 4.26 allows us to write equation 4.25 as

$$\text{prob}(F) \propto \exp\left(-\frac{1}{2}\lambda^2\|L(F - F_0)\|_2^2\right). \quad (4.27)$$

According to Bayes' theorem (equation 4.22), the posterior becomes

$$\text{prob}(F|S) \propto \exp\left(-\frac{1}{2}\|WF - S\|_2^2 - \frac{1}{2}\lambda^2\|L(F - F_0)\|_2^2\right) \quad (4.28)$$

where we dropped the unimportant evidence term. Maximizing the posterior probability is equivalent to solving the minimization problem in equation 4.3. We have hence recovered the Tikhonov problem from the Bayesian formulation. Equation 4.26 shows how to obtain the covariance matrix C , from the penalty matrix L in Tikhonov's problem. Conversely, given C , we can find L to within a factor λ by symmetric matrix decomposition. Perhaps the simplest example is the zeroth-order Tikhonov problem where L is the identity matrix. Then C is a diagonal matrix with $1/\lambda^2$ on the diagonal, so that the entries in F are uncorrelated. For first-order or higher-order Tikhonov regularization, we can likewise use equation 4.26 to calculate C which is useful to implement Tikhonov regularization in Bayesian inference methods, e.g. to interpret CTS measurements in current tokamaks and ITER [126].

CHAPTER 5

Discussion, conclusions, and outlook

This thesis demonstrates measurements of 2D fast-ion velocity distribution functions in magnetized fusion plasmas. Such measurements are essential to understand the physics of fast ions and hence to eventually operate high-performance plasmas for harvesting energy. Fast-ion velocity distribution functions are often anisotropic and have local maxima. This can drive instabilities causing anomalous fast-ion transport that can be detrimental to the plasma performance.

Up to now fast-ion diagnostics have never measured 2D velocity distribution functions. Experimental results have conventionally been presented in terms of spectra of diagnostic quantities, e.g. spectral power density of scattered radiation, FIDA radiance or γ -ray count rates. Results in terms of such quantities of secondary interest are often hard to interpret. The spectra consist of hundreds of data points that have different relationships to the velocity distribution function and additionally depend on nuisance parameters. To directly consider this wealth of data on an equal footing is intractable for humans.

Velocity-space tomography transforms the rich diagnostic data to a 2D image that is straightforward to interpret for all physicists rather than just diagnostic specialists. The technique borrows from standard medical tomography techniques implemented in CAT or MRI scanners, but applies them to measure velocities rather than positions. The obtained 2D image of the velocity distribution function is the best useful fit to hundreds of simultaneous measurements. It shows the fundamental quantity of interest rather than measured quantities of secondary interest. Data from different diagnostics are combined, and nuisance parameters are accounted for.

This development has been published in my papers reprinted with this brief overview [1–15] and in papers by my PhD students [16–23] and collaborators [24–38]. Recent review and tutorial papers on fast-ion diagnostics [39] and on analytic velocity distribution functions in various coordinate systems [40] provide comprehensive technical background information.

Paper [1] is an example of how fast-ion measurements are traditionally analyzed. The unsatisfactory connection between fast-ion measurements and the 2D velocity distribution function in this paper illustrates the basic problem addressed by velocity-space tomography. The development of diagnostic weight functions allowed a more detailed analysis in velocity space [73]. Weight functions of the major fast-ion diagnostics were subsequently derived in papers [2, 6, 8, 9, 17, 21, 36]. Weight functions not only allow velocity-space tomography but also provide new ways to understand and analyze fast-ion measurements.

The velocity-space tomography method based on such weight functions was presented in papers [2–4]. Different inversion methods were compared in [20]. The state-of-the-art now is high-definition velocity-space tomography which uses prior information together with Tikhonov regularization to improve results compared with cases without extra prior information. This further allows the analysis of sparse data, even if parts of velocity space are observed by only one or two detectors [10, 22, 23].

Experimentally, measurements by the diagnostics FIDA, CTS, GRS, NES, and FILD installed at the tokamaks ASDEX Upgrade, JET, MAST, DIII-

D, and EAST have been interpreted using velocity-space tomography up to now. The method was introduced at ASDEX Upgrade based on three simultaneously measured FIDA spectra [5, 7]. Now four to five simultaneously measured FIDA spectra are routinely used [10, 19, 20, 25, 27, 29, 31, 33]. Integrated data analysis by combining different fast-ion diagnostics [4] has been experimentally demonstrated for FIDA and CTS measurements at ASDEX Upgrade [20, 31] and for GRS and NES at JET [11]. We have measured non-Maxwellian, strongly anisotropic fast-ion velocity distribution functions in the keV-range in plasmas heated by NBI [5, 7, 10, 19, 20, 25, 27, 29, 31] and up to the MeV-range in plasmas heated by ICRF [11, 13, 33].

The interaction of fast ions and magnetohydrodynamic instabilities could be studied in unprecedented detail. In particular sawteeth have been extensively studied [10, 19, 20, 25, 27, 29, 31], revealing strong selectivity of the interaction in velocity space. Initial studies of neoclassical tearing modes and Alfvén eigenmodes have been made. Fast-ion densities and energy spectra have been measured for the first time [10, 15, 24]. First movies of fast-ion velocity distribution functions at ASDEX Upgrade in a sawtooth plasma [10], during NBI start-up [10], and rotating and locked neoclassical tearing modes have been presented. Automation could make such movies available in the control room minutes after a discharge in the future to aid the immediate decision-making in future experiments in ITER or present tokamaks.

The focus of much of fusion energy research is now the ITER tokamak. Velocity-space tomography was demonstrated to be a useful analysis tool for ITER [14], and its further development in ongoing Joint Experiments under the ITPA Topical Group for Energetic Particles is requested by the ITER Organization. It was found that co-passing and counter-passing particles, which are two out of three major classes of ions, cannot be told apart at ITER, unless a detector with an oblique line-of-sight is installed [14]. It remains to be seen, if this can be done.

To make optimal use of the diagnostic set at ITER or present tokamaks, we must develop 1D, 2D, and 3D inversion tools and be familiar with the use of prior information depending on the situation. Measurements of α -particle energy spectra in ITER, as requested by the ITER mea-

surement requirements [112], should be possible by velocity-space tomography for energies from 1.7 MeV upwards based on GRS and CTS [14]. Below α -particle energies of 1.7 MeV, GRS is not sensitive and CTS will be the only diagnostic for α -particles, so that 2D or 3D inference will be challenging if not impossible. Here 1D inversion techniques akin to 2D velocity-space tomography can be used to determine energy spectra and α -particles without assuming a functional form [14, 15]. It is now becoming possible to measure 3D phase-space distribution functions by orbit tomography [68, 69]. This approach requires many measurements to cover the 3D target phase space, but with appropriate prior information it will hopefully be useful at ITER.

The original scope of velocity-space tomography has also broadened, and similar methods have been applied in other fields in fusion plasmas. A comparison with astrophysical Doppler tomography [7] inspired a way to deal with perpendicular drift velocities [13, 40, 127]. Measurements of the total ion velocity distribution function allowed measurements of main-ion densities, parallel drift velocities and anisotropic temperatures by taking its lowest moments [12]. These basic plasma parameters are not easily measurable by other means. Anisotropic temperatures in a fusion plasma have never been measured before. Furthermore, we applied methods of velocity-space tomography to interpret γ -ray measurements of relativistic runaway electrons [37]. Lastly, we deblurred measured images of FILD measurements using velocity-space tomography [35, 36]. A FILD system is foreseen for ITER.

In conclusion, this thesis provides a new meeting ground between theory and observation which is far more easily accessible by a broad community. Measurements of 1D, 2D and 3D distribution functions of ions will help us understand anomalous transport of energetic and thermal particles in plasmas and are foreseen for the interpretation of diagnostic data at ITER.

Bibliography

- [1] M. Salewski *et al.* Comparison of fast ion collective Thomson scattering measurements at ASDEX Upgrade with numerical simulations. *Nucl. Fusion*, 50(3):035012, March 2010.
- [2] M. Salewski *et al.* On velocity space interrogation regions of fast-ion collective Thomson scattering at ITER. *Nucl. Fusion*, 51(8):083014, 2011.
- [3] M. Salewski *et al.* Tomography of fast-ion velocity-space distributions from synthetic CTS and FIDA measurements. *Nucl. Fusion*, 52(10):103008, October 2012.
- [4] M. Salewski *et al.* Combination of fast-ion diagnostics in velocity-space tomographies. *Nucl. Fusion*, 53(6):063019, June 2013.
- [5] M. Salewski *et al.* Measurement of a 2D fast-ion velocity distribution function by tomographic inversion of fast-ion D-alpha spectra. *Nucl. Fusion*, 54(2):023005, February 2014.
- [6] M. Salewski *et al.* On velocity-space sensitivity of fast-ion D-alpha spectroscopy. *Plasma Phys. Control. Fusion*, 56(10):105005, October 2014.
- [7] M. Salewski *et al.* Doppler tomography in fusion plasmas and astrophysics. *Plasma Phys. Control. Fusion*, 57(1):014021, January 2015.

-
- [8] M. Salewski *et al.* Velocity-space observation regions of high-resolution two-step reaction gamma-ray spectroscopy. *Nucl. Fusion*, 55(9):093029, 2015.
- [9] M. Salewski *et al.* Fast-ion energy resolution by one-step reaction gamma-ray spectrometry. *Nucl. Fusion*, 56:046009, 2016.
- [10] M. Salewski *et al.* High-definition velocity-space tomography of fast-ion dynamics. *Nucl. Fusion*, 56:106024, 2016.
- [11] M. Salewski *et al.* MeV-range velocity-space tomography from gamma-ray and neutron emission spectrometry measurements at JET. *Nucl. Fusion*, 57:056001, 2017.
- [12] M. Salewski *et al.* Deuterium temperature, drift velocity, and density measurements in non-Maxwellian plasmas at ASDEX Upgrade. *Nucl. Fusion*, 58:036017, 2018.
- [13] M. Salewski *et al.* Bayesian integrated data analysis of fast-ion measurements by velocity-space tomography. *Fusion Sci. Tech.*, 74:23–36, 2018.
- [14] M. Salewski *et al.* Alpha-particle velocity-space diagnostic in ITER. *Nucl. Fusion*, 58:096019, 2018.
- [15] M. Salewski *et al.* Diagnostic of fast-ion energy spectra and densities in magnetized plasmas. *J. Instrum.*, submitted.
- [16] A. S. Jacobsen *et al.* Velocity-space sensitivity of the time-of-flight neutron spectrometer at JET. *Rev. Sci. Instrum.*, 85(11):11E103, November 2014.
- [17] A. S. Jacobsen *et al.* Velocity-space sensitivity of neutron spectrometry measurements. *Nucl. Fusion*, 55(5):053013, May 2015.
- [18] A.S. Jacobsen. Methods to determine fast-ion distribution functions from multi-diagnostic measurements. *PhD thesis*, 2015.
- [19] A. S. Jacobsen *et al.* Benchmark and combined velocity-space tomography of fast-ion D-Alpha spectroscopy and collective Thomson scattering measurements. *Plasma Phys. Control. Fusion*, 58:042002, 2016.

- [20] A. S. Jacobsen *et al.* Inversion methods for fast-ion velocity-space tomography in fusion plasmas. *Plasma Phys. Control. Fusion*, 58:045016, 2016.
- [21] A. S. Jacobsen *et al.* Velocity-space sensitivities of neutron emission spectrometers at JET and ASDEX Upgrade. *Rev. Sci. Instrum.*, 88:073506, 2017.
- [22] B. Madsen *et al.* Velocity-space tomography using prior information at MAST. *Rev. Sci. Instrum.*, 89:10D125, 2018.
- [23] B. Madsen *et al.* Velocity-space tomography at DIII-D. *in preparation*, 2019.
- [24] B. Geiger *et al.* Quantification of the impact of large and small-scale instabilities on the fast-ion confinement in ASDEX Upgrade. *Plasma Phys. Control. Fusion*, 57(1):014018, January 2015.
- [25] B. Geiger *et al.* Fast-ion transport and neutral beam current drive in ASDEX Upgrade. *Nucl. Fusion*, 55:083001, 2015.
- [26] J. Eriksson *et al.* Dual sightline measurements of MeV range deuterons with neutron and gamma-ray spectroscopy at JET. *Nucl. Fusion*, 55(12):123026, 2015.
- [27] M. Weiland *et al.* Enhancement of the FIDA diagnostic at ASDEX Upgrade for velocity-space tomography. *Plasma Phys. Control. Fusion*, 58:025012, 2016.
- [28] M. Schneider *et al.* Modelling third harmonic ion cyclotron acceleration of deuterium beams for jet fusion product studies experiments. *Nucl. Fusion*, 56:112022, 2016.
- [29] F. Jaulmes *et al.* Numerical and experimental study of the redistribution of energetic and impurity ions by sawteeth in ASDEX Upgrade. *Nucl. Fusion*, 56:112012, 2016.
- [30] J. Rasmussen *et al.* Consistency between real and synthetic fast-ion measurements at ASDEX Upgrade. *Plasma Phys. Control. Fusion*, 57:075014, 2015.

- [31] J. Rasmussen *et al.* Collective Thomson scattering measurements of fast-ion transport due to sawtooth crashes in ASDEX Upgrade. *Nucl. Fusion*, 56:112014, 2016.
- [32] B. Geiger *et al.* Study of the fast-ion distribution function in the tcv tokamak based on fida spectroscopy and the transp code. *Plasma Phys. Control. Fusion*, 59:115002, 2017.
- [33] M. Weiland *et al.* Phase-space resolved measurement of 2nd harmonic ion cyclotron heating using fida tomography at the asdex upgrade tokamak. *Nucl. Fusion*, 57:116058, 2017.
- [34] M. Nocente *et al.* Conceptual design of the radial gamma ray spectrometers system for alpha-particle and runaway electron measurements at ITER. *Nucl. Fusion*, 57:076016, 2017.
- [35] J. Galdon-Quiroga *et al.* Beam-Ion Acceleration during Edge Localized Modes in the ASDEX Upgrade Tokamak. *Phys. Rev. Lett.*, 121:025002, 2018.
- [36] J. Galdon-Quiroga *et al.* Velocity-space sensitivity and tomography of scintillator-based fast-ion loss detectors. *Plasma Phys. Control. Fusion*, 60:105005, 2018.
- [37] M. Nocente *et al.* High resolution gamma-ray spectrometer with MHz capabilities for runaway electron studies at ASDEX Upgrade. *Rev. Sci. Instrum.*, 89:10I124, 2018.
- [38] J. Eriksson *et al.* Measuring fast ions in fusion plasmas with neutron diagnostics at JET. *Plasma Phys. Control. Fusion*, 61:014027, 2019.
- [39] D. Moseev, M. Salewski, M. Garcia-Munoz, B. Geiger, and M. Nocente. Recent progress in fast-ion diagnostics for magnetically confined plasmas. *Rev. Mod. Plasma Phys.*, 2:7, December 2018.
- [40] D. Moseev and M. Salewski. Bi-maxwellian, slowing-down, and ring velocity distributions of fast ions in magnetized plasmas. *Phys. Plasma*, 26:020901, 2019.
- [41] International Energy Agency. *Key World Energy Statistics 2018*. IEA, Paris, 2018.

- [42] International Energy Agency. *World Energy Outlook 2016*. OECD Publishing, Paris/IEA, Paris, 2016.
- [43] Intergovernmental Panel on Climate Change, [Core Writing Team, R.K. Pachauri and L.A. Meyer (eds.)]. *Climate Change 2014: Synthesis Report. Contribution of Working Groups I, II and III to the Fifth Assessment Report of the Intergovernmental Panel on Climate Change*. IPCC, Geneva, Switzerland, 2014.
- [44] K.-H. Kim *et al.* A review on the human health impact of airborne particulate matter. *Environment International*, 74:136–143, 2015.
- [45] J. D. Lawson. Some Criteria for a Power Producing Thermonuclear Reactor. *Proc. Phys. Soc. B.*, 70:6, 1957.
- [46] M. Shimada *et al.* Progress in the ITER Physics Basis Chapter 1: Overview and Summary. *Nucl. Fusion*, 47:S1–S17, 2007.
- [47] G. Giruzzi *et al.* Modelling of pulsed and steady-state DEMO scenarios. *Nucl. Fusion*, 55:073002, 2015.
- [48] R. Wenninger *et al.* Advances in the physics basis for the European DEMO design. *Nucl. Fusion*, 55:063003, 2015.
- [49] R. Wenninger *et al.* The physics and technology basis entering European system code studies for DEMO. *Nucl. Fusion*, 57:016011, 2017.
- [50] www.euro-fusion.org. accessed in December 2018.
- [51] T. Klinger *et al.* Overview of first Wendelstein 7-X high-performance operation. *Nucl. Fusion*, 59:at press, 2019.
- [52] ITER Organization. ITER Research Plan within the Staged Approach. 2018.
- [53] M. Keilhacker *et al.* High fusion performance from deuterium-tritium plasmas in JET. *Nucl. Fusion*, 39:209–234, 1999.
- [54] F. Romanelli. Overview of the JET results. *Nucl. Fusion*, 55(10):104001, October 2015.
- [55] X. Litaudon *et al.* Overview of the JET results in support to ITER. *Nucl. Fusion*, 57:102001, 2017.

- [56] W.W. Heidbrink and G.J. Sadler. The behaviour of fast ions in tokamak experiments. *Nucl. Fusion*, 34(4):535–615, April 1994.
- [57] K.-L. Wong. A review of Alfvén eigenmode observations in toroidal plasmas. *Plasma Phys. Control. Fusion*, 41:R1, 1999.
- [58] J. Jacquinot *et al.* ITER Physics Basis Chapter 5: Physics of energetic ions. *Nuclear Fusion*, 39(12):2471–2495, 1999.
- [59] S.J. Zweben *et al.* Alpha particle physics experiments in the Tokamak Fusion Test Reactor. *Nucl. Fusion*, 40:91–149, 2000.
- [60] A. Fasoli *et al.* Progress in the ITER Physics Basis Chapter 5: Physics of energetic ions. *Nucl. Fusion*, 47:S264–S284, 2007.
- [61] B.N. Breizman and S.E. Sharapov. Major minority: energetic particles in fusion plasmas. *Plasma Phys. Control. Fusion*, 53:054001, 2011.
- [62] S.E. Sharapov *et al.* Energetic particle instabilities in fusion plasmas. *Nucl. Fusion*, 53(10):104022, 2013.
- [63] N.N. Gorelenkov, S.D. Pinches, and K. Toi. Energetic particle physics in fusion research in preparation for burning plasma experiments. *Nuclear Fusion*, 54:125001, 2014.
- [64] S.D. Pinches *et al.* Energetic ions in ITER plasmas. *Physics of Plasmas*, 22:021807, 2015.
- [65] L. Chen and F. Zonca. *Rev. Mod. Phys.*, 88:015008, 2016.
- [66] K.G. McClements and E.D. Fredrickson. Energetic particles in spherical tokamak plasmas. *Plasma Phys. Control. Fusion*, 59:053001, 2017.
- [67] Y. Todo. Introduction to the interaction between energetic particles and alfvén eigenmodes in toroidal plasmas. *Rev. Mod. Plasma Phys.*, 3:1, 2019.
- [68] L. Stagner and W.W. Heidbrink. Action-angle formulation of generalized, orbit-based, fast-ion diagnostic weight functions. *Phys. Plasmas*, 24:092505, 2017.

- [69] L.E. Stagner. Inference of the fast-ion distribution function. *PhD thesis*, 2018.
- [70] A. Pankin *et al.* The tokamak Monte Carlo fast ion module NUBEAM in the National Transport Code Collaboration library. *Comp. Phys. Comm.*, 159(3):157–184, June 2004.
- [71] S.B. Korsholm *et al.* Collective Thomson scattering capabilities to diagnose fusion plasmas. *Nucl. Instrum. Meth. Phys. Res. A*, 623(2):677–680, November 2010.
- [72] S.K. Nielsen *et al.* Measurements of the fast-ion distribution function at ASDEX upgrade by collective Thomson scattering (CTS) using active and passive views. *Plasma Phys. Control. Fusion*, 57(3):035009, March 2015.
- [73] W.W. Heidbrink *et al.* Measurements of fast-ion acceleration at cyclotron harmonics using Balmer-alpha spectroscopy. *Plasma Phys. Control. Fusion*, 49(9):1457–1475, September 2007.
- [74] M. Nocente. *Neutron and gamma-ray emission spectroscopy as fast ion diagnostics in fusion plasmas*. PhD thesis, 2012.
- [75] J. Eriksson *et al.* Calculating fusion neutron energy spectra from arbitrary reactant distributions. *Comp. Phys. Comm.*, 199:40–46, 2016.
- [76] M. Gatu Johnson *et al.* The 2.5-MeV neutron time-of-flight spectrometer TOFOR for experiments at JET. *Nucl. Inst. Meth. Phys. Res. A*, 591:417–430, 2008.
- [77] F. Binda *et al.* Forward fitting of experimental data from a NE213 neutron detector installed with the magnetic proton recoil upgraded spectrometer at JETa). *Rev. Sci. Instrum.*, 85:11E123, 2014.
- [78] C. Cazzaniga *et al.* Single crystal diamond detector measurements of deuterium-deuterium and deuterium-tritium neutrons in Joint European Torus fusion plasmas. *Review of Scientific Instruments*, 85:043506, 2014.
- [79] M. Nocente *et al.* Fast ion energy distribution from third harmonic radio frequency heating measured with a single crystal diamond

- detector at the Joint European Torus. *Review of Scientific Instruments*, 86:103501, 2015.
- [80] A. Muraro *et al.* First neutron spectroscopy measurements with a pixelated diamond detector at JET. *Review of Scientific Instruments*, 87:11D833, 2016.
- [81] V.G. Kiptily, F.E. Cecil, and S.S. Medley. Gamma ray diagnostics of high temperature magnetically confined fusion plasmas. *Plasma Phys. Control. Fusion*, 48(8):R59–R82, August 2006.
- [82] M. Tardocchi, M. Nocente, and G. Gorini. Diagnosis of physical parameters of fast particles in high power fusion plasmas with high resolution neutron and gamma-ray spectroscopy. *Plasma Phys. Control. Fusion*, 55(7):074014, July 2013.
- [83] V.G. Kiptilyj. Capabilities of Gamma Spectroscopy for Fast Alpha-Particle Diagnostics. *Fusion Science and Technology*, 18(4):583–590, December 1990.
- [84] V.G. Kiptilyj *et al.* In-Beam Study of the ${}^9\text{Be}(\alpha, n\gamma){}^{12}\text{C}$ Reaction and Alpha-Particle Diagnostics. *Fusion Science and Technology*, 22(4):454–460, December 1992.
- [85] W.W. Heidbrink *et al.* Hydrogenic fast-ion diagnostic using Balmer-alpha light. *Plasma Phys. Control. Fusion*, 46(12):1855–1875, December 2004.
- [86] W.W. Heidbrink. Fast-ion $D\alpha$ measurements of the fast-ion distribution (invited). *Rev. Sci. Instrum.*, 81(10):10D727, October 2010.
- [87] W.W. Heidbrink *et al.* ‘Beam-emission spectroscopy’ diagnostics also measure edge fast-ion light. *Plasma Phys. Control. Fusion*, 53(8):085007, August 2011.
- [88] E. Fermi. Quantum theory of radiation. *Rev. Mod. Phys.*, 4:87–132, 1932.
- [89] M. García-Muñoz. Fast Response Scintillator Based Detector for MHD Induced Energetic Ion Losses in ASDEX Upgrade. *PhD thesis*, 2006.

- [90] W.W. Heidbrink *et al.* A new fast-ion D(alpha) diagnostic for DIII-D. *Rev. Sci. Instrum.*, 79(10):10E520, October 2008.
- [91] W.W. Heidbrink *et al.* Fast-ion D-alpha diagnostic for NSTX. *Rev. Sci. Instrum.*, 77(10):10F120, October 2006.
- [92] Y. Luo *et al.* Measurement of the D alpha spectrum produced by fast ions in DIII-D. *Rev. Sci. Instrum.*, 78(3):033505, March 2007.
- [93] M. Podestaá *et al.* The NSTX fast-ion D-alpha diagnostic. *Rev. Sci. Instrum.*, 79(10):10E521, October 2008.
- [94] M.A. Van Zeeland *et al.* Fast ion D α imaging in the DIII-D tokamak. *Plasma Phys. Control. Fusion*, 51(5):055001, May 2009.
- [95] M. Podestá *et al.* Experimental studies on fast-ion transport by Alfvé wave avalanches on the National Spherical Torus Experiment. *Physics of Plasmas*, 16(5):056104, March 2009.
- [96] M.A. Van Zeeland *et al.* Imaging key aspects of fast ion physics in the DIII-D tokamak. *Nucl. Fusion*, 50(8):084002, August 2010.
- [97] A. Bortolon *et al.* A tangentially viewing fast ion D-alpha diagnostic for NSTX. *Rev. Sci. Instrum.*, 81(10):10D728, October 2010.
- [98] C.A. Michael *et al.* Dual view FIDA measurements on MAST. *Plasma Phys. Control. Fusion*, 55(9):095007, September 2013.
- [99] O.M. Jones *et al.* Measurements and modelling of fast-ion redistribution due to MHD instabilities in the Mega-Amp Spherical Tokamak. *Plasma Phys. Control. Fusion*, 57:125009, 2015.
- [100] M. García-Muñoz *et al.* Fast-ion transport induced by Alfvén eigenmodes in the ASDEX Upgrade tokamak. *Nucl. Fusion*, 51(10):103013, October 2011.
- [101] B. Geiger *et al.* Fast-ion D-alpha measurements at ASDEX Upgrade. *Plasma Phys. Control. Fusion*, 53(6):065010, June 2011.
- [102] C.M. Muscatello *et al.* Velocity-space studies of fast-ion transport at a sawtooth crash in neutral-beam heated plasmas. *Plasma Phys. Control. Fusion*, 54(2):025006, February 2012.

- [103] B. Geiger *et al.* Multi-view fast-ion D-alpha spectroscopy diagnostic at ASDEX Upgrade. *Rev. Sci. Instrum.*, 84(11):113502, November 2013.
- [104] D.C. Pace *et al.* Energetic ion transport by microturbulence is insignificant in tokamaks. *Physics of Plasmas*, 20(5):056108, May 2013.
- [105] W.W. Heidbrink *et al.* Confinement degradation by Alfvén-eigenmode induced fast-ion transport in steady-state scenario discharges. *Plasma Phys. Control. Fusion*, 56(9):095030, September 2014.
- [106] B. Geiger *et al.* Fast-ion transport in the presence of magnetic reconnection induced by sawtooth oscillations in ASDEX Upgrade. *Nucl. Fusion*, 54(2):022005, February 2014.
- [107] B. Geiger. *Fast-ion transport studies using FIDA spectroscopy at the ASDEX Upgrade tokamak*. Phd, Ludwig-Maximilians-Universität München, 2013.
- [108] M. Weiland. Influence of RF heating and MHD instabilities on the fast-ion distribution in ASDEX Upgrade. *PhD thesis*, 2016.
- [109] L.J. Ge *et al.* Velocity-space sensitivity of time-of-flight neutron spectrometer at EAST in deuterium plasma. *Rev. Sci. Instrum.*, 89:10I143, 2018.
- [110] Y.M. Zhang *et al.* Velocity-space sensitivity of the compact neutron emission spectrometers at EAST. *Rev. Sci. Instrum.*, 89:10I141, 2018.
- [111] M. Nocente *et al.* Gamma-ray emission spectrum from thermonuclear fusion reactions without intrinsic broadening. *Nucl. Fusion*, 55(12):123009, nov 2015.
- [112] A.J.H. Donné *et al.* Progress in the ITER Physics Basis Chapter 7: Diagnostics. Chapter 7: Diagnostics. *Nucl. Fusion*, 47(6):S337–S384, June 2007.
- [113] W.W. Heidbrink *et al.* A Code that Simulates Fast-Ion D(alpha) and Neutral Particle Measurements. *COMMUNICATIONS IN COMPUTATIONAL PHYSICS*, 10(3):716–741, 2011.

- [114] R. McWilliams and R. Koslover. Laboratory Observation of Ion Conics by Velocity-Space Tomography of a Plasma. *Phys. Rev. Lett.*, 58(1):37–40, 1987.
- [115] T.R. Marsh and K. Horne. IMAGES OF ACCRETION DISKS .2. DOPPLER TOMOGRAPHY. *MONTHLY NOTICES OF THE ROYAL ASTRONOMICAL SOCIETY*, 235(1):269 – 286, 1988.
- [116] T.R. Marsh. Doppler Tomography. In *LNP Vol. 573: Astrotomography, Indirect Imaging Methods in Observational Astronomy*, pages 1–26. 2001.
- [117] T.R. Marsh. Doppler Tomography. *Astrophysics and Space Science*, 296(1-4):403–415, April 2005.
- [118] D. Steeghs. Doppler tomography of accretion in binaries. *Astronomische Nachrichten*, 325(3):185–188, March 2004.
- [119] L. Morales-Rueda. Doppler tomography of cataclysmic variables. *Astronomische Nachrichten*, 325(3):193–196, March 2004.
- [120] A.D. Schwope *et al.* Indirect imaging of polars. *Astronomische Nachrichten*, 325(3):197–200, March 2004.
- [121] M. T. Richards. Doppler tomography of Algols. *Astronomische Nachrichten*, 325(3):229–232, March 2004.
- [122] S.D. Vrtílek *et al.* Doppler Tomography of X-ray binaries. *Astronomische Nachrichten*, 325(3):209–212, March 2004.
- [123] J. Egedal and H. Bindslev. Reconstruction of gyrotropic phase-space distributions from one-dimensional projections. *Physics of Plasmas*, 11(5):2191, April 2004.
- [124] P.C. Hansen. *Discrete Inverse Problems*. SIAM, Philadelphia, US, 2010.
- [125] C.L. Lawson and R.J. Hanson. *Solving Least Squares Problems*. Prentic-Hall, Englewood Cliffs, NJ, 1974.
- [126] H. Bindslev. *Rev. Sci. Instrum.*, 70:1093, 1999.

- [127] I. Abramovic *et al.* Collective Thomson Scattering Model For Arbitrarily Drifting Bi-Maxwellian Velocity Distributions. *AIP Advances*, 9:at press, 2019.

Reference [1]

[1]. M Salewski et al. (2010) *Nuclear Fusion* **50** 035012. Comparison of fast ion collective Thomson scattering measurements at ASDEX Upgrade with numerical simulations

Comparison of fast ion collective Thomson scattering measurements at ASDEX Upgrade with numerical simulations

M. Salewski¹, F. Meo¹, M. Stejner¹, O. Asunta², H. Bindslev¹,
V. Furtula¹, S.B. Korsholm¹, T. Kurki-Suonio², F. Leipold¹,
F. Leuterer³, P.K. Michelsen¹, D. Moseev¹, S.K. Nielsen¹,
J. Stober³, G. Tardini³, D. Wagner³, P. Woskov⁴ and the
ASDEX Upgrade team³

¹ Association Euratom - Risø National Laboratory for Sustainable Energy, Technical University of Denmark, DK-4000 Roskilde, Denmark

² Association Euratom - TEKES, Helsinki University of Technology, FI-02015 TKK, Finland

³ Association Euratom-Max-Planck-Institut für Plasmaphysik, D-85748 Garching, Germany

⁴ MIT Plasma Science and Fusion Center, Cambridge, MA 02139, USA

E-mail: msal@risoe.dtu.dk

Received 19 November 2009, accepted for publication 2 February 2010

Published 5 March 2010

Online at stacks.iop.org/NF/50/035012

Abstract

Collective Thomson scattering (CTS) experiments were carried out at ASDEX Upgrade to measure the one-dimensional velocity distribution functions of fast ion populations. These measurements are compared with simulations using the codes TRANSP/NUBEAM and ASCOT for two different neutral beam injection (NBI) configurations: two NBI sources and only one NBI source. The measured CTS spectra as well as the inferred one-dimensional fast ion velocity distribution functions are clearly asymmetric as a consequence of the anisotropy of the beam ion populations and the selected geometry of the experiment. As expected, the one-beam configuration can clearly be distinguished from the two-beam configuration. The fast ion population is smaller and the asymmetry is less pronounced for the one-beam configuration. Salient features of the numerical simulation results agree with the CTS measurements while quantitative discrepancies in absolute values and gradients are found.

PACS numbers: 52.25.Os, 52.40.Db, 52.50.Gj, 52.65.Cc, 52.70.Gw

1. Introduction

Medium-sized tokamaks such as ASDEX Upgrade are designed to confine hot plasmas with temperatures in the kiloelectronvolt range and are usually equipped with powerful auxiliary heating systems: neutral beam injection (NBI), ion cyclotron resonance heating (ICRH) or electron cyclotron resonance heating (ECRH) [1, 2]. The energetic ions generated by NBI and ICRH play a key role in heating the bulk plasma, and understanding fast ion physics is therefore essential. However, reliable predictions of fast ion motion still face many challenges: fast ions exhibit collective behaviour [3, 4] and can interact with magnetohydrodynamic (MHD) activity such as the family of Alfvén eigenmodes [5–8], sawteeth [9–12], kinetic ballooning modes [6, 13, 14], neoclassical tearing modes [6, 15] or the sierpes mode [16]. Fast

ions may also interact with turbulent fluctuations [17–19]. Theories describing such phenomena need to be tested against experimental data. The implications for ITER and tokamaks beyond are also far-reaching: the confinement of the bulk plasma and the fast ions may degrade due to such effects. Measurements of fast ion distributions have therefore been recognized as a milestone towards understanding plasmas in the burning regime [20, 21]. Millimetre wave collective Thomson scattering (CTS) has been demonstrated to provide measurements of one-dimensional velocity distribution functions of confined fast ions in various selected directions and locations in the plasma at JET [22], TEXTOR [23, 24] and ASDEX Upgrade [25, 26]; a fast ion CTS system at ITER is also foreseen [27–32]. CTS experiments at other machines have further contributed to the experience with millimetre wave CTS diagnostics [33–36]. For example, the ion temperature

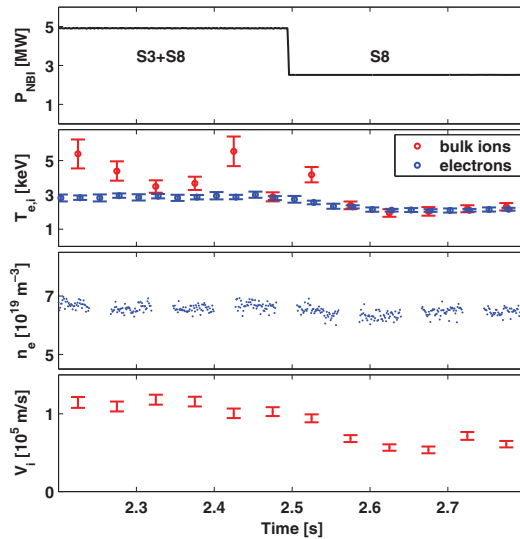


Figure 1. Time traces of NBI power, ion and electron temperatures, electron density and toroidal bulk ion drift velocity in the plasma centre in discharge 24089. Neutral beams S3 and S8 heated the plasma up to 2.5 s when beam S3 was switched off.

has been estimated by millimetre wave CTS at the W7-AS stellarator [37].

Here we report recent fast ion velocity distribution results obtained by CTS for different NBI configurations at ASDEX Upgrade. We compare the measurements with numerical simulations and describe methods for such a comparison. The experimental conditions are summarized in section 2 and the methods in section 3. The measured spectral power densities of scattered radiation are compared with synthetic CTS spectra calculated with a scattering model [38, 39] using fast ion velocity distributions obtained with the simulation codes TRANSP/NUBEAM [40, 41] or ASCOT [42, 43] (section 4.1). Moreover, the inferred one-dimensional fast ion velocity distributions obtained for this experiment are presented and compared with the simulations (section 4.2). We discuss perspectives and draw conclusions in sections 5 and 6.

2. CTS experiment at ASDEX Upgrade

2.1. Plasma parameters

The CTS measurements were carried out in a co-current NBI heated, standard H-mode plasma (discharge 24089). ASDEX Upgrade is equipped with two-beam boxes each containing four neutral beam injectors [44]. We used two of the injectors, namely source 3 (S3) and source 8 (S8). S3 and S8 have full acceleration energies of 60 keV and 93 keV in deuterium, respectively, and they have similar injection geometries. Both NBI sources (S3+S8) injected deuterium with a total power of about 5 MW (2×2.5 MW), until S3 was switched off. Fast ion populations in the plasma centre for both NBI configurations (S3+S8 and S8 only) were measured by CTS.

CTS spectra of scattered radiation depend not only on the fast ion velocity distribution function—the parameters

of interest—but also on other parameters which are not the goal of the measurement and encumber the data analysis—the nuisance parameters. Among the nuisance parameters are several bulk plasma parameters which we discuss here. Figure 1 shows time traces of the NBI power, the electron and ion temperatures, the electron density and the toroidal bulk ion drift velocity. The temperatures and the drift velocity decreased when beam S3 was turned off whereas the electron density was feedback controlled. From here on we shall use representative values to characterize the plasma for both NBI configurations: two beams (S3+S8) versus one beam (S8). These representative values and their 1σ confidence levels are given in table 1, which also contains additional plasma parameters affecting the CTS spectra: the magnetic field, the isotope ratio and impurity concentrations. The ion temperature and bulk ion drift velocity were obtained from the charge exchange diagnostic, the electron temperature from (non-collective) Thomson scattering [45], the electron density from the integrated data analysis (IDA) [46–49], the isotope ratio from a neutral particle analyzer, and the impurity content was estimated by spectroscopy [50].

2.2. CTS experiment description

In CTS experiments at ASDEX Upgrade, a probe beam of millimetre waves is launched into the plasma, and radiation is scattered off microscopic fluctuations in the plasma. Part of this scattered radiation is collected by a receiver with a quasi-optical antenna and resolved into frequency intervals. The acceptance cone of the antenna, referred to as the receiver beam, is defined by the antenna design. Information about the fast ions can be inferred from the spectral power density of the scattered radiation. The measurement is spatially resolved at the location where probe and receiver beam patterns intersect. This location is called the scattering volume and lies near the plasma centre at $R = 1.7$ m and $z = 0.1$ m in this experiment. The scattering geometry is sketched in poloidal and toroidal views in figures 2(a) and (b), respectively. CTS enables measuring the fast ion velocity distribution projected onto the fluctuation wave vector $k^\delta = k^s - k^i$ where the superscripts s and i refer to scattered and incident radiation, respectively. The spectral content of the scattered radiation bears a signature of the ion velocity distribution since the CTS system at ASDEX Upgrade satisfies Salpeter's condition [51]: $|\lambda_D k^\delta| < 1$ where λ_D is the Debye length. A frequency shift in scattered radiation, ν^δ , can be approximately related to an ion velocity, v_{ion} , by $\nu^\delta = \nu^s - \nu^i \approx v_{ion} \cdot k^\delta / 2\pi$.

In discharge 24089 the incident gyrotron power was $P_i = 250$ kW at an average frequency of $F_i = 104.93$ GHz [25, 26, 52]. The geometry and gyrotron parameters for the CTS experiment and their estimated uncertainties are summarized in table 2. The resolved angle $\phi = \angle(k^\delta, B)$, the scattering angle $\theta = \angle(k^i, k^s)$ and the less important azimuthal angle ψ describe the scattering geometry. The so-called beam overlap O_b accounts for the effects of the widths of the probe and receiver beam patterns and for the extent to which they overlap in the plasma [38, 39]. The role of the overlap in our comparison is explained in section 4.1. This set of CTS system parameters (table 2) and the set of plasma parameters (table 1) form the set of nuisance parameters mentioned in section 2.1.

Table 1. Parameters of the plasma in discharge 24089 at the location of the CTS scattering volume ($\rho_{\text{pol}} = 0$) and their estimated 1σ uncertainties. The parameters are given separately for the NBI configurations with two beams (S3+S8) and one beam (S8). Z stands for the impurity ion charge and m for the mass.

Parameter	Symbol	2 NBIs	1 NBI
Magnetic field	B_{mod}	2.6 ± 0.1 T	2.6 ± 0.1 T
Electron density	n_e	$6.6 \pm 0.3 \times 10^{19} \text{ m}^{-3}$	$6.5 \pm 0.3 \times 10^{19} \text{ m}^{-3}$
Electron temperature	T_e	2.9 ± 0.3 keV	2.2 ± 0.3 keV
Ion temperature	T_i	3.7 ± 0.5 keV	2.1 ± 0.5 keV
Ion drift velocity	V_i	$1.1 \pm 0.6 \times 10^5 \text{ m s}^{-1}$	$0.6 \pm 0.6 \times 10^5 \text{ m s}^{-1}$
Isotope ratio $n_{\text{H}}/(n_{\text{H}} + n_{\text{D}})$	R_i	0.03 ± 0.02	0.03 ± 0.02
Impurity ($Z/m = 6/12$) n_{11}/n_e	N_{11}	0.005 ± 0.005	0.005 ± 0.005
Impurity ($Z/m = 50/184$) n_{12}/n_e	N_{12}	0.0005 ± 0.0005	0.0005 ± 0.0005

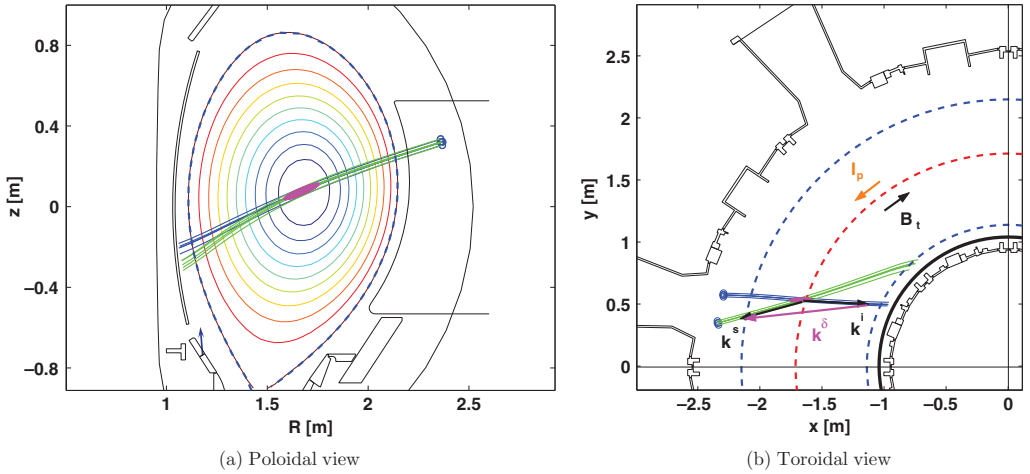


Figure 2. Ray tracing for the scattering geometry in discharge 24089 projected into the poloidal and toroidal planes, respectively. The probe beam is plotted in blue, the receiver beam in green. Both have O-mode polarization. The scattering volume lies at the intersection of probe and receiver beams and is illustrated in magenta. In (b) viewing the torus from the top, the directions of the toroidal magnetic field B_t , the plasma current I_p and the projected wave vectors k^δ , k^i and k^s are indicated. The dashed lines represent the magnetic axis (red) and the last closed flux surface (blue).

Table 2. CTS system parameters for the experiment in discharge 24089 and their estimated 1σ confidence intervals. The orientations of the vectors k^δ , k^i , k^s and B are sketched in figure 2(b).

Parameter	Symbol	Value
Resolved angle $\angle(k^\delta, B)$	ϕ	$122 \pm 1^\circ$
Scattering angle $\angle(k^i, k^s)$	θ	$161 \pm 1^\circ$
Azimuthal angle of B when $\hat{z} \parallel k^\delta$ and $\hat{x} \parallel (k^i \times k^s)$	ψ	$-95 \pm 1^\circ$
Gyrotron power	P_i	250 ± 20 kW
Gyrotron frequency	F_i	104.93 ± 0.01 GHz
Beam overlap	O_b	$70 \pm 30 \text{ m}^{-1}$

The magnetic field in discharge 24089 was 2.6 T on axis, placing the cold electron cyclotron resonances near the plasma edge so as to avoid large levels of electron cyclotron emission (ECE) background radiation and plasma heating. The ECE background is the largest contribution to CTS noise and amounts to several tens of electronvolts against which a CTS signal on the order of 1–10 eV has to be observed (for large frequency shift). The gyrotron is modulated in order

to estimate the ECE background. The ECE background in the periods in which the gyrotron fires can then be estimated from the ECE background in the periods in which the gyrotron is off. The ECE background estimation turned out to be more cumbersome for ASDEX Upgrade plasmas compared with TEXTOR plasmas [23, 24] due to the fast time-scale MHD activity in typical ASDEX Upgrade plasmas, and a new approach to estimate the ECE background was adopted [26]. The ECE background is estimated using channels in which no CTS signal is expected. The uncertainty due to the ECE background subtraction was estimated by applying the formalism to plasmas without gyrotron operation. Here the estimated ECE background could be compared with the measured ECE background. The discrepancies between the estimated and measured ECE background were found to be smaller than the pulse-to-pulse variation of the measured CTS signal. In this work we present data which are averaged over 15 gyrotron pulses spanning 75 ms, and the uncertainty of the measurement in each channel is given by the standard deviation of the time series. The radial extent of the scattering volume in this experiment was approximately 10 cm as illustrated in

figure 2. A more detailed description of the system parameters and the capabilities of CTS at ASDEX Upgrade can be found in [25, 26].

3. Methods for CTS data analysis

Experimental CTS results can be compared with theoretical expectations in two complementary ways: either in frequency space, if a synthetic CTS spectrum is calculated from theoretical ion and electron velocity distributions, or in velocity space, if the one-dimensional fast ion velocity distribution $g(u)$ is inferred from the experimental CTS spectra. The velocity space comparison has the advantage that it is the velocity distribution $g(u)$ that one is actually interested in. On the other hand, the frequency space comparison has the advantage that the spectral power density is the quantity that is directly measured with the CTS receiver. The latter option is presented in section 4.1 and the former in section 4.2. We thus need to find the experimental and the simulated $g(u)$ and the experimental and the synthetic spectral power densities which are obtained by methods explained in the following three sections.

3.1. Forward model of CTS and synthetic spectra

The forward model provides a mapping from velocity space to frequency space [38, 39]: if the velocity distributions of fast ions (see section 3.2), bulk ions and electrons as well as the nuisance parameters are known, the expected CTS spectrum can be calculated [31, 53]. Not only do calculated spectra rely on this forward model but also the estimation of $g(u)$ from the measured spectra (section 3.3). The comparison of experimental and numerical data therefore also depends on the forward model. Predicted spectra are calculated using the best available estimates for the plasma and CTS system parameters (tables 1 and 2). The spectral power density of the scattered radiation $\partial P^s / \partial \nu^s$ is calculated as

$$\frac{\partial P^s}{\partial \nu^s} = P_i O_b n_e \lambda_0^i r_e^2 \frac{1}{2\pi} \Sigma, \quad (1)$$

where λ_0^i is the vacuum wavelength of the probe radiation, r_e the classical electron radius and Σ the scattering function that gives the spectral shape [38, 39]. This forward model is derived from a kinetic, fully electromagnetic description of the scattering process, and it accounts for fluctuations in electron density, in the electric and magnetic fields, and in the electron current density.

Figure 3 shows a synthetic CTS spectrum calculated using this forward model for the NBI configuration with two beams (S3+S8). The bulk ion species are assumed to consist of deuterium, hydrogen, carbon and tungsten with Maxwellian velocity distributions parametrized by a common bulk ion temperature and toroidal drift velocity with densities of the various ion species as given in table 1. However, the deuterium velocity distribution function is the sum of the beam ion velocity distribution function $g(u)$ (section 3.2) and the Maxwellian distribution for the bulk deuterium. The electrons are assumed to have a Maxwellian distribution characterized by the electron temperature and density. The various species in the plasma each contribute a component to the CTS spectrum given by their assumed velocity distributions. The bulk ion feature

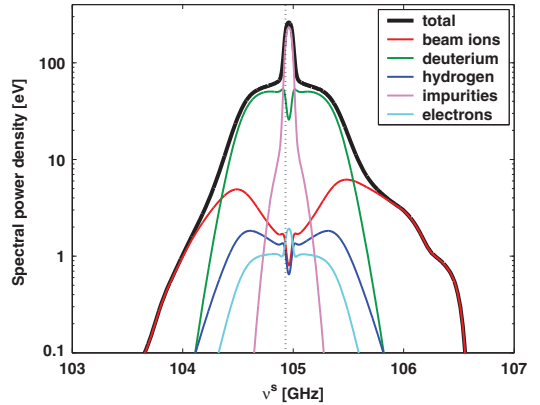


Figure 3. Synthetic CTS spectrum for the two-beam phase (S3+S8) in discharge 24089. The spectrum was calculated using the data from tables 1 and 2 and the fast ion distribution simulated with TRANSP/NUBEAM shown in figure 4(a). The total signal is the sum of the individual contributions indicated in this figure. The dotted line marks the gyrotron frequency.

dominates the spectrum from 104.3 to 105.5 GHz, the main contributions coming from deuterium and impurities. Note that the bulk ion feature has a small frequency shift from the gyrotron frequency due to the assumed bulk ion drift velocity. The beam ions are clearly the largest contributor to the CTS spectrum for frequencies above 105.5 and below 104.3 GHz in this configuration. The asymmetry of the fast ion feature is a consequence of the asymmetry of the one-dimensional beam ion velocity distribution function to be discussed in section 3.2.

3.2. Simulation models for the fast ion velocity distributions

In this section we describe how to obtain one-dimensional velocity distribution functions $g(u)$ from numerical simulation with the help of the widely used transport code TRANSP coupled with the neutral beam module NUBEAM [40, 41] or the test-particle Monte Carlo code ASCOT [42, 43]. The simulation codes compute the two-dimensional fast ion distribution $f(v_{\parallel}, v_{\perp})$ at the location of the scattering volume where v_{\parallel} and v_{\perp} refer to the velocity components parallel and perpendicular to the magnetic field, respectively. We compare the CTS results with both sets of simulation results (from TRANSP/NUBEAM and from ASCOT). A full comparison of the two codes is, however, beyond the scope of this work. The steady-state velocity space distribution of beam ions originating from S3 and S8, as computed with ASCOT and TRANSP/NUBEAM, is presented in figure 4. The largest velocity space densities for these beams are found at a pitch angle of 120° . The rotationally symmetric distribution $f(v_{\parallel}, v_{\perp})$ is then projected onto the resolved direction \mathbf{k}^δ indicated in figure 4. The projection $g(u)$ of the full velocity distribution function $f(v_{\parallel}, v_{\perp})$ along the direction of \mathbf{k}^δ is given by

$$g(u) = \int d\mathbf{v} f \delta \left(\frac{\mathbf{v} \cdot \mathbf{k}^\delta}{k^\delta} - u \right), \quad (2)$$

where $\delta()$ is the Dirac δ -function and u is the resolved one-dimensional velocity component.

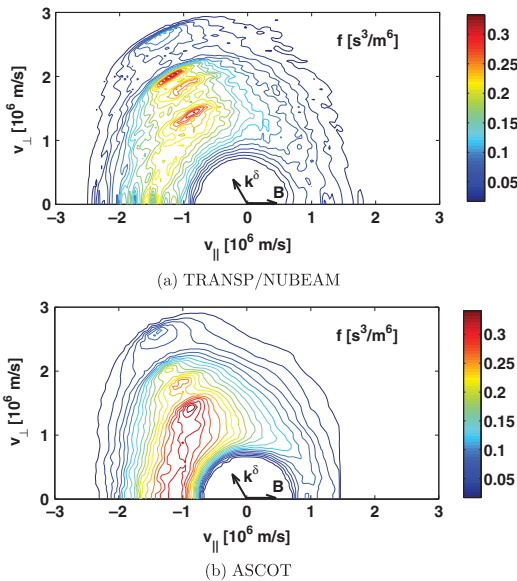


Figure 4. Equally spaced contours of the beam ion velocity distribution f in the scattering volume ($R = 1.7$ m, $z = 0.1$ m) computed with TRANSP/NUBEAM (a) and ASCOT (b) for heating with S3 and S8. The bulk ion distribution is not plotted in this figure, leading to low densities near the origin. The directions of the magnetic field B and k^δ are indicated.

We illustrate the projection of the rotationally invariant function f onto k^δ in figure 5, using ASCOT data as an example. The rotation axis B and k^δ define a plane which slices through the three-dimensional, rotationally invariant function f . The resolved angle in the experiment was $\phi = \angle(k^\delta, B) = 122^\circ$ indicated as the bold red line in figure 5(a). Additionally, other options for resolved directions are shown for illustration: $\phi = 20^\circ$, $\phi = 90^\circ$ and $\phi = 160^\circ$. Resolved angles of $\phi = 20^\circ$ and $\phi = 160^\circ$ are at the limits of the steering capability of the CTS antenna system at ASDEX Upgrade. The corresponding projections $g(u)$ onto these resolved directions k^δ are plotted in figure 5(b). If the resolved direction is $\phi = 90^\circ$, the projection of f onto k^δ will be symmetric about $u = 0$. For resolution as close to parallel to the magnetic field as possible, $\phi = 20^\circ$ or $\phi = 160^\circ$, the projection becomes very asymmetric. These two projections are mirror images of each other. For the resolved angle chosen in this experiment, $\phi = 122^\circ$, $g(u)$ is asymmetric about $u = 0$ which leads to the asymmetry in the computed spectra described in section 3.1. For this angle a finite phase space density exists at the largest values of the velocity component u . Scattering is then found at the largest possible frequency upshift with this angle. Thus, the spectral range of the CTS receiver for frequency upshift is exploited optimally for this angle.

3.3. Inference of the fast ion velocity distribution from CTS measurements

The inference of the one-dimensional fast ion velocity distribution $g(u)$ and of its estimated uncertainty—

demands the solution to an inverse problem. Direct operators mapping from frequency space (the measured CTS spectrum) to velocity space are not available whereas a forward model mapping from velocity space to frequency space has been formulated (section 3.1) [38, 39]. The velocity distribution $g(u)$ is obtained from the measured spectra by a least square fitting procedure using this forward model. Uncertainties in the nuisance parameters and in the measured spectral power density are accounted for. Assuming normal distributions for the measured spectral power densities and the nuisance parameters, one can derive expressions for the misfit between the experimental data and the expectation [54]. The nuisance parameters and their uncertainties are summarized in tables 1 and 2.

We demonstrate the inference in figure 6 for the simulated one-dimensional fast ion distribution function $g(u)$. A synthetic spectrum based on this distribution function and the nuisance parameters in tables 1 and 2 was displayed in figure 3. We infer $g(u)$, given only the synthetic spectrum and the nuisance parameters as well as their uncertainties. We assume the uncertainties of the synthetic spectrum to be given by the measurement uncertainties of the actual experiment. In the inference we make use of the full spectrum, except for the parts which are blocked by the notch filter in the experiment. In this way the inference is demonstrated for experimental conditions. The inference should then ideally be identical to the fast ion distribution function used to calculate the synthetic spectrum. Figure 6 demonstrates that the underlying fast ion distributions can be inferred from the synthetic spectra with good accuracy.

4. Results

4.1. Comparison of measured and synthetic CTS spectra

Figure 7 presents a comparison of experimentally obtained spectra against synthetically generated spectra, such as the one shown in figure 3, for both NBI configurations (S3+S8 and S8 only). The synthetic spectra obtained on the basis of TRANSP/NUBEAM or ASCOT simulations agree reasonably well with each other, especially for large frequency shifts. We note several points of agreement between the simulations and the measurements. First, there is a clear asymmetry about the gyrotron frequency due to the presence of beam ions in the measurement and in the simulation, the reason for which we explained in sections 3.1 and 3.2. Second, the larger particle density of beam ions in the two-beam phase (S3+S8) is reflected in the larger spectral power densities for frequencies above 105.5 GHz. When neutral beam S3 is switched off, the spectral power density above 105.5 GHz drops significantly compared with the error bars. We attribute this to a smaller population of fast ions (see section 4.2). Measurements and simulations agree in this respect. Third, the bulk ion feature from 104.3 to 105.5 GHz is measured to be narrower due to the ion temperature drop after 2.5 s as was expected according to simulation.

However, there are quantitative discrepancies between the simulation and the experiment. To point these out, we need to address the sensitivity of the synthetic spectra to changes in plasma parameters affecting the spectra. The sensitivity of the

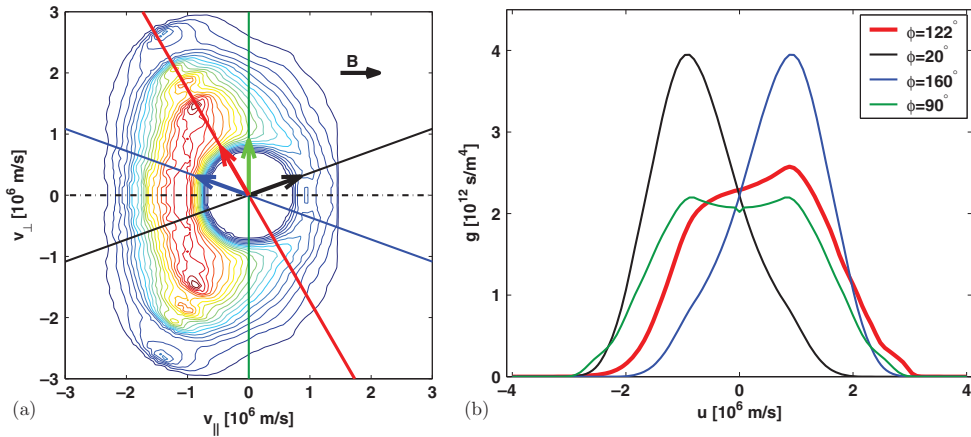


Figure 5. Illustration of the projection of the rotationally symmetric function f from ASCOT onto k^δ . The straight coloured lines represent various options for the resolved angle $\phi = \angle(k^\delta, B)$. The bold red line is at an angle of $\phi = 122^\circ$ and is selected for this experiment. (a) Slice through the rotationally symmetric fast ion distribution plotted in figure 4(b). The plane contains k^δ and the rotation axis B . (b) Corresponding one-dimensional fast ion distribution functions $g(u)$ for various resolved angles ϕ . The entire three-dimensional rotationally symmetric function f is projected onto k^δ .

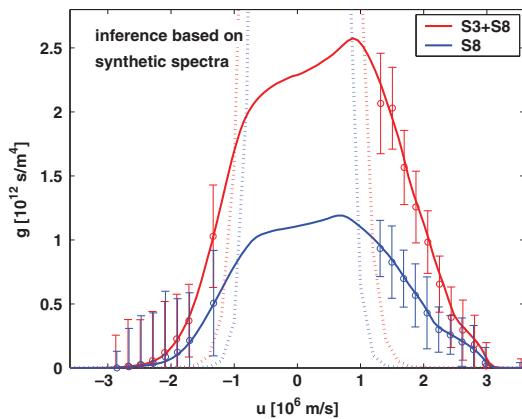


Figure 6. Comparison of the simulated one-dimensional fast ion velocity distributions $g(u)$ and the inference from synthetic spectra based on these simulated distributions. The plasma is assumed to be heated by two beams (S3+S8, red) and one beam (S8, blue). —, ASCOT; \circ , inference based on synthetic spectrum; \cdots , bulk ions. We plot the inferred fast ion distributions for velocities larger than typical for the bulk ions.

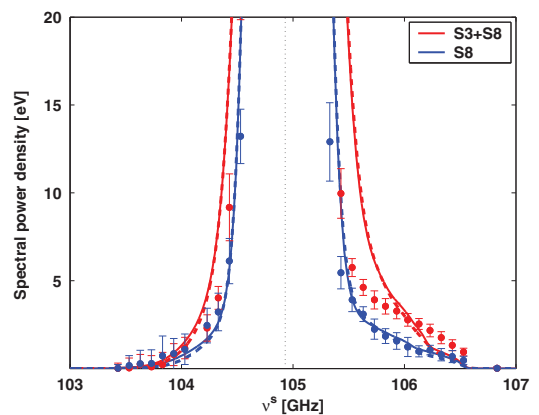


Figure 7. Comparison of measured and synthetic CTS spectra for discharge 24089 for auxiliary heating with two NBI sources (S3+S8, red) and one NBI source (S8, blue). —, TRANSP/NUBEAM; - - -, ASCOT; \circ , measurement; \cdots , gyrotron frequency. CTS measurements were averaged over 15 gyrotron pulses. The two-beam configuration is also presented in logarithmic scale in figure 8 as reference.

spectra to changes in a selection of such plasma parameters is shown in figure 8 for the two-beam phase together with experimental data. Each parameter is varied while the other parameters are kept constant. Figure 8(a) shows that changes in the fast ion density affect mainly large frequency shifts beyond the bulk ion feature. Contrarily, the ion temperature has an impact on the width of the bulk ion feature and has only a small influence on the spectral power density for large frequency shifts (figure 8(b)). These two effects were observed in figure 7. Another important issue is the uncertainty due to an incompletely known frequency independent scaling factor. Equation (1) asserts that the measured spectral power

density is directly proportional to the probing power P_1 and the beam overlap O_b (the electron density n_e also appears in the scattering function Σ). The uncertainties in the probing power and the beam overlap can be combined with the uncertainty in the receiver calibration and have the effect of a frequency independent scaling factor. We show the sensitivities to the electron density and this scaling factor in figures 8(c) and (d), respectively.

An uncertainty of a factor of two in this scaling factor seems possible due to mainly systematic uncertainties whereas the stochastic error due to launcher control is significantly smaller (accuracy $<0.1^\circ$). One source of such systematic

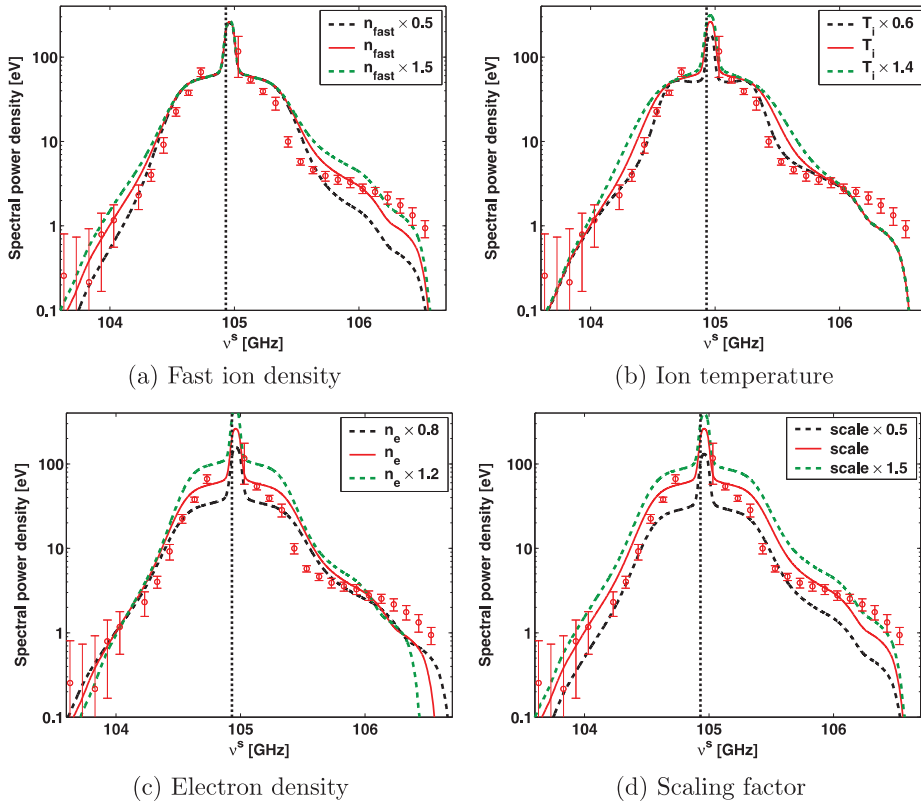


Figure 8. Sensitivity of the spectra to changes in the fast ion density, the ion temperature, the electron density and the frequency independent scaling factor for the two-NBI configuration. The spectra are here presented in logarithmic scale. The baseline spectrum (red) was also displayed in linear scale in figure 7. One parameter is varied in each figure as indicated. The fast ion velocity distribution function has not been recomputed in each case.

uncertainty is the antenna characteristic of the receiver beam which is only known for the component of radiation which excites an HE11-mode in the transmission line. Another systematic uncertainty is due to beam diffraction by transverse density gradients. A third systematic uncertainty is due to the power measurement of the probe beam using the embedded directional coupler which may not be accurate for short pulses. A direct calorimetric measurement of a short sequence of these pulses is in principle possible and should reduce this error component significantly ($<5\%$). An additional source of uncertainty lies in the calibration of the CTS receiver.

Due to the relatively large uncertainties in the scaling factor illustrated in figure 8(d), one should only consider the shape of a CTS spectrum when comparing with a simulation and allow an overall multiplicative factor. Such a frequency independent scaling factor will move the spectrum up or down in the logarithmic plot and scale the values and the gradients in a linear plot. In figure 7 we use the nominal values as the best guess before consideration of the CTS data. Note that any deviation from these nominal values should be the same for the cases with one and with two beam sources shown in figure 7 since the antenna setting is unchanged, the density profiles are very similar and the nominal ECRH power is

identical. This means that there is essentially only one common scaling factor to be applied to the simulated data. We will come back to this point in the discussion of figure 10 at the end of section 4.2. We do not comment on the sensitivities to other nuisance parameters further here even though these also have a bearing on the uncertainty of the measurement results [54]. An additional uncertainty originates from the finite size of the scattering volume which implies a distribution of k^δ . In the experiment the CTS signal will be measured for a convolution over the distribution of k^δ whereas only the nominal k^δ is assumed in our model. Moreover, we note that the nuisance parameters may not be constant within our scattering volume. However, these uncertainties can be shown to be small compared with the uncertainty due to uncertain nominal values of the nuisance parameters.

For the discussion of figure 7 we keep in mind that the simulation results are uncertain with respect to an overall scaling factor between 0.5 and 2. We note that the computation predicts a significantly steeper gradient in the spectra for the two-NBI configuration (S3+S8) compared with the one-NBI configuration (S8). This difference in gradient is smaller in the measured spectra. A second difference is that the measured bulk ion feature has a tendency to be narrower than the expected

bulk ion feature as is also visible in figure 8. It can furthermore be noted that the expected decrease in spectral power densities, after S3 is switched off, for negative frequency shift is too small to be measured. The error bars in this frequency range (below 104.3 GHz) are larger due to the higher ECE background levels for these frequencies in this experiment.

4.2. Comparison of measured and simulated fast ion velocity distributions

In figure 9 we present the inferred fast ion distributions from the CTS measurements and compare them with the simulated fast ion distribution from TRANSP/NUBEAM or ASCOT. Also in velocity space the simulations and experiments agree in several points. First, the projection of the beam ion distribution function onto the resolved direction is asymmetric: the measured $g(u)$ is larger for positive u compared with negative u which was expected from the simulations. Second, $g(u)$ decreases for positive u when neutral beam S3 is turned off as expected. This decrease is only evident for positive u whereas $g(u)$ for both NBI configurations coincides for negative u within the asserted confidence. The different shape of $g(u)$ for each NBI configuration can be clearly observed and originates from the different beam energies. The asymmetry is more pronounced in the two-beam configuration. There are also some discrepancies: there is a tendency that the simulated fast ion velocity distributions lie below the measured ones. Furthermore, the difference in the gradients between the two-beam and one-beam phases for positive u is larger in the computations than in the CTS measurements. The causes of these tendencies are presently under investigation.

As noted before, the projections $g(u)$ of the simulation results from TRANSP/NUBEAM and ASCOT onto k^δ are very similar for large u (see figure 9). They cannot be told apart with the CTS diagnostic in this experiment as the discrepancies between TRANSP/NUBEAM and ASCOT are below the uncertainty of the experimental results for large u . We stress that small velocity components u are not necessarily related to small ion velocities: the δ -function in equation (2) picks out $u = v \cdot k^\delta / k^\delta$, and hence u will be small even for large ion velocities v if v and k^δ span a large angle. The bulk ions mask this fast ion information for small u components. Therefore, the inferred fast ion velocity distribution is plotted only for velocities beyond the Maxwellian bulk indicated in figure 9. The error bars show the 1σ confidence interval for the phase space density of fast ions at each velocity. They are affected by the measurement uncertainties of the spectral power density and also those of the nuisance parameters. The uncertainties in the velocity distribution are correlated and are mostly such that they could be represented by uncertainty in a scaling factor for the velocity distribution. It can be shown to mostly originate from the uncertain frequency independent scaling factor of the spectral power density discussed in section 4.1 in combination with other uncertainties in the nuisance parameters [54]. Considering the uncertainties of both theory and experiment, these first comparisons of CTS results to numerical plasma simulations show a reasonable level of agreement.

Finally, we revise our comparison between the simulations and the experiments in frequency space after consideration

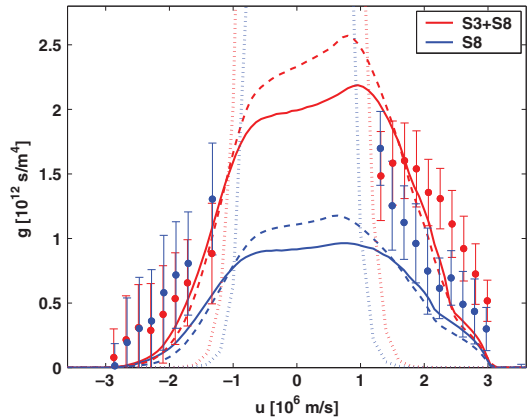


Figure 9. Comparison of the measured and computed one-dimensional fast ion velocity distributions $g(u)$ for plasma heating by two beams (S3+S8, red) and one beam (S8, blue). —, TRANSP/NUBEAM; - - -, ASCOT; O, measurement; ·····, bulk ions. The measured distribution is restricted to outside indicated bulk ion distributions. The beam ion energies 60 keV and 93 keV correspond to $2.4 \times 10^6 \text{ m s}^{-1}$ and $3 \times 10^6 \text{ m s}^{-1}$ for $\mathcal{L}(v_{\text{ion}}, k^\delta) = 0$, respectively.

of the measured spectral power densities. The comparison before consideration of the measured spectral power densities was shown in figure 7, which was therefore a prediction of the signal to be observed. Here we pick the comparison of the measurement with NUBEAM data and compare the prediction before the experiment with the newly computed maximum likelihood estimate. The maximum likelihood solution for all parameters also contains revised estimates for the nuisance parameters, in particular the magnitude of the frequency independent scaling factor. The maximum likelihood solution suggests this factor to be smaller than estimated originally. The measured spectral power densities for small frequency shifts are lower than the predicted values which leads to a downward revision of the magnitude of the frequency independent scaling factor by 30%. Therefore, the simulated levels of spectral power densities are overall lower after consideration of the CTS data as shown in figure 10. This downward revision was also illustrated in figure 8(d). We note that the scaling factors determined with the maximum likelihood solution are very similar for both NBI configurations as expected from the discussion on the nature of the scaling uncertainty in section 4.1. Thus we reconciled the comparison in frequency space with our maximum likelihood solution of the one-dimensional velocity distribution.

5. Discussion

We have noted some points of agreement and some points of disagreement between measurements and simulations. We observe agreement among the ASCOT and TRANSP/NUBEAM simulation codes in experimentally accessible parameters. However, it may be possible to find a heating scenario for which the two codes make different predictions which could be experimentally distinguishable by CTS. This will require some benchmarking efforts among the codes

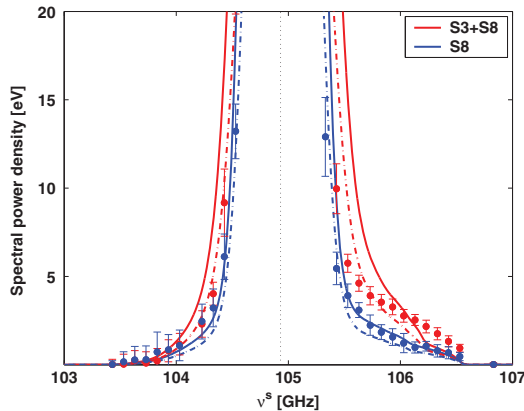


Figure 10. Comparison of measured and synthetic CTS spectra for discharge 24089 for auxiliary heating with two NBI sources (S3+S8, red) and one NBI source (S8, blue). —, TRANSP/NUBEAM before consideration of the CTS data; — —, TRANSP/NUBEAM after consideration of the CTS data consistent with the corresponding $g(u)$ from figure 9; \circ , measurement; \cdots , gyrotron frequency.

and additional CTS experiments which is beyond the scope of this work. In future experiments the results of simulations could be compared with CTS measurements for several locations in the plasma and several resolved directions for various heating scenarios. Furthermore, it will be feasible to reduce the uncertainties of the CTS measurements. Recent modifications of the CTS receiver will allow the spectral power density to be measured with higher accuracy. Additionally, CTS data analysis will benefit from more accurate measurements of the nuisance parameters. In this work the full capabilities of the CTS system have not yet been fully exploited: the signal-to-noise ratio has been increased at the expense of time resolution. In future experiments it may be possible to inject higher gyrotron powers [52] which may improve the signal-to-noise ratio and thus enable us to increase the time resolution. This may allow detailed studies of plasma dynamics on millisecond time scales by CTS—the results of which may be interesting to compare with numerical simulations. It would also be of considerable benefit to add a second receiver to the CTS system at ASDEX Upgrade. A second receiver located in a different port would enable CTS measurements resolving simultaneously two directions and would allow a reconstruction of two-dimensional fast ion velocity distribution functions [55].

6. Conclusions

The fast ion populations in the plasma centre of ASDEX Upgrade were compared for two-NBI configurations: one neutral beam versus two neutral beams. One-dimensional fast ion velocity distributions $g(u)$ were inferred for both NBI configurations. The inferred $g(u)$ and the measured CTS spectra for both heating regimes have different shapes and can, as expected, clearly be distinguished. The CTS measurements were compared with simulations using the TRANSP/NUBEAM and ASCOT codes. Salient

features of the measured spectral power densities and one-dimensional fast ion velocity distributions are in reasonable agreement with the simulations within the limits of the given uncertainties. Quantitative discrepancies between measurement and simulation in absolute values and gradients were observed which will drive future activities in the development of the diagnostic and the codes.

Acknowledgments

This work, supported by the European Communities under the contract of Association between EURATOM and Risø DTU, was partly carried out within the framework of the European Fusion Development Agreement. The views and opinions expressed herein do not necessarily reflect those of the European Commission. The computing facilities of the Finnish IT Centre for Science (CSC) used in this work are gratefully acknowledged. This work was partially funded by The Finnish Academy project No 121371.

References

- [1] Herrmann A. and Gruber O. 2003 *Fusion Sci. Technol.* **44** 569–77
- [2] Gruber O. et al 2007 *Nucl. Fusion* **47** S622–34
- [3] Chen L. 1994 *Phys. Plasma* **1** 1519–22
- [4] Briguglio S. et al 2007 *Phys. Plasma* **14** 055904–055904
- [5] Heidbrink W.W. and Sadler G.J. 1994 *Nucl. Fusion* **34** 535
- [6] Zweben S.J. et al 2000 *Nucl. Fusion* **40** 91–149
- [7] Heidbrink W.W. 2002 *Phys. Plasma* **9** 2213–9
- [8] Pinches S.D. et al 2004 *Plasma Phys. Control. Fusion* **46** B187–B200
- [9] Campbell D.J. et al 1988 *Phys. Rev. Lett.* **60** 2148–51
- [10] Marcus F.B. et al 1994 *Nucl. Fusion* **34** 687–701
- [11] Kolesnichenko Y.I., Lutsenko V.V., White R.B. and Yakovenko Y.V. 2000 *Nucl. Fusion* **40** 1325–41
- [12] Graves J. et al 2005 *Plasma Phys. Control. Fusion* **47** B121–33
- [13] Chang Z. et al 1996 *Phys. Rev. Lett.* **76** 1071
- [14] Nazikian R. et al 1996 *Phys. Plasma* **3** 593–605
- [15] García-Muñoz M. et al 2007 *Nucl. Fusion* **47** L10–5
- [16] García-Muñoz M. et al 2008 *Phys. Rev. Lett.* **100** 055005
- [17] Günter S. et al 2007 *Nucl. Fusion* **47** 920–8
- [18] Hauff T., Poeschel M.J., Dannert T. and Jenko F. 2009 *Phys. Rev. Lett.* **102** 075004
- [19] Heidbrink W.W. et al 2009 *Phys. Rev. Lett.* **103** 175001
- [20] ITER Physics Expert Group on Energetic Particles, Heating and Current Drive 1999 *Nucl. Fusion* **39** 2471–95
- [21] Fasoli A. et al 2007 *Nucl. Fusion* **47** S264–84
- [22] Bindslev H. et al 1999 *Phys. Rev. Lett.* **83** 3206–9
- [23] Bindslev H. et al 2006 *Phys. Rev. Lett.* **97** 205005
- [24] Nielsen S.K. et al 2008 *Phys. Rev. E* **77** 016407
- [25] Meo F. et al 2008 *Rev. Sci. Instrum.* **79** 10E501
- [26] Meo F. et al 2010 First results and analysis of collective Thomson scattering (CTS) fast ion distribution measurements on ASDEX Upgrade 14th Int. Symp. on Laser-Aided Plasma Diagnostics J. Phys.: Conf. Ser. submitted
- [27] Bindslev H. et al 2004 *Rev. Sci. Instrum.* **75** 3598–600
- [28] Meo F. et al 2004 *Rev. Sci. Instrum.* **75** 3585–8
- [29] Korsholm S.B. et al 2008 Burning plasma diagnostics AIP Conf. Proc. **988** 118–22
- [30] Salewski M. et al 2008 *Rev. Sci. Instrum.* **79** 10E729
- [31] Salewski M. et al 2009 *Plasma Phys. Control. Fusion* **51** 035006
- [32] Leipold F. et al 2009 *Rev. Sci. Instrum.* **80** 093501
- [33] Machuzak J. et al 1997 *Rev. Sci. Instrum.* **68** 458–61
- [34] Tartari U. et al 2006 *Nucl. Fusion* **46** 928

- [35] Westerhof E. *et al* 2009 *Phys. Rev. Lett.* **103** 125001
- [36] Nishiura M. *et al* 2008 *Rev. Sci. Instrum.* **79** 10E731
- [37] Suvorov E. *et al* 1995 *Plasma Phys. Control. Fusion* **37** 1207
- [38] Bindslev H. 1993 *Plasma Phys. Control. Fusion* **35** 1615–40
- [39] Bindslev H. 1996 *J. Atmos. Terr. Phys.* **58** 983
- [40] Budny R.V. *et al* 1995 *Nucl. Fusion* **35** 1497
- [41] Pankin A., McCune D., Andre R. and Kritz A. 2004 *Comput. Phys. Commun.* **159** 157–84
- [42] Heikkinen J.A. and Sipilä S.K. 1995 *Phys. Plasma* **2** 3724–33
- [43] Heikkinen J.A. *et al* 2001 *J. Comput. Phys.* **173** 527–48
- [44] Streibl B. *et al* 2003 *Fusion Sci. Technol.* **44** 578–92
- [45] Murmann H. *et al* 1992 *Rev. Sci. Instrum.* **63** 4941–3
- [46] Fischer R., Dinklage A. and Pasch E. 2003 *Plasma Phys. Control. Fusion* **45** 1095–111
- [47] Fischer R. *et al* 2008 *Plasma Phys. Control. Fusion* **50** 085009
- [48] Fischer R. *et al* 2008 Integrated density profile analysis in ASDEX upgrade H-modes *Europhys. Conf. Abstracts* vol 32D p P4.010
- [49] Fischer R. *et al* 2009 Multiple diagnostic data analysis of density and temperature profiles in ASDEX Upgrade *Europhys. Conf. Abstracts* vol 33E P1.159
- [50] Dux R. 2003 *Fusion Sci. Technol.* **44** 708–15
- [51] Salpeter E.E. 1960 *Phys. Rev.* **120** 1528–35
- [52] Wagner D.H. *et al* 2008 *IEEE Trans. Plasma Sci.* **36** 324–31
- [53] Salewski M. *et al* 2009 *Nucl. Fusion* **49** 025006
- [54] Bindslev H. 1999 *Rev. Sci. Instrum.* **70** 1093–9
- [55] Egedal J. and Bindslev H. 2004 *Phys. Plasma* **11** 2191–8

Reference [2]

[2]. M Salewski et al. (2011) *Nuclear Fusion* **51** 083014. On velocity space interrogation regions of fast-ion collective Thomson scattering at ITER

On velocity space interrogation regions of fast-ion collective Thomson scattering at ITER

M. Salewski¹, S.K. Nielsen¹, H. Bindslev¹, V. Furtula¹,
N.N. Gorelenkov², S.B. Korsholm¹, F. Leipold¹, F. Meo¹,
P.K. Michelsen¹, D. Moseev¹ and M. Stejner¹

¹ Association Euratom-Risø National Laboratory for Sustainable Energy, Technical University of Denmark, DK-4000 Roskilde, Denmark

² Princeton Plasma Physics Laboratory, Princeton, NJ 08543-045, USA

E-mail: msal@risoe.dtu.dk

Received 15 April 2011, accepted for publication 9 June 2011

Published 7 July 2011

Online at stacks.iop.org/NF/51/083014

Abstract

The collective Thomson scattering (CTS) diagnostic proposed for ITER is designed to measure projected 1D fast-ion velocity distribution functions at several spatial locations simultaneously. The frequency shift of scattered radiation and the scattering geometry place fast ions that caused the collective scattering in well-defined regions in velocity space, here dubbed interrogation regions. Since the CTS instrument measures entire spectra of scattered radiation, many different interrogation regions are probed simultaneously. We here give analytic expressions for weight functions describing the interrogation regions, and we show typical interrogation regions of the proposed ITER CTS system. The backscattering system with receivers on the low-field side is sensitive to fast ions with pitch $|p| = |v_{\parallel}/v| < 0.5\text{--}0.9$ depending on the ion energy and the frequency shift of the scattered radiation. A forward scattering system with receivers on the high-field side would be sensitive to co- and counter-passing fast ions in narrow interrogation regions with pitch $|p| > 0.6\text{--}0.8$. Additionally, we use weight functions to reconstruct 2D fast-ion distribution functions, given two projected 1D velocity distribution functions from simulated simultaneous measurements with the back- and forward scattering systems.

(Some figures in this article are in colour only in the electronic version)

1. Introduction

In burning plasmas in ITER, fast ions from fusion reactions, from neutral beam injection (NBI) and from ion cyclotron resonance heating (ICRH) will provide more than 2/3 of the total heating by transferring most of their energy to the bulk plasma. However, many aspects of fast-ion behaviour, which still pose challenges to theory, may lead to enhanced energy and fast-ion losses. For example, fast ions can develop energetic particle modes [1, 2] and can interact with Alfvén eigenmodes [3–7], with sawteeth instabilities [8–11], with kinetic ballooning modes [4, 12, 13], with neoclassical tearing modes [4, 14] or with turbulent fluctuations [15–17]. The extrapolation of such phenomena to ITER plasmas is even more uncertain, and measurements of fast-ion velocity distributions in ITER are therefore essential [18, 19]. Millimetre-wave collective Thomson scattering (CTS) has been demonstrated to provide such measurements at JET [20], TEXTOR [10, 11, 21–23] and ASDEX Upgrade [24–26].

The proposed ITER CTS system comprises a forward scattering system with receivers on the high-field side and a backscattering system with receivers on the low-field side [27–32]. Each system is designed to measure fast-ion velocity distributions in 7–10 measurement volumes distributed along the minor radius a on both the high-field side and the low-field side simultaneously, satisfying the ITER measurement requirements on resolution for fusion alpha diagnostic (time: 100 ms, space: $a/10$) [33]. The CTS backscattering system is an enabled ITER diagnostic, and its in-port components are part of the updated ITER baseline design [34]. The forward scattering system [29, 32], however, is not enabled. CTS measurements are sensitive to the fast-ion velocity distribution function projected onto the wave vector $k^{\delta} = k^s - k^i$, where s and i refer to scattered and incident radiation, respectively. A frequency shift ν^{δ} of scattered radiation can be related to an ion velocity v^p projected onto k^{δ} : $\nu^{\delta} = \nu^s - \nu^i \approx v^p \cdot k^{\delta}/2\pi$. The detected frequency shift and the projection angle between k^{δ} and the magnetic field B , $\phi = \angle(k^{\delta}, B)$, place the ions

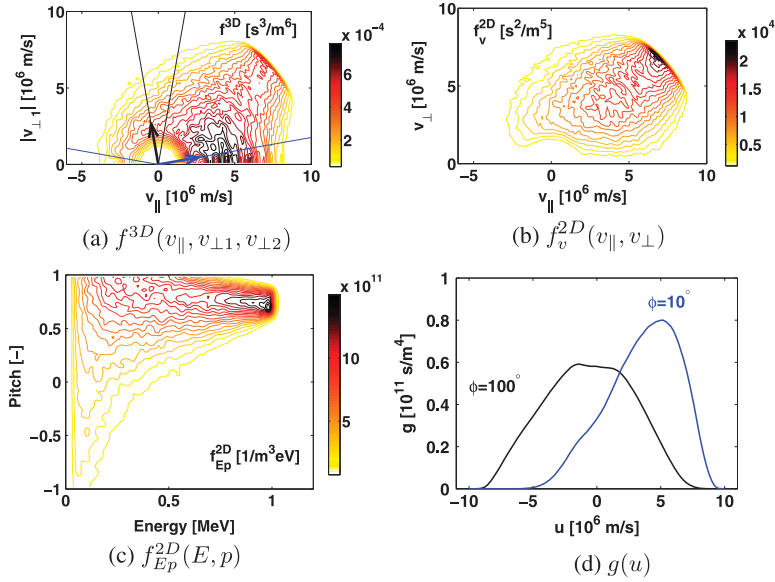


Figure 1. An ITER NBI ion distribution function at the minor radius coordinate $r/a = 0.25$ in the midplane on the high-field side computed with TRANSP shown in four coordinate systems. (a) Slice through the 3D, rotation invariant velocity distribution function $f^{3D}(v_{\parallel}, v_{\perp 1}, v_{\perp 2})$. The projection directions are indicated by the vector k^{δ} and thin straight lines for $\phi = 100^\circ$ (black) and $\phi = 10^\circ$ (blue). Positive u -coordinates are on the branches containing the arrows and negative u -coordinates lie on the mirror-reflected branches. (b) 2D velocity distribution function $f_v^{2D}(v_{\parallel}, v_{\perp})$. (c) 2D velocity distribution function $f_{Ep}^{2D}(E, p)$. (d) 1D projected velocity distribution functions $g(u)$ corresponding to the projection directions indicated in (a).

that caused the collective scattering in a well-defined region in velocity space, here dubbed the interrogation region. Typical interrogation regions of the back- and forward scattering ITER CTS systems are presented using weight functions such as those used for fast-ion $D\alpha$ (FIDA) diagnostics [35–38]. Weight functions are a convenient and illustrative way to relate the fast-ion distribution function and the geometry of the experiment to the measured CTS signal.

To develop analytic expressions for CTS weight functions in section 4, we define relevant coordinate systems in section 2 and illustrate the projection of velocity distribution functions onto k^{δ} in section 3. The analytic expressions derived here should also be useful for FIDA because CTS weight functions are identical with the geometric (Doppler shift) part of FIDA weight functions [38]. In section 5 we show, using weight functions, that the ITER CTS backscattering system is sensitive to dynamics of fast ions with pitch $|p| = |v_{\parallel}|/v < 0.5$ –0.9, depending on the ion energy and the frequency shift of the scattered radiation. Here v_{\parallel} is the velocity component parallel to \mathbf{B} and v is the velocity magnitude. The proposed forward scattering system would reveal dynamics of co- and counter-passing fast ions in narrow interrogation regions with pitch $|p| > 0.6$ –0.8 as opposed to the backscattering system where the interrogation regions cover broad ranges of pitch angle and energy. CTS signals at ITER are dominated by alpha particles [31, 30]. For a central alpha distribution function computed with TRANSP [39], most of the CTS signal at various frequency shifts originates from the low energy end of the interrogation regions which are thus effectively probed (section 5). Simultaneous measurements with both systems

would even make it possible to study anisotropy in the fast-ion velocity distribution and to reconstruct 2D velocity distributions (section 6). We conclude in section 7.

2. Coordinate systems

In CTS experiments 1D projections $g(u)$ of full 3D fast-ion velocity distribution functions $f^{3D}(v_{\parallel}, v_{\perp 1}, v_{\perp 2})$ along k^{δ} are estimated by measuring the spectral power density of scattered radiation. The Cartesian velocity component v_{\parallel} is parallel to \mathbf{B} and $v_{\perp 1}$ and $v_{\perp 2}$ are perpendicular to \mathbf{B} , and u is the 1D velocity component in the direction of k^{δ} . The projection is given by

$$g(u) = \int f^{3D}(v) \delta\left(\frac{v \cdot k^{\delta}}{k^{\delta}} - u\right) dv, \quad (1)$$

where v is the velocity and $\delta()$ is the Dirac delta function. The u -coordinate determines the frequency shift of scattered radiation in CTS experiments:

$$v^{\delta} \approx uk^{\delta}/2\pi. \quad (2)$$

Figure 1 shows an NBI ion distribution function in four different representations. The distribution function has been computed with TRANSP simulating an ITER plasma during the injection. Figure 1(a) is a 2D slice through the 3D distribution function $f^{3D}(v_{\parallel}, v_{\perp 1}, v_{\perp 2})$. As we assume f^{3D} to be rotationally symmetric about \mathbf{B} , we are free to choose $v_{\perp 1}$ to lie in the plane spanned by k^{δ} and \mathbf{B} . For the same reason we can choose $|v_{\perp 1}|$ as the coordinate axis since the half plane with

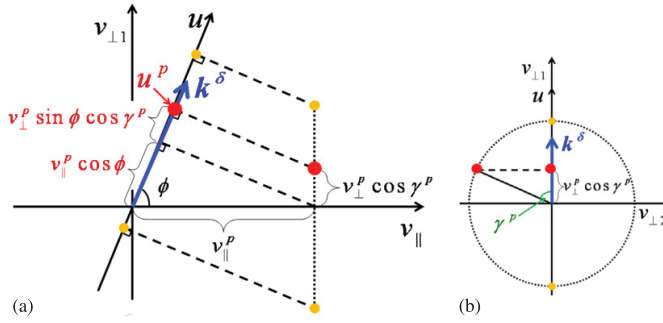


Figure 2. Illustration of the mapping from $(v_{\parallel}, v_{\perp 1}, v_{\perp 2})$ -space onto u -space along k^{δ} (blue). (a) $(v_{\parallel}, v_{\perp 1})$ -plane: the point $(v_{\parallel}^p, v_{\perp 1}^p \cos \gamma^p)$ (large red dot), which is always on the dotted line between the extremal points $(v_{\parallel}^p, v_{\perp 1}^p)$ and $(v_{\parallel}^p, -v_{\perp 1}^p)$ (small orange dots), is projected onto the u -coordinate at angle ϕ to the v_{\parallel} -axis. The dashed lines are perpendicular to the u -axis. As $\cos \gamma^p \in [-1, 1]$, $u^p \in [v_{\parallel}^p \cos \phi - v_{\perp 1}^p \sin \phi, v_{\parallel}^p \cos \phi + v_{\perp 1}^p \sin \phi]$. (b) $(v_{\perp 1}, v_{\perp 2})$ -plane: projection of a point $(v_{\perp 1}^p, v_{\perp 2}^p)$ (large red dot) representing an ion on a gyroorbit into the $(v_{\parallel}, v_{\perp 1})$ -plane. The $v_{\perp 1}$ -coordinate is $v_{\perp 1}^p \cos \gamma^p$. The u -axis along k^{δ} (blue) lies in the $(v_{\parallel}, v_{\perp 1})$ -plane and so is usually not identical to the $v_{\perp 1}$ -axis.

negative $v_{\perp 1}$ is a mirror reflection of that with positive $v_{\perp 1}$. Two typical projection directions for a forward- and backscattering ITER CTS system are indicated by vector arrows and two branches of thin straight lines for each projection angle in figure 1(a). The corresponding 1D distribution functions g are shown in figure 1(d). As the relation between f^{3D} and g is by no means obvious, we will elaborate on the mapping from $(v_{\parallel}, v_{\perp 1}, v_{\perp 2})$ -coordinates of f^{3D} onto the u -coordinate of g in the following section.

As we assume the fast-ion distribution function to be rotationally invariant about B , it is sufficient and convenient to work with the fast-ion distribution functions $f_v^{2D}(v_{\parallel}, v_{\perp})$ and $f_{Ep}^{2D}(E, p)$ shown in figure 1(b) and (c). The perpendicular velocity components $v_{\perp 1}$ and $v_{\perp 2}$ are related to v_{\perp} through the gyroangle γ by $v_{\perp 1} = v_{\perp} \cos \gamma$ and $v_{\perp 2} = v_{\perp} \sin \gamma$, so $v_{\perp}^2 = v_{\perp 1}^2 + v_{\perp 2}^2$. The energy is $E = \frac{1}{2}mv^2$, and the pitch is $p = \frac{v_{\parallel}}{v}$ with $v^2 = v_{\parallel}^2 + v_{\perp}^2$. The (E, p) - and $(v_{\parallel}, v_{\perp})$ -coordinate systems are truly 2D with no implied third direction. We derive weight functions describing the interrogation regions in these coordinate systems (section 5). The representations of the fast-ion distribution function in figures 1(a)–(c) are equivalent. One can obtain the velocity distribution function f_v^{2D} from f^{3D} by transforming to cylindrical coordinates and integrating over by the assumption ignorable gyroangle γ , $f_v^{2D} = 2\pi v_{\perp} f^{3D}$, and the velocity distribution function f_{Ep}^{2D} is related to f_v^{2D} through a 2D coordinate transformation. The respective Jacobians are included in the definitions f_v^{2D} and f_{Ep}^{2D} , so that the ion particle density is, respectively, given by

$$\begin{aligned} n &= \int f^{3D}(v_{\parallel}, v_{\perp 1}, v_{\perp 2}) dv_{\perp 1} dv_{\perp 2} dv_{\parallel} \\ &= \int f_v^{2D}(v_{\parallel}, v_{\perp}) dv_{\perp} dv_{\parallel} \\ &= \int f_{Ep}^{2D}(E, p) dE dp = \int g(u) du. \end{aligned} \quad (3)$$

3. Mapping from $(v_{\parallel}, v_{\perp 1}, v_{\perp 2})$ -coordinates and $(v_{\parallel}, v_{\perp})$ -coordinates onto u -coordinates

We illustrate the projection trace of a gyrating ion in $(v_{\parallel}, v_{\perp 1}, v_{\perp 2})$ -space onto u -space along k^{δ} in figure 2.

The gyroorbit about the v_{\parallel} -axis can be parametrized by $(v_{\parallel}^p, v_{\perp}^p, \gamma^p)$, where v_{\parallel}^p and v_{\perp}^p are constants and $\gamma^p \in [0, 360^\circ]$ with respect to the $v_{\perp 1}$ -axis. The gyroorbit then intersects the $(v_{\parallel}, v_{\perp 1})$ -plane at $(v_{\parallel}^p, v_{\perp 1}^p)$ for $\gamma^p = 0^\circ$ and at its mirror image $(v_{\parallel}^p, -v_{\perp 1}^p)$ for $\gamma^p = 180^\circ$. For arbitrary gyroangles the projection into the $(v_{\parallel}, v_{\perp 1})$ -plane is $(v_{\parallel}^p, v_{\perp 1}^p \cos \gamma^p)$. It is then a matter of plane geometry to find the projected velocity u^p as a function of the gyroangle γ^p (see figure 2):

$$u^p = v_{\parallel}^p \cos \phi + v_{\perp 1}^p \sin \phi \cos \gamma^p. \quad (4)$$

A single point in 2D velocity space with coordinates $(v_{\parallel}^p, v_{\perp 1}^p)$ thus maps onto an interval of width $2v_{\perp 1}^p \sin \phi$ centred on $v_{\parallel}^p \cos \phi$ in u -space as $\cos \gamma^p$ takes values from -1 to 1 . If the projection direction is perpendicular to the magnetic field ($\phi = 90^\circ$), the interval in u is at its widest, going from $u^p = -v_{\perp 1}^p$ to $u^p = +v_{\perp 1}^p$, and is symmetric about $u = 0$. In the other extreme, if the projection direction is parallel to the magnetic field ($\phi = 0^\circ$), the width of the interval goes to zero. In this case the point in $(v_{\parallel}, v_{\perp 1})$ -space will map onto a single point in u -space: $u^p = v_{\parallel}^p$. These intervals in u determine in which frequency channels an ion with given $(v_{\parallel}^p, v_{\perp 1}^p)$ will elicit a response at given ϕ .

Figure 3(a) shows three Maxwellian bumps as simple test velocity distribution functions in $(v_{\parallel}, v_{\perp 1}, v_{\perp 2})$ -space representing distinct populations of fast ions: trapped particles (T), passing particles (P) and particles near the trapped-passing-boundary (TP). These populations should be taken as illustrations only. The bulk part of a typical ITER plasma is modelled as an isotropic deuterium Maxwellian distribution function with an ion temperature $T = 20$ keV and an ion density $n = 10^{20} \text{ m}^{-3}$. Figures 3(b)–(d) illustrate the projections of these velocity distribution functions onto k^{δ} . The projection directions, represented by the vector arrows and thin straight lines as in figure 1(a), are typical for the proposed ITER CTS system. The projections g of the test functions onto these two projection directions are plotted in figures 3(b)–(d). For $\phi = 100^\circ$ the intervals are much broader than for $\phi = 10^\circ$ as their widths are $2v_{\perp 1} \sin \phi$. Since the integral of g always gives the fast-ion particle density (equation (3)) and is therefore

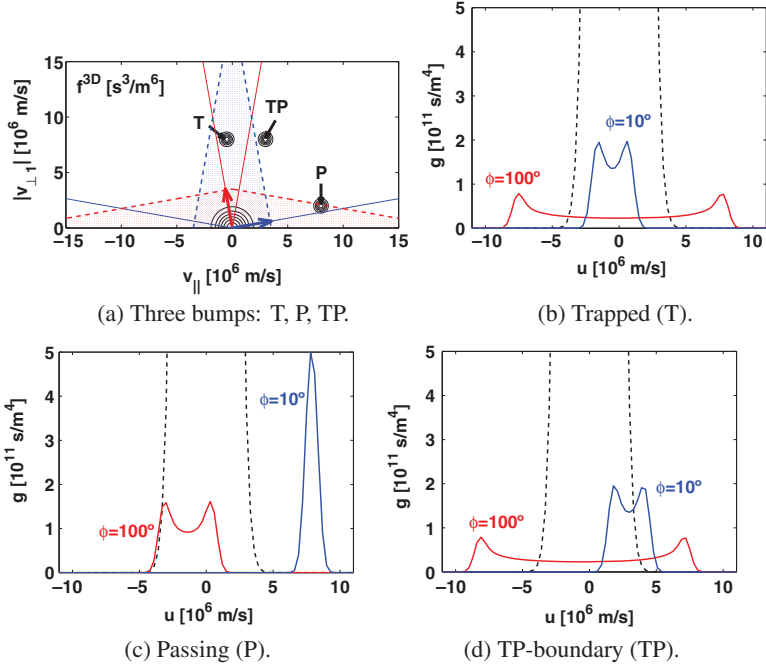


Figure 3. (a) Populations of trapped particles (T), passing particles (P), and particles near the trapped-passing-boundary (TP) are shown in a 2D slice of a 3D coordinate system. The concentric circles about the origin represent the bulk-ion distribution. The projection directions used for (b)–(d) are shown as vector arrows and thin straight lines for $\phi = 10^\circ$ (blue) and $\phi = 100^\circ$ (red). These directions are typical for the forward scattering and backscattering systems, respectively. The dashed lines enclose triangular regions in which the much more numerous bulk ions hamper the detection of fast ions for each ϕ . (b) Projections g for the bump of trapped particles (T). (c) Projections g for the bump of passing particles (P). (d) Projections g for the bump of particles near the trapped-passing-boundary (TP). The dashed lines in (b)–(d) are the projections of the bulk plasma distribution function.

the same for any ϕ , the curves are flatter for $\phi = 100^\circ$ than those for $\phi = 10^\circ$. For $\phi = 10^\circ$ the curves are more lopsided about $u = 0$ than those for $\phi = 100^\circ$ because the centre of each interval is $v_{\parallel} \cos \phi$.

The projection of the isotropic Maxwellian bulk-ion distribution function is a Maxwellian (dashed lines in figures 3(b) to (d)) described by the bulk-ion temperature and particle density. As the bulk-ion particle density is much larger than that of fast ions, the scattered radiation related to bulk ions will obscure that of fast ions for values of

$$|u| = |v_{\parallel} \cos \phi + v_{\perp} \sin \phi \cos \gamma| < A \times v_{th}, \quad (5)$$

where the factor A reflects a velocity level one chooses below which little fast-ion information can be extracted (usually $A \sim 2$). The bulk ions thus create an obscure region—a triangle in $(v_{\parallel}, v_{\perp})$ -space or a bicone in $(v_{\parallel}, v_{\perp 1}, v_{\perp 2})$ -space—in which the fast ions are very difficult to detect. The shape of such triangles depends on ϕ and is given by the three sides

$$v_{\perp} = \frac{A \times v_{th} \pm v_{\parallel} \cos \phi}{\sin \phi}, \quad (6)$$

$$v_{\perp} = 0. \quad (7)$$

Two such triangles are plotted for $\phi = 10^\circ$ and for $\phi = 100^\circ$ in figure 3(a) as dashed lines enclosing shaded regions. The

bump of trapped particles (T) can be well detected with the backscattering system ($\phi \approx 100^\circ$), but the bulk ions hamper detection with the forward scattering system ($\phi \approx 10^\circ$). Co- and counter-passing particles (P) with pitch near ± 1 , on the other hand, are well detectable with the forward scattering system, but the bulk ions hamper detection with the backscattering system. Particles assumed to be near the trapped-passing-boundary (TP) in our illustration are well detectable with either system.

4. Weight functions

In section 3 we discussed the question: given an ion in 2D velocity space, where is it in u -space or in which frequency channels of the CTS receiver will it elicit a response? In this section we ask the reciprocal question: given a fast-ion phase space density at a particular u —or a detected spectral power density in a particular frequency channel—where could the ions that caused the collective scattering be in 2D velocity space? The answer is expressed in terms of plasma independent weight functions which are positive in the velocity space interrogation regions and zero in the velocity space regions where the ion cannot be for given u and ϕ . Weight functions w_v in $(v_{\parallel}, v_{\perp})$ -space are defined

such that

$$g(u, \phi) = \int_{-\infty}^{\infty} \int_0^{\infty} w_v(u, \phi, v_{\parallel}, v_{\perp}) f_v^{2D}(v_{\parallel}, v_{\perp}) dv_{\perp} dv_{\parallel} \quad (8)$$

or correspondingly w_{Ep} in (E, p) -space

$$g(u, \phi) = \int_{-1}^1 \int_0^{\infty} w_{Ep}(u, \phi, E, p) f_{Ep}^{2D}(E, p) dE dp. \quad (9)$$

The product of a plasma independent weight function and a fast-ion 2D distribution function of a particular plasma (the integrand in equation (8) or equation (9)) represents the relative contributions of regions in 2D velocity space to g for given u and ϕ .

To find analytic expressions for weight functions in $(v_{\parallel}, v_{\perp})$ -space, we compare equation (1) with equation (8). The $(v_{\parallel}, v_{\perp 1}, v_{\perp 2})$ -coordinate system is chosen such that the v_{\parallel} -axis is aligned with \mathbf{B} and the $v_{\perp 1}$ -axis lies in the plane spanned by \mathbf{k}^{δ} and \mathbf{B} (figure 2). The $k_{\perp 2}$ component of \mathbf{k}^{δ} is then zero and equation (1) becomes

$$\begin{aligned} g(u, \phi) &= \int_{-\infty}^{\infty} \int_{-\infty}^{\infty} \int_{-\infty}^{\infty} f^{3D}(v_{\parallel}, v_{\perp 1}, v_{\perp 2}) \delta\left(\frac{\mathbf{v} \cdot \mathbf{k}^{\delta}}{k^{\delta}} - u\right) \\ &\quad \times dv_{\parallel} dv_{\perp 1} dv_{\perp 2} \\ &= \int_{-\infty}^{\infty} \int_{-\infty}^{\infty} \int_{-\infty}^{\infty} f^{3D}(v_{\parallel}, v_{\perp 1}, v_{\perp 2}) \\ &\quad \times \delta(v_{\parallel} \cos \phi + v_{\perp 1} \sin \phi - u) dv_{\parallel} dv_{\perp 1} dv_{\perp 2} \\ &= \int_{-\infty}^{\infty} \int_0^{\infty} f_v^{2D}(v_{\parallel}, v_{\perp}) \frac{1}{2\pi} \\ &\quad \times \int_0^{2\pi} \delta(v_{\parallel} \cos \phi + v_{\perp} \sin \phi \cos \gamma - u) \\ &\quad \times d\gamma dv_{\perp} dv_{\parallel}. \end{aligned}$$

The expression for the weight function is by comparison with equation (8)

$$w_v^a(u, \phi, v_{\parallel}, v_{\perp}) = \frac{1}{2\pi} \int_0^{2\pi} \delta(v_{\parallel} \cos \phi + v_{\perp} \sin \phi \cos \gamma - u) d\gamma. \quad (10)$$

The superscript a denotes that w_v^a is an analytic expression. The weight function is positive at those locations in $(v_{\parallel}, v_{\perp})$ -space where a gyroangle γ exists that satisfies equation (4) for the given u and ϕ . The argument of the Dirac delta function is then zero. If no such gyroangle exists for given $(u, \phi, v_{\parallel}, v_{\perp})$, the delta function argument is never zero, and the weight function is then zero at $(v_{\parallel}, v_{\perp})$ for the given u and ϕ . If a delta function argument has roots, the delta function can be rewritten using

$$\delta(h(x)) = \sum_k \frac{\delta(x - x_k)}{|h'(x_k)|}, \quad (11)$$

where x_k are the roots of h , and the prime denotes a derivative. If roots γ_k of the delta function argument in equation (10) exist, they are given by

$$\cos \gamma_k = \frac{u - v_{\parallel} \cos \phi}{v_{\perp} \sin \phi}, \quad (12)$$

and so the weight function can be written

$$\begin{aligned} w_v^a(u, \phi, v_{\parallel}, v_{\perp}) &= \frac{1}{2\pi} \int_0^{2\pi} \sum_k \frac{\delta(\gamma - \gamma_k)}{v_{\perp} \sin \phi \sin \gamma_k} d\gamma \quad (13) \\ &= \frac{1}{2\pi v_{\perp} \sin \phi \sqrt{1 - \left(\frac{u - v_{\parallel} \cos \phi}{v_{\perp} \sin \phi}\right)^2}} \sum_k \int_0^{2\pi} \delta(\gamma - \gamma_k) d\gamma. \end{aligned} \quad (14)$$

There are then always two roots in the interval $[0, 2\pi]$ so that the weight function becomes

$$w_v^a(u, \phi, v_{\parallel}, v_{\perp}) = \frac{1}{\pi v_{\perp} \sin \phi \sqrt{1 - \left(\frac{u - v_{\parallel} \cos \phi}{v_{\perp} \sin \phi}\right)^2}}. \quad (15)$$

Equation (15) is valid in the velocity space regions where the delta function argument in equation (10) has roots. These are the velocity space interrogation regions. Otherwise $w_v^a(u, \phi, v_{\parallel}, v_{\perp}) = 0$, describing velocity space regions in which ions cannot be observed at given u and ϕ .

An alternative way to arrive at this result is by noting the geometrical relationship between u and γ illustrated in figure 2. Due to the assumed rotational invariance of f^{3D} , every gyroangle of the ion is equally likely. We may consider the gyroangle γ a random variable with the probability density function $p_{\gamma}(\gamma) = 1/(2\pi)$. In this picture u is also a random variable, and we get the probability density function of u , given ϕ, v_{\parallel} and v_{\perp} , by the transformation

$$p_u(u|\phi, v_{\parallel}, v_{\perp}) = p_{\gamma}(\gamma) \left| \frac{d\gamma}{du} \right|, \quad (16)$$

where the derivative is found from equation (4). The right-hand side turns out identical to that of equation (15). The weight function is thus the probability density function of the random variable u , given ϕ, v_{\parallel} and v_{\perp} .

The weight function $w_v^a(u, \phi, v_{\parallel}, v_{\perp})$ is singular near its limits in u for which the values are positive. However, the integral $\int w_v^a(u, \phi, v_{\parallel}, v_{\perp}) du$ can easily be shown to be finite. It is unity as for every probability density function. We will exploit this fact to construct approximate weight functions w_v^b by binning. The weight functions and their finite integrals explain the double-peak structure of the curves in figure 3.

It is useful to find these expressions in (E, p) -coordinates. equation (4) expressed in (E, p) is

$$u = \left(p \cos \phi + \sqrt{1 - p^2} \sin \phi \cos \gamma \right) \sqrt{2E/m}, \quad (17)$$

and equation (15) expressed in (E, p) is

$$\begin{aligned} w_{Ep}^a(u, \phi, E, p) &= \frac{1}{\pi \sqrt{2E/m(1 - p^2)} \sin \phi \sqrt{1 - \left(\frac{u/\sqrt{2E/m} - p \cos \phi}{\sqrt{1 - p^2} \sin \phi}\right)^2}}. \end{aligned} \quad (18)$$

This result is consistent with the proportionality relation in the appendix of [36]. Here we give a complete analytic expression.

Figure 4 shows weight functions for several projection angles ϕ and a given velocity $u = 6 \times 10^6 \text{ m s}^{-1}$ as examples. The upper row shows weight functions in $(v_{\parallel}, v_{\perp})$ -coordinates,

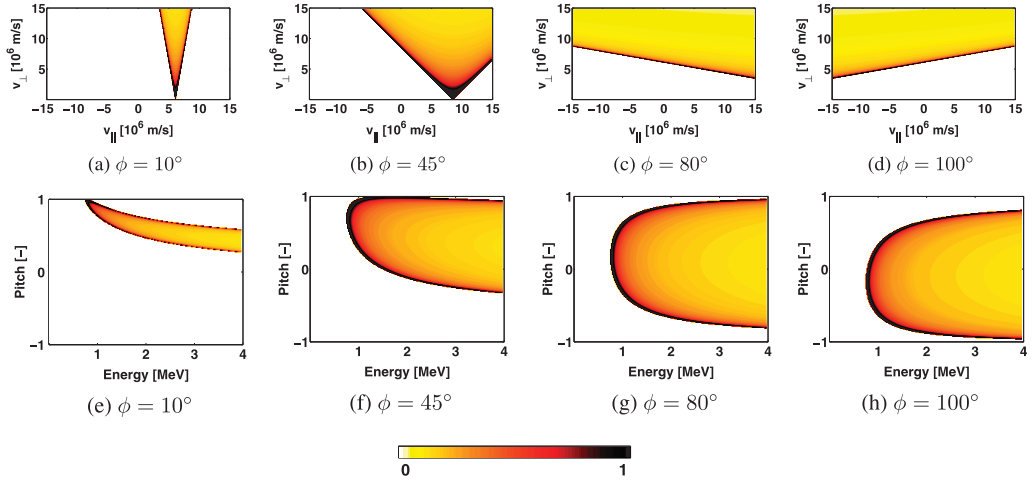


Figure 4. Weight functions in $(v_{\parallel}, v_{\perp})$ -coordinates ((a)–(d)) for $u = 6 \times 10^6 \text{ m s}^{-1}$ and various projection angles ϕ . The corresponding weight functions in (E, p) -coordinates are shown in (e)–(f). The angles $\phi = 10^\circ$ and $\phi = 100^\circ$ are typical for the forward- and backscattering ITER CTS systems, respectively, while the angles 45° and 80° are shown for illustrative purpose. The coloured regions are interrogation regions while the white regions are unobservable for the given ϕ and u .

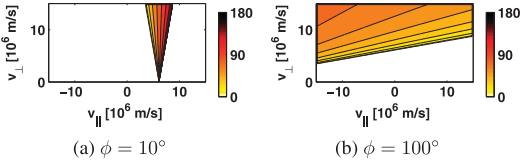


Figure 5. Contours of the gyroangle within the interrogation regions shown in figure 4(a) and (d), respectively. The colours show the necessary gyroangle $\gamma \in [0^\circ, 180^\circ]$ to map onto $u = 6 \times 10^6 \text{ m s}^{-1}$ for the given ϕ in $(v_{\parallel}, v_{\perp})$ -space. For $\gamma \in [180^\circ, 360^\circ]$ similar maps can be found as $\cos(360^\circ - \gamma) = \cos \gamma$.

and the lower row corresponding weight functions in (E, p) -coordinates. The weight functions have positive values in the coloured regions which we call interrogation regions. Ions within these regions are observable for the given u and ϕ . On the other hand, ions in white regions, where the weight functions are zero, are unobservable. Explicit expressions for the limiting lines separating the velocity space interrogation regions from the unobservable regions in $(v_{\parallel}, v_{\perp})$ -space are found by solving equation (4) for v_{\perp} .

$$v_{\perp} = \frac{u - v_{\parallel} \cos \phi}{\sin \phi \cos \gamma}. \quad (19)$$

For each gyroangle γ , there is a line of constant slope in $(v_{\parallel}, v_{\perp})$ -space along which ions with that γ project onto a given u for a given ϕ . Such lines are shown in figure 5. Two limiting lines with $\gamma = 0^\circ$ or $\gamma = 180^\circ$ are

$$v_{\perp} = \pm \frac{u - v_{\parallel} \cos \phi}{\sin \phi}. \quad (20)$$

These two lines intersect the v_{\parallel} -axis at $v_{\parallel} = u / \cos \phi$ and have the slopes $\pm v_{\perp} / \tan \phi$. Their closest distance to the origin is u . Points below these lines cannot map onto u . The weight functions are largest just above these lines at which

the gyroangle is $\gamma = 0^\circ$ or $\gamma = 180^\circ$. These large values near the limits are expected [40].

Weight functions w_v for any ϕ (except for $\phi = 0^\circ, 90^\circ, 180^\circ, 270^\circ$) and u are qualitatively similar: they are triangles in $(v_{\parallel}, v_{\perp})$ -space (figures 4(a)–(d)). If the v_{\parallel} -intercept $u / \cos \phi$ of the triangle is larger than any ion velocity (if $\phi \sim 90^\circ$), then only one of the limiting lines is relevant to the experiment such as for the proposed ITER CTS fast-ion system for $\phi \approx 100^\circ$ (figure 4(d)). The interrogation region then covers a fairly large region of the velocity distribution function in velocity space. In contrast, the weight function picks out a narrow triangle in velocity space for the forward scattering system with $\phi \approx 10^\circ$ (figure 4(a)). The projection angles $\phi = 45^\circ$ and $\phi = 80^\circ$ are shown for illustrative purpose (figures 4(b) and (c)). For $\phi = 45^\circ$ the triangle is wider than for $\phi = 10^\circ$ and intercepts the v_{\parallel} -axis at larger values. For $\phi = 80^\circ$ the triangle is yet wider and the v_{\parallel} -intercept yet larger, and the triangle is a mirror image of that for $\phi = 100^\circ$. The seemingly different shapes of the four corresponding weight functions w_{Ep} in (E, p) coordinates can likewise be explained (figures 4(e)–(h)).

The analytic weight functions are singular on the limiting lines given by equation (20) and so are inconvenient for numerical work. However, equation (15) can be integrated over u , and the integral can be shown to be unity. This is also expected since the weight function is a probability density function. We can therefore find corresponding binning weight functions $w_v^b(u, \phi, v_{\parallel}, v_{\perp})$ and $w_{Ep}^b(u, \phi, E, p)$ by binning u into intervals for $\gamma = [0, 2\pi]$ using equation (4). To do this we find contributions of Maxwellian bumps distributed in $(v_{\parallel}, v_{\perp})$ -space to a given $g(u)$ at the projected velocity u . Three such bumps were illustrated in figure 3. The weight functions are then normalized to satisfy equation (8). If the characteristic width of the Maxwellians and the bin width go to zero, the analytic weight functions are recovered with very large values near the limiting lines. We use a characteristic

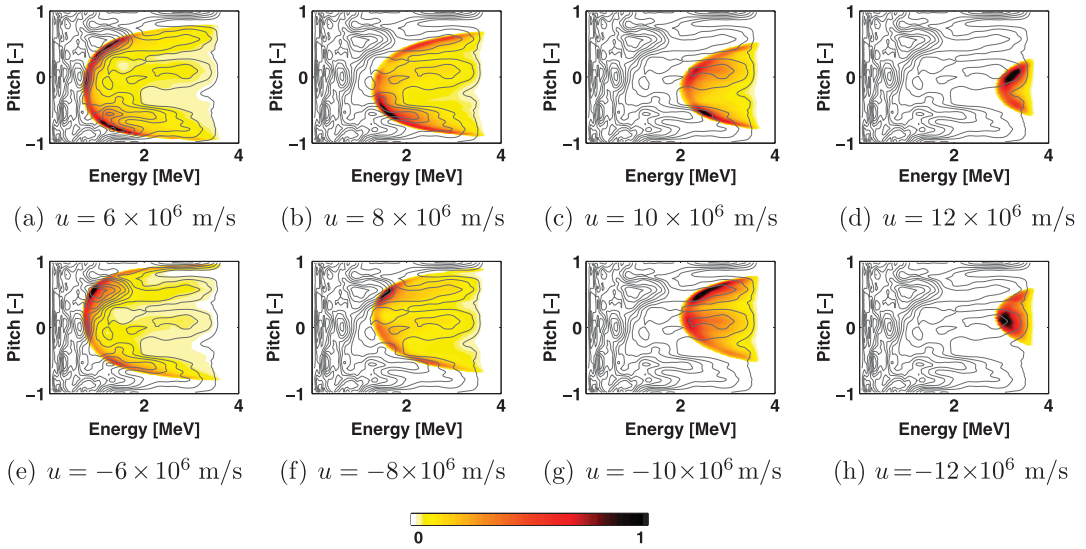


Figure 6. Relative contributions from the interrogation regions in (E, p) -space for $\phi = 100^\circ$ and various velocities u . The coloured regions show the integrand of equation (9), i.e. the product of the weight functions and a central alpha distribution function ($r/a = 0$) computed with TRANSP. The integrands have been normalized. The alpha distribution function is illustrated as grey isocontours.

width corresponding approximately to the typical resolution of numerical simulations.

5. Velocity space interrogation regions of the proposed forward- and backscattering ITER CTS systems

Figure 6 shows example interrogation regions of a single CTS spectrum for a central measurement volume of the proposed backscattering system in a standard ITER burning plasma. The colours show the integrand of equation (9) (the relative contributions to g) for $\phi = 100^\circ$ for eight example u values. The central alpha distribution function has been computed with TRANSP. The integrands in the interrogation region tend to be larger towards the small energy values because the alpha distribution function tends to be larger there. We have not converged the statistics of the alpha distribution function to be completely smooth to show the effect of small-scale features in the alpha velocity distribution. The CTS signal will then come mostly from those regions within the interrogation regions where the alphas are most numerous and the weight functions are largest. The regions without colours are unobservable with the CTS diagnostic at the given u and ϕ . The positive and negative velocities u interrogate similar regions for the backscattering system, and the 1D projections g will then be nearly symmetric. Figure 7 shows corresponding plots for the proposed forward scattering system. Co-passing ions with positive pitch at several energies can be measured for positive u and counter-passing ions with negative pitch for negative u . The interrogation regions of the forward scattering system cover a narrower region in (E, p) -space compared with those of the backscattering system.

While the weight functions are plasma independent, the integrand of equation (9) is also proportional to the particular

fast-ion distribution function. A comparison of figure 8(a) with figure 7(a) and figure 8(b) with figure 6(a) illustrates that the region from which most of the CTS signal at the given u and ϕ originates—the region which is effectively probed—can be very different for other fast-ion distributions. The weight functions in each pair are identical, but it is multiplied with the alpha distribution in figures 6 and 7 and with the NBI distribution from figure 1 in figure 8.

6. Reconstruction of the fast-ion velocity distribution function from two 1D projections

Weight functions can be used to reconstruct the fast-ion velocity distribution function from two 1D distributions along different projection directions. This problem has no unique solution [41], but it is possible to find reasonable reconstructions. Here we present an iteration algorithm to find such reconstructions by exploiting the knowledge contained in weight functions. Figure 9(a) shows three bumps in (E, p) -space as a simple test model, and figure 9(d) shows the NBI ion distribution function from figure 1 as a second test model. The aim is to reconstruct these target 2D test functions, given only two 1D projections g with different projection angles. In an actual experiment, two target 1D projections g can be obtained from two simultaneous CTS measurements with different projection angles. Here we choose the angles to be $\phi = 10^\circ$ and $\phi = 100^\circ$ corresponding to the forward- and backscattering ITER CTS systems and use only information that would not be masked by the bulk ions in ITER and are hence outside the shaded triangles in figure 3, i.e. $|u| > 3 \times 10^6 \text{ m s}^{-1}$. After an initial guess, two projections g are computed from the iterated 2D velocity distribution function. The next iteration is obtained by adding or subtracting small multiples of the weight functions for each u and ϕ to the

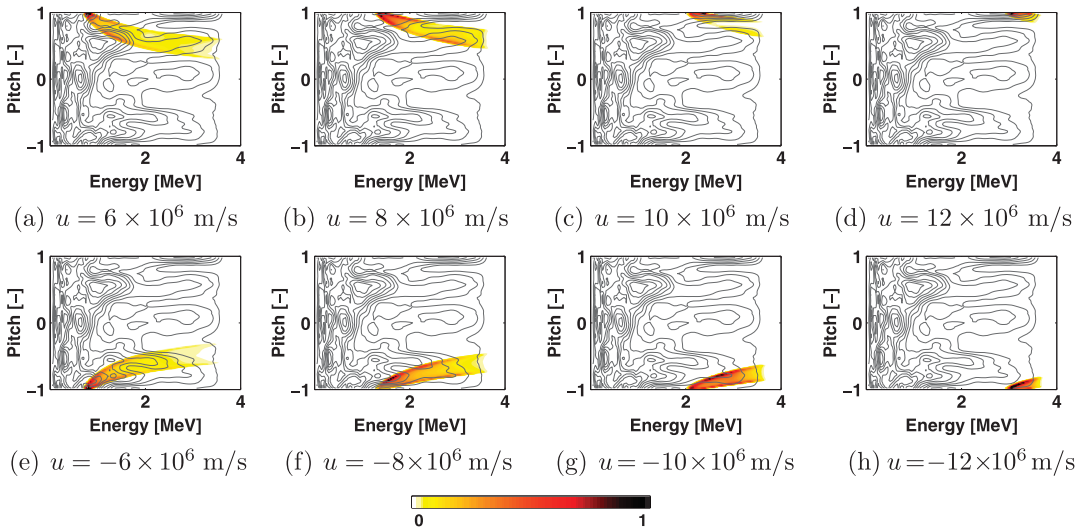


Figure 7. Relative contributions from the interrogation regions in (E, p) -space for $\phi = 10^\circ$ and various velocities u . The coloured regions show the integrand of equation (9), i.e. the product of the weight functions and a central alpha distribution function ($r/a = 0$) computed with TRANSP. The integrands have been normalized. The alpha distribution function is illustrated as grey isocontours.

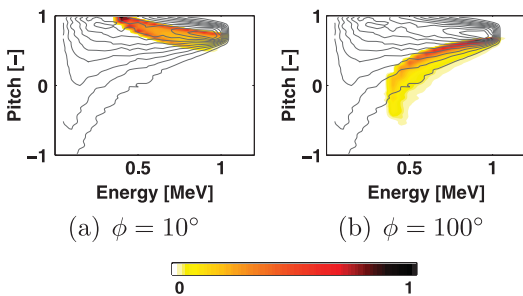


Figure 8. Relative contributions from the interrogation regions in (E, p) -space for $\phi = 10^\circ$ and $\phi = 100^\circ$ with $u = 6 \times 10^6 \text{ m s}^{-1}$. The coloured regions show the integrand of equation (9), i.e. the product of the weight functions and the high field side NBI distribution function at $r/a = 0.25$ computed with TRANSP (see figure 1(d)). The integrands have been normalized. The NBI distribution function is illustrated as grey isocontours.

2D velocity distribution function, depending on whether the corresponding iterated g is larger or smaller than the target g , respectively. The iterated solution depends on the initial guess for which we choose zeros everywhere. Reasonable reconstructions are then reliably obtained for a wide range of target functions compared with other initial guesses. Figure 9 demonstrates that large-scale features of the simple 2D test functions can reasonably be reconstructed, given only two 1D projections with $|u| > 3 \times 10^6 \text{ m s}^{-1}$ (figures 9(b) and (e)).

To demonstrate that measurements from other fast-ion diagnostics could be included in the algorithm, we use a third g for a hypothetical third projection angle ($\phi = 45^\circ$) for the reconstruction (figures 9(c) and (f)). This CTS geometry is not feasible in ITER due to refraction. However, the hypothetical extra CTS measurement serves as an example of

the possible extension of the algorithm. The reconstruction of the more complicated NBI ion distribution function improves due to the extra information. The reconstruction algorithm and its extension will be used in future experiments at ASDEX Upgrade where a second CTS receiver is currently being installed and FIDA is available [42].

7. Conclusions

Here we show the velocity space interrogation regions of the proposed ITER CTS system. The backscattering system with receivers on the low-field side is an enabled ITER diagnostic, whereas the forward scattering system with receivers on the high-field side is not. The backscattering system is sensitive to fast ions with pitch $|p| < 0.5\text{--}0.9$, depending on the ion energy and the frequency shift of the scattered radiation. Its viewing geometry makes it easy to retrofit it with a CTS-based fuel ion ratio diagnostic [43–46]. On the other hand, the forward scattering system would be sensitive to co- and counter-passing fast ions at various energies with pitch $|p| > 0.6\text{--}0.8$. Its interrogation regions in 2D velocity space are narrow compared with those for the backscattering system which cover broad ranges in (E, p) -space. The relative contributions of different regions in 2D velocity space to the CTS signal have been computed using weight functions and TRANSP simulations of the alpha and NBI ion distributions in ITER, showing the regions which are effectively probed. The interrogation regions are described by weight functions. We here derive analytic expressions for the weight functions which should also be useful for FIDA since CTS weight functions are identical to the geometric (Doppler shift) part of FIDA weight functions [35–38]. Moreover, it is shown that weight functions can efficiently be used as base functions in reconstructions of 2D fast-ion distribution functions, given two simultaneous CTS measurements with different scattering geometries. The

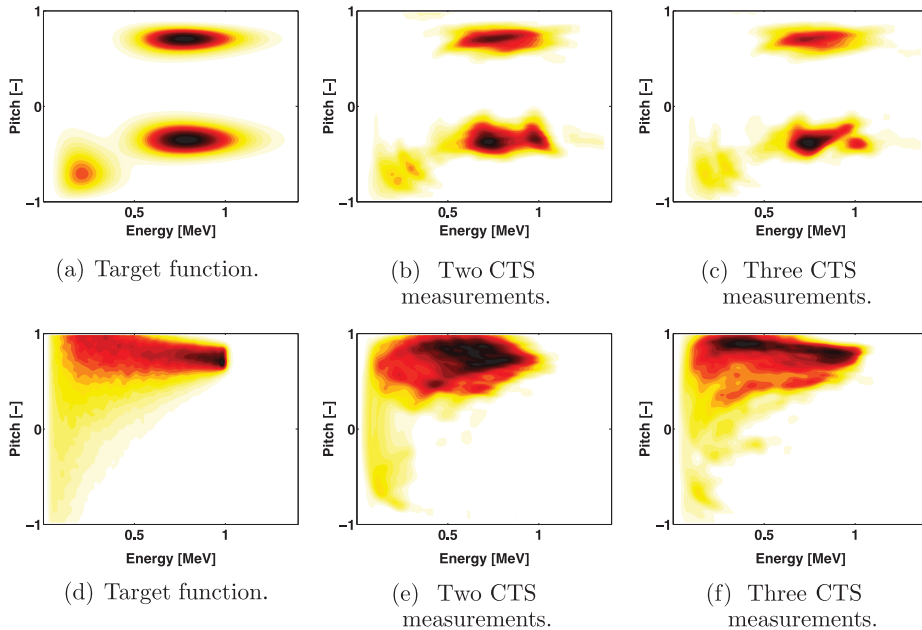


Figure 9. Reconstruction of a target function ((a) and (d)) given only the information obtained from two 1D projections g ((b) and (e)) or three 1D projections g ((c) and (f)) with $|u| > 3 \times 10^6 \text{ m s}^{-1}$. The projection angles of the two 1D projections were $\phi = 10^\circ$ and $\phi = 100^\circ$ in (b) and (c). In (c) and (f) additionally a projection with $\phi = 45^\circ$.

quality of such reconstructions can be improved by including fast-ion measurements from other diagnostics in the iteration algorithm. Thus, we have shown the benefits of the back- and forward scattering ITER CTS systems and their combination. Much added information could be gained from a forward scattering system, allowing measurements of co- and counter-passing ions with high velocity space resolution, revealing anisotropy in the fast-ion populations and even allowing reconstruction of 2D fast-ion distribution functions.

Acknowledgments

This work supported by the European Communities under the contract of Association between Euratom and Risø DTU was partly carried out within the framework of the European Fusion Development Agreement. The views and opinions expressed herein do not necessarily reflect those of the European Commission. We acknowledge the discussions on this topic within the Integrated Tokamak Modelling Activities (ITPA) Group for Energetic Particles which initiated this study.

References

- [1] Chen L. 1994 *Phys. Plasma* **1** 1519–22
- [2] Briguglio S. et al 2007 *Phys. Plasma* **14** 055904
- [3] Heidbrink W.W. and Sadler G.J. 1994 *Nucl. Fusion* **34** 535
- [4] Zweben S.J. et al 2000 *Nucl. Fusion* **40** 91–149
- [5] Heidbrink W.W. 2002 *Phys. Plasma* **9** 2113–9
- [6] Pinches S.D. et al 2004 *Plasma Phys. Control. Fusion* **46** B187–200
- [7] Gorelenkov N.N., Berk H.L. and Budny R.V. 2005 *Nucl. Fusion* **45** 226–37
- [8] Campbell D.J. et al 1988 *Phys. Rev. Lett.* **60** 2148–51
- [9] Marcus F.B. et al 1994 *Nucl. Fusion* **34** 687–701
- [10] Nielsen S.K. et al 2010 *Plasma Phys. Control. Fusion* **52** 092001
- [11] Nielsen S.K. et al 2011 *Nucl. Fusion* **51** 063014
- [12] Chang Z. et al 1996 *Phys. Rev. Lett.* **76** 1071
- [13] Nazikian R. et al 1996 *Phys. Plasma* **3** 593–605
- [14] García-Muñoz M. et al 2007 *Nucl. Fusion* **47** L10–L15
- [15] Günter S. et al 2007 *Nucl. Fusion* **47** 920–8
- [16] Hauff T., Püeschel M.J., Dannert T. and Jenko F. 2009 *Phys. Rev. Lett.* **102** 075004
- [17] Heidbrink W.W. et al 2009 *Phys. Rev. Lett.* **103** 175001
- [18] ITER Physics Expert Group on Energetic Particles, Heating and Current Drive 1999 *Nucl. Fusion* **39** 2471–95
- [19] Fasoli A. et al 2007 Progress in the ITER Physics Basis Chapter 5: Physics of energetic ions *Nucl. Fusion* **47** S264
- [20] Bindslev H. et al 1999 *Phys. Rev. Lett.* **83** 3206–9
- [21] Bindslev H. et al 2006 *Phys. Rev. Lett.* **97** 205005
- [22] Nielsen S.K. et al 2008 *Phys. Rev. E* **77** 016407
- [23] Moseev D. et al 2011 Comparison of measured and simulated fast ion velocity distributions in the TEXTOR tokamak *Plasma Phys. Control. Fusion* submitted
- [24] Meo F. et al 2008 *Rev. Sci. Instrum.* **79** 10E501
- [25] Salewski M. et al 2010 *Nucl. Fusion* **50** 035012
- [26] Meo F. et al 2010 *J. Phys.: Conf. Ser.* **227** 012010
- [27] Meo F. et al 2004 *Rev. Sci. Instrum.* **75** 3585–8
- [28] Korsholm S.B. et al 2008 Burning plasma diagnostics AIP *Conf. Proc.* **988** 118–22
- [29] Salewski M. et al 2008 *Rev. Sci. Instrum.* **79** 10E729
- [30] Salewski M. et al 2009 *Plasma Phys. Control. Fusion* **51** 035006
- [31] Salewski M. et al 2009 *Nucl. Fusion* **49** 025006
- [32] Leipold F. et al 2009 *Rev. Sci. Instrum.* **80** 093501
- [33] Donne A.J.H. et al 2007 Progress in the ITER Physics Basis Chapter 7: Diagnostics *Nucl. Fusion* **47** S337

- [34] Costley A. *et al* 2008 *Fusion Energy Proc. 22nd Int. Conf. on Fusion Energy (Geneva, Switzerland, 2008)* (Vienna: IAEA) CD-ROM file IT/1-5 and <http://www-naweb.iaea.org/nape/physics/FEC/FEC2008/html/index.htm>
- [35] Luo Y. *et al* 2007 *Rev. Sci. Instrum.* **78** 033505
- [36] Heidbrink W.W. *et al* 2007 *Plasma Phys. Control. Fusion* **49** 1457–75
- [37] van Zeeland M.A., Heidbrink W.W. and Yu J.H. 2009 *Plasma Phys. Control. Fusion* **51** 055001
- [38] Heidbrink W.W. 2010 *Rev. Sci. Instrum.* **81** 10D727
- [39] Pankin A., McCune D., Andre R. and Kritiz A. 2004 *Comput. Phys. Commun.* **159** 157–84
- [40] Heidbrink W.W. 1984 *Nucl. Fusion* **24** 636
- [41] Egedal J. and Bindslev H. 2004 *Phys. Plasma* **11** 2191–8
- [42] Geiger B. *et al* 2011 *Plasma Phys. Control. Fusion* **53** 065010
- [43] Korsholm S.B. *et al* 2010 *Rev. Sci. Instrum.* **81** 10D323
- [44] Stejner M. *et al* 2010 *Rev. Sci. Instrum.* **81** 10D515
- [45] Korsholm S.B. *et al* 2011 *Phys. Rev. Lett.* **106** 165004
- [46] Korsholm S.B. *et al* 2010 *Nucl. Instrum. Methods Phys. Res. A* **623** 677

Reference [3]

[3]. M Salewski et al. (2012) *Nuclear Fusion* **52** 103008. Tomography of fast-ion velocity-space distributions from synthetic CTS and FIDA measurements

Tomography of fast-ion velocity-space distributions from synthetic CTS and FIDA measurements

M. Salewski¹, B. Geiger², S.K. Nielsen¹, H. Bindslev³,
M. García-Muñoz², W.W. Heidbrink⁴, S.B. Korsholm¹,
F. Leipold¹, F. Meo¹, P.K. Michelsen¹, D. Moseev^{2,5}, M. Stejner¹,
G. Tardini² and the ASDEX Upgrade team²

¹ Association Euratom-DTU, Technical University of Denmark, Department of Physics, DTU Risø Campus, DK-4000 Roskilde, Denmark

² Association Euratom-Max-Planck-Institut für Plasmaphysik, D-85748 Garching, Germany

³ Faculty of Sciences and Technology, Aarhus University, DK-8000 Aarhus C, Denmark

⁴ Department of Physics and Astronomy, University of California, Irvine, CA 92697, USA

⁵ Association Euratom-FOM Institute DIFFER, 3430 BE Nieuwegein, The Netherlands

E-mail: msal@fysik.dtu.dk

Received 10 May 2012, accepted for publication 1 August 2012

Published 21 August 2012

Online at stacks.iop.org/NF/52/103008

Abstract

We compute tomographies of 2D fast-ion velocity distribution functions from synthetic collective Thomson scattering (CTS) and fast-ion D_α (FIDA) 1D measurements using a new reconstruction prescription. Contradicting conventional wisdom we demonstrate that one single 1D CTS or FIDA view suffices to compute accurate tomographies of arbitrary 2D functions under idealized conditions. Under simulated experimental conditions, single-view tomographies do not resemble the original fast-ion velocity distribution functions but nevertheless show their coarsest features. For CTS or FIDA systems with many simultaneous views on the same measurement volume, the resemblance improves with the number of available views, even if the resolution in each view is varied inversely proportional to the number of views, so that the total number of measurements in all views is the same. With a realistic four-view system, tomographies of a beam ion velocity distribution function at ASDEX Upgrade reproduce the general shape of the function and the location of the maxima at full and half injection energy of the beam ions. By applying our method to real many-view CTS or FIDA measurements, one could determine tomographies of 2D fast-ion velocity distribution functions experimentally.

(Some figures may appear in colour only in the online journal)

1. Introduction

Fast ions play a key role in high performance plasmas: they mediate energy from external heating sources or fusion reactions to the bulk plasma and so maintain the high temperatures typical for fusion-relevant plasmas. The fast-ion orbits can be perturbed by fluctuations in the plasma, and the ions can then be prematurely ejected from the plasma, leading to undesired local heating of the first wall instead of plasma heating. Several types of modes selectively deplete or reorganize fast ions in particular velocity-space regions, for example sawteeth [1–3], Alfvén eigenmodes [4–6] and neoclassical tearing modes [7]. Turbulence also ejects ions selectively depending on their energy [8, 9]. In particular, it is this selectivity of fast-ion depletion or reorganization in velocity space that can be quantified with velocity-space tomography. Additionally, velocity-space tomography could

be used to monitor phase-space engineering of fast-ion velocity distribution functions which has enabled control of sawteeth and of neoclassical tearing modes [10]. We show velocity-space tomographies using parameters typical for the ASDEX Upgrade collective Thomson scattering (CTS) [11–15] and fast-ion D_α (FIDA) diagnostics [16].

CTS and FIDA diagnostics are sensitive to 1D functions g of local fast-ion velocity distribution functions f in magnetically confined plasmas. The spatial resolution of the CTS diagnostic at ASDEX Upgrade is about 10 cm, and the measurement location can be moved freely in the plasma core by means of steerable antennas. The time resolution has often been set to 4 ms. CTS diagnostics are sensitive to the 1D projection of f onto the wave vector $\mathbf{k}^\delta = \mathbf{k}^s - \mathbf{k}^i$ which is the difference between the wave vectors of scattered radiation \mathbf{k}^s and incident radiation \mathbf{k}^i . The most important angle to describe the pre-selected projection direction given by \mathbf{k}^δ is

the projection angle $\phi_{\text{CTS}} = \angle(\mathbf{k}^\delta, \mathbf{B})$ where \mathbf{B} is the magnetic field. In CTS experiments the ions leave spectral signatures in the scattered radiation. A frequency shift ν^δ of scattered radiation can be related to an ion velocity v projected onto \mathbf{k}^δ :

$$\nu^\delta = \nu^s - \nu^i \approx v \cdot \mathbf{k}^\delta / 2\pi = uk^\delta / 2\pi \quad (1)$$

where u is the projected velocity and $k^\delta = |\mathbf{k}^\delta|$. We define here a CTS *measurement* as detection of the fast-ion phase-space density in a particular interval in u that is related to an interval in ν^δ via equation (1). We define a *view* as a set of measurements taken in a projection direction described by ϕ_{CTS} . A second CTS receiver has been installed at ASDEX Upgrade in 2012, so that two simultaneous views with independently variable projection angles ϕ_{CTS} are available.

The location of a FIDA measurement is determined by the intersection of the injected neutral beam (NBI) and the line-of-sight (LOS) of the optical head. The spatial resolution of the FIDA diagnostic at ASDEX Upgrade is about 7 cm, and the time resolution is 2 ms. Beam source S3 is observed in the plasma core at two different fixed angles $\phi_{\text{FIDA}} = \angle(\mathbf{k}^{\text{LOS}}, \mathbf{B})$ where \mathbf{k}^{LOS} represents the wave vector along the LOS of the optical heads. The toroidal LOS has an angle of $\phi_{\text{FIDA}} = 11^\circ$, and the new poloidal LOS has $\phi_{\text{FIDA}} = 64^\circ$. The angles ϕ_{CTS} and ϕ_{FIDA} are analogue and will hereafter simply be called ϕ . FIDA diagnostics are also sensitive to 1D functions of f as the fast ions likewise leave a spectral signature in the detected light by Doppler shift and Stark splitting. For FIDA diagnostics no simple relation between the projected velocity u and the wavelength λ exists, so we define here as FIDA *measurement* the detection of Doppler- and Stark-shifted light in a particular wavelength interval.

Computed tomography in real space is used in many applications, for example in medical imaging in x-ray computed axial tomography (CAT or CT) scanners, positron emission tomography (PET) scanners or magnetic resonance imaging (MRI) scanners [17, 18]. It is also widely used in nuclear fusion research [19, 20]. We give a new prescription for tomographic reconstruction in velocity space that is analogue to those in real space. The prescription is based on CTS or FIDA weight functions [21–23] which were not available in previous work [24]. In [24] reconstructions from two and three synthetic CTS views have been shown to contain salient features of the underlying 2D fast-ion velocity distribution functions in idealized situations. It has since become conventional wisdom that a 2D velocity distribution function could not be found from one single 1D CTS or FIDA view and that at least two CTS or FIDA views with different projection directions would be necessary for that [12, 22–32]. We demonstrate that in fact just one single 1D CTS or FIDA view theoretically suffices to compute tomographies of almost the entire discrete 2D velocity distribution function under idealized conditions. Nevertheless, in simulated tokamak experiments with many CTS or FIDA views, the resemblance of tomographies and the original functions improves with the number of available views. Several tokamaks have been equipped with multiple FIDA views, for example DIII-D [33], NSTX [34], MAST or ASDEX Upgrade which is now also equipped with two CTS receivers. With our prescription we can compute tomographies for any set of fast-ion measurements, in particular those obtained with CTS or

FIDA or other fast-ion charge exchange spectroscopy (FICXS) that detects other light than D_α . A mix of diagnostics would also be possible as will be relevant to the CTS/FIDA system at ASDEX Upgrade, the CTS/FICXS system at LHD [35, 36] and the proposed two-view CTS system for ITER [37–40] in particular if it can be combined with FICXS [32]. However, only one of the two CTS views is an enabled ITER diagnostic. One could also include neutral particle analysers (NPAs) or other fast-ion diagnostics in such mixes. We will study tomographies from such diagnostic mixes elsewhere.

In section 2 we will argue that one single 1D set of CTS measurements at different frequencies in fact theoretically suffices to reconstruct the original 2D velocity distribution function under ideal conditions. As weight functions form the core of our tomographic reconstruction prescription to be presented in section 4, we briefly review their meaning and use in section 3. Tomographic reconstructions of a variety of functions from synthetic CTS measurements under idealized conditions are demonstrated in section 5 and under simulated experimental conditions in section 6. In section 7 we show that tomographies can likewise be computed from synthetic FIDA measurements. We discuss the analogy of velocity-space tomography to real-space tomography in section 8 and draw conclusions in section 9.

2. Velocity-space tomography gedankenexperiment

First we perform a gedankenexperiment to motivate how one single 1D projection can in fact contain enough information to reconstruct the underlying 2D velocity-space distribution function in discrete problems. Suppose that Alice has a way to construct a 2D velocity-space distribution function f ion by ion and that Bob has a way to measure the 1D velocity distribution function g by CTS every time a new ion has been added. Bob will only know his own measurements obtained in a single CTS view. Alice adds an ion at some coordinate pair $(v_{\parallel}, v_{\perp})$ of her choice, for example at the location chosen in figure 1(a). Bob then measures g which would have the characteristic hammock shape shown in figure 1(b) [23, 41]. Bob can now work out the $(v_{\parallel}, v_{\perp})$ -coordinates using

$$u = v_{\parallel} \cos \phi + v_{\perp} \sin \phi \cos \gamma, \quad (2)$$

where γ is the gyrophase of the ion [23]. Since $\cos \gamma$ takes values from -1 to 1 , the width of the interval in which Bob detects the ion is $2v_{\perp} \sin \phi$. The centre of the interval is $v_{\parallel} \cos \phi$. Knowing his projection angle ϕ and the width and centre of his measured function g , he can tell at which coordinates $(v_{\parallel}, v_{\perp})$ Alice has added the ion. Alice then adds a second ion at a velocity-space location of her choice, and Bob again measures g by CTS. Now the function g looks more complicated but Bob can subtract his previous function g and has again a simple hammock-shaped function from which he can deduce the location of the second ion. This procedure can be repeated until the entire 2D velocity distribution function is constructed ion by ion, and Bob will know the entire function exactly, looking just at his 1D measurements. Alice could also construct f by adding collections of ions with identical velocities instead of single ions. Bob could then tell how many

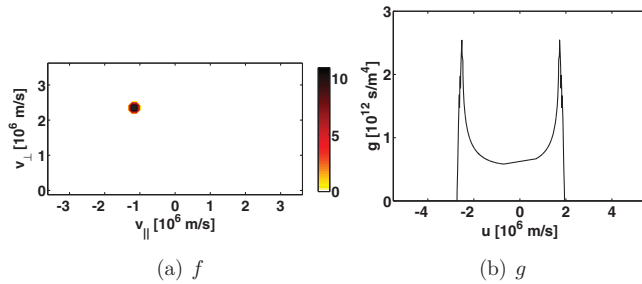


Figure 1. (a) Example function f consisting of a single pixel in arbitrary units. (b) Projection g of the pixel function for a projection angle of $\phi = 70^\circ$.

ions have been added since the integral over u is proportional to the number of ions:

$$n = \int g \, du = \int \int f \, dv_{\parallel} \, dv_{\perp}. \quad (3)$$

This gedankenexperiment shows that one single 1D CTS view can in fact contain enough information for accurate reconstruction firstly in simple situations and secondly also in arbitrarily complicated situations if the complexity is added step by step. In real experiments only the complicated situation can be generated, and it is not immediately obvious that the 1D function g can contain enough information about the 2D function f . But we will demonstrate that we can compute accurate tomographies from one single CTS or FIDA view using our tomography reconstruction prescription if just enough information is available.

3. Discrete weight functions for CTS and FIDA

Discrete weight functions will lead to the tomographic reconstruction prescription presented in section 4. The reconstruction prescription in [24] did not use weight functions and was made tractable by expansion of the 1D (synthetic) measurements as well as the 2D fast-ion velocity distribution functions into orthonormal sets of base functions. Bessel functions have been used but other choices would be possible [24]. Exploiting CTS or FIDA weight functions [21–23] we will give a simpler reconstruction prescription that is inherently tractable and obviates the use of such expansions. Weight functions have previously been used in an alternative reconstruction prescription where the tomography was found by iteration. This has the disadvantage that the solution depends on the arbitrary start conditions of the iteration [23]. The new prescription we present gives unique solutions. In this section we define weight functions in discrete form.

Assuming f to be rotationally symmetric about the v_{\perp} -axis, weight functions describe the mapping from 2D velocity-space distribution functions f to 1D functions g that are measured with CTS [23] or FIDA [22]. We here treat a discrete tomography problem and so also deal with discrete functions. The coordinates $(u, \phi, v_{\parallel}, v_{\perp})$ are discretized in $(u_i, \phi_j, v_{\parallel k}, v_{\perp l})$ where the subscripts i, j, k, l run from 1 to the corresponding upper case letter I, J, K, L . I is the number of measurements at different u_i in a CTS or FIDA view, J is the number of available views, and (K, L) are the number

of grid points in $(v_{\parallel}, v_{\perp})$, respectively. $g_{ij} = g(u_i, \phi_j)$ is a matrix of discrete 1D functions in u_i for each viewing angle ϕ_j . $f_{kl} = f(v_{\parallel k}, v_{\perp l})$ is the discrete 2D velocity-space distribution function. g_{ij} and f_{kl} are related by discrete CTS or FIDA weight functions w_{ijkl} analogue to the continuous weight functions [23] so that

$$g_{ij} = \sum_{k=1}^K \sum_{l=1}^L w_{ijkl} f_{kl} \Delta v_{\perp} \Delta v_{\parallel}. \quad (4)$$

Weight functions pick out and assign weights to the velocity-space interrogation region that is observed for a particular projection angle ϕ_j and a projected velocity range at u_i (observed in a frequency range at f_i) for CTS or a wavelength range at λ_i for FIDA. In $(v_{\parallel}, v_{\perp})$ -coordinates CTS weight functions have a nearly triangular shape as shown in figure 2 for $u_i = 2 \times 10^6 \text{ m s}^{-1}$ and four typical projection angles ϕ_j . Weight functions describing CTS measurements quantify the probability that a gyrating ion with velocity $(v_{\parallel}, v_{\perp})$ is observed in a particular projected velocity range at u_i for a given projection angle ϕ_j . The scattering must always originate from the coloured triangular region. A comprehensive discussion of weight functions for fast-ion CTS measurements is given elsewhere [23]. The weight functions describing FIDA measurements are more complicated and account for the charge exchange probability, the probability of photon emission from atomic level $n = 3$ to $n = 2$, Doppler shift of radiation originating from a gyrating particle, Stark splitting of the deuterium Balmer alpha line, and the instrument function of the FIDA spectrometer [16, 21, 22, 26, 29]. The Doppler shift part of FIDA weight functions is analogous to the CTS weight functions [23].

4. Tomographic reconstruction prescription

To find tomographies from CTS or FIDA measurements, we rewrite equation (4) to formulate a linear algebra problem of the form

$$W_{mn} F_n = G_m. \quad (5)$$

The matrix elements G_m , F_n and W_{mn} are, respectively, obtained from the matrix elements g_{ij} , f_{kl} and w_{ijkl} by

$$G_m = g_{ij} \quad (6)$$

$$F_n = f_{kl} \quad (7)$$

$$W_{mn} = w_{ijkl} \quad (8)$$

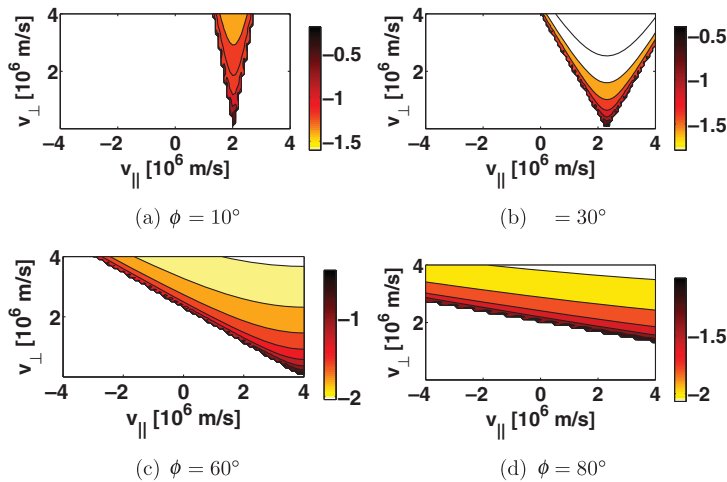


Figure 2. Gyromotion weight functions w for $u = 2 \times 10^6 \text{ m s}^{-1}$ and various projection angles ϕ . The colourbar shows the base 10 logarithm.

using the assignment rules

$$m = (i - 1) \times J + j \quad (9)$$

$$n = (k - 1) \times L + l. \quad (10)$$

F is a column matrix of size $N \times 1$ obtained from the discrete 2D fast-ion velocity distribution function described by $N = K \times L$ points. G is a column matrix of size $M \times 1$ obtained from the discrete 1D functions measured with CTS or FIDA. If J views are available and I measurements in u_i (CTS) or λ_i (FIDA) are taken in each view, then the total number of measurements is $M = I \times J$. W is then a transfer matrix of size $M \times N$ taking F into G . The prescription given here corresponds to stacking lines or rows on top of each other but the order of this reorganization of the matrices is arbitrary as long as we obey equation (4). The forward problem to determine g from f or equivalently G from F is straightforward given that w and consequently W are known. An example of the action of the transfer matrix W on a pixel function F is illustrated in figure 1. The projection angle ϕ_j of this single-view example ($J = 1$) is set to 70° , and we compute a weight function for each u_i to obtain the value of G from the inner product WF . The 1D function G for a pixel function has the characteristic hammock shape shown in figure 1. The inverse problem to determine f from g or equivalently F from G is more complicated: we have to find an optimum solution F^+ to the under- or overdetermined system of linear equations (equation (5)) where W and G are known. We then also know f^+ because we know F^+ and the reorganization procedure.

We find an optimum solution to $WF = G$ for any size of W from the Moore–Penrose pseudoinverse or generalized inverse W^+ under positivity constraint. W^+ is a unique $N \times M$ matrix [42–44]. It can be computed from the singular value decomposition (SVD) of W : an $M \times N$ matrix W can always be decomposed uniquely as

$$W = U \Sigma V^T \quad (11)$$

where U is the normalized eigenvector matrix of WW^T (an orthogonal $M \times M$ matrix), V is the normalized eigenvector matrix of $W^T W$ (an orthogonal $N \times N$ matrix), V^T denotes the transpose of V , and Σ is a diagonal (but rectangular) $M \times N$ matrix [44]. The diagonal entries $\sigma_1, \sigma_2, \dots, \sigma_R$ are the singular values of W , and R is the rank of W . The other entries of Σ are zero. The Moore–Penrose pseudoinverse is then

$$W^+ = V \Sigma^+ U^T \quad (12)$$

Σ^+ is a diagonal (but also rectangular) $N \times M$ matrix, and the diagonal entries are $1/\sigma_1, 1/\sigma_2, \dots, 1/\sigma_R$, i.e. the reciprocals of corresponding entries of Σ . The other entries of Σ^+ are zero. The computed tomography is then

$$F^+ = W^+ G. \quad (13)$$

This is the equation from which we could determine F^+ from actual measurements. If W is invertible, then W^+ is identical to the inverse W^{-1} . But W is generally a rectangular $M \times N$ matrix that cannot be inverted. If the system $WF = G$ is overdetermined, F^+ gives the minimum 2-norm of the residual $|WF - G|_2$. If the system $WF = G$ is underdetermined, F^+ is the particular solution with minimum 2-norm $|F|_2$ out of infinitely many solutions (the one with no nullspace component).

5. Tomographies under ideal conditions

In this section we firstly demonstrate that our prescription for computed tomography in velocity space can reproduce a variety of functions—any function we tested—in an idealized situation. Secondly, we also demonstrate that just one single synthetic CTS or FIDA view on that function suffices to construct an accurate tomography. We assume that the function can be described accurately on a numerical 2D grid, i.e. the grid size is so fine that even features on the smallest scale are accurately described. We also assume that there is no

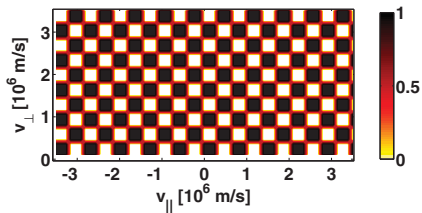


Figure 3. The original checkerboard function shown here is digitized in $N = 30 \times 61$ pixels. Typical 1D projections are shown in figure 4. Tomographies are shown in figure 5.

noise. The effects of insufficient resolution and noise will be discussed in section 6. Under these idealized conditions, we set the numerical grid of the tomography equal to that of the original function. As will be shown in section 6, these assumptions will not give a realistic picture of the recoverable information in real experiments. Nevertheless, previous work used identical grids for tomography and the original function [23, 24], and the results found in this section give an upper limit of the quality that can be achieved and demonstrate that one single view is enough under ideal conditions. Our prescription immediately suggests that the tomography should be very accurate in this case if just $M > N$ (more measurements than pixels). If the numerical grids of the original function and the tomography are equal, we can give a simple relation between F and F^+ . One can substitute for G and use the orthogonality of U .

$$F^+ = W^+G = W^+WF = V\Sigma^+U^T U\Sigma V^T F = V\Sigma^+\Sigma V^T F \quad (14)$$

$\Sigma^+\Sigma$ has as R ones on the diagonal and otherwise zeros. Therefore, only the first R columns and rows of V and V^T will be used in the reconstruction. In that sense the reconstruction for identical numerical grids is analogue to lossy data compression using SVD [44].

Under these assumptions, we reconstruct a checkerboard function (figure 3) and a pacman function (figure 6) using just one single view. We choose these test functions because it is easy to spot differences between the original function and the tomography. The checkerboard pattern in figure 3 covers the velocity-space region for $-3.5 \times 10^6 \text{ m s}^{-1} < v_{\parallel} < 3.5 \times 10^6 \text{ m s}^{-1}$ and $0 < v_{\perp} < 3.5 \times 10^6 \text{ m s}^{-1}$ and is digitized in $N = 30 \times 61 = 1830$ pixels. This resolution is typical for simulated fast-ion velocity distribution functions today. We distribute M measurements evenly in the interval $-5 \times 10^6 \text{ m s}^{-1} < u < 5 \times 10^6 \text{ m s}^{-1}$ to ensure complete coverage of the velocity-space region we show here for any ϕ . Synthetic measurements in one single view for $\phi = 30^\circ$ and $M = 101$ to $M = 2501$ are illustrated in figure 4. By increasing the resolution one can capture an increasingly more fine-grained structure of g that contains recoverable information about the 2D function f . We stress that the noisy looking curve ($M = 2501$) is the accurate one whereas the smooth looking curve ($M = 101$) contains the least information. Actually the smooth curve has a large noise level originating from the discretization. The resolution in the u coordinate for $M = 101$ corresponds roughly to the resolution of most of the channels of the ASDEX Upgrade

CTS receivers. Over 2500 measurements in one view seem possible in high-frequency resolution measurements that were demonstrated at TEXTOR [45–47].

Single-view tomographies computed from M synthetic measurements such as those in figure 4 are presented in figure 5. For any resolution they contain a fine-grained structure that is similar to that in the original in figure 3. Even for $M \sim N/20$ ($M = 101$), the tomography contains evenly distributed small-scale structures but they are larger than those in the original by a factor of two. The checkerboard pattern at a correct scale begins to emerge when $M \sim N/2$ ($M = 1001$). For $M \sim N$ the tomography closely resembles the original with minor defects, and for $M \sim 4N/3$ they are indistinguishable. The reconstruction prescription in previous work [24] failed to reconstruct the original function for low v_{\perp} corresponding to about $v_{\perp} < 10^6 \text{ m s}^{-1}$ in our graphs. The checkerboard patterns in figure 5 demonstrate that our prescription works for all v_{\perp} about evenly.

Figure 7 shows single-view tomographies of the pacman function (figure 6), which we consider to be quite complex, for a various number of measurements M . From here on we do not use measurements in the interval $-0.7 \times 10^6 < u < 0.7 \times 10^6 \text{ m s}^{-1}$. CTS due to bulk ions makes unambiguous detection of fast ions very difficult if not impossible in this interval, and so we block it in the synthetic diagnostic. This loss of information results in the appearance of triangular regions that are not experimentally accessible (figures 7(a)–(d)). The shape of such triangles depends on the projection angle ϕ . The sides of these triangles are given by $v_{\perp} = (\text{const} \times v_{\text{th}} \pm v_{\parallel} \cos \phi) / \sin \phi$ and $v_{\perp} = 0$ [23]. The original pacman function contains complicated structures with a scale separation of one order of magnitude between the large-scale structures (pacman head, spook) and the small-scale fine details (eyes and mouth, zick zack pattern of the spook fringe). The tomography of the pacman function is also an accurate reproduction of the original function if M is large enough. The required number of measurements M for accurate tomographies is similar to the required M for the checkerboard—and in fact for any function we tested—and does not significantly depend on whether an interval in u has been blocked.

Lastly, we note that the projection angle ϕ is not very important in the idealized situation except for at $\phi = 90^\circ$ when all information about v_{\parallel} is lost and at $\phi = 0^\circ$ where the weight functions are singular. No advantage is gained from having many views for an equal total number of measurements M in the idealized situation. For example a tomography from two views each with 1000 measurements ($M = 2 \times 1000 = 2000$) roughly resembles the original as much as the tomography from one view with $M = 2000$ measurements. Likewise, the angles are not important for many-view systems either if just the resolution of the measurements is high enough. The quality of the tomography for any number of views depends mostly on the total number of measurements M in the idealized situation.

6. Tomographies for heavily under-diagnosed fast-ion distribution functions

The previous section demonstrated that our tomography prescription will work in an idealized situation. The original function had the same number of grid points as

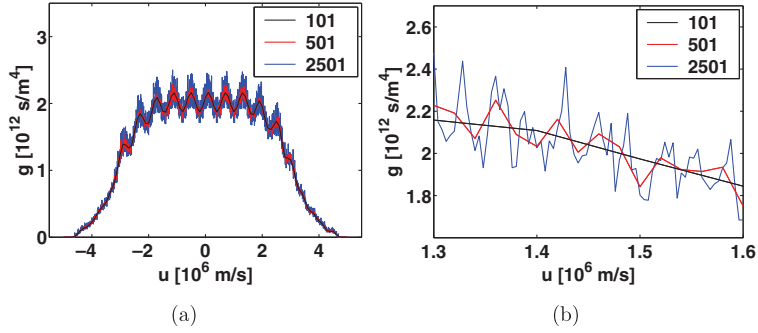


Figure 4. Projections of the checkerboard function (figure 3) for $\phi = 30^\circ$ with $M = 101, 501$ and 2501 measurements in one view g . (a) Zoomed out showing the entire functions g . (b) Zoomed in showing that fine-scale structure can be resolved with $M = 2501$ measurements, which is sufficient to compute an accurate tomography.

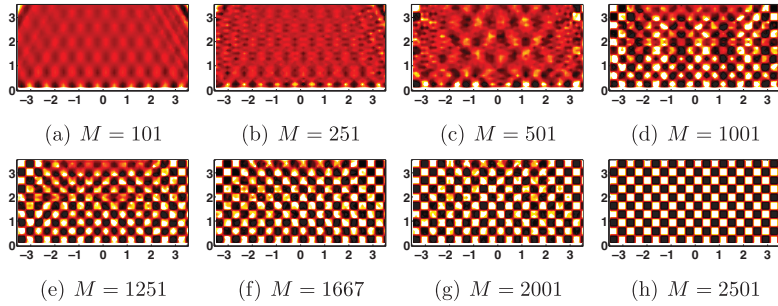


Figure 5. Single-view tomographies of a checkerboard function in $N = 30 \times 61 = 1830$ pixels giving only M measurements at $\phi = 30^\circ$. The M measurements are evenly spaced in $-5 \times 10^6 \text{ m s}^{-1} < u < 5 \times 10^6 \text{ m s}^{-1}$. The number of measurements is varied from $M = 101$ to $M = 2501$. The axes and colourbars are identical to those for the original in figure 3.

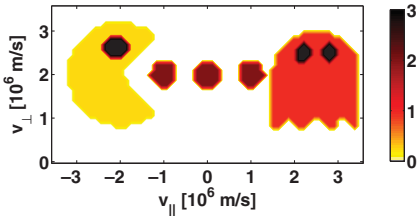


Figure 6. The original pacman function shown here is digitized in $N = 30 \times 61 = 1830$ pixels. Tomographies are shown in figure 7.

the reconstructions as in previous work [23, 24]. The 2D velocity distribution function in an actual tokamak experiment will have a fine-grained structure. It is then practically impossible to make enough CTS or FIDA measurements to carry all information about the fine-grained f . To simulate experimental conditions, we first construct a 1D projection g with M synthetic measurements from a finely resolved 2D distribution:

$$G = W_1 F. \quad (15)$$

Here we discretize f in $N_1 = 350 \times 701 \sim 250\,000$ grid points and take $M \sim 3400$ or $M \sim 340$ measurements leaving f under-diagnosed by a factor on the order of 100 or 1000, respectively. Accurate tomographies are impossible for such

under-diagnosed f . Then we compute a tomography with a much lower number of grid points than N_1 : $N_2 = 30 \times 61 = 1830 \ll N_1$.

$$F^+ = W_2^+ G. \quad (16)$$

Substitution of G now gives

$$F^+ = V_2 \Sigma_2^+ U_2^T W_1 F. \quad (17)$$

Substitution of the SVD of $W_1 = U_1 \Sigma_1 V_1^T$ does not lead to simplifications as in equation (14) since $U_2^T U_1$ does not disappear. If the grids for the tomography and the original function are not identical, it is necessary to truncate the SVD and use only singular values above a selected level. This is effectively also a lossy data compression technique since we find a lower rank approximation of the transfer matrix W_2 that has about rank $R \sim 1700$ in our example. Reference [24] used such a lossy data compression technique to simulate the effects of noise, noting that noise decreases the information content of the smallest singular values. The effect of noise and of under-diagnosing, i.e. computing the tomography on a much coarser grid than the original, are similar. $G = W_1 F$ is different from $G^+ = W_2^+ F^+$, and this difference can be interpreted as noise originating from the discretization.

Figure 8 shows a typical beam ion velocity distribution function at ASDEX Upgrade resolved on $N_1 = 350 \times 701$ grid points for which we present tomographies from CTS

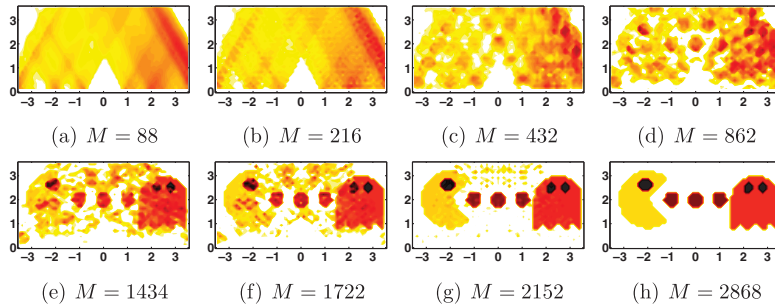


Figure 7. Single-view tomographies of a pacman function in 1830 pixels giving only M measurements at $\phi = 30^\circ$. The M measurements are evenly spaced in $-5 \times 10^6 \text{ m s}^{-1} < u < -0.7 \times 10^6 \text{ m s}^{-1}$ and $0.7 \times 10^6 \text{ m s}^{-1} < u < 5 \times 10^6 \text{ m s}^{-1}$. The number of measurements is varied from $M = 88$ to $M = 2868$. The axes and colourbars are identical to those in figure 6.

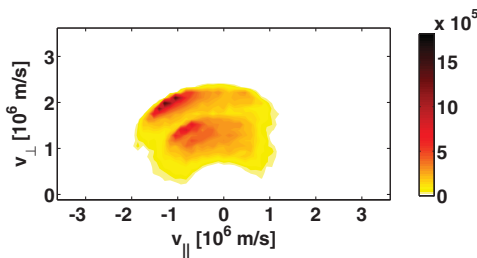


Figure 8. Typical beam ion distribution function for beam S3 at ASDEX Upgrade computed with TRANSP/NUBEAM. The distribution function is shown on a grid with 350×701 pixels.

measurements here. The original function has peaks at full and half injection energy of 60 keV in deuterium. We plot tomographies ($N_2 = 30 \times 61 = 1830$ grid points) of the original function in figure 9 for a various number of available views J and measurements M . The three-view and four-view CTS tomographies are proxies for mixed CTS/FIDA tomographies that can be reconstructed from the two available CTS views and the two available FIDA views at ASDEX Upgrade. The combination of different diagnostics in our method will be discussed elsewhere. We set the number of measurements per view inversely proportional to the number of views so that the total number of measurements M is almost the same in each column of figure 9. The left column shows tomographies for one to four views with about $M \sim 340$ measurements in total ($M < N$), and the right column with about $M \sim 3400$ measurements in total ($M > N$). In the idealized situation the number of views J is unimportant; only the number of measurements M matters. Therefore, just one view suffices for accurate tomographies in the idealized situation. However, under simulated experimental conditions, the number of views J is highly important for the relevance of the tomography to the original function. The single-view tomographies do not resemble the original function but they resemble rather the weight functions, and taking more measurements M in that one view does not help significantly. Nevertheless, the lopsidedness towards negative velocities is correctly reconstructed in the tomographies. For two views the region of the beam ions is roughly identifiable, and two maxima emerge. The four-view tomographies resemble the original

function best. To quantify the difference between the original function and the tomography, we define an error measure as

$$Q_{\text{tom}} = \frac{1}{n_{\text{fast}}} \int \int |f - f^+| dv_{\parallel} dv_{\perp} \quad (18)$$

$$n_{\text{fast}} = \int \int f dv_{\parallel} dv_{\perp} \quad (19)$$

which is a single number quantifying the resemblance of the tomography with the original function. $Q_{\text{tom}} = 0$ means that the match is perfect, and $Q_{\text{tom}} \sim 1$ means that f^+ does not resemble the original function f . In this example $Q_{\text{tom}} = 1$ for one view, $Q_{\text{tom}} = 0.8$ for two views, $Q_{\text{tom}} = 0.7$ for three views and $Q_{\text{tom}} = 0.5$ for four views, but the particular values depend on the particular distribution function and the diagnostic setup. This measure should be useful for future optimization studies. Comparing the low resolution column ($M < N$) with the high resolution column ($M > N$), we find that taking ten times more measurements per view does not help improving the tomographies much whereas adding extra views does. For the high resolution cases with $M \sim 3400$ only 340 singular values are useful whereas about 300 are useful in the low resolution cases with $M \sim 340$.

We now illustrate tomographies of a simpler function from synthetic CTS measurements. Figure 11 shows tomographies of a drifting Maxwellian function with $N_1 = 350 \times 701$ pixels (figure 10) that we then diagnose in one to four views, and we seek tomographies with $N_2 = 30 \times 61 = 1830$ pixels. Even though the number of measurements $M \sim 2000$ is again almost the same for the four cases, the tomographies improve with the number of views. One view is not enough to give tomographies that resemble the original. Nevertheless, the tomography for just one single view correctly identifies the location of the Maxwellian peak, so we can conclude that measurements in one single view contain relevant information about f even under simulated experimental conditions.

7. Tomographies from FIDA measurements

So far we have built the transfer matrix W from gyromotion weight functions, and these are sufficient to describe CTS measurements. Analytic expressions for these CTS weight functions are available [23]. Weight functions relevant to FIDA measurements are more complicated and are calculated

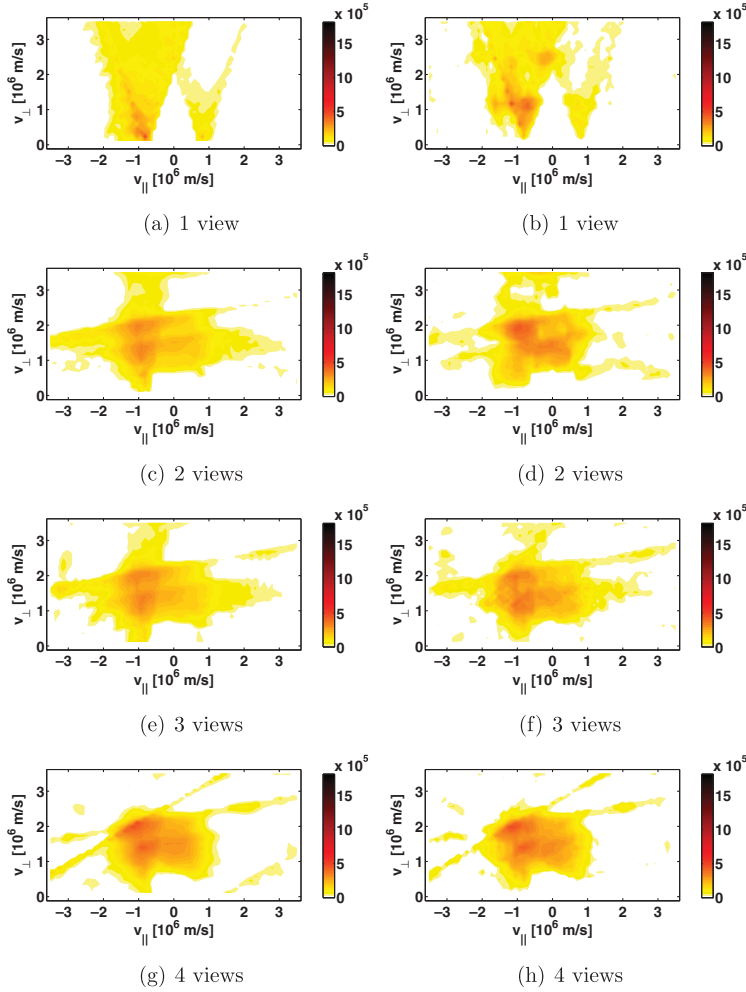


Figure 9. Tomographies ($N_2 = 30 \times 61$ pixels) of a typical beam ion distribution function ($N_1 = 350 \times 701$ pixels) for various numbers of views and measurements M . The total number of measurements M is similar in each column. In the left column (a), (c), (e), (g) $M \sim 340$ whereas in the right column (b), (d), (f), (h) $M \sim 3400$. The viewing angles are $\phi = 20^\circ$ for one view, $\phi = (10^\circ, 80^\circ)$ for two views, $\phi = (10^\circ, 40^\circ, 80^\circ)$ for three views and $\phi = (10^\circ, 30^\circ, 60^\circ, 80^\circ)$ for four views.

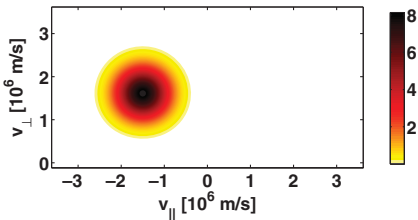


Figure 10. A drifting Maxwellian resolved in 350×701 pixels.

by counting photons in the different wavelength intervals. FIDA weight functions therefore contain numerical noise that decreases with the square root of the computer time allowed for their computation. We use $\phi = (11^\circ, 64^\circ)$ for the two FIDA

views available at ASDEX Upgrade. The measurements M are evenly distributed in the wavelength intervals $649 \text{ nm} < \lambda < 654 \text{ nm}$ and $659 \text{ nm} < \lambda < 663 \text{ nm}$. FIDA light cannot be observed in the wavelength interval $654 \text{ nm} < \lambda < 659 \text{ nm}$ due to beam emission and halo neutrals [16], and so we exclude this wavelength range also in the synthetic measurements. Figure 12 shows a tomography of the original function (figure 8) from synthetic measurements for the two-view FIDA system at ASDEX Upgrade and demonstrates that our prescription also works for FIDA measurements. The original has $N_1 = 350 \times 701$ grid points which was here diagnosed by $M = 2 \times 90 = 180$ measurements, and the tomography in figure 12 has $N_2 = 30 \times 61 = 1830$ grid points. We here use the largest 80 singular values for the computation of the Moore–Penrose pseudoinverse.

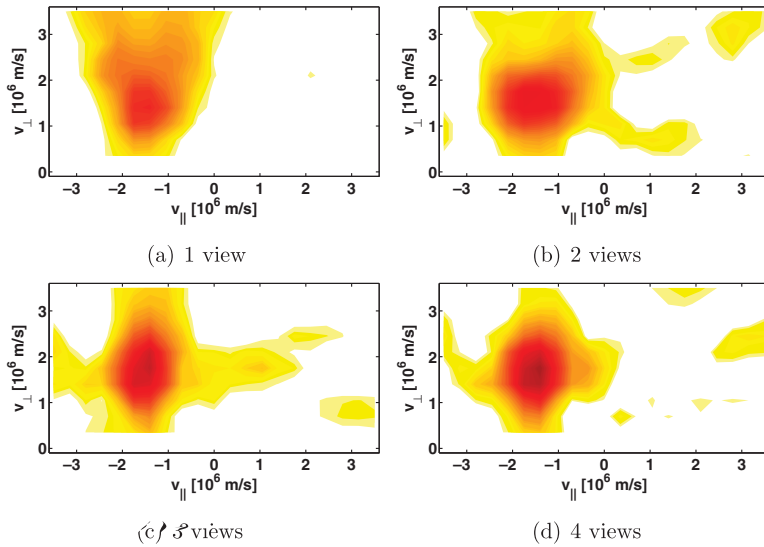


Figure 11. Tomographies in $N_2 = 30 \times 61 = 1830$ pixels for the drifting Maxwellian shown in figure 10 for $M \sim 2000$ evenly distributed on the available views. The viewing angles are $\phi = 20^\circ$ for one view, $\phi = (30^\circ, 60^\circ)$ for two views, $\phi = (10^\circ, 40^\circ, 80^\circ)$ for three views and $\phi = (10^\circ, 30^\circ, 60^\circ, 80^\circ)$ for four views.

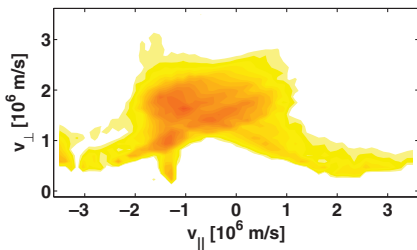


Figure 12. Tomography with $N_2 = 30 \times 61$ pixels from the two-view FIDA system with $\phi = (11^\circ, 64^\circ)$ and $M = 2 \times 90 = 180$ simulated measurements.

8. Analogy between real-space tomography and velocity-space tomography

Computed tomography in real space is a well-developed technique with applications in medical diagnostics, geo- and astrophysics, material science and many other disciplines [17, 18]. An important application is medical imaging in x-ray CT scanners, in MRI scanners, or in PET scanners. For example, x-ray CT scanners measure the absorption of several narrow x-ray beams through the patient. The absorption of x-rays depends on the tissue type, e.g. bones, muscle tissue, or fatty tissue. CT with x-rays may be carried out using a single x-ray source and a detector that are moved together to scan a beam through the patient. One viewing angle on the patient is not enough because the measurement is line-integrated and it is not known where along the LOS the x-rays have been absorbed. In CT scanners the source–detector arrangement is rotated, and the patient is scanned at another angle. By scanning the patient at many angles one can deduce a tomography of absorption coefficients that in turn give the tissue type. We note

that tomographies in medical imaging thankfully operate with overdetermined systems of equations to obtain their accurate results.

It would be misleading to identify the FIDA or CTS projection angle ϕ with the viewing angle of the rotating apparatus of medical CT scanners. In plasmas in fact we have an intrinsic rotation of the object that allows a multitude of measurements: the gyration of the ions about the magnetic field. This gyration allows measurements of an ion at different frequency shifts via equations (1) and (2). It is this multitude of frequency-space measurements in velocity-space tomography that is analogue to the different viewing angles in real-space tomography. Many viewing angles in velocity space improve tomographies under realistic conditions but they are not essential under idealized conditions. For that reason one single CTS or FIDA view suffices for a tomography of the velocity-space distribution function in an idealized situation if just the resolution of the frequency-space measurements is high enough.

9. Conclusions

We have presented a new prescription for tomographic reconstruction of 2D fast-ion velocity distribution functions from CTS and FIDA measurements. By computing tomographies from synthetic measurements, we have demonstrated our prescription to give accurate tomographies of arbitrary functions in an idealized situation, and we have shown promise and limits of its application to real experiments. Our tomographic and theoretical results contradict the conventional wisdom that at least two CTS or FIDA views would necessarily be required for tomography of fast-ion velocity distribution functions [12, 22–32]. In an idealized situation in fact just one single CTS or FIDA view suffices to compute an accurate

tomography. Under simulated experimental conditions, tomographies contain salient features of the original fast-ion velocity distribution function showing that 2D information can be recovered from the 1D measurements in one single view. The lopsidedness of a beam ion velocity distribution and the peak location of a drifting Maxwellian function can correctly be reproduced in single-view tomographies for a range of angles but otherwise single-view tomographies do not resemble the original functions. For many-view systems the resemblance of the tomography and the original improves each time a new CTS or FIDA view is added, even if the resolution is varied inversely proportional to the number of views so that the total number of measurements in all views is constant. For a four-view system, the tomography of a realistic beam ion velocity distribution function at ASDEX Upgrade resembles the original function well in general shape and location of the beam injection sources at full and half energies. By applying our prescription to a set of real CTS or FIDA measurements with many views, one could determine a tomography of the 2D fast-ion velocity distribution function experimentally.

Acknowledgments

This work, supported by the European Communities under the contract of Association between Euratom and DTU was partly carried out within the framework of the European Fusion Development Agreement. The views and opinions expressed herein do not necessarily reflect those of the European Commission.

References

- [1] Nielsen S.K. et al 2010 Fast-ion redistribution due to sawtooth crash in the TEXTOR tokamak measured by collective Thomson scattering *Plasma Phys. Control. Fusion* **52** 092001
- [2] Nielsen S.K. et al 2011 Dynamics of fast ions during sawtooth oscillations in the TEXTOR tokamak measured by collective Thomson scattering *Nucl. Fusion* **51** 063014
- [3] Muscatello C.M., Heidbrink W.W., Kolesnichenko Ya.I., Lutsenko V.V., Van Zeeland M.A. and Yakovenko Yu.V. 2012 Velocity-space studies of fast-ion transport at a sawtooth crash in neutral-beam heated plasmas *Plasma Phys. Control. Fusion* **54** 025006
- [4] García-Munoz M. et al 2011 Fast-ion transport induced by Alfvén eigenmodes in the ASDEX Upgrade tokamak *Nucl. Fusion* **51** 103013
- [5] Van Zeeland M.A. et al 2011 Measurements and modeling of Alfvén eigenmode induced fast ion transport and loss in DIII-D and ASDEX Upgrade *Phys. Plasmas* **18** 056114
- [6] Pace D.C., Fisher R.K., García-Muñoz M., Heidbrink W.W. and Van Zeeland M.A. 2011 Convective beam ion losses due to Alfvén eigenmodes in DIII-D reversed-shear plasmas *Plasma Phys. Control. Fusion* **53** 062001
- [7] García-Muñoz M., Martín P., Fahrback H.-U., Gobbin M., Günter S., Maraschek M., Marrelli L., Zohm H. and the ASDEX Upgrade Team 2007 NTM induced fast ion losses in ASDEX Upgrade *Nucl. Fusion* **47** L10–5
- [8] Hauff T., Pueschel M., Dannert T. and Jenko F. 2009 Electrostatic and magnetic transport of energetic ions in turbulent plasmas *Phys. Rev. Lett.* **102** 075004
- [9] Heidbrink W., Park J., Murakami M., Petty C., Holcomb C. and Van Zeeland M. 2009 Evidence for fast-ion transport by microturbulence *Phys. Rev. Lett.* **103** 175001
- [10] Graves J.P., Chapman I.T., Coda S., Lennholm M., Albergante M. and Jucker M. 2012 Control of magnetohydrodynamic stability by phase space engineering of energetic ions in tokamak plasmas *Nature Commun.* **3** 624
- [11] Meo F. et al 2008 Commissioning activities and first results from the collective Thomson scattering diagnostic on ASDEX Upgrade (invited) *Rev. Sci. Instrum.* **79** 10E501
- [12] Salewski M. et al 2010 Comparison of fast ion collective Thomson scattering measurements at ASDEX Upgrade with numerical simulations *Nucl. Fusion* **50** 035012
- [13] Meo F. et al and The Asdex Upgrade Team 2010 First results and analysis of collective Thomson scattering (CTS) fast ion distribution measurements on ASDEX Upgrade *J. Phys.: Conf. Ser.* **227** 012010
- [14] Furtula V., Salewski M., Leipold F., Michelsen P.K., Korsholm S.B., Meo F., Moseev D., Nielsen S.K., Stejner M. and Johansen T. 2012 Design and performance of the collective Thomson scattering receiver at ASDEX Upgrade *Rev. Sci. Instrum.* **83** 013507
- [15] Furtula V., Leipold F., Salewski M., Michelsen P.K., Korsholm S.B., Meo F., Moseev D., Nielsen S.K., Stejner M. and Johansen T. 2012 Performance measurements of the collective Thomson scattering receiver at ASDEX Upgrade *J. Instrum.* **7** C02039
- [16] Geiger B., Garcia-Munoz M., Heidbrink W.W., McDermott R.M., Tardini G., Dux R., Fischer R. and Igochine V. 2011 Fast-ion D-alpha measurements at ASDEX Upgrade *Plasma Phys. Control. Fusion* **53** 065010
- [17] Kak A.C. and Slaney M. 1998 *Principles of Computerized Tomographic Imaging* (New York: IEEE Press)
- [18] Herman G.T. 2009 *Fundamentals of Computerized Tomography* 2nd edn (Berlin: Springer)
- [19] Anton M., Weisen H., Dutch M.J., von der Linden W., Buhlmann F., Chavan R., Marletaz B., Marmillod P. and Paris P. 1996 X-ray tomography on the TCV tokamak *Plasma Phys. Control. Fusion* **38** 1849–78
- [20] Ingesson L.C., Alper B., Chen H., Edwards A.W., Fehmers G.C., Fuchs J.C., Giannella R., Gill R.D., Lauro-Taroni L. and Romanelli M. 1998 Soft x ray tomography during ELMs and impurity injection in JET *Nucl. Fusion* **38** 1675–94
- [21] Heidbrink W.W., Luo Y., Burrell K.H., Harvey R.W., Pinsker R.I. and Ruskov E. 2007 Measurements of fast-ion acceleration at cyclotron harmonics using Balmer-alpha spectroscopy *Plasma Phys. Control. Fusion* **49** 1457–75
- [22] Heidbrink W.W. 2010 Fast-ion D α measurements of the fast-ion distribution (invited) *Rev. Sci. Instrum.* **81** 10D727
- [23] Salewski M. et al 2011 On velocity space interrogation regions of fast-ion collective Thomson scattering at ITER *Nucl. Fusion* **51** 083014
- [24] Egedal J. and Bindslev H. 2004 Reconstruction of gyrotropic phase-space distributions from one-dimensional projections *Phys. Plasmas* **11** 2191
- [25] Heidbrink W.W., Bell R.E., Luo Y. and Solomon W. 2006 Fast-ion D-alpha diagnostic for NSTX *Rev. Sci. Instrum.* **77** 10F120
- [26] Luo Y., Heidbrink W.W., Burrell K.H., Kaplan D.H. and Gohil P. 2007 Measurement of the D alpha spectrum produced by fast ions in DIII-D *Rev. Sci. Instrum.* **78** 033505
- [27] Luo Y., Heidbrink W.W., Burrell K.H., Ruskov E. and Solomon W.M. 2007 Fast-ion D α measurements and simulations in quiet plasmas *Phys. Plasmas* **14** 112503
- [28] Podestà M., Heidbrink W.W., Bell R.E. and Feder R. 2008 The NSTX fast-ion D-alpha diagnostic *Rev. Sci. Instrum.* **79** 10E521
- [29] Van Zeeland M.A., Heidbrink W.W. and Yu J.H. 2009 Fast ion D α imaging in the DIII-D tokamak *Plasma Phys. Control. Fusion* **51** 055001
- [30] Van Zeeland M.A. 2010 Imaging key aspects of fast ion physics in the DIII-D tokamak *Nucl. Fusion* **50** 084002

- [31] Heidbrink W.W., Liu D., Luo Y., Ruskov E. and Geiger B. 2011 A code that simulates fast-ion D(alpha) and neutral particle measurements *Commun. Comput. Phys.* **10** 716–41
- [32] Kappatou A., Delabie E., Jaspers R.J.E. and von Hellermann M.G. 2012 Feasibility of non-thermal helium measurements with charge exchange spectroscopy on ITER *Nucl. Fusion* **52** 043007
- [33] Muscatello C.M., Heidbrink W.W., Taussig D. and Burrell K.H. 2010 Extended fast-ion D-alpha diagnostic on DIII-D *Rev. Sci. Instrum.* **81** 10D316
- [34] Bortolon A., Heidbrink W.W. and Podestà M. 2010 A tangentially viewing fast ion D-alpha diagnostic for NSTX *Rev. Sci. Instrum.* **81** 10D728
- [35] Kubo S. *et al* 2010 Collective Thomson scattering of a high power electron cyclotron resonance heating beam in LHD (invited) *Rev. Sci. Instrum.* **81** 10D535
- [36] Ito T., Osakabe M., Ida K., Yoshinuma M., Kobayashi M., Murakami S., Goto M., Takeiri Y., Reiter D. and Okamura S. 2012 Effect of halo neutrals on fast-ion charge exchange spectroscopy measurements in LHD *Plasma Fusion Res.* **5** S2099
- [37] Salewski M., Meo F., Bindslev H., Furtula V., Korsholm S.B., Lauritzen B., Leipold F., Michelsen P.K., Nielsen S.K. and Nonbø I.E. 2008 Investigation of first mirror heating for the collective Thomson scattering diagnostic in ITER *Rev. Sci. Instrum.* **79** 10E729
- [38] Salewski M. *et al* 2009 Comparison of collective Thomson scattering signals due to fast ions in ITER scenarios with fusion and auxiliary heating *Plasma Phys. Control. Fusion* **51** 035006
- [39] Salewski M., Eriksson L.-G., Bindslev H., Korsholm S.B., Leipold F., Meo F., Michelsen P.K. and Nielsen S.K. 2009 Impact of ICRH on the measurement of fusion alphas by collective Thomson scattering in ITER *Nucl. Fusion* **49** 025006
- [40] Leipold F., Furtula V., Salewski M., Bindslev H., Korsholm S.B., Meo F., Michelsen P.K., Moseev D., Nielsen S.K. and Stejner M. 2009 Antenna design for fast ion collective Thomson scattering diagnostic for the international thermonuclear experimental reactor *Rev. Sci. Instrum.* **80** 093501
- [41] Heidbrink W.W., Burrell K.H., Luo Y., Pablant N.A. and Ruskov E. 2004 Hydrogenic fast-ion diagnostic using Balmer-alpha light *Plasma Phys. Control. Fusion* **46** 1855–75
- [42] Moore E.H. 1920 The fourteenth western meeting of the American Mathematical Society *Bull. Am. Math. Soc.* **26** 385–96
- [43] Penrose R. 1955 A generalized inverse for matrices *Math. Proc. Camb. Phil. Soc.* **51** 406–13
- [44] Strang G. 1988 *Linear Algebra and its Applications* (Orlando, FL: Harcourt Brace Jovanovich)
- [45] Stejner M. *et al* 2010 Collective Thomson scattering measurements with high frequency resolution at TEXTOR *Rev. Sci. Instrum.* **81** 10D515
- [46] Korsholm S.B. *et al* 2011 Measurements of intrinsic ion Bernstein waves in tokamak by collective Thomson scattering *Phys. Rev. Lett.* **106** 165004
- [47] Stejner M. *et al* 2012 Measurements of plasma composition in the TEXTOR tokamak by collective Thomson scattering *Plasma Phys. Control. Fusion* **54** 015008

Reference [4]

[4]. M Salewski et al. (2013) *Nuclear Fusion* **53** 063019. Combination of fast-ion diagnostics in velocity-space tomographies

Combination of fast-ion diagnostics in velocity-space tomographies

M. Salewski¹, B. Geiger², S.K. Nielsen¹, H. Bindslev³,
 M. García-Muñoz², W.W. Heidbrink⁴, S.B. Korsholm¹,
 F. Leipold¹, J. Madsen¹, F. Meo¹, P.K. Michelsen¹, D. Moseev^{2,5},
 M. Stejner¹, G. Tardini² and the ASDEX Upgrade Team²

¹ Association Euratom-DTU, Technical University of Denmark, Department of Physics, DTU Risø Campus, DK-4000 Roskilde, Denmark

² Association Euratom-Max-Planck-Institut für Plasmaphysik, D-85748 Garching, Germany

³ Aarhus University, Faculty of Science and Technology, DK-8000 Aarhus C, Denmark

⁴ University of California, Irvine, Department of Physics and Astronomy, CA 92697, USA

⁵ Association Euratom-FOM Institute DIFFER, 3430 BE Nieuwegein, The Netherlands

E-mail: msal@fysik.dtu.dk

Received 22 October 2012, accepted for publication 17 April 2013

Published 14 May 2013

Online at stacks.iop.org/NF/53/063019

Abstract

Fast-ion D_α (FIDA) and collective Thomson scattering (CTS) diagnostics provide indirect measurements of fast-ion velocity distribution functions in magnetically confined plasmas. Here we present the first prescription for velocity-space tomographic inversion of CTS and FIDA measurements that can use CTS and FIDA measurements together and that takes uncertainties in such measurements into account. Our prescription is general and could be applied to other diagnostics. We demonstrate tomographic reconstructions of an ASDEX Upgrade beam ion velocity distribution function. First, we compute synthetic measurements from two CTS views and two FIDA views using a TRANSP/NUBEAM simulation, and then we compute joint tomographic inversions in velocity-space from these. The overall shape of the 2D velocity distribution function and the location of the maxima at full and half beam injection energy are well reproduced in velocity-space tomographic inversions, if the noise level in the measurements is below 10%. Our results suggest that 2D fast-ion velocity distribution functions can be directly inferred from fast-ion measurements and their uncertainties, even if the measurements are taken with different diagnostic methods.

(Some figures may appear in colour only in the online journal)

1. Introduction

ASDEX Upgrade is a medium-size tokamak that is equipped with powerful and versatile auxiliary heating systems: a variety of fast-ion populations can be generated by eight neutral beam injection (NBI) sources with a total power of 20 MW and four ion cyclotron resonance heating (ICRH) antennas with a total power of 6 MW [1–3]. ASDEX Upgrade is also equipped with a suite of fast-ion diagnostics: fast-ion loss detectors (FILDs) [4–6], fast-ion D_α (FIDA) [7], collective Thomson scattering (CTS) [8–13], neutron spectrometry [14, 15], neutral particle analysers (NPA) [16, 17] and γ -ray spectrometry [18]. These auxiliary heating systems and fast-ion diagnostics give unique opportunities to study fast ions in tokamak plasmas. Each diagnostic observes fast ions in different, restricted parts of configuration space and velocity space. CTS and FIDA diagnose confined fast ions in small volumes relative to the plasma size. FILDs are sensitive to lost fast ions near the

plasma edge that strike the scintillator plates. Passive NPAs, neutron spectrometers and γ -ray spectrometers detect confined fast ions anywhere along the lines-of-sight.

We focus here on CTS and FIDA measurements that could be made at roughly the same location in configuration space. CTS and FIDA measure spectra of scattered and emitted radiation, respectively, that constitute 1D functions of the fast-ion velocity distribution function. Traditionally, fast-ion CTS or FIDA measurements are often compared with simulated spectra to investigate if the measurements match the expectation or if they are anomalous [9, 19, 20]. Orbit-following codes such as TRANSP/NUBEAM provide the local 2D fast-ion velocity distribution function f , and then synthetic measurements are calculated from f . However, if the real measurements disagree with the synthetic measurements, it is often unclear what caused this discrepancy. Our final goal is to experimentally determine f , and this might help establish where in 2D velocity space the measurements

disagree with the simulation. Inference of tomographic inversions in velocity space from CTS or FIDA measurements was recently shown to be an achievable goal [13]. Velocity-space tomographic inversions are the best fit to the CTS and FIDA measurements under a regularization condition. It was also shown that the resemblance of the inversions with the original 2D ion velocity distribution function improves with the number of available views, and this motivates the combination of CTS and FIDA measurements in joint velocity-space tomographic inversions. Here we derive a new prescription for velocity-space tomography that allows such a combination of diagnostics which was not possible with previous methods [13]. Our new prescription is also the first to account for uncertainty in the individual measurements. Lastly, we here present a method to estimate uncertainty levels in the tomographic inversions.

Among the most wide-spread applications of computed tomography in configuration space are medical imaging, e.g. x-ray computed axial tomography (CAT or CT) scanners, positron emission tomography (PET) scanners or magnetic resonance imaging (MRI) scanners [21, 22], and it is also widely used in nuclear fusion research [23–32]. Velocity-space tomography is less developed [13, 33, 34] but could be particularly useful in studies of selective ejection or redistribution in velocity space. Several types of modes affect ions in only part of velocity space, for example sawteeth [35–38], Alfvén eigenmodes [6, 39–43] and neoclassical tearing modes [4, 5]. Turbulent transport of fast ions also depends on the ion energy [44–47]. Additionally, velocity-space tomography could be used to monitor phase-space engineering of fast-ion velocity distribution functions which has enabled control of sawteeth and neoclassical tearing modes [48].

We compute joint tomographic inversions of 2D fast-ion velocity distribution functions from synthetic 1D CTS and FIDA measurements. The use of synthetic diagnostics gives us the advantage that we can compare the underlying, known 2D velocity distribution functions with the inversions. The synthetic measurements were calculated from a TRANSP/NUBEAM simulation for the combined four-view FIDA/CTS system at ASDEX Upgrade. Our joint tomography method could also combine the fast-ion charge exchange spectroscopy (FICXS) (that detects light other than D_α but is otherwise similar to FIDA) and the CTS diagnostics at the Large Helical Device (LHD) [49, 50]. Moreover, joint tomographic inversions could be directly relevant to ITER where the proposed FICXS [51] and the CTS system [52–55] could be combined even if there is only one CTS view. Measurements from any other fast-ion diagnostic could be included in our joint tomography prescription, if quantitative weight functions describing the measurements such as those for CTS [34] or FIDA [20, 56] can be formulated. Our joint tomography method would then also be applicable to other tokamaks with many-view FIDA systems and additional fast-ion diagnostics, for example DIII-D [57, 58], NSTX [59] and MAST. Here we make a start by combining CTS and FIDA.

In section 2 we describe the four-view CTS and FIDA system at ASDEX Upgrade, and in section 3 we discuss the combination of CTS and FIDA measurements and their uncertainties in a joint tomography prescription.

Joint tomographic inversions of a simulated beam ion distribution function from combined synthetic CTS and FIDA measurements and their uncertainties are presented in section 4, and in section 5 we study the effect of noise. Finally, we discuss the intrinsically complementary nature of CTS and FIDA measurements in section 6, and we draw conclusions in section 7.

2. CTS and FIDA measurements at ASDEX Upgrade

The CTS system at ASDEX Upgrade has two receivers after installations in 2012, and likewise the FIDA system has two optical heads. CTS and FIDA measurements are sensitive to the velocity-space distribution in small measurement volumes. Except for different shapes and sizes of the measurement volumes, which we ignore here assuming measurements in spatial points, the CTS and FIDA measurements could be made at the same position assuming toroidal symmetry. Hence, four simultaneous views of the 2D fast-ion distribution function are now available if the CTS views and the FIDA views are used together. The spatial resolution of the CTS diagnostic at ASDEX Upgrade is about 10 cm which is given by the size of the intersection pattern of the probe beam from a gyrotron and the receiver field of view. The measurement positions can be moved freely in the plasma core by means of steerable antennas. The measurement locations of the two CTS views can be similar in the poloidal (R, Z) plane if two probe beams are used. The time resolution is often set to 4 ms given by the gyrotron modulation frequency. The position of a FIDA measurement is determined by the intersection of the NBI S3 beam path and the line-of-sight (LOS) of the optical head. The spatial resolution of the FIDA diagnostic at ASDEX Upgrade is about 7 cm, and the time resolution is 2 ms.

CTS and FIDA measure 1D functions g which depend on the respective projection angles ϕ_{CTS} and ϕ_{FIDA} and the fast-ion 2D velocity-space distribution function f that we assume to be rotationally symmetric about the magnetic field direction. CTS and FIDA weight functions relate the 2D fast-ion velocity distribution function f to the 1D measurements g [34, 56]. CTS and FIDA weight functions w are defined by

$$g_{\text{CTS}}(u, \phi_{\text{CTS}}) = \int_{-\infty}^{\infty} \int_0^{\infty} w_{\text{CTS}}(u, \phi_{\text{CTS}}, v_{\parallel}, v_{\perp}) f(v_{\parallel}, v_{\perp}) dv_{\perp} dv_{\parallel}, \quad (1)$$

$$g_{\text{FIDA}}(\lambda, \phi_{\text{FIDA}}) = \int_{-\infty}^{\infty} \int_0^{\infty} w_{\text{FIDA}}(\lambda, \phi_{\text{FIDA}}, v_{\parallel}, v_{\perp}) f(v_{\parallel}, v_{\perp}) dv_{\perp} dv_{\parallel} \quad (2)$$

where u is the projected velocity and λ is the wavelength of detected FIDA light. Examples of weight functions for CTS and FIDA for $\phi_{\text{CTS}} = \phi_{\text{FIDA}} = 64^\circ$ are shown in figure 1.

CTS diagnostics are sensitive to 1D projections of f onto the wave vector $\mathbf{k}^\delta = \mathbf{k}^s - \mathbf{k}^i$ which is the difference between the wave vectors of scattered radiation \mathbf{k}^s and incident radiation \mathbf{k}^i . The most important angle to describe the pre-selected projection direction given by \mathbf{k}^δ is the projection angle $\phi_{\text{CTS}} = \angle(\mathbf{k}^\delta, \mathbf{B})$ where \mathbf{B} is the magnetic field. A frequency shift ν^δ of scattered radiation can be related to the ion velocity v projected onto \mathbf{k}^δ :

$$\nu^\delta = \nu^s - \nu^i \approx v \cdot \mathbf{k}^\delta / 2\pi = uk^\delta / 2\pi, \quad (3)$$

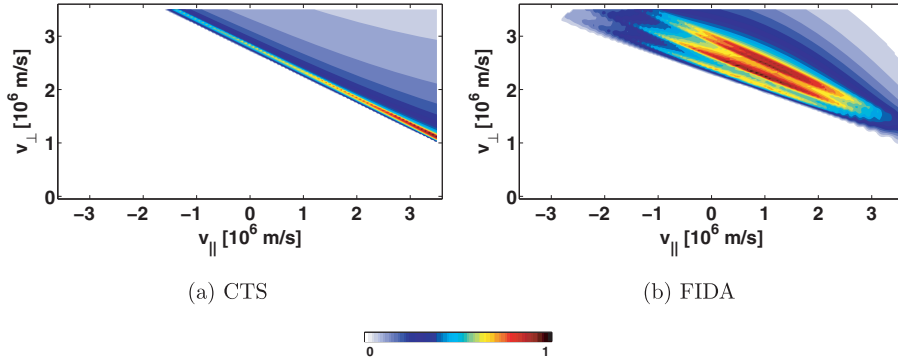


Figure 1. Weight functions [a.u.] at a projection angle of $\phi_{\text{CTS}} = \phi_{\text{FIDA}} = 64^\circ$ for (a) CTS and (b) FIDA and a particular velocity or wavelength interval.

where $k^\delta = |k^\delta|$. We define here a CTS *measurement* as detection of the fast-ion phase-space density in a particular interval in u that is related to an interval in v^δ via equation (3). The projection angles ϕ_{CTS} of the two CTS views can be varied independently if two probe beams are used.

For FIDA, the fast ions likewise leave a spectral signature in the detected light by Doppler shift and Stark splitting. FIDA weight functions are directly parametrized by the wavelength of detected radiation λ instead of u [20, 56]. Hence we define here as FIDA *measurement* the detection of Doppler- and Stark-shifted light in a particular wavelength interval. The FIDA optical head observes NBI source S3 in the plasma core at two different fixed angles $\phi_{\text{FIDA}} = \angle(k^{\text{LOS}}, \mathbf{B})$ where k^{LOS} is the wave vector along the LOS of the optical heads. The toroidal LOS has an angle of $\phi_{\text{FIDA}} = 11^\circ$, and the poloidal LOS, that was installed in 2012, has $\phi_{\text{FIDA}} = 64^\circ$. The angles ϕ_{CTS} and ϕ_{FIDA} describing the *view*, the measurements g_{CTS} and g_{FIDA} , and the weight functions w_{CTS} and w_{FIDA} are analogous and will hereafter simply be called ϕ , g and w , respectively. The analogy between CTS and FIDA measurements is reflected in the form of the weight functions that can be chosen to be quite similar as we show in figure 1. We will discuss the differences between the CTS and FIDA weight functions with identical projection angle ϕ in section 6.

3. Prescription for joint tomographic reconstruction from measurements and their uncertainties

We discretize f and the measurements g from CTS and FIDA into f_{kl} and g_{ij} and the coordinates $(u, \phi, v_{\parallel}, v_{\perp})$ into $(u_i, \phi_j, v_{\parallel k}, v_{\perp l})$. The discrete functions f_{kl} and g_{ij} are written into the column matrices F and G , respectively, similarly to the procedure in [13]. F is a column matrix of size $N \times 1$ obtained from the discrete 2D fast-ion velocity distribution function described by $N = K \times L$ grid points (K grid points in v_{\perp} and L in v_{\parallel}). G is a column matrix of size $M \times 1$ consisting of the discrete 1D functions measured with CTS or FIDA. M is the total number of measurements in u_i (CTS) and λ_i (FIDA) made in the J views with projection angles ϕ_j . The subscripts i, j, k, l, m, n run from 1 to the corresponding upper case letter I, J, K, L, M, N . The discretized form of

equations (1) and (2) is

$$g_{ij} = \sum_{k=1}^K \sum_{l=1}^L w_{ijkl} f_{kl} \Delta v_{\perp} \Delta v_{\parallel}, \quad (4)$$

where Δv_{\perp} and Δv_{\parallel} are the cell sizes in v_{\perp} and v_{\parallel} , respectively. Using these discrete weight functions, we can immediately write down an $M \times N$ transfer matrix W taking F into G [13], and we obtain the linear system of equations

$$WF = G. \quad (5)$$

In real experiments the transfer matrix W and the measurements G are known, and tomographies can be found by solving the inverse problem in equation (5). If the measurements G contain noise, there is no exact solution irrespective of whether the system of equations is underdetermined or overdetermined, but we can find a best fit F^* by minimizing a figure of merit χ^2 . Whereas in [13] we assumed identical uncertainties in all measurements, we here allow for individual uncertainties $\sigma_{G,m}$ in each measurement. For correlated uncertainties in the measurements, the χ^2 figure of merit is determined by the covariance matrix of the measurements C_G and the misfit of the measurements [60]:

$$\chi^2 = \sum_{m,m'} \left(G_m - \sum_n W_{mn} F_n \right) C_{G,mm'}^{-1} \times \left(G_{m'} - \sum_{n'} W_{m'n'} F_{n'} \right), \quad (6)$$

where the subscripts denote the matrix elements. We here assume the uncertainties to be uncorrelated and get the usual least-squares figure of merit in which the misfit of each measurement is divided by its uncertainty:

$$\chi^2 = \sum_m \left(\frac{G_m - \sum_n W_{mn} F_n}{\sigma_{G,m}} \right)^2 = \sum_m \left(\frac{G_m}{\sigma_{G,m}} - \sum_n \frac{W_{mn}}{\sigma_{G,m}} F_n \right)^2. \quad (7)$$

In matrix form this becomes

$$\chi^2 = |\hat{G} - \hat{W}F|^2. \quad (8)$$

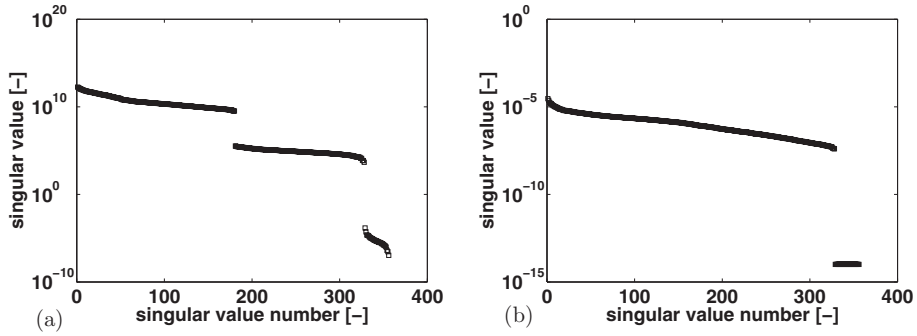


Figure 2. (a) Singular values of the transfer matrix W for combined CTS and FIDA measurements (before normalization with the uncertainties). (b) Singular values of the transfer matrix \hat{W} for combined CTS and FIDA measurements (after normalization with the uncertainties).

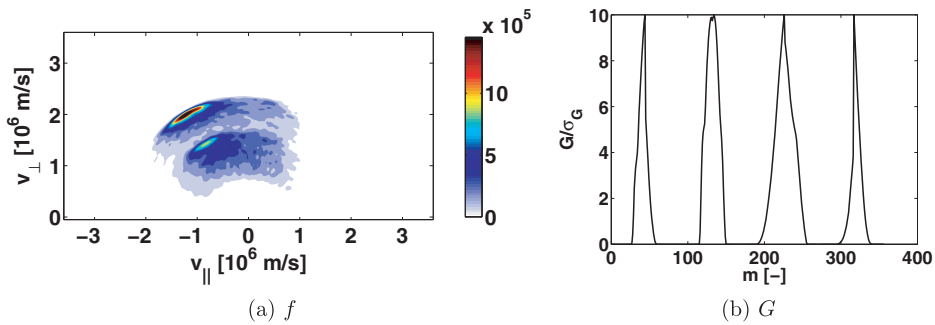


Figure 3. (a) 2D velocity distribution function f on a very fine grid (300×601). (b) Synthetic measurement data in G from two CTS views with $\phi = (33^\circ, 85^\circ)$ (left bumps) and two FIDA views with $\phi = (11^\circ, 64^\circ)$ (right bumps). m is the index of the measurement.

The matrix elements of \hat{G} and \hat{W} are given by

$$\hat{G}_m = G_m / \sigma_{G,m} \quad (9)$$

$$\hat{W}_{mn} = W_{mn} / \sigma_{G,m}, \quad (10)$$

where repeated indices do *not* imply summation. We find a minimum χ^2 figure of merit under minimum two-norm regularization and positivity constraint using the Moore–Penrose pseudoinverse \hat{W}^+ [61, 62] computed from the singular value decomposition of \hat{W} [63]. Therefore, the tomographic inversion F^+ is determined from the measurements and their uncertainties by

$$F^+ = \hat{W}^+ \hat{G}. \quad (11)$$

F^+ is the least-squares fit to the normalized set of equations

$$\hat{W} F = \hat{G}. \quad (12)$$

In [13] the figure of merit was simply

$$\chi^2 = \|G - WF\|^2 \quad (13)$$

which is minimized by

$$F^+ = W^+ G \quad (14)$$

as the best-fit solution to equation (5). Equations (5) and (12) are equivalent, but here the figure of merit χ^2 (equation (8))

is different than in [13] (equation (13)). By this normalization of W and G with σ_G here we take the uncertainties of the individual measurements into account. If all uncertainties are equal, the reconstruction prescription in [13] is recovered.

The normalization of the measurements and the weight functions by their respective uncertainties is also essential to improve the conditioning of the transfer matrix. Without this normalization the conditioning of W would usually be poor for combined CTS and FIDA measurements because CTS and FIDA measure different physical quantities, and their weight functions are usually given in different units and have amplitudes that differ by orders of magnitude. The conditioning of \hat{W} , in contrast, should usually be good, and this well-conditioned transfer matrix allows the combination of CTS and FIDA measurements. The singular values before and after the normalization by the uncertainties are shown in figure 2. Here we assume the uncertainty in each view to be 10% of the maximum value of the respective view.

4. Joint tomographic inversion from combined CTS and FIDA measurements

First we illustrate the data we use for the inference of F^+ . Figure 3(a) shows a beam ion velocity distribution function for NBI source S3 (60 keV, 2.5 MW) at ASDEX Upgrade computed with TRANSP/NUBEAM, and figure 3(b) shows a set of normalized, synthetic CTS and FIDA measurements of that function. The resolution of the original function, from

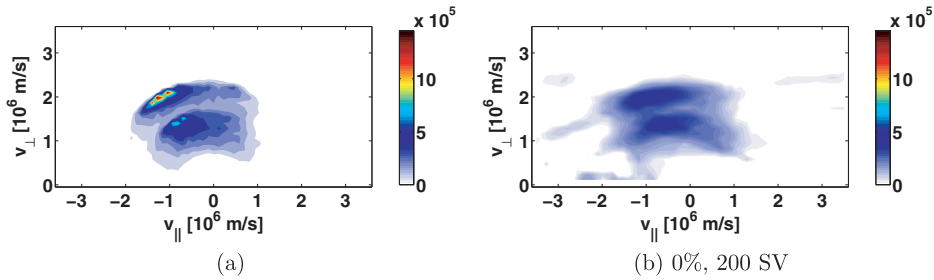


Figure 4. (a) Interpolation of the original function from figure 3(a) to the 30×61 grid of the tomographic inversion. (b) Inversion using 200 singular values. No additional noise has been added to G . The colour scales in (a) and (b) are identical. Figure 5(e) presents the inversion with a different colour scale.

which we take the synthetic measurements, is 300×601 grid points. The two bumps to the left in figure 3(b) represent CTS measurements taken in two views at $\phi = (33^\circ, 85^\circ)$, and the two bumps to the right represent FIDA measurements at $\phi = (11^\circ, 64^\circ)$ for the two FIDA views. The CTS measurements are distributed in the u -intervals $-5 \times 10^6 < u < -0.7 \times 10^6 \text{ m s}^{-1}$ and $0.7 \times 10^6 < u < 5 \times 10^6 \text{ m s}^{-1}$ with a resolution of $\Delta u = 0.1 \times 10^6 \text{ m s}^{-1}$ that is roughly achievable with the filterbank receivers at ASDEX Upgrade. We do not use CTS measurements in the interval $-0.7 \times 10^6 < u < 0.7 \times 10^6 \text{ m s}^{-1}$ because bulk ions make unambiguous detection of fast ions very difficult if not impossible in this interval. The FIDA measurements are evenly distributed in the wavelength intervals $649 \text{ nm} < \lambda < 654 \text{ nm}$ and $659 \text{ nm} < \lambda < 663 \text{ nm}$. FIDA light cannot be observed in the wavelength interval $654 \text{ nm} < \lambda < 659 \text{ nm}$ due to beam emission and halo neutrals [7], and we likewise exclude this wavelength range in the synthetic measurements. Figure 3(b) contains the synthetic normalized measurements that we use for the inference of the tomographic inversions. The abscissa is the measurement index label m that runs from 1 to M , and the ordinate is the corresponding CTS or FIDA measurement normalized by the uncertainty of the measurement (10% of the maxima of each CTS or FIDA view as explained above).

The inversions are calculated on a much coarser grid with 30×61 grid points corresponding to velocity-space resolution of typical simulations. The original function has been interpolated to the coarser grid of the inversion in figure 4(a) to illustrate an upper limit of the achievable resemblance between the inversion and the original function. If the data are noisy, it is necessary to truncate the SVD and use lower rank approximations to the Moore–Penrose pseudoinverse. Explicit noise will be added in section 5 whereas in this section the noise originates from the different discretizations of the original function (300×601) and the inversion (30×61). Here the transfer matrix W has a rank of about 320, corresponding to 320 significant singular values (see figure 2(b)). In truncated SVD, only the largest singular values are used. Figure 4(b) shows an inversion using 200 singular values. The joint inversion from a mix of CTS and FIDA measurements reproduces the overall shape of the underlying function including the location of the peaks at full and half beam injection energy. However, these peaks are broader in the inversion than in the original function, and their amplitudes are approximately 3–4 times smaller.

Figure 5 shows inversions computed with various truncation levels from 40 singular values to 320 singular values.

From here on we use different colour scales in the inversions to emphasize the shape of the inferred inversions more clearly. The two peaks at full and half beam injection energies emerge if about 80 singular values are used. The peak amplitudes become larger if more singular values are used, but they never become quite as large as in the original. Using more singular values, however, also tends to increase the jitter in the inversion.

It should be possible to improve the resemblance of the inversions with the original velocity distribution function by adding more CTS or FIDA views or other fast-ion measurements and by increasing the frequency resolution of the measurements [13]. High-frequency resolution CTS measurements on the order of 1 MHz were recently demonstrated which give a few thousand measurements in frequency space per view [64–66].

5. Joint tomographic inversions from noisy measurements

In the following we investigate inversions computed from noisy measurements. Noise makes the smallest singular values useless, and the inversions then have to be inferred using only the largest singular values. The lower the noise level, the more singular values can be used. We add various levels of uncorrelated Gaussian noise to the synthetic measurements and infer inversions at various truncation levels of the SVD.

Figure 6 shows inversions computed for a Gaussian noise level of 2%. The two beam injection peaks again emerge if about 80 singular values are used. About 240 singular values contain useful information at 2% noise. In figure 7 we infer inversions at various noise levels up to 50%. The two peaks at full and half beam injection energy are visible for 100 singular values at noise levels of 4% (figure 7(a)). At 10% noise (figure 7(b)), the form of the peaks is distorted by the noise, and for larger noise levels such as 20% they completely disappear (figure 7(c)) in the jitter. Nevertheless, even at a noise level of 50%, the inversion based on 20 singular values still reveals the coarsest anisotropy features of the original function (figure 7(d)).

For a matrix equation of the form $F^+ = \hat{W}^+ \hat{G}$, we can investigate the propagation of errors from the normalized measurements \hat{G} to the inversion F^+ . The measurements can contain correlated noise that can be summarized in the $m \times m$

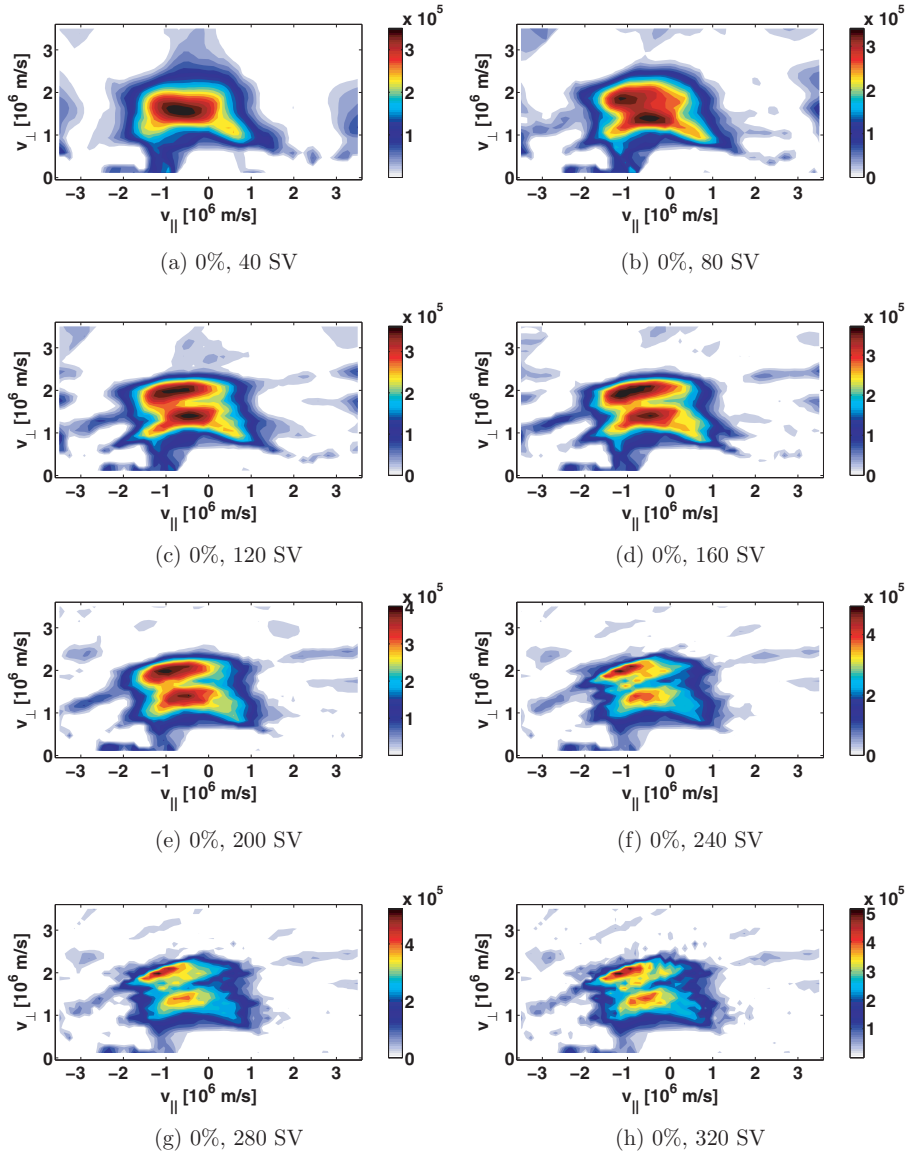


Figure 5. Tomographic inversions inferred from the synthetic CTS/FIDA four-view data in figure 3(b). 40–320 singular values are used in (a) to (h). No additional noise has been added to G . The colour scales are different from that of the original in figure 4.

covariance matrix \hat{C}_G . We then use standard error propagation methods [60] to find the $n \times n$ covariance matrix C_F^+ of F^+ :

$$C_F^+ = \hat{W}^+ \hat{C}_G (\hat{W}^+)^T. \quad (15)$$

For uncorrelated noise in the measurements, the diagonal elements $(\sigma_{F,n}^+)^2$ of C_F^+ are given by

$$(\sigma_{F,n}^+)^2 = \sum_m (\hat{W}_{nm}^+)^2 \hat{\sigma}_{G,m}^2. \quad (16)$$

Figure 8 shows standard deviations σ_f^+ , which are immediately given by the vectors $\sigma_{F,n}^+$, using 100 singular values (a) and 300 singular values (b). Tomographic inferences

using only the largest singular values are less sensitive to noise than those using many singular values. For 100 singular values, the values of f are well above the noise level σ_f^+ , and hence a tomographic inversion f^+ using 100 singular values is dominated by the measured values g . In contrast, for 300 singular values, the values of f are below the noise level σ_f^+ , and hence this inversion f^+ is strongly influenced by noise.

6. The complementary nature of CTS and FIDA measurements

Lastly, we remark that the velocity-space interrogation regions of CTS and FIDA measurements and the relative weightings

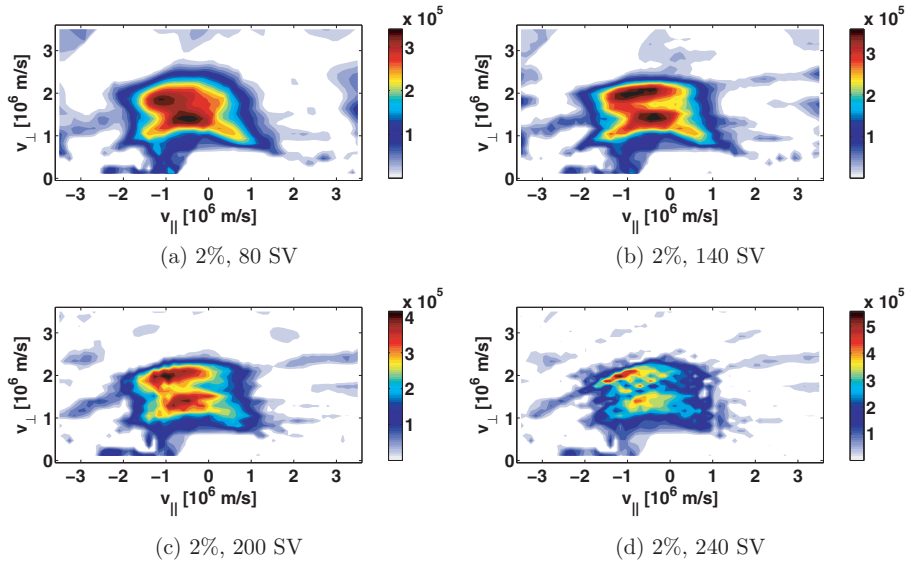


Figure 6. Tomographic inversions inferred from the synthetic CTS/FIDA four-view data in figure 3(b) with 2% Gaussian noise. 80–240 singular values are used. The colour scales are different from that of the original in figure 4.

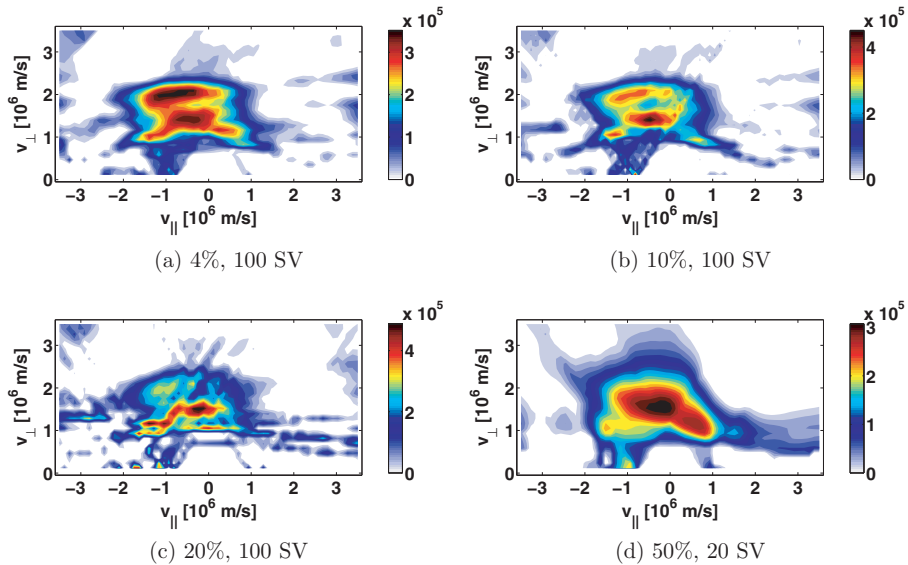


Figure 7. Tomographic inversions inferred from the synthetic CTS/FIDA four-view data in figure 3(b) with 4–50% Gaussian noise. In (a) to (c) we use 100 singular values, in (d) we use 20 singular values. The colour scales are different from that of the original in figure 4.

within these can in fact never coincide, irrespective of how we choose the scattering geometry. These weightings are described by the weight functions w that relate the 2D velocity-space $(v_{\parallel}, v_{\perp})$ to the 1D CTS or FIDA measurements of a spectrum of radiation. CTS and FIDA measurements g are sensitive to products of their respective weight functions and the ion velocity distribution function f according to equations (1) and (2). The basic shapes of CTS and FIDA velocity-space interrogation regions were illustrated in figure 1. They are given by 1D projections of velocities of gyrating ions determining the frequency shifts of detectable

radiation [34]. Despite the identical projection angle in figure 1, the boundaries of the triangular velocity-space interrogation region of FIDA have a smaller slope than those for CTS due to Stark splitting: Stark splitting broadens the FIDA velocity-space interrogation regions compared with those of CTS. The weights are also different due to Stark splitting, the charge-exchange probability, and the probability of a Balmer alpha photon emission. Figure 1 suggests that the observable signals emphasize different velocity-space regions even if the interrogation regions are chosen to be as similar as possible. This makes direct comparisons of CTS and FIDA

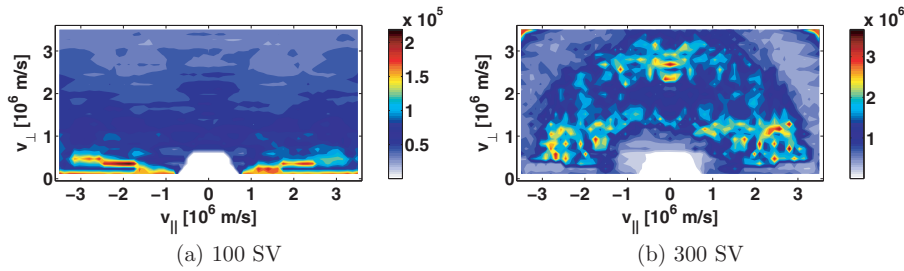


Figure 8. Standard deviation σ_f^+ of the inversion obtained from the diagonal elements of the covariance matrix for (a) 100 singular values and (b) 300 singular values.

measurements difficult as these measurements can never be redundant; they are complementary irrespective of the viewing geometry. But the combination of the measurements in joint inversions turns this intrinsically complementary nature of the measurements into an advantage. One may then speculate how to set the projection angles of the available CTS and FIDA views to obtain the best possible inversion and how many views are really required. It is firstly beneficial to increase the number of views and secondly to select very different projection angles in each view as one would intuitively expect. It is, however, outside the scope of this work to find optimum projection angles or number of views, and we will give comprehensive discussion of these topics elsewhere.

7. Conclusions

We have demonstrated that diagnostic information from CTS and FIDA measurements can be combined in joint velocity-space tomographic inversions that provide the best fit to the measurements under a regularization condition. To enable this combination of diagnostic methods, we have derived a new velocity-space tomography prescription that can use information from any fast-ion diagnostic and that takes uncertainties in the measurements into account. We infer tomographic reconstructions using synthetic measurements with the combined four-view CTS/FIDA system at ASDEX Upgrade. The synthetic measurements are based on a beam ion velocity distribution function simulated with TRANSP/NUBEAM. The overall shape of the distribution function and the location of the maxima at full and half beam injection energy are reproduced well in tomographic inversions, if uncorrelated Gaussian noise in the measurements has a level below 10%. Joint tomography using real fast-ion measurements can combine different diagnostic methods—also other than CTS and FIDA—and can yield an experimentally determined 2D fast-ion velocity distribution function.

Acknowledgments

This work, supported by the European Communities under the contract of Association between Euratom and DTU, was partly carried out within the framework of the European Fusion Development Agreement. The views and opinions expressed herein do not necessarily reflect those of the European Commission.

References

- [1] Gruber O. 2007 Overview of ASDEX Upgrade results *Nucl. Fusion* **47** S622–34
- [2] Kallenbach A. *et al* 2012 Recent ASDEX Upgrade results and future extension plans *IEEE Trans. Plasma Sci.* **40** 605–13
- [3] Stroth U. *et al* 2013 Overview of ASDEX Upgrade results *Proc. 24th Conf. on Fusion Energy (San Diego, 8–13 October 2012)* www-naweb.iaea.org/napc/physics/FEC/FEC2012/html/fec12.htm; *Nucl. Fusion* at press
- [4] García-Muñoz M., Martin P., Fahrbach H.-U., Gobbin M., Günter S., Maraschek M., Marrelli L., Zohm H. and the ASDEX Upgrade Team 2007 NTM induced fast ion losses in ASDEX Upgrade *Nucl. Fusion* **47** L10–5
- [5] García-Muñoz M. *et al* 2009 MHD induced fast-ion losses on ASDEX Upgrade *Nucl. Fusion* **49** 085014
- [6] Garcia-Munoz M. *et al* 2011 Fast-ion transport induced by Alfvén eigenmodes in the ASDEX Upgrade tokamak *Nucl. Fusion* **51** 103013
- [7] Geiger B., Garcia-Munoz M., Heidbrink W.W., McDermott R.M., Tardini G., Dux R., Fischer R. and Igochine V. 2011 Fast-ion D-alpha measurements at ASDEX Upgrade *Plasma Phys. Control. Fusion* **53** 065010
- [8] Meo F. *et al* 2008 Commissioning activities and first results from the collective Thomson scattering diagnostic on ASDEX Upgrade (invited) *Rev. Sci. Instrum.* **79** 10E501
- [9] Salewski M. *et al* 2010 Comparison of fast ion collective Thomson scattering measurements at ASDEX Upgrade with numerical simulations *Nucl. Fusion* **50** 035012
- [10] Meo F. *et al* and The Asdex Upgrade Team 2010 First results and analysis of collective Thomson scattering (CTS) fast ion distribution measurements on ASDEX Upgrade *J. Phys.: Conf. Ser.* **227** 012010
- [11] Furtula V., Salewski M., Leipold F., Michelsen P.K., Korsholm S.B., Meo F., Moseev D., Nielsen S.K., Stejner M. and Johansen T. 2012 Design and performance of the collective Thomson scattering receiver at ASDEX Upgrade *Rev. Sci. Instrum.* **83** 013507
- [12] Furtula V., Leipold F., Salewski M., Michelsen P.K., Korsholm S.B., Meo F., Moseev D., Nielsen S.K., Stejner M. and Johansen T. 2012 Performance measurements of the collective Thomson scattering receiver at ASDEX Upgrade *J. Instrum.* **7** C02039
- [13] Salewski M. *et al* 2012 Tomography of fast-ion velocity-space distributions from synthetic CTS and FIDA measurements *Nucl. Fusion* **52** 103008
- [14] Giacomelli L., Zimbal A., Tittelmeier K., Schuhmacher H., Tardini G. and Neu R. 2011 The compact neutron spectrometer at ASDEX Upgrade *Rev. Sci. Instrum.* **82** 123504
- [15] Tardini G., Zimbal A., Esposito B., Gagnon-Moisan F., Marocco D., Neu R., Schuhmacher H. and the

- ASDEX Upgrade Team 2012 First neutron spectrometry measurements in the ASDEX Upgrade tokamak *J. Instrum.* **7** C03004
- [16] Kurki-Suonio T., Hynönen V., Suttrop W., Fahrbach H.-U., Stober J. and the ASDEX Upgrade Team 2006 Edge fast ion distribution benchmarking ASCOT against experimental NPA data on ASDEX Upgrade *Europhys. Conf. Abstracts* vol 30I p P2.145
- [17] Äkäslompolo S., Hirvijoki E., Kurki-Suonio T. and the ASDEX Upgrade Team 2010 Implementing beam-beam CX-reactions in the ASCOT-code and prediction of active NPA measurement *Europhys. Conf. Abstracts* vol 34A p P5.113
- [18] Nocente M. *et al* and the ASDEX Upgrade Team 2012 Gamma-ray spectroscopy measurements of confined fast ions on ASDEX upgrade *Nucl. Fusion* **52** 094021
- [19] Moseev D. *et al* 2011 Comparison of measured and simulated fast ion velocity distributions in the TEXTOR tokamak *Plasma Phys. Control. Fusion* **53** 105004
- [20] Heidbrink W.W. 2010 Fast-ion $D\alpha$ measurements of the fast-ion distribution (invited) *Rev. Sci. Instrum.* **81** 10D727
- [21] Kak A.C. and Slaney M. 1988 *Principles of Computerized Tomographic Imaging* (New York: IEEE Press)
- [22] Herman G.T. 2009 *Fundamentals of Computerized Tomography* 2nd edn (Berlin: Springer)
- [23] Ertl K., von der Linden W., Dose V. and Weller A. 1996 Maximum entropy based reconstruction of soft x-ray emissivity profiles in W7-AS *Nucl. Fusion* **36** 1477–88
- [24] Anton M., Weisen H., Dutch M.J., von der Linden W., Buhlmann F., Chavan R., Marletaz B., Marmillot P. and Paris P. 1996 X-ray tomography on the TCV tokamak *Plasma Phys. Control. Fusion* **38** 1849–78
- [25] Ingesson L.C., Alper B., Chen H., Edwards A.W., Fehmers G.C., Fuchs J.C., Giannella R., Gill R.D., Lauro-Taroni L. and Romanelli M. 1998 Soft x ray tomography during ELMs and impurity injection in JET *Nucl. Fusion* **38** 1675–94
- [26] Nagayama Y., Taylor G., Yamada M., Fredrickson E.D., Janos A.C. and McGuire K.M. 1996 ECE image reconstruction of partial sawtooth crashes in ohmic plasmas *Nucl. Fusion* **36** 521–6
- [27] Howard J. 1996 Vector tomography applications in plasma diagnostics *Plasma Phys. Control. Fusion* **38** 489–503
- [28] Konoshima S., Leonard A.W., Ishijima T., Shimizu K., Kamata I., Meyer W.H., Sakurai S., Kubo H., Hosogane N. and Tamai H. 2001 Tomographic reconstruction of bolometry for JT-60U diverted tokamak characterization *Plasma Phys. Control. Fusion* **43** 959–83
- [29] Peterson B.J., Kostrioukov A.Yu., Ashikawa N., Liu Y., Yuhong Xu., Osakabe M., Watanabe K.Y., Shimozuma T., Sudo S. and the LHD Experiment Group 2003 Bolometer diagnostics for one- and two-dimensional measurements of radiated power on the Large Helical Device *Plasma Phys. Control. Fusion* **45** 1167–82
- [30] Furno I., Weisen H., Carey C., Angioni C., Behn R., Fable E., Zabolotsky A., the TCV Team, and JET-EFDA Contributors 2005 A new method for the inversion of interferometry data using basis functions derived from singular value decomposition of local measurements in tokamak plasmas *Plasma Phys. Control. Fusion* **47** 49–69
- [31] Bonheure G., Popovichev S., Bertalot L., Murari A., Conroy S., Mlynar J., Voitsekhoivitch I. and JET-EFDA Contributors 2006 Neutron profiles and fuel ratio n T/n D measurements in JET ELMy H-mode plasmas with tritium puff *Nucl. Fusion* **46** 725–40
- [32] Svensson J. and Werner A. 2008 Current tomography for axisymmetric plasmas *Plasma Phys. Control. Fusion* **50** 085002
- [33] Egedal J. and Bindslev H. 2004 Reconstruction of gyrotronic phase-space distributions from one-dimensional projections *Phys. Plasmas* **11** 2191
- [34] Salewski M. *et al* 2011 On velocity space interrogation regions of fast-ion collective Thomson scattering at ITER *Nucl. Fusion* **51** 083014
- [35] Nielsen S.K. *et al* 2010 Fast-ion redistribution due to sawtooth crash in the TEXTOR tokamak measured by collective Thomson scattering *Plasma Phys. Control. Fusion* **52** 092001
- [36] Nielsen S.K. *et al* 2011 Dynamics of fast ions during sawtooth oscillations in the TEXTOR tokamak measured by collective Thomson scattering *Nucl. Fusion* **51** 063014
- [37] Pace D.C. *et al* 2011 Transport of energetic ions due to sawteeth, Alfvén eigenmodes and microturbulence *Nucl. Fusion* **51** 043012
- [38] Muscatello C.M., Heidbrink W.W., Kolesnichenko Ya.I., Lutsenko V.V., Van Zeeland M.A. and Yakovenko Yu.V. 2012 Velocity-space studies of fast-ion transport at a sawtooth crash in neutral-beam heated plasmas *Plasma Phys. Control. Fusion* **54** 025006
- [39] Heidbrink W.W. and Sadler G.J. 1994 The behaviour of fast ions in tokamak experiments *Nucl. Fusion* **34** 535–615
- [40] Zweben S.J., Budny R.V., Darrow D.S., Medley S.S., Nazikian R., Stratton B.C., Synakowski E.J. and Taylor G. for the TFTR Group 2000 Alpha particle physics experiments in the Tokamak Fusion Test Reactor *Nucl. Fusion* **40** 91–149
- [41] Nabais F., Borba D., Garcia-Muñoz M., Johnson T., Kiptily V.G., Reich M., Nave M.F.F., Pinches S.D. and Sharapov S.E. 2010 Impact of strongly driven fishbones and Alfvén eigenmodes on fast ion losses *Nucl. Fusion* **50** 115006
- [42] Van Zeeland M.A. *et al* 2011 Measurements and modeling of Alfvén eigenmode induced fast ion transport and loss in DIII-D and ASDEX Upgrade 2011 *Phys. Plasmas* **18** 056114
- [43] Pace D.C., Fisher R.K., García-Muñoz M., Heidbrink W.W. and Van Zeeland M.A. 2011 Convective beam ion losses due to Alfvén eigenmodes in DIII-D reversed-shear plasmas *Plasma Phys. Control. Fusion* **53** 062001
- [44] Günter S. *et al* and the ASDEX Upgrade Team 2007 Interaction of energetic particles with large and small scale instabilities *Nucl. Fusion* **47** 920–8
- [45] Dannert T., Günter S., Hauff T., Jenko F., Lapillonne X. and Lauber P. 2008 Turbulent transport of beam ions *Phys. Plasmas* **15** 062508
- [46] Hauff T. and Jenko F. 2008 Mechanisms and scalings of energetic ion transport via tokamak microturbulence *Phys. Plasmas* **15** 112307
- [47] Hauff T., Pueschel M., Dannert T. and Jenko F. 2009 Electrostatic and magnetic transport of energetic ions in turbulent plasmas *Phys. Rev. Lett.* **102** 075004
- [48] Graves J.P., Chapman I.T., Coda S., Lennholm M., Albergante M. and Jucker M. 2012 Control of magnetohydrodynamic stability by phase space engineering of energetic ions in tokamak plasmas *Nature Commun.* **3** 624
- [49] Kubo S. *et al* 2010 Collective Thomson scattering of a high power electron cyclotron resonance heating beam in LHD (invited) *Rev. Sci. Instrum.* **81** 10D535
- [50] Ito T., Osakabe M., Ida K., Yoshinuma M., Kobayashi M., Murakami S., Goto M., Takeiri Y., Reiter D. and Okamura S. 2012 Effect of halo neutrals on fast-ion charge exchange spectroscopy measurements in LHD *Plasma Fusion Res.* **5** S2099
- [51] Kappatou A., Delabie E., Jaspers R.J.E. and von Hellermann M.G. 2012 Feasibility of non-thermal helium measurements with charge exchange spectroscopy on ITER *Nucl. Fusion* **52** 043007

- [52] Salewski M., Meo F., Bindslev H., Furtula V., Korsholm S.B., Lauritzen B., Leipold F., Michelsen P.K., Nielsen S.K. and Nonbø I E. 2008 Investigation of first mirror heating for the collective Thomson scattering diagnostic in ITER *Rev. Sci. Instrum.* **79** 10E729
- [53] Salewski M. *et al* 2009 Comparison of collective Thomson scattering signals due to fast ions in ITER scenarios with fusion and auxiliary heating *Plasma Phys. Control. Fusion* **51** 035006
- [54] Salewski M., Eriksson L.-G., Bindslev H., Korsholm S.B., Leipold F., Meo F., Michelsen P.K. and Nielsen S.K. 2009 Impact of ICRH on the measurement of fusion alphas by collective Thomson scattering in ITER *Nucl. Fusion* **49** 025006
- [55] Leipold F., Furtula V., Salewski M., Bindslev H., Korsholm S.B., Meo F., Michelsen P.K., Moseev D., Nielsen S.K. and Stejner M. 2009 Antenna design for fast ion collective Thomson scattering diagnostic for the international thermonuclear experimental reactor *Rev. Sci. Instrum.* **80** 093501
- [56] Heidbrink W.W., Luo Y., Burrell K.H., Harvey R.W., Pinsky R.I. and Ruskov E. 2007 Measurements of fast-ion acceleration at cyclotron harmonics using Balmer-alpha spectroscopy *Plasma Phys. Control. Fusion* **49** 1457–75
- [57] Heidbrink W.W. *et al* 2008 Central flattening of the fast-ion profile in reversed-shear DIII-D discharges *Nucl. Fusion* **48** 084001
- [58] Muscatello C.M., Heidbrink W.W., Taussig D. and Burrell K.H. 2010 Extended fast-ion D-alpha diagnostic on DIII-D *Rev. Sci. Instrum.* **81** 10D316
- [59] Bortolon A., Heidbrink W.W. and Podestà M. 2010 A tangentially viewing fast ion D-alpha diagnostic for NSTX *Rev. Sci. Instrum.* **81** 10D728
- [60] Barlow R.J. 1989 *Statistics* (New York: Wiley)
- [61] Moore E.H. 1920 14th Western Meeting of the American Mathematical Society *Bull. Am. Math. Soc.* **26** 385–96
- [62] Penrose R. 1955 A generalized inverse for matrices *Math. Proc. Cambridge Phil. Soc.* **51** 406–13
- [63] Strang G. 1988 *Linear Algebra and its Applications* (Orlando, FL: Harcourt Brace Jovanovich)
- [64] Stejner M. *et al* 2010 Collective Thomson scattering measurements with high frequency resolution at TEXTOR *Rev. Sci. Instrum.* **81** 10D515
- [65] Korsholm S.B. *et al* 2011 Measurements of intrinsic ion Bernstein waves in a tokamak by collective Thomson scattering *Phys. Rev. Lett.* **106** 165004
- [66] Stejner M. *et al* 2012 Measurements of plasma composition in the TEXTOR tokamak by collective Thomson scattering *Plasma Phys. Control. Fusion* **54** 015008

Reference [5]

[5]. M Salewski et al. (2014) *Nuclear Fusion* **54** 023005. Measurement of a 2D fast-ion velocity distribution function by tomographic inversion of fast-ion D-alpha spectra

Measurement of a 2D fast-ion velocity distribution function by tomographic inversion of fast-ion D-alpha spectra

M. Salewski¹, B. Geiger², A.S. Jacobsen¹, M. García-Muñoz³,
W.W. Heidbrink⁴, S.B. Korsholm¹, F. Leipold¹, J. Madsen¹,
D. Moseev², S.K. Nielsen¹, J. Rasmussen¹, M. Stejner¹,
G. Tardini², M. Weiland² and the ASDEX Upgrade Team²

¹ Association Euratom - DTU, Technical University of Denmark, Department of Physics, DK-2800 Kgs. Lyngby, Denmark

² Association Euratom - Max-Planck-Institut für Plasmaphysik, D-85748 Garching, Germany

³ Department of Physics, University of Seville, Seville, Spain

⁴ University of California, Department of Physics and Astronomy, Irvine, CA 92697, USA

E-mail: msal@fysik.dtu.dk

Received 6 September 2013, revised 12 December 2013

Accepted for publication 12 December 2013

Published 21 January 2014

Abstract

We present the first measurement of a local fast-ion 2D velocity distribution function $f(v_{\parallel}, v_{\perp})$. To this end, we heated a plasma in ASDEX Upgrade by neutral beam injection and measured spectra of fast-ion D_{α} (FIDA) light from the plasma centre in three views simultaneously. The measured spectra agree very well with synthetic spectra calculated from a TRANSP/NUBEAM simulation. Based on the measured FIDA spectra alone, we infer $f(v_{\parallel}, v_{\perp})$ by tomographic inversion. Salient features of our measurement of $f(v_{\parallel}, v_{\perp})$ agree reasonably well with the simulation: the measured as well as the simulated $f(v_{\parallel}, v_{\perp})$ are lopsided towards negative velocities parallel to the magnetic field, and they have similar shapes. Further, the peaks in the simulation of $f(v_{\parallel}, v_{\perp})$ at full and half injection energies of the neutral beam also appear in the measurement at similar velocity-space locations. We expect that we can measure spectra in up to seven views simultaneously in the next ASDEX Upgrade campaign which would further improve measurements of $f(v_{\parallel}, v_{\perp})$ by tomographic inversion.

Keywords: fast-ion velocity distribution function, tomography, inverse problems, fast ions in tokamaks

(Some figures may appear in colour only in the online journal)

1. Introduction

The fast-ion phase-space distribution function is often the key to understanding many aspects of plasma behaviour but it can only be incompletely diagnosed. Here we discuss fast-ion D_{α} (FIDA) spectroscopy which measures spectra of D_{α} light at large Doppler shifts [1]. FIDA spectra are 1D functions of the 3D fast-ion velocity distribution function in small measurement volumes. In strongly magnetized plasmas, the 3D velocity distribution function can be regarded as 2D by decoupling the fast, quasi-periodic gyro-motion from the drift motion [2]. Hence we consider local 2D fast-ion velocity distribution functions $f(v_{\parallel}, v_{\perp})$ where v_{\parallel} and v_{\perp} are velocities parallel and perpendicular to the magnetic field, respectively. We have recently shown theoretically that $f(v_{\parallel}, v_{\perp})$ can be inferred from FIDA spectra by tomographic inversion [3]. Tomography is a standard analysis method in nuclear fusion research [4–13] as well as in many fields

throughout physical and medical sciences [14, 15]. Fast-ion velocity-space tomography in nuclear fusion research has until now only been investigated theoretically [3, 16–18]. Here we apply this method to measure $f(v_{\parallel}, v_{\perp})$ for the first time.

Our velocity-space tomography approach seeks to make up for shortcomings in conventional FIDA data analysis procedures. FIDA measurements are often compared with numerical simulations to judge if a measurement is consistent with a theoretical model or not. This is conventionally done by means of synthetic diagnostics using forward modelling in which the expected FIDA spectrum is modelled on the basis of a simulation of the fast-ion distribution, for example by the FIDASIM code [19] on the basis of a TRANSP/NUBEAM simulation [20]. If the FIDA measurements agree with synthetic FIDA measurements [21–30], it is argued that $f(v_{\parallel}, v_{\perp})$ in the experiment corresponds to the simulation and that the fast-ion behaviour therefore is understood—at least in the interrogation regions of the measurements. However,

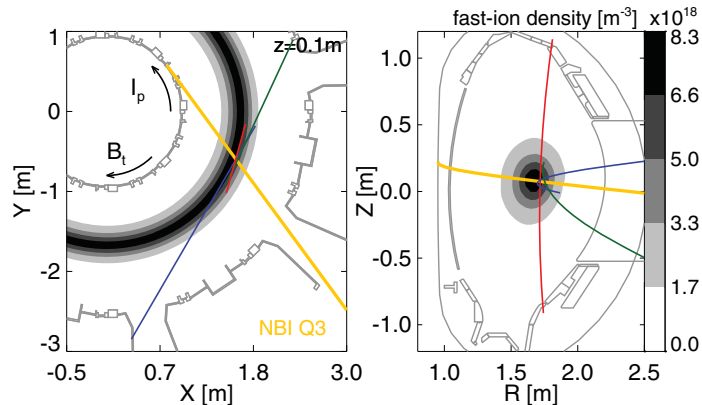


Figure 1. The geometry of the three FIDA lines-of-sight (red: $\phi = 69^\circ$, $R = 1.720$ m; green: $\phi = 156^\circ$, $R = 1.749$ m; blue: $\phi = 12^\circ$, $R = 1.728$ m) and NBI Q3 (yellow) are shown in a toroidal view to the left and in a poloidal view to the right. The FIDA measurements are localized where NBI Q3 intersects the lines-of-sight. The fast-ion density from a TRANSP/NUBEAM simulation is illustrated in grey. The directions of the plasma current and the toroidal magnetic field are indicated in the left figure.

if they disagree [31–42], it is unclear how the experimental and simulated functions $f(v_{\parallel}, v_{\perp})$ are different. In this case, we would rather solve the inverse problem to know what the measured FIDA spectra imply about $f(v_{\parallel}, v_{\perp})$. The tomographic inversion of the FIDA spectra is a solution to this inverse problem and provides a measurement of $f(v_{\parallel}, v_{\perp})$. We could then examine in which parts of 2D velocity space the simulation and the measurement disagree.

Nevertheless, here we chose a discharge with very good agreement between measured and synthetic spectra so that the TRANSP/NUBEAM simulation should be a good model for the discharge and should resemble our measurement of $f(v_{\parallel}, v_{\perp})$. In section 2 we discuss the experimental conditions and the three-view FIDA diagnostic. In section 3 we briefly review the inversion method. We demonstrate in section 4 that salient features of our measurement of $f(v_{\parallel}, v_{\perp})$ agree with the simulation. Lastly, in section 5 we discuss the potential of tomographic inversion of FIDA and other measurements, and we draw conclusions in section 6.

2. Three-view FIDA measurements

FIDA measurements at ASDEX Upgrade were described in references [27, 43]. For our experiment in discharge 29578, we selected a plasma scenario with very low plasma density of about $n = 1.8 \times 10^{19} \text{ m}^{-3}$ in the plasma centre in order to limit bremsstrahlung and the very bright so-called passive D_{α} light from excited deuterium at the plasma edge [43]. The discharge in deuterium was heated by the co-current neutral beam injection (NBI) source Q3 that was switched on 70 ms before the measurement. NBI Q3 has an injection energy of 60 keV and a power of 2.5 MW. The toroidal magnetic field was $B_t = 1.8$ T, and the current was $I_p = 0.8$ MA. The plasma was in L-mode at the time of our measurements.

Figure 1 illustrates the geometry of the three-view FIDA measurements in a toroidal and a poloidal view. FIDA light is generated along the path of the neutral beam where many neutrals can undergo charge exchange reactions with fast ions. FIDA measurement volumes are located at the intersections

of the lines-of-sight and the path of NBI Q3. Here we choose the lines-of-sight such that the measurement volumes in each view are very similar. The spatial resolution of the three FIDA views is about 3–6 cm, and the centres of the three measurement volumes are within 3 cm of each other. The three FIDA views therefore observe approximately the same spatial volume in the plasma centre. The velocity-space interrogation regions in a FIDA view are determined by the wavelength range and the viewing angle ϕ between the line-of-sight and the magnetic field [1, 17, 22]. The three views have viewing angles (12° , 156° , 69°) which is equivalent to (12° , 24° , 69°) since a spectrum at $\phi = 24^\circ$ is a mirror image of that at $\phi = 156^\circ$. The FIDA light is collected by fibres placed in the vacuum vessel and is guided to a single 180 mm Czerny-Turner-like spectrometer with a grating with $2000 \text{ lines mm}^{-1}$. The spectrometer is optimized for high photon throughput ($f/2.8$). The spectrally dispersed radiation is measured by a low-noise electron-multiplying charge-coupled device (EM-CCD) camera with 2 ms exposure time. We used a neon lamp for the wavelength calibration and the beam emission appearing in the three spectra for the absolute intensity calibration.

In figures 2 and 3 we plot measured spectra together with synthetic spectra calculated from TRANSP/NUBEAM simulations. In figure 2 we use logarithmic intensity axes to show the contributions due to FIDA light, halo emission, beam emission, and a flat background of bremsstrahlung. In figure 3 we focus on the FIDA contributions with uncertainties using linear intensity axes. The measured spectra are averages over three frames from $t = 0.861$ – 0.867 s. Hence the time resolution is 6 ms. Figure 2 shows that the sum of these four contributions in the synthetic spectra agrees very well with the measured spectra. The levels of bremsstrahlung and passive D_{α} light were so low that we could detect red-shifted as well as blue-shifted FIDA light in all three spectra. However, line radiation from the plasma edge is not taken into account in the model and hence causes discrepancies between measurements and simulations in particular wavelength ranges. The dominating line is the cold D_{α} line at 656.1 nm in all three views. In figures 2(b) and (c) two carbon lines appear

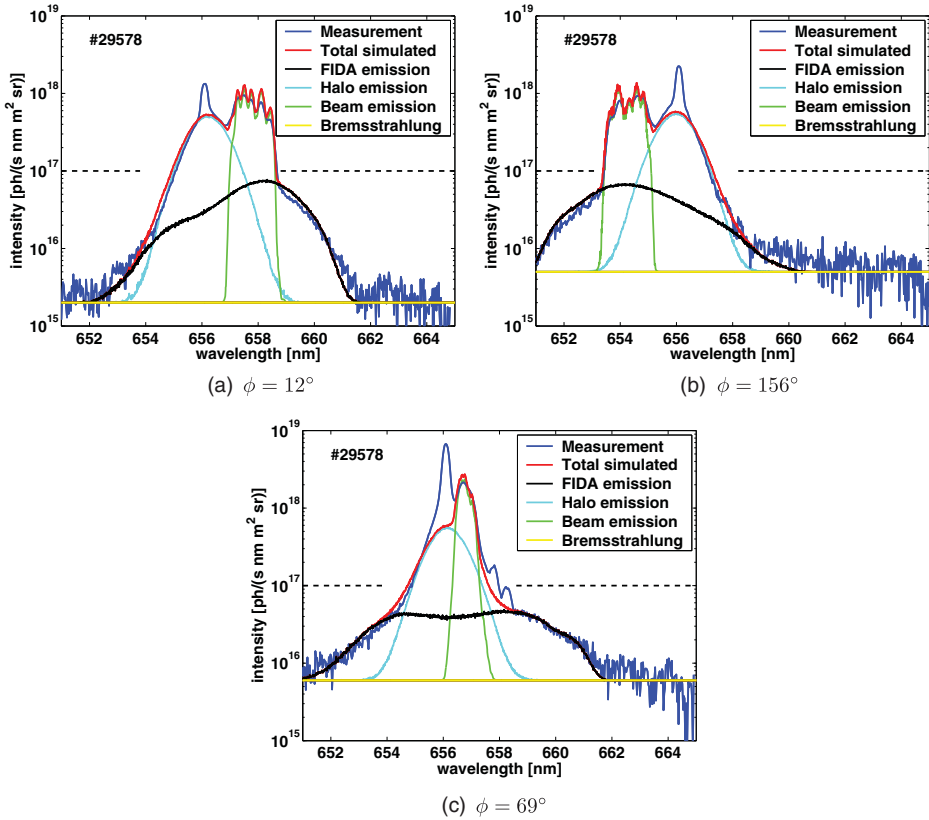


Figure 2. Measured and synthetic FIDA spectra based on TRANSP/NUBEAM simulations are shown for the three FIDA views. The total simulated spectra are the sums of the contributions from FIDA, halo, and beam emissions and bremsstrahlung. The dashed lines indicate the wavelength ranges used for the inversion. The FIDA emission curves are plotted with linear axes in figure 3.

at 657.8 nm and 658.3 nm [44]. Figure 3 confirms that in particular the measured and synthetic FIDA emission contributions to the spectra, which we use for the tomographic inversion, agree very well despite the detected weak MHD activity at the frequency of Alfvén modes. The Alfvén modes may be the reason for the slight tendency of the measured spectra to lie below the synthetic spectra, but this minor discrepancy is within the experimental uncertainty.

3. Tomographic inversion method

We use the inversion prescription discussed in references [3, 18]. The tomographic inversion F^+ , i.e. our estimate of the fast-ion distribution function leading to the FIDA measurements, is given by

$$F^+ = \hat{W}^+ \hat{G}. \quad (1)$$

\hat{G} is a matrix containing the FIDA measurements normalized by their uncertainties, \hat{W}^+ is the Moore-Penrose pseudoinverse of the transfer matrix \hat{W} which is composed of likewise normalized weight functions, and F^+ is a matrix containing the discretized function $f(v_{\parallel}, v_{\perp})$ [18]. The weight functions relate $f(v_{\parallel}, v_{\perp})$ to the fast-ion measurements [1, 17, 22]. The

weight functions are determined by Doppler shift and Stark splitting of the emitted D_{α} light as well as charge exchange and photon emission probabilities of fast ions based on averaged neutral densities in the measurement volume as calculated by FIDASIM. The uncertainties are here given by the diagnostic read-out-noise and by the photon noise. \hat{W}^+ is found by singular value decomposition of \hat{W} using the largest 65 singular values whereas the remaining singular values have been truncated. The inversion F^+ minimizes the least-square figure of merit χ^2 in which the misfit of each measurement is normalized by its uncertainty:

$$\chi^2 = |\hat{G} - \hat{W}F|^2. \quad (2)$$

Based on the achievable spectral resolution of the FIDA measurements, we divide the spectral range in a FIDA view into 160 wavelength intervals. Each wavelength interval monitors a particular velocity-space region described by a weight function. As we use three FIDA views, we have in total 480 weight functions. Of these, 217 weight functions cover the velocity-space of interest and spectral ranges which are dominated by FIDA light and bremsstrahlung or just by bremsstrahlung (see figure 2). The tomographic information lies in the amplitudes of the FIDA light. Beam emission, halo

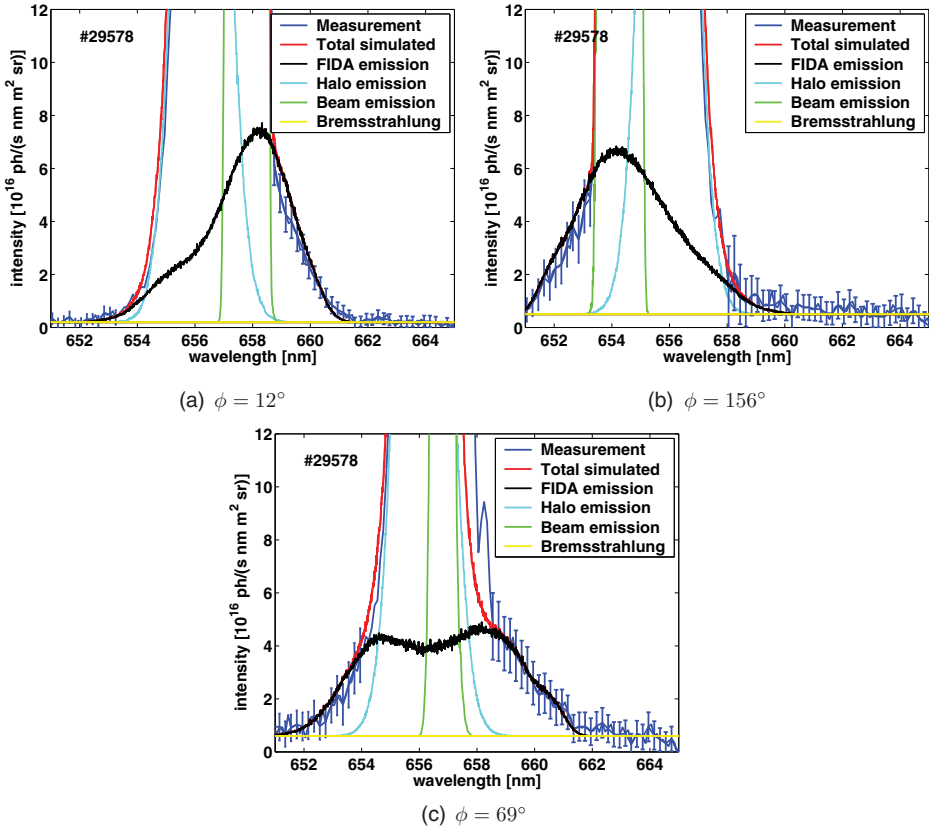


Figure 3. Measured and synthetic FIDA spectra based on TRANSP/NUBEAM simulations are shown for the three FIDA views in linear scale. The uncertainties of every second measurement are indicated. The graphs are presented with logarithmic intensities in figure 2.

emission, or impurity lines dominate the other spectral ranges. These contributions cannot be subtracted accurately enough from the total measured signal to extract a useful estimate for the FIDA signal, and hence we do not use these spectral ranges. We are free to choose the numerical grid to describe $f(v_{\parallel}, v_{\perp})$. On the one hand, we would like to describe $f(v_{\parallel}, v_{\perp})$ in high resolution and so would prefer a fine grid with many grid points. On the other hand, there is a limited number of measurements to infer useful values for F^+ at these grid points. If there are more grid points than measurements or even if the numbers are comparable, signatures of weight functions appear in the tomographic inversion [3]. These are systematic artefacts in the inversion which can be identified but which we avoid here. We therefore choose a discretization with 17×8 grid points in $(v_{\parallel}, v_{\perp})$ such that the number of grid points (136) is lower than the number of measurements (217).

4. Tomographic inversion of three-view FIDA measurements

The three measured FIDA spectra in discharge 29578 agreed very well with synthetic FIDA spectra based on a TRANSP/NUBEAM simulation. Therefore the simulation should be a realistic model of $f(v_{\parallel}, v_{\perp})$ in the experiment,

and the measurement of $f(v_{\parallel}, v_{\perp})$ by tomographic inversion should resemble the TRANSP/NUBEAM simulation.

Figure 4(a) shows the TRANSP/NUBEAM simulation of $f(v_{\parallel}, v_{\perp})$ discretized on 61×30 grid points in $(v_{\parallel}, v_{\perp})$. This resolution is high enough to capture essential features of $f(v_{\parallel}, v_{\perp})$. The function shows three peaks at full, half and one-third beam injection energies of NBI Q3 ($E = 60$ keV, $E/2 = 30$ keV and $E/3 = 20$ keV). As NBI Q3 is injected against the direction of the magnetic field (co-current), these beam injection peaks have negative v_{\parallel} coordinates. Hence the function is lopsided towards negative v_{\parallel} . We choose to calculate the inversion of the FIDA measurements on a coarser grid with 17×8 grid points in $(v_{\parallel}, v_{\perp})$ so that we infer 136 values from 217 measurements. In figure 4(b) we interpolate the TRANSP/NUBEAM simulation to the coarse grid. On this grid the peaks at $E/2$ and $E/3$ merge to become a single dominant peak in $f(v_{\parallel}, v_{\perp})$ due to the lower resolution. This interpolation in figure 4(b) shows how well a measurement of $f(v_{\parallel}, v_{\perp})$ could at best resemble the simulation in figure 4(a) for our choice of grid for the inversion, given that the TRANSP simulation is a good model for $f(v_{\parallel}, v_{\perp})$ in discharge 29578 and that the measurements are noise-free and cover the entire 2D velocity-space.

Figure 4(c) shows a tomographic inversion of the synthetic spectra based on the TRANSP/NUBEAM simulation. We use

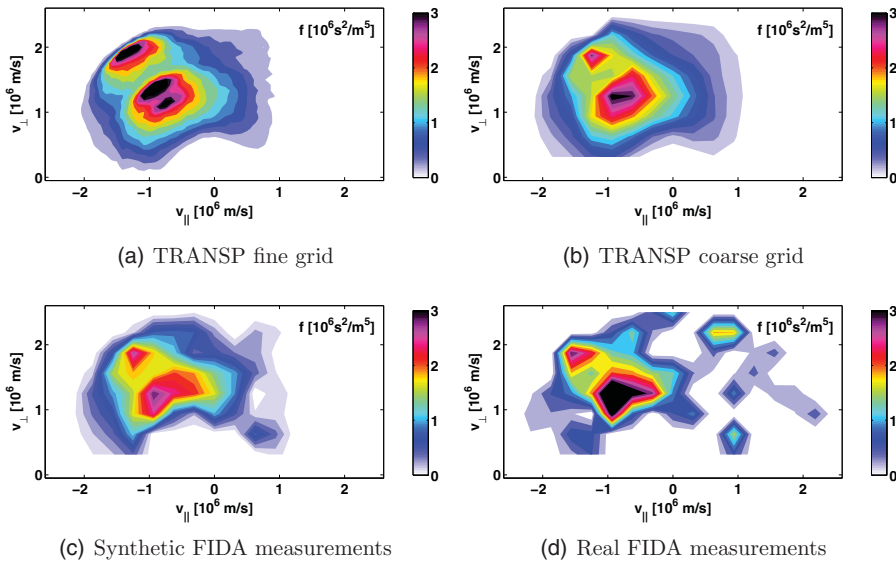


Figure 4. Simulation of $f(v_{\parallel}, v_{\perp})$ as well as measurement of $f(v_{\parallel}, v_{\perp})$ by tomographic inversion. (a) TRANSP/NUBEAM simulation discretized by 61×30 grid points. (b) TRANSP/NUBEAM simulation discretized by 17×8 grid points. (c) Inversion of synthetic FIDA spectra based on the TRANSP/NUBEAM simulation. (d) Measurement of $f(v_{\parallel}, v_{\perp})$ by tomographic inversion of FIDA spectra.

only synthetic spectral data from experimentally accessible wavelength intervals for our three-view FIDA measurements. This inversion is an idealized prediction for the measurement of $f(v_{\parallel}, v_{\perp})$ in figure 4(d) and represents how well our measurement of $f(v_{\parallel}, v_{\perp})$ with our particular three-view FIDA instrument could at best resemble the simulation in figure 4(a), given noise-free measurements and that the TRANSP simulation is a good model for $f(v_{\parallel}, v_{\perp})$ in discharge 29578. As expected, the inversion from synthetic spectra resembles the TRANSP simulation very well [3].

In figure 4(d) we present the measurement of $f(v_{\parallel}, v_{\perp})$ by tomographic inversion of FIDA spectra. The TRANSP/NUBEAM simulation and the measurement of $f(v_{\parallel}, v_{\perp})$ agree reasonably well. The shapes of the measured and simulated functions $f(v_{\parallel}, v_{\perp})$ are similar, and the measured function $f(v_{\parallel}, v_{\perp})$ is also lopsided towards negative v_{\parallel} . The beam injection peaks at E and $E/2$ appear in the measurement very close to the velocity-space positions in the simulation. The differences between figures 4(c) and 4(d) originate from the slight systematic differences between the measured and the synthetic FIDA spectra and from noise in the measurements. We interpret the jitter appearing in figure 4(d) not to be physical but rather to be artefacts generated by noise.

To conclude, we find remarkable agreement between the measurement and the simulation of $f(v_{\parallel}, v_{\perp})$. The overall shape of $f(v_{\parallel}, v_{\perp})$ including the positions of the beam injection peaks can be revealed by tomographic inversion but not by conventional inspection of the FIDA spectra in figure 2.

5. Discussion

In this section we suggest how to improve tomographic inversions further and discuss the potential of tomographic

inversions to study physical phenomena in plasmas. In the experiment reported here, three FIDA spectra with different viewing angles were simultaneously measured and inverted. Two additional FIDA views should become available in the next ASDEX Upgrade campaign. Moreover, we can increase the signal-to-noise ratio of the FIDA measurements. Here we allowed the cold D_{α} line to enter the spectrometer together with the FIDA signal. It will benefit the signal-to-noise ratio to block the cold D_{α} line as then the EM-CCD camera can be operated at higher gain without saturation.

Further, our analysis method is not restricted to FIDA measurements. Likewise, 1D collective Thomson scattering (CTS) measurements can be inverted [3], as can combinations of CTS and FIDA measurements [18]. Traditional CTS data analysis procedures also rely on synthetic diagnostics [45, 46], and our velocity-space tomography approach will have the same benefits for the interpretation of CTS spectra. The next step will be to include the CTS diagnostic installed at ASDEX Upgrade [46–50] which we recently upgraded with a second radiometer. Hence a total of seven views should become available for a combined FIDA and CTS system in the next campaign. The additional four views would improve the inversions, in particular if they have large viewing angles to complement the viewing angles at 12° and 24° . CTS measurements at very high frequency resolution, such as those demonstrated at TEXTOR [51–53], are also possible at ASDEX Upgrade. High resolution CTS measurements have so far been restricted to bulk-ion measurements since the bandwidth and the bit resolution were not large enough to measure fast ions. High resolution spectra should contain a wealth of information suitable for tomographic inversion of future CTS measurements [3]. Measurements from other fast-ion diagnostics at ASDEX Upgrade could also be included in the inversion if weight functions describing these can be

formulated, for example neutron spectroscopy [54, 55] and neutron count measurements [56], γ spectroscopy [57], neutral particle analysers [58], or fast-ion loss detectors [37, 59]. Lastly, we could likely achieve further improvements of the tomography method by using alternative inversion algorithms such as those in other branches of tomography [4–15].

Several other machines have multi-view FIDA systems installed or are planning to install or upgrade multi-view FIDA systems. Similar measurements of $f(v_{\parallel}, v_{\perp})$ could be done on DIII-D (three FIDA views [38, 60]), NSTX (two FIDA views [61]), MAST (two FIDA views [40, 62]), LHD (one CTS view [63, 64] and two FIDA views [65, 66]) and ITER (one CTS view [67–70] and possibly charge exchange measurements of fast α particles [71]).

The velocity-space tomography approach can potentially reveal new physics in cases with anomalous transport of fast ions, in particular if this transport depends on the position of the fast ions in velocity space. Our measurement of $f(v_{\parallel}, v_{\perp})$ was made in a plasma with relatively weak Alfvén modes. A TRANSP/NUBEAM simulation assuming neoclassical transport matched the FIDA measurements well, and we could demonstrate that it is possible to measure $f(v_{\parallel}, v_{\perp})$. Stronger Alfvén eigenmodes than the ones reported here are known to affect ions in specific parts of velocity space [37, 60, 72–75]. The amplitude of the anomalous transport due to resonant interaction of the modes with the fast ions depends on the position in velocity space as only ions fulfilling a resonance condition with the modes are affected. Several other types of modes also affect ions selectively in velocity space, for example sawteeth, neoclassical tearing modes, and or fishbones. Sawtooth crashes redistribute passing ions more than trapped ions [41, 42, 76, 77]. Strong and coherent fast-ion losses observed in the presence of neoclassical tearing modes have shown that these modes selectively redistribute fast particles under resonance conditions [59, 78]. Fishbones [72, 79] and off-axis fishbones [80] have also been demonstrated to act selectively in velocity space. However, the underlying mechanisms leading to enhanced fast-ion transport in the presence of these MHD instabilities are still not understood well. Likewise, any anomalous fast-ion transport in the presence of microinstabilities is thought to be selective in velocity space and is not well understood [30, 33, 81]. Our tomography approach can pinpoint the origin of any observed discrepancies between FIDA measurements and simulation in velocity space which has not been possible before. This can give clues to reveal the underlying mechanisms and can enable us to improve the forward modelling, either in cases where existing theory is wrong or even if there is no theory yet.

6. Conclusions

We demonstrated that it is possible to measure salient features of a 2D fast-ion velocity distribution function $f(v_{\parallel}, v_{\perp})$. For this purpose we measured spectra of FIDA light from the plasma centre at ASDEX Upgrade simultaneously in three views and calculated a tomographic inversion of these measurements. The measured spectra agree very well with synthetic spectra based on a TRANSP/NUBEAM simulation, and the tomographic inversion therefore agrees reasonably well with the simulation. The inversion as well as the simulation are

lopsided towards negative v_{\parallel} , and the overall shapes also agree reasonably well. The velocity-space locations of the beam injection peaks at E and $E/2$ in the inversion are very close to those in the simulation. We hope to measure $f(v_{\parallel}, v_{\perp})$ in seven views simultaneously in the next ASDEX Upgrade campaign, and this would further improve the diagnostic potential of tomographic inversion to measure 2D fast-ion velocity-space distribution functions $f(v_{\parallel}, v_{\perp})$.

Acknowledgments

This work, supported by the European Communities under the contract of Association between Euratom and DTU was partly carried out within the framework of the European Fusion Development Agreement. The views and opinions expressed herein do not necessarily reflect those of the European Commission.

References

- [1] Heidbrink W.W. 2010 *Rev. Sci. Instrum.* **81** 10D727
- [2] Alfvén H. 1940 *Ark. Mat. Astron. Fys.* **27A** 1
- [3] Salewski M. et al 2012 *Nucl. Fusion* **52** 103008
- [4] Ertl K., von der Linden W., Dose V. and Weller A. 1996 *Nucl. Fusion* **36** 1477–88
- [5] Anton M. et al 1996 *Plasma Phys. Control. Fusion* **38** 1849–78
- [6] Ingesson L.C. et al 1998 *Nucl. Fusion* **38** 1675–94
- [7] Nagayama Y. et al 1996 *Nucl. Fusion* **36** 521–6
- [8] Howard J. 1996 *Plasma Phys. Control. Fusion* **38** 489–503
- [9] Konoshima S. et al 2001 *Plasma Phys. Control. Fusion* **43** 959–83
- [10] Peterson B.J. et al 2003 *Plasma Phys. Control. Fusion* **45** 1167–82
- [11] Furno I. et al 2005 *Plasma Phys. Control. Fusion* **47** 49–69
- [12] Bonheure G. et al 2006 *Nucl. Fusion* **46** 725–40
- [13] Svensson J. and Werner A. 2008 *Plasma Phys. Control. Fusion* **50** 085002
- [14] Kak A. C. and Slaney M. 1988 *Principles of Computerized Tomographic Imaging* (Piscataway, NJ: IEEE Press)
- [15] Herman G.T. 2009 *Fundamentals of Computerized Tomography* (Berlin: Springer) 2nd edn
- [16] Egedal J. and Bindslev H. 2004 *Phys. Plasmas* **11** 2191
- [17] Salewski M. et al 2011 *Nucl. Fusion* **51** 083014
- [18] Salewski M. et al 2013 *Nucl. Fusion* **53** 063019
- [19] Heidbrink W.W. et al 2011 *Commun. Comp. Phys.* **10** 716–41
- [20] Pankin A. et al 2004 *Comp. Phys. Commun.* **159** 157–84
- [21] Heidbrink W.W. et al 2004 *Plasma Phys. Control. Fusion* **46** 1855–75
- [22] Heidbrink W.W. et al 2007 *Plasma Phys. Control. Fusion* **49** 1457–75
- [23] Luo Y. et al 2007 *Phys. Plasmas* **14** 112503
- [24] Muscatello C.M. et al 2010 *Rev. Sci. Instrum.* **81** 10D316
- [25] Van Zeeland M.A., Heidbrink W.W. and Yu J.H. 2009 *Plasma Phys. Control. Fusion* **51** 055001
- [26] Park J.M. et al 2009 *Phys. Plasmas* **16** 092508
- [27] Geiger B. et al 2011 *Plasma Phys. Control. Fusion* **53** 065010
- [28] Grierson B.A. et al 2012 *Phys. Plasmas* **19** 056107
- [29] Grierson B.A. et al 2012 *Rev. Sci. Instrum.* **83** 10D529
- [30] Pace D.C. et al 2013 *Phys. Plasmas* **20** 056108
- [31] Heidbrink W.W. et al 2009 *Plasma Phys. Control. Fusion* **51** 125001
- [32] Heidbrink W.W. et al 2007 *Phys. Rev. Lett.* **99** 245002
- [33] Heidbrink W.W. et al 2009 *Phys. Rev. Lett.* **103** 175001
- [34] Heidbrink W.W. et al 2008 *Nucl. Fusion* **48** 084001
- [35] Gorelenkov N.N. et al 2009 *Phys. Plasmas* **16** 056107
- [36] Liu D. et al 2010 *Plasma Phys. Control. Fusion* **52** 025006

- [37] García-Muñoz M *et al* 2011 *Nucl. Fusion* **51** 103013
- [38] Heidbrink W.W. *et al* 2012 *Nucl. Fusion* **52** 094005
- [39] Heidbrink W.W. *et al* 2012 *Rev. Sci. Instrum.* **83** 10D903
- [40] Michael C.A. 2013 *Plasma Phys. Control. Fusion* **55** 095007
- [41] Pace D.C. *et al* 2011 *Nucl. Fusion* **51** 043012
- [42] Muscatello C.M. *et al* 2012 *Plasma Phys. Control. Fusion* **54** 025006
- [43] Geiger B. *et al* 2013 *Rev. Sci. Instrum.* **84** 113502
- [44] Moore C.E. 1970 *National Standard Reference Data Series NSRDS-NBS 3 (Sect. 3)* (Washington, DC: National Bureau Standards)
- [45] Moseev D. *et al* 2011 *Plasma Phys. Control. Fusion* **53** 105004
- [46] Salewski M. *et al* 2010 *Nucl. Fusion* **50** 035012
- [47] Meo F. *et al* 2008 *Rev. Sci. Instrum.* **79** 10E501
- [48] Meo F. *et al* 2010 *J. Phys.: Conf. Ser.* **227** 012010
- [49] Furtula V. *et al* 2012 *Rev. Sci. Instrum.* **83** 013507
- [50] Furtula V. *et al* 2012 *J. Instrum.* **7** C02039
- [51] Stejner M. *et al* 2010 *Rev. Sci. Instrum.* **81** 10D515
- [52] Korsholm S.B. *et al* 2011 *Phys. Rev. Lett.* **106** 165004
- [53] Stejner M. *et al* 2013 *Plasma Phys. Control. Fusion* **55** 085002
- [54] Giacomelli L. *et al* 2011 *Rev. Sci. Instrum.* **82** 123504
- [55] Tardini G. *et al* 2012 *J. Instrum.* **7** C03004
- [56] Tardini G. *et al* 2013 *Nucl. Fusion* **53** 063027
- [57] Nocente M. *et al* 2012 *Nucl. Fusion* **52** 063009
- [58] Äkäslompolo S. *et al* 2010 *Europhysics Conf. Abstracts (Dublin)* vol 34A P5.113 <http://ocs.ciemat.es/EPS2010PAP/pdf/P5.113.pdf>
- [59] García-Muñoz M. *et al* 2007 *Nucl. Fusion* **47** L10–5
- [60] Pace D.C. *et al* 2011 *Plasma Phys. Control. Fusion* **53** 062001
- [61] Bortolon A., Heidbrink W.W. and Podestà M. 2010 *Rev. Sci. Instrum.* **81** 10D728
- [62] Jones O.M. *et al* 2013 *Plasma Phys. Control. Fusion* **55** 085009
- [63] Kubo S. *et al* 2010 *Rev. Sci. Instrum.* **81** 10D535
- [64] Nishiura M. *et al* 2014 Spectrum response and analysis of 77-GHz band collective Thomson scattering diagnostic for bulk and fast ions in LHD plasmas *Nucl. Fusion* **54** 023006
- [65] Ito T. *et al* 2010 *Rev. Sci. Instrum.* **81** 10D327
- [66] Ito T. *et al* 2012 *Plasma Fusion Res.* **5** S2099
- [67] Salewski M. *et al* 2009 *Plasma Phys. Control. Fusion* **51** 035006
- [68] Salewski M. *et al* 2009 *Nucl. Fusion* **49** 025006
- [69] Salewski M. *et al* 2008 *Rev. Sci. Instrum.* **79** 10E729
- [70] Leipold F. *et al* 2009 *Rev. Sci. Instrum.* **80** 093501
- [71] Kappatou A. *et al* 2012 *Nucl. Fusion* **52** 043007
- [72] Heidbrink W.W. and Sadler G.J. 1994 *Nucl. Fusion* **34** 535–615
- [73] Zweben S.J. *et al* 2000 *Nucl. Fusion* **40** 91–149
- [74] Nabais F. *et al* 2010 *Nucl. Fusion* **50** 115006
- [75] Van Zeeland M.A. *et al* 2011 *Phys. Plasmas* **18** 056114
- [76] Nielsen S.K. *et al* 2010 *Plasma Phys. Control. Fusion* **52** 092001
- [77] Nielsen S.K. *et al* 2011 *Nucl. Fusion* **51** 063014
- [78] García-Muñoz M. *et al* 2009 *Nucl. Fusion* **49** 085014
- [79] Perez von Thun C. *et al* 2012 *Nucl. Fusion* **52** 094010
- [80] Heidbrink W.W. *et al* 2011 *Plasma Phys. Control. Fusion* **53** 085028
- [81] Hauff T. *et al* 2009 *Phys. Rev. Lett.* **102** 075004

Reference [6]

- [6]. M Salewski et al. (2014) *Plasma Physics and Controlled Fusion* **56** 105005. On velocity-space sensitivity of fast-ion D-alpha spectroscopy

On velocity-space sensitivity of fast-ion D-alpha spectroscopy

M Salewski¹, B Geiger², D Moseev^{2,3}, W W Heidbrink⁴, A S Jacobsen¹, S B Korsholm¹, F Leipold¹, J Madsen¹, S K Nielsen¹, J Rasmussen¹, M Stejner¹, M Weiland² and the ASDEX Upgrade Team²

¹ Technical University of Denmark, Department of Physics, DK-2800 Kgs. Lyngby, Denmark

² Max-Planck-Institut für Plasmaphysik, D-85748 Garching, Germany

³ FOM Institute DIFFER, 3430 BE Nieuwegein, The Netherlands

⁴ University of California, Department of Physics and Astronomy, Irvine, CA 92697, USA

E-mail: msal@fysik.dtu.dk

Received 19 May 2014, revised 18 July 2014

Accepted for publication 13 August 2014

Published 8 September 2014

Abstract

The velocity-space observation regions and sensitivities in fast-ion D α (FIDA) spectroscopy measurements are often described by so-called weight functions. Here we derive expressions for FIDA weight functions accounting for the Doppler shift, Stark splitting, and the charge-exchange reaction and electron transition probabilities. Our approach yields an efficient way to calculate correctly scaled FIDA weight functions and implies simple analytic expressions for their boundaries that separate the triangular observable regions in (v_{\parallel} , v_{\perp})-space from the unobservable regions. These boundaries are determined by the Doppler shift and Stark splitting and could until now only be found by numeric simulation.

Keywords: fast-ion D-alpha spectroscopy, FIDA, charge-exchange recombination spectroscopy, fast ions, velocity space

(Some figures may appear in colour only in the online journal)

1. Introduction

Fast-ion D α (FIDA) spectroscopy [1–3] is an application of charge-exchange recombination (CER) spectroscopy [4, 5] based on deuterium [6–11]. Deuterium ions in the plasma are neutralized in charge-exchange reactions with deuterium atoms from a neutral beam injector (NBI). The neutralized deuterium atoms are often in excited states, and hence they can emit D α -photons which are Doppler-shifted due to the motion of the excited atoms. As the excited atoms inherit the velocities of the deuterium ions before the charge-exchange reaction, spectra of Doppler-shifted D α -light are sensitive to the velocity distribution function of deuterium ions in the plasma. The measurement volume is given by the intersection of the NBI path and the line-of-sight of the CER diagnostic. D α -photons due to bulk deuterium ions typically have Doppler shifts of about 1–2 nm whereas D α -photons due to fast deuterium, which is the FIDA light, can have Doppler shifts of several nanometers. This paper deals with FIDA light but as the physics of D α -light due to bulk deuterium ions is the same,

our methods also apply to deuterium-based CER spectroscopy. The FIDA or CER-D α light is sometimes obscured by Doppler shifted D α -light from the NBI, unshifted D α -light from the plasma edge, bremsstrahlung or line radiation from impurities.

FIDA spectra can be related to 2D velocity space by so-called weight functions [2, 3, 12]. Weight functions have been used in four ways: first, they quantify the velocity-space sensitivity of FIDA measurements, and hence they also separate the observable region in velocity space for a particular wavelength range from the unobservable region [2, 3, 13–29]. Second, they reveal how much FIDA light is emitted resolved in velocity space for a given fast-ion velocity distribution function [2, 3, 24–30]. The ions in the regions with the brightest FIDA light are then argued to dominate the measurement. Third, weight functions have been used to calculate FIDA spectra from given fast-ion velocity distribution functions [14, 31–33], eliminating the Monte-Carlo approach of the standard FIDA analysis code FIDASIM [34]. Fourth, recent tomographic inversion algorithms to infer 2D fast-ion velocity distribution

functions directly from the measurements rely heavily on weight functions [12, 31–33, 35].

Here we present a comprehensive discussion of FIDA weight functions and derive analytic expressions describing them. FIDA weight functions have often been presented in arbitrary units, relative units or without any units [2, 3, 15–28, 30] which is sufficient for their use as indicator of the velocity-space interrogation region or of the velocity-space origin of FIDA light. However, correctly scaled FIDA weight functions, which are necessary to calculate FIDA spectra or tomographic inversions, have only been implemented in the FIDASIM code recently [13, 14, 29, 31–33]. Weight functions are traditionally calculated using the FIDASIM code by computing the FIDA light from an ion on a fine grid in 2D velocity space and gyroangle. It is then counted how many photons contribute to a particular wavelength range for a given observation angle and point in velocity space using models for the Doppler shift, Stark splitting, charge-exchange probabilities and electron transition probabilities.

In section 2 we define weight functions and motivate their interpretation in terms of probabilities. Our viewpoint provides insights into functional dependencies between wavelength space and 2D velocity space that are not revealed by the traditional numerical calculation approach using FIDASIM. As a consequence we demonstrate how Doppler shift, Stark splitting, charge-exchange probabilities as well as the electron transition probabilities contribute to the velocity-space sensitivity of FIDA measurements. Section 3 focuses on weight functions implied by the Doppler shift alone as a relatively simple approximation. In section 4 we additionally treat Stark splitting and in section 5 the charge-exchange and the electron transition processes. In section 6 we present full FIDA weight functions accounting for these four effects. In section 7 we deduce exact analytic expressions for the boundaries of FIDA weight functions. We discuss the applicability of our results to CER spectroscopy and other fast-ion diagnostics in section 8 and conclude in section 9.

2. Definitions of weight functions

The velocity-space interrogation or observation regions of FIDA diagnostics are described by weight functions w_{vol} which are determined by charge-exchange probabilities, electron transition probabilities, Stark splitting and the Doppler shift. They thereby depend on position space and velocity space. Weight functions are defined to obey [2, 3, 12]

$$I(\lambda_1, \lambda_2, \phi) = \int_{\text{vol}} \int_0^\infty \int_{-\infty}^\infty w_{\text{vol}}(\lambda_1, \lambda_2, \phi, v_{\parallel}, v_{\perp}, \mathbf{x}) \times f(v_{\parallel}, v_{\perp}, \mathbf{x}) dv_{\parallel} dv_{\perp} d\mathbf{x}. \quad (1)$$

$I(\lambda_1, \lambda_2, \phi)$ is the intensity of FIDA light in the wavelength range $\lambda_1 < \lambda < \lambda_2$ with a viewing angle ϕ between the line-of-sight of the FIDA diagnostic and the magnetic field. $(v_{\parallel}, v_{\perp})$ denote velocities parallel and perpendicular to the magnetic field, respectively, and \mathbf{x} denotes the spatial coordinates. Here we use $(v_{\parallel}, v_{\perp})$ -coordinates rather than the more widespread (E, p) -coordinates (energy, pitch) since our mathematical

expressions are simpler in $(v_{\parallel}, v_{\perp})$ -coordinates. The energy and the pitch are defined as

$$E = \frac{1}{2} m_{\text{D}} (v_{\parallel}^2 + v_{\perp}^2) \quad (2)$$

$$p = -\frac{v_{\parallel}}{v} \quad (3)$$

where m_{D} is the mass of a deuteron and $v = \sqrt{v_{\parallel}^2 + v_{\perp}^2}$ is the velocity magnitude. Note that the pitch is positive for co-current particles as usual. Key expressions are given in (E, p) -coordinates in the appendix. We assume $w_{\text{vol}}(\lambda_1, \lambda_2, \phi, v_{\parallel}, v_{\perp}, \mathbf{x})$ and the fast-ion distribution function $f(v_{\parallel}, v_{\perp}, \mathbf{x})$ to be spatially uniform within the small measurement volume V . This may be violated near the foot of the pedestal where the density gradient length scale could be comparable with the mean free path of the emitters, but it should be fulfilled in the core plasma. With

$$w(\lambda_1, \lambda_2, \phi, v_{\parallel}, v_{\perp}) = V w_{\text{vol}}(\lambda_1, \lambda_2, \phi, v_{\parallel}, v_{\perp}, \mathbf{x}) \quad (4)$$

equation (1) becomes

$$I(\lambda_1, \lambda_2, \phi) = \int_0^\infty \int_{-\infty}^\infty w(\lambda_1, \lambda_2, \phi, v_{\parallel}, v_{\perp}) f(v_{\parallel}, v_{\perp}) dv_{\parallel} dv_{\perp}. \quad (5)$$

Weight functions w relate the FIDA intensity $I(\lambda_1, \lambda_2, \phi)$ with units $[N_{\text{ph}}/(\text{s} \times \text{sr} \times \text{m}^2)]$ to the 2D fast-ion velocity distribution function with units $[N_{\text{i}}/(\text{m}^3 \times (\text{m}/\text{s})^2)]$. The units of FIDA weight functions w are hence $[N_{\text{ph}}/(\text{s} \times \text{sr} \times \text{m}^2 \times N_{\text{i}}/\text{m}^3)]$, i.e. FIDA weight functions w quantify the *FIDA intensity per unit ion density* in the wavelength range $\lambda_1 < \lambda < \lambda_2$ for a viewing angle ϕ as a function of the ion velocity $(v_{\parallel}, v_{\perp})$. The units of FIDA weight functions w_{vol} are $[N_{\text{ph}}/(\text{s} \times \text{sr} \times \text{m}^2 \times N_{\text{i}})]$, i.e. the *FIDA intensity per ion* in $\lambda_1 < \lambda < \lambda_2$ for a viewing angle ϕ as function of $(v_{\parallel}, v_{\perp})$. We will split FIDA weight functions w into a FIDA intensity function $R(v_{\parallel}, v_{\perp})$ and a probability $\text{prob}(\lambda_1 < \lambda < \lambda_2 | \phi, v_{\parallel}, v_{\perp})$ according to

$$w(\lambda_1, \lambda_2, \phi, v_{\parallel}, v_{\perp}) = R(v_{\parallel}, v_{\perp}) \text{prob}(\lambda_1 < \lambda < \lambda_2 | \phi, v_{\parallel}, v_{\perp}). \quad (6)$$

$R(v_{\parallel}, v_{\perp})$ determines the total FIDA intensity for any wavelength of the photons per unit ion density. It depends only on the charge-exchange and electron transition processes, but not on the Doppler shift or Stark splitting that only change the wavelength of the photons. $\text{prob}(\lambda_1 < \lambda < \lambda_2 | \phi, v_{\parallel}, v_{\perp})$ determines the probability that a randomly selected detected photon has a wavelength in a particular range $\lambda_1 < \lambda < \lambda_2$ for a given projection angle ϕ and $(v_{\parallel}, v_{\perp})$ -coordinates. The conditioning symbol ‘|’ means ‘given’. The subject of this paper is the derivation of this probability. $\text{prob}(\lambda_1 < \lambda < \lambda_2 | \phi, v_{\parallel}, v_{\perp})$ depends on the Doppler shift and Stark Splitting as well as on the charge-exchange and electron transition processes which in turn all depend on the gyroangle γ of the ion at the time of the charge-exchange reaction. We treat $\gamma \in [0, 2\pi]$ as a random variable since we do not know the phases of all ions in the plasma, i.e. the initial conditions of any set of equations determining the ion motion are unknown as always in problems with a very large number of degrees of freedom. Since λ is determined by γ , it is also treated

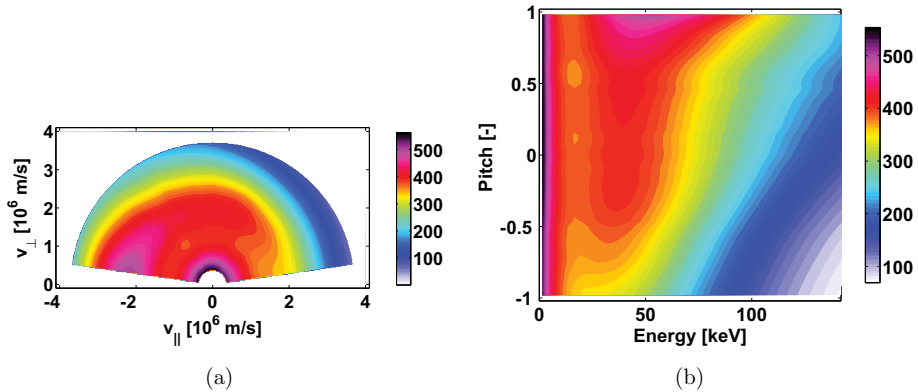


Figure 1. The FIDA intensity function R shows the total FIDA intensity per unit ion density as function of (a) $(v_{\parallel}, v_{\perp})$ -coordinates and (b) (E, p) -coordinates. The units are $[N_{\text{ph}}/(\text{s} \times \text{sr} \times \text{m}^2 \times N_i/\text{m}^3)]$. The Balmer-alpha photons can have any Doppler-shifted wavelength. We computed R using FIDASIM for NBI Q3 at ASDEX Upgrade. Q3 has an injection energy of 60 keV.

as random variable. Probabilities are always dimensionless numbers in the interval $[0,1]$, and hence the FIDA intensity function $R(v_{\parallel}, v_{\perp})$ has the same units as weight functions.

$R(v_{\parallel}, v_{\perp})$ is a common factor of all weight functions for a given ϕ at any wavelength. On the contrary, the probability function depends on the wavelength range and the projection angle ϕ and hence contains the spectral information. We compute $R(v_{\parallel}, v_{\perp})$ using FIDASIM by modeling the charge-exchange and the electron transition processes. Examples of the FIDA intensity function for NBI Q3 at ASDEX Upgrade, which is used for FIDA measurements, are shown in figure 1(a) in $(v_{\parallel}, v_{\perp})$ -coordinates and in figure 1(b) in (E, p) -coordinates. The sensitivity of FIDA is low for very large ion energies where few photons are generated per ion. Ions with positive pitch generate more photons per ion than ions with negative pitch for Q3.

Usually one measures spectral or specific intensities I_{λ} , i.e. the intensity per wavelength with units $[N_{\text{ph}}/(\text{s} \times \text{sr} \times \text{m}^2 \times \text{nm})]$. The intensity and the spectral intensity are related by

$$I(\lambda_1, \lambda_2, \phi) = \int_{\lambda_1}^{\lambda_2} I_{\lambda}(\lambda, \phi) d\lambda. \quad (7)$$

The spectral intensity $I_{\lambda}(\lambda, \phi)$ can likewise be related to $f(v_{\parallel}, v_{\perp})$ by a probability density function $\text{pdf}(\lambda|\phi, v_{\parallel}, v_{\perp})$ that then leads to a differential weight function dw as

$$I_{\lambda}(\lambda, \phi) = \int_0^{\infty} \int_{-\infty}^{\infty} dw(\lambda, \phi, v_{\parallel}, v_{\perp}) f(v_{\parallel}, v_{\perp}) dv_{\parallel} dv_{\perp} \quad (8)$$

with

$$dw(\lambda, \phi, v_{\parallel}, v_{\perp}) = R(v_{\parallel}, v_{\perp}) \text{pdf}(\lambda|\phi, v_{\parallel}, v_{\perp}). \quad (9)$$

However, the weight functions we discuss here are related to a wavelength range rather than a particular wavelength since FIDA intensity measurements can only be made for a wavelength range and not for a single wavelength. Mathematically this is reflected in the always finite amplitudes of w whereas dw is singular at its boundary.

3. Doppler shift

An approximate shape of FIDA weight functions can be found by considering only the Doppler shift $\lambda - \lambda_0$ where $\lambda_0 = 656.1 \text{ nm}$ is the wavelength of the unshifted D_{α} -line and λ is the Doppler-shifted wavelength. In this section we derive this approximate shape by neglecting Stark splitting and by assuming that the D_{α} -photon emission is equally likely for all gyroangles γ of the ion at the time of the charge-exchange reaction. The probability density function in γ of randomly selected detected D_{α} photons is

$$\text{pdf}_{D_{\alpha}}(\gamma | v_{\parallel}, v_{\perp}) = 1/2\pi. \quad (10)$$

Stark splitting and an arbitrary $\text{pdf}_{D_{\alpha}}$ describing charge-exchange and electron transition probabilities will be introduced into the model in the next two sections. The Doppler shift depends on the projected velocity u of the ion along the line-of-sight according to

$$\lambda - \lambda_0 = u\lambda_0/c \quad (11)$$

where c is the speed of light. Equation (11) assumes $u \ll c$. Consider a gyrating ion with velocity $(v_{\parallel}, v_{\perp})$ in a magnetic field. The ion is neutralized in a charge-exchange reaction which ultimately leads to emission of a D_{α} -photon. We define a coordinate system such that for $\gamma = 0$ the velocity vector of the ion is in the plane defined by the unit vector along the line-of-sight \hat{u} and \mathbf{B} such that $\mathbf{v} \cdot \hat{u} > 0$. Then the ion velocity is

$$\mathbf{v} = v_{\parallel} \hat{\mathbf{B}} + v_{\perp} \cos \gamma \hat{\mathbf{v}}_{\perp 1} - v_{\perp} \sin \gamma \hat{\mathbf{v}}_{\perp 2} \quad (12)$$

and the unit vector along the line-of-sight is

$$\hat{u} = \cos \phi \hat{\mathbf{B}} + \sin \phi \hat{\mathbf{v}}_{\perp 1}. \quad (13)$$

The velocity component u of the ion along the line-of-sight at a projection angle ϕ to the magnetic field is then given by [12]

$$u = \mathbf{v} \cdot \hat{u} = v_{\parallel} \cos \phi + v_{\perp} \sin \phi \cos \gamma. \quad (14)$$

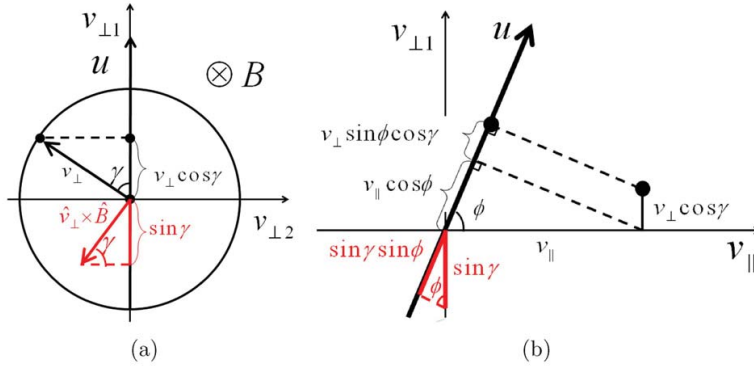


Figure 2. Projection of the ion velocity (v_{\parallel} , v_{\perp}) and the unit vector $\hat{v} \times \hat{B}$ onto the line-of-sight. The latter is required for the treatment of Stark splitting discussed in section 4.

The projections of the ion velocity v and the unit vector $\hat{v} \times \hat{B}$ (relevant for Stark splitting) onto the line-of-sight in this coordinate system are illustrated in figure 2. Equation (14) shows that u is a random variable which depends on the random variable $\gamma \in [0, 2\pi]$. We now calculate the probability $\text{prob}(u_1 < u < u_2 | \phi, v_{\parallel}, v_{\perp})$ that the ion has a projected velocity between u_1 and u_2 at the time of the charge-exchange reaction and therefore a Doppler-shifted D_{α} -line wavelength between λ_1 and λ_2 according to equation (11). For given $(v_{\parallel}, v_{\perp})$ with $v_{\perp} \neq 0$ and projection angle $\phi \neq 0$, the projected velocity depends on the gyroangle γ . Conversely, we can calculate the gyroangles that lead to a given projected velocity u by solving equation (14) for γ :

$$\gamma = \arccos \frac{u - v_{\parallel} \cos \phi}{v_{\perp} \sin \phi}. \quad (15)$$

The arccos function is defined for $0 < \gamma < \pi$, and a second solution in $\pi < \gamma' < 2\pi$ is given by

$$\gamma' = 2\pi - \gamma. \quad (16)$$

Using equations (15) and (16) we can calculate gyroangles γ_1 and γ_2 and γ'_1 and γ'_2 corresponding to the limits u_1 and u_2 and transform the calculation of the probability to γ -space:

$$\begin{aligned} & \text{prob}(u_1 < u < u_2 | \phi, v_{\parallel}, v_{\perp}) \\ &= \text{prob}(\gamma_2 < \gamma < \gamma_1 | v_{\parallel}, v_{\perp}) + \text{prob}(\gamma'_1 < \gamma < \gamma'_2 | v_{\parallel}, v_{\perp}) \\ &= \int_{\gamma_2}^{\gamma_1} \text{pdf}_{D_{\alpha}}(\gamma | v_{\parallel}, v_{\perp}) d\gamma + \int_{\gamma'_1}^{\gamma'_2} \text{pdf}_{D_{\alpha}}(\gamma | v_{\parallel}, v_{\perp}) d\gamma. \end{aligned} \quad (17)$$

As we here assume a uniform probability density, we can integrate equation (17) analytically:

$$\begin{aligned} \text{prob}(u_1 < u < u_2 | \phi, v_{\parallel}, v_{\perp}) &= \frac{\gamma_1 - \gamma_2}{2\pi} + \frac{\gamma'_2 - \gamma'_1}{2\pi} \\ &= \frac{\gamma_1 - \gamma_2}{\pi}. \end{aligned} \quad (18)$$

The probability $\text{prob}(u_1 < u < u_2 | \phi, v_{\parallel}, v_{\perp})$ is thus the fraction of the gyro-orbit that leads to a projected velocity

between u_1 and u_2 . Substitution of γ using equation (15) gives

$$\begin{aligned} & \text{prob}(u_1 < u < u_2 | \phi, v_{\parallel}, v_{\perp}) \\ &= \frac{1}{\pi} \left(\arccos \frac{u_1 - v_{\parallel} \cos \phi}{v_{\perp} \sin \phi} - \arccos \frac{u_2 - v_{\parallel} \cos \phi}{v_{\perp} \sin \phi} \right). \end{aligned} \quad (19)$$

Equation (19) is singular for $v_{\perp} = 0$ or $\phi = 0$. If $\phi = 0$, the projected velocity is just the parallel velocity as equation (14) reduces to $u = v_{\parallel}$. Then the probability function becomes

$$\text{prob}(u_1 < u < u_2 | \phi = 0, v_{\parallel}, v_{\perp}) = \begin{cases} 1 & \text{for } u_1 < v_{\parallel} < u_2 \\ 0 & \text{otherwise} \end{cases} \quad (20)$$

which is identical to equation (19) in the limit $\phi \rightarrow 0$. For $v_{\perp} = 0$, i.e. on the v_{\parallel} -axis corresponding to ions not actually gyrating, equation (14) reduces to $u = v_{\parallel} \cos \phi$, and the probability function becomes

$$\begin{aligned} & \text{prob}(u_1 < u < u_2 | \phi, v_{\parallel}, v_{\perp} = 0) \\ &= \begin{cases} 1 & \text{for } u_1 / \cos \phi < v_{\parallel} < u_2 / \cos \phi \\ 0 & \text{otherwise.} \end{cases} \end{aligned} \quad (21)$$

Lastly, we note that the argument of the arccos function is often outside the range $[-1; 1]$. In this case the arccos is complex, and we take the real part to obtain physically meaningful quantities. Equation (19) is a weight function describing just the projection onto the line-of-sight. We have previously derived the corresponding probability density function $\text{pdf}(u | \phi, v_{\parallel}, v_{\perp})$ to describe the velocity-space sensitivity of collective Thomson scattering (CTS) measurements [12]. The pdf can be found from the probability function by letting $u_1, u_2 \rightarrow u$:

$$\begin{aligned} \text{pdf}(u | \phi, v_{\parallel}, v_{\perp}) &= \lim_{u_1, u_2 \rightarrow u} \frac{\text{prob}(u_1 < u < u_2 | \phi, v_{\parallel}, v_{\perp})}{u_2 - u_1} \\ &= \frac{1}{\pi v_{\perp} \sin \phi \sqrt{1 - \left(\frac{u - v_{\parallel} \cos \phi}{v_{\perp} \sin \phi} \right)^2}}. \end{aligned} \quad (22)$$

Equations (19) to (22) have been used to interpret CTS measurements at TEXTOR [36] and should have great utility

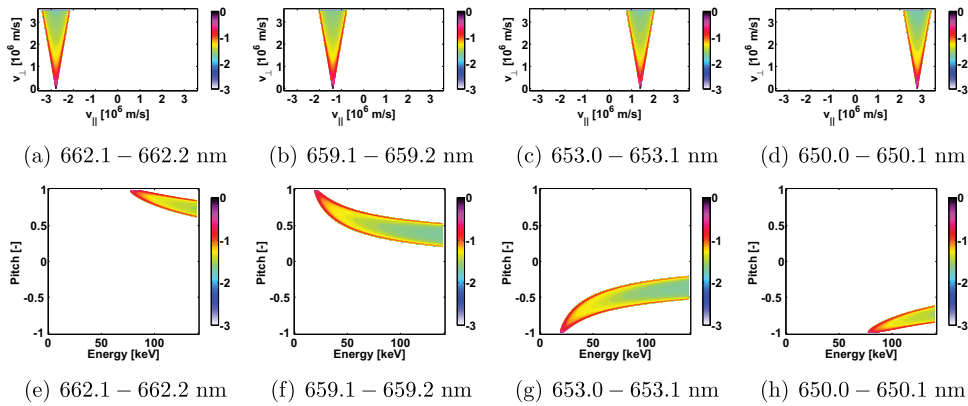


Figure 3. Probability functions after ((a)–(d)) equation (24) and ((e)–(h)) equation (68) for various Doppler shifts and a narrow wavelength range $\lambda_2 - \lambda_1 = 0.1$ nm. The projection angle is $\phi = 10^\circ$. The colorbar shows the base ten logarithm of the probability function $\log_{10}(\text{prob}(\lambda_1 < \lambda < \lambda_2 | \phi, v_{\parallel}, v_{\perp}))$.

for CTS measurements at ASDEX Upgrade [37–39], LHD [40, 41] or ITER [42–44].

To obtain the probability function in λ -space, we first find the integration limits by substituting u in equation (15) using equation (11):

$$\gamma = \arccos \frac{c \left(\frac{\lambda}{\lambda_0} - 1 \right) - v_{\parallel} \cos \phi}{v_{\perp} \sin \phi}. \quad (23)$$

Hence the probability function in λ -space becomes

$$\begin{aligned} \text{prob}(\lambda_1 < \lambda < \lambda_2 | \phi, v_{\parallel}, v_{\perp}) &= \frac{\gamma_1 - \gamma_2}{\pi} \\ &= \frac{1}{\pi} \left(\arccos \frac{c \left(\frac{\lambda_1}{\lambda_0} - 1 \right) - v_{\parallel} \cos \phi}{v_{\perp} \sin \phi} \right. \\ &\quad \left. - \arccos \frac{c \left(\frac{\lambda_2}{\lambda_0} - 1 \right) - v_{\parallel} \cos \phi}{v_{\perp} \sin \phi} \right). \end{aligned} \quad (24)$$

This is a simple approximation to the probability part of FIDA weight functions neglecting Stark splitting and non-uniformity in pdf_{D_n} due to charge-exchange and electron transition probabilities.

Figures 3((a)–(d)) show $\text{prob}(\lambda_1 < \lambda < \lambda_2 | \phi, v_{\parallel}, v_{\perp})$ for a narrow wavelength range of 0.1 nm at various Doppler shifts. Figures 3((e)–(h)) show the corresponding probabilities $\text{prob}(\lambda_1 < \lambda < \lambda_2 | \phi, E, p)$. The observable regions or interrogation regions are colored whereas the unobservable regions are white. The viewing angle is $\phi = 10^\circ$. The wavelength interval width $\lambda_2 - \lambda_1 = 0.1$ nm is comparable to the achievable spectral resolution of FIDA measurements at ASDEX Upgrade and is typical for tomographic measurements of 2D fast-ion velocity distribution functions [33]. The shape of the probability functions is triangular and symmetric in $(v_{\parallel}, v_{\perp})$ -coordinates, but the very tip of the triangle is cut off by the v_{\parallel} -axis as we will show more clearly in figure 5. The opening angle of the triangles is $2\phi = 20^\circ$ as the two sides have inclination angles of $\pm\phi$ with respect to the v_{\perp} -axis [12]. The location of the interrogation region changes substantially with the magnitude of the Doppler

shift. In figures 3((e)–(h)) we show the same probability functions in (E, p) -coordinates since FIDA weight functions are traditionally given in these coordinates. The probability functions have more complicated shapes in (E, p) -coordinates. In figure 4 we vary the viewing angle ϕ . The larger the viewing angle, the larger the opening angle (2ϕ) of the triangular regions in $(v_{\parallel}, v_{\perp})$ -space, and the lower the probabilities that a detected photon has a wavelength in the particular wavelength range. These probabilities decrease for increasing projection angle ϕ since the spectrum of projected velocities of the ion and therefore wavelengths of the photons broaden according to equation (11) while the integral over the spectrum is the same. Figure 5 shows probability functions for broader wavelength ranges up to $\lambda_2 - \lambda_1 = 1$ nm typical for the traditional use of weight functions as sensitivity or signal origin indicators. The inclinations of the sides of the triangle are not affected by the larger wavelength range, but a larger tip of the triangle is now cut off by the v_{\parallel} -axis as figure 5(d) shows most clearly. The larger the wavelength range, the larger the probabilities become since larger fractions of the ion orbits can produce Doppler shifts within the wavelength limits. In the limit of wavelength ranges covering very large red- and blue-shifts, the probability function becomes unity. Figures 3–5 show that patterns in the velocity-space sensitivity of FIDA measurements are easier to spot in $(v_{\parallel}, v_{\perp})$ -space where FIDA weight functions always have triangular shapes.

Equations (14), (15) and (16) transform the problem of finding a probability in λ -space into the simpler problem of finding a probability in γ -space. We will use this transformation when we account for Stark splitting and non-uniform charge-exchange and electron transition probabilities in the next two sections.

4. Stark splitting

An electron Balmer alpha transition from the $n = 3$ to $n = 2$ state of a moving D-atom in the magnetic field of a tokamak leads to light emission at 15 distinct wavelengths

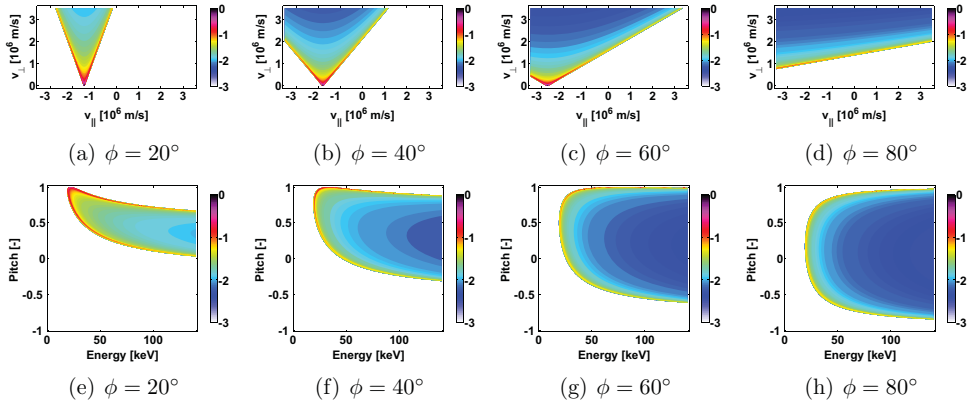


Figure 4. Probability functions after ((a)–(d)) equation (24) and ((e)–(h)) equation (68) for various projection angles ϕ and a narrow wavelength range $\lambda_2 - \lambda_1 = 659.1 - 659.0 \text{ nm} = 0.1 \text{ nm}$. The colorbar shows the base ten logarithm of the probability function $\log_{10}(\text{prob}(\lambda_1 < \lambda < \lambda_2 | \phi, v_{\parallel}, v_{\perp}))$.

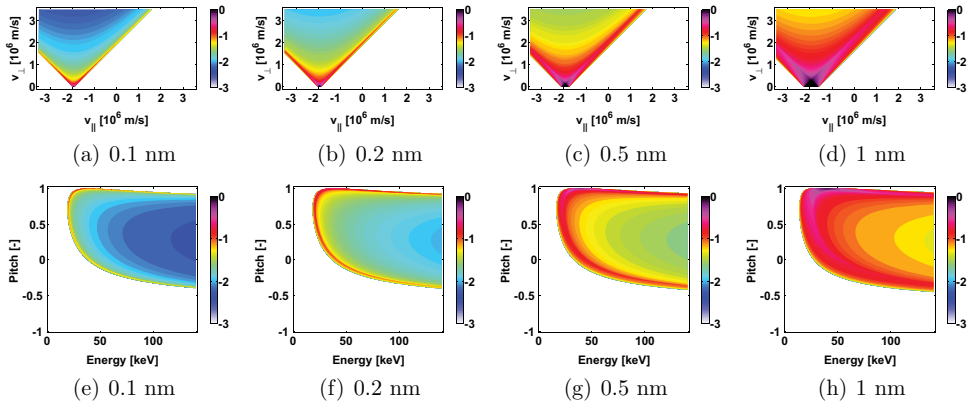


Figure 5. Probability functions after ((a)–(d)) equation (24) and ((e)–(h)) equation (68) for various wavelength ranges $\lambda_2 - \lambda_1$. The wavelength ranges are centered at 659.1 nm . The projection angle is $\phi = 45^\circ$. The colorbar shows the base ten logarithm of the probability function $\log_{10}(\text{prob}(\lambda_1 < \lambda < \lambda_2 | \phi, v_{\parallel}, v_{\perp}))$.

λ_l . This is referred to as Stark splitting since the splitting occurs due to the electric field in the reference frame of the moving D-atom. Zeeman splitting is negligible in the analysis of FIDA measurements as it is much weaker than Stark splitting [34]. In this section we treat Stark splitting of the D_α -line. For this we find the integration limits for the 15 lines, find their probabilities and then sum over all possibilities. The magnitude of the Stark splitting wavelength shift is proportional to the magnitude of the electric field \tilde{E} in the reference frame of the neutral:

$$\lambda_l = \lambda_0 + s_l \tilde{E} \quad (25)$$

where l is a number from 1 to 15 corresponding to the 15 lines and the constants s_l are [45, 46]

$$s_{l=1,\dots,15} = \left(-220.2, -165.2, -137.7, -110.2, -82.64, -55.1, -27.56, 0, 27.57, 55.15, 82.74, 110.3, 138.0, 165.6, 220.9 \right) \times 10^{-18} \frac{\text{m}^2}{\text{V}}. \quad (26)$$

Lines 1, 4–6, 10–12 and 15 are so-called π -lines, and lines 2, 3, 7–9, 13 and 14 are so-called σ -lines. Line 8 is the unshifted wavelength with $s_8 = 0$. The electric field \tilde{E} in the reference frame of the neutral is

$$\tilde{E} = \hat{E} + v \times B. \quad (27)$$

where \hat{E} is the electric field in the lab frame. In components this is

$$\begin{aligned} \begin{pmatrix} \tilde{E}_{\perp 1} \\ \tilde{E}_{\perp 2} \\ \tilde{E}_{\parallel} \end{pmatrix} &= \begin{pmatrix} \hat{E}_{\perp 1} \\ \hat{E}_{\perp 2} \\ \hat{E}_{\parallel} \end{pmatrix} + \begin{pmatrix} v_{\perp} \cos \gamma \\ v_{\perp} \sin \gamma \\ v_{\parallel} \end{pmatrix} \times \begin{pmatrix} 0 \\ 0 \\ B \end{pmatrix} \\ &= \begin{pmatrix} \hat{E}_{\perp 1} + B v_{\perp} \sin \gamma \\ \hat{E}_{\perp 2} - B v_{\perp} \cos \gamma \\ \hat{E}_{\parallel} \end{pmatrix}. \end{aligned} \quad (28)$$

The magnitude of the electric field in the frame of the neutral is

$$\tilde{E} = \sqrt{\hat{E}^2 + v_{\perp}^2 B^2 + 2v_{\perp} B (\hat{E}_{\perp 1} \sin \gamma - \hat{E}_{\perp 2} \cos \gamma)}. \quad (29)$$

Suppose we make a FIDA measurement at a particular wavelength λ . The photon could have been emitted from any of the 15 lines with wavelength λ_l that is then Doppler shifted. Each of the 15 lines has a particular Stark wavelength shift corresponding to a particular Doppler shift with projected velocity u_l to be observable at λ . The 15 Doppler shift conditions are

$$\lambda = \lambda_l \left(1 + \frac{u_l}{c} \right) \quad (30)$$

which in combination with equation (25) yields

$$\lambda = \left(\lambda_0 + s_l \tilde{E} \right) \left(1 + \frac{u_l}{c} \right). \quad (31)$$

The projected velocity u_l and the electric field in the frame of the particle \tilde{E} depend on the gyroangle. Substitution of \tilde{E} using equation (29) and of u_l using equation (14) shows the relation between λ , ϕ , v_\perp , v_\parallel , γ_l and s_l :

$$\lambda = \left(\lambda_0 + s_l \sqrt{\tilde{E}^2 + v_\perp^2 B^2 + 2v_\perp B (\hat{E}_{\perp 1} \sin \gamma_l - \hat{E}_{\perp 2} \cos \gamma_l)} \right) \times \left(1 + \frac{1}{c} (v_\parallel \cos \phi + v_\perp \sin \phi \cos \gamma_l) \right). \quad (32)$$

This relation describes not only the Doppler effect but also Stark splitting, the two effects changing the wavelength of a detectable photon. It can be used to transform integration limits in λ to γ -space where the integration is easier to do. Here we include Stark splitting neglecting any electric field in the laboratory frame of reference. This reveals the most important effects and is often a good approximation in a tokamak as $|\hat{E}| \ll |v \times B|$, in particular for fast ions with large v_\perp . In FIDASIM simulations this approximation is usually made. If there is no electric field in the laboratory reference frame, the electric field in the reference frame of the particle is

$$\tilde{E} = v_\perp B \quad (33)$$

and the Stark shift is just proportional to v_\perp :

$$\lambda_l = \lambda_0 + s_l v_\perp B. \quad (34)$$

The functional dependence between λ and γ in equation (32) simplifies, and λ becomes a cosine function of γ as in the relation between u and γ in equation (14). Equation (32) becomes

$$\lambda = (\lambda_0 + s_l v_\perp B) \left(1 + \frac{1}{c} (v_\parallel \cos \phi + v_\perp \sin \phi \cos \gamma_l) \right). \quad (35)$$

Equation (35) implies an equation for the exact shape of FIDA weight functions neglecting the electric field in the lab frame but accounting for Stark splitting as we will show in section 7. The inverse function is

$$\gamma_l = \arccos \frac{c \left(\frac{\lambda}{\lambda_0 + s_l v_\perp B} - 1 \right) - v_\parallel \cos \phi}{v_\perp \sin \phi} \quad (36)$$

which gives a solution for $0 < \gamma < \pi$. A second solution is given by equation (16). These are integration limits in γ_l for each of the 15 lines. The relative intensities $I_l(\gamma)$ of π -lines

and σ -lines depend on the gyroangle γ and can be written as [14]

$$\sigma : I_l(\gamma) = C_l (1 + \cos^2(\hat{u}, \hat{v} \times \hat{B})) = C_l (1 + \sin^2 \phi \sin^2 \gamma) \quad (37)$$

$$\pi : I_l(\gamma) = C_l (1 - \cos^2(\hat{u}, \hat{v} \times \hat{B})) = C_l (1 - \sin^2 \phi \sin^2 \gamma) \quad (38)$$

where \hat{u} , \hat{v} and \hat{B} are unit vectors and the constants C_l are [14, 45, 47]

$$C_{l=1, \dots, 15} = \left(1, 18, 16, 1681, 2304, 729, 1936, 5490, 1936, 729, 2304, 1681, 16, 18, 1 \right). \quad (39)$$

The expression of the projection of $\hat{v} \times \hat{B}$ onto the line-of-sight vector \hat{u} in terms of the gyroangle γ is illustrated in figure 2. The probabilities $\text{prob}(l|\gamma)$ that a detected photon comes from line l given the gyroangle γ can be calculated from the relative intensities:

$$\text{prob}(l|\gamma) = \frac{I_l(\gamma)}{\sum I_l(\gamma)}. \quad (40)$$

Since $\sum I_l(\gamma) = 18860$ is a constant independent of γ , we can write the probabilities of line l as

$$\text{prob}(l|\gamma) = \hat{C}_l (1 \pm \sin^2 \phi \sin^2 \gamma) \quad (41)$$

where the plus is used for the σ -lines and minus for the π -lines and

$$\hat{C}_l = \frac{C_l}{\sum_{n=1}^{15} C_l}. \quad (42)$$

The probability part of full FIDA weight functions accounting for Doppler and Stark effects for arbitrary pdf_{D_α} can now be calculated according to

$$\begin{aligned} & \text{prob}(\lambda_1 < \lambda < \lambda_2 | \phi, v_\parallel, v_\perp) \\ &= \sum_{l=1}^{15} \left(\int_{\gamma_{2,l}}^{\gamma_{1,l}} \text{prob}(l|\gamma) \text{pdf}_{D_\alpha}(\gamma | v_\parallel, v_\perp) d\gamma \right. \\ & \quad \left. + \int_{\gamma'_{1,l}}^{\gamma'_{2,l}} \text{prob}(l|\gamma) \text{pdf}_{D_\alpha}(\gamma | v_\parallel, v_\perp) d\gamma \right). \end{aligned} \quad (43)$$

We will discuss the nature of the pdf_{D_α} in FIDA measurements in the following section. Here we study basic effects by assuming a uniform $\text{pdf}_{D_\alpha} = 1/(2\pi)$ for which we can solve the integrals in equation (43) analytically:

$$\begin{aligned} & \text{prob}(\lambda_1 < \lambda < \lambda_2 | \phi, v_\parallel, v_\perp) \\ &= \sum_{l=1}^{15} \frac{1}{2\pi} \left(\int_{\gamma_{2,l}}^{\gamma_{1,l}} \hat{C}_l (1 \pm \sin^2 \phi \sin^2 \gamma) d\gamma \right. \\ & \quad \left. + \int_{\gamma'_{1,l}}^{\gamma'_{2,l}} \hat{C}_l (1 \pm \sin^2 \phi \sin^2 \gamma) d\gamma \right) \\ &= \sum_{l=1}^{15} \hat{C}_l \left(\frac{\gamma_{1,l} - \gamma_{2,l}}{\pi} \pm \frac{\sin^2 \phi}{2} \right. \\ & \quad \left. \times \left(\frac{\gamma_{1,l} - \gamma_{2,l}}{\pi} - \frac{\sin(2\gamma_{1,l}) - \sin(2\gamma_{2,l})}{2\pi} \right) \right). \end{aligned} \quad (44)$$

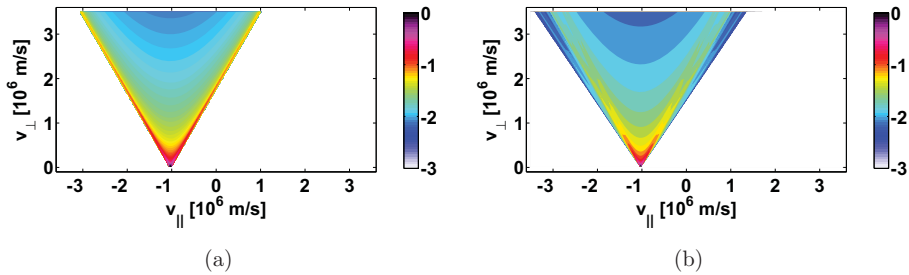


Figure 6. The probability functions $\text{prob}(\lambda_1 < \lambda < \lambda_2 | \phi, v_{\parallel}, v_{\perp})$ for $\text{pdf}_{D_{\alpha}} = 1/(2\pi)$: (a) without Stark splitting (equation (24)), (b) with Stark splitting (equation (44)). The wavelength range is $\lambda_2 - \lambda_1 = 0.1$ nm. The magnetic field is 1.74 T. The projection angle is $\phi = 30^\circ$. The colorbar shows the base ten logarithm of the probability part of the weight function $\log_{10}(\text{prob}(\lambda_1 < \lambda < \lambda_2 | \phi, v_{\parallel}, v_{\perp}))$.

We leave the probability function in this form as substitution of the gyroangles using equation (36) provides no new insights. The probability function is calculated as a weighted sum over the 15 Stark splitting lines. The first fraction accounts for 15 different probability functions for the uniform distribution where the integration limits change for each Stark splitting line. The second term is a small correction due to the changing relative intensities of the 15 Stark splitting lines over the gyroangle. The corrections due to σ -lines and π -lines have different signs and hence partly cancel. For $\phi = 0$ this correction disappears.

Figure 6 demonstrates the effects of Stark splitting for a uniform $\text{pdf}_{D_{\alpha}}$ and a magnetic field of 1.74 T. The observation angle is $\phi = 30^\circ$ and the wavelength range is 658.0–658.1 nm in both figures. Stark splitting widens the interrogation region and changes the probabilities. The effect of the 15 Stark splitting lines shows most clearly close to the boundary of the observable region where several local maxima in the probability are formed. Since Stark splitting can be calculated accurately, it actually does not limit the spectral resolution of FIDA measurements as was sometimes asserted [3, 15, 16, 24, 48, 49] but rather just changes the velocity-space sensitivities.

5. Charge-exchange reaction and D_{α} -emission

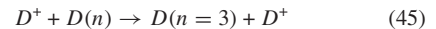
The probability density $\text{pdf}_{D_{\alpha}}(\gamma | v_{\parallel}, v_{\perp})$ is in fact not uniform as we assumed until now but is a complicated function depending on the charge-exchange probabilities and the electron transition probabilities and hence ultimately on the particular NBI as well as on the ion and electron temperatures and drift velocities. We hence find $\text{pdf}_{D_{\alpha}}(\gamma | v_{\parallel}, v_{\perp})$ and the FIDA intensity per unit ion density $R(v_{\parallel}, v_{\perp})$ irrespective of the detected wavelength by numeric computation using FIDASIM. Here we discuss the nature of these contributions.

The probability of a charge-exchange reaction between an ion and a neutral depends on their relative velocity as well as on the particular charge-exchange reaction. For an ion with given $(v_{\parallel}, v_{\perp})$, the probability density of a charge-exchange reaction $\text{pdf}_{\text{CX}}(\gamma | v_{\parallel}, v_{\perp})$ therefore depends on the gyroangle γ . Since FIDA light comes from a fast neutral that has been created from a fast ion in a charge-exchange reaction, FIDA does not sample the gyroangles of the ions uniformly, but favors

those gyroangles for which the ion velocity vectors are similar to those of the neutrals. The charge-exchange probability density depends on the distribution of injected neutrals and halo neutrals and therefore on the particular NBI heating geometry.

The gyroangle probability densities that an ion at a particular gyroangle ultimately leads to a detection of a D_{α} -photon are further influenced by the electron transition probability densities $\text{pdf}_{m \rightarrow n}(\gamma | v_{\parallel}, v_{\perp})$ from energy level m to n . The $n = 3$ state can be populated and depopulated from any other energy state whereas only the $n = 3 \rightarrow 2$ leads to D_{α} -emission. These electron transition probabilities also depend on the velocity due to collisions. The probability density $\text{pdf}_{D_{\alpha}}(\gamma | v_{\parallel}, v_{\perp})$ is hence found numerically using FIDASIM.

Before we proceed to such a full numeric computation of the relevant charge-exchange reactions and electron transitions, we study essential features using a simplified model. We consider the charge-exchange reaction



where the donor neutral $D(n)$ is in the n th excited state and the product neutral $D(n=3)$ is in the $n=3$ state and so can directly emit a D_{α} -photon. We emphasize that the $n=3$ state can also be populated via any electron transition. However, in our simplified model we neglect electron transitions and consider only the direct population of the $n=3$ state via the charge-exchange reaction. The charge-exchange reaction cross sections σ and the reactivities σv_{rel} strongly depend on the relative velocity v_{rel} which is usually expressed as the relative energy

$$E_{\text{rel}} = \frac{1}{2} m_D v_{\text{rel}}^2. \quad (46)$$

Figure 7 illustrates the cross sections σ_m and the reactivities $\sigma_m v_{\text{rel}}$ for charge-exchange reactions with a donor neutral in state m directly resulting in an excited $n=3$ neutral [14, 50–52]. In these reactions the donor neutral was in one of the first six excited states. The reactivities strongly depend on the relative velocities which in turn depend on the gyroangle. For simplicity, we treat a single source of injected neutrals neglecting that in reality there are sources at full, half and third injection energy. In the coordinate system from figure 2 the velocity of the beam neutrals is

$$v_b = v_{b,\parallel} \hat{B} + v_{b,\perp 1} \hat{v}_{\perp 1} + v_{b,\perp 2} \hat{v}_{\perp 2} \quad (47)$$

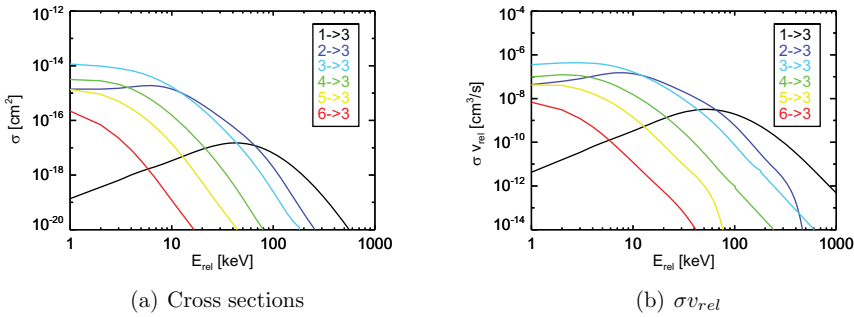


Figure 7. Cross sections and reactivities σv_{rel} of the charge-exchange reactions of ions with donor neutrals in the first six excited states directly resulting in an excited neutral in the $n = 3$ state.

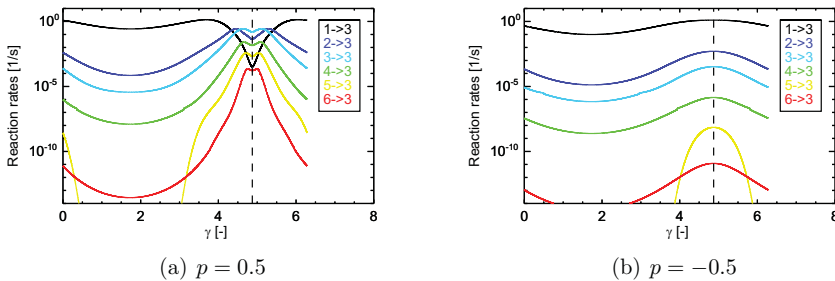


Figure 8. Reaction rates $\sigma_m v_{rel} n_{neut,m}$ as function of the gyroangle γ for an energy of $E = 60$ keV and pitches of $p = \pm 0.5$. The donor neutral population is here from the full injection energy peak of NBI Q3 while we neglect donor neutrals from half or third injection energies. Here we show rates for reactions with these beam neutrals in the first six excited states directly resulting in an excited neutral in the $n = 3$ state.

and the fast-ion velocity is given by equation (12). The relative velocity is then

$$v_{rel} = \sqrt{(v_{b,\parallel} - v_{\parallel})^2 + (v_{b,\perp 1} - v_{\perp} \cos \gamma)^2 + (v_{b,\perp 2} - v_{\perp} \sin \gamma)^2}. \quad (48)$$

To find extremal values in v_{rel} , we set

$$\frac{dv_{rel}}{d\gamma} = 0 \quad (49)$$

and find that the gyroangle γ is then given by

$$\tan \gamma = \frac{v_{b,\perp 2}}{v_{b,\perp 1}}. \quad (50)$$

If the reactivity $\sigma_m v_{rel}$ were monotonic in the range of interest, the extrema of $\sigma_m v_{rel}$ would correspond to the extrema of v_{rel} . However, figure 7 shows that the reactivities in particular of the charge-exchange reactions $1 \rightarrow 3$ and $2 \rightarrow 3$ are not monotonic but have maxima in the energy range of interest. Since the density of neutrals $n_{neut,m=1}$ in the first energy state is by far largest, this charge-exchange reaction often dominates. The reaction rates per ion are given by

$$r_m = \sigma_m v_{rel} n_{neut,m}. \quad (51)$$

In figure 8 we show these reaction rates for the six charge-exchange reactions for an energy of $E = 60$ keV and pitches

of $p = \pm 0.5$. The reaction rates strongly depend on the gyroangle and have local maxima and minima. The dashed line shows the minima of the relative velocities given by equation (50) which coincides well with the local minima or maxima in the corresponding reaction rates. An extreme case is illustrated in figure 8(a) where the relative velocity goes to zero for a particular gyroangle. Figure 8(b) illustrates the reaction rates for velocity space coordinates far away from the donor neutral velocities.

Up to now we have not considered electron transition processes. In the following we calculate the full $\text{pdf}_{D\alpha}$ with FIDASIM where we model the important charge-exchange reactions and electron transitions as well as the beam geometry and energy distribution. Figure 9 shows such numerically calculated $\text{pdf}_{D\alpha}$ for a few energies and pitches. They often coarsely resemble phase-shifted cosine curves if one disregards local minima and maxima and Monte-Carlo noise. To study the effects of the non-uniform gyroangle distributions by simple models, we assume a model pdf to take the form

$$\text{pdf}_{D\alpha}(\gamma | v_{\parallel}, v_{\perp}) = 1/2\pi + a \cos(\gamma + \bar{\gamma}) \quad (52)$$

where $a < 1/2\pi$ is an amplitude and $\bar{\gamma}$ is a phase shift. The integrals in equation (17) can be solved assuming $\text{pdf}_{D\alpha}$ from

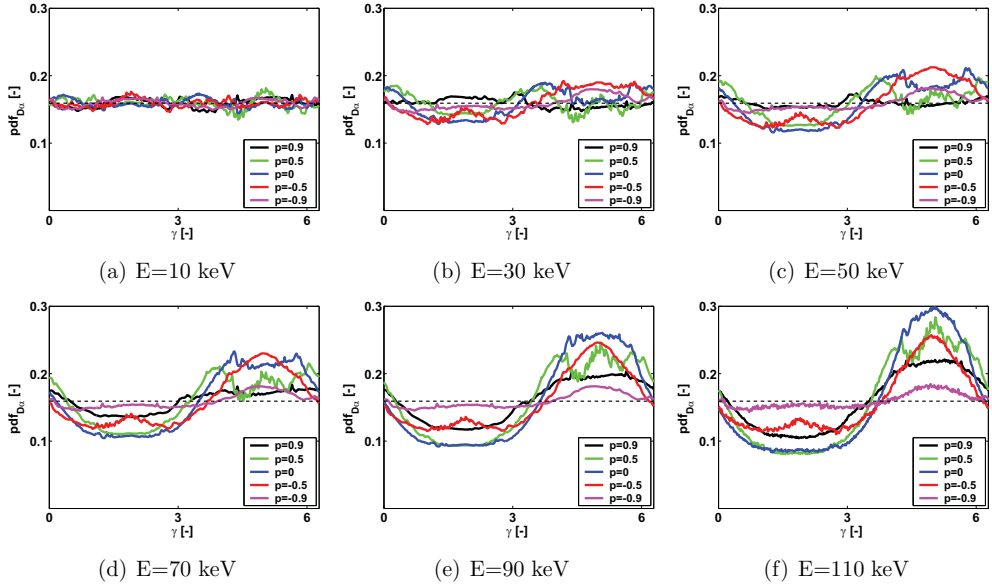


Figure 9. Probability density functions pdf_{D_n} at various positions in (E, p) -space (energy, pitch). The functions have been computed with FIDASIM. The NBI Q3 has an injection energy of 60 keV and an injection angle of about 120° . The thin dashed line is the uniform distribution assumed up to now.

equation (52):

$$\begin{aligned} \text{prob}(\lambda_1 < \lambda < \lambda_2 | \phi, v_{\parallel}, v_{\perp}) &= \int_{\gamma_2}^{\gamma_1} 1/2\pi + a \cos(\gamma + \bar{\gamma}) d\gamma \\ &+ \int_{\gamma'_1}^{\gamma'_2} 1/2\pi + a \cos(\gamma + \bar{\gamma}) d\gamma \\ &= \frac{\gamma_1 - \gamma_2}{\pi} + 2a \cos \bar{\gamma} (\sin \gamma_1 - \sin \gamma_2). \end{aligned} \quad (53)$$

Again we leave the probability function in this form and do not substitute the gyroangles. The first term in equation (53) also appears for the uniform pdf whereas the second term accounts for cosine shape. It is proportional to the amplitude a and to the cosine of the phase shift $\cos \bar{\gamma}$. We can also integrate our model pdf accounting for Stark splitting. Equation (43) becomes

$$\begin{aligned} \text{prob}(\lambda_1 < \lambda < \lambda_2 | \phi, v_{\parallel}, v_{\perp}) &= \sum_{l=1}^{15} \left(\int_{\gamma_{2,l}}^{\gamma_{1,l}} \hat{C}_l (1 \pm \sin^2 \phi \sin^2 \gamma) \right. \\ &\times \left(\frac{1}{2\pi} + a \cos(\gamma + \bar{\gamma}) \right) d\gamma \\ &+ \left. \int_{\gamma'_{1,l}}^{\gamma'_{2,l}} \hat{C}_l (1 \pm \sin^2 \phi \sin^2 \gamma) \left(\frac{1}{2\pi} + a \cos(\gamma + \bar{\gamma}) \right) d\gamma \right) \\ &= \sum_{l=1}^{15} \hat{C}_l \left(\frac{\gamma_{1,l} - \gamma_{2,l}}{\pi} \pm \frac{\sin^2 \phi}{2} \right. \\ &\times \left. \left(\frac{\gamma_{1,l} - \gamma_{2,l}}{\pi} - \frac{\sin(2\gamma_{1,l}) - \sin(2\gamma_{2,l})}{2\pi} \right) \right) \end{aligned}$$

$$\begin{aligned} &+ 2a \cos \bar{\gamma} \left(\sin \gamma_{1,l} - \sin \gamma_{2,l} \pm \frac{\sin^2 \phi}{3} \right. \\ &\times \left. \left(\sin^3 \gamma_{1,l} - \sin^3 \gamma_{2,l} \right) \right). \end{aligned} \quad (54)$$

Equation (54) contains all terms of equation (44) as well as the term accounting for the cosine shape from equation (53). Additionally, another correction term arises accounting for changing intensities of the Stark splitting lines and varying amplitude due to the cosine function. This term has again different signs for σ -lines and π -lines and disappears for $\phi = 0$.

As already mentioned, the phase shift $\bar{\gamma}$ in equation (52) can be found approximately from geometric considerations. Further, we construct a model for the amplitude so that it increases with energy and decreases with the magnitude of the pitch as motivated by figure 9 where these trends appear:

$$a = \frac{E}{E_0} (1 - p^2) = \frac{v_{\perp}^2}{v_{\perp 0}^2}. \quad (55)$$

This model for the amplitude has E_0 as the only free parameter. It has units of energy to non-dimensionalize the energy coordinate. The amplitude a of the cosine function in equation (52) is inversely proportional to E_0 . For $E_0 = 1$ MeV the amplitudes of the probability density functions roughly correspond to the FIDASIM calculation over the relevant energy range up to 90 keV as we show in figure 10. Figure 11 shows that the typical large-scale cosine-like shape of pdf_{D_n} leads to lopsided probabilities. In this particular case ions close to the right side of the triangular weight functions have higher

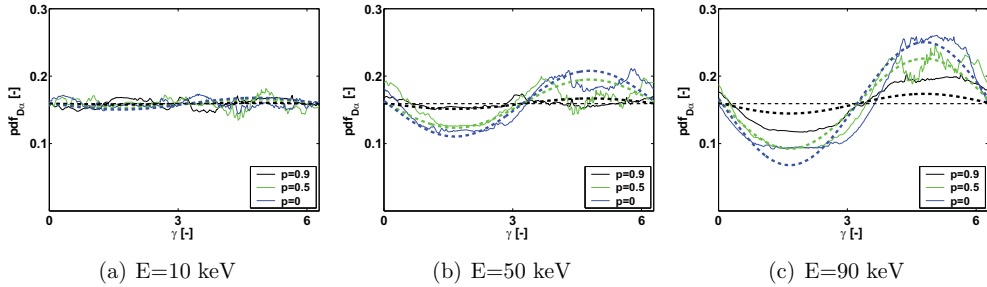


Figure 10. Comparison of pdf_{D_α} as computed with FIDASIM with the cosine model pdf_{D_α} (equation (52)) at various positions in velocity space. The thick dashed lines are the model cosine, and the thin dashed line is the uniform distribution.

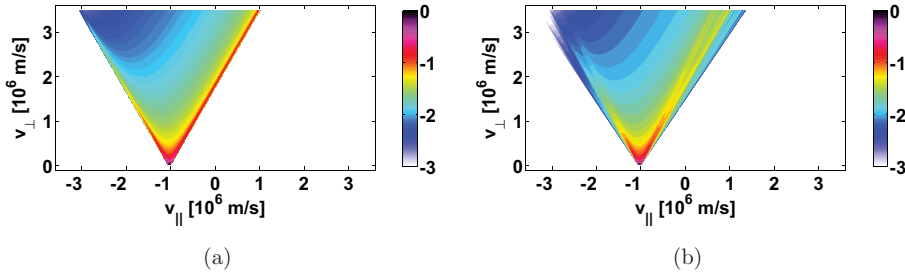


Figure 11. The probability functions $\text{prob}(\lambda_1 < \lambda < \lambda_2 | \phi, v_{\parallel}, v_{\perp})$ for pdf_{D_α} given by equation (52): (a) without Stark splitting (equation (53)), (b) with Stark splitting (equation (54)). The wavelength range is $\lambda_2 - \lambda_1 = 0.1$ nm. The magnetic field is 1.74 T. The projection angle is $\phi = 30^\circ$. The colorbar shows the base ten logarithm of the probability part of the weight function $\log_{10}(\text{prob}(\lambda_1 < \lambda < \lambda_2 | \phi, v_{\parallel}, v_{\perp}))$.

probabilities to emit light in the particular wavelength range than those close to the left side of the triangle. The phase angle $\bar{\gamma}$ determines how lopsided the probability function becomes. In figure 11(a) we show one of the extreme cases as $\cos(\bar{\gamma}) = 1$. For $\cos(\bar{\gamma}) = 0$ the probability function is symmetric and the same as that for the uniform distribution. Figure 11(b) shows the probability function for the model pdf_{D_α} given by equation (52) and accounting for Stark splitting. The effect of Stark splitting is similar to that observed for the uniform pdf_{D_α} . Lastly, we note that any arbitrary pdf_{D_α} can be expanded into a Fourier series and then analytical, smooth FIDA weight functions could be constructed from the Fourier components which each can be integrated as in equation (54).

6. Full FIDA weight functions

Substitution of equation (43) into equation (6) gives an analytic expression for full FIDA weight functions accounting for Doppler and Stark effects and allowing for arbitrary pdf_{D_α} :

$$w(\lambda_1, \lambda_2, \phi, v_{\parallel}, v_{\perp}) = R(v_{\parallel}, v_{\perp}) \times \sum_{l=1}^{15} \left(\int_{\gamma_{2,l}}^{\gamma_{1,l}} \text{prob}(l|\gamma) \text{pdf}_{D_\alpha}(\gamma | v_{\parallel}, v_{\perp}) d\gamma + \int_{\gamma'_{1,l}}^{\gamma'_{2,l}} \text{prob}(l|\gamma) \text{pdf}_{D_\alpha}(\gamma | v_{\parallel}, v_{\perp}) d\gamma \right). \quad (56)$$

Equation (56) is general whereas the assumptions of the FIDASIM code are used to calculate R and pdf_{D_α} [14, 34]. In

particular, the calculation of the weight functions assumes that the FIDA emission comes from a small volume in configuration space. Practically, R and pdf_{D_α} are calculated from the distribution function $f_{D_\alpha}(\gamma | v_{\parallel}, v_{\perp})$ of the FIDA intensity per unit ion density over γ which we calculate numerically using FIDASIM. Then

$$R(v_{\parallel}, v_{\perp}) = \int_0^{2\pi} f_{D_\alpha}(\gamma | v_{\parallel}, v_{\perp}) d\gamma, \quad (57)$$

$$\text{pdf}_{D_\alpha}(\gamma | v_{\parallel}, v_{\perp}) = \frac{f_{D_\alpha}(\gamma | v_{\parallel}, v_{\perp})}{R(v_{\parallel}, v_{\perp})}. \quad (58)$$

We prefer not to substitute equation (58) into equation (56) to emphasize that R is a factor common to any weight function with any wavelength range. We compare full FIDA weight functions as computed with our formalism with the traditional weight function as computed with FIDASIM in figure 12. The two approaches give the same result within small and controllable discretization errors and Monte Carlo noise from the sampling of the neutral beam particles in FIDASIM below 5%. This shows that our new formalism is consistent with the traditional FIDASIM computation as expected since the physics assumptions are the same. However, our approach provides additional insight into functional dependencies not revealed by the traditional brute-force computation. It also leads to faster computations if weight functions in several wavelength ranges are to be computed since the time-consuming collisional–radiative model only has to be evaluated once to find R and pdf_{D_α} , and weight functions

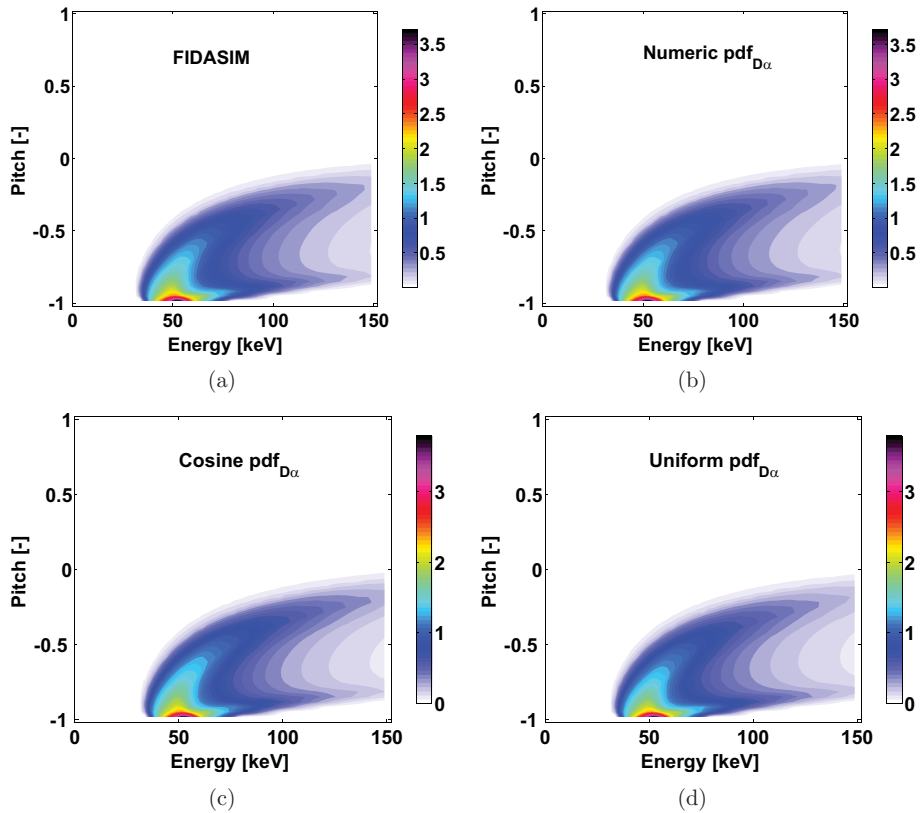


Figure 12. Full FIDA weight functions as computed with (a) traditional FIDASIM, (b) equation (56) for numerically computed $\text{pdf}_{D_{\alpha}}$ using FIDASIM, (c) equation (56) for the cosine model $\text{pdf}_{D_{\alpha}}$, (d) equation (56) for the uniform model $\text{pdf}_{D_{\alpha}}$. The projection angle is $\phi = 155^\circ$. The wavelength range is 660–661 nm. The magnetic field is 1.74 T.

for any wavelength range can then be computed rapidly using equation (56). Additionally, we compare these full FIDA weight functions based on numerically computed $\text{pdf}_{D_{\alpha}}$ using FIDASIM with full weight functions given by the uniform $\text{pdf}_{D_{\alpha}}$ and the cosine $\text{pdf}_{D_{\alpha}}$ which match the full computation to within 20%.

7. Boundaries of FIDA weight functions

Often it is useful to know the velocity-space interrogation regions of FIDA measurements. Until now these observable regions in velocity space had to be found by numerical simulations with the FIDASIM code. Here we show that these velocity-space interrogation regions are in fact completely determined by a simple analytic expression accounting for the Doppler shift and Stark splitting. The boundaries of FIDA weight functions are found by solving equation (35) for v_{\parallel} and setting $\cos \gamma = \pm 1$ and $l = 1$ or $l = 15$ which gives the largest possible Doppler shift and Stark splitting wavelength shift, respectively. The boundaries for arbitrary l are

$$v_{\parallel} = \pm v_{\perp} \tan \phi + \frac{c}{\cos \phi} \left(\frac{\lambda}{\lambda_0 + s_{\perp} v_{\perp} B} - 1 \right). \quad (59)$$

This is a hyperbolic equation. Nevertheless, for $v_{\perp} \ll c$ we have $s_{\perp} v_{\perp} B \ll \lambda_0$, and we can expand the right hand side in a Taylor series:

$$v_{\parallel} \approx \left(\pm \tan \phi - \frac{c}{\cos \phi} \frac{\lambda}{\lambda_0} \frac{s_{\perp} B}{\lambda_0} \right) v_{\perp} + \frac{c}{\cos \phi} \frac{\lambda - \lambda_0}{\lambda_0}. \quad (60)$$

For $v_{\perp} \ll c$ the FIDA weight functions are thus approximately bounded by straight lines in $(v_{\parallel}, v_{\perp})$ -coordinates. The v_{\parallel} -intercept is $\frac{c}{\cos \phi} \frac{\lambda - \lambda_0}{\lambda_0}$ and the slope is given by the term in the bracket. In figure 13 we compare the outer boundary given by equation (60) with the corresponding FIDA weight function in (E, p) -coordinates. The outermost boundaries are found for $l = 1$ and $l = 15$. However, since the outermost three lines on each side correspond to Stark lines with tiny intensities (see equation (39)), the effective boundaries of the velocity-space interrogation region could be considered to be defined by $l = 4$ and $l = 12$ as indicated by dashed lines. Stark splitting has always been neglected in previous work where boundaries of weight functions or minimum energies below which the weight function is zero have been discussed [2, 3, 15, 16, 18, 19, 22, 28]. Figure 13 demonstrates that the effect of Stark splitting can be substantial as it decreases the minimum energy below which the weight function is zero by

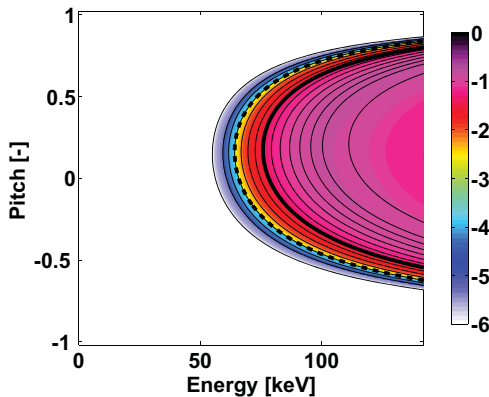


Figure 13. Boundaries of a FIDA weight function compared with the corresponding weight function for $\phi = 80^\circ$, 662–663 nm, and $B = 1.74$ T. For each of the 15 Stark splitting lines there is a boundary shown by thin black lines. The thick black line denotes $l = 8$ (no Stark shift). The thick dashed black lines denote $l = 4$ and $l = 12$. Note that here we show probabilities down to 10^{-6} .

10–20 keV depending on whether we define the boundary by $l = 1, 15$ or by $l = 4, 12$. In Figure 13 the thick lines correspond to previous models with no Stark splitting (here $l = 8$). The outermost lines set the interrogation region accounting for Stark splitting ($l = 1, 15$), and dashed lines correspond to the Stark lines $l = 4, 12$.

8. Discussion

8.1. Fast-ion studies

ASDEX Upgrade has five FIDA views. Correctly scaled FIDA weight functions, as we present here, allow measurements of 2D fast-ion velocity distribution functions by tomographic inversion [33]. This will allow velocity-space studies of fast-ion distributions which are generated by up to 20 MW of neutral beam injection power and 6 MW of ion cyclotron heating power [53–55]. Moreover, weight functions are not specific to FIDA and have also been given for CTS [12], neutron count rate measurements [2], neutral particle analyzers (NPAs) [2], fast-ion loss detectors [56], neutron spectroscopy [57, 58] and beam emission spectroscopy [59]. If weight functions for the other diagnostics are correctly scaled, as those for FIDA and CTS [12], the fast-ion diagnostics can be combined in joint measurements of 2D fast-ion velocity distribution functions using the available diagnostics [32]. For example, ASDEX Upgrade is equipped with fast-ion loss detectors (FILD) [26, 60, 61], fast-ion D_α (FIDA) [13, 27, 29, 33], CTS [31, 32, 37–39, 62, 63], neutron energy spectrometry [64, 65], NPAs [66, 67], and γ -ray spectrometry [68].

8.2. CER spectroscopy of the bulk ions

Weight functions describing FIDA diagnostics will also describe D_α -based CER spectroscopy of the bulk deuterium ions [6–11] and would then also be applicable to CER spectroscopy based on impurity species [4, 5] if the path of

the emitter from the charge-exchange reaction to the photon emission does not curve significantly. Hence we could also show velocity-space interrogation regions of particular wavelength intervals in CER spectroscopy with our approach, estimate where in velocity space most signal comes for a given ion velocity distribution function, calculate spectra, and—perhaps the most interesting application—calculate velocity-space tomographies of bulk-ion velocity distribution functions of the emitting species. A temperature, density and drift parallel to the magnetic field could be found by fitting a 2D Maxwellian to the tomography of the ion distribution functions, and this could provide an alternative to standard methods. This method would be even more interesting if parallel and perpendicular ion temperatures are discrepant as sometimes observed in MAST [69] or JET [70] or if the ions do not have a Maxwellian distribution.

9. Conclusions

The velocity-space sensitivity of FIDA measurements can be described by weight functions. We derive correctly scaled expressions for FIDA weight functions accounting for the Doppler shift, Stark splitting, and the charge-exchange and the electron transition probabilities. Our approach provides insight not revealed by the traditional numerical computation of weight functions implemented in the FIDASIM code. By using simple analytic models we show how these physical effects contribute to the velocity-space sensitivities of FIDA measurements. The Doppler shift determines an approximate shape of the observable region in $(v_{\parallel}, v_{\perp})$ -space which is triangular and mirror symmetric. Stark splitting broadens this triangular observable region whereas the charge-exchange and electron transition probabilities do not change the boundaries of FIDA weight functions separating the observable region from the unobservable region in velocity space. Our approach implies exact analytic expressions for these boundaries that take Stark splitting into account and therefore differ by up to 10–20 keV in (energy, pitch)-space from similar expressions in previous work. We show that Stark splitting changes the sensitivity of the measurement, but this does not limit the achievable spectral resolution of FIDA measurements as has sometimes been asserted [3, 15, 16, 24, 48, 49]. Weight functions as we deduce here can be used to rapidly compute synthetic FIDA spectra from a 2D velocity distribution function. This lays the groundwork for the solution of the inverse problem to determine 2D velocity distribution functions from FIDA measurements. Lastly, our methods are immediately applicable to charge-exchange recombination spectroscopy measurements of D_α -light from the bulk deuterium population to determine their temperature and drift velocity as well as any anisotropy.

Acknowledgments

Dmitry Moseev was supported by an EFDA fellowship. This work has received funding from the European Union's Horizon 2020 research and innovation program under grant agreement number 633053. The views and opinions expressed herein do not necessarily reflect those of the European Commission.

Appendix

Here we give key expressions in the widespread (E, p) -coordinates (Energy, pitch) that are used in the TRANSP code. They can be obtained by substituting

$$v_{\parallel} = -p\sqrt{2E/m} \quad (61)$$

$$v_{\perp} = \sqrt{(1-p^2)2E/m} \quad (62)$$

into the corresponding expressions in $(v_{\parallel}, v_{\perp})$ -coordinates. Weight functions in (E, p) -coordinates are defined as

$$I(\lambda_1, \lambda_2, \phi) = \int \int \int w(\lambda_1, \lambda_2, \phi, E, p) f(E, p) dE dp. \quad (63)$$

They can be written as

$$w(\lambda_1, \lambda_2, \phi, E, p) = R(E, p) \text{prob}(\lambda_1 < \lambda < \lambda_2 | \phi, E, p). \quad (64)$$

The projected velocity u along the line-of-sight is

$$u = \left(-p \cos \phi + \sqrt{1-p^2} \sin \phi \cos \gamma \right) \sqrt{2E/m}. \quad (65)$$

If there is no static electric field, the observed wavelength as function of gyroangle becomes

$$\lambda = \left(\lambda_0 + s_l B \sqrt{(1-p^2)2E/m} \right) \times \left(1 + \frac{1}{c} (-p \cos \phi + \sqrt{1-p^2} \sin \phi \cos \gamma_l) \sqrt{2E/m} \right) \quad (66)$$

and the inverse function is

$$\gamma_l = \arccos \frac{\frac{c}{\sqrt{2E/m}} \left(\frac{\lambda}{\lambda_0 + s_l B \sqrt{(1-p^2)2E/m}} - 1 \right) + p \cos \phi}{\sqrt{1-p^2} \sin \phi}. \quad (67)$$

The probability function for a uniform gyroangle distribution and no Stark splitting becomes

$$\begin{aligned} \text{prob}(\lambda_1 < \lambda < \lambda_2 | \phi, E, p) &= \frac{1}{\pi} \left(\arccos \frac{\frac{c}{\sqrt{2E/m}} \left(\frac{\lambda_1}{\lambda_0} - 1 \right) + p \cos \phi}{\sqrt{1-p^2} \sin \phi} \right. \\ &\quad \left. - \arccos \frac{\frac{c}{\sqrt{2E/m}} \left(\frac{\lambda_2}{\lambda_0} - 1 \right) + p \cos \phi}{\sqrt{1-p^2} \sin \phi} \right) \end{aligned} \quad (68)$$

and the pdf is expressed in (E, p) as

$$\begin{aligned} \text{pdf}(\lambda, \phi, E, p) &= \frac{1}{\pi \sqrt{2E/m} (1-p^2) \sin \phi \sqrt{1 - \left(\frac{\frac{c}{\sqrt{2E/m}} \left(\frac{\lambda}{\lambda_0} - 1 \right) + p \cos \phi}{\sqrt{1-p^2} \sin \phi} \right)^2}}. \end{aligned} \quad (69)$$

For an arbitrary gyroangle distribution and no Stark splitting the probability function becomes

$$\begin{aligned} \text{prob}(\lambda_1 < \lambda < \lambda_2 | \phi, E, p) &= \int_{\gamma_{2,l}}^{\gamma_{1,l}} \text{pdf}_{D_a}(\gamma | E, p) d\gamma + \int_{\gamma'_{1,l}}^{\gamma'_{2,l}} \text{pdf}_{D_a}(\gamma | E, p) d\gamma. \end{aligned} \quad (70)$$

The general expression of the probability function for an arbitrary gyroangle distribution and accounting for Stark splitting is

$$\begin{aligned} \text{prob}(\lambda_1 < \lambda < \lambda_2 | \phi, E, p) &= \sum_{l=1}^{15} \left(\int_{\gamma_{2,l}}^{\gamma_{1,l}} \text{prob}(l|\gamma) \text{pdf}_{D_a}(\gamma | E, p) d\gamma \right. \\ &\quad \left. + \int_{\gamma'_{1,l}}^{\gamma'_{2,l}} \text{prob}(l|\gamma) \text{pdf}_{D_a}(\gamma | E, p) d\gamma \right). \end{aligned} \quad (71)$$

The general expression of FIDA weight functions is

$$\begin{aligned} w(\lambda_1, \lambda_2, \phi, E, p) &= R(E, p) \\ &\quad \times \sum_{l=1}^{15} \left(\int_{\gamma_{2,l}}^{\gamma_{1,l}} \text{prob}(l|\gamma) \text{pdf}_{D_a}(\gamma | E, p) d\gamma \right. \\ &\quad \left. + \int_{\gamma'_{1,l}}^{\gamma'_{2,l}} \text{prob}(l|\gamma) \text{pdf}_{D_a}(\gamma | E, p) d\gamma \right) \end{aligned} \quad (72)$$

and their boundaries are given by

$$E = \frac{mc^2(\lambda - \lambda_0)^2}{2(1-p^2) \times \left(\lambda_0 \cos \phi \left(\pm \tan \phi - p + \frac{c\lambda_l B}{\lambda_0^2 \cos \phi} \right) \right)^2}. \quad (73)$$

References

- [1] Heidbrink W W, Burrell K H, Luo Y, Pablant N A and Ruskov E 2004 *Plasma Phys. Control. Fusion* **46** 1855–75
- [2] Heidbrink W W, Luo Y, Burrell K H, Harvey R W, Pinsker R I and Ruskov E 2007 *Plasma Phys. Control. Fusion* **49** 1457–75
- [3] Heidbrink W W 2010 *Rev. Sci. Instrum.* **81** 10D727
- [4] Fonck R, Darrow D and Jaehnic K 1984 *Phys. Rev. A* **29** 3288–309
- [5] Isler R C 1994 *Plasma Phys. Control. Fusion* **36** 171
- [6] Busche E, Euringer H and Jaspers R 1997 *Plasma Phys. Control. Fusion* **39** 1327–38
- [7] Pütterich T, Wolfgram E, Dux R and Maggi C 2009 *Phys. Rev. Lett.* **102** 025001
- [8] Grierson B A, Burrell K H, Solomon W M and Pablant N A 2010 *Rev. Sci. Instrum.* **81** 10D735
- [9] Grierson B A, Burrell K H, Chrystal C, Groebner R J, Kaplan D H, Heidbrink W W, Muñoz Burgos J M, Pablant N A, Solomon W M and Van Zeeland M A 2012 *Rev. Sci. Instrum.* **83** 10D529
- [10] Grierson B A, Burrell K H, Heidbrink W W, Lanctot M J, Pablant N A and Solomon W M 2012 *Phys. Plasmas* **19** 056107
- [11] Grierson B, Burrell K, Solomon W, Budny R and Candy J 2013 *Nucl. Fusion* **53** 063010
- [12] Salewski M *et al* 2011 *Nucl. Fusion* **51** 083014
- [13] Geiger B *et al* 2014 *Nucl. Fusion* **54** 022005
- [14] Geiger B 2013 Fast-ion transport studies using FIDA spectroscopy at the ASDEX Upgrade tokamak *PhD Thesis* Ludwig-Maximilians-Universität München
- [15] Heidbrink W W, Bell R E, Luo Y and Solomon W 2006 *Rev. Sci. Instrum.* **77** 10F120
- [16] Luo Y, Heidbrink W W, Burrell K H, Kaplan D H and Gohil P 2007 *Rev. Sci. Instrum.* **78** 033505
- [17] Podestà M, Heidbrink W W, Bell R E and Feder R 2008 *Rev. Sci. Instrum.* **79** 10E521
- [18] Van Zeeland M A, Heidbrink W W and Yu J H 2009 *Plasma Phys. Control. Fusion* **51** 055001

- [19] Van Zeeland M *et al* 2010 *Nucl. Fusion* **50** 084002
- [20] Bortolon A, Heidbrink W W and Podestà M 2010 *Rev. Sci. Instrum.* **81** 10D728
- [21] Heidbrink W W, McKee G R, Smith D R and Bortolon A 2011 *Plasma Phys. Control. Fusion* **53** 085007
- [22] Michael C A *et al* 2013 *Plasma Phys. Control. Fusion* **55** 095007
- [23] Jones O M *et al* and the MAST Team 2014 [arXiv:1401.6864](https://arxiv.org/abs/1401.6864)
- [24] Heidbrink W W, Luo Y, Muscatello C M, Zhu Y and Burrell K H 2008 *Rev. Sci. Instrum.* **79** 10E520
- [25] Podesta M *et al* 2009 *Phys. Plasmas* **16** 056104
- [26] Garcia-Munoz M *et al* 2011 *Nucl. Fusion* **51** 103013
- [27] Geiger B, Garcia-Munoz M, Heidbrink W W, McDermott R M, Tardini G, Dux R, Fischer R and Igochine V 2011 *Plasma Phys. Control. Fusion* **53** 065010
- [28] Muscatello C M, Heidbrink W W, Kolesnichenko Y I, Lutsenko V V, Van Zeeland M A and Yakovenko Y V 2012 *Plasma Phys. Control. Fusion* **54** 025006
- [29] Geiger B, Dux R, McDermott R M, Potzel S, Reich M, Ryter F, Weiland M, Wunderlich D and Garcia-Munoz M 2013 *Rev. Sci. Instrum.* **84** 113502
- [30] Pace D C *et al* 2013 *Phys. Plasmas* **20** 056108
- [31] Salewski M *et al* 2012 *Nucl. Fusion* **52** 103008
- [32] Salewski M *et al* 2013 *Nucl. Fusion* **53** 063019
- [33] Salewski M *et al* 2014 *Nucl. Fusion* **54** 023005
- [34] Heidbrink W, Liu D, Luo Y, Ruskov E and Geiger B 2011 *Commun. Comput. Phys.* **10** 716–41
- [35] Salewski M *et al* 2014 Doppler tomography in fusion plasmas and astrophysics, submitted
- [36] Nielsen S K *et al* 2011 *Nucl. Fusion* **51** 063014
- [37] Meo F *et al* 2008 *Rev. Sci. Instrum.* **79** 10E501
- [38] Salewski M *et al* 2010 *Nucl. Fusion* **50** 035012
- [39] Meo F *et al* and the ASDEX Upgrade Team 2010 *J. Phys.: Conf. Ser.* **227** 012010
- [40] Kubo S *et al* 2010 *Rev. Sci. Instrum.* **81** 10D535
- [41] Nishiura M *et al* 2014 *Nucl. Fusion* **54** 023006
- [42] Salewski M, Meo F, Bindslev H, Furtula V, Korsholm S B, Lauritzen B, Leipold F, Michelsen P K, Nielsen S K and Nonbø I E 2008 *Rev. Sci. Instrum.* **79** 10E729
- [43] Salewski M, Eriksson L G, Bindslev H, Korsholm S, Leipold F, Meo F, Michelsen P and Nielsen S 2009 *Nucl. Fusion* **49** 025006
- [44] Salewski M *et al* 2009 *Plasma Phys. Control. Fusion* **51** 035006
- [45] Schrödinger E 1926 *Ann. Phys.* **385** 437–90
- [46] Epstein P 1926 *Phys. Rev.* **28** 695–710
- [47] Foster J S and Chalk L 1929 *Proc. R. Soc. A* **123** 108–18
- [48] Luo Y, Heidbrink W W and Burrell K H 2004 *Rev. Sci. Instrum.* **75** 3468–70
- [49] Muscatello C M, Heidbrink W W, Taussig D and Burrell K H 2010 *Rev. Sci. Instrum.* **81** 10D316
- [50] 2012 www.adas.ac.uk
- [51] Janev R K and Smith J J 1993 *Atomic and Plasma–Material Interaction Data for Fusion* vol 4 (Vienna: IAEA)
- [52] Janev R K, Reiter D and Samm U *Technical Report Jül- 4105* Forschungszentrum Jülich
- [53] Gruber O *et al* 2007 *Nucl. Fusion* **47** S622–34
- [54] Kallenbach A *et al* 2012 *IEEE Trans. Plasma Sci.* **40** 605–13
- [55] Stroth U *et al* 2013 *Nucl. Fusion* **53** 104003
- [56] Pace D C *et al* 2012 *Rev. Sci. Instrum.* **83** 073501
- [57] Jacobsen A S *et al* 2014 Velocity-space sensitivity of neutron emission spectrometry, in preparation
- [58] Jacobsen A S *et al* 2014 *Rev. Sci. Instrum.* **85** 11E103
- [59] Pace D, Pinsker R, Heidbrink W, Fisher R, Van Zeeland M, Austin M, McKee G and Garcia-Munoz M 2012 *Nucl. Fusion* **52** 063019
- [60] García-Muñoz M, Martin P, Fahrbach H U, Gobbin M, Günter S, Maraschek M, Marrelli L, Zohm H and the ASDEX Upgrade Team 2007 *Nucl. Fusion* **47** L10–15
- [61] García-Muñoz M *et al* 2009 *Nucl. Fusion* **49** 085014
- [62] Furtula V, Salewski M, Leipold F, Michelsen P K, Korsholm S B, Meo F, Moseev D, Nielsen S K, Stejner M and Johansen T 2012 *Rev. Sci. Instrum.* **83** 013507
- [63] Furtula V, Leipold F, Salewski M, Michelsen P K, Korsholm S B, Meo F, Moseev D, Nielsen S K, Stejner M and Johansen T 2012 *J. Instrum.* **7** C02039
- [64] Giacomelli L, Zimbal A, Tittelmeier K, Schuhmacher H, Tardini G and Neu R 2011 *Rev. Sci. Instrum.* **82** 123504
- [65] Tardini G, Zimbal A, Esposito B, Gagnon-Moisan F, Marocco D, Neu R, Schuhmacher H and the ASDEX Upgrade Team 2012 *J. Instrum.* **7** C03004
- [66] Kurki-Suonio T, Hynönen V, Suttrop W, Fahrbach H U, Stober J and the ASDEX Upgrade Team 2006 *Europhysics Conference Abstracts* vol 30I, p P2.145
- [67] Äkäslompolo S, Hirvijoki E, Kurki-Suonio T and the ASDEX Upgrade Team 2010 *Europhysics Conference Abstracts* vol 34A, p P5.113
- [68] Nocente M *et al* 2012 *Nucl. Fusion* **52** 094021
- [69] Hole M J, von Nessi G, Fitzgerald M, McClements K G and Svensson J 2011 *Plasma Phys. Control. Fusion* **53** 074021
- [70] von Hellermann M G, Core W G F, Frieling J, Horton L D, König R W T, Mandl W and Summers H P 1993 *Plasma Phys. Control. Fusion* **35** 799–824

Reference [7]

[7]. M Salewski et al. (2015) *Plasma Physics and Controlled Fusion* **57**
014021. Doppler tomography in fusion plasmas and astrophysics

Doppler tomography in fusion plasmas and astrophysics

M Salewski¹, B Geiger², W W Heidbrink³, A S Jacobsen¹, S B Korsholm¹,
F Leipold¹, J Madsen¹, D Moseev^{2,4}, S K Nielsen¹, J Rasmussen¹,
L Stagner³, D Steeghs⁵, M Stejner¹, G Tardini², M Weiland² and
the ASDEX Upgrade Team²

¹ Technical University of Denmark, Department of Physics, 2800 Kgs.

Lyngby, Denmark

² Max Planck Institute for Plasma Physics, Boltzmannstr. 2, D-85748 Garching, Germany

³ University of California, Irvine, CA 92697, USA

⁴ FOM Institute DIFFER, PO Box 1207, NL-3430 BE Nieuwegein, The Netherlands

⁵ Department of Physics, University of Warwick, Coventry, CV4 7AL, UK

E-mail: msal@fysik.dtu.dk

Received 26 June 2014, revised 3 September 2014

Accepted for publication 22 September 2014

Published 28 November 2014



CrossMark

Abstract

Doppler tomography is a well-known method in astrophysics to image the accretion flow, often in the shape of thin discs, in compact binary stars. As accretion discs rotate, all emitted line radiation is Doppler-shifted. In fast-ion D α (FIDA) spectroscopy measurements in magnetically confined plasma, the D α -photons are likewise Doppler-shifted ultimately due to gyration of the fast ions. In either case, spectra of Doppler-shifted line emission are sensitive to the velocity distribution of the emitters. Astrophysical Doppler tomography has led to images of accretion discs of binaries revealing bright spots, spiral structures and flow patterns. Fusion plasma Doppler tomography has led to an image of the fast-ion velocity distribution function in the tokamak ASDEX Upgrade. This image matched numerical simulations very well. Here we discuss achievements of the Doppler tomography approach, its promise and limits, analogies and differences in astrophysical and fusion plasma Doppler tomography and what can be learned by comparison of these applications.

Keywords: tomography, fast ions, accretion discs, spectroscopy, fast ion D-alpha spectroscopy, tokamak

(Some figures may appear in colour only in the online journal)

1. Introduction

Doppler tomography has been used to image a fast-ion velocity distribution function in a fusion plasma [1]. While this application of Doppler tomography is in its infancy, it has been used to study astrophysical accretion discs for more than 25 years [2–4]. Readily observable accretion discs form in pairs of stars, called interacting binaries, in which matter flows from one star to its companion. Angular momentum tends to confine these discs within the orbital plane of the binary with the gas orbiting around the more massive, compact component in the system, often a stellar remnant. They form when this

compact object pulls matter towards it. Angular momentum in the accretion disc is transported outwards and hence matter spirals inwards and eventually reaches the accretor. Astrophysical Doppler tomography has provided images of accretion discs for several classes of binaries [3–9].

Magnetically confined laboratory plasmas are heated to ~ 10 keV mostly by fast ions generated by injected energetic neutrals (~ 30 keV–1 MeV), by electromagnetic wave acceleration (up to MeVs), or finally in a fusion power plant by the DT fusion reaction (3.5 MeV). Fast ions are magnetically forced on twisted trajectories within the donut-shaped plasma until they become part of the thermal ions. At the

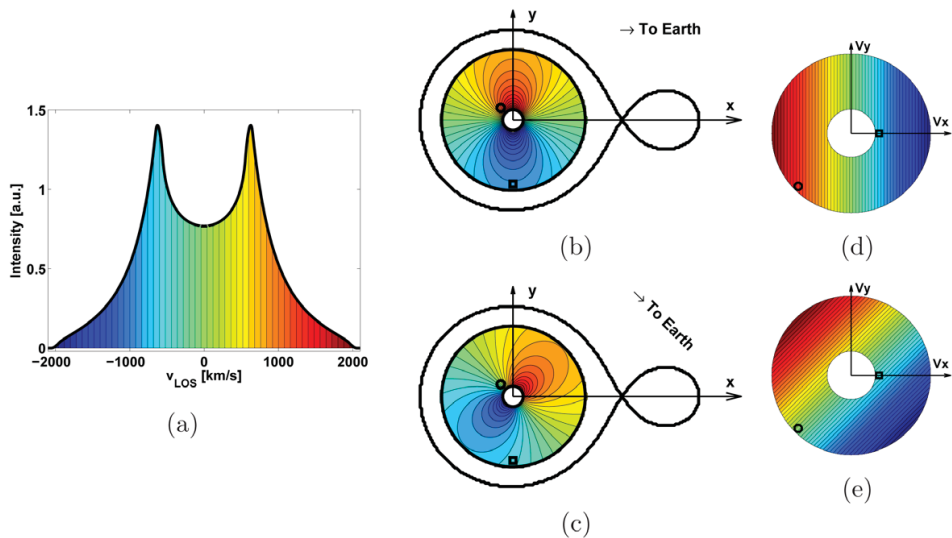


Figure 1. (a) Model spectrum from an accretion disc in LOS velocity space. Negative v_{LOS} corresponds to blue-shift and positive v_{LOS} to red-shift. (b)–(d) show where these v_{LOS} appear on the disc in position space and in velocity space in the same colours as in (a). (b) and (c) show the disc and the Roche lobe of a binary in position space at different phases. The Roche lobe is an equipotential surface of the rotating two-body system. Matter within the Roche lobe of a star is gravitationally bound to this star. (d) and (e) show the same accretion disc in velocity space at the phases of (b) and (c), respectively. The circles and the squares illustrate the mapping from position space to velocity space.

tokamak ASDEX Upgrade we can generate a variety of fast-ion populations by using neutral beams or electromagnetic waves at the ion cyclotron frequency [10–12].

Doppler tomography is analogous to standard tomography, but the images are constructed in velocity space rather than in position space. This is possible due to the Doppler shift of line radiation from emitters on trajectories with a near-circular component. Such trajectories are typical for rotating accretion discs of binary stars and gyrating ions in magnetized plasma that have locally helical trajectories. The velocity vector of the emitter and its projected velocity v_{LOS} onto the line-of-sight (LOS) of a detector depend on the angular position of the emitter in its orbit with respect to the line-of-sight. We refer to this angle as phase angle $[0, 2\pi]$ or alternatively as phase $[0, 1]$ following the astrophysical literature. The wavelength shift of emitted photons is proportional to v_{LOS} according to the Doppler shift $\lambda - \lambda_0 = v_{LOS} \lambda_0/c$ where c is the speed of light, λ_0 is the unshifted wavelength of the line emission and λ is its Doppler-shifted wavelength. The goal of Doppler tomography is to infer 2D velocity distributions of the emitters from spectroscopic measurements. In fusion plasmas such spectra are measured by fast-ion D_α (FIDA) spectroscopy [1, 13–19] where fast ions are neutralized to become excited neutrals emitting D_α -photons. The Doppler shift is determined by the phase angle of the fast ion at the time of the charge-exchange reaction.

The available measurements in astrophysical and fusion plasma Doppler tomography lead to different flavours of Doppler tomography. Since the two stars in an interacting binary orbit each other, we can view the binary at any phase angle in their orbit. The observations are made mostly using ground-based telescopes but sometimes also satellite-based

telescopes such as the Hubble space telescope. Provided observations are obtained across a substantial fraction of the period of the binary system, spectra for various phase angles can be adequately sampled using time-series observations. These spectra change with the phase since several prominent features in the accretion disc are phase-locked to the binary. Astrophysical Doppler images are then inferred for two velocity coordinates in the orbital plane of the binary. The out-of-plane velocity component of matter in the disc is negligible as the disc is thin compared with its diameter. On the contrary, line radiation from fusion plasmas comes from many emitters at all phases and hence spectra are not phase-resolved but phase-averaged. But since the ion velocity distribution function is to a good approximation rotationally symmetric about the strong and slowly varying local magnetic field, resolution of different phases is not necessary. Fusion plasma Doppler tomograms are imaged in velocity components parallel and perpendicular to the magnetic field. Astrophysical Doppler tomograms are 2D by assuming zero out-of-plane velocity whereas fusion plasma Doppler tomograms are 2D by assuming rotational symmetry.

The incentives for imaging in velocity space are different in the two fields. In astrophysical Doppler tomography one is actually interested in the spatial structure of accretion discs. Each point of an accretion disc can be mapped onto velocity space by for example assuming flow velocities obeying Kepler’s law which may, however, be a crude assumption. Such Keplerian mapping is illustrated in figure 1. Here we observe that typical rotational speeds in the disc are much larger than the thermal speed of the atoms, so that the line broadening is mostly caused by the rotation of the accretion disc. Tomographic reconstructions in velocity space are

preferable as they do not require any mapping assumptions and make the method applicable to a wide range of flow geometries including emission sources not originating within discs. In fusion plasma Doppler tomography, on the contrary, knowledge of the fast-ion phase-space distribution function $f(\mathbf{u}, \mathbf{x})$ itself is essential for the successful operation of a fusion power plant.

In this paper we discuss Doppler tomography in astrophysical and nuclear fusion applications. In section 2 we discuss general principles appearing in both applications as well as their differences. We compare the equations describing the projection onto the LOS, the forward models and the most wide-spread inversion methods. In section 3 we highlight achievements of astrophysical Doppler tomography and in section 4 we present fusion plasma Doppler images. In section 5 we discuss the two applications of the Doppler tomography method in light of each other and what can be learned by comparison. In section 6 we draw conclusions.

2. Principles of velocity-space tomography

2.1. Line-of-sight velocity

Here we derive how v_{LOS} relates to the astrophysical 2D velocity space of the orbital plane (v_x, v_y) and to the fusion plasma 2D velocity space $(u_{\parallel}, u_{\perp})$. Consider a coordinate system with unit vectors $(\hat{\mathbf{u}}_x, \hat{\mathbf{u}}_y, \hat{\mathbf{u}}_z)$ and components (u_x, u_y, u_z) in velocity space as illustrated in figure 1 where the u_z -axis is aligned with the rotation axis. The orientation of u_x and u_y -axes is arbitrary for fusion plasma due to rotational symmetry. Let the LOS be at an inclination angle i to the rotation axis and have an azimuthal angle ϕ from the $(\hat{\mathbf{u}}_x, \hat{\mathbf{u}}_y)$ -plane and let γ be a systemic or drift velocity along the LOS. Then the unit vector along the LOS $\hat{\mathbf{v}}$ and the emitter velocity \mathbf{u} are

$$\hat{\mathbf{v}} = -\cos\phi \sin i \hat{\mathbf{u}}_x + \sin\phi \sin i \hat{\mathbf{u}}_y - \cos i \hat{\mathbf{u}}_z, \quad (1)$$

$$\mathbf{u} = \gamma \hat{\mathbf{v}} + u_x \hat{\mathbf{u}}_x + u_y \hat{\mathbf{u}}_y + u_z \hat{\mathbf{u}}_z. \quad (2)$$

The projected velocity v_{LOS} along the LOS from 3D velocity space is then [2]

$$v_{\text{LOS}} = \gamma - u_x \sin i \cos\phi + u_y \sin i \sin\phi - u_z \cos i. \quad (3)$$

In the following we make further assumptions to deduce simplified projection equations for astrophysical and fusion plasma Doppler tomography. In astrophysics the inclination i of the accretion disc is often unknown and so one substitutes [2]

$$v_x = u_x \sin i, \quad v_y = u_y \sin i, \quad v_z = u_z \cos i \quad (4)$$

to get a projection equation not containing the inclination:

$$v_{\text{LOS}} = \gamma - v_x \cos\phi + v_y \sin\phi - v_z. \quad (5)$$

Further, the out-of-plane flow v_z is assumed to be zero and we arrive at the projection equation used in many astrophysical applications [2]:

$$v_{\text{LOS}} = \gamma - v_x \cos\phi + v_y \sin\phi. \quad (6)$$

In fusion plasma Doppler tomography, the magnetic field and the LOS vectors and hence the inclination i are known, making transformation to (v_x, v_y, v_z) -coordinates unnecessary. To exploit rotational symmetry, we transform to cylindrical coordinates:

$$u_x = u_{\perp} \cos\bar{\phi}, \quad u_y = u_{\perp} \sin\bar{\phi}, \quad u_z = u_{\parallel} \quad (7)$$

so that the projection equation becomes

$$\begin{aligned} v_{\text{LOS}} &= \gamma - u_{\perp} \cos\phi \sin i \cos\bar{\phi} + u_{\perp} \sin\phi \sin i \sin\bar{\phi} - u_{\parallel} \cos i \\ &= \gamma - u_{\perp} \sin i \cos(\phi + \bar{\phi}) - u_{\parallel} \cos i. \end{aligned} \quad (8)$$

As the distribution is rotationally symmetric, we can choose $\phi = 0$. Further, it is assumed that there is no systemic or drift velocity γ . Hence we obtain the usual projection equation used for Doppler tomography in fusion plasma

$$v_{\text{LOS}} = -(u_{\parallel} \cos i + u_{\perp} \sin i \cos\bar{\phi}) \quad (9)$$

where normally the vector along the LOS is defined in the opposite direction so that the minus disappears [19, 20]. Thus the two projection equations are consistently derived but describe projections from different image planes and rely on different assumptions.

2.2. Forward models

The projection of an arbitrary 3D function f_u^{3D} onto the LOS is [2, 20]

$$\begin{aligned} f_{v,\text{LOS}}(v, \phi) &= \int_{-\infty}^{\infty} \int_{-\infty}^{\infty} \int_{-\infty}^{\infty} f_u^{3D}(u_x, u_y, u_z) \\ &\quad \times \delta(v - v_{\text{LOS}}) du_x du_y du_z. \end{aligned} \quad (10)$$

We now reduce equation (10) by making the same assumptions as in the previous section. In astrophysics we transform the velocity coordinates to (v_x, v_y, v_z) using equation (4) and substitute for v_{LOS} using equation (5):

$$\begin{aligned} f_{v,\text{LOS}}(v, \phi) &= \int_{-\infty}^{\infty} \int_{-\infty}^{\infty} \int_{-\infty}^{\infty} f_v^{3D}(v_x, v_y, v_z) \\ &\quad \times \delta(v - \gamma + v_x \cos\phi - v_y \sin\phi + v_z) dv_x dv_y dv_z. \end{aligned} \quad (11)$$

Assuming the out-of-plane velocity to be negligible, we write

$$f_v^{3D}(v_x, v_y, v_z) = f_v^{2D}(v_x, v_y) \delta(v_z) \quad (12)$$

and integrate over v_z to find the common astrophysical 2D projection equation [3]

$$\begin{aligned} f_{v,\text{LOS}}(v, \phi) &= \int_{-\infty}^{\infty} \int_{-\infty}^{\infty} f_v^{2D}(v_x, v_y) \\ &\quad \times \delta(v - \gamma + v_x \cos\phi - v_y \sin\phi) dv_x dv_y. \end{aligned} \quad (13)$$

In fusion plasma physics, u_z is allowed to be arbitrary, but we assume the $f_u^{3D}(u_x, u_y, u_z)$ to be rotationally symmetric so that it can be described by two coordinates $(u_{\parallel}, u_{\perp})$. We define a 2D velocity distribution function

$$f_u^{2D}(u_{\parallel}, u_{\perp}) = \int_0^{2\pi} f_u^{3D}(u_{\parallel}, u_{\perp}) u_{\perp} d\phi = 2\pi u_{\perp} f_u^{3D}(u_{\parallel}, u_{\perp}), \quad (14)$$

transform equation (10) to cylindrical coordinates and substitute equation (14) [20]

$$f_{v, \text{LOS}}(v, i) = \int_{-\infty}^{\infty} \int_0^{\infty} \frac{1}{2\pi} \int_0^{2\pi} \delta(u_{\parallel} \cos i + u_{\perp} \sin i \times \cos \phi - v) d\phi f_u^{2D}(u_{\parallel}, u_{\perp}) du_{\parallel} du_{\perp}. \quad (15)$$

As one actually measures the number of photons in a small wavelength range rather than at one wavelength, the measurable quantity is the integral of f_v over a small velocity range [19]. Noting that $f_u^{2D}(u_{\parallel}, u_{\perp})$ does not depend on v , we arrive at the forward model used in fusion plasma Doppler tomography:

$$\begin{aligned} f_{\text{LOS}}(v_1, v_2, i) &= \int_{v_1}^{v_2} f_{v, \text{LOS}}(v, i) dv \\ &= \int_0^{\infty} \int_{-\infty}^{\infty} w(v_1, v_2, i, u_{\parallel}, u_{\perp}) f_u^{2D}(u_{\parallel}, u_{\perp}) du_{\parallel} du_{\perp} \end{aligned} \quad (16)$$

where we have introduced a weight function w in analogy with position-space tomography. The weight function can be explicitly calculated [19, 20]:

$$\begin{aligned} w(v_1, v_2, i, u_{\parallel}, u_{\perp}) &= \int_{v_1}^{v_2} \frac{1}{2\pi} \int_0^{2\pi} \delta(u_{\parallel} \cos i + u_{\perp} \sin i \cos \phi - v) d\phi dv \\ &= \int_{v_1}^{v_2} \frac{1}{\pi u_{\perp} \sin i \sqrt{1 - \left(\frac{v - u_{\parallel} \cos i}{u_{\perp} \sin i}\right)^2}} dv \\ &= \frac{1}{\pi} \left(\arccos \frac{v_1 - u_{\parallel} \cos i}{u_{\perp} \sin i} - \arccos \frac{v_2 - u_{\parallel} \cos i}{u_{\perp} \sin i} \right). \end{aligned} \quad (17)$$

Weight functions in this form enable us to construct a transfer matrix W with which we can rapidly calculate the implied function f_{LOS} from an arbitrary image in 2D velocity space f_u^{2D} . The forward model can be written as a matrix equation of the form

$$F_{\text{LOS}} = W F_u^{2D} \quad (18)$$

where F_{LOS} is a vector holding the measurements and F_u^{2D} is a vector holding the image pixel values [1, 20–22]. Refined forward models accounting for Stark splitting, charge-exchange reaction probabilities and electron transition probabilities are discussed in reference [19]. In this paper we focus on the Doppler shift to emphasize the analogy between astrophysical and fusion plasma Doppler tomography.

2.3. A rotationally symmetric accretion disc with no out-of-plane flow

Here we derive explicit formulas for the observable spectrum of a rotationally symmetric accretion disc with velocities from $v_{\perp 1}$ to $v_{\perp 2}$ and no out-of-plane flow so that $f_v^{2D}(v_{\perp}, v_{\parallel}) = f_v^{1D}(v_{\perp}) \delta(v_{\parallel})$. Exploiting the analogy with fusion plasma Doppler tomography, we integrate equation (16) over v_{\parallel} using equation (17):

$$f_{\text{LOS}}(v) = \int_0^{\infty} \frac{1}{\pi} \left(\arccos \frac{v_1}{v_{\perp}} - \arccos \frac{v_2}{v_{\perp}} \right) f_v^{1D}(v_{\perp}) dv_{\perp}. \quad (19)$$

We can evaluate the integral over v_{\perp} by assuming a functional form of f_v^{1D} . Similar models used position coordinates [23–26] whereas we use velocity coordinates. In these earlier treatments power laws were assumed and then matched to experimental data. As for Keplerian flow power laws in position space map to power laws in velocity space, we also take the emitted intensity to follow a power law of the form $f_v^{1D}(v_{\perp}) = f_0 / v_{\perp}^a$ between $v_{\perp 1}$ and $v_{\perp 2}$. Hence we find theoretical spectra for rotationally symmetric discs with no out-of-plane flow for $a = (0, 2, 4)$:

$$\begin{aligned} f_0 \rightarrow f_{\text{LOS}}(v_1, v_2) &= \frac{f_0}{\pi} \left(v \operatorname{arctanh} \frac{1}{\sqrt{1 - \left(\frac{v}{v_{\perp}}\right)^2}} - v_{\perp} \arccos \frac{v}{v_{\perp}} \right) \Big|_{v_{\perp 1} = v_1}^{v_{\perp 2} = v_2} \Big|_{v_{\perp 1} = v_1}^{v_{\perp 2} = v_2} \end{aligned} \quad (20)$$

$$\begin{aligned} \frac{f_0}{v_{\perp}^2} \rightarrow f_{\text{LOS}}(v_1, v_2) &= \frac{f_0}{\pi} \left(\frac{1}{v_{\perp}} \arccos \frac{v}{v_{\perp}} - \frac{1}{v} \sqrt{1 - \left(\frac{v}{v_{\perp}}\right)^2} \right) \Big|_{v_{\perp 1} = v_1}^{v_{\perp 2} = v_2} \Big|_{v_{\perp 1} = v_1}^{v_{\perp 2} = v_2} \end{aligned} \quad (21)$$

$$\begin{aligned} \frac{f_0}{v_{\perp}^4} \rightarrow f_{\text{LOS}}(v_1, v_2) &= \frac{f_0}{\pi} \left(\frac{1}{3v_{\perp}^3} \arccos \frac{v}{v_{\perp}} - \frac{1}{9v} \left(\frac{1}{v_{\perp}^2} - \frac{2}{v^2} \right) \sqrt{1 - \left(\frac{v}{v_{\perp}}\right)^2} \right) \Big|_{v_{\perp 1} = v_1}^{v_{\perp 2} = v_2} \Big|_{v_{\perp 1} = v_1}^{v_{\perp 2} = v_2} \end{aligned} \quad (22)$$

These spectra are shown in figure 2. The value of a is unknown and could be found by matching experimental data. For $a = 0$ the 1D velocity distribution is uniform corresponding to a $1/v$ curve in 2D velocity space. For $a = 4$ very little emission comes from the rapidly rotating regions of the accretion disc which cover only a small area close to the accretor in position space. The models reproduce the characteristic often observed double-peak. This illustrates the analogy between astrophysical and fusion plasma Doppler tomography as we derived the astrophysical observation from the fusion plasma formula. Further, the model gives direct insight in the relation between 2D velocity space of the accretion disc and the line-of-sight velocity space of the measurement and it can be used to validate inversion algorithms. The detailed shape of the double-peak is also influenced by the optical depth [25] and magnetohydrodynamic turbulence [26].

2.4. Inversion methods

Several inversion methods have been applied to solve the velocity-space tomography problem. Astrophysical applications usually apply the maximum entropy method [2] or filtered back-projection method [3]. Nuclear fusion applications of velocity space tomography have relied on the singular value decomposition [1, 21, 22], an iterative technique akin to the back-projection method [20] and a maximum entropy method [27]. In all methods velocity space

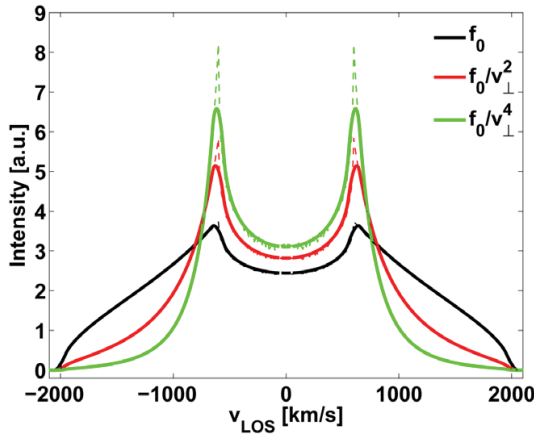


Figure 2. Theoretical spectra of rotationally symmetric accretion discs with no out-of-plane flow and intensities following power laws of the form $f \sim f_0 / v_{\perp}^q$. Solid lines show the analytic formulas and dashed lines the numeric integration of the velocity image not accounting for finite resolution.

is divided into many elements or pixels. In the maximum entropy method we calculate synthetic data for possible images and quantify the difference between the synthetic data with the measured data by a goodness-of-fit parameter χ^2 . χ^2 could be decreased to very low values by changing the image, but this tends to amplify noise in the images. Instead we set a target χ^2 such that we judge the synthetic and the measured data to be consistent. The reduced χ^2 should then be of order one but the precise value is open for discussion. Out of the many tomograms that achieve this target χ^2 one selects the one with maximum entropy which can be found using Lagrange multipliers in an iterative procedure [28]. The standard definition of entropy

$$S = - \sum p_i \ln p_i, \quad p_i = f_i / \sum_j f_j \quad (23)$$

selects the most uniform image [2]. In astrophysical Doppler tomography one frequently instead uses a modified entropy

$$S = - \sum p_i \ln \frac{p_i}{q_i}, \quad p_i = f_i / \sum_j f_j, \quad q_i = D_i / \sum_j D_j \quad (24)$$

where D is a default image [2]. Prior information can be encoded in the default image which can be set to be for example axisymmetric or a heavily blurred version of the image. Such adaptive defaults are better than axisymmetric defaults as the Doppler images have well-defined spots of emission and discs can be strongly asymmetric. An advantage of the maximum entropy method is the enforced positivity that reduces high frequency jitter in the image which is often found in linear methods.

The filtered back-projection method is a linear method in which the inversion is computed in two steps. First the spectra are filtered to damp high frequency components which would otherwise lead to jitter in the tomogram. This step also blurs the tomogram. The filtered profiles $\tilde{f}(v, \phi)$ are

$$\tilde{f}(v, \phi) = \int F(\hat{v}, v) f(v - \hat{v}, \phi) d\hat{v}. \quad (25)$$

where F is the filter function. The second step is the so-called back-projection which is

$$f(v_x, v_y) = \int_0^{0.5} \tilde{f}(\gamma - v_x \cos 2\pi\phi' + v_y \sin 2\pi\phi', \phi') d\phi'. \quad (26)$$

In this method each image value is found by integrating the 2D function $\tilde{f}(v, \phi)$ over the sinusoidal path which would be traced out by a bright light source with the velocity coordinates of the image point. One may also regard this as smearing the filtered profile measured at the angle ϕ across the image at the same angle ϕ .

The singular value decomposition method is another linear method, in which we formulate a forward model based on weight functions as a matrix equation. The tomographic inversion is then given by

$$F^+ = \hat{W}^+ \hat{F}_{\text{LOS}}. \quad (27)$$

\hat{W}^+ is the truncated Moore–Penrose pseudoinverse found by singular value decomposition of the transfer matrix \hat{W} from equation (18).

3. Doppler tomography of accreting binary stars

Astrophysical Doppler tomography is a standard technique to image accretions discs of binary star systems such as cataclysmic variables [6], Algols [8] and x-ray binaries [9] including neutron stars [29, 30] and black holes [31, 32]. It is also very useful to map the magnetically controlled accretion stream in polars where the strong magnetic fields prevent formation of an accretion disc [7] or in intermediate polars [33]. Often spectra of the strong emission lines from H and He are measured, but recently spectra of the $CaII$ line even revealed the presence of the faint donor star [34]. Here we highlight two particularly instructive achievements of astrophysical Doppler tomography. Figure 3 shows the observed time-series of emission line profiles, so-called trailed spectra, and the corresponding Doppler tomogram of the interacting binary CE315. The maximum entropy method was used for the inversion of the 34 measured spectra. The strong emission near 0 km s^{-1} comes from the compact, massive white dwarf. The trailed spectra in figure 3(a) have a half-width of about 1000 km s^{-1} . They show the characteristic S-curve of a bright source of emission that is phase-locked to the binary. Figure 3(b) shows the Doppler image constructed from the trailed spectra. The accretion disk appears as a ring with velocities between 400 km s^{-1} and 1000 km s^{-1} . The highest speeds show emission from the inner edge of the disc in position space that is close to the white dwarf. The lowest speeds show emission from the outer edge of the disc in position space. The accreting white dwarf sits at the center of the Doppler image. The mass donor sits at $v_y = 400 \text{ km s}^{-1}$ and by definition of the coordinate system at $v_x = 0$. The Doppler image reveals a bright spot causing the S-curve in the trailed spectra. At this location the gas flow from the donor star to the white dwarf

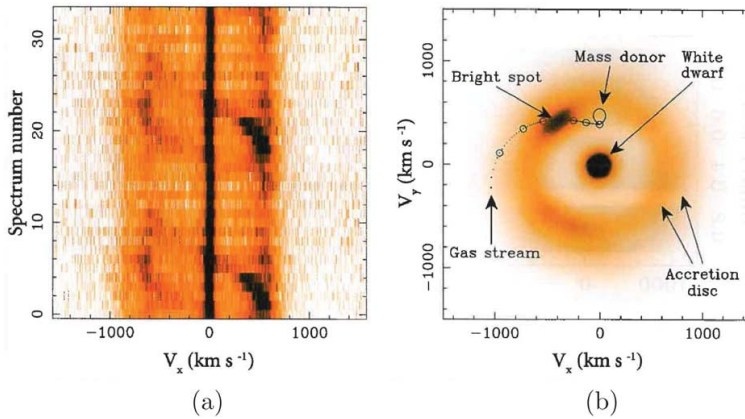


Figure 3. (a) The observed line emission from CE315 as a function of the binary orientation and projected velocity which is here called V_x [4]. Each of the 34 spectra is measured for a new phase angle of the binary, corresponding to a new line-of-sight. (b) The corresponding Doppler image reveals a bright spot where the gas stream from the donor to the accretor hits the accretion disc. The dotted line shows a calculated ballistic trajectory of the gas stream where the circles show 10% steps of the distance which the gas stream covers [4]. The V_x -coordinate in (a) corresponds to the V_x -coordinate in (b) for one particular phase.

hits the disc. In the Doppler image this gas flows from the L1 Lagrange point between the donor and the accretor to the high-speed outer edge of the disc which, in position space, corresponds to the inner edge of the disc close to the accretor.

In figure 4 we show an example of the very variable spectra observed over the binary phase of the binary IP Peg [35–37]. The Doppler images reveal that these variable spectra, which would otherwise be very hard if not impossible to interpret, are due to spiral arms in the accretion disc [35]. A numerical simulation and derived synthetic observations match respectively the Doppler image and observations well. These spiral arms are phase-locked to the binary suggesting they are some form of tidal wave [35], perhaps tidally induced shock waves [37]. However, the nature of the spiral arms is still controversial. Spiral arms have been observed in many other binaries, e.g. [33]. Other asymmetric features in the discs have also been observed, e.g. eccentricity [38] or alternating radial flow velocities [39]. These examples illustrate how the complex emissivity profiles observed from binaries can be conveniently mapped into images that are much more straightforward to interpret and at the same time offer quantitative tests against models.

4. Doppler tomography of fast-ion velocity distribution functions

Tomography in position space is a standard analysis method in nuclear fusion research [40, 41] just as in other fields throughout physical and medical sciences [42, 43]. Fusion plasma Doppler tomography has been studied theoretically for some years [20–22, 44]. The method has been theoretically demonstrated and made tractable by formulating the forward model in terms of weight functions [20] previously used to estimate the velocity-space sensitivity of FIDA measurements [14, 19, 45].

Figure 5 shows Doppler images of the fast-ion velocity distribution function in ASDEX Upgrade discharge 29578

on 17×8 grid points. Here we study the number of singular values and the effect of filtering the spectra as in the filtered back-projection method. From the uppermost row to the bottom row the number of singular values in the tomogram decreases. In the left column we use synthetic measurements, in the center column actual measurements and in the right column filtered actual measurements.

We measured in three FIDA views and used the singular value decomposition method to invert the spectra [1]. We used experimentally accessible parts of the spectrum with red- and blue shifts with a wavelength resolution of 0.1 nm over 16 nm. Of the resulting 3×160 measurement points, 217 were not obscured by other features in the FIDA spectra and covered the velocity-space region of interest. The inclination angles i of the three FIDA LOS are 12° , 69° and 156° . The left column in figure 5 shows reconstructions from synthetic FIDA measurements computed from a simulated fast-ion velocity distribution function using the FIDASIM code [46]. Figure 5(a) closely matches simulations which we show in reference [1].

This distribution function is typical for fast ions generated by neutral beam injection and its form can be explained by classical slowing down due to collisions. Neutral deuterium atoms at $E = 60$ keV are injected and ionized to D ions, forming a peak at about $(v_{\parallel}, v_{\perp}) \approx (-1, 2) \times 10^6$ m s $^{-1}$. D_2 and D_3 in the neutral beam lead to further injection peaks at $E/2 = 30$ keV and $E/3 = 20$ keV which are merged to form the second, larger peak at about $(v_{\parallel}, v_{\perp}) \approx (-1, 1) \times 10^6$ m s $^{-1}$. These injection peaks are the sources of fast ions which then slow down due to collisions. In collisions with electrons the ions lose energy while their pitch $p = -v_{\parallel} / \sqrt{v_{\parallel}^2 + v_{\perp}^2}$ does not change significantly. In collisions with ions the pitch also changes.

The Doppler images of the synthetic measurements show as expected that the larger the number of singular values, the finer features of the functions can be reconstructed but the more the noise is amplified. 50 singular values are not enough to recover the two peaks in the functions whereas for

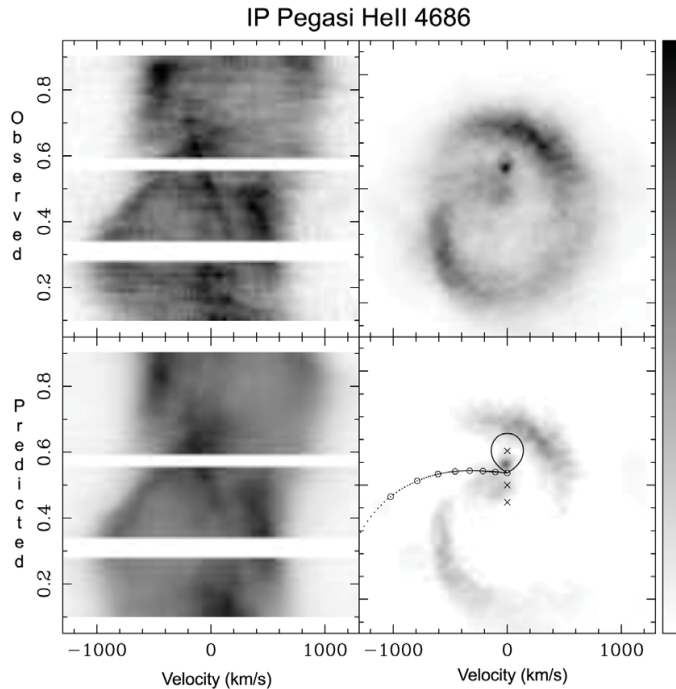


Figure 4. In the upper panels we show the observed line emission from IP Peg as a function of the binary orientation and projected velocity (left) and corresponding Doppler image revealing spiral arms in the accretion disc (right) [37]. The binary phase in the left panel runs from 0 to 1 during a period of the binary. Both axes of the Doppler image in the right panel are in identical units. The velocities are defined analogous to those in figure 3. The lower panels show a numerical simulation of the disc (right) and the implied observable line emission (left). The gas stream is marked as in figure 3.

60–70 singular values the two peaks appear. For more than 70 singular values the Doppler images become hard to interpret due to noise. There is no obvious objective rationale to choose the number of singular values and this is a weakness of the method. A possible remedy could be the L-curve technique [47]. The center column in figure 5 shows Doppler images from actual FIDA measurements at ASDEX Upgrade. The large-scale shape of the function including the location of the beam injection peaks are reproduced well if 60–70 singular values are used as predicted. The right column shows Doppler images calculated from filtered spectra as in the filtered back-projection method. We use a box filter with a stencil of three points. The filter decreases the amplitude of the jitter as expected.

In figure 6 we present a maximum entropy reconstruction of a fast-ion velocity distribution typical for the tokamak DIII-D on a 25×25 element energy-pitch grid from noisy synthetic measurements. Here we used four views with viewing angles of 8° , 19° , 45° and 95° , a mean signal-to-noise ratio of 20:1 and a wavelength resolution of 0.14 nm over 14 nm, which corresponds to a total of 4×100 measurement points in the spectra. This simulated distribution assumes a 60 keV NBI in co-current direction (positive pitch) and an 80 keV NBI in counter-current direction (negative pitch) which generate the dominant beam injection peaks. Further peaks appear at half and third energies for both beams. The overall shape of the

reconstruction matches the original function used to compute the synthetic measurements well, in particular for positive pitch. The peak at 80 keV at negative pitch in the reconstruction is barely visible, blurred and much smaller than in the original function. In the actual experiment the spectrum will be obscured by other emissions at small Doppler shifts. An experimental demonstration of the Doppler tomography method on DIII-D with these or similar parameters is in preparation.

5. Discussion

Doppler tomography in nuclear fusion research and astrophysics rely on the same techniques, but substantially different measurement data lead to different implementations of the method. The imaging plane is the orbital plane in astrophysics. The reduction from 3D is achieved by assuming that the out-of-plane velocity components are much smaller than the flow within the binary plane. Several researchers have attempted 3D imaging using all three velocity coordinates, though this is a much less well-constrained inversion problem from the observable time-series of 1D spectra. The assumption of rotational symmetry in fusion plasmas is rather good, so it would likely not lead to new insight to do 3D imaging in velocity space. Nevertheless, the inclusion of a spatial

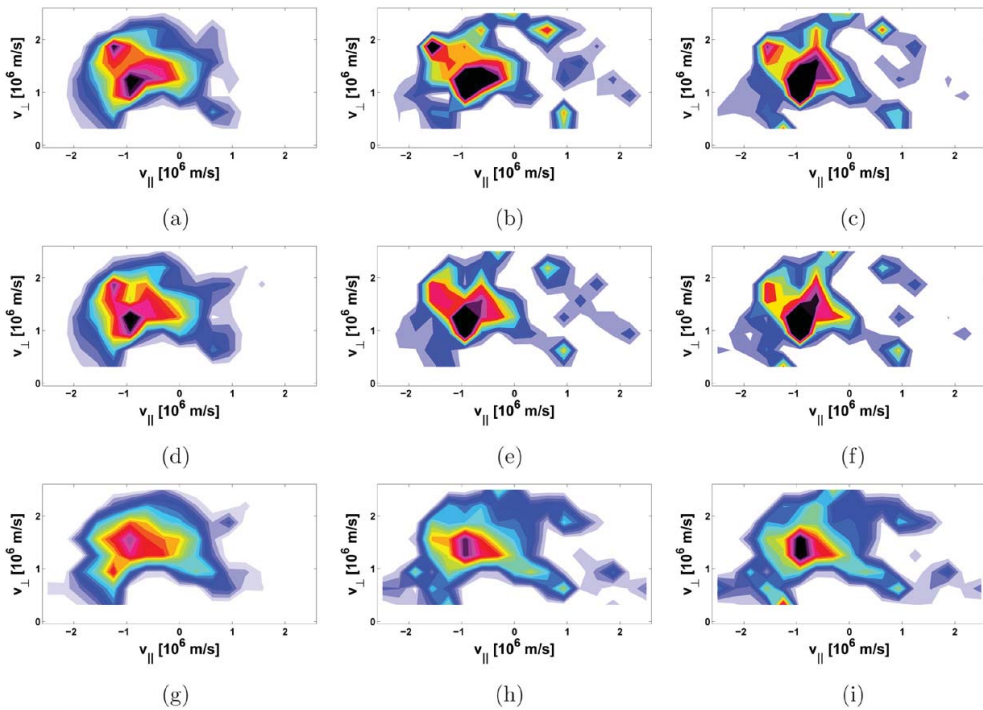


Figure 5. Doppler images from synthetic FIDA spectra (left column), from measured FIDA spectra (center column) and from filtered, measured FIDA spectra (right column). The number of singular values is 70 in the uppermost row, 60 in the center row and 50 in the bottom row. (a) Synthetic, 70 SV, (b) measured, 70 SV, (c) filtered, 70 SV, (d) synthetic, 60 SV, (e) measured, 60 SV, (f) filtered, 60 SV, (g) synthetic, 50 SV, (h) measured, 50 SV, (i) filtered, 50 SV.

dimension in fusion plasma Doppler tomography would likely improve the inference.

Astrophysical and fusion plasma Doppler tomography are photon-starved compared with many position-space tomography applications: The data is often scarce and the signal-to-noise ratio unfavourable. A spectrum in astrophysical Doppler tomography is analogous to a set of measurements with parallel or fanned beams along a LOS in position-space tomography. In astrophysical Doppler tomography the number of spectra or LOS's is limited by the signal-to-noise ratio, so that typically much fewer LOS's are used in astrophysical Doppler tomography (tens) than in position-space tomography (hundreds). In fusion plasmas actually only one LOS would be necessary for a measurement without noise since the fast-ion velocity distribution function is rotationally symmetric to a good approximation. However, due to noise in practise we need to use all available fast-ion measurements. So far three LOS's have been used and this may be increased to seven or eight LOS's in the future. In fusion plasma Doppler tomography at ASDEX Upgrade, we can combine the FIDA measurements with other measurements [22] such as collective Thomson scattering [20, 48–51], neutron emission spectroscopy or neutron yield measurements [52–56] or gamma-ray spectroscopy [57]. Similar combinations are possible at the tokamak DIII-D [27, 45], the stellarator LHD [58–60] or the spherical tokamak MAST [61–63]

as well as the next step fusion experiment ITER [64–69]. In astrophysical Doppler tomography, one can use several emission lines from various elements such as hydrogen, helium, or calcium [34].

The astrophysical Doppler tomography allows for a systemic velocity γ along the LOS. This velocity is analogous to perpendicular drift in tokamak plasmas, such as the often dominant $\mathbf{E} \times \mathbf{B}$ -drift or the often smaller grad-B, curvature or polarization drifts. Since parallel velocities are allowed in fusion plasma Doppler tomography, any drift velocities parallel to the magnetic field can already be handled, but not perpendicular drift velocities. It should be possible and beneficial to introduce a perpendicular drift velocity in the fusion plasma Doppler tomography approach as well, in particular when applied to the thermal ion population. This would possibly allow us to infer the perpendicular drift velocity and would probably also improve the Doppler image itself.

If there is a significant magnetic field, the line emission has finer structure. A moving D-atom in a magnetic field experiences an electric field in its own rest frame which causes the Balmer alpha line to split into 15 lines. This is referred to as Stark splitting. Stark shifts are usually substantially larger than Zeeman shifts which occur due to the magnetic field. Stark shifts are routinely accounted for in fusion plasma Doppler tomography by calculating the emission from the 15 lines and summing over them whereas Zeeman

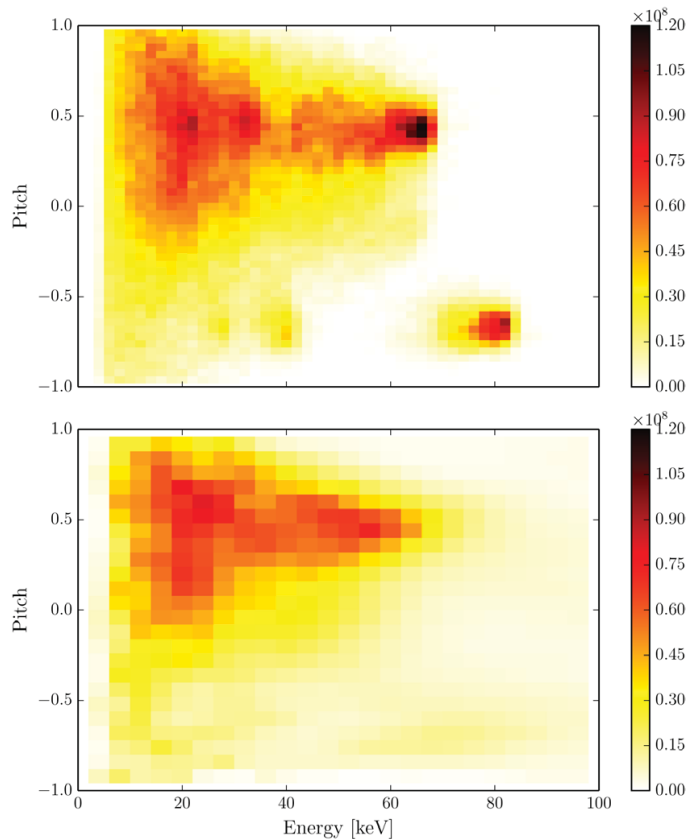


Figure 6. Simulation (up) and Doppler image (below) from synthetic measurements of a fast-ion velocity distribution function at the tokamak DIII-D. Here the function is presented in the widespread (energy, pitch)-coordinates with $E = 1/2 mv^2$ and $p = -v_{\parallel}/v$.

shifts are neglected. The effect of Stark splitting is significant for fusion plasmas [19]. In astrophysical Doppler tomography, Stark and Zeeman shifts have so far been neglected in Doppler tomography in binaries due to the large bulk velocities of the gas in the disc though Zeeman Doppler imaging has been successfully applied to resolve the stellar surfaces of magnetic stars. If the magnetic fields are strong, Stark and Zeeman shifts might also be a nuisance for Doppler tomography in binaries. They could be taken into account in astrophysical Doppler tomography in binaries analogous to fusion plasma Doppler tomography.

Finally, the inversion algorithms are readily transferable between astrophysical and nuclear fusion Doppler tomography. The formulation as a matrix problem is possible in astrophysics. Maximum entropy inversion algorithms are already used in both fields. The filtered back-projection method is widely used in astrophysics. A closely related method also using back-projection has been used in nuclear fusion Doppler tomography [20]. In this paper we borrowed the idea to filter the spectra and found that improvements may be possible with this technique. Filtering the measurement data is also a common technique in position-space

tomography. Improvement of inversion algorithms will clearly benefit both fields.

6. Conclusions

We outline basic principles of astrophysical and fusion plasma Doppler tomography by deriving projection equations and forward models from their common 3D framework. This enables us to derive the shape of observed spectra of light coming from accretion discs from the forward model of fusion plasma Doppler tomography. We present inversions of filtered measured spectra from the tokamak ASDEX Upgrade with the singular value decomposition method and of synthetic spectra with the maximum entropy method in preparation of Doppler tomography on the tokamak DIII-D. Prominent astrophysical Doppler images are discussed and compared with simulations. We already highlighted an example where an idea from one discipline was applied to the other. We further find that an inclusion of a perpendicular drift velocity in the fusion plasma forward model analogous to the systemic velocity of the binary in astrophysics will be valuable. Further, Stark and Zeeman splitting have so far been neglected in astrophysical Doppler

tomography of binaries whereas Stark splitting is routinely accounted for in fusion plasma Doppler tomography. One could introduce similar models for the line splitting in astrophysical Doppler tomography even though additional models of the magnetic field would be required. Similar approaches have been successfully applied to image stellar surfaces of magnetic stars. Ideas in the inversion algorithms are readily transferable, for example the formulation as matrix equation used for fusion plasmas, filtering in linear methods to reduce noise, or different formulations of the entropy. In conclusion, using Doppler tomography we can conveniently map measured spectra into images that are much more straightforward to interpret and at the same time offer quantitative tests against models.

Acknowledgments

This project has received funding from the Euratom research and training programme 2014–2018 and from the European Union’s Horizon 2020 research and innovation programme under grant agreement number 633053. The views and opinions expressed herein do not necessarily reflect those of the European Commission.

References

- [1] Salewski M *et al* 2014 *Nucl. Fusion* **54** 023005
- [2] Marsh T and Horne K 1988 *Mon. Not. R. Astron. Soc.* **235** 269–86
- [3] Marsh T 2001 *Astromotography, Indirect Imaging Methods in Observational Astronomy, Doppler tomography Lecture Notes in Physics* vol 573 (Berlin: Springer) pp 1–26
- [4] Marsh T R 2005 *Astrophys. Space Sci.* **296** 403–15
- [5] Steeghs D 2004 *Astronomische Nachr.* **325** 185–8
- [6] Morales-Rueda L 2004 *Astronomische Nachr.* **325** 193–6
- [7] Schwöpe A D *et al* 2004 *Astronomische Nachr.* **325** 197–200
- [8] Richards M T 2004 *Astronomische Nachr.* **325** 229–32
- [9] VrtiLek S *et al* 2004 *Astronomische Nachr.* **325** 209–12
- [10] Gruber O *et al* 2007 *Nucl. Fusion* **47** S622–34
- [11] Kallenbach A *et al* 2012 *IEEE Trans. Plasma Sci.* **40** 605–13
- [12] Stroth U *et al* 2013 *Nucl. Fusion* **53** 104003
- [13] Heidbrink W W *et al* 2004 *Plasma Phys. Control. Fusion* **46** 1855–75
- [14] Heidbrink W W 2010 *Rev. Sci. Instrum.* **81** 10D727
- [15] Geiger B *et al* 2011 *Plasma Phys. Control. Fusion* **53** 065010
- [16] Geiger B *et al* 2013 *Rev. Sci. Instrum.* **84** 113502
- [17] Geiger B *et al* 2014 *Nucl. Fusion* **54** 022005
- [18] Geiger B *et al* 2014 Quantification of the impact of large and small scale instabilities on the fast-ion confinement in ASDEX Upgrade, submitted
- [19] Salewski M *et al* 2014 *Plasma Phys. Control. Fusion* **56** 105005
- [20] Salewski M *et al* 2011 *Nucl. Fusion* **51** 083014
- [21] Salewski M *et al* 2012 *Nucl. Fusion* **52** 103008
- [22] Salewski M *et al* 2013 *Nucl. Fusion* **53** 063019
- [23] Smak J 1969 *Acta Astron.* **19** 155–64
- [24] Smak J 1981 *Acta Astron.* **31** 395–408
- [25] Horne K and Marsh T R 1986 *Mon. Not. R. Astron. Soc.* **218** 761–73
- [26] Horne K 1995 *Astron. Astrophys.* **297** 273–84
- [27] Stagner L *et al* 2013 *Bull. Am. Phys. Soc.* **58** BP8.00104
- [28] Skilling J and Bryan R K 1984 *Mon. Not. R. Astron. Soc.* **211** 111
- [29] Steeghs D and Casares J 2002 *Astrophys. J.* **568** 273–8
- [30] Bassa C G *et al* 2009 *Mon. Not. R. Astron. Soc.* **399** 2055–62
- [31] Marsh T, Robinson E and Wood J 1994 *Mon. Not. R. Astron. Soc.* **266** 137–54
- [32] Neilsen J, Steeghs D and Vrtilek S D 2008 *Mon. Not. R. Astron. Soc.* **384** 849–62
- [33] Bloemen S *et al* 2010 *Mon. Not. R. Astron. Soc.* **407** 1903–12
- [34] van Spaendonk L *et al* 2010 *Mon. Not. R. Astron. Soc.* **401** 1857–68
- [35] Steeghs D, Harlaftis E T and Horne K 1997 *Mon. Not. R. Astron. Soc.* **290** L28–32 (arXiv: astro-ph/9708005)
- [36] Steeghs D and Stehle R 1999 *Mon. Not. R. Astron. Soc.* **307** 99–110
- [37] Harlaftis E T *et al* 1999 *Mon. Not. R. Astron. Soc.* **306** 348–52
- [38] Roelofs G H A *et al* 2006 *Mon. Not. R. Astron. Soc.* **371** 1231–42
- [39] Copperwheat C M *et al* 2012 *Mon. Not. R. Astron. Soc.* **421** 149–58
- [40] Ertl K *et al* 1996 *Nucl. Fusion* **36** 1477–88
- [41] Anton M *et al* 1996 *Plasma Phys. Control. Fusion* **38** 1849–78
- [42] Kak A and Slaney M 1988 *Principles of Computerized Tomographic Imaging* (New York: IEEE Press)
- [43] Herman G 2009 *Fundamentals of Computerized Tomography* 2nd edn (New York: Springer)
- [44] Egedal J and Bindslev H 2004 *Phys. Plasmas* **11** 2191
- [45] Heidbrink W W *et al* 2007 *Plasma Phys. Control. Fusion* **49** 1457–75
- [46] Heidbrink W W *et al* 2011 *Commun. Comput. Phys.* **10** 716–41
- [47] Hansen P C 1992 *SIAM Rev.* **34** 561–80
- [48] Meo F *et al* 2008 *Rev. Sci. Instrum.* **79** 10E501
- [49] Salewski M *et al* 2010 *Nucl. Fusion* **50** 035012
- [50] Meo F *et al* 2010 *J. Phys.: Conf. Ser.* **227** 012010
- [51] Furtula V *et al* 2012 *Rev. Sci. Instrum.* **83** 013507
- [52] Giacomelli L *et al* 2011 *Rev. Sci. Instrum.* **82** 123504
- [53] Tardini G *et al* 2012 *J. Instrum.* **7** C03004
- [54] Tardini G *et al* 2013 *Nucl. Fusion* **53** 063027
- [55] Jacobsen A S *et al* 2014 *Rev. Sci. Instrum.* **85** 11E103
- [56] Jacobsen A S 2014 Velocity-space sensitivity of neutron emission spectroscopy, submitted
- [57] Nocente M *et al* 2012 *Nucl. Fusion* **52** 094021
- [58] Kubo S *et al* 2010 *Rev. Sci. Instrum.* **81** 10D535
- [59] Nishiura M *et al* 2014 *Nucl. Fusion* **54** 023006
- [60] Ito T *et al* 2010 *Rev. Sci. Instrum.* **81** 10D327
- [61] Michael C A *et al* 2013 *Plasma Phys. Control. Fusion* **55** 095007
- [62] Jones O M *et al* 2013 *Plasma Phys. Control. Fusion* **55** 085009
- [63] Jones O M *et al* 2014 arXiv: 1401.6864
- [64] Salewski M *et al* 2008 *Rev. Sci. Instrum.* **79** 10E729
- [65] Salewski M *et al* 2009 *Nucl. Fusion* **49** 025006
- [66] Salewski M *et al* 2009 *Plasma Phys. Control. Fusion* **51** 035006
- [67] Kappatou A *et al* 2012 *Nucl. Fusion* **52** 043007
- [68] Bertalot L *et al* 2012 *J. Instrum.* **7** C04012
- [69] Chugunov I N *et al* 2011 *Nucl. Fusion* **51** 083010

Reference [8]

[8]. M Salewski et al. (2015) *Nuclear Fusion* **55** 093029. Velocity-space observation regions of high-resolution two-step reaction gamma-ray spectroscopy

Velocity-space observation regions of high-resolution two-step reaction gamma-ray spectroscopy

M. Salewski¹, M. Nocente^{2,3}, G. Gorini^{2,3}, A.S. Jacobsen¹, V.G. Kiptily⁴, S.B. Korsholm¹, F. Leipold¹, J. Madsen¹, D. Moseev⁵, S.K. Nielsen¹, J. Rasmussen¹, M. Stejner¹, M. Tardocchi³ and JET Contributors^{6,a}

¹ Department of Physics, Technical University of Denmark, DK-2800 Kgs. Lyngby, Denmark

² Department of Physics, University of Milano Bicocca, 20126 Milano, Italy

³ Istituto di Fisica del Plasma, Consiglio Nazionale delle Ricerche, 20125 Milano, Italy

⁴ CCFE, Culham Science Centre, Abingdon, Oxfordshire, OX14 3DB, UK

⁵ Max Planck Institute for Plasma Physics, 17491 Greifswald, Germany

⁶ EUROfusion Consortium, JET, Culham Science Centre, Abingdon, Oxfordshire, OX14 3DB, UK

E-mail: msal@fysik.dtu.dk

Received 18 May 2015, revised 15 July 2015

Accepted for publication 21 July 2015

Published 21 August 2015



CrossMark

Abstract

High-resolution γ -ray spectroscopy (GRS) measurements resolve spectral shapes of Doppler-broadened γ -rays. We calculate weight functions describing velocity-space sensitivities of any two-step reaction GRS measurements in magnetized plasmas using the resonant nuclear reaction ${}^9\text{Be}(\alpha, n\gamma){}^{12}\text{C}$ as an example. The energy-dependent cross sections of this reaction suggest that GRS is sensitive to alpha particles above about 1.7 MeV and highly sensitive to alpha particles at the resonance energies of the reaction. Here we demonstrate that high-resolution two-step reaction GRS measurements are not only selective in energy but also in pitch angle. They can be highly sensitive in particular pitch angle ranges and completely insensitive in others. Moreover, GRS weight functions allow rapid calculation of γ -ray energy spectra from fast-ion distribution functions, additionally revealing how many photons any given alpha-particle velocity-space region contributes to the measurements in each γ -ray energy bin.

Keywords: gamma-ray spectroscopy, energetic particles, tokamaks

(Some figures may appear in colour only in the online journal)

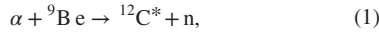
1. Introduction

Gamma-ray spectroscopy (GRS) is an essential diagnostic to study fast ions in fusion plasmas [1, 2]. Early GRS measurements in tokamaks have been made at Doublet-III [3], TFTR [4], JET [5–13] and JT-60U [14, 15]. More recently, high-resolution GRS measurements have been made at JET [16–21] and ASDEX Upgrade [22] thanks to the development of new detectors [18, 23]. GRS is particularly well-suited for large, hot devices such as JET [5–13, 16–21], ITER [24] or DEMO [25] since high temperatures enhance fusion reaction rates and hence γ -ray fluxes [1, 2].

^a See the appendix of [83].

Many nuclear reactions in hot fusion plasmas lead to γ -ray emission [1, 2]. At JET, several species including alpha particles, helium-3, deuterium or hydrogen have been measured using GRS [5–13, 16–21]. These fast ions are generated in fusion reactions, by ion cyclotron resonance heating (ICRH) or by neutral beam injection (NBI) [7]. γ -rays are emitted when fast ions react with bulk plasma ions or with low-mass impurities such as lithium, beryllium, boron, carbon or oxygen [7]. Fast alpha particles are of particular interest as they are produced at an energy of 3.5 MeV in the most important fusion reaction $\text{T}(\text{D},\text{n})\alpha$, which will release most of the fusion power in future burning plasmas. Fast alpha particles can undergo resonant nuclear reactions with low-mass

impurities allowing GRS measurements with high signal-to-noise ratio [26]. Here we consider the reaction ${}^9\text{Be}(\alpha, n\gamma){}^{12}\text{C}$ [8, 27], which has been proposed for studies of alpha particles in ITER where beryllium is the first-wall material. This reaction has regularly been studied at JET [7–10, 12, 16, 17, 19, 21] and has become all the more important at JET since the installation of the ITER-like beryllium wall [28, 29]. The reaction happens in two steps. (1) An alpha particle and ${}^9\text{Be}$ react to form excited ${}^{12}\text{C}^*$ and a neutron. (2) The excited ${}^{12}\text{C}^*$ rapidly decays to ground-state ${}^{12}\text{C}$ emitting a γ -photon:



The energy release of the reaction is $Q = 5.70$ MeV of which $E_{\gamma 0} = 4.44$ MeV is required to populate the excited state ${}^{12}\text{C}^*$. This is also the rest frame energy of the γ -photon that is emitted when ${}^{12}\text{C}^*$ decays to the ground state. The remaining $Q^* = 1.26$ MeV becomes kinetic energy of the reaction products ${}^{12}\text{C}^*$ and the neutron in addition to the initial kinetic energies of the fast alpha and the thermal ${}^9\text{Be}$. γ -photons are Doppler-shifted due to the velocity component u_C of the ${}^{12}\text{C}^*$ nucleus along the line-of-sight of the detector. The Doppler-shifted energy E_γ of the detected γ -photon is

$$E_\gamma = E_{\gamma 0} \left(1 + \frac{u_C}{c} \right) \quad (3)$$

where c is the speed of light and u_C/c is typically on the order of 1%.

Each nuclear reaction emitting γ -rays forms a peak in the measured energy spectra. Such peaks are hence broadened by the Doppler shift according to equation (3). Recently, it has become possible to measure the spectral shapes of such peaks using high-resolution γ -ray spectrometers [2, 16–21]. Here we study sensitivities of such high-resolution GRS measurements to 2D fast-ion distribution functions typical for hot, magnetized plasmas. It is known from the energy dependence of the reaction cross sections (figure 1) that GRS measurements are highly sensitive to alpha particles near the resonance energies of the reaction at 1.9 MeV, 2.6 MeV, 4.0 MeV, 4.5 MeV, 5.0 MeV, 5.3 MeV and 5.75 MeV [30]. As the energies of thermal ${}^9\text{Be}$ impurities are negligible compared with the alpha particle energies, resonance peaks appear as semi-circular ridges in figure 1. The sensitivity to alpha particles with energies below 1.7 MeV is poor. (At 1.7 MeV the sensitivity is about 10% of the sensitivity at the resonance maximum at 1.9 MeV). In this paper we show that the energies of the measured γ -photons from a particular reaction indicate not only the energies of the alpha particles but also their pitches. The pitch is defined as $p = v_{\parallel}/v$ where v_{\parallel} is the velocity component parallel to the magnetic field and v is the velocity magnitude. Energy and momentum conservation imply, together with the reaction cross sections, the existence of regions in 2D velocity space to which a measurement in a given energy range of the γ -photon is sensitive as well as regions to which the measurement is completely insensitive.

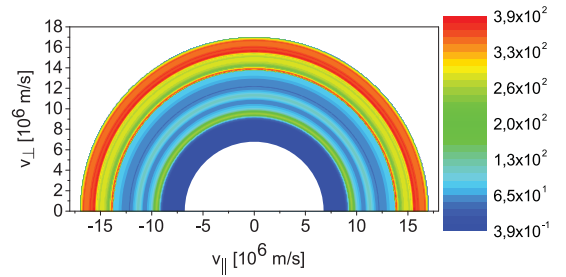


Figure 1. Reaction cross sections (millibarn) of the ${}^9\text{Be}(\alpha, n\gamma){}^{12}\text{C}$ reaction as a function of $(v_{\parallel}, v_{\perp})$ of the alpha particle for energies up to 6 MeV corresponding to a velocity magnitude $v = 17 \times 10^6 \text{ m s}^{-1}$. The resonances appear at $v = (9.5, 11.1, 13.8, 14.7, 15.5, 15.9, 16.6) \times 10^6 \text{ m s}^{-1}$. Below the resonance at 1.9 MeV ($v = 9 \times 10^6 \text{ m s}^{-1}$) the cross sections become very small, and hence GRS is insensitive to particles populating the inner white region.

Such 2D velocity-space sensitivities of two-step reaction GRS measurements are described by weight functions analogous to those of fast-ion D_α (FIDA) [31, 32], collective Thomson scattering (CTS) [32, 33] and neutron emission spectrometry (NES) measurements [34, 35]. Our final goal is to infer 2D fast-ion velocity distribution functions by tomographic inversion using weight functions as we present here for GRS [33, 36, 37]. Whereas full tomographic inversion of GRS measurements cannot yet be achieved, the general method has been demonstrated using FIDA measurements at ASDEX Upgrade in MHD quiescent plasmas [37, 38] and in plasmas with sawteeth [39]. A comparison of the tomographic inversion before and after a sawtooth crash showed a strong dependence of the fast-ion redistribution on pitch. Whereas these measurements relied on FIDA, all available fast-ion diagnostics can in principle be combined, provided their weight functions are known [40]. Here we focus on three other useful applications of weight functions. First, weight functions provide significant insight into the velocity-space sensitivity of the diagnostic. They separate observable velocity-space regions from unobservable regions [31–35, 41–51, 52–62]. Second, they reveal the velocity-space origin of a measurement for a given 2D fast-ion velocity distribution function [31–35, 41, 56–61, 63]. Third, they allow rapid calculation of synthetic measurements [32–35]. The formalism we present here allows these applications for two-step reaction GRS measurements.

In section 2 we show how to calculate GRS weight functions numerically using the GENESIS code as forward model [20, 64]. We present numerically calculated GRS weight functions to show the velocity-space observation regions typical for high-resolution GRS measurements at JET in section 3. To gain insight into the numerically calculated GRS weight functions, we consider the kinematics of the ${}^9\text{Be}(\alpha, n\gamma){}^{12}\text{C}$ reaction based on energy and momentum conservation in section 4, which allows us to construct a tractable simplified model showing observable regions in section 5. We compare analytical and numerical approaches in section 6.

In section 7 we study the dependence of the GRS velocity-space sensitivities on key parameters. We calculate GRS measurements using weight functions in section 8 and show where in velocity space the measurements originate from for typical JET parameters. We discuss the potential application of GRS weight functions in future burning plasmas in section 9 and conclude in section 10.

2. Numeric computation of GRS weight functions

Weight functions, w , relate 2D fast-ion distribution functions, f , to measurements, s , according to [31–35, 41]

$$s(E_{\gamma,1}, E_{\gamma,2}, \phi) = \int_{\text{vol}} \int_0^\infty \int_{-\infty}^\infty w(E_{\gamma,1}, E_{\gamma,2}, \phi, v_{\parallel}, v_{\perp}, \mathbf{x}) f(v_{\parallel}, v_{\perp}, \mathbf{x}) dv_{\parallel} dv_{\perp} d\mathbf{x}. \quad (4)$$

For GRS measurements, $s(E_{\gamma,1}, E_{\gamma,2}, \phi)$ is the detection rate of γ -rays [photons/s] in the energy range $E_{\gamma,1} < E_{\gamma} < E_{\gamma,2}$ with a viewing angle ϕ between the line-of-sight of the GRS diagnostic and the magnetic field. $(v_{\parallel}, v_{\perp})$ are the velocities parallel and perpendicular to the magnetic field, respectively, and \mathbf{x} describes the spatial coordinates. We use 2D $(v_{\parallel}, v_{\perp})$ -coordinates rather than the equivalent and more widespread (energy, pitch)-coordinates for example used in the TRANSP code as our expressions are simpler in $(v_{\parallel}, v_{\perp})$ -coordinates. The fast-ion velocity distribution function f is a 2D function due to rotational symmetry of the full 3D fast-ion velocity distribution function. It is obtained by transforming to cylindrical coordinates and integrating over the ignorable gyroangle Γ : $f^{2D} = 2\pi v_{\perp} f^{3D}$. In cylindrical coordinates v_{\parallel} can be negative or positive whereas v_{\perp} is always positive. The units of f in equation (4) are $[\text{s}^2\text{m}^{-5}]$ due to multiplication of f^{3D} with the Jacobian v_{\perp} . The units of GRS weight functions are thus $(\text{photons}/(\alpha\text{-particle} \times \text{s}))$.

Weight functions of any fast-ion diagnostic can be found numerically using a forward model that can predict a measurement for an arbitrary fast-ion distribution function. In this numerical approach we calculate energy spectra of γ -rays emitted due to a small collection of N_f fast alpha particles whose velocities $(v_{\parallel}, v_{\perp})$ are varied to scan the area of interest in velocity space. This formalism is analogous to numeric computation of weight functions for FIDA [31, 38], CTS [33] and NES [34, 35]. This collection of fast ions at phase-space position $(\mathbf{x}_0, v_{\parallel 0}, v_{\perp 0})$ has a fast-ion distribution function f_{δ} of the form

$$f_{\delta}(v_{\parallel}, v_{\perp}, \mathbf{x}) = N_f \delta(v_{\parallel} - v_{\parallel 0}) \delta(v_{\perp} - v_{\perp 0}) \delta(\mathbf{x} - \mathbf{x}_0). \quad (5)$$

Substitution into equation (4) and integration gives the amplitude of the weight function at phase-space position $(\mathbf{x}_0, v_{\parallel 0}, v_{\perp 0})$:

$$w(E_{\gamma,1}, E_{\gamma,2}, \phi, v_{\parallel 0}, v_{\perp 0}, \mathbf{x}_0) = \frac{s_{\delta}(E_{\gamma,1}, E_{\gamma,2}, \phi)}{N_f}. \quad (6)$$

GRS weight functions show the incident rate of γ -photons between two γ -ray energies viewed at angle ϕ per alpha particle at phase-space position $(\mathbf{x}_0, v_{\parallel 0}, v_{\perp 0})$.

3. Observable regions of GRS measurements at JET

In this section we calculate GRS weight functions by the numerical approach given in equation (6) using the GENESIS code. Figures 2 and 3 show weight functions for observation angles of respectively $\phi = 90^\circ$ and $\phi = 30^\circ$ at Doppler shifts typical for high-resolution GRS measurements at JET. The coloured regions are observable whereas the white regions are unobservable. The amplitude shows the sensitivity of the measurement in $(\text{photons}/(\alpha\text{-particle} \times \text{s}))$. GRS measurements are indeed insensitive to energies below about 1.7 MeV and are most sensitive to alpha particles with energies at the resonance energies. These features are inherited from the cross sections of the reaction shown in figure 1. However, the weight functions reveal that GRS measurements are also highly selective in pitch.

For an observation angle of $\phi = 90^\circ$ and large Doppler shifts ($\Delta E_{\gamma} = E_{\gamma} - E_{\gamma 0} \gtrsim 45$ keV), GRS measurements are completely insensitive to ions with pitches $\sim \pm 1$. The unobservable regions become larger for larger Doppler shifts such that for very large Doppler shifts ($\Delta E_{\gamma} \sim 90$ keV), the measurements are only sensitive to pitches around zero. We will show in the following sections that the energy and momentum equations cannot be obeyed in the unobservable regions between 1.7 MeV and 6 MeV. Hence γ -photons with the given Doppler shifts cannot originate from these regions. For a Doppler shift of $\Delta E_{\gamma} \sim 30$ keV, the sensitivity of GRS measurements depends only weakly on the pitch. For low Doppler shifts ($\Delta E_{\gamma} \lesssim 15$ keV), the measurements are most sensitive to particles with pitches close to ± 1 on all resonances. We will explain this perhaps surprising result as a consequence of energy and momentum conservation as well as the projection of \mathbf{v}_c onto the line-of-sight in section 7. The redshifted side is identical to the blueshifted side at the same Doppler shift magnitude (figures 2(a) and (c)) corresponding to the expectation to observe spectra that are symmetric about the peak energy.

We illustrate typical velocity-space observation regions of the other high-resolution γ -ray spectrometer at an observation angle $\phi = 30^\circ$ and various Doppler shifts in figure 3. For any Doppler shift there are pitch ranges that are completely unobservable at $\phi = 30^\circ$. As for $\phi = 90^\circ$ the unobservable regions grow with the Doppler shift. The observable regions are now biased towards either positive or negative pitches. The blueshifted side ($\Delta E_{\gamma} > 0$) is most sensitive to co-going particles for large Doppler shifts ($\Delta E_{\gamma} \gtrsim 30$ keV). For very large Doppler shifts ($\Delta E_{\gamma} \gtrsim 75$ keV) the measurement is not sensitive to particles with negative pitches at all. The redshifted side is always a mirror image of the blueshifted side at the same Doppler shift magnitude (figures 3(a) and (c)). For low Doppler shifts ($\Delta E_{\gamma} \lesssim 15$ keV), the measurements are most sensitive to trapped particles with pitches close to zero. This again perhaps surprising result will also be explained in section 7.

Thus we find that firstly GRS measurements are highly selective in pitch depending on the observation angle and the Doppler shift. Secondly, the pitch selectivity for both view

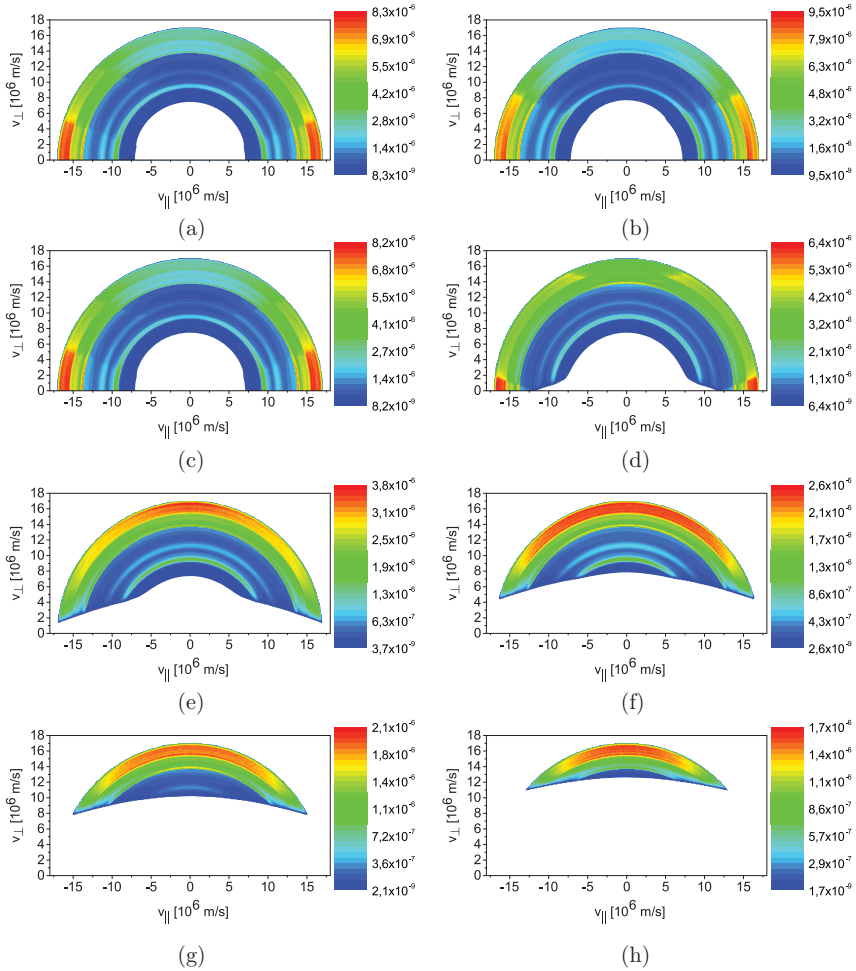


Figure 2. Full GRS weight functions w (photons/ $(\alpha$ -particle \times s)) for $\phi = 90^\circ$ and various Doppler-shifted energies ΔE_γ of the γ -photons. The γ -ray energy bin width is $E_{\gamma,1} - E_{\gamma,2} = 1$ keV. We assume $n_{Be} = 10^{18} \text{ m}^{-3}$. Note that the colour scale is different in each plot. (a) $\Delta E_\gamma = -15$ keV. (b) $\Delta E_\gamma = 0$ keV. (c) $\Delta E_\gamma = 15$ keV. (d) $\Delta E_\gamma = 30$ keV. (e) $\Delta E_\gamma = 45$ keV. (f) $\Delta E_\gamma = 60$ keV. (g) $\Delta E_\gamma = 75$ keV. (h) $\Delta E_\gamma = 90$ keV.

changes depending on the Doppler shift. The latter is perhaps a surprising result that we will study using an analytic approach in the following sections.

4. Kinematics of the ${}^9\text{Be}(\alpha, n\gamma){}^{12}\text{C}$ reaction

The numeric computations of GRS weight functions is the most accurate way to characterize the velocity-space sensitivity of GRS measurements as the numeric GRS weight functions account for all physics modelled in the GENESIS code including the anisotropic differential cross sections of the ${}^9\text{Be}(\alpha, n\gamma){}^{12}\text{C}$ reaction [65]. However, the numeric approach provides limited insight and, for example, does not explain why large pitch ranges are not observable. In the following sections we seek to gain insight into the velocity-space

sensitivity of GRS measurements by constructing a simplified model of GRS weight functions based on the kinematics of the ${}^9\text{Be}(\alpha, n\gamma){}^{12}\text{C}$ reaction. The gyro-angle Γ of the alpha particle at the time of the reaction influences the measurable Doppler-shifted energy E_γ of a γ -photon emitted by ${}^{12}\text{C}^*$ due to conservation of energy and momentum. Motion of the alpha towards the detector tends to lead to blueshift whereas motion of the alpha away from the detector tends to lead to redshift. Here we establish this functional dependence. E_γ depends linearly on the line-of-sight velocity u_C of the carbon nucleus according to equation (3). u_C in turn can be related to the gyro-angle Γ of the alpha particle by energy and momentum conservation.

Our formalism is analogous to that for neutron emission spectrometry (NES) [35]. However, two nuisance parameters appear as the reaction kinematics in two-step reaction GRS is less constrained than in NES which relies on one-step

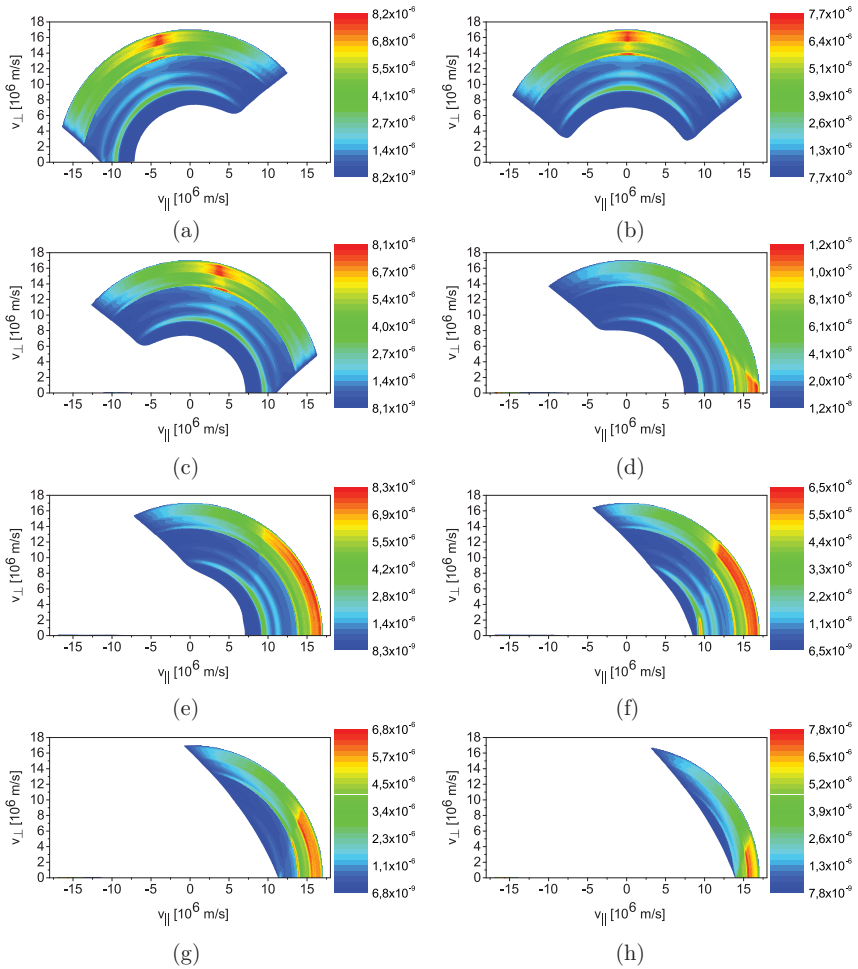


Figure 3. Full GRS weight functions w (photons/ $(\alpha$ -particle \times s)) for $\phi = 30^\circ$ and various Doppler-shifted energies ΔE_γ of the γ -photons. The γ -ray energy bin width is $E_{\gamma,1} - E_{\gamma,2} = 1$ keV. We assume $n_{Be} = 10^{18} \text{ m}^{-3}$. Note that the colour scale is different in each plot. (a) $\Delta E_\gamma = -15$ keV. (b) $\Delta E_\gamma = 0$ keV. (c) $\Delta E_\gamma = 15$ keV. (d) $\Delta E_\gamma = 30$ keV. (e) $\Delta E_\gamma = 45$ keV. (f) $\Delta E_\gamma = 60$ keV. (g) $\Delta E_\gamma = 75$ keV. (h) $\Delta E_\gamma = 90$ keV.

reactions. In one-step reaction NES we know the energy as well as the momentum of the neutrons produced in the reaction since only neutrons moving along the line-of-sight towards the detector are measured. In two-step reaction GRS measurements we neither know the energy nor the momentum of the $^{12}\text{C}^*$ produced in the reaction, but we know its velocity component u_C along the line-of-sight of the γ -ray detector as we know the energy of the γ -photon. The other two directions are described by the unknown angles β and ζ . These angles and the velocities and line-of-sight velocities of the $^{12}\text{C}^*$ and of the alpha particle relative to the line-of-sight and the local magnetic field are sketched in figure 4.

We neglect the gyro-motion of the $^{12}\text{C}^*$ as it decays after much shorter time than the cyclotron period. The decay time can be estimated from the intrinsic half-width of the 4.44 MeV level, $\Delta E_{\gamma,0} = 5.4$ meV, to $\hbar/\Delta E_{\gamma,0} \sim 61$ fs [66] where \hbar is the

reduced Planck constant. The cyclotron period of fully ionized $^{12}\text{C}^*$ is about 60 ns for a magnetic field of 2.2 T, i.e. $\sim 10^6$ times larger. In our simplified model, we further neglect the energy and momentum of the thermal ^9Be impurities compared with the energy and momentum of the alpha particle. For a beryllium temperature of ~ 10 keV and an alpha particle energy of 2 MeV, the alpha-to-beryllium energy ratio is ~ 200 and the momentum ratio is ~ 10 . The GENESIS code accounts for the non-zero energy and momentum of beryllium. A calculation showed that non-zero beryllium temperatures blur the GRS weight functions somewhat but preserve their large-scale features. We do not show these temperature effects for brevity.

Hence the energy and momentum conservation equations for the first step (equation (1)) of the two-step reaction become, respectively,

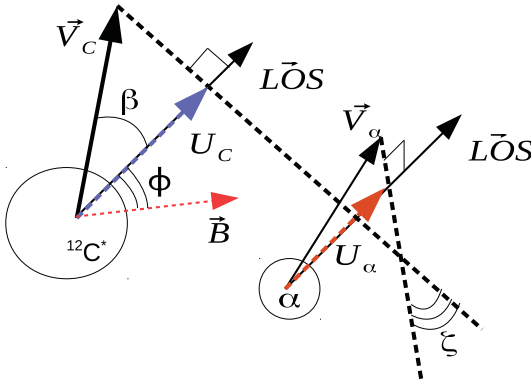


Figure 4. Sketch of the geometric relation between the magnetic field, the line-of-sight (LOS) and the velocities of the $^{12}\text{C}^*$ nucleus, \mathbf{v}_C , and the alpha particle, \mathbf{v}_α . The respective line-of-sight velocities are u_C and u_α . The dashed lines are perpendicular to the line-of-sight. The angles ϕ , β , ζ are defined as $\phi = \angle(\hat{\mathbf{v}}_{\text{LOS}}, \mathbf{B})$, $\beta = \angle(\hat{\mathbf{v}}_{\text{LOS}}, \mathbf{v}_C)$ and $\zeta = \angle(\hat{\mathbf{v}}_{\alpha, \text{LOS}}, \hat{\mathbf{v}}_{\text{LOS}})$.

$$\frac{1}{2}m_\alpha v_\alpha^2 + Q^* = \frac{1}{2}m_C v_C^2 + \frac{1}{2}m_n v_n^2, \quad (7)$$

$$m_\alpha \mathbf{v}_\alpha = m_C \mathbf{v}_C + m_n \mathbf{v}_n \quad (8)$$

where subscripts α , C and n refer to the alpha particle, the ^{12}C and the neutron, respectively. We solve equation (8) for \mathbf{v}_n and eliminate v_n^2 from the energy equation:

$$\frac{1}{2}m_\alpha v_\alpha^2 + Q^* = \frac{1}{2}m_C v_C^2 + \frac{1}{2m_n}(m_\alpha^2 v_\alpha^2 + m_C^2 v_C^2 - 2m_\alpha m_C \mathbf{v}_\alpha \cdot \mathbf{v}_C). \quad (9)$$

When equation (9) is solved for v_α , the solution may not conserve momentum but instead comply with $m_\alpha \mathbf{v}_\alpha = m_C \mathbf{v}_C - m_n \mathbf{v}_n$ rather than the correct momentum equation. This is checked for and excluded below. The dot product $\mathbf{v}_\alpha \cdot \mathbf{v}_C$ in equation (9) is calculated by introducing the line-of-sight velocities. The line-of-sight velocity u_C of ^{12}C can at once be calculated from the measured energies E_γ in high-resolution GRS according to equation (3). The line-of-sight velocity u_α of the alpha leaves a signature in the γ -ray spectra through the momentum and the energy equations whereas its velocity perpendicular to the line-of-sight enters through the energy equation only. Motivated by this observation, we split the velocity vectors of the ^{12}C and the alpha into components parallel and perpendicular to the line-of-sight,

$$\mathbf{v}_\alpha = u_\alpha \hat{\mathbf{v}}_{\text{LOS}} + \sqrt{v_\alpha^2 - u_\alpha^2} \hat{\mathbf{v}}_{\perp \alpha, \text{LOS}}, \quad (10)$$

$$\mathbf{v}_C = u_C \hat{\mathbf{v}}_{\text{LOS}} + \sqrt{v_C^2 - u_C^2} \hat{\mathbf{v}}_{\perp C, \text{LOS}} \quad (11)$$

where $\hat{\mathbf{v}}_{\text{LOS}}$ is the unit vector along the line-of-sight towards the detector and $\hat{\mathbf{v}}_{\perp \alpha, \text{LOS}}$ and $\hat{\mathbf{v}}_{\perp C, \text{LOS}}$ are unit vectors of the velocity components of the alpha particle and the carbon nucleus perpendicular to the line-of-sight, respectively. The line-of-sight velocity u_C and the total velocity v_C can be related according to

$$u_C = v_C \cos \beta \quad (12)$$

where $\beta \in [0, \pi]$ is the angle between $\hat{\mathbf{v}}_C$ and $\hat{\mathbf{v}}_{\text{LOS}}$ as sketched in figure 4. β is a random variable with a probability distribution which we will sample by Monte Carlo simulations. As v_C is the magnitude of \mathbf{v}_C , u_C and $\cos \beta$ have the same sign.

The dot product in equation (9) becomes

$$\mathbf{v}_\alpha \cdot \mathbf{v}_C = u_\alpha u_C + \cos \zeta \sqrt{(v_\alpha^2 - u_\alpha^2)(v_C^2 - u_C^2)} \quad (13)$$

where $\zeta \in [0, 2\pi]$ is the angle between $\hat{\mathbf{v}}_{\perp \alpha, \text{LOS}}$ and $\hat{\mathbf{v}}_{\perp C, \text{LOS}}$ as sketched in figure 4. ζ is, as β , a random variable with a probability distribution which we sample by Monte Carlo simulation. For the special cases that \mathbf{v}_α or \mathbf{v}_C has no velocity component perpendicular to the line-of-sight, the dot product becomes

$$\mathbf{v}_\alpha \cdot \mathbf{v}_C = u_\alpha u_C \quad (14)$$

as $u_\alpha^2 = v_\alpha^2$ or $u_C^2 = v_C^2$. Then ζ is not defined, and the simplified dot product must be used. This simplified dot product appears for NES weight functions because detectable neutrons always move along the line-of-sight [35]. Substituting equation (13) into equation (9) we get

$$\frac{1}{2} \left(m_\alpha - \frac{m_\alpha^2}{m_n} \right) v_\alpha^2 + Q^* = \frac{1}{2} \left(m_C + \frac{m_C^2}{m_n} \right) v_C^2 - \frac{m_\alpha m_C}{m_n} \left(u_\alpha u_C + \cos \zeta \sqrt{(v_\alpha^2 - u_\alpha^2)(v_C^2 - u_C^2)} \right). \quad (15)$$

We eliminate v_C for $\beta \neq \pi/2$:

$$\frac{1}{2} \left(m_\alpha - \frac{m_\alpha^2}{m_n} \right) v_\alpha^2 + Q^* = \frac{1}{2} \left(m_C + \frac{m_C^2}{m_n} \right) \frac{u_C^2}{\cos^2 \beta} - \frac{m_\alpha m_C}{m_n} \left(u_\alpha u_C + \cos \zeta \sqrt{(v_\alpha^2 - u_\alpha^2)(u_C^2 / \cos^2 \beta - u_C^2)} \right). \quad (16)$$

For $\beta = \pi/2$, $u_C = 0$ according to equation (12). The measured Doppler shift is zero for particles moving perpendicular to the line-of-sight. To simplify the algebra, we take $m_\alpha = 4m_n$ and $m_C = 12m_n$. Using $1/\cos^2 \beta - 1 = \tan^2 \beta$ we find

$$\frac{Q^*}{6m_n} - v_\alpha^2 - 13 \frac{u_C^2}{\cos^2 \beta} + 8 \left(u_\alpha u_C + \cos \zeta \sqrt{(v_\alpha^2 - u_\alpha^2) u_C^2 \tan^2 \beta} \right) = 0. \quad (17)$$

v_α and u_α are given by

$$v_\alpha^2 = v_{\parallel}^2 + v_{\perp}^2 \quad (18)$$

and [33]

$$u_\alpha = v_{\parallel} \cos \phi + v_{\perp} \sin \phi \cos \Gamma \quad (19)$$

where ϕ is the angle between the line-of-sight and the magnetic field at the position we consider as sketched in figure 4. Γ is the gyro-angle. Substitution gives

$$\begin{aligned} \frac{Q^*}{6m_n} - v_{\parallel}^2 - v_{\perp}^2 - 13 \frac{u_C^2}{\cos^2 \beta} + 8(v_{\parallel} \cos \phi + v_{\perp} \sin \phi \cos \Gamma) u_C \\ + 8 \cos \zeta \sqrt{(v_{\parallel}^2 + v_{\perp}^2 - (v_{\parallel} \cos \phi + v_{\perp} \sin \phi \cos \Gamma)^2) u_C^2 \tan^2 \beta} \\ = 0. \end{aligned} \quad (20)$$

This is an implicit functional relationship between the gyro-angle Γ of the alpha particle and the measurable u_C showing that the measurable energy E_γ depends on the gyro-angle Γ of the alpha particle for each point in 2D velocity space.

5. Analytic model of GRS probability functions

Equation (20) contains the gyroangle Γ which can take any value in $[0, 2\pi]$. The probability distribution is uniform to a good approximation:

$$\text{pdf}_\Gamma = \frac{1}{2\pi}. \quad (21)$$

The relation between the measurable u_C and the gyro-angle Γ of the alpha particle in equation (20) then allows us to calculate the probability that a detected γ -photon lies in a given energy range between $E_{\gamma,1}$ and $E_{\gamma,2}$ as we will show in this section. As this probability is a function of the observation angle ϕ and the position in velocity space, it is written as $\text{prob}(E_{\gamma,1} < E_\gamma < E_{\gamma,2} | \phi, v_{\parallel}, v_{\perp})$ where the conditioning symbol $|$ means ‘given’. The probability function is related to the weight function by a detection rate function $R(v_{\parallel}, v_{\perp}, \mathbf{x})$ defined as the detection rate of photons per alpha particle per second irrespective of the γ -ray energy in units (photons/ $(\alpha$ -particle \times s)). The weight function w is obtained if we multiply the total detection rate per ion R with the probability that the detected γ -photon is in a particular energy range:

$$w(E_{\gamma,1}, E_{\gamma,2}, \phi, v_{\parallel}, v_{\perp}, \mathbf{x}) = R(v_{\parallel}, v_{\perp}, \mathbf{x}) \times \text{prob}(E_{\gamma,1} < E_\gamma < E_{\gamma,2} | \phi, v_{\parallel}, v_{\perp}). \quad (22)$$

This relation has similarly been introduced to normalize FIDA and NES weight functions [32, 35]. $R(v_{\parallel}, v_{\perp}, \mathbf{x})$ hence has the same units as weight functions whereas the probabilities functions are dimensionless numbers between 0 and 1. $R(v_{\parallel}, v_{\perp}, \mathbf{x})$ depends on the production rate of γ -photons per alpha particle, on how many of the produced γ -photons reach the detector, and on how efficiently the γ -photons at the detector are detected. Energy and momentum conservation determine the boundaries of the probability functions $\text{prob}(E_{\gamma,1} < E_\gamma < E_{\gamma,2} | \phi, v_{\parallel}, v_{\perp})$ in $(v_{\parallel}, v_{\perp})$ -space and hence ultimately the boundaries of weight functions separating the observable regions from the unobservable regions. The amplitudes of the probability functions and the full weight functions also depend on the reaction cross sections.

We compute $R(v_{\parallel}, v_{\perp}, \mathbf{x})$ using the GENESIS code by allowing all possible E_γ :

$$R(v_{\parallel 0}, v_{\perp 0}, \mathbf{x}_0) = \frac{s_\delta(E_{\gamma,1} = 0, E_{\gamma,2} \rightarrow \infty, \phi)}{N_\gamma}. \quad (23)$$

An example of a numerically calculated rate function for the ${}^9\text{Be}(\alpha, n\gamma){}^{12}\text{C}$ reaction is shown in figure 5. The rate function is, as the cross sections, symmetric in pitch angle. The numbers of detectable γ -photons per ion are enhanced at the resonances.

In the following we calculate probability functions introduced in equation (22) using equation (20). The angles β

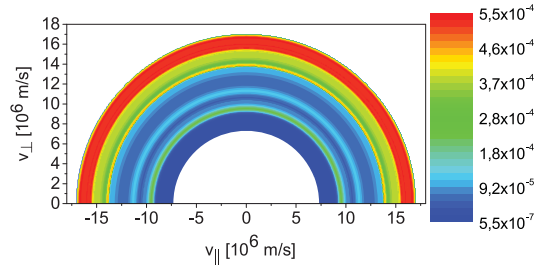


Figure 5. Rate function R (photons/ $(\alpha$ -particle \times s)) showing the number of detectable γ -photons per alpha particle at $\phi = 90^\circ$ as a function of alpha particle velocities. The photons can have any energy. We assume $n_{\text{Be}} = 10^{18} \text{ m}^{-3}$. The resonances appear at $v = (9.5, 11.1, 13.8, 14.7, 15.5, 15.9, 16.6) \times 10^6 \text{ m s}^{-1}$.

and ζ are random variables for which probability distribution functions $\text{pdf}(\beta, \zeta | v_{\parallel}, v_{\perp}, \phi)$ can be computed numerically using the GENESIS code. The probability function $\text{prob}(E_{\gamma,1} < E_\gamma < E_{\gamma,2} | v_{\parallel}, v_{\perp}, \phi)$ can be calculated by transforming to probabilities in u_C according to

$$\begin{aligned} \text{prob}(E_{\gamma,1} < E_\gamma < E_{\gamma,2} | v_{\parallel}, v_{\perp}, \phi) &= \text{prob}(u_{C,1} < u_C < u_{C,2} | v_{\parallel}, v_{\perp}, \phi) \\ &= \int_{u_{C,1}}^{u_{C,2}} \text{pdf}(u_C | v_{\parallel}, v_{\perp}, \phi) du_C \\ &= \int_{\beta, \zeta} \int_{u_{C,1}}^{u_{C,2}} \text{pdf}(u_C | v_{\parallel}, v_{\perp}, \phi, \beta, \zeta) \text{pdf}(\beta, \zeta | v_{\parallel}, v_{\perp}, \phi) du_C d\beta d\zeta \end{aligned} \quad (24)$$

The integration limits in u_C can be directly calculated from equation (3) for the energy range of interest. The probability density function $\text{pdf}(u_C | v_{\parallel}, v_{\perp}, \phi, \beta, \zeta)$ can be calculated by solving equation (20) for u_C and then by sampling from the uniform probability density function in gyro-angle Γ (equation (21)).

To solve for u_C , we pull the always positive product $u_C \tan \beta$ in equation (17) in front of the square root:

$$\frac{Q^*}{6m_n} - v_\alpha^2 - 13 \frac{u_C^2}{\cos^2 \beta} + 8 \left(u_\alpha u_C + u_C \tan \beta \sqrt{v_\alpha^2 - u_\alpha^2} \cos \zeta \right) = 0. \quad (25)$$

The solutions of the quadratic equation in u_C are

$$\begin{aligned} u_C &= \frac{4}{13} \cos \beta \left(u_\alpha \cos \beta + \sin \beta \cos \zeta \sqrt{v_\alpha^2 - u_\alpha^2} \right) \\ &\pm \sqrt{\frac{\cos^2 \beta}{13} \left(\frac{16}{13} \left(u_\alpha \cos \beta + \sin \beta \cos \zeta \sqrt{v_\alpha^2 - u_\alpha^2} \right)^2 + \frac{Q^*}{6m_n} - v_\alpha^2 \right)}. \end{aligned} \quad (26)$$

A second option to calculate $\text{prob}(E_{\gamma,1} < E_\gamma < E_{\gamma,2} | v_{\parallel}, v_{\perp}, \phi)$ is to transform the problem from u_C -space to Γ -space according to

$$\text{pdf}(u_C | v_{\parallel}, v_{\perp}, \phi, \beta, \zeta) = \text{pdf}_\Gamma \left| \frac{d\Gamma}{du_C} \right| \quad (27)$$

which has the advantage that the integration of the constant pdf_Γ is straightforward. Hence the probability function can alternatively be calculated according to

$$\begin{aligned}
& \text{prob}(E_{\gamma,1} < E_{\gamma} < E_{\gamma,2} | v_{\parallel}, v_{\perp}, \phi) \\
&= \int_{\beta, \zeta} \sum_i \left| \int_{\Gamma_{1,i}}^{\Gamma_{2,i}} \text{pdf}_{\Gamma} \text{pdf}(\beta, \zeta | v_{\parallel}, v_{\perp}, \phi) d\Gamma \right| d\beta d\zeta \\
&= \int_{\beta, \zeta} \text{pdf}(\beta, \zeta | v_{\parallel}, v_{\perp}, \phi) \sum_i \left| \int_{\Gamma_{1,i}}^{\Gamma_{2,i}} \text{pdf}_{\Gamma} d\Gamma \right| d\beta d\zeta. \quad (28)
\end{aligned}$$

The integration limits in Γ must still be calculated. There are zero to four possible ranges in Γ corresponding to the range in u_C as we will show next. These are indicated as a sum over the index i in equation (28). As these ranges in Γ do not overlap, we sum over the mutually exclusive probabilities. We take the absolute value of the integral in Γ as the integral represents a probability and hence must be positive while we have $\Gamma_{1,i} > \Gamma_{2,i}$ for at least one interval, if there is a solution. In the last step we have used that $\text{pdf}(\beta, \zeta | v_{\parallel}, v_{\perp}, \phi)$ does not depend on Γ . We can now evaluate the integral in Γ :

$$\begin{aligned}
& \text{prob}(E_{\gamma,1} < E_{\gamma} < E_{\gamma,2} | v_{\parallel}, v_{\perp}, \phi) \\
&= \int_{\beta, \zeta} \text{pdf}(\beta, \zeta | v_{\parallel}, v_{\perp}, \phi) \sum_i \left| \frac{\Gamma_{2,i} - \Gamma_{1,i}}{2\pi} \right| d\beta d\zeta \quad (29)
\end{aligned}$$

To find the integration limits in Γ in equations (28) and (29), we isolate the square root in equation (17) and square:

$$\begin{aligned}
& \left(\frac{Q^*}{6m_n} - v_{\alpha}^2 - 13 \frac{u_C^2}{\cos^2 \beta} \right)^2 + 16u_C \left(\frac{Q^*}{6m_n} - v_{\alpha}^2 - 13 \frac{u_C^2}{\cos^2 \beta} \right) u_{\alpha} \\
&+ 64u_C^2 u_{\alpha}^2 \\
&= 64u_C^2 \tan^2 \beta \cos^2 \zeta (v_{\alpha}^2 - u_{\alpha}^2). \quad (30)
\end{aligned}$$

The solutions in u_{α} are for $u_C(\cos^2 \beta + \sin^2 \beta \cos^2 \zeta) \neq 0$

$$\begin{aligned}
u_{\alpha} &= \frac{13u_C^2 + \cos^2 \beta \left(v_{\alpha}^2 - \frac{Q^*}{6m_n} \right)}{8u_C(\cos^2 \beta + \sin^2 \beta \cos^2 \zeta)} \\
&\pm \sqrt{\frac{\sin^2 \beta \cos^2 \zeta \left(64u_C^2 v_{\alpha}^2 \cos^2 \beta (\cos^2 \beta + \sin^2 \beta \cos^2 \zeta) \right.}{64u_C^2 \cos^2 \beta (\cos^2 \beta + \sin^2 \beta \cos^2 \zeta)^2} \\
&\quad \left. - \left(\cos^2 \beta \left(\frac{Q^*}{6m_n} - v_{\alpha}^2 \right) - 13u_C^2 \right)^2 \right)}{64u_C^2 \cos^2 \beta (\cos^2 \beta + \sin^2 \beta \cos^2 \zeta)^2}. \quad (31)
\end{aligned}$$

Γ is then found from u_{α} by

$$\Gamma = \arccos \frac{u_{\alpha} - v_{\parallel} \cos \phi}{v_{\perp} \sin \phi}. \quad (32)$$

A second pair of solutions for $\Gamma \in [\pi, 2\pi]$ is given by

$$\Gamma' = 2\pi - \Gamma \quad (33)$$

as $\cos(2\pi - \Gamma) = \cos \Gamma$ and the arccosine function is defined in $[0, \pi]$ whereas $\Gamma \in [0, 2\pi]$. This is the functional dependence between Γ and u_C required to transform the integration limits. However, taking the square again introduces a spurious solution, i.e. a solution of the squared equation (30) but not of the original non-squared equation (17), which we check for and exclude below.

We note that our solution for Γ is valid for not completely parallel observation ($\sin \phi \neq 0$), velocity-space positions not exactly on the v_{\parallel} -axis ($v_{\perp} \neq 0$), non-zero Doppler-shifts ($u_C \neq 0, \cos \beta \neq 0$), and particles not moving exactly parallel to the line-of-sight ($u_{\alpha}^2 \neq v_{\alpha}^2$ and $u_C^2 \neq v_C^2$). The special cases not fulfilling these conditions could be treated individually, but we omit these special cases for brevity.

6. Comparison of analytically and numerically calculated GRS probability functions for given (β, ζ)

In this section we compare probability functions for given (β, ζ) as computed by the analytical and the numerical approaches. Equation (28) shows that the full probability function $\text{prob}(E_{\gamma,1} < E_{\gamma} < E_{\gamma,2} | v_{\parallel}, v_{\perp}, \phi)$ requires knowledge of the probability density function $\text{pdf}(\beta, \zeta | v_{\parallel}, v_{\perp}, \phi)$. Nevertheless, equation (20) allows analytic computation of probability functions for given (β, ζ) ,

$$\text{prob}(E_{\gamma,1} < E_{\gamma} < E_{\gamma,2} | \phi, v_{\parallel}, v_{\perp}, \beta, \zeta) = \sum_i \left| \frac{\Gamma_{2,i} - \Gamma_{1,i}}{2\pi} \right| \quad (34)$$

which must be integrated over (β, ζ) to obtain the full probability function:

$$\begin{aligned}
& \text{prob}(E_{\gamma,1} < E_{\gamma} < E_{\gamma,2} | v_{\parallel}, v_{\perp}, \phi) \\
&= \int_{\beta, \zeta} \text{pdf}(\beta, \zeta | v_{\parallel}, v_{\perp}, \phi) \text{prob}(E_{\gamma,1} < E_{\gamma} < E_{\gamma,2} | \phi, v_{\parallel}, v_{\perp}, \beta, \zeta) d\beta d\zeta \quad (35)
\end{aligned}$$

Both probability functions can be calculated with the numerical approach. The full probability function can be calculated from the numerically calculated quantities w and R according to

$$\begin{aligned}
& \text{prob}(E_{\gamma,1} < E_{\gamma} < E_{\gamma,2} | \phi, v_{\parallel 0}, v_{\perp 0}, \mathbf{x}_0) \\
&= \frac{w(E_{\gamma,1}, E_{\gamma,2}, \phi, v_{\parallel 0}, v_{\perp 0}, \mathbf{x}_0)}{R(v_{\parallel 0}, v_{\perp 0}, \mathbf{x}_0)}. \quad (36)
\end{aligned}$$

The probability $\text{prob}(E_{\gamma,1} < E_{\gamma} < E_{\gamma,2} | \phi, v_{\parallel}, v_{\perp}, \beta, \zeta)$ can also be calculated using the numerical approach by allowing only the given (β, ζ) -pair:

$$\begin{aligned}
& \text{prob}(E_{\gamma,1} < E_{\gamma} < E_{\gamma,2} | \phi, v_{\parallel}, v_{\perp}, \beta, \zeta) = \frac{w(E_{\gamma,1}, E_{\gamma,2}, \phi, v_{\parallel}, v_{\perp}, \mathbf{x}, \beta, \zeta)}{R(v_{\parallel}, v_{\perp}, \mathbf{x}, \beta, \zeta)} \\
&= \frac{s(E_{\gamma,1}, E_{\gamma,2}, \phi, \beta, \zeta)}{N_f R(v_{\parallel}, v_{\perp}, \mathbf{x}, \beta, \zeta)}. \quad (37)
\end{aligned}$$

As $\text{pdf}(\beta, \zeta | v_{\parallel}, v_{\perp}, \phi)$ is not known analytically, it is best to compare analytic and the numerical approach at given (β, ζ) . The probability functions $\text{prob}(E_{\gamma,1} < E_{\gamma} < E_{\gamma,2} | \phi, v_{\parallel}, v_{\perp}, \beta, \zeta)$ may be regarded as basic building blocks of full probability functions $\text{prob}(E_{\gamma,1} < E_{\gamma} < E_{\gamma,2} | \phi, v_{\parallel}, v_{\perp})$. As probability functions based on equation (20) neglect the momentum and energy of the thermal beryllium impurity, we also neglect these in the numeric computation by setting the beryllium temperature to zero. A comparison of the analytical and numerical probability functions for given (β, ζ) is presented in figure 6. The amplitudes are the probabilities of detected γ -photons

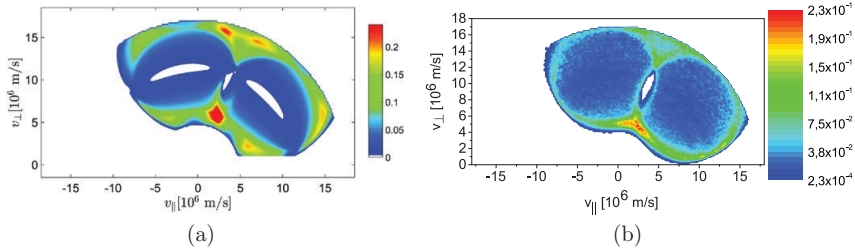


Figure 6. $\text{prob}(E_{\gamma,1} < E_{\gamma} < E_{\gamma,2} | \phi, v_{\parallel}, v_{\perp}, \beta, \zeta)$ for $E_{\gamma} = 15$ keV, $E_{\gamma,2} - E_{\gamma,1} = 1$ keV, $\phi = 30^{\circ}$, $\beta = 70^{\circ}$ and $\zeta = 10^{\circ}$ as computed by the analytic and numerical approaches. (a) Analytic. (b) Numeric.

to be within the given energy range. The analytical and the numerical approaches find the complex shape of this probability function in very good agreement. The amplitudes of the analytical and numerical probability functions are slightly different because (β, ζ) are not given in exact values but rather in a small ranges due to the finite numerical resolution. We have calculated the probability functions up to energies of 6 MeV corresponding to 17×10^6 m s⁻¹ as larger energies are usually not of interest. We have used this particular pair of (β, ζ) as this probability function has a particularly complex shape. The simpler shapes of probability functions for other (β, ζ) pairs computed with the numerical and the analytical approaches are similarly in very good agreement.

7. Parametric studies of the velocity-space sensitivity of GRS

In this section we study the velocity-space sensitivity of GRS measurements using simplified analytic expressions as shown in section 5. First we show examples of probability functions for fixed values of β and ζ . We will further present a simplified model for a full probability function by assuming a uniform probability distribution of (β, ζ) .

Figure 7 shows the impact of the observation angle ϕ and the Doppler-shifted energy of the γ -rays for $\beta = \angle(\hat{\mathbf{v}}_{\text{LOS}}, \mathbf{v}_{\text{C}}) = 10^{\circ}$ and $\zeta = \angle(\hat{\mathbf{v}}_{\perp, \text{LOS}}, \hat{\mathbf{v}}_{\perp, \text{C, LOS}}) = 0^{\circ}$. Typical observation angles for the two high-resolution GRS diagnostics at JET are $\phi = 90^{\circ}$ and $\phi = 30^{\circ}$. The Doppler shifts of the γ -rays are varied from $\Delta E_{\gamma} = -15$ keV to $\Delta E_{\gamma} = 60$ keV corresponding to projected velocities of the ¹²C from $u_{\text{C}} = -10^6$ m s⁻¹ to $u_{\text{C}} = 4 \times 10^6$ m s⁻¹ (equation (3)). These values are also typical for GRS measurements at JET. Blueshifted γ -rays have positive ΔE_{γ} whereas redshifted γ -rays have negative ΔE_{γ} . The forms and positions of these probability functions $\text{prob}(E_{\gamma,1} < E_{\gamma} < E_{\gamma,2} | \phi, v_{\parallel}, v_{\perp}, \beta, \zeta)$ are highly dependent on the Doppler-shifted energies and the observation angles. The amplitudes of $\text{prob}(E_{\gamma,1} < E_{\gamma} < E_{\gamma,2} | \phi, v_{\parallel}, v_{\perp}, \beta, \zeta)$ are large near their boundaries. This is also observed for CTS, FIDA, and NES weight functions for the typical spectral resolution of the measurements and is explained by the projection of the circular gyro-motion onto the line-of-sight which leads to high probabilities to observe velocities near the extremal values [32, 33, 35]. We further note the appearance of a low sensitivity region at a particular alpha particle energy in each probability

function which does not occur for FIDA, CTS or NES weight functions. For $\phi = 90^{\circ}$ (figures 7(a)–(c)) the probability functions are mirror symmetric about $v_{\parallel} = 0$ since v_{\parallel} appears only as the squared quantity v_{\parallel}^2 in equation (20) whereas the linear terms in v_{\parallel} vanish. The larger ΔE_{γ} is (or equivalently the larger u_{C} is), the larger the observable area covered by the probability functions is in alpha velocity space and the larger the velocities are. For the oblique line-of-sight with respect to the magnetic field at $\phi = 60^{\circ}$ (figures 7(d)–(f)), a bias towards positive v_{\parallel} for blueshifted E_{γ} is introduced into the probability functions. This bias comes from the terms $v_{\parallel} \cos \phi$ in equation (20). It becomes even stronger for $\phi = 30^{\circ}$ (figures 7(g)–(i)). These biases for oblique lines-of-sight occur for any β and ζ and hence leave a signature in the full GRS weight functions and make GRS measurements with oblique lines-of-sight selective in pitch towards either co-going or counter-going alpha particles. Lastly, we find that the observation regions for given β and ζ and redshift are mirror images of those for corresponding blueshifts (figures 7(j)–(l)) as also follows from equation (20). Similarly, observation regions for fixed β and ζ for an observation angle $\phi' = 180^{\circ} - \phi$ are mirror images to those at ϕ at the same Doppler shift.

In the following we calculate a simplified model of full probability functions $\text{prob}(E_{\gamma,1} < E_{\gamma} < E_{\gamma,2} | \phi, v_{\parallel}, v_{\perp})$ assuming that all angles β and ζ are equally likely. Then the pdf $(\beta, \zeta | v_{\parallel}, v_{\perp}, \phi)$ is uniform. Our results show that salient features of the GRS weight functions in figure 2 are reflected in similar features of either the rate function R in figure 5 or the corresponding probability function. The elevated sensitivity of weight functions at the resonances is inherited from the rate functions. In contrast, the pitch selectivity is inherited from the probability functions $\text{prob}(E_{\gamma,1} < E_{\gamma} < E_{\gamma,2} | \phi, v_{\parallel}, v_{\perp})$.

In figure 8 we show a simplified model of the full probability function $\text{prob}(E_{\gamma,1} < E_{\gamma} < E_{\gamma,2} | \phi, v_{\parallel}, v_{\perp})$ for a perpendicular observation angle $\phi = 90^{\circ}$ assuming uniform probability densities in (β, ζ) . The Doppler shifts are varied from 15 keV to 75 keV. The boundaries of the simplified probability functions are identical with the boundaries of full probability functions computed with the GENESIS code whereas the amplitudes may be different for probability densities in (β, ζ) accounting for anisotropic cross sections. The probability functions reveal completely unobservable regions as well as local maxima with elevated sensitivity. The local maxima in the probability functions make the GRS measurements highly

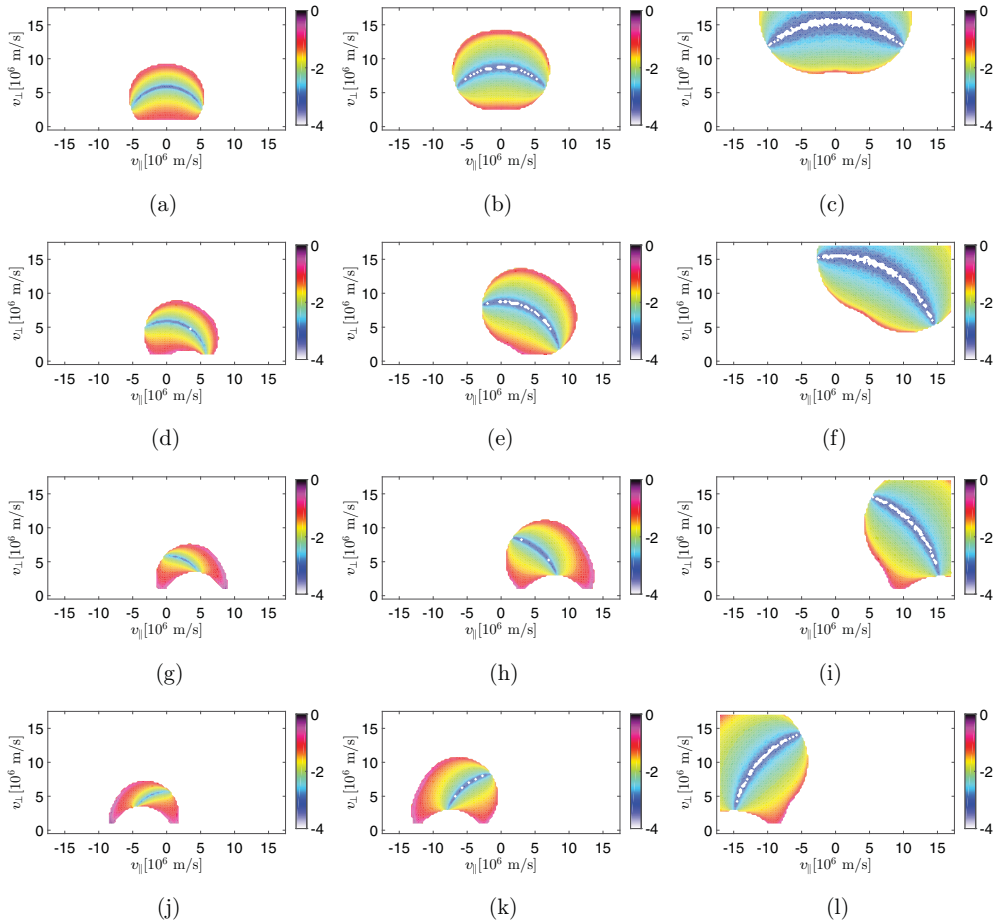


Figure 7. $\text{prob}(E_{\gamma,1} < E_{\gamma} < E_{\gamma,2} | \phi, v_{\parallel}, v_{\perp}, \beta, \zeta)$ for various projection angles $\phi = (30^\circ, 60^\circ, 90^\circ)$ and Doppler shifts $\Delta E_{\gamma} = (-15, 15, 30, 60)$ keV in base ten logarithm, see subfigure captions. $E_{\gamma,2} - E_{\gamma,1} = 1.5$ keV and $\zeta = 0^\circ$ are kept fixed. The angle between \hat{v}_{LOS} and v_{C} is set to $\beta = 10^\circ$ for blueshift ($\Delta E_{\gamma} > 0$) and to the supplementary angle $\beta = 170^\circ$ for redshift ($\Delta E_{\gamma} < 0$). The probability functions for redshift and blueshift with the same magnitude are mirror images about $v_{\parallel} = 0$. (a) $\phi = 90^\circ$, $\Delta E_{\gamma} = 15$ keV. (b) $\phi = 90^\circ$, $\Delta E_{\gamma} = 30$ keV. (c) $\phi = 90^\circ$, $\Delta E_{\gamma} = 60$ keV. (d) $\phi = 60^\circ$, $\Delta E_{\gamma} = 15$ keV. (e) $\phi = 60^\circ$, $\Delta E_{\gamma} = 30$ keV. (f) $\phi = 60^\circ$, $\Delta E_{\gamma} = 60$ keV. (g) $\phi = 30^\circ$, $\Delta E_{\gamma} = 15$ keV. (h) $\phi = 30^\circ$, $\Delta E_{\gamma} = 30$ keV. (i) $\phi = 30^\circ$, $\Delta E_{\gamma} = 60$ keV. (j) $\phi = 30^\circ$, $\Delta E_{\gamma} = -15$ keV. (k) $\phi = 30^\circ$, $\Delta E_{\gamma} = -30$ keV. (l) $\phi = 30^\circ$, $\Delta E_{\gamma} = -60$ keV.

sensitive in particular pitch ranges whereas areas with no solution of energy and momentum equations make the GRS measurements completely insensitive in other pitch ranges. We note that the probability functions $\text{prob}(E_{\gamma,1} < E_{\gamma} < E_{\gamma,2} | \phi, v_{\parallel}, v_{\perp})$ presented here assume uniform probability densities in β and ζ in the allowed regions whereas in section 3 we fully accounted for the anisotropic differential cross sections.

For $\Delta E_{\gamma} = 15$ keV the entire velocity space is observable. The strong upper local maximum would suggest strong sensitivity for pitches near zero, but this maximum lies below the energy of the first resonance and is hence in a region producing few detectable γ -rays. For alpha particle energies larger than 1.9 MeV we find that the GRS measurements should be most sensitive to co-going and counter-going particles (low v_{\perp}) rather than trapped particles. This perhaps surprising result

was also found by calculating full GRS weight functions in section 3. For larger Doppler shifts, completely unobservable regions appear at low v_{\perp} (corresponding to pitches $\sim \pm 1$). In these regions energy and momentum conservation do not allow the emission of γ -photons with these Doppler shifts. The sizes of these unobservable regions increase with the Doppler shift consistent with the corresponding weight functions. Further, there are particular regions with very large probabilities. We find two local maxima whose distances to the origin also increase with the Doppler shift. For $\Delta E_{\gamma} \sim 30$ keV the upper maximum lies in the region with significant γ -photon production whereas the lower maximum is still below the first resonance at 1.9 MeV. For $\Delta E_{\gamma} \sim 45$ keV the upper and lower local maxima at pitches around zero cover several resonances making the GRS measurements highly sensitive for pitches

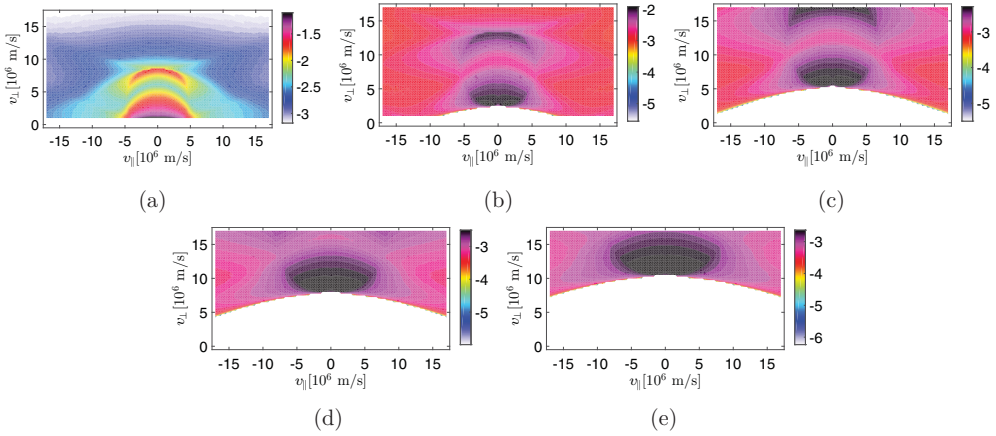


Figure 8. $\text{prob}(E_{\gamma,1} < E_{\gamma} < E_{\gamma,2} | \phi, v_{\parallel}, v_{\perp})$ assuming uniform probability densities in (β, ζ) for $\phi = 90^\circ$ and various Doppler shifts $\Delta E_{\gamma} = (15, 30, 45, 60, 75)$ keV in base ten logarithm. $E_{\gamma,2} - E_{\gamma,1} = 1.5$ keV is kept fixed. Note that we choose different scales for each plot. (a) $\Delta E_{\gamma} = 15$ keV. (b) $\Delta E_{\gamma} = 30$ keV. (c) $\Delta E_{\gamma} = 45$ keV. (d) $\Delta E_{\gamma} = 60$ keV. (e) $\Delta E_{\gamma} = 75$ keV.

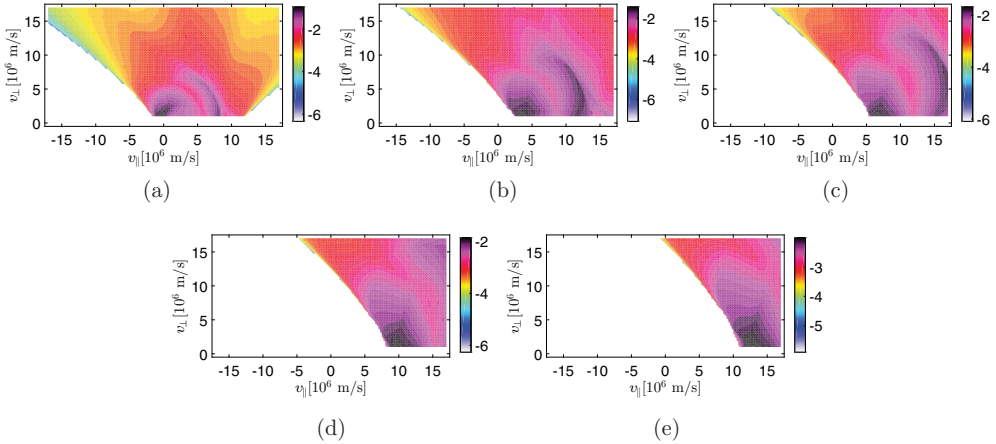


Figure 9. $\text{prob}(E_{\gamma,1} < E_{\gamma} < E_{\gamma,2} | \phi, v_{\parallel}, v_{\perp})$ assuming uniform probability densities in (β, ζ) for $\phi = 30^\circ$ and various Doppler shifts $\Delta E_{\gamma} = (15, 30, 45, 60, 75)$ keV in base 10 logarithm. $E_{\gamma,2} - E_{\gamma,1} = 1.5$ keV is kept fixed. We assume uniform probability densities in (β, ζ) . Note that we choose different scales for each plot. (a) $\Delta E_{\gamma} = 15$ keV. (b) $\Delta E_{\gamma} = 30$ keV. (c) $\Delta E_{\gamma} = 45$ keV. (d) $\Delta E_{\gamma} = 60$ keV. (e) $\Delta E_{\gamma} = 75$ keV.

around zero. For $\Delta E_{\gamma} \sim 60$ keV the lower local maximum is in the region with significant γ -photon production. The elevated detection probabilities make GRS spectrometers observing at $\phi = 90^\circ$ for Doppler shifts of about 45 keV or larger particularly sensitive to ions with pitches close to zero and rather insensitive or completely insensitive to ions with pitch close to ± 1 . We stress that the most sensitive pitch range thus strongly depends on the Doppler shift.

We illustrate typical velocity-space observation regions of the other high-resolution γ -ray spectrometer at an observation angle $\phi = 30^\circ$ and various Doppler shifts in figure 9. Completely unobservable regions appear even at small Doppler shifts ($\Delta E_{\gamma} \sim 15$ keV). These blueshifted γ -photons

cannot be produced due to alpha particles with $p \sim -1$ and very high energy alpha particles with $p \sim 1$. Two local maxima with elevated detection probabilities again appear that are biased towards positive v_{\parallel} for blueshift and $\phi = 30^\circ$. Further we find elevated probabilities for pitches near zero explaining why the weight functions for low Doppler shift and $\phi = 30^\circ$ are actually most sensitive to trapped particles. For Doppler shifts of $\Delta E_{\gamma} \gtrsim 30$ keV, the probability functions show the expected bias. The blueshifted side is most sensitive to co-going particles. For large Doppler shifts the measurement is not sensitive to counter-going particles at all. The probabilities are also rather small for trapped alpha particles. As already mentioned GRS weight functions for

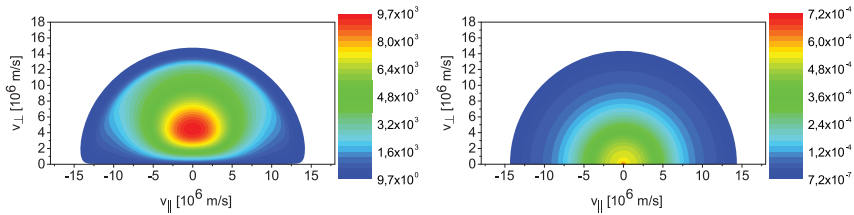


Figure 10. Alpha particle slowing-down distribution represented (left) as a slice of a 3D function [$\text{s}^3 \text{m}^{-6}$] and (right) as 2D function [$\text{s}^2 \text{m}^{-5}$]. We assume $n_\alpha = 10^{18} \text{m}^{-3}$, $n_e = 10^{20} \text{m}^{-3}$, $n_D = n_T = n_e/2$ and $T_D = T_T = T_e = 20 \text{keV}$. The velocity distribution function f^{2D} from f^{3D} by transforming to cylindrical coordinates and integrating over the by assumption ignorable gyroangle Γ , $f^{2D} = 2\pi v_\perp f^{3D}$.

redshifts are mirror images of those with the corresponding blueshift.

8. Applications of GRS weight functions for a slowing-down distribution

Traditionally high resolution GRS spectra are calculated by computationally demanding Monte Carlo simulation using the GENESIS code. GRS spectra can also be calculated using weight functions. In this approach weight functions are calculated for each Doppler-shifted energy bin. Once the weight functions are known, the spectra can be rapidly calculated by matrix multiplication for any f . The matrix multiplication method is significantly faster than the Monte Carlo simulation [32, 33, 35]. This becomes very advantageous if spectra for many distributions functions are to be calculated. We illustrate the two approaches to calculate spectra for an alpha particle slowing down distribution. This distribution is illustrated in figure 10 as a slice of a 3D function [$\text{s}^3 \text{m}^{-6}$] and as 2D function with no implied third direction [$\text{s}^2 \text{m}^{-5}$]. The slowing down distribution is given by

$$f^{3D}(v_{\parallel}, v_{\perp}) = \frac{\tau_s}{(v_{\parallel}^2 + v_{\perp}^2)^{3/2} + v_c^3} \int_0^{\infty} \bar{v}^2 S(\bar{v}) d\bar{v} \quad (38)$$

where τ_s is the slowing-down time, v_c is the critical velocity and S is the alpha particle source spectrum, which we calculated using a Monte Carlo approach.

Figure 11 demonstrates that spectra calculated using weight functions and using the Monte Carlo approach agree within the Monte Carlo noise level. This verifies that the GRS weight functions are in agreement with the traditional Monte Carlo simulation. The weight function method additionally shows the alpha particle velocity space origin of the signal in a particular γ -photon energy bin. This is shown by the product of the particular weight function for this γ -photon energy bin and the fast-ion velocity distribution function $w \times f$ at that point. Figures 12 and 13 illustrate these regions for $\phi = 90^\circ$ and $\phi = 30^\circ$ for a few Doppler-shifted energies, respectively. For the adopted slowing-down distribution, most γ -photons with Doppler shifts below $\lesssim 60 \text{keV}$ are produced near the 1.9 MeV resonance. Most γ -photons with Doppler shifts larger than 60 keV are produced near the 4 MeV resonance as energy and momentum conservation do not permit the production of γ at the 1.9 MeV resonance. We further find

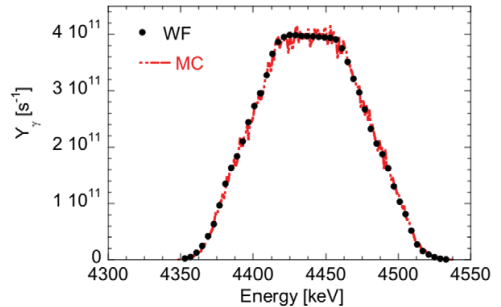


Figure 11. Energy spectrum for the $E_{\gamma,0} = 4.44 \text{MeV}$ level for the alpha particle slowing-down distribution from figure 10 as calculated using Monte Carlo simulations (MC) and by weight functions (WF). The spectrum shows the number of detected γ -photons per second [photons/s] in small energy bins of widths $E_{\gamma,2} - E_{\gamma,1} = 1 \text{keV}$. We assume emission from a point source in position space.

the strong pitch dependence inherited from the corresponding weight functions.

9. Discussion

Weight functions are widely used to interpret FIDA and CTS measurements [31–35, 41–61]. Recently, NES weight functions have been derived and applied to interpret measurements with the time-of-flight neutron spectrometer TOFOR at JET [34, 35]. GRS weight functions should likewise prove useful for GRS measurements at JET. Alpha particles accelerated to high energies by ICRH likely have pitches quite close to zero and can hence be measured well using the detector with the perpendicular line-of-sight ($\phi = 90^\circ$) at large Doppler shifts. However, alpha particles generated in burning plasma in the upcoming DT campaign at JET should be quite evenly distributed in pitch. GRS weight functions show that measurements at $\phi = 90^\circ$ and large Doppler shifts will preferentially detect trapped fast particles with low pitches ($p \sim 0$) whereas measurements at $\phi = 30^\circ$ and large Doppler shifts will preferentially detect co- and counter-going fast particles on the blue- and redshifted sides of the peak, respectively.

Weight functions are further used to measure 2D fast-ion distribution functions by tomographic inversion. This was demonstrated for FIDA measurements at ASDEX Upgrade in NBI heated MHD quiescent discharges as well as discharges

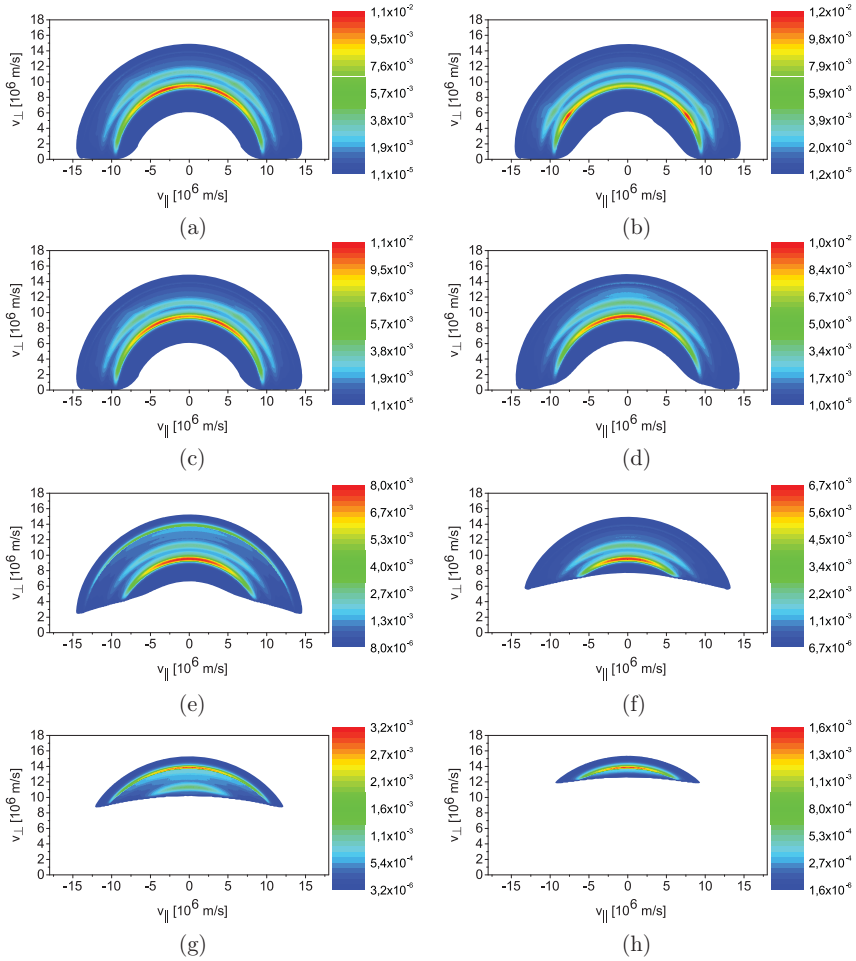


Figure 12. The products $w \times f$ of the functions shown in figures 2 and 10(b) illustrate how many γ -photons detected at each Doppler shift ΔE_γ were produced resolved in 2D velocity-space for this slowing-down distribution function. The units are (photons \times s m^{-3}). The γ -ray energy bin width is $E_{\gamma,1} - E_{\gamma,2} = 1$ keV, and the observation angle is $\phi = 90^\circ$. We assume $n_{\text{Be}} = 10^{18} \text{ m}^{-3}$ and $T_{\text{Be}} = 0$ keV. (a) $\Delta E_\gamma = -15$ keV. (b) $\Delta E_\gamma = 0$ keV. (c) $\Delta E_\gamma = 15$ keV. (d) $\Delta E_\gamma = 30$ keV. (e) $\Delta E_\gamma = 45$ keV. (f) $\Delta E_\gamma = 60$ keV. (g) $\Delta E_\gamma = 75$ keV. (h) $\Delta E_\gamma = 90$ keV.

with sawtooth activity. JET has two high-resolution γ -ray spectrometers as well as two high-resolution neutron emission spectrometers. These diagnostics could be combined to measure 2D fast-ion distribution functions in JET discharges. This could provide direct measurements of 2D velocity distribution functions of fast ions in the MeV range generated by ICRH or even of an alpha distribution function in burning plasma in the upcoming DT campaign at JET. However, this is beyond the scope of this paper. We must still investigate if the signal-to-noise ratio is high enough for tomographic inversion. Further, GRS and NES measurements have no spatial resolution along their lines-of-sight, and hence measurements in small spatial volumes as for FIDA are not possible with this diagnostic set. At JET the tomographic inversion would determine a spatial average of the 2D velocity distribution function in the plasma core assuming most fusion products are formed there.

GRS weight functions could also prove useful for tomographic inversion at ASDEX Upgrade [67, 68] where up to six FIDA views [39, 55, 61], two CTS views [54, 62, 69–73], one NES view [74, 75], one GRS view [22], one neutral particle analyzer as well as three FILD diagnostics [76, 77] provide excellent fast-ion velocity-space coverage. Here the GRS weight functions enable us to use GRS together with the other diagnostics to measure 2D fast-ion distribution functions.

Lastly, our formalism will show the velocity-space sensitivity of GRS measurements on ITER [24] and DEMO [25] and fusion reactors beyond. ITER will also be equipped with NES [78] and CTS [79–81] diagnostics, and diagnostics based on charge-exchange reactions will also likely give valuable information about fast ions [82]. GRS weight functions should make it possible to measure 2D fast-ion velocity distribution functions on ITER in combination with the other fast-ion diagnostics.

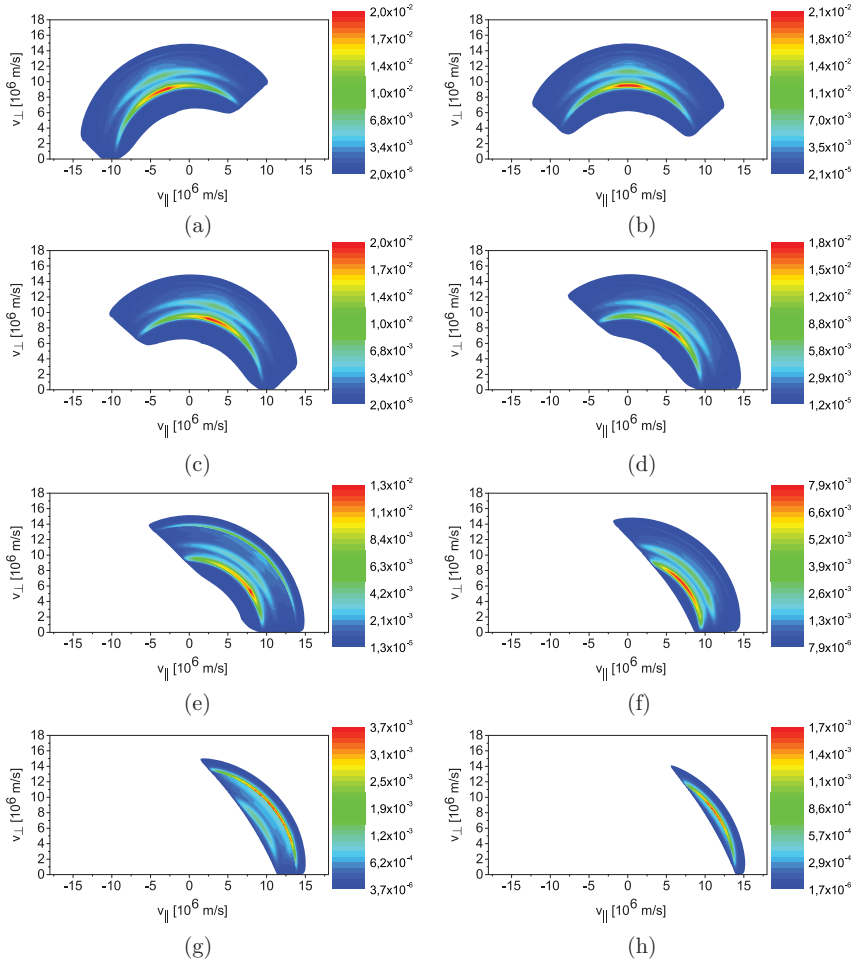


Figure 13. The products $w \times f$ of the functions shown in figures 3 and 10(b) illustrate how many γ -photons detected at each Doppler shift ΔE_γ were produced resolved in 2D velocity-space for this slowing-down distribution function. The units are (photons \times s m^{-5}). The γ -ray energy bin width is $E_{\gamma,1} - E_{\gamma,2} = 1$ keV, and the observation angle is $\phi = 30^\circ$. We assume $n_{Be} = 10^{18} \text{ m}^{-3}$ and $T_{Be} = 0$ keV. (a) $\Delta E_\gamma = -15$ keV. (b) $\Delta E_\gamma = 0$ keV. (c) $\Delta E_\gamma = 15$ keV. (d) $\Delta E_\gamma = 30$ keV. (e) $\Delta E_\gamma = 45$ keV. (f) $\Delta E_\gamma = 60$ keV. (g) $\Delta E_\gamma = 75$ keV. (h) $\Delta E_\gamma = 90$ keV.

10. Conclusions

Here we calculated weight functions revealing velocity-space sensitivities of GRS measurements. GRS weight functions show how many γ -photons can be detected per ion and hence which velocity-space regions are observable and which are unobservable. Given a simulated fast-ion distribution function, GRS weight functions allow rapid calculation of γ -ray spectra additionally showing how many γ -rays are produced for each alpha particle velocity. We focussed on the ${}^9\text{Be}(\alpha, n){}^{12}\text{C}$ reaction, but our formalism is valid for any two-step reaction producing γ -rays.

It is known that GRS measurements of the ${}^9\text{Be}(\alpha, n){}^{12}\text{C}$ reaction are highly sensitive to alpha particles with energies near the resonance energies of the reaction. Here we demonstrate that the GRS measurements are also highly selective in pitch depending on the orientation of the line-of-sight and the

Doppler-shifted energy. The pitch selectivity originates from the conservation of energy and momentum and the Doppler shift condition as we demonstrate by constructing a tractable simplified model.

The two high-resolution γ -ray spectrometers at JET have a perpendicular ($\phi = 90^\circ$) and an oblique line-of-sight ($\phi = 30^\circ$) with respect to the central magnetic field, respectively. GRS measurements with perpendicular lines-of-sight are highly sensitive to ions with pitches close to zero for large Doppler shifts. Perhaps surprisingly, for small Doppler shifts they are most sensitive to ions with pitch close to ± 1 . On the contrary, for the oblique lines-of-sight the blueshifted side of the spectrum is sensitive to co-going ions and the redshifted to counter-going ions for large Doppler shifts. At very large Doppler shifts, these measurements are completely insensitive not only to ions passing in the opposite direction but even to ions with pitches near zero. For smaller Doppler shifts the

measurements are biased in the same sense but still sensitive to both sides of the spectrum. Again perhaps surprisingly, measurements for the oblique line-of-sight at small Doppler shifts are most sensitive to particles with pitches around zero.

The energy selectivity and pitch selectivity make GRS measurements highly sensitive in rather small regions in velocity space. This selectivity in 2D velocity space suggests that GRS measurements could be highly valuable in measurements of 2D velocity distribution functions by tomographic inversion.

Acknowledgments

This work has been carried out within the framework of the EUROfusion Consortium and has received funding from the Euratom research and training programme 2014–2018 under grant agreement No 633053. The views and opinions expressed herein do not necessarily reflect those of the European Commission.

References

- [1] Kiptily V.G., Cecil F.E. and Medley S.S. 2006 *Plasma Phys. Control. Fusion* **48** R59–82
- [2] Tardocchi M., Nocente M. and Gorini G. 2013 *Plasma Phys. Control. Fusion* **55** 074014
- [3] Newman D.E. and Cecil F. 1984 *Nucl. Instrum. Methods Phys. Res. A* **227** 339–41
- [4] Cecil F.E. and Medley S.S. 1988 *Nucl. Instrum. Methods Phys. Res. A* **271** 628–35
- [5] Boyd D.A. et al 1989 *Nucl. Fusion* **29** 593–604
- [6] Jarvis O.N. et al 1996 *Nucl. Fusion* **36** 1513–30
- [7] Kiptily V.G., Cecil F.E., Jarvis O.N. and Mantsinen M.J. 2002 *Nucl. Fusion* **42** 999–1007
- [8] Kiptily V.G. et al 2003 *Rev. Sci. Instrum.* **74** 1753
- [9] Kiptily V.G. et al 2004 *Phys. Rev. Lett.* **93** 115001
- [10] Kiptily V.G. et al 2005 *Nucl. Fusion* **45** L21–5
- [11] Kiptily V.G. et al 2009 *Nucl. Fusion* **49** 065030
- [12] Kiptily V.G. et al 2012 *Plasma Phys. Control. Fusion* **54** 074010
- [13] Kiptily V.G. et al 2013 *Plasma Fusion Res.* **8** 2502071
- [14] Kondoh T. et al 1997 *J. Nucl. Mater.* **241–3** 564–8
- [15] Nishitani T., Tobita K., Kusama Y. and Shibata Y. 2001 *Rev. Sci. Instrum.* **72** 877
- [16] Kiptily V.G. et al 2010 *Nucl. Fusion* **50** 084001
- [17] Murari A. et al 2010 *Rev. Sci. Instrum.* **81** 10E136
- [18] Nocente M. et al 2010 *Rev. Sci. Instrum.* **81** 10D321
- [19] Nocente M. et al 2012 *Nucl. Fusion* **52** 063009
- [20] Tardocchi M. et al 2011 *Phys. Rev. Lett.* **107** 205002
- [21] Shevelev A.E. et al 2013 *Nucl. Fusion* **53** 123004
- [22] Nocente M. et al 2012 *Nucl. Fusion* **52** 094021
- [23] Nocente M. et al 2013 *IEEE Trans. Nucl. Sci.* **60** 1408–15
- [24] Chugunov I.N. et al 2011 *Nucl. Fusion* **51** 083010
- [25] Kiptily V. 2015 *Nucl. Fusion* **55** 023008
- [26] Cecil F., Zweben S. and Medley S. 1986 *Nucl. Instrum. Methods Phys. Res. A* **245** 547–52
- [27] Kiptily V.G. 1990 *Fusion Sci. Technol.* **18** 583–90
- [28] Romanelli F. 2013 *Nucl. Fusion* **53** 104002
- [29] Romanelli F. 2015 *Nucl. Fusion* **55** 104001
- [30] Ajzenberg-Selove F. 1991 *Nucl. Phys. A* **523** 1–196
- [31] Heidbrink W.W. et al 2007 *Plasma Phys. Control. Fusion* **49** 1457–75
- [32] Salewski M. et al 2014 *Plasma Phys. Control. Fusion* **56** 105005
- [33] Salewski M. et al 2011 *Nucl. Fusion* **51** 083014
- [34] Jacobsen A.S. et al 2014 *Rev. Sci. Instrum.* **85** 11E103
- [35] Jacobsen A.S. et al 2015 *Nucl. Fusion* **55** 053013
- [36] Salewski M. et al 2012 *Nucl. Fusion* **52** 103008
- [37] Salewski M. et al 2015 *Plasma Phys. Control. Fusion* **57** 014021
- [38] Salewski M. et al 2014 *Nucl. Fusion* **54** 023005
- [39] Geiger B. et al 2015 *Nucl. Fusion* **55** 083001
- [40] Salewski M. et al 2013 *Nucl. Fusion* **53** 063019
- [41] Heidbrink W.W. 2010 *Rev. Sci. Instrum.* **81** 10D727
- [42] Geiger B. et al 2014 *Nucl. Fusion* **54** 022005
- [43] Geiger B. 2013 Fast-ion transport studies using FIDA spectroscopy at the ASDEX Upgrade tokamak *PhD Thesis* Ludwig-Maximilians-Universität München
- [44] Heidbrink W.W. et al 2006 *Rev. Sci. Instrum.* **77** 10F120
- [45] Luo Y. et al 2007 *Rev. Sci. Instrum.* **78** 033505
- [46] Podestà M. et al 2008 *Rev. Sci. Instrum.* **79** 10E521
- [47] Van Zeeland M.A. et al 2009 *Plasma Phys. Control. Fusion* **51** 055001
- [48] Van Zeeland M.A. et al 2010 *Nucl. Fusion* **50** 084002
- [49] Bortolon A. et al 2010 *Rev. Sci. Instrum.* **81** 10D728
- [50] Heidbrink W.W. et al 2011 *Plasma Phys. Control. Fusion* **53** 085007
- [51] Michael C.A. et al 2013 *Plasma Phys. Control. Fusion* **55** 095007
- [52] Jones O.M. et al 2014 arXiv:1401.6864
- [53] Heidbrink W.W. et al 2014 *Plasma Phys. Control. Fusion* **56** 095030
- [54] Nielsen S.K. et al 2015 *Plasma Phys. Control. Fusion* **57** 035009
- [55] Geiger B. et al 2015 *Plasma Phys. Control. Fusion* **57** 014018
- [56] Heidbrink W.W. et al 2008 *Rev. Sci. Instrum.* **79** 10E520
- [57] Podesta M. et al 2009 *Phys. Plasmas* **16** 056104
- [58] Garcia-Munoz M. et al 2011 *Nucl. Fusion* **51** 103013
- [59] Geiger B. et al 2011 *Plasma Phys. Control. Fusion* **53** 065010
- [60] Muscatello C.M. et al 2012 *Plasma Phys. Control. Fusion* **54** 025006
- [61] Geiger B. et al 2013 *Rev. Sci. Instrum.* **84** 113502
- [62] Rasmussen J. et al 2015 *Plasma Phys. Control. Fusion* **57** 075014
- [63] Pace D.C. et al 2013 *Phys. Plasmas* **20** 056108
- [64] Nocente M. 2012 Neutron and gamma-ray emission spectroscopy as fast ion diagnostics in fusion plasmas *PhD Thesis* University of Milano Bicocca, Italy (<https://boa.unimib.it/handle/10281/28397>)
- [65] Proverbio I. et al 2010 *Rev. Sci. Instrum.* **81** 10D320
- [66] Kozlovsky B. et al 2002 *Astrophys. J. Suppl. Ser.* **141** 523–41
- [67] Stroth U. et al 2013 *Nucl. Fusion* **53** 104003
- [68] Zohm H. 2015 *Nucl. Fusion* **55** 104010
- [69] Meo F. et al 2008 *Rev. Sci. Instrum.* **79** 10E501
- [70] Meo F. et al 2010 *J. Phys.: Conf. Ser.* **227** 012010
- [71] Salewski M. et al 2010 *Nucl. Fusion* **50** 035012
- [72] Furtula V. et al 2012 *Rev. Sci. Instrum.* **83** 013507
- [73] Stejner M. et al 2015 *Plasma Phys. Control. Fusion* **57** 062001
- [74] Tardini G. et al 2012 *J. Instrum.* **7** C03004
- [75] Tardini G. et al 2013 *Nucl. Fusion* **53** 063027
- [76] Garcia-Munoz M. et al 2013 *Nucl. Fusion* **53** 123008
- [77] Garcia-Munoz M. et al 2013 *Plasma Phys. Control. Fusion* **55** 124014
- [78] Donné A.J.H. et al 2007 Progress in the ITER physics basis chapter 7: diagnostics *Nucl. Fusion* **47** S337–84
- [79] Salewski M. et al 2008 *Rev. Sci. Instrum.* **79** 10E729
- [80] Salewski M. et al 2009 *Plasma Phys. Control. Fusion* **51** 035006
- [81] Salewski M. et al 2009 *Nucl. Fusion* **49** 025006
- [82] Kappatou A. et al 2012 *Nucl. Fusion* **52** 043007
- [83] Romanelli F. et al 2014 *Proc. 25th IAEA Conf. on Fusion Energy (Saint Petersburg, Russia, 13–18 October 2014)*

Reference [9]

[9]. M Salewski et al. (2016) *Nuclear Fusion* **56** 046009. Fast-ion energy resolution by one-step reaction gamma-ray spectrometry

Fast-ion energy resolution by one-step reaction gamma-ray spectrometry

M. Salewski¹, M. Nocente^{2,3}, G. Gorini^{2,3}, A.S. Jacobsen¹, V.G. Kiptily⁴,
S.B. Korsholm¹, F. Leipold¹, J. Madsen¹, D. Moseev⁵, S.K. Nielsen¹,
J. Rasmussen¹, M. Stejner¹, M. Tardocchi³ and JET Contributors^{6,7}

¹ Department of Physics, Technical University of Denmark, DK-2800 Kgs. Lyngby, Denmark

² Department of Physics, University of Milano Bicocca, Milano 20126, Italy

³ Istituto di Fisica del Plasma, Consiglio Nazionale delle Ricerche, Milano 20125, Italy

⁴ CCFE, Culham Science Centre, Abingdon, Oxon, X14 3DB, UK

⁵ Max Planck Institute for Plasma Physics, 17491 Greifswald, Germany

⁶ EUROfusion Consortium, JET, Culham Science Centre, Abingdon, OX14 3DB, UK

E-mail: msal@fysik.dtu.dk

Received 21 December 2015, revised 26 January 2016

Accepted for publication 9 February 2016

Published 2 March 2016



Abstract

The spectral broadening of γ -rays from fusion plasmas can be measured in high-resolution gamma-ray spectrometry (GRS). We derive weight functions that determine the observable velocity space and quantify the velocity-space sensitivity of one-step reaction high-resolution GRS measurements in magnetized fusion plasmas. The weight functions suggest that GRS resolves the energies of fast ions directly without the need for tomographic inversion for selected one-step reactions at moderate plasma temperatures. The $D(p,\gamma)^3\text{He}$ reaction allows the best direct fast-ion energy resolution. We illustrate our general formalism using reactions with and without intrinsic broadening of the γ -rays for the GRS diagnostic at JET.

Keywords: gamma-ray spectrometry, tokamak, fast-ion diagnostics

(Some figures may appear in colour only in the online journal)

1. Introduction

Resolution of the energies of fast particles in fusion plasmas is a long-standing problem in present energetic-particle diagnostics. For example, the ITER measurement requirements entail resolution of the energy spectrum of confined α -particles [2]. However, recent studies of the velocity-space sensitivity of available core plasma fast-ion diagnostics suggest that this goal cannot be achieved by traditional measurements and analysis techniques as there is no direct one-to-one correspondence between fast-ion energy and measured signals [3–8]. In fact, fast-ion charge-exchange recombination spectroscopy (e.g. fast-ion D_α (FIDA) [3, 4]), collective Thomson scattering (CTS) [4, 5], neutron emission spectrometry (NES) [6, 7] and two-step reaction γ -ray spectrometry (GRS) [8] are not sensitive to distinct energies or pitches but to large regions in 2D velocity space covering a wide range of energies and

pitches. Neutral particle analyzers (NPA) are a notable exception and resolve fast-ion energies for the observable narrow pitch range [3]. Here we demonstrate that fast-ion energies for all pitches can be resolved directly by one-step reaction GRS. However, good direct energy resolution is achievable only for selected one-step reactions, such as the $D(p,\gamma)^3\text{He}$ reaction with fast protons. Further, the plasma temperature needs to be moderate. Hence direct energy resolution in burning plasmas in ITER remains elusive. Nevertheless, energy resolution of fast ions is possibly achievable by tomographic inversion in velocity space [9–13].

In GRS the γ -rays emitted by fusion plasmas are spectrally analyzed [14, 15]. Today the highest γ -ray fluxes from fusion plasmas are achieved at JET where GRS is routinely used [16–32]. The high nuclear reaction rates in the upcoming DT campaign at JET [1, 33] and later in burning plasmas at ITER and DEMO will further enhance the γ -ray emission [14, 15, 34, 35]. GRS measurements have traditionally been made at moderate spectral resolution just sufficient to identify peaks

⁷ See the appendix of [1].

Table 1. One-step fusion reactions discussed in this paper.

Reaction	Q (MeV)	σ_Q (MeV)	Remark
D(p, γ) ³ He	5.5	0.0	Well-established cross sections, often analysed
D(D, γ) ⁴ He	23.8	0.0	Peak has not been found at JET
D(T, γ) ⁵ He	16.85	0.648	Intrinsic broadening
T(p, γ) ⁴ He	19.7	0.0	Suggested for DEMO, good for H in DT plasma

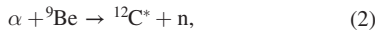
Note: The Q -value is the energy released in the reaction. σ_Q stands for the intrinsic non-zero mass width of the nuclear reaction product.

appearing at characteristic γ -ray energies in the spectra. Each peak can be related to a nuclear reaction by the γ -ray energy. GRS measurements at moderate spectral resolution have been made at Doublet-III [36], TFTR [37], JET [16–24] and JT-60U [38, 39]. New detectors [27, 40] allow GRS measurements at very high spectral resolution sufficient to resolve the spectral shapes of the individual peaks as demonstrated at JET [25–31] and ASDEX Upgrade [41].

Nuclear reactions emitting γ -rays can be divided into one-step reactions and two-step reactions based on their reaction kinematics [14]. In one-step reactions the γ -ray is a primary reaction product, as e.g. in D(p, γ)³He which can also be written as



In two-step reactions the γ -ray is a secondary reaction product, as e.g. in ⁹Be(α , n γ)¹²C. The two steps of this reaction are:



As this reaction releases high γ -ray fluxes in tokamaks with strong alpha particle populations and beryllium as a main plasma impurity, it is foreseen for alpha particle studies in the upcoming DT campaign at JET and at ITER [19, 42].

We have recently shown that two-step reaction high-resolution GRS measurements observe rather large regions in velocity space [8]. The measurements are sensitive to energies near the nuclear resonances in selected pitch ranges. As γ -rays at measured energies E_γ can be produced on several nuclear resonances, two-step reaction GRS actually provides no direct resolution of fast-ion energies. Here we demonstrate that selected one-step reaction GRS measurements, on the contrary, directly provide resolution of the fast-ion energies at moderate plasma temperatures. We will consider the D(p, γ)³He reaction as the main example as well as the reactions summarized in table 1.

The sensitivity in 2D velocity-space of fast-ion diagnostics can be described by weight functions. At present, weight functions have been developed for FIDA [3, 4], NPA [3], CTS [4, 5], fast-ion loss detectors [43] and NES [6, 7] as well as for two-step reaction GRS [8]. Weight functions have been used in four ways. First, they show the velocity-space

sensitivity of the diagnostic separating the observable velocity-space regions from unobservable regions [3–8, 31, 44–63]. Second, assuming a 2D fast-ion velocity distribution function, the velocity-space distribution of the ions generating a given measurement can be calculated [3–8, 31, 44, 57–62, 64]. Third, they allow rapid calculation of synthetic measurements [4–8]. Fourth, given enough measurements and sufficiently high signal-to-noise ratio, it is possible to infer 2D fast-ion velocity distribution functions by tomographic inversion [5, 9–13, 65, 66]. The formalism we present here allows these applications for one-step reaction GRS measurements.

This paper is organized as follows. In section 2 we consider the kinematics of one-step reactions. In section 3 we present analytic weight functions describing the velocity-space sensitivity of high-resolution one-step reaction GRS measurements. Section 4 illustrates typical observable velocity-space of the GRS spectrometer at JET for the D(p, γ)³He reaction. In section 5 we derive analytic expressions for the boundaries of the observable regions and explain the energy resolution of one-step reaction GRS by energy and momentum conservation. In section 6 we benchmark our formalism against numerical simulations. Section 7 discusses other nuclear reactions with and without so-called intrinsic broadening. Similarly, in section 8 the impact of thermal broadening is discussed. Finally, in section 9 we discuss implications of our formalism, and in section 10 we draw conclusions.

2. Kinematics of one-step reactions

The reaction kinematics determines the spectral broadening of the peak in the spectrum for reactions without intrinsic broadening [67]. Here we derive the relationship between the line-of-sight velocity u_f , the energy of the fast ion and the energy E_γ of the detected γ -ray by considering the reaction kinematics. As u_f depends on the gyroangle Γ of the fast ion, we can relate the energy E_γ to the gyroangle Γ of the fast ion. For a generic one-step reaction between species 1 and species 2 to form a reaction product, pr , releasing a γ -ray, the non-relativistic energy and momentum conservation equations are, respectively,

$$\frac{1}{2}m_1v_1^2 + \frac{1}{2}m_2v_2^2 + Q = \frac{1}{2}m_{pr}v_{pr}^2 + E_\gamma, \quad (4)$$

$$m_1\mathbf{v}_1 + m_2\mathbf{v}_2 = m_{pr}\mathbf{v}_{pr} + \mathbf{p}_\gamma. \quad (5)$$

E_γ and \mathbf{p}_γ are respectively the energy and momentum of the emitted γ -ray, and Q is the energy released in the reaction. We now assume that one species is fast and the other thermal. Neglecting the energy and momentum of the thermal species and denoting the mass of the fast species to m_f and its velocity to \mathbf{v}_f , the energy and momentum equations become

$$\frac{1}{2}m_f v_f^2 + Q = \frac{1}{2}m_{pr} v_{pr}^2 + E_\gamma, \quad (6)$$

$$m_f \mathbf{v}_f = m_{pr} \mathbf{v}_{pr} + \mathbf{p}_\gamma. \quad (7)$$

The effects of non-zero temperature will be calculated in section 8 using the GENESIS code [29, 68]. Elimination of v_{pr}^2 in equation (6) using equation (7) gives

$$\frac{1}{2}m_f v_f^2 + Q = \frac{1}{2m_{pr}}(m_f^2 v_f^2 - 2m_f \mathbf{p}_\gamma \cdot \mathbf{v}_f + p_\gamma^2) + E_\gamma \quad (8)$$

where $p_\gamma = |\mathbf{p}_\gamma|$. Equation (8) could also be obtained from the erroneous equation $m_f \mathbf{v}_f = -m_{pr} \mathbf{v}_{pr} + \mathbf{p}_\gamma$ instead of momentum conservation (equation (5)). This is checked for and excluded below. The dot product $\mathbf{p}_\gamma \cdot \mathbf{v}_f$ can be expressed in terms of the line-of-sight velocity u_f by introducing the unit vector along the line-of-sight $\hat{\mathbf{p}}_\gamma$:

$$\mathbf{p}_\gamma \cdot \mathbf{v}_f = p_\gamma \hat{\mathbf{p}}_\gamma \cdot \mathbf{v}_f = p_\gamma u_f. \quad (9)$$

The magnitude of the momentum p_γ and the energy of the γ -ray are related by

$$p_\gamma = E_\gamma/c \quad (10)$$

where c is the speed of light. Substitution of equations (9) and (10) into equation (8) gives

$$\frac{1}{2}m_f v_f^2 + Q = \frac{1}{2m_{pr}} \left(m_f^2 v_f^2 - 2m_f \frac{E_\gamma}{c} u_f + \frac{E_\gamma^2}{c^2} \right) + E_\gamma. \quad (11)$$

Equation (11) relates the line-of-sight velocity u_f of the fast ion to the measurable energy E_γ of the γ -photon. We solve equation (11) for u_f and express v_f^2 in $(v_{\parallel}, v_{\perp})$ -coordinates with respect to the total magnetic field as $v_f^2 = v_{\parallel}^2 + v_{\perp}^2$:

$$u_f = \frac{(m_f - m_{pr})c}{2E_\gamma} (v_{\parallel}^2 + v_{\perp}^2) + \frac{E_\gamma}{2m_f c} + \frac{m_{pr}c(E_\gamma - Q)}{m_f E_\gamma}. \quad (12)$$

The line-of-sight velocity u_f is determined by the gyroangle Γ according to [5, 7, 11]

$$u_f = v_{\parallel} \cos \phi + v_{\perp} \sin \phi \cos \Gamma \quad (13)$$

where ϕ is the observation angle between the line-of-sight and the magnetic field. We eliminate u_f from equations (12) and (13) and solve for $\Gamma \in [0, \pi]$:

$$\Gamma = \arccos \frac{\frac{(m_f - m_{pr})c}{2E_\gamma} (v_{\parallel}^2 + v_{\perp}^2) + \frac{E_\gamma}{2m_f c} + \frac{m_{pr}c(E_\gamma - Q)}{m_f E_\gamma} - v_{\parallel} \cos \phi}{v_{\perp} \sin \phi}. \quad (14)$$

This relation allows us to calculate the gyroangle $\Gamma \in [0, \pi]$ of the fast ion leading to the detected energy E_γ of the γ -ray. A second solution for $\Gamma' \in [\pi, 2\pi]$ is given by [5]

$$\Gamma' = 2\pi - \Gamma. \quad (15)$$

3. One-step reaction GRS weight functions

The relation between fast-ion measurements, s , and fast-ion distribution functions, f , can be expressed as an integral over phase space,

$$s(E_{\gamma,1}, E_{\gamma,2}, \phi) = \int_{\text{vol}} \int_0^\infty \int_{-\infty}^\infty w(E_{\gamma,1}, E_{\gamma,2}, \phi, v_{\parallel}, v_{\perp}, \mathbf{x}) \times f(v_{\parallel}, v_{\perp}, \mathbf{x}) dv_{\parallel} dv_{\perp} d\mathbf{x} \quad (16)$$

where w is the weight function [3–8, 44] and \mathbf{x} denotes the spatial coordinates. For GRS measurements, $s(E_{\gamma,1}, E_{\gamma,2}, \phi)$ is the detection rate of γ -rays (photons s^{-1}) in the energy range $E_{\gamma,1} < E_\gamma < E_{\gamma,2}$ with an observation angle ϕ . The units of $f(v_{\parallel}, v_{\perp}, \mathbf{x})$ are (fast ions $\times \text{s}^2 \text{m}^{-5}$). The units of GRS weight functions are thus (photons / (fast ion $\times \text{s}$)) describing the velocity-space sensitivity of the diagnostic. Analogous to two-step reaction GRS weight functions as well as FIDA and NES weight functions [4, 7, 8], we factor GRS weight functions w into a detection rate function $R(v_{\parallel}, v_{\perp}, \phi, \mathbf{x})$ and a probability $\text{prob}(E_{\gamma,1} < E_\gamma < E_{\gamma,2} | \phi, v_{\parallel}, v_{\perp})$:

$$w(E_{\gamma,1}, E_{\gamma,2}, \phi, v_{\parallel}, v_{\perp}, \mathbf{x}) = R(v_{\parallel}, v_{\perp}, \phi, \mathbf{x}) \times \text{prob}(E_{\gamma,1} < E_\gamma < E_{\gamma,2} | \phi, v_{\parallel}, v_{\perp}). \quad (17)$$

$R(v_{\parallel}, v_{\perp}, \phi, \mathbf{x})$ describes incident rates in (photons / (fast ion $\times \text{s}$)) irrespective of the γ -ray energy [8]. $R(v_{\parallel}, v_{\perp}, \phi, \mathbf{x})$ hence has the same units as weight functions whereas the probabilities are dimensionless numbers between 0 and 1. The laws of energy and momentum conservation determine the boundaries of the probability functions $\text{prob}(E_{\gamma,1} < E_\gamma < E_{\gamma,2} | \phi, v_{\parallel}, v_{\perp})$ in $(v_{\parallel}, v_{\perp})$ -space and hence ultimately the boundaries of weight functions which separate the observable regions from the unobservable regions.

Before we calculate probability functions, we briefly discuss the rate function R . Assuming a fast reactant with velocity $(v_{\parallel}, v_{\perp})$ and a thermal reactant at rest and neglecting any angle dependence of the cross section σ , the rate function can be calculated according to [7]

$$R(v_{\parallel}, v_{\perp}, \mathbf{x}) = \frac{\Omega}{4\pi} n_t \sqrt{v_{\parallel}^2 + v_{\perp}^2} \sigma \left(\sqrt{v_{\parallel}^2 + v_{\perp}^2} \right). \quad (18)$$

where Ω is the solid angle of the detector as seen from position \mathbf{x} and n_t is the density of the thermal ions. The cross section can be modelled as [41]

$$\sigma(E) = \frac{S}{E} \exp(-\beta_G \sqrt{E}) \quad (19)$$

where $E = \frac{1}{2}m(v_{\parallel}^2 + v_{\perp}^2)$ is the energy (which depends on the velocity-space position), β_G is the Gamow constant and S is the so-called astrophysical factor which is a slowly varying function of energy [69, 70]. For the $\text{D}(\text{p}, \gamma)^3\text{He}$ reaction, S is modelled as a fifth-order polynomial for which the coefficients are given in reference [41]. The rate function is illustrated in figure 1.

The probability function $\text{prob}(E_{\gamma,1} < E_\gamma < E_{\gamma,2} | \phi, v_{\parallel}, v_{\perp})$ can be calculated by transforming to probabilities in Γ using equation (14). This transformation is advantageous as the gyroangle has, to a good approximation, a uniform distribution:

$$\text{pdf}_\Gamma = \frac{1}{2\pi}. \quad (20)$$

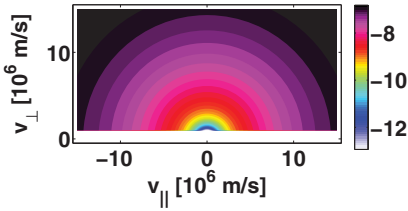


Figure 1. Rate function R in units (γ -photons / (ion \times s)). The magnitude is shown in base 10 logarithm.

We write the probability function as an integral over the corresponding probability density function and transform to probability densities in Γ :

$$\begin{aligned} \text{prob}(E_{\gamma,1} < E_{\gamma} < E_{\gamma,2} | \phi, v_{\parallel}, v_{\perp}) &= \int_{E_{\gamma,1}}^{E_{\gamma,2}} \text{pdf}(E_{\gamma} | \phi, v_{\parallel}, v_{\perp}) dE_{\gamma} \\ &= \int_{\Gamma_2}^{\Gamma_1} \text{pdf}_{\Gamma} d\Gamma + \int_{2\pi-\Gamma_1}^{2\pi-\Gamma_2} \text{pdf}_{\Gamma} d\Gamma = \frac{\Gamma_1 - \Gamma_2}{\pi}. \end{aligned} \quad (21)$$

We have used that

$$\text{pdf}(E_{\gamma} | \phi, v_{\parallel}, v_{\perp}) = \text{pdf}_{\Gamma} \left| \frac{d\Gamma}{dE_{\gamma}} \right|. \quad (22)$$

The second integral in Γ arises due to the second solution in Γ shown in equation (15). The integration limits Γ_1 and Γ_2 are respectively given by the energies $E_{\gamma,1}$ and $E_{\gamma,2}$ according to equation (14). We stress that the probability function depends only on the observation angle ϕ , the considered γ -ray energy range and the reaction kinematics but not on the reaction cross sections.

4. Observable velocity-space regions for the $D(p,\gamma)^3\text{He}$ reaction at JET

Typical observation angles for the two high-resolution GRS diagnostics at JET are about $\phi = 90^\circ$ and $\phi = 30^\circ$ with respect to the magnetic field in the plasma centre. The observation angle varies along the line-of-sight. However, as most γ -rays are generated in the plasma centre, we neglect these spatial variations here. Figure 2 shows probability functions for the $D(p,\gamma)^3\text{He}$ reaction with fast protons and thermal deuterium for these angles and various γ -ray energy ranges. In this case the proton velocity is much larger than the deuterium velocity ($v_p \gg v_D$). This reaction is often studied for plasma scenarios with ICRH hydrogen minority heating in deuterium plasma [18, 41, 67]. The observation regions are similar for the two views and are bounded by circular arcs that have their centers close to the origin as we will show in section 5. Hence fast ions in narrow energy ranges are observable in each γ -ray energy range. The radius of each circular arc as well as the distance of its center to the origin are independent of ϕ . For $\phi = 90^\circ$ the probability functions are symmetric about $v_{\parallel} = 0$. For $\phi = 30^\circ$ the center is tilted towards negative parallel velocities, and hence the observation regions are slightly biased towards negative parallel velocities. We also observe that the probability functions for $\phi = 30^\circ$ are narrower and have larger amplitudes than those at $\phi = 90^\circ$. The arcs for

$\phi = 30^\circ$ are narrower as the impact of the gyromotion is smaller according to equation (13). The shapes and amplitudes of the probability functions suggest good resolution of the fast ion energies for all pitches in contrast to other fast-ion diagnostics. Weight functions with perfect energy resolution would be bounded by concentric circular arcs about the origin in $(v_{\parallel}, v_{\perp})$ -coordinates.

Figure 3 shows the corresponding weight functions, i.e. the product of each probability function from figure 2 with the rate function R from figure 1. As R covers the entire velocity space, the forms of the probability functions and the corresponding weight functions are identical. However, as the cross sections and hence R increase with energy, the weight functions have their largest amplitudes in the parts furthest away from the origin.

5. Boundaries of one-step reaction GRS weight functions

Boundaries of weight functions are found by inserting $\cos \Gamma = \pm 1$ in equation (13) as then the line-of-sight velocity is at extremal values for given ϕ . Substitution of u_f into equation (12) then gives

$$\begin{aligned} E_{\gamma}^2 + 2m_{pr}c^2(E_{\gamma} - Q) - 2m_f c(v_{\parallel} \cos \phi \pm v_{\perp} \sin \phi) E_{\gamma} \\ - m_f(m_{pr} - m_f)c^2(v_{\parallel}^2 + v_{\perp}^2) = 0. \end{aligned} \quad (23)$$

Equation (23) can be written in the form $(v_{\parallel} - v_{\parallel,0})^2 + (v_{\perp} - v_{\perp,0})^2 = r_v^2$.

$$\begin{aligned} \left(v_{\parallel} + \frac{\cos \phi E_{\gamma}}{(m_{pr} - m_f)c} \right)^2 + \left(v_{\perp} \pm \frac{\sin \phi E_{\gamma}}{(m_{pr} - m_f)c} \right)^2 \\ = \frac{m_{pr}E_{\gamma}^2 + 2m_{pr}(m_{pr} - m_f)c^2(E_{\gamma} - Q)}{m_f(m_{pr} - m_f)^2c^2}. \end{aligned} \quad (24)$$

The weight functions are hence bounded by the circular arcs with $v_{\perp} > 0$. The center and the radius r_v are given by

$$v_{\parallel,0} = -\frac{\cos \phi E_{\gamma}}{(m_{pr} - m_f)c}, \quad (25)$$

$$v_{\perp,0} = \pm \frac{\sin \phi E_{\gamma}}{(m_{pr} - m_f)c}, \quad (26)$$

$$r_v = \sqrt{\frac{m_{pr}}{m_f} \left(\frac{E_{\gamma}^2}{(m_{pr} - m_f)^2c^2} + \frac{2(E_{\gamma} - Q)}{m_{pr} - m_f} \right)}. \quad (27)$$

The distance of the center of the circular arcs to the origin is

$$v_0 = \frac{E_{\gamma}}{(m_{pr} - m_f)c}. \quad (28)$$

The radicand in equation (27) must be positive which implies a minimum energy of the observable γ -rays:

$$\begin{aligned} E_{\gamma} \geq E_{\gamma,\min} = \sqrt{2(m_{pr} - m_f)c^2Q + (m_{pr} - m_f)^2c^4} \\ - (m_{pr} - m_f)c^2. \end{aligned} \quad (29)$$

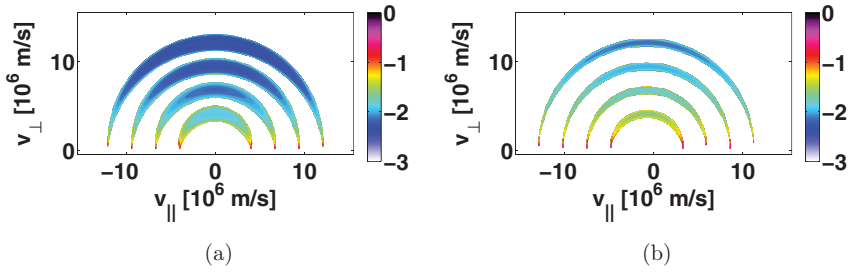


Figure 2. Probability functions $\text{prob}(E_{\gamma,1} < E_{\gamma} < E_{\gamma,2} | \phi, v_{||}, v_{\perp})$ of $\text{D}(p,\gamma)^3\text{He}$ with $v_p \gg v_D$ for two observation angles ϕ and various γ -ray energies in base 10 logarithm. In each figure we plot four probability functions showing the observation regions at four γ -ray energy ranges with fixed width $E_{\gamma,2} - E_{\gamma,1} = 1$ keV. From inside to outside: $E_{\gamma,1} - Q = 50$ keV, 150 keV, 300 keV, 500 keV. (a) $\phi = 90^\circ$. (b) $\phi = 30^\circ$.

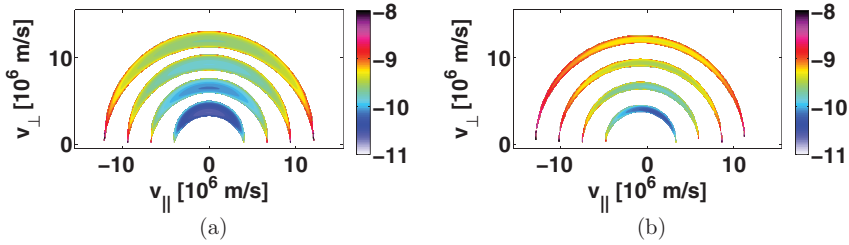


Figure 3. Weight functions of $\text{D}(p,\gamma)^3\text{He}$ with $v_p \gg v_D$ for two observation angles ϕ and various γ -ray energy ranges of fixed width $E_{\gamma,2} - E_{\gamma,1} = 1$ keV in units (γ -photons / (ion \times s)) in base ten logarithm. From inside to outside: $E_{\gamma,1} - Q = 50$ keV, 150 keV, 300 keV, 500 keV. The weight functions are obtained from equation (17). R is shown in figure 1 and $\text{prob}(E_{\gamma,1} < E_{\gamma} < E_{\gamma,2} | \phi, v_{||}, v_{\perp})$ in figure 2. (a) $\phi = 90^\circ$. (b) $\phi = 30^\circ$.

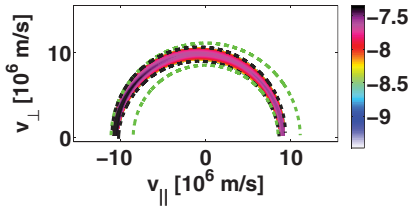


Figure 4. Probability function of $\text{D}(p,\gamma)^3\text{He}$ with $v_p \gg v_D$ for $\phi = 30^\circ$ and $E_{\gamma,1} - Q = 300$ keV in units (γ -photons / (ion \times s)) in base ten logarithm. We set $E_{\gamma,2} - E_{\gamma,1} = 50$ keV, so that the low-energy and high-energy boundaries are more easily distinguishable. Black dashed lines: boundaries. Green dashed lines: Upper and lower energy limits.

For example, for the $\text{D}(p,\gamma)^3\text{He}$ reaction with fast protons and thermal deuterium $E_{\gamma,\min} = 5.480$ MeV (for $Q = 5.488$ MeV). This minimum energy is only a few keV below the released energy Q whereas there are no maximum energies. The peak is strongly asymmetric with a much larger high-energy tail than low-energy tail as has been observed previously [67]. As the low-energy tail is close to the spectral resolution, we consider the nominal peak energy and the high-energy tail in the following. For NES an analogous minimum energy of observable neutrons was found to be $E_n > Q/2$ [7] which implies a considerably more prominent low-energy tail in neutron emission energy spectra.

As observed in figure 3 and in equations (25)–(28), the radius and the distance of the center to the origin do not

depend on the observation angle ϕ , but the pitch coordinate $v_{||}/v$ of the center does. For a given energy E_{γ} we can now give upper and lower energy limits on the fast proton leading to the γ -ray emission. The center of the upper circular boundary has $v_{\perp,0} > 0$, whereas the center of the lower circular boundary has $v_{\perp,0} < 0$ (see equation (26)). Hence the largest and smallest possible proton energies E_{\max} and E_{\min} for a given γ -ray energy E_{γ} are

$$E_{\min} = \frac{1}{2}m_f(r_v - v_0)^2, \quad (30)$$

$$E_{\max} = \frac{1}{2}m_f(r_v + v_0)^2 \quad (31)$$

where r_v and v_0 are given by equations (27) and (28), respectively. The fast-ion energy limits for a given γ -ray energy range are found at the extremal values of the considered γ -ray energies. In figure 4 we plot an example of a probability function together with its boundaries as calculated in equations (25)–(27) as well as the upper and lower limits on the proton energies according to equations (30) and (31). In $(v_{||}, v_{\perp})$ -coordinates the upper and lower energy limits show as the two circles about the origin that each touch the probability function. These upper and lower proton energy limits are plotted as a function of the measured γ -ray energy E_{γ} for the $\text{D}(p,\gamma)^3\text{He}$ reaction in figure 5, illustrating the fast-ion energy resolution of the measurement for each γ -ray energy. This reaction is useful for tail temperatures $T_{\perp} < 400$ keV. At higher tail temperatures the peak tends to become difficult

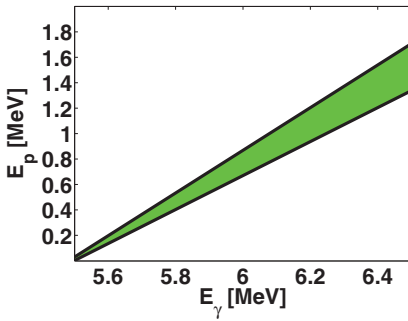


Figure 5. Proton energy resolution of the GRS measurement. The green region shows possible proton energies E_p for a given measured γ -ray energy E_γ . This neglects the energy of the thermal species. Here we set $E_{\gamma,2} - E_{\gamma,1} = 1$ keV.

to separate from the background [18]. The energy limits are valid for zero temperature of the deuterium. We note that in JET there are often also fast deuterium ions in the plasma. Fast hydrogen is generated by first harmonic ICRH. If fast deuterium ions due to NBI are in the plasma, they will also be accelerated to high energies by second harmonic ICRH. Under some conditions fast deuterium can even be generated without NBI [18].

The fast-ion energy resolution of the measurement is good if $r_v \gg v_0$. This is indeed the case for large or even moderate energy shifts. The ratio r_v/v_0 is

$$\frac{r_v}{v_0} = \sqrt{\frac{m_{pr}}{m_f} \left(1 + \frac{E_\gamma - Q}{E_\gamma} \times \frac{2(m_{pr} - m_f)c^2}{E_\gamma} \right)}. \quad (32)$$

At the nominal peak energy $E_\gamma = Q$, the radius becomes $r_v = \sqrt{\frac{m_{pr}}{m_f}} v_0$. This will also hold approximately when the energy shift $E_\gamma - Q$ is so small that the first term in equation (27) dominates. The second term dominates at large energy shifts, i.e. if

$$\frac{E_\gamma - Q}{E_\gamma} \gg \frac{E_\gamma}{2(m_{pr} - m_f)c^2}. \quad (33)$$

For example for fast protons in $D(p,\gamma)^3\text{He}$, $2(m_{pr} - m_f)c^2 \sim 4$ GeV and $E_\gamma \sim 5.5$ MeV, and hence the fraction $E_\gamma/(2(m_{pr} - m_f)c^2)$ is of order 10^{-3} . The radius is larger than the distance of the circular arc to the origin, unless the E_γ is very close to the minimum energy $E_{\gamma,\min}$. For large energy shifts according to equation (33), we find $r_v \gg v_0$, i.e. the centers of the circular arcs are close to the origin compared with the radius. Equation (32) suggests that low Q -values (and hence typical $E_\gamma \sim Q$), large m_{pr}/m_f and large $m_{pr} - m_f$ are beneficial for the energy resolution. NES weight functions are analogously bounded by circular arcs. But for the GRS weight function of the $D(p,\gamma)^3\text{He}$ reaction, the center of the circle lies very close to the origin compared with the radius. Hence for this and other selected one-step reaction GRS, the measured γ -energies can be related to particular fast-ion energies in rather narrow bands. The reaction kinematics of NES and one-step reaction GRS are very similar. The significant differences

originate from the ratios between energies and momenta for neutron and γ -ray fusion products:

$$E_n = p_n \frac{v_n}{2}, \quad (34)$$

$$E_\gamma = p_\gamma c \quad (35)$$

For example, for the 2.45 MeV neutrons from $D(D,n)^3\text{He}$, $E_n/p_n \lesssim c/20$. For one-step reactions releasing γ -rays, $E_\gamma/p_\gamma = c$ as always. One may estimate how much of the initial fast-ion momentum a released γ -ray or neutron can carry:

$$\frac{p_\gamma}{p_f} = \frac{E_\gamma v_f}{E_f 2c}, \quad (36)$$

$$\frac{p_n}{p_f} = \frac{E_n v_f}{E_f v_n}. \quad (37)$$

As $v_n/2c \ll 1$ and if $E_n \sim E_\gamma$, the γ -rays carry a much smaller fraction of the total momentum after the reaction compared with a neutron in a similar reaction. The γ -ray therefore tends to carry a significant fraction of the energy, but a small fraction of the momentum compared with neutrons. For the $D(p,\gamma)^3\text{He}$ reaction with $E_p \sim 1$ MeV and $E_\gamma \sim Q \sim 5.5$ MeV, we get $p_\gamma/p_p \sim 0.13$. For the $D(D,\gamma)^4\text{He}$ reaction with $E_D \sim 1$ MeV and $E_\gamma \sim Q \sim 23.8$ MeV, we get $p_\gamma/p_D \sim 0.39$. As comparison, for the $D(D,n)^3\text{He}$ reaction releasing 2.45 MeV neutrons and $E_D \sim 1$ MeV, we get $p_n/p_D \sim 1.1$. Hence the observation regions become strongly selective in energy and only weakly selective in pitch, as reflected by the circular shapes centered close to the origin, for one-step reactions releasing γ -rays with low Q -value when the momentum carried by the γ -ray is comparatively low. Examples of probability functions for various reactions illustrating their energy resolution will be shown in section 7.

6. Numerically calculated weight functions with anisotropic cross sections

Weight functions can also be calculated numerically using the GENESIS code that predicts a GRS measurement for an arbitrary fast-ion distribution function [29, 68]. In this numerical approach, we calculate a γ -ray spectrum for a collection of N_f fast ions located at a single point in velocity space and then scan the location of this point through velocity space. This formalism has been presented for two-step reaction GRS measurements [8] and is analogous to numeric computation of weight functions for FIDA [3, 11], CTS [5] and NES [6, 7]. The amplitude of the weight function at phase-space position $(\mathbf{x}_p, v_{\parallel p}, v_{\perp p})$ is [7]

$$w(E_{\gamma,1}, E_{\gamma,2}, \phi, v_{\parallel p}, v_{\perp p}, \mathbf{x}_p) = \frac{s(E_{\gamma,1}, E_{\gamma,2}, \phi)}{N_f}. \quad (38)$$

GRS weight functions show the incident rate s of γ -photons between two γ -ray energies viewed at angle ϕ per alpha particle at phase-space position $(\mathbf{x}_p, v_{\parallel p}, v_{\perp p})$. In the numerical approach we take anisotropy of the cross sections into account

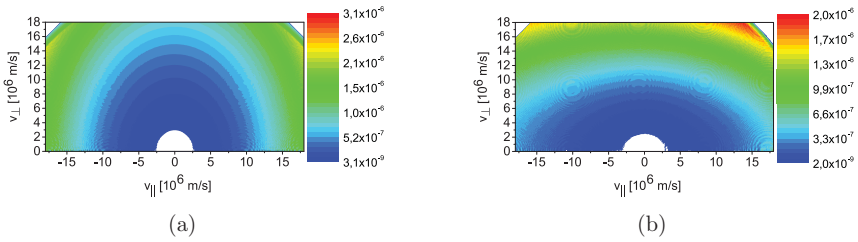


Figure 6. Rate function R in units (γ -photons / (ion \times s)) for two observation angles. Anisotropic cross sections are accounted for. (a) $\phi = 90^\circ$. (b) $\phi = 30^\circ$.

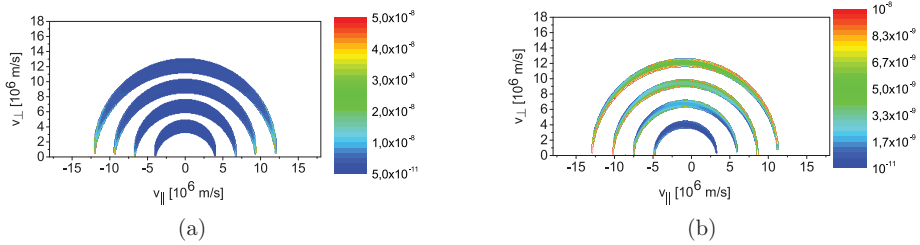


Figure 7. Numerically calculated weight function in units (γ -photons / (ion \times s)) for two observation angles covering various energy ranges of fixed width $E_{\gamma,2} - E_{\gamma,1} = 1$ keV. From inside to outside: $E_{\gamma,1} - Q = 50$ keV, 150 keV, 300 keV, 500 keV. Anisotropic cross sections are accounted for. (a) $\phi = 90^\circ$. (b) $\phi = 30^\circ$.

[71]. Figure 6 shows the rate function R for the two observation angles $\phi = 90^\circ$ and $\phi = 30^\circ$ illustrating the strong anisotropy of the cross sections. For isotropic cross sections the isolines are concentric circles (see figure 1). Figure 7 shows numerically calculated weight functions at these angles. While the shapes of the numerically calculated weight functions agree with the analytic model at the same angles (see figure 3), the amplitudes are different due to the anisotropic cross sections.

Fast-ion distribution functions typical for ICRH are often characterized by a so-called tail temperature. We model the tail of such a distribution function as strongly biased bi-Maxwellian with a tail temperature $T_{\perp} = 150$ keV and $T_{\parallel} = 15$ keV as illustrated in figure 8. The product of weight functions and a given fast-ion velocity distribution functions $w \times f$ resolves the origin of the γ -rays in 2D velocity space of the fast ions for this given f as illustrated in figure 9. The narrow probability functions at $\phi = 30^\circ$ provide a better energy resolution for narrow velocity distribution functions with $v_{\parallel} \ll v_{\perp}$, such as the bi-Maxwellian from figure 8.

Figure 10 shows spectra as calculated by traditional Monte Carlo simulations and by weight functions. The energy and momentum of the thermal species are here neglected. As expected, the two approaches give very similar results and differ only due to Monte Carlo noise. The weight function approach has two advantages. First, the velocity-space region generating the γ -ray at each energy can be identified (see figure 9). Second, once the weight functions are calculated, the weight function approach is significantly faster as it requires only a matrix multiplication instead of Monte Carlo simulations. Hence spectra of many fast-ion velocity distribution functions can rapidly be calculated.

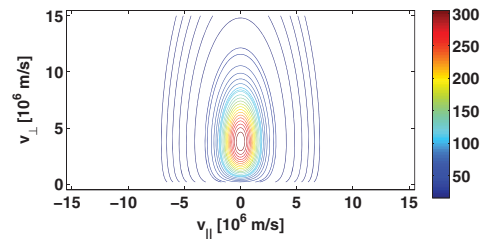


Figure 8. 2D bi-Maxwellian in units (fast ions \times s $^{-2}$ m $^{-5}$). The 2D bi-Maxwellian f^{2D} is related to the corresponding 3D bi-Maxwellian f^{3D} by $f^{2D} = 2\pi v_{\perp} f^{3D}$ assuming rotational symmetry about the magnetic field vector.

7. Other reactions and excited charged reaction products

Our formalism is general and applies to any one-step reaction GRS measurement, including reactions where the charged reaction product has an intrinsic mass width. This leads to so-called intrinsic broadening of the reaction energy peak such as in $D(T,\gamma)^5\text{He}$. For many reactions the energy dependence of the reaction cross sections is described by only few data points. We can nevertheless draw conclusions about the velocity-space sensitivity for such one-step reactions. The cross sections enter only into the calculation of the rate function R whereas probability functions are calculated based on the conservation of energy and momentum and do not depend on the cross sections. Hence we can calculate the probability functions and the boundaries of weight functions exactly even

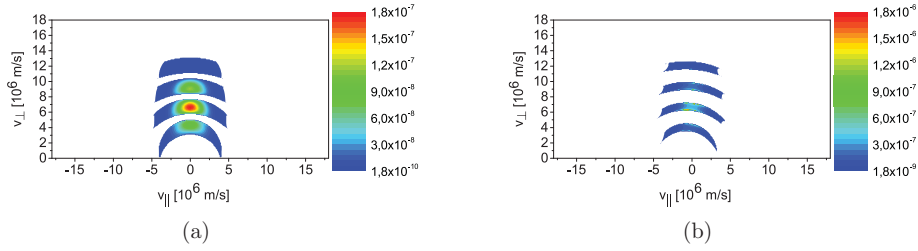


Figure 9. Products $w \times f$ of the weight functions illustrated in figure 7 and the bi-Maxwellian illustrated in figure 8. The observation angles are (a) $\phi = 90^\circ$ and (b) $\phi = 30^\circ$. The γ -rays observed in each narrow energy range originate from small regions in velocity space. (a) $\phi = 90^\circ$. (b) $\phi = 30^\circ$.

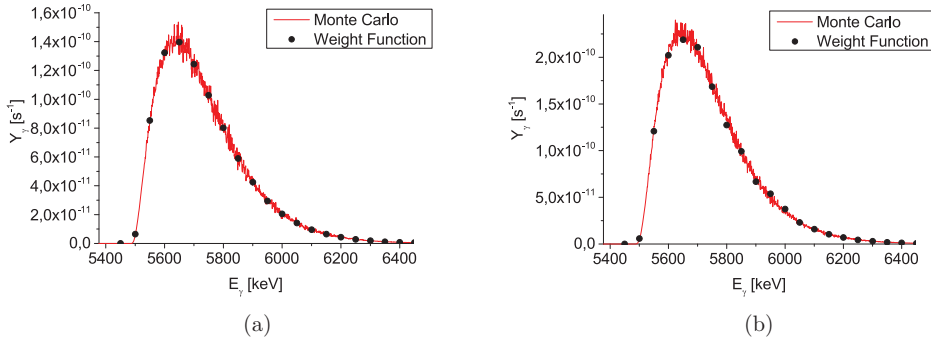


Figure 10. Energy spectra for the bi-Maxwellian distribution from figure 8 as calculated using Monte Carlo simulations and by weight functions for (a) $\phi = 90^\circ$ and (b) $\phi = 30^\circ$. The spectrum shows the number of detected γ -photons per second (photons s^{-1}) in small energy bins of widths $E_{\gamma,2} - E_{\gamma,1} = 1$ keV. (a) $\phi = 90^\circ$. (b) $\phi = 30^\circ$.

if the cross sections are poorly known. Three examples of one-step reactions with less well established cross sections are $D(D,\gamma)^4\text{He}$, $D(T,\gamma)^5\text{He}$ and $T(p,\gamma)^4\text{He}$. The highly energetic γ -rays from these reactions (see table 1) could be observable at ITER as deuterium and tritium are the main constituents of ITER plasmas and the continuum emission above 10 MeV in ITER is practically zero.

Some example probability functions of the $D(p,\gamma)^3\text{He}$, $D(D,\gamma)^4\text{He}$ and $T(p,\gamma)^4\text{He}$ reactions are illustrated in figure 11. The $D(p,\gamma)^3\text{He}$ reactions with fast protons provides the narrowest weight functions suggesting direct fast-proton energy resolution. $D(p,\gamma)^3\text{He}$ with fast deuterium and thermal protons (as might be useful in the low-activation phase of ITER with hydrogen plasmas and deuterium beam injection) and $T(p,\gamma)^4\text{He}$ have somewhat broader weight functions tilted towards negative pitches. The $D(D,\gamma)^4\text{He}$ reaction provides the lowest fast-ion energy resolution.

Reactions with so-called intrinsic broadening require special attention, for example the $D(T,\gamma)^5\text{He}$ reaction. The ground state of the ^5He nucleus has a broad energy width due to its very short lifetime after which it decays to ^4He and a neutron. The energy of the ground state is then defined as Lorentzian with a width $\sigma_Q^* = 0.648$ MeV obeying the uncertainty principle. In this case DT gamma-ray energies also follow a Lorentzian distribution centered about the nominal energy $Q = 16.85$ MeV:

$$\text{pdf}(Q^*) = \frac{1}{\pi} \frac{\frac{1}{2}\sigma_Q^*}{(Q - Q^*)^2 + (\frac{1}{2}\sigma_Q^*)^2}. \quad (39)$$

We account for this effect by introducing Q^* as nuisance parameter:

$$\begin{aligned} \text{prob}(E_{\gamma,1} < E_\gamma < E_{\gamma,2} | \phi, v_{\parallel}, v_{\perp}) \\ &= \int_{Q^*} \text{prob}(E_{\gamma,1} < E_\gamma < E_{\gamma,2} | \phi, v_{\parallel}, v_{\perp}, Q^*) \times \text{pdf}(Q^*) dQ^* \\ &= \int_{Q^*} \left| \frac{\Gamma_2(Q^*, \dots) - \Gamma_1(Q^*, \dots)}{\pi} \right| \text{pdf}(Q^*) dQ^*. \end{aligned} \quad (40)$$

An example probability function for the $D(T,\gamma)^5\text{He}$ reaction is shown in figure 12. The intrinsic broadening of the peak broadens the observable velocity space, such that ions with any energy could result in the given γ -ray energy. Nevertheless, the measurement is significantly more sensitive in some regions compared with others.

8. Blurring due to high temperatures

In our model we assumed that the energy and momentum of the thermal species are negligible. Non-zero temperatures can be accounted for by the Monte-Carlo sampling approach as previously shown for NES [7] where it was found that non-zero

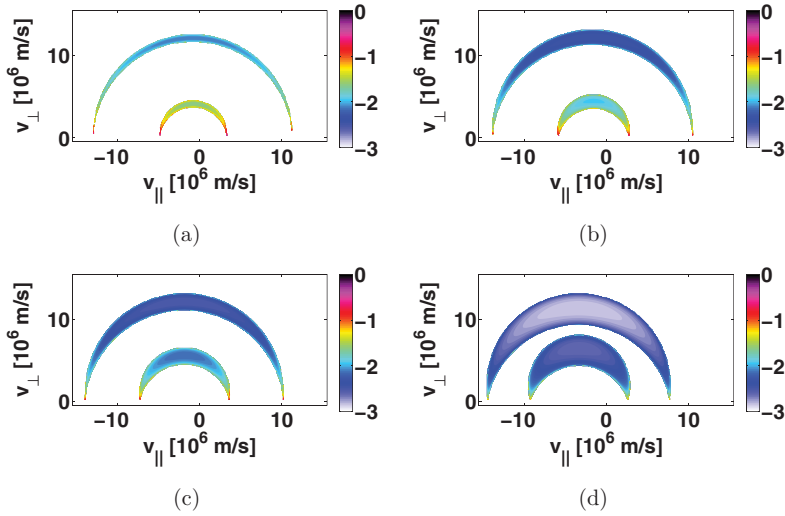


Figure 11. Probability functions $\text{prob}(E_{\gamma,1} < E_{\gamma} < E_{\gamma,2} | \phi, v_{\parallel}, v_{\perp})$ in base 10 logarithm for the various reactions: (a) $\text{D}(p,\gamma)^3\text{He}$ with fast p; (b) $\text{D}(p,\gamma)^3\text{He}$ with fast D; (c) $\text{T}(p,\gamma)^4\text{He}$ with fast p; (d) $\text{D}(D,\gamma)^4\text{He}$. The inner probability functions is at $E_{\gamma,1} - Q = 50$ keV for each reaction, and the outer at 500 keV. The observation angle is $\phi = 30^\circ$, and $E_{\gamma,2} - E_{\gamma,1} = 1$ keV.

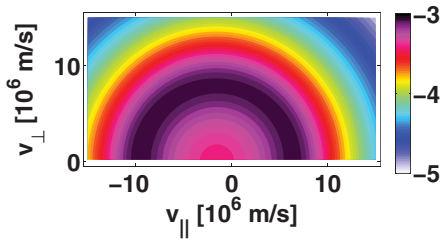


Figure 12. Probability function $\text{prob}(E_{\gamma,1} < E_{\gamma} < E_{\gamma,2} | \phi, v_{\parallel}, v_{\perp})$ of the $\text{D}(T,\gamma)^5\text{He}$ reaction for $\phi = 30^\circ$, $E_{\gamma,1} - Q = 0.35$ MeV, $E_{\gamma,2} - E_{\gamma,1} = 1$ keV in base 10 logarithm. The intrinsic width of the line is 648 keV.

temperatures blur the weight functions. In figure 13 we illustrate the blurring effect for one-step reaction GRS weight functions for a typical JET ion temperature of 5 keV. The blurring due to thermal broadening decreases the fast-ion energy resolution, but some energy resolution can still be provided at these typical temperatures. The strength of the blurring can be assessed by comparing the momenta and energies of the fast ions to those of the thermal reaction partners. Our analytical model from section 2 neglected the energies and momenta of the thermal ions (equations (4)–(7)). These approximations improve with the fast-ion velocity at given temperature. This suggests that at larger fast-ion energies the blurring effect is less pronounced and the fast-ion energy resolution thus less affected.

9. Discussion

Weight functions have previously been calculated for FIDA [3, 4], NPA [3], CTS [4, 5], FILD [43] and NES measurements [6, 7] as well as for two-step reaction GRS [8]. The

substantial differences between the weight functions of each diagnostic imply that the diagnostics complement each other well. FIDA, CTS, NES and two-step reaction GRS observe large regions in velocity space which do not allow energy resolution of the measurements unless tomographic techniques in velocity space are used [9–13]. In contrast, the velocity-space positions of the narrow weight functions of selected one-step reaction GRS measurements demonstrate that GRS can provide energy resolution of the fast-ion population, even without tomographic techniques. The fast-ion energy resolution is a strong asset of one-step reaction high resolution GRS measurements that could be highly important for further fast-ion studies at JET, ITER or other large-size tokamaks with significant γ -ray fluxes. However, the temperature should be as low as possible for good energy resolution. Figure 13 illustrates that the fast-ion energy resolution at a plasma temperature of 5 keV is degraded compared with the 0 keV case. This temperature is likely the upper limit for useful energy resolution. At the very high temperatures of burning plasmas ($T \sim 20$ keV) it is likely that tomographic inversion techniques will be required to provide useful energy resolution.

We have argued that the ITER measurement requirements on resolution of the confined α -particle energies [2] are not achievable by major core fast-ion diagnostics (FIDA [56, 65], CTS [72, 73], NES [7, 32] or two-step reaction GRS [7, 32]) without resorting to tomographic inversion in velocity space. A notable exception is NPA that can provide good energy resolution for a narrow observed pitch range if the signal-to-noise ratio is high enough. Our results would suggest that energy resolution of confined α -particles could in principle be achievable at moderate temperatures for one-step reactions involving α -particles. However, the chances to observe such peaks at ITER are bleak. The capture reactions $\alpha(\text{D},\gamma)^6\text{Li}$ and $\alpha(\text{T},\gamma)^7\text{Li}$ have much lower cross sections than

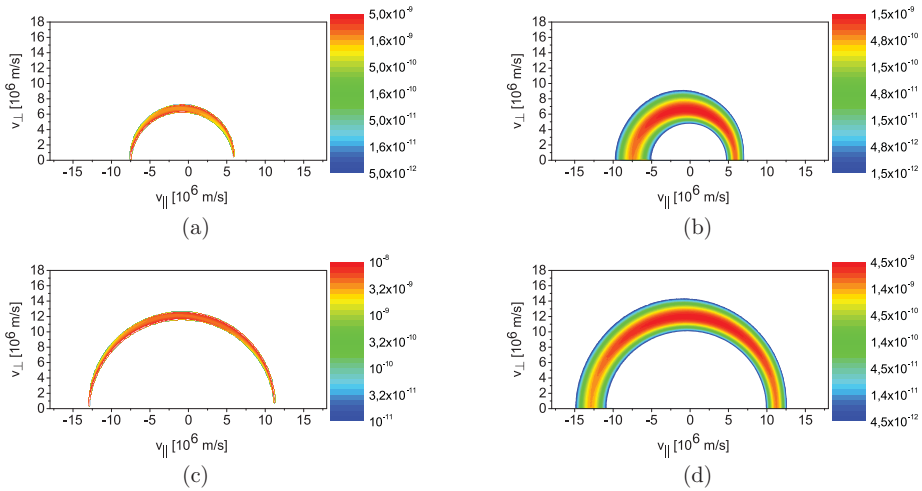


Figure 13. Comparison of numerically calculated weight functions at 0 keV and 5 keV at two γ -ray energy shifts $E_{\gamma,1} - Q$. (a) $E_{\gamma,1} - Q = 150$ keV, $T = 0$ keV. (b) $E_{\gamma,1} - Q = 150$ keV, $T = 5$ keV. (c) $E_{\gamma,1} - Q = 500$ keV, $T = 0$ keV. (d) $E_{\gamma,1} - Q = 500$ keV, $T = 5$ keV.

${}^9\text{Be}(\alpha, n\gamma){}^{12}\text{C}$ by about five to six orders of magnitude at the resonances. As deuterium and tritium will be about 100 times more abundant than beryllium in ITER and the velocity-space observation regions have comparable sizes, the emission will be about three to four orders of magnitude smaller. We can expect counting rates on the order of 1 Hz in a spectral range (1–3 MeV) where the background counting rates are on the order of 100 kHz. Hence the observation of one-step reaction peaks involving α -particles at ITER will be extremely difficult if not impossible. Hence one-step reaction GRS will likely not be able to meet the ITER measurement requirement on energy resolution of confined α -particles either. Nevertheless, other fast ions should be readily observable at ITER and DEMO. $\text{T}(p, \gamma){}^4\text{He}$ has been highlighted as a very promising reaction in DT plasmas [35] as may be demonstrated using ICRH minority heating in the upcoming tritium campaign at JET. The $\text{D}(T, \gamma){}^5\text{He}$ reaction should be observable, as count rates on the order of 1 kHz are expected in a high-energy spectral range (>10 MeV) where the background is practically zero. Other ions accelerated by ion cyclotron resonance heating, e.g. ${}^3\text{He}$, could also be readily observable. The $\text{D}(D, \gamma){}^4\text{He}$ reaction peak could so far not be detected in JET discharges, but might appear at ITER.

Weight functions are now available for all major core fast-ion diagnostics. At ASDEX Upgrade [74], full tomographic inversion of fast-ion measurements to infer fast-ion distribution functions based on weight functions has already been demonstrated [11]. Such a full tomographic inversion is not likely to be achievable based on one-step reaction GRS measurements by themselves. However, ASDEX Upgrade has up to six FIDA views [56, 62, 65], two CTS views [55, 63, 75–78] one NES view [79, 80], one GRS view [41], one NPA [81] as well as three FILD diagnostics [82, 83]. We can in principle combine the one-step reaction GRS with the other fast-ion measurements [10, 84]. This approach is also promising for

JET which is equipped with two NES views, two GRS views as well as an NPA [31, 32]. Lastly, we will be able to show the velocity-space sensitivity of GRS measurements at ITER [34] and DEMO [35]. ITER will be equipped with GRS, NES [2] and CTS [85–87] as well as fast-ion charge-exchange recombination spectroscopy [88]. With this set of diagnostics, measurements of the 2D fast-ion velocity distribution functions on ITER, and hence energy resolution, should be in reach.

10. Conclusions

We derived analytic expressions, so-called weight functions, describing the velocity-space observation regions of one-step reaction GRS measurements. The spectral resolution of the γ -rays achievable with modern detectors allows energy resolution of the fast ion distribution for all pitches for selected one-step reactions at moderate plasma temperatures. One-step reaction GRS is the only major core fast-ion diagnostic that can provide energy resolution directly without tomographic inversion in velocity space which is a strong asset of this diagnostic. The $\text{D}(p, \gamma){}^3\text{He}$ reaction with fast protons has the best direct energy resolution. The $\text{D}(D, \gamma){}^4\text{He}$ allows somewhat coarser energy resolution. The direct energy resolution is worst for reactions with intrinsic broadening. High plasma temperatures as expected in ITER also strongly degrade the direct energy resolution. Nevertheless, one-step reaction GRS weight functions provide additional information on fast-ion velocity space for any machine with substantial γ -ray fluxes, such as JET, ITER and DEMO. Weight functions are now available for the major fast-ion diagnostics: FIDA, NPA, CTS, NES, and one- and two-step reaction GRS. Hence all major fast-ion diagnostics can now in principle be combined to determine fast-ion velocity distribution functions experimentally.

Acknowledgments

This work has been carried out within the framework of the EUROfusion Consortium and has received funding from the Euratom research and training programme 2014–2018 under grant agreement No 633053. The views and opinions expressed herein do not necessarily reflect those of the European Commission.

References

- [1] Romanelli F. 2015 *Nucl. Fusion* **55** 104001
- [2] Donn e A.J.H. et al 2007 Progress in the ITER physics basis chapter 7: diagnostics *Nucl. Fusion* **47** S337–84
- [3] Heidbrink W.W. et al 2007 *Plasma Phys. Control. Fusion* **49** 1457–75
- [4] Salewski M. et al 2014 *Plasma Phys. Control. Fusion* **56** 105005
- [5] Salewski M. et al 2011 *Nucl. Fusion* **51** 083014
- [6] Jacobsen A.S. et al 2014 *Rev. Sci. Instrum.* **85** 11E103
- [7] Jacobsen A.S. et al 2015 *Nucl. Fusion* **55** 053013
- [8] Salewski M. et al 2015 *Nucl. Fusion* **55** 093029
- [9] Salewski M. et al 2012 *Nucl. Fusion* **52** 103008
- [10] Salewski M. et al 2013 *Nucl. Fusion* **53** 063019
- [11] Salewski M. et al 2014 *Nucl. Fusion* **54** 023005
- [12] Salewski M. et al 2015 *Plasma Phys. Control. Fusion* **57** 014021
- [13] Jacobsen A.S. et al 2016 *Plasma Phys. Control. Fusion* **58** 045106
- [14] Kiptily V.G. et al 2006 *Plasma Phys. Control. Fusion* **48** R59–82
- [15] Tardocchi M. et al 2013 *Plasma Phys. Control. Fusion* **55** 074014
- [16] Boyd D.A. et al 1989 *Nucl. Fusion* **29** 593–604
- [17] Jarvis O.N. et al 1996 *Nucl. Fusion* **36** 1513–30
- [18] Kiptily V.G. et al 2002 *Nucl. Fusion* **42** 999–1007
- [19] Kiptily V.G. et al 2003 *Rev. Sci. Instrum.* **74** 1753
- [20] Kiptily V.G. et al 2004 *Phys. Rev. Lett.* **93** 115001
- [21] Kiptily V.G. et al 2005 *Nucl. Fusion* **45** L21–5
- [22] Kiptily V.G. et al 2009 *Nucl. Fusion* **49** 065030
- [23] Kiptily V.G. et al 2012 *Plasma Phys. Control. Fusion* **54** 074010
- [24] Kiptily V.G. et al 2013 *Plasma Fusion Res.* **8** 2502071
- [25] Kiptily V.G. et al 2010 *Nucl. Fusion* **50** 084001
- [26] Murari A. et al 2010 *Rev. Sci. Instrum.* **81** 10E136
- [27] Nocente M. et al 2010 *Rev. Sci. Instrum.* **81** 10D321
- [28] Nocente M. et al 2012 *Nucl. Fusion* **52** 063009
- [29] Tardocchi M. et al 2011 *Phys. Rev. Lett.* **107** 205002
- [30] Shevelev A.E. et al 2013 *Nucl. Fusion* **53** 123004
- [31] Eriksson J. et al 2015 *Nucl. Fusion* **55** 123026
- [32] Schneider M. et al 2016 Modelling third harmonic ion cyclotron acceleration of deuterium beams for JET fusion product studies experiments submitted
- [33] Romanelli F. 2013 *Nucl. Fusion* **53** 104002
- [34] Chugunov I.N. et al 2011 *Nucl. Fusion* **51** 083010
- [35] Kiptily V. 2015 *Nucl. Fusion* **55** 023008
- [36] Newman D.E. and Cecil F. 1984 *Nucl. Instrum. Methods Phys. Res. A* **227** 339
- [37] Cecil F.E. and Medley S.S. 1988 *Nucl. Instrum. Methods Phys. Res. A* **271** 628
- [38] Kondoh T. et al 1997 *J. Nucl. Mater.* **241–3** 564
- [39] Nishitani T. et al 2001 *Rev. Sci. Instrum.* **72** 877
- [40] Nocente M. et al 2013 *IEEE Trans. Nucl. Sci.* **60** 1408
- [41] Nocente M. et al 2012 *Nucl. Fusion* **52** 094021
- [42] Kiptily V.G. 1990 *Fusion Sci. Tech.* **18** 583
- [43] Pace D.C. et al 2012 *Rev. Sci. Instrum.* **83** 073501
- [44] Heidbrink W.W. 2010 *Rev. Sci. Instrum.* **81** 10D727
- [45] Geiger B. et al 2014 *Nucl. Fusion* **54** 022005
- [46] Heidbrink W.W. et al 2006 *Rev. Sci. Instrum.* **77** 10F120
- [47] Luo Y. et al 2007 *Rev. Sci. Instrum.* **78** 033505
- [48] Podest a M. et al 2008 *Rev. Sci. Instrum.* **79** 10E521
- [49] Van Zeeland M.A. et al 2009 *Plasma Phys. Control. Fusion* **51** 055001
- [50] Van Zeeland M.A. et al 2010 *Nucl. Fusion* **50** 084002
- [51] Bortolon A. et al 2010 *Rev. Sci. Instrum.* **81** 10D728
- [52] Heidbrink W.W. et al 2011 *Plasma Phys. Control. Fusion* **53** 085007
- [53] Michael C.A. et al 2013 *Plasma Phys. Control. Fusion* **55** 095007
- [54] Heidbrink W.W. et al 2014 *Plasma Phys. Control. Fusion* **56** 095030
- [55] Nielsen S.K. et al 2015 *Plasma Phys. Control. Fusion* **57** 035009
- [56] Geiger B. et al 2015 *Plasma Phys. Control. Fusion* **57** 014018
- [57] Heidbrink W.W. et al 2008 *Rev. Sci. Instrum.* **79** 10E520
- [58] Podesta M. et al 2009 *Phys. Plasmas* **16** 056104
- [59] Garcia-Munoz M. et al 2011 *Nucl. Fusion* **51** 103013
- [60] Geiger B. et al 2011 *Plasma Phys. Control. Fusion* **53** 065010
- [61] Muscatello C.M. et al 2012 *Plasma Phys. Control. Fusion* **54** 025006
- [62] Geiger B. et al 2013 *Rev. Sci. Instrum.* **84** 113502
- [63] Rasmussen J. et al 2015 *Plasma Phys. Control. Fusion* **57** 075014
- [64] Pace D.C. et al 2013 *Phys. Plasmas* **20** 056108
- [65] Geiger B. et al 2015 *Nucl. Fusion* **55** 083001
- [66] Weiland M. et al 2016 *Plasma Phys. Control. Fusion* **58** 025012
- [67] Nocente M. et al 2015 *Nucl. Fusion* **55** 123009
- [68] Nocente M. 2012 Neutron and gamma-ray emission spectroscopy as fast ion diagnostics in fusion plasmas *PhD Thesis* University of Milano Bicocca <https://boa.unimib.it/handle/10281/28397>
- [69] Burbidge E.M. et al 1957 *Rev. Mod. Phys.* **29** 547–650
- [70] Bosch H.S. and Hale G. 1992 *Nucl. Fusion* **32** 611–31
- [71] Proverbio I. et al 2010 *Rev. Sci. Instrum.* **81** 10D320
- [72] Moseev D. et al 2011 *Plasma Phys. Control. Fusion* **53** 105004
- [73] Nishiura M. et al 2014 *Nucl. Fusion* **54** 023006
- [74] Stroth U. et al 2013 *Nucl. Fusion* **53** 104003
- [75] Meo F. et al 2008 *Rev. Sci. Instrum.* **79** 10E501
- [76] Meo F. et al 2010 *J. Phys.: Conf. Ser.* **227** 012010
- [77] Salewski M. et al 2010 *Nucl. Fusion* **50** 035012
- [78] Furtula V. et al 2012 *Rev. Sci. Instrum.* **83** 013507
- [79] Tardini G. et al 2012 *J. Instrum.* **7** C03004
- [80] Tardini G. et al 2013 *Nucl. Fusion* **53** 063027
- [81] Schneider P.A. et al 2015 *Rev. Sci. Instrum.* **86** 073508
- [82] Garcia-Munoz M. et al 2013 *Nucl. Fusion* **53** 123008
- [83] Garcia-Munoz M. et al 2013 *Plasma Phys. Control. Fusion* **55** 124014
- [84] Jacobsen A.S. et al 2016 *Plasma Phys. Control. Fusion* **58** 042002
- [85] Salewski M. et al 2008 *Rev. Sci. Instrum.* **79** 10E729
- [86] Salewski M. et al 2009 *Plasma Phys. Control. Fusion* **51** 035006
- [87] Salewski M. et al 2009 *Nucl. Fusion* **49** 025006
- [88] Kappatou A. et al 2012 *Nucl. Fusion* **52** 043007

Reference [10]

[10]. M Salewski et al. (2016) *Nuclear Fusion* **56** 106024. High-definition velocity-space tomography of fast-ion dynamics

High-definition velocity-space tomography of fast-ion dynamics

M. Salewski¹, B. Geiger², A.S. Jacobsen², P.C. Hansen³, W.W. Heidbrink⁴,
S.B. Korsholm¹, F. Leipold¹, J. Madsen¹, D. Moseev⁵, S.K. Nielsen¹,
M. Nocente^{6,7}, T. Odstrčil², J. Rasmussen¹, L. Stagner⁴, M. Stejner¹,
M. Weiland² and the ASDEX Upgrade team²

¹ Department of Physics, Technical University of Denmark, Kgs. Lyngby, Denmark

² Max-Planck-Institut für Plasmaphysik, Garching, Germany

³ Department of Applied Mathematics and Computer Science, Technical University of Denmark, Kgs. Lyngby, Denmark

⁴ University of California Irvine, Irvine, CA, USA

⁵ Max-Planck-Institut für Plasmaphysik, Greifswald, Germany

⁶ Department of Physics, University of Milano Bicocca, Milano, Italy

⁷ Istituto di Fisica del Plasma, Consiglio Nazionale delle Ricerche, Milano, Italy

E-mail: msal@fysik.dtu.dk

Received 25 May 2016, revised 11 July 2016

Accepted for publication 18 July 2016

Published 19 August 2016



CrossMark

Abstract

Velocity-space tomography of the fast-ion distribution function in a fusion plasma is usually a photon-starved tomography method due to limited optical access and signal-to-noise ratio of fast-ion D_α (FIDA) spectroscopy as well as the strive for high-resolution images. In high-definition tomography, prior information makes up for this lack of data. We restrict the target velocity space through the measured absence of FIDA light, impose phase-space densities to be non-negative, and encode the known geometry of neutral beam injection (NBI) sources. We further use a numerical simulation as prior information to reconstruct where in velocity space the measurements and the simulation disagree. This alternative approach is demonstrated for four-view as well as for two-view FIDA measurements. The high-definition tomography tools allow us to study fast ions in sawtoothed plasmas and the formation of NBI peaks at full, half and one-third energy by time-resolved tomographic movies.

Keywords: fast ions, tomography, tokamaks, sawteeth, neutral beam injection, fast-ion D-alpha spectroscopy

 Online supplementary data available from stacks.iop.org/NF/56/106024/mmedia

(Some figures may appear in colour only in the online journal)

1. Introduction

It is often convenient to split ion distribution functions in magnetized fusion plasmas into two parts. One part contains fast ions from fusion reactions or auxiliary heating and the other part thermal ions. The latter is by definition described by a Maxwellian distribution and thus fully determined by a temperature T_i , a density n_i and a drift velocity \mathbf{v}_i . As T_i and n_i are nearly constant on a flux surface, bulk-ion measurements often refer to flux surface measurements of these fundamental

parameters [1–4]. Fast-ion velocity distribution functions are much more complex. They are not flux functions due to the large drift excursions of fast ions, and they are in general 6D functions in phase space. Nevertheless, the cyclotron motion in strongly magnetized plasmas implies an approximate rotational symmetry which effectively reduces the dimensionality of velocity space to two. Usually fast-ion measurements do not refer to measurements of the fundamental high-dimensional fast-ion distribution functions but rather to measurements of local 1D projections or other derived quantities such as the

measured spectra in collective Thomson scattering (CTS) [5–8], fast-ion D_α spectroscopy (FIDA) [9–11], neutron emission spectrometry (NES) [12–15] and γ -ray spectrometry (GRS) [16–19]. This is in contrast to bulk-ion measurements where the fundamental parameters T_i , n_i and \mathbf{v}_i are inferred from the spectra and presented as measurements whereas the spectra themselves are of secondary interest.

Velocity-space tomography allows us to infer the fundamental 2D fast-ion velocity distribution functions from measured spectra in analogy to bulk-ion measurements [20–30, 31]. The 2D velocity distribution function is spatially localized in a small measurement volume which we take to be a single point in position space. The fast-ion measurements depend on phase space in a complicated way illustrated by so-called weight functions which have been formulated for FIDA [10, 32], neutral particle analyzers (NPA) [10], CTS [21], fast-ion loss detectors [33], NES [34, 35] and GRS [36, 37]. To exploit the rich information about fast ions contained in the measurements by traditional procedures, we need to consider hundreds of data points, e.g. spectral bins, together with the corresponding weight functions. Further, the spectral measurements also depend on nuisance parameters such as bulk-ion densities or temperatures.

Velocity-space tomography provides a way to process this wealth of information at once by inverting the data. It provides a 2D image that is straightforward to interpret, that is the best useful fit to hundreds of simultaneous measurements from different diagnostics, that shows the fundamental quantity of interest rather than derived quantities, and that accounts for nuisance parameters. The tomography approach also allows an alternative way to compare fast-ion measurements and numerical simulations. Traditionally, this is done by comparing the measurements with simulated measurements in units particular to the diagnostic, e.g. the spectral density of the measured neutron or photon fluxes (D_α , γ , or mm-wave). Velocity-space tomography allows us to use the fundamental 2D velocity distribution function as a meeting ground between theory and observation for any combination of fast-ion diagnostics [23, 29, 31].

Until now velocity-space tomography has relied on standard inversion methods such as truncated singular value decomposition (TSVD), the maximum entropy method, and variants of the Tikhonov regularization [24, 25, 27, 28]. For measurements with high data quality and signal-to-noise ratio, these inversion methods work well. We have previously shown that it is possible to correctly reconstruct the injection energy in plasma heated by neutral beam injection (NBI), and good agreement with TRANSP predictions was found in the absence of strong magnetohydrodynamic (MHD) activity [24, 27]. Fast-ion velocity-space redistribution patterns of sawtooth crashes could also be reconstructed with confidence [26–31]. However, velocity-space tomography is usually a photon-starved enterprise since the signal-to-noise ratio is often low compared with many other tomography applications and the optical access to tokamak plasmas is limited. The FIDA emission is weak compared with other components of the measured spectra, e.g. the beam emission. In addition,

the spectra are often polluted with strong background contributions from bremsstrahlung and impurity line radiation. This hampers the analysis in plasmas with high electron density or high impurity content. In conflict with the limited amount of data, we strive for high-resolution images requiring the inference of many unknowns. Consequently, the inversions based on standard methods have been plagued by artifacts, for example non-zero phase-space densities at energies larger than the NBI energy or negative phase-space densities, even though artifacts can be minimized in optimized discharges usually based on L-mode plasmas with low density and low heating power [24, 26–28]. Artifacts can be attenuated by increasing the number of measurement data points by installation of additional fast-ion diagnostics [22, 27]. However, often economic or technical constraints do not allow this. In high-definition velocity-space tomography we make up for the lack of data through various types of prior information. This not only improves results for the five-view FIDA diagnostic at the tokamak ASDEX Upgrade [38], but it also allows the use of inversion techniques for more common FIDA systems with two or three views. The attenuation of artifacts through the use of prior information further allows an increased resolution of the images.

We discuss prior information for velocity-space tomography in section 2 and the choice of the regularization strength using current inversion techniques in section 3. Substantial improvements brought about by prior information are demonstrated in sections 4 and 5. In section 6 we study fast-ion velocity distributions in NBI heated plasmas and dynamics in sawtooth plasmas using high-definition movies applying our new techniques. Finally, we draw conclusions in section 7.

2. Prior information for velocity-space tomography

Velocity-space tomography entails the solution of an ill-posed problem in which we seek F^* solving the matrix equation

$$WF^* = S \quad (1)$$

where W and S are known [22], F^* is the fast-ion velocity distribution function discretized in n pixels, S holds m fast-ion measurements, and W is an $m \times n$ matrix composed of weight functions. S and W are normalized by the uncertainties of the measurements [23]. Noise in the measurements makes the rows of the matrix equation (1) inconsistent, so that there is no solution irrespective of the choice of n ($n = m$, $n < m$, or $n > m$). One might have hoped that one could instead solve the related least-squares problem

$$F_{LS}^* = \arg \min_F \|WF - S\|_2, \quad (2)$$

where F is an arbitrary fast-ion velocity distribution function and F_{LS}^* is the least-squares solution. However, this is also useless since the matrix W is ill-conditioned and hence the solution F_{LS}^* is not stable. This means that small perturbations in S can lead to large perturbations in F_{LS}^* which is therefore dominated by random jitter. Nevertheless, we can construct a related well-conditioned problem by imposing additional requirements that reflect prior assumptions about the solution

Table 1. Prior information used in this article, their benefits and risks.

Prior	Benefits	Risks
L (1 st -order)	Good for smooth functions.	Misses spikes and ridges.
$F > 0$	Always true, improves solutions.	$F < 0$ could point to data errors that are now missed.
$F(E_0, p_0) = 0$	Avoids artifacts in null-measurement region.	Misses marginal densities of fast ions in null-measurement region. Possibly artifacts at the boundary.
$\kappa(E, p)$	Accounts well for NBI peaks.	Misses any peak displacement. Might introduce spurious peaks.
F_{sim}	Good at locating discrepancies in velocity space.	Possible misinterpretation if the absolute scaling is wrong.

Note: Each prior is optionally used when appropriate.

and that provide useful and stable solutions. This is called regularization. A popular regularization method in plasma physics is the Tikhonov regularization [28, 39, 40] in which we solve the minimization problem

$$F^* = \arg \min_F \{ \|WF - S\|_2^2 + \lambda^2 \|LF\|_2^2 \}. \quad (3)$$

In equation (3), F^* minimizes the sum of the residual of the original ill-posed problem (first term) and the norm of the additional requirement on the solution (second term). A common choice is to require that the norm of the gradients in F^* is small, i.e. that the solution is smooth. In this so-called first-order Tikhonov regularization, the penalty matrix L is a matrix operator effecting a finite difference approximation of a gradient [28]. We calculate the gradient in $(v_{\parallel}, v_{\perp})$ -space where parallel and perpendicular denote directions with respect to the magnetic field [28]. The free regularization parameter λ balances how well the solution should fit the noisy data and how much it should obey the regularization constraint. Equation (3) shows that for small λ 's the residual of the original problem dominates whereas for large λ 's the norm of the regularization constraint dominates. The challenge now is to select λ leading to a useful and stable solution as we will discuss in section 3. An equivalent formulation of Tikhonov's minimization problem in equation (3) is

$$F^* = \arg \min_F \left\| \begin{pmatrix} W \\ \lambda L \end{pmatrix} F - \begin{pmatrix} S \\ 0 \end{pmatrix} \right\|_2. \quad (4)$$

Our computations of Tikhonov solutions in the following will be based on the formulation in equation (4) as it is most stable and best suited for numerical computations. Our exposition will focus on Tikhonov regularization, but our methods are applicable to other regularization methods as we will demonstrate for TSVD. The types of prior information presented in the following sections are summarized in table 1 together with their benefits and risks. Each type of prior information can be optionally added when appropriate.

2.1. Null measurements

FIDA measures Doppler-shifted D_{α} -light emitted when a fast deuterium neutral is formed in a charge-exchange reaction from a fast deuterium ion and then decays from the third to the second excited state [9]. In many experiments, there is an upper limit to the observed Doppler shifts. Parts of a spectrum where no FIDA light is observed above the noise

floor are referred to as null measurements. The wavelength ranges of null measurements are related to velocity-space regions through weight functions [32]. We refer to such weight functions as null-measurement weight functions. If treated on an equal footing with detections of FIDA light, null measurements already contribute strongly to the reconstruction of the large-scale shape of the velocity distribution function since they tend to decrease the reconstructed phase-space densities in the velocity space covered by the null-measurement weight functions. For that reason the FIDA system at ASDEX Upgrade was upgraded to measure red- and blue-shifted light in all spectra so that the absence of FIDA light could be measured [27]. Still, inversions are plagued by artifacts in velocity-space regions covered by null-measurement weight functions where the phase-space densities should be negligible [24].

Here we remedy such artifacts by analyzing the measurements in two stages. In the first stage we identify regions in velocity space where null measurements suggest phase-space densities below the detection limit of the diagnostic according to

$$\int w_0 F_{\text{true}} dE dp = S \leq \epsilon \quad (5)$$

where w_0 is the null-measurement weight function, F_{true} is the unknown true fast-ion velocity distribution function, S is the measured signal, and ϵ is the noise floor. As is customary, w_0 and F_{true} are given in energy-pitch coordinates (E, p) , where E is the energy of the fast ions and p is the pitch defined as $p = \frac{v_{\parallel}}{v}$. v is the fast-ion speed, and v_{\parallel} the velocity component anti-parallel to the magnetic field. The non-negativity of w_0 and F_{true} would allow us to conclude from an absolutely certain null-measurement (i.e. $\epsilon = 0$) that F_{true} must be zero in the regions covered by the null-measurement weight function. If noise is present, the strict argument does not hold. Nevertheless, we can still assert that the velocity space covered by the null-measurement weight function contains so few ions that they cannot be detected against the noise floor and thus neglect the small phase-space densities in these regions. This stage does not require the solution of an inverse problem and is thus very reliable if null-measurements can be told apart from measurements of small FIDA intensities, i.e. if the measurement uncertainties can be quantified reliably. In the second stage we solve the tomography problem neglecting the phase-space

densities in the regions covered by null-measurement weight functions:

$$F^* = \arg \min_F \left\| \begin{pmatrix} W \\ \lambda L \end{pmatrix} F - \begin{pmatrix} S \\ 0 \end{pmatrix} \right\|_2 \quad \text{subject to } F^*(E_0, p_0) = 0. \quad (6)$$

E_0 and p_0 are the energies and pitches covered by the null-measurement weight functions, and $F^*(E_0, p_0)$ are the elements of the vector F^* that represent the null-measurement region. This condition determines an upper energy boundary of the target velocity space that we seek to reconstruct (figure 1). As weight functions are not bounded in energy, the target velocity space has also been judiciously restricted at some energy in previous work. A common choice is 10–50 keV above the injection energy of 60 keV or 90 keV as phase-space densities at larger energies are supposed to be small. Null-measurement weight functions allow us to determine this upper boundary in energies from the measurements in an optimal way that does not allow artifacts in the null-measurement region and that minimizes the number of unknowns in the inversion. This upper boundary is a strong function of pitch (figure 1). Neoclassical simulations by TRANSP [41] agree very well with the shape of the null-measurement velocity space (figure 2). Maxima of the velocity distribution function simulated by TRANSP appear at 60 keV and at 30 keV, corresponding to the full and half injection energy, whereas here no peak appears at 20 keV (one-third energy) as the TRANSP model removes thermalized particles in this region due to the high temperature.

The null-measurement idea is based on the presence of a sharp transition to zero in the fast-ion velocity distribution function. This is fulfilled in NBI discharges at the highest injection energy. In experiments with ion cyclotron resonance heating, the fast-ion distribution function is not expected to have a sharp transition within the energy range accessible to FIDA, such that the null-measurement technique cannot be used here. Nevertheless, we note that null measurements are often found in NES and GRS measurements in plasmas with third harmonic ICRH at JET as these diagnostics can easily detect MeV-range ions [14].

2.2. Non-negativity

One of the advantages of maximum entropy regularization is that it does not allow negative phase-space densities. The TSVD and variants of the Tikhonov regularization (one of which is inspired by Fisher information) do allow negative phase-space densities and in fact inversions based on those methods often contain regions with small negative phase-space densities. Negative phase-space densities have usually been ignored [11, 22–25, 28–31]. In a recent study such negative densities were strongly attenuated by a new approach [27]. It used fictitious measurements with pixelized weight functions covering the most negative values in the inversions. These fictitious measurements were given enough weight to iteratively force the phase-space densities

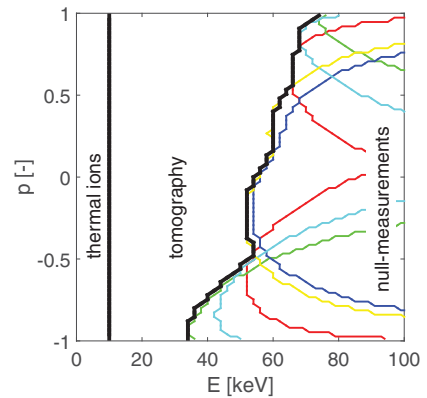


Figure 1. The coloured lines circumscribe the regions covered by null-measurement FIDA weight functions for ASDEX Upgrade discharge #31557 where the five colours represent the five views. These null-measurements suggest negligible fast-ion densities for energies above the black line to the right. The vertical black line at 10 keV is defined as the border between fast and thermal ions. The phase-space densities between the black lines are found by tomographic inversion.

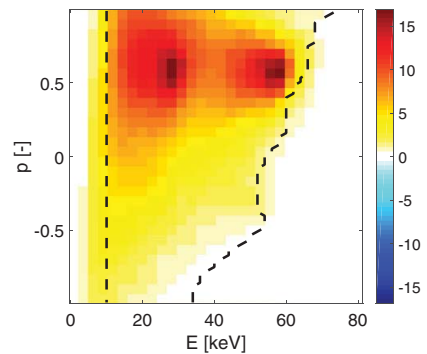


Figure 2. Comparison of the target velocity space identified in figure 1 with a TRANSP simulation of the fast-ion velocity distribution function ($10^{16} \text{ keV}^{-1} \text{ m}^{-3}$). The simulation confirms the form of the null-measurement region with negligible phase-space densities. The colorbar is linear and includes positive phase-space densities as well as negative phase-space densities to allow comparisons with figures 4 and 5.

to negligible, yet still negative, values. Here we simply impose the constraint that the solution be non-negative and solve the minimization problem

$$F^* = \arg \min_F \left\| \begin{pmatrix} W \\ \lambda L \end{pmatrix} F - \begin{pmatrix} S \\ 0 \end{pmatrix} \right\|_2 \quad \text{subject to } F^* \geq 0 \quad (7)$$

using a standard non-negative least-squares algorithm [42]. The implementation as constraint has the advantage that no assumptions about the negative regions are needed. We will in the following also impose non-negativity and null-measurement constraints together:

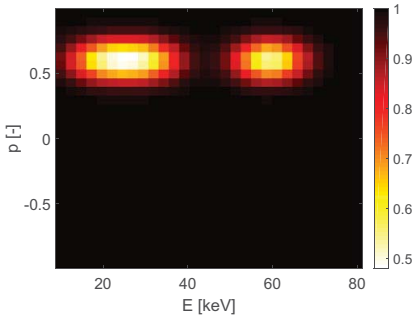


Figure 3. The known positions of the beam injection peaks are encoded by using a 2D regularization given by $\kappa(E, p)$ [-]. The total regularization strength is given by $\lambda\kappa(E, p)$. The half- and one-third energy injection peaks merge due to the low resolution.

$$F^* = \arg \min_F \left\| \begin{pmatrix} W \\ \lambda L \end{pmatrix} F - \begin{pmatrix} S \\ 0 \end{pmatrix} \right\|_2 \quad \text{subject to} \quad \begin{cases} F^*(E_0, p_0) = 0 \\ F^* \geq 0 \end{cases}. \quad (8)$$

2.3. Positions of neutral beam injection peaks

Often the fast-ion distribution function has peaks at full-, half and one-third NBI energy which are difficult to reconstruct. We will show a reconstruction of all three NBI peaks based on TSVD exploiting null-measurements in section 4. First-order Tikhonov regularization, which penalizes steep gradients typical for NBI peaks, will tend to reduce the peaks. The positions of the NBI peaks, if present, are actually very well known from the geometry and energy of the beams. Three peaks are expected at $E = (20, 30, 60)$ keV and $p = 0.6$ for NBI Q3 in the plasma center. Here we encode the known geometry of the NBI by using a 2D function $\kappa(E, p)$ varying between 0.5 and 1 and solve the minimization problem

$$F^* = \arg \min_F \left\| \begin{pmatrix} W \\ \lambda\kappa(E, p)L \end{pmatrix} F - \begin{pmatrix} S \\ 0 \end{pmatrix} \right\|_2 \quad \text{subject to} \quad \begin{cases} F^*(E_0, p_0) = 0 \\ F^* \geq 0 \end{cases}. \quad (9)$$

This reduces the penalty by a factor of about two at the position of the NBI sources, where we expect large gradients (figure 3), compared with the penalty elsewhere. In this way no prior knowledge of the size of the peak is used, and in fact even a negative peak would equally well be supported by $\kappa(E, p)$.

2.4. Numerical simulations as prior information

In previous studies of velocity-space tomography based on three to five FIDA views or a mix of FIDA and CTS views, it was possible to find useful and stable inversions and hence provide measurements of the fast-ion velocity distribution function and derived quantities such as the fast-ion density [26, 28]. However, if fewer views are available or if the signal-to-noise ratio is unfavourable, this is sometimes out of reach. Here we propose a new goal of the tomography approach for such highly photon-starved situations. Rather than inferring

the full 2D velocity distribution function, we only seek to infer the distribution of any discrepancy between a numerical simulation and the measurement in velocity space. Firstly, this is a simpler task that is possible with fewer views as we will show. Secondly, deviations from a numerical simulation is often what we are actually interested in. For example, the TRANSP code accounts for neoclassical transport and likely provides a good picture of the distribution function in MHD quiescent discharges. In MHD active discharges, we often observe discrepancies from such neoclassical simulations. The discrepancies are attributed to anomalous transport in addition to the neoclassical transport which still serves as a baseline. To locate the distribution of any disagreement in velocity space, we penalize differences from the simulated velocity distribution function F_{sim} and solve the minimization problem

$$F^* = \arg \min_F \left\| \begin{pmatrix} W \\ \lambda\kappa L \end{pmatrix} F - \begin{pmatrix} S \\ \lambda\kappa L F_{\text{sim}} \end{pmatrix} \right\|_2 \quad \text{subject to} \quad \begin{cases} F^* \geq 0 \\ F^*(E_0, p_0) = 0 \end{cases}. \quad (10)$$

For very small λ 's the inversion is underregularized and is dominated by random jitter as in the previously discussed Tikhonov problems. For very large λ 's the solution is overregularized, but here the inversion then approaches the numerical simulation as equation (10) shows. The problem is now again to select λ assigning an appropriate balance between the measurements and the simulation which we will discuss in section 3. The solution F^* represents our estimate of the 2D velocity distribution function considering the simulation and the measurements. As our goal is to locate discrepancies between simulation and measurements in velocity space, we calculate

$$\Delta F^* = F^* - F_{\text{sim}} \quad (11)$$

which shows how the simulation should be modified according to the measurements. Examples will be shown in sections 5 and 6.

3. Standard inversions and the choice of the regularization parameter λ

The number of measurement data points and the number of unknowns in fast-ion velocity-space tomography is fairly small compared with many other tomography problems. Quick automatic inversion of FIDA spectra based on a library of approximate weight functions after each plasma discharge is therefore possible and will be implemented in future work. For that purpose the regularization parameter λ must be computed automatically from the data. In traditional tomography, two popular methods among many are the L-curve method [43, 44] and the generalized cross-validation (GCV) method [45]. The L-curve method has been applied to velocity-space tomography previously [28]. The GCV method seeks to minimize the prediction error by asserting that an arbitrary measurement S_i should be predicted well by the regularized solution based on the other measurements in S and that orthogonal transformations of S should not affect the choice of the

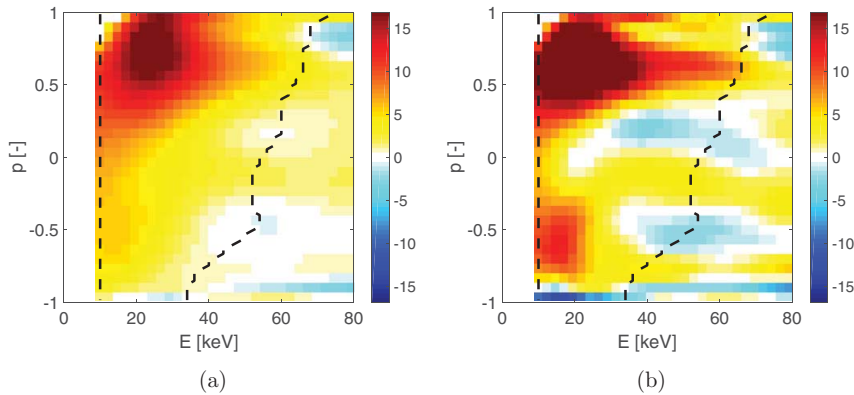


Figure 4. Unconstrained first-order Tikhonov tomographic inversions of FIDA measurements in five views in ASDEX Upgrade discharge #31557 in units ($10^{16} \text{ keV}^{-1} \text{ m}^{-3}$). The regularization parameter λ is chosen by two different methods: (a) L-curve. (b) GCV.

regularization parameter λ [45]. Recall that the Tikhonov solution $F^* = F^*(\lambda)$ is a function of the regularization parameter λ and that, for the unconstrained problem (equation (4)), we can write $F^*(\lambda) = W^\#(\lambda)S$ where the matrix $W^\#(\lambda)$ defines the solution. Then λ minimizes the GCV function

$$G(\lambda) = \frac{\|WF^*(\lambda) - S\|_2^2}{(\text{trace}(I - WW^\#(\lambda)))^2}, \quad (12)$$

where I is the identity matrix.

Figure 4 shows two unconstrained first-order Tikhonov inversions of FIDA measurements in ASDEX Upgrade discharge #31557. The level of regularization was respectively selected by the L-curve method and the GCV method. The discharge and the five-view FIDA measurements have been discussed previously [28]. The plasma was heated by NBI with the 2.5 MW source Q3 at 60 keV. The five-view FIDA measurements here and throughout the paper were made in the center of the plasma. Figure 2 shows a corresponding TRANSP simulation.

The unconstrained inversion with first-order Tikhonov regularization and L-curve regularization parameter selection in figure 4(a) shows the usual characteristics for this method. The inversion is smooth, and the overall shape, including the anisotropy and the location of the merged 20 keV and 30 keV NBI peaks, is close to our expectation. However, there are also limitations of the unconstrained inversion. First, the NBI peak at full injection energy (60 keV) does not appear. It is known that the sharp NBI peaks tend to be attenuated by first-order Tikhonov regularization [28]. Second, there are substantial phase-space densities at energies well in the null-measurement region. Here we plot up to 20 keV above the full injection energy. As already mentioned, TRANSP/NUBEAM predicts almost zero phase-space densities in the null-measurement region (figure 2), which further corroborates the hypothesis that the inferred phase-space densities are artifacts. Third, small patches of unphysical negative fast-ion phase-space densities appear, in this case in the null-measurement region. These three features of the inversions are very likely artifacts since they also appear erroneously in inversions of synthetic data where the true solution is known [22, 24, 28].

The GCV method tends to regularize less than the L-curve method (figure 4(b)) and roughly produces a regularization level as was sometimes judiciously selected [11, 24, 27]. The full energy beam injection peak (60 keV) does not appear but there is a clear ridge of large phase-space densities between the expected locations of the beam injection peaks. The ridge does not extend to energies larger than 60 keV as expected. The form of the ridge is consistent with the presence of fast ions that are slowing down due to collisions with electrons, i.e. they lose energy without significant pitch angle scattering. Nevertheless, as the critical energy is about 60 keV, collisions with thermal ions are also important leading to pitch-angle scattering as is apparent in figure 4. The unphysical negative regions are larger than for the L-curve method. A peak appears at $p = -0.5$ which is not expected according to the TRANSP simulation (figure 2) and is likely an artifact.

In velocity-space tomography, the regularization parameter has up to now been set either by judicious choice or by the L-curve method. The choice of regularization parameter or of a method to calculate it remains an open problem as one never knows *a priori* which method works best. Our criteria for good reconstruction of velocity-space distribution functions in NBI heated plasma are that there are no significant negative phase-space densities, that there are no significant phase-space densities far above the beam injection energies, that the distribution function is smooth and that the beam injection peaks are reconstructed well. Neither the L-curve nor the GCV method is consistently superior. Both methods are fairly robust but do not always work. The L-curve method can be applied irrespective of the incorporated prior information. However, the GCV method requires the existence of a regularized inverse matrix mapping the measurement space to the solution space, and so it is not directly applicable to the non-negative least-squares problem formulation or maximum entropy methods. Here we apply either method, depending on what works best for the given problem. For inversions not using a TRANSP simulation as prior information we will choose the regularization parameter λ by the GCV method applied to the unconstrained least-square problem (figure 4(b)), and then

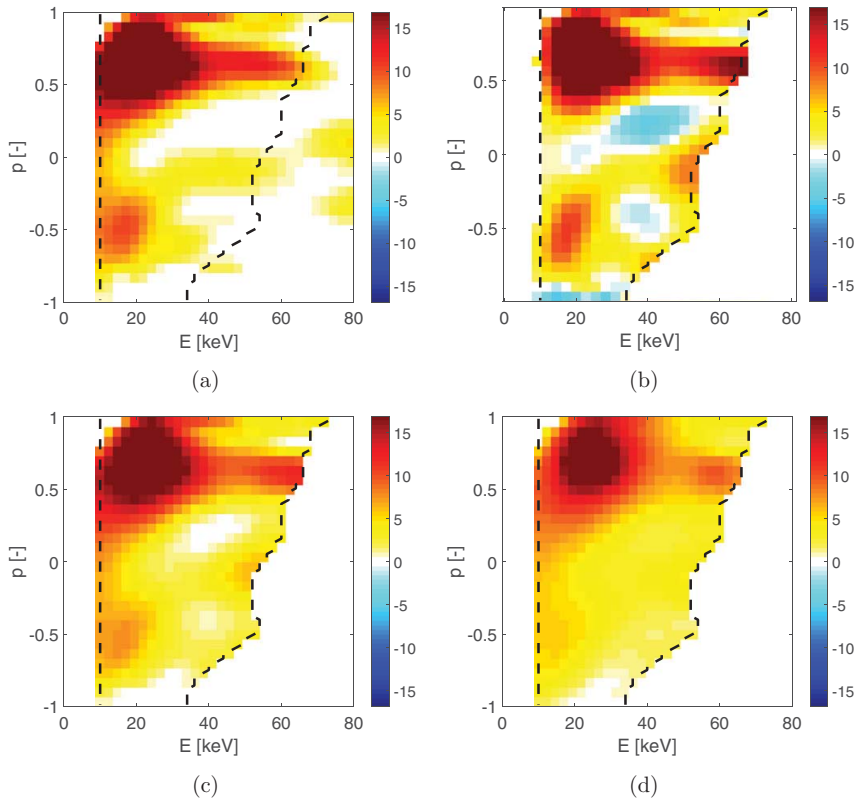


Figure 5. First-order Tikhonov tomographic inversions based on five-view FIDA measurements in ASDEX Upgrade discharge #31557. The units are $(10^{16} \text{ keV}^{-1} \text{ m}^{-3})$. Various types of prior information are used. (a) Non-negativity: $F^* \geq 0$. (b) Null-measurement constraints: $F^*(E_0, p_0) = 0$. (c) $F^* \geq 0$ and $F^*(E_0, p_0) = 0$. (d) $F^* \geq 0$, $F^*(E_0, p_0) = 0$ and known peak locations: $\kappa(E, p)$.

solve the non-negative least-squares problem with that λ . However, we apply the L-curve method for the inversions using the TRANSP simulations as prior information.

4. High-definition inversions using prior information

In this section we show that prior information based on non-negativity, null measurements and the NBI geometry improves inversions substantially. The effect of prior information based on a numerical simulation is presented in section 5. The inversions in this section represent an estimate of the 2D fast-ion velocity distribution functions based on measurements alone. The inversions in section 5 represent an estimate based on measurements and simulations or, more interestingly, of how a given simulation needs to be modified to match best with the measurements.

Figure 5(a) shows a first-order Tikhonov inversion with non-negativity constraint according to equation (7). The non-negativity constraint improves the inversions without any visible disadvantages compared with the unconstrained inversions in figure 4. By virtue of the constraint, there are

no negative regions. Erroneous phase-space densities in the null-measurement region are reduced compared with the unconstrained inversions. The full energy beam injection peak is almost invisible, but there is a clear drop in phase-space densities above the full NBI energy. A possibly spurious peak at $p = -0.5$ is present as also observed in figure 4(b).

Figure 5(b) shows a first-order Tikhonov inversion with the null-measurement constraint according to equation (6). The inversion shows a clear peak at full injection energy and a clear ridge consistent with ions slowing down due to collisions with electrons. By virtue of the constraint, the phase-space densities in the null-measurement region are zero. Regions of erroneously negative phase-space densities are present at this regularization level. It is unclear if the two peaks appearing at negative pitches are real or if they are artifacts. The peak at $p = -0.5$ also appears as in figures 4(b) and 5(a).

Figure 5(c) shows a first-order Tikhonov inversion with non-negativity and null-measurement constraints according to equation (8). By construction there are no artifacts in the null-measurement region and there are no negative phase-space densities. The white patches of very low fast-ion density circumscribed by larger fast-ion densities seem physically unlikely and would suggest that slightly more regularization

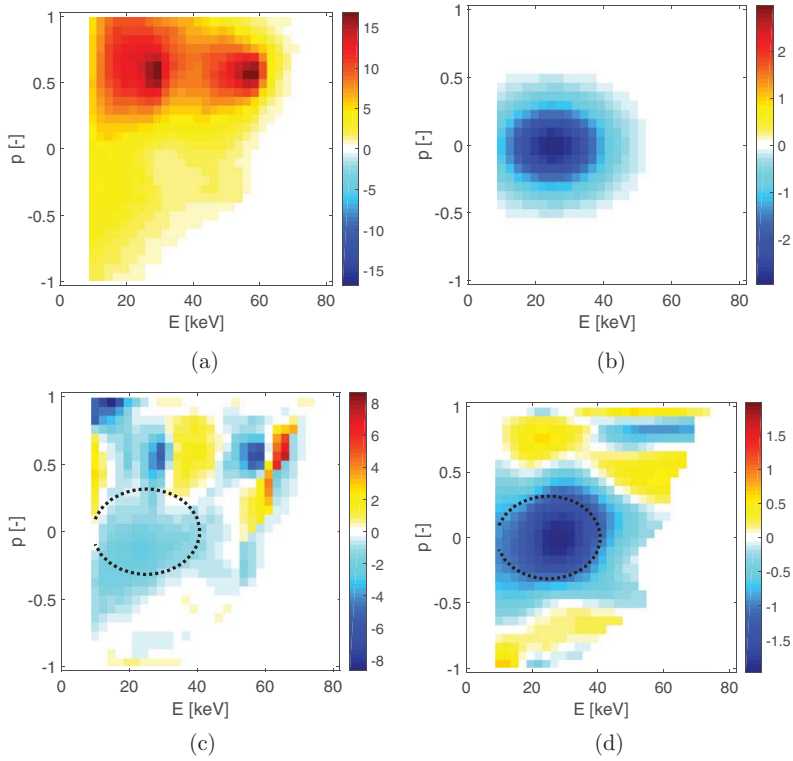


Figure 6. First-order Tikhonov tomographic inversions using a simulation as prior information. The units are $(10^{16} \text{ keV}^{-1} \text{ m}^{-3})$. (a) F_{true} which is a modified TRANSP simulation with selective ejection of particles. (b) $\Delta F = F_{\text{true}} - F_{\text{sim}}$. (c) + (d) Inversion $\Delta F^* = F^* - F_{\text{sim}}$ based on synthetic measurements of F_{true} with 5% Gaussian noise for a five-view FIDA system (c) without and (d) with the TRANSP simulation as prior information.

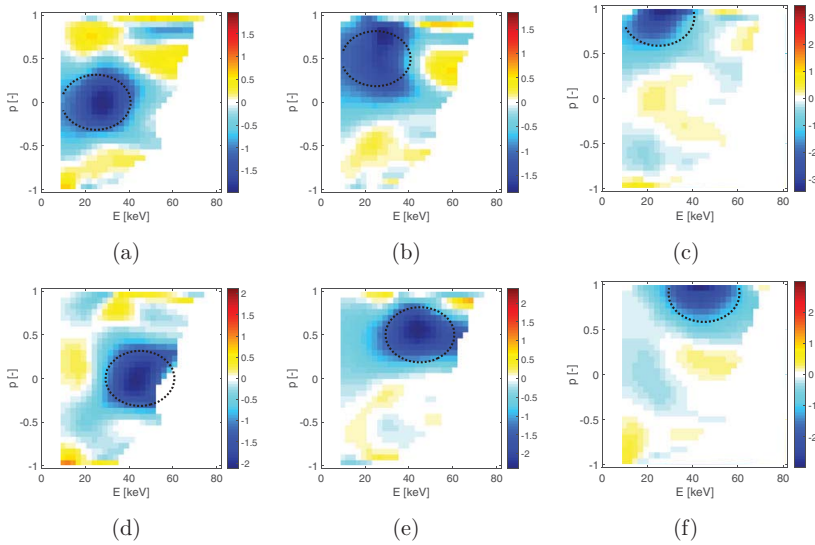


Figure 7. $\Delta F^* = F^* - F_{\text{sim}}$ where F^* is calculated as in figure 6(d). In each subfigure the black dotted line shows the true location of the discrepancy. The units are $(10^{16} \text{ keV}^{-1} \text{ m}^{-3})$. The colorbar is different for each plot.

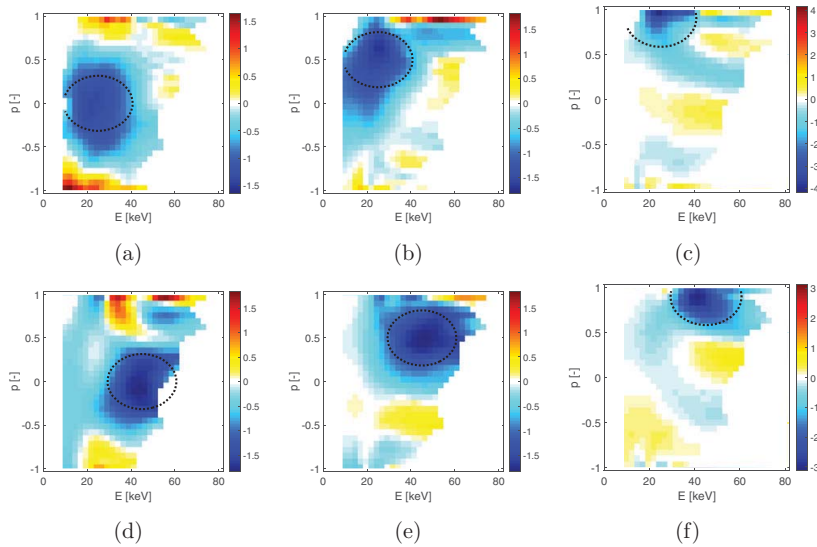


Figure 8. As figure 7, but using only two FIDA views. The angles of the lines-of-sight to the magnetic field are $\phi = [73^\circ, 153^\circ]$. The colorbar is different for each plot.

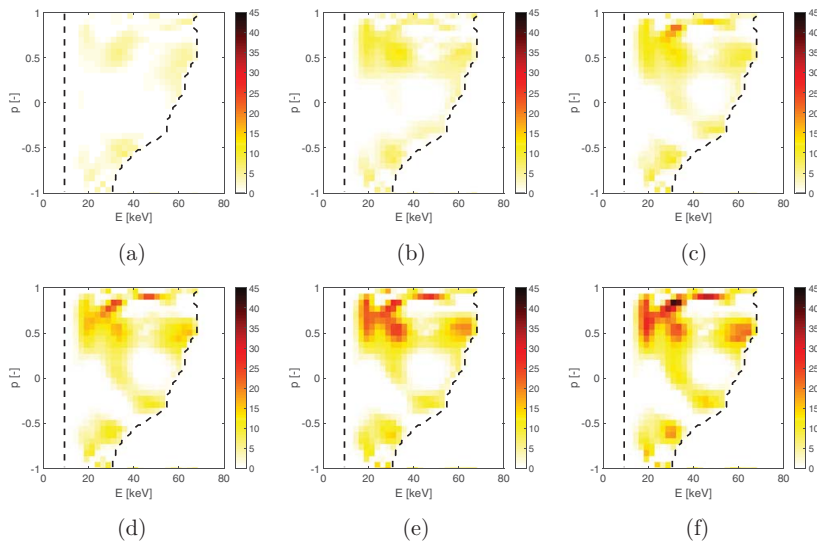


Figure 9. Inversions by TSVD with null-measurement constraint after NBI Q3 was turned on in discharge #33138 at $t = 0.4$ s. A movie is provided as supplementary material to this paper (movie 1) (stacks.iop.org/NF/56/106024/mmedia). NBI peaks at full, half, and one-third energy are gradually formed. The units are $(10^{16} \text{ keV}^{-1} \text{ m}^{-3})$. (a) 0.40 s, (b) 0.42 s, (c) 0.44 s, (d) 0.47 s, (e) 0.49 s, (f) 0.52 s.

would benefit the solution. The non-negativity constraint also tends to attenuate positive peaks because it reduces high-frequency components of the inversion and hence negative as well as positive extrema. The peak at full injection energy is present but weaker than in figure 5(b), and the ridge connecting the beam injection peaks is weaker than in figure 5(b). The two small peaks at negative pitches are attenuated compared with figure 5(b).

Finally, figure 5(d) shows a first-order Tikhonov inversion with non-negativity and null-measurement constraints and known NBI geometry according to equation (9). Two NBI peaks as well as the ridge connecting them appear. No clear artifacts, such as peaks or low-density patches at unexpected locations, appear in this inversion, and by construction there are again no artifacts in the null-measurement region and there are no negative phase-space densities. In the NBI peak

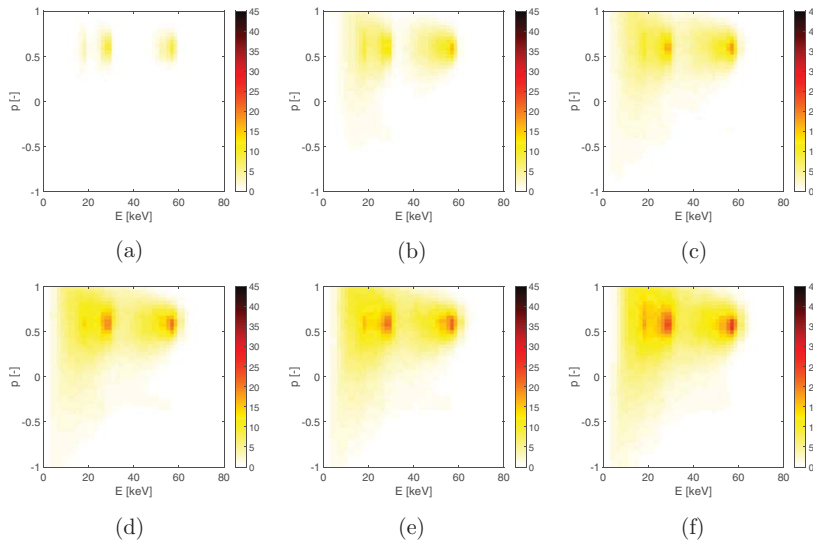


Figure 10. TRANSP simulation ($10^{16} \text{ keV}^{-1} \text{ m}^{-3}$) as in figure 9 after NBI Q3 was turned on in discharge #33138 at $t = 0.4$ s. NBI peaks at full, half, and one-third energy appear in the simulation. (a) 0.40 s, (b) 0.42 s, (c) 0.44 s, (d) 0.47 s, (e) 0.49 s, (f) 0.52 s.

region the regularization is comparatively weak so that high-definition features appear. In the regions far from the peaks the solution is smooth due to the stronger regularization. Overall, this inversion resembles the TRANSP simulation from figure 2 the most. This use of prior information will likely make inversions possible at many other tokamaks, where fewer fast-ion data than at ASDEX Upgrade is available.

5. Inversions using numerical simulations as prior information

Inversion techniques can be used to identify differences between theory and observation in velocity space. This could give clues on which physics is not adequately described in the simulation or which systematic error confounds the measurements. For this goal it is advantageous to use the numerical simulation as prior information. Figure 6 illustrates two different ways to locate differences between measurements and simulation in velocity space. Figure 6(a) shows a true distribution function F_{true} which we would like to know but which in an experiment is never known. Here we assume a modified TRANSP simulation. We have added the negative Gaussian function shown in figure 6(b) to the known TRANSP simulation F_{sim} (figure 2). This selective reduction in phase-space density is a toy model for an assumed anomalous transport phenomenon localized in velocity space which is not modelled in the TRANSP simulation F_{sim} . Hence figure 6(b) shows the difference

$$\Delta F_{\text{true}} = F_{\text{true}} - F_{\text{sim}}. \quad (13)$$

The goal is now to reconstruct ΔF_{true} , given synthetic measurements of F_{true} in five FIDA views and F_{sim} . We add 5% Gaussian noise to each synthetic measurement which is

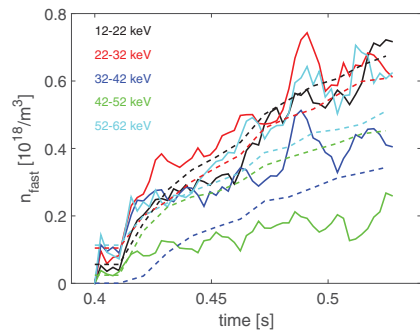


Figure 11. Measured (full lines) and simulated (dashed lines) increases in the fast-ion density for $p \in [0.3, 0.7]$ and five 10 keV wide energy intervals in ASDEX Upgrade discharge #33138 right after the NBI is switched on. The fast-ion densities are obtained by integration of the high-definition tomographic inversion in the specified regions in velocity space. The fast-ion densities in the regions containing NBI peaks grow faster.

a realistic noise level for FIDA measurements at ASDEX Upgrade. The discrepancy between measurement and simulation ΔF^* is calculated according to equation (11) without and with using the TRANSP simulation as prior information, i.e. respectively using equations (9) and (10). Figure 6(c) shows ΔF^* for the case without the TRANSP simulation as prior. In the region of the true difference, ΔF^* is negative and has approximately correct amplitudes. However, ΔF^* is dominated by large negative values at the beam injection peaks reflecting the difficulty in reconstructing the NBI peaks. The reconstructed difference ΔF^* therefore does not resemble the true difference ΔF_{true} . Figure 6(d) presents ΔF^* for the case where the TRANSP simulation has been used as prior information (equation (10)). In this case the approximate location of the discrepancy between the true distribution and

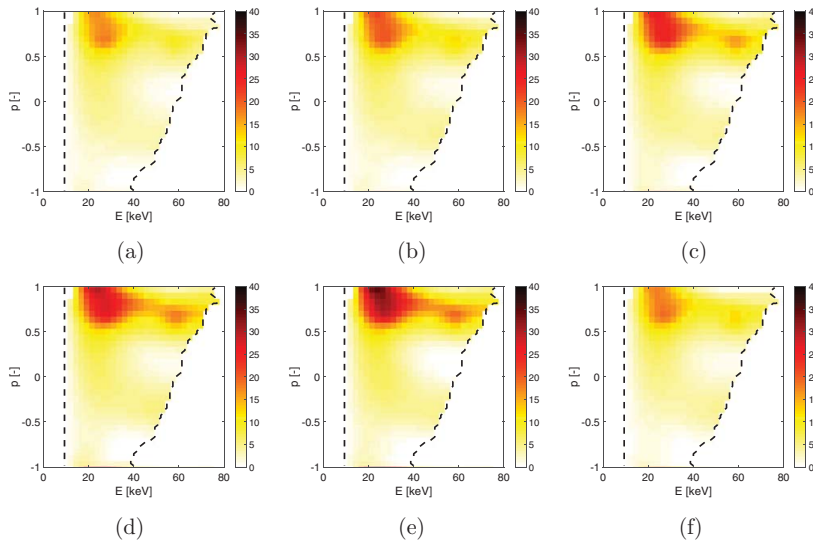


Figure 12. High-definition first-order Tikhonov tomographic inversions based on four-view FIDA measurements in ASDEX Upgrade discharge #32323. The units are ($10^{16} \text{ keV}^{-1} \text{ m}^{-3}$). 100 frames are supplied in a sawtooth crash movie attached as supplementary material to the paper (movie 2) (stacks.iop.org/NF/56/106024/mmedia). The crash occurs at $t = 2.23$ s. (a) 2.1 s. (b) 2.13 s. (c) 2.16 s. (d) 2.19 s. (e) 2.22 s. (f) 2.25 s.

the TRANSP simulation is found based on experimentally accessible quantities. However, artifacts are present and the amplitudes in the reconstruction are too low by about 30%. The success of this approach does not depend strongly on the position of the discrepancy in velocity space for the five-view FIDA system as we illustrate in figure 7. Each case shows the true location of the discrepancy and the reconstruction using the simulation as prior information. The approximate location of the discrepancy is in each case identified as the region with the lowest amplitudes.

Many FIDA systems have two or three viewing directions rather than the five available at ASDEX Upgrade. DIII-D has three FIDA views [46, 47] and MAST [48, 49], NSTX [50], EAST [51], and LHD have two views [52, 53]. In figure 8 we reconstruct the six cases from figure 7 using just two FIDA views to show that this approach could be useful for other machines. The approximate location of the ΔF_{true} is reconstructed in each case, even though the amplitudes of negative phase-space densities are not reconstructed as well as for the five-view case. The reconstruction of ΔF^* does not require as many measurements as the reconstruction of F^* since the simulation provides cogent prior information about the approximate basic shape. Hence this alternative approach to tomographic reconstruction should be highly useful for FIDA systems with few viewing directions as is common on many machines. Further, the approach should also work for many combinations of fast ion diagnostics installed on many machines [23, 29, 31], for example based on FIDA and CTS at LHD [54, 55], CTS, FIDA, NPA, NES, and GRS at ASDEX Upgrade [5, 7, 11, 56–62], NES, GRS and NPA at JET [14, 15, 63], CTS, GRS, NES, NPA and possibly fast-ion charge-exchange recombination spectroscopy at ITER [64–69]. We will demonstrate this method for the two-view FIDA case using experimental data in the next section.

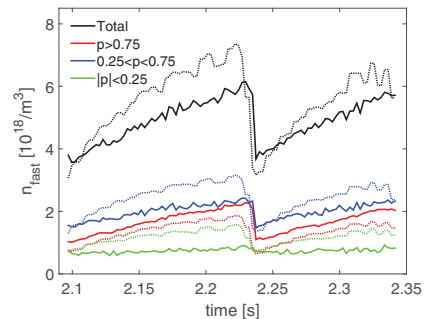


Figure 13. The measured (full lines) and simulated (dashed lines) total fast-ion densities and the fast-ion densities in selected pitch ranges in ASDEX Upgrade discharge #32323.

6. Studies of neutral beam injection and sawtooth dynamics

Prior information allows us to study the formation and presence of NBI peaks at full, half, and one-third injection energy and the fast-ion dynamics associated with sawteeth. NBI peaks are here reconstructed by TSVD which is well-suited for fine-scale features at the expense of the appearance of some jitter. The target velocity-space is restricted using null-measurements. The beam positions are *not* used as prior information here, and neither is the TRANSP simulation. Negative phase-space densities are present in the TSVD, but they are fairly small and simply ignored as usual for TSVD. The TSVD study confirms the positions of the NBI peaks which we will use as prior information in the Tikhonov inversions of fast-ion dynamics in sawtooth plasma.

In discharge #33138, FIDA measurements in five views were made just after switching on NBI Q3 to study the

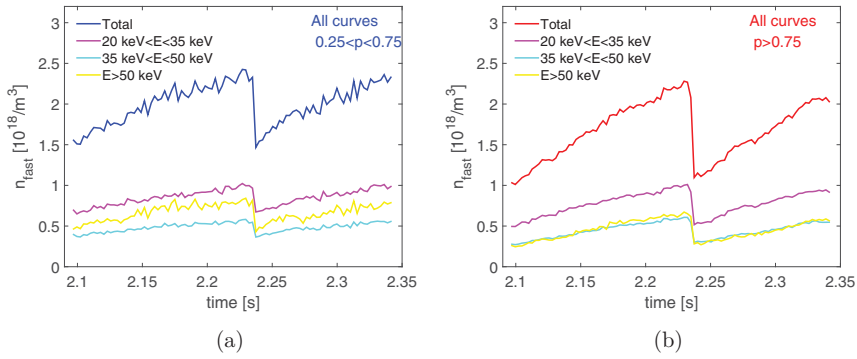


Figure 14. The measured fast-ion densities in selected pitch and energy ranges in ASDEX Upgrade discharge #32323. The red and blue curves also appear in figure 13 and are here split into different energy intervals. (a) $0.25 < p < 0.75$. (b) $p > 0.75$.

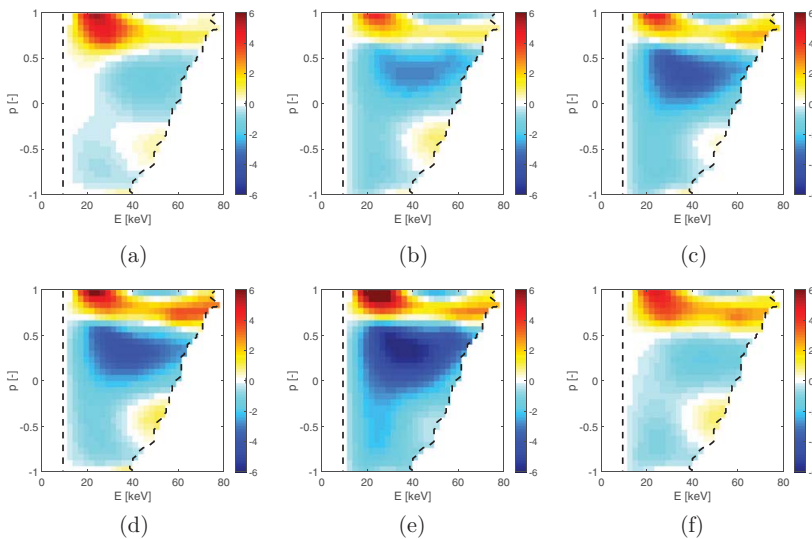


Figure 15. Reconstruction of the velocity-space distribution of the differences between the measurements and the TRANSP simulation $\Delta F^* = F^* - F_{\text{sim}}$ ($10^{16} \text{ keV}^{-1} \text{ m}^{-3}$) according to equation (10). Here the TRANSP simulations were used as prior information in the inversion. The crash occurs at $t = 2.23$ s. A movie is supplied as supplementary material to this paper (movie 3) (stacks.iop.org/NF/56/106024/mmedia). (a) 2.1 s. (b) 2.13 s. (c) 2.16 s. (d) 2.19 s. (e) 2.22 s. (f) 2.25 s.

appearance of the beam injection peaks in the plasma center. The time resolution of the measurements was 2.5 ms. Figure 9 shows six inversions after the NBI was switched on at $t = 0.4$ s. A movie showing the formation of the three NBI peaks in 50 frames is provided as supplementary material to this paper (movie 1) (stacks.iop.org/NF/56/106024/mmedia). The same level of regularization is used for all frames. The NBI peaks at full, half, and one-third injection energy appear reliably at the expected pitch and energies at 20 keV, 30 keV and 60 keV. Even though three peaks do not always appear in inversions, the well-understood locations and the large-scale coherence suggest that the peaks are not artifacts but are supported by the FIDA measurements. Figure 10 shows that a TRANSP simulation of the discharge also predicts the formation of three peaks in agreement with the measured result.

To study the increase of fast-ion density in time at selected positions in velocity space due to switching on the NBI, we integrate the inversion in $p \in [0.3, 0.7]$ and in five 10 keV wide energy intervals (figure 11). The fast-ion density builds up quickly and steadily for the intervals containing the NBI peaks at 20, 30 and 60 keV whereas the intermediate intervals from 32 to 52 keV increase more slowly in agreement with the TRANSP simulation. Simulations and measurements agree very well for the intervals containing the 20 keV and 30 keV NBI peaks whereas the 60 keV interval is predicted to be slightly less populated. The TRANSP simulation shows larger fast-ion densities at 42–52 keV than at 32–42 keV as these intervals are fuelled mostly by slowing down of 60 keV ions and there is some pitch angle scattering. The inversion does not show this behaviour. It should be noted that TSVD

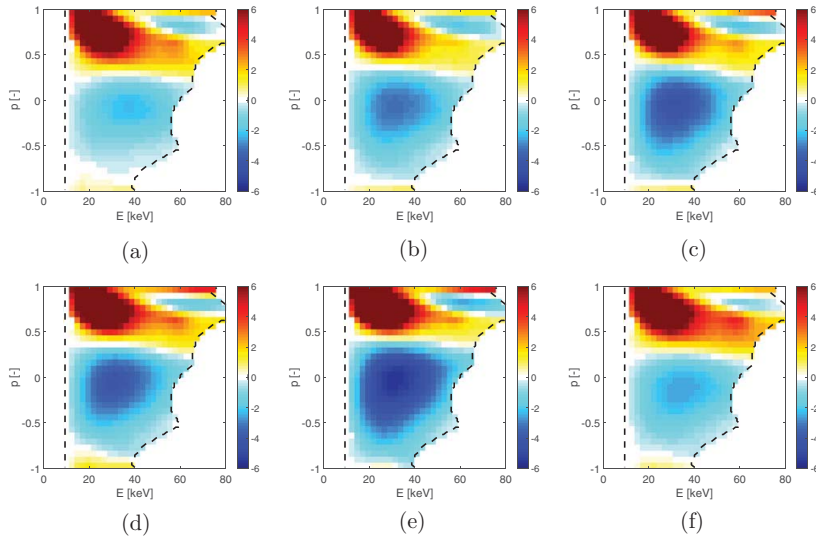


Figure 16. As for figure 15, but using only two FIDA views. The angles of the lines-of-sight to the magnetic field are $\phi = [14^\circ, 73^\circ]$. (a) 2.1 s. (b) 2.13 s. (c) 2.16 s. (d) 2.19 s. (e) 2.22 s. (f) 2.25 s.

showing NBI peaks typically also have undulations elsewhere, which may bias a comparison between the different energy curves. All in all, the TRANSP simulation agrees fairly well with the measurements, and both show the formation of three NBI peaks at the expected locations.

Now we turn to study fast-ion dynamics in the sawtooth plasma by high-definition first-order Tikhonov inversions using all methods discussed in section 2. First we will use null-measurements, non-negativity, and the NBI peak positions, but *not* the TRANSP simulation, in pure inversions of the data. Then we will use the TRANSP simulation as prior information and locate the distribution of discrepancies between the measurements and the TRANSP simulation. Previous inversions focussed on the redistribution due to the crash [26–31] whereas we here study the dynamics in the entire sawtooth period. In this discharge only four views had a time resolution of 2.5 ms whereas the fifth view had a time resolution of 25 ms as the camera did not allow faster data acquisition in this discharge, and hence we only use four views here. Figure 12 shows first-order Tikhonov inversions with prior information from non-negativity, null-measurements and the position of the NBI peaks but *not* from any simulation. The same level of regularization is used for all frames. Figure 12 covers one sawtooth cycle, and figures 12(a) and (f) are right after crashes. A movie showing 100 frames covering two sawtooth cycles is supplied as supplementary material to this paper (movie 2) (stacks.iop.org/NF/56/106024/mmedia). The 2D velocity distribution function is strongly depleted at the sawtooth crashes and builds up due to the continuous fuelling by the NBI particle sources at 20 keV, 30 keV and 60 keV between the crashes. The 60 keV peak almost disappears right after the crashes. It gradually builds up as the fast-ion density increases during the sawtooth cycle. The ridge between the beam injection peaks also becomes stronger during the sawtooth cycle.

Figure 13 compares measured total fast-ion densities as well as fast-ion densities in selected pitch intervals with a TRANSP simulation. Here we have added drifting Maxwellian distribution functions to the fast-ion TRANSP simulation as one always measures the complete ion velocity distribution function. The tails of the Maxwellian here make a significant contribution due to the very high ion temperatures of up to 10 keV with sawtooth time traces. The fast ion densities are obtained by integration of the inversions over all energies and over pitches in the selected intervals. The measured and simulated total fast-ion densities are similar right after the crashes. However, the measured total fast-ion density increases less than the simulated one during the sawtooth cycle. For $p > 0.75$ the measurement and the TRANSP simulation show clear sawteeth in good agreement though the TRANSP simulation is consistently lower than the FIDA measurement. For the intermediate pitch range $0.25 < p < 0.75$ the agreement is also good, but here the TRANSP simulation is consistently higher than the FIDA measurement. For $|p| < 0.25$ the measurements show no evidence of sawteeth, whereas the simulation shows clear sawteeth. We stress that variations in measured signals are much more reliable than their absolute values, and hence we are confident in the presence or absence of sawteeth in the time traces. The previous velocity-space tomography studies of sawtooth crashes have consistently found that fast ions with pitches close to zero are much less affected by the crash than ions with pitches close to one which is consistent with our results [26–31]. Figure 14 subdivides the $p > 0.75$ interval as well as the $0.25 < p < 0.75$ interval into three energy intervals. Sawtooth time traces are evident at all energies, and we find no strong selection in energy.

In figure 15 we examine the results from figures 13 and 14 by reconstructing the difference $\Delta F^* = F^* - F_{\text{sim}}$ between the

TRANSP simulation and the high-definition inversions using the TRANSP simulation as prior information. As above we have added a drifting Maxwellian to the TRANSP simulation to account for the thermal ions. We use the available four FIDA views. A movie covering two sawtooth cycles is supplied as supplementary material to this paper (movie 3) (stacks.iop.org/NF/56/106024/mmedia). The results obtained by using and not using the TRANSP simulation as prior information are consistent. The inversions and the simulations agree relatively well right after the crashes. The differences then grow during the sawtooth cycle in the region where the TRANSP simulation underpredicts the measurements ($p > 0.75$) as well as in the region where the TRANSP simulation overpredicts the measurements ($p < 0.75$). Finally, in figure 16 we repeat the tomographic reconstructions of the difference $\Delta F^* = F^* - F_{\text{sim}}$ from figure 15, but only using two FIDA views as available on many other machines. Salient large-scale features such as the regions of overprediction and underprediction as well as the approximate location of the extrema are well reconstructed using only two views. However, the detailed shape of ΔF^* is somewhat different, and there is a tendency to find larger discrepancies.

7. Conclusions

Velocity-space tomography is usually a highly photon-starved enterprise since the optical access to tokamaks and hence the number of simultaneous measurements is limited and since the signal-to-noise ratio of the measurements is often low compared with many other tomography applications. At the same time, we would like to infer the 2D velocity distribution function in high resolution and hence need to infer as many unknown parameters as the measurement data support. Here we make up for the lack of measurements by using additional prior information. The inversions are substantially improved by using three types of prior information: 1. The non-negativity of phase-space densities. 2. The measured absence of FIDA light restricting the target velocity space. 3. The velocity-space position of NBI peaks.

An inversion based on truncated singular value decomposition using null-measurements but not the other types of prior information reconstructs the three NBI peaks at full, half and one-third energy at the expected locations, and their appearance after switching on an NBI could be studied resolved in time. We could further study the dynamics of the fast-ion velocity distribution function in a sawtooth plasma resolved in time in unprecedented detail. TRANSP simulations underpredict the measurements for $p > 0.75$ and overpredict the measurements for $p < 0.75$. Measurements show no evidence of sawteeth for $p < 0.25$ in disagreement with the TRANSP simulation. The time-resolved tomographic inversion movies efficiently summarize up to 50000 data points using all presented prior information.

Lastly, we demonstrate an alternative approach to velocity-space tomography. We infer the 2D fast-ion distribution function considering the measurements as well as a simulation. In this case tomographic inversion uses the simulation as

prior information. If the measurements and the simulation are inconsistent, the most likely velocity-space distribution of the discrepancies can then be found by subtracting the simulation from the inversion with the simulation as prior information. This could not be achieved with the pure velocity-space tomography approach, which does not use the simulation, even with five FIDA views. The experimental results obtained with this alternative approach are consistent with results obtained by velocity-space tomography that does not use the simulation as prior information. Experimental results obtained with this approach using only two FIDA views suggest that velocity-space tomography methods can be applied to two-view FIDA systems which are common on many machines.

Acknowledgments

This work has been carried out within the framework of the EUROfusion Consortium and has received funding from the Euratom research and training programme 2014–2018 under grant agreement No 633053. The views and opinions expressed herein do not necessarily reflect those of the European Commission.

References

- [1] Grierson B.A. et al 2012 *Phys. Plasmas* **19** 056107
- [2] Grierson B.A. et al 2012 *Rev. Sci. Instrum.* **83** 10D529
- [3] Stejner M. et al 2013 *Plasma Phys. Control. Fusion* **55** 085002
- [4] Stejner M. et al 2015 *Plasma Phys. Control. Fusion* **57** 062001
- [5] Salewski M. et al 2010 *Nucl. Fusion* **50** 035012
- [6] Moseev D. et al 2011 *Plasma Phys. Control. Fusion* **53** 105004
- [7] Nielsen S.K. et al 2015 *Plasma Phys. Control. Fusion* **57** 035009
- [8] Rasmussen J. et al 2015 *Plasma Phys. Control. Fusion* **57** 075014
- [9] Heidbrink W.W. et al 2004 *Plasma Phys. Control. Fusion* **46** 1855–75
- [10] Heidbrink W.W. et al 2007 *Plasma Phys. Control. Fusion* **49** 1457–75
- [11] Geiger B. et al 2015 *Plasma Phys. Control. Fusion* **57** 014018
- [12] Hellesen C. et al 2010 *Nucl. Fusion* **50** 084006
- [13] Hellesen C. et al 2013 *Nucl. Fusion* **53** 113009
- [14] Eriksson J. et al 2015 *Nucl. Fusion* **55** 123026
- [15] Schneider M. et al 2016 Modelling third harmonic ion cyclotron acceleration of deuterium beams for JET fusion product studies experiments *Nucl. Fusion* submitted
- [16] Kiptily V.G. et al 2010 *Nucl. Fusion* **50** 084001
- [17] Tardocchi M. et al 2011 *Phys. Rev. Lett.* **107** 205002
- [18] Nocente M. et al 2012 *Nucl. Fusion* **52** 063009
- [19] Nocente M. et al 2015 *Nucl. Fusion* **55** 123009
- [20] Egedal J. and Bindslev H. 2004 *Phys. Plasmas* **11** 2191
- [21] Salewski M. et al 2011 *Nucl. Fusion* **51** 083014
- [22] Salewski M. et al 2012 *Nucl. Fusion* **52** 103008
- [23] Salewski M. et al 2013 *Nucl. Fusion* **53** 063019
- [24] Salewski M. et al 2014 *Nucl. Fusion* **54** 023005
- [25] Salewski M. et al 2015 *Plasma Phys. Control. Fusion* **57** 014021
- [26] Geiger B. et al 2015 *Nucl. Fusion* **55** 083001

- [27] Weiland M. et al 2016 *Plasma Phys. Control. Fusion* **58** 025012
- [28] Jacobsen A.S. et al 2016 *Plasma Phys. Control. Fusion* **58** 045016
- [29] Jacobsen A.S. et al 2016 *Plasma Phys. Control. Fusion* **58** 042002
- [30] Jaulmes F. et al 2016 *Nucl. Fusion* **56** 112012
- [31] Rasmussen J. et al 2016 *Nucl. Fusion* **56** 112014
- [32] Salewski M. et al 2014 *Plasma Phys. Control. Fusion* **56** 105005
- [33] Pace D.C. et al 2012 *Rev. Sci. Instrum.* **83** 073501
- [34] Jacobsen A.S. et al 2014 *Rev. Sci. Instrum.* **85** 11E103
- [35] Jacobsen A.S. et al 2015 *Nucl. Fusion* **55** 053013
- [36] Salewski M. et al 2015 *Nucl. Fusion* **55** 093029
- [37] Salewski M. et al 2016 *Nucl. Fusion* **56** 046009
- [38] Stroth U. et al 2013 *Nucl. Fusion* **53** 104003
- [39] Anton M. et al 1996 *Plasma Phys. Control. Fusion* **38** 1849–78
- [40] Craciunescu T. et al 2009 *Nucl. Instrum. Methods Phys. Res. A* **605** 374–83
- [41] Pankin A. et al 2004 *Comput. Phys. Commun.* **159** 157–84
- [42] Lawson C. and Hanson R. 1974 *Solving Least Squares Problems* (Englewood Cliffs, NJ: Prentice-Hall)
- [43] Hansen P.C. 1992 *SIAM Rev.* **34** 561–80
- [44] Hansen P.C. and O’Leary D.P. 1993 *SIAM J. Sci. Comput.* **14** 1487–503
- [45] Golub G., Heath M. and Wahba G. 1979 *Technometrics* **21** 215–23
- [46] Heidbrink W.W. et al 2012 *Nucl. Fusion* **52** 094005
- [47] Pace D.C. et al 2011 *Plasma Phys. Control. Fusion* **53** 062001
- [48] Michael C.A. et al 2013 *Plasma Phys. Control. Fusion* **55** 095007
- [49] Jones O.M. et al 2015 *Plasma Phys. Control. Fusion* **57** 125009
- [50] Bortolon A. et al 2010 *Rev. Sci. Instrum.* **81** 10D728
- [51] Huang J. et al 2014 *Rev. Sci. Instrum.* **85** 11E407
- [52] Ito T. et al 2010 *Rev. Sci. Instrum.* **81** 10D327
- [53] Ito T. et al 2012 *Plasma Fusion Res.* **5** S2099
- [54] Kubo S. et al 2010 *Rev. Sci. Instrum.* **81** 10D535
- [55] Nishiura M. et al 2014 *Nucl. Fusion* **54** 023006
- [56] Meo F. et al 2008 *Rev. Sci. Instrum.* **79** 10E501
- [57] Meo F. et al 2010 *J. Phys.: Conf. Ser.* **227** 012010
- [58] Furtula V. et al 2012 *Rev. Sci. Instrum.* **83** 013507
- [59] Schneider P.A. et al 2015 *Rev. Sci. Instrum.* **86** 073508
- [60] Tardini G. et al 2012 *J. Instrum.* **7** C03004
- [61] Tardini G. et al 2013 *Nucl. Fusion* **53** 063027
- [62] Nocente M. et al 2012 *Nucl. Fusion* **52** 094021
- [63] Romanelli F. 2015 *Nucl. Fusion* **55** 104001
- [64] Chugunov I.N. et al 2011 *Nucl. Fusion* **51** 083010
- [65] Donné A.J.H. et al 2007 Progress in the ITER Physics Basis Chapter 7: diagnostics *Nucl. Fusion* **47** S337–84
- [66] Salewski M. et al 2008 *Rev. Sci. Instrum.* **79** 10E729
- [67] Salewski M. et al 2009 *Plasma Phys. Control. Fusion* **51** 035006
- [68] Salewski M. et al 2009 *Nucl. Fusion* **49** 025006
- [69] Kappatou A. et al 2012 *Nucl. Fusion* **52** 043007

Reference [11]

[11]. M Salewski et al. (2017) *Nuclear Fusion* **57** 056001. MeV-range velocity-space tomography from gamma-ray and neutron emission spectrometry measurements at JET

MeV-range velocity-space tomography from gamma-ray and neutron emission spectrometry measurements at JET

M. Salewski¹, M. Nocente^{2,3}, A.S. Jacobsen⁴, F. Binda⁵, C. Cazzaniga⁶, G. Ericsson⁵, J. Eriksson⁵, G. Gorini^{2,3}, C. Hellesen⁵, A. Hjalmarsson⁵, V.G. Kiptily⁷, T. Koskela^{8,9}, S.B. Korsholm¹, T. Kurki-Suonio⁸, F. Leipold¹, J. Madsen¹, D. Moseev¹⁰, S.K. Nielsen¹, J. Rasmussen¹, M. Schneider¹¹, S.E. Sharapov⁷, M. Stejner¹, M. Tardocchi³ and JET Contributors^a

EUROfusion Consortium, JET, Culham Science Centre, Abingdon, OX14 3DB, United Kingdom

¹ Department of Physics, Technical University of Denmark, Kgs. Lyngby, Denmark

² Department of Physics, University of Milano Bicocca, Milano, Italy

³ Istituto di Fisica del Plasma, Consiglio Nazionale delle Ricerche, Milano, Italy

⁴ Max-Planck-Institut für Plasmaphysik, Garching, Germany

⁵ Department of Physics and Astronomy, Uppsala University, Sweden

⁶ ISIS Facility, Science and Technology Facilities Council, Rutherford Appleton Laboratory, Didcot, United Kingdom

⁷ CCFE, Culham Science Centre, Abingdon, Oxon, United Kingdom

⁸ Department of Applied Physics, Aalto University, Aalto, Finland

⁹ NERSC, Lawrence Berkeley National Laboratory, Berkeley, CA, United States of America

¹⁰ Max-Planck-Institut für Plasmaphysik, Greifswald, Germany

¹¹ ITER Organization, St Paul-lez-Durance Cedex, France

E-mail: msal@fysik.dtu.dk

Received 24 November 2016, revised 6 February 2017

Accepted for publication 15 February 2017

Published 14 March 2017



CrossMark

Abstract

We demonstrate the measurement of a 2D MeV-range ion velocity distribution function by velocity-space tomography at JET. Deuterium ions were accelerated into the MeV-range by third harmonic ion cyclotron resonance heating. We made measurements with three neutron emission spectrometers and a high-resolution γ -ray spectrometer detecting the γ -rays released in two reactions. The tomographic inversion based on these five spectra is in excellent agreement with numerical simulations with the ASCOT-RFOF and the SPOT-RFOF codes. The length of the measured fast-ion tail corroborates the prediction that very few particles are accelerated above 2 MeV due to the weak wave-particle interaction at higher energies.

Keywords: γ -ray spectrometry, neutron emission spectrometry, velocity-space tomography, fast ions, tokamak

(Some figures may appear in colour only in the online journal)

1. Introduction

The era of burning plasmas is approaching with the construction of the ITER tokamak. Burning plasmas will offer new challenges since the temperature and density profiles are

self-consistently determined by α -particle heating rather than controlled by auxiliary heating. Furthermore, MeV-range ions can drive a zoo of instabilities deteriorating the plasma performance [2–8]. Hence the development of diagnostics capable of measuring MeV-range ions is essential.

MeV-range ions are routinely generated by waves in the ion cyclotron range of frequencies (ICRF) and diagnosed

^a See the appendix of [1]

by high-resolution γ -ray spectrometry (GRS) and neutron emission spectrometry (NES) at JET. Substantial densities of MeV-range α -particles are expected in the upcoming DT campaign [9]. The fast-ion phase-space distribution function can be related to energy spectra of neutrons and γ -rays, respectively [10–24]. Traditionally the measured 1D spectra are compared with simulated 1D spectra to obtain information about the fast ion phase-space distribution function. If the spectra agree, the simulation is thought to be a good model of the fast ions in the discharge. However, any disagreement is enormously difficult to interpret for several reasons. First, if several simultaneously acquired spectra are available, the amount of data one has to consider is rather large, often hundreds of data points. Second, each data point samples large regions of fast-ion phase space as illustrated by NES and GRS weight functions, and hence it is difficult to pinpoint the sources of any disagreement in phase space [25–28]. Third, the spectra also depend on nuisance parameters which are not of direct interest in fast-ion measurements, such as the thermal ion parameters.

Velocity-space tomography is a method to overcome these difficulties [29–42]. The method provides a measurement of the 2D velocity distribution function averaged over a spatial measurement volume. The rich and complex spectral measurement data are converted into 2D images of the velocity distribution function that are straightforward to interpret. The 2D images are the best useful fit to hundreds of simultaneously acquired data points, and nuisance parameters are accounted for. ASDEX upgrade [43] is equipped with collective Thomson scattering (CTS) and fast-ion D_α (FIDA) spectroscopy diagnostics [33, 44–48]. Velocity-space tomography is becoming a standard tool to visualize and analyze FIDA and CTS measurements [32–42]. While FIDA spectroscopy works well for ion energies on the order of 100 keV, it suffers from the low charge-exchange cross sections at MeV-range energies [49–51]. Hence velocity-space tomography has so far been limited to ion energies below 120 keV. At JET, 1D distribution functions of fast-ion velocities perpendicular to the magnetic field have been inferred from measurements with the time-of-flight neutron emission spectrometer TOFOR [15–17]. These 1D inversions are based on the assumption that all ion velocities parallel to the magnetic field are zero. Here we demonstrate velocity-space tomography in the MeV-range based on GRS and NES at JET and measure a core-averaged 2D velocity distribution function of fast ions generated by third harmonic ICRF.

Section 2 describes the JET discharge, the diagnostic set-up and the NES and GRS measurements. In section 3 we discuss the velocity-space sensitivity of our detectors and how we select measurement data for the inversion. In section 4 we outline the velocity-space tomography approach. A measurement of a 2D MeV-range velocity distribution function and benchmarks with the ASCOT–RFOF [20, 52] and the SPOT–RFOF [22] codes are presented in section 5. We discuss the potential and limitations of our approach in section 6 and draw conclusions in section 7.

2. NES and GRS measurements at JET

Deuterium ions are routinely accelerated into the MeV-range by third harmonic ICRF heating at JET [15, 19, 20]. The wave-particle interaction for third harmonic ICRF heating is much stronger for moderately energetic ions than for thermal ions [22]. Hence JET discharge #86459 was heated by 4.5 MW of neutral beam injection (NBI) with beam injection energies of 80 keV, 100 keV and 120 keV providing the seed fast-ion population as well as 3 MW of third harmonic ICRF heating accelerating the ions into the MeV range. As the magnetic field on the magnetic axis was $B = 2.25$ T, the ICRF wave frequency was 51 MHz. The electron density was about $4 \times 10^{19} \text{ m}^{-3}$.

The energetic deuterium tail formed in such plasma scenarios was simultaneously measured by three NES detectors and one high-purity Germanium (HpGe) GRS detector from 50.5 s to 52.1 s in discharge #86459 (figure 1). The three neutron emission spectrometers detect neutrons with energies near 2.5 MeV from the $D(D,n)^3\text{He}$ reaction. The time-of-flight spectrometer TOFOR is mounted in the roof laboratory and views the plasma perpendicularly to the magnetic field [53]. The other two neutron emission spectrometers detect neutrons through reactions with a synthetic single-crystal diamond [54–56] and the liquid organic scintillator material NE213 [57], respectively. Both neutron emission spectrometers have compact designs and are mounted in the back of the magnetic proton recoil (MPR) deuterium-tritium neutron emission spectrometer (which is not used here). The lines-of-sight of the two compact neutron emission spectrometers are oblique forming an angle of 47° with the magnetic field on the magnetic axis.

The high-resolution HpGe GRS detector is mounted just behind TOFOR sharing the same line-of-sight [12, 58]. Here we use measurements of the two competing two-step reactions $^9\text{Be}(D,n\gamma)^{10}\text{B}$ and $^9\text{Be}(D,p\gamma)^{10}\text{Be}$. Beryllium is the first-wall surface material and therefore a major impurity at JET. It is also planned as first-wall surface material in ITER. Basic parameters of the reactions relevant to this study are summarized in table 1.

Figure 2 presents the NES measurements for the three spectrometers. The y -axes are the number of event counts per bin in all cases. However, the x -axes are given in units particular to each instrument as we will explain below. The instrumental units are related to the neutron energies via known instrumental response matrices which reflect that a recorded event could originate from neutrons in a wide range of possible energies. The determination of neutron energy spectra from the measurements is therefore an inverse problem in itself. We incorporated this inverse problem into the velocity-space tomography problem by formulating instrumental weight functions that include the instrumental response matrix and hence directly relate the instrumental units to velocity space [25, 59]. The parts of the spectra that are used for the inversion are chosen based on weight functions and are highlighted in each case (see section 3).

The measurements are shown together with synthetic measurements based on a numerical simulation with the

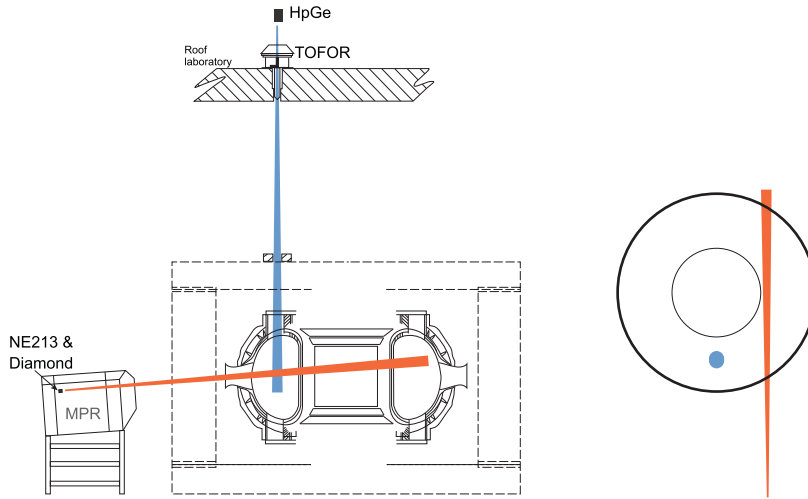


Figure 1. Cutaway view (left) and top view (right) of the lines-of-sight of the three neutron spectrometers (TOFOR, diamond, NE213) and the HpGe GRS detector. The angle between the lines-of-sight and the magnetic field is about 90° for TOFOR and the HpGe detector and about 47° for the compact diamond and NE213 spectrometers.

Table 1. Reactions producing the measured neutron and γ -ray spectra.

Reaction	Energy release	Neutron or γ energy
$D(D,n)^3He$	$Q = 3.27$ MeV	$E_n = 2.5$ MeV
$^9Be(D,n\gamma)^{10}B$	$Q^* = (4.36-3.59)$ MeV	$E_\gamma = 2.868$ MeV
$^9Be(D,p\gamma)^{10}Be$	$Q^* = (4.59-3.37)$ MeV	$E_\gamma = 3.367$ MeV

ASCOT-RFOF code [20]. The absolute calibration of the measurements is comparatively uncertain. Hence we fitted the synthetic spectra to the measured spectra by multiplication with a single scaling factor per spectrum. This allows comparisons of the spectral shapes disregarding the absolute scaling.

TOFOR measures the distribution of times-of-flight of neutrons covering the distance between two detectors (figure 2(a)). Ideally, the energy E_n of an incoming neutron before scattering in the first detector can be related to the time-of-flight of the scattered neutrons between the two detectors by [53]

$$E_n = 2m_n \frac{R_s^2}{t_{tof}^2} \quad (1)$$

where t_{tof} is the time-of-flight, m_n is the neutron mass and $R_s = 0.705$ m is the radius of the constant time-of-flight sphere on which both detectors are situated. The geometry leading to equation (1) is illustrated in reference [53]. Plugging in the parameters leads to the handy formula for TOFOR

$$E_n \approx \left(\frac{100 \text{ ns}}{t_{tof}} \right)^2 \text{ MeV}. \quad (2)$$

However, the detailed instrumental response accounting for multiple scattering is more complicated as summarized in the instrumental response matrix [53, 59] which we will account

for. Equations (1) and (2) are useful because they describe the by far most likely response of TOFOR. Such a relation between the measured variable and the neutron energies does not exist for the diamond and the liquid scintillator spectrometers. We use the time-of-flight data between 22 ns and 58 ns. Hardly any neutrons with times-of-flight below 42 ns are detected. Measurements of the absence of neutrons contain strong information about 2D velocity space (see section 3).

Figure 2(b) shows the measurements made with the single-crystal diamond detector. The detector measures distributions of energies deposited by neutrons in the diamond. In this case the instrumental response matrix reflects that neutrons in a wide range of possible energies above a threshold energy can deposit a particular energy in the diamond ($E_{dep} < 0.284E_n$) [59]. Here we use the data with deposited energies between 0.8 MeV and 2 MeV though hardly any detections are made above about $E_{dep} = 1.4$ MeV.

Figure 2(c) shows the measurements with the liquid scintillator NE213 detector. This detector is sensitive to neutron energies by measuring the emitted light produced when a neutron hits the scintillator material. The commonly used unit of this measurement is mega-electronvolt electron equivalent (MeVee) which is the energy of a hypothetical electron producing the emitted light. A particular flash of emitted light can again be produced by neutrons in a wide range of possible energies [59]. We use the data between 0.9 and 2.2 MeVee. Hardly any detections are made above about 2 MeVee.

Finally, the GRS measurements are made with a high-resolution HpGe detector, which can provide 1 keV energy bins in the bandwidth of 10 MeV. Its fine instrumental response allows us to neglect it without loss of accuracy. The entire GRS data containing many γ -ray peaks is presented in figure 3. The tiny highlighted regions show the spectral range that we use for velocity-space tomography. Figure 3 illustrates that measurement data from many other reactions can be

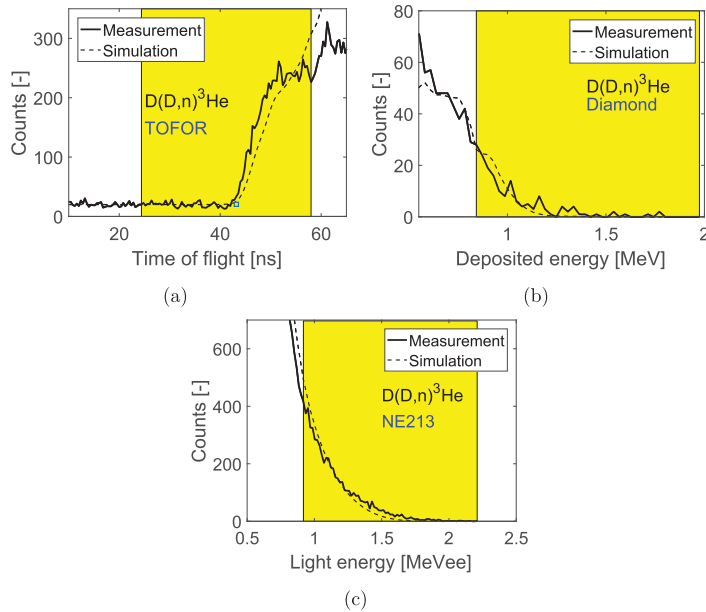


Figure 2. NES measurements in JET discharge #86459 with three different neutron detectors together with synthetic measurements based on the ASCOT-RFOF code. The data used for the inversion is highlighted in yellow. (a) TOFOR. (b) Diamond. (c) Liquid scintillator NE213.

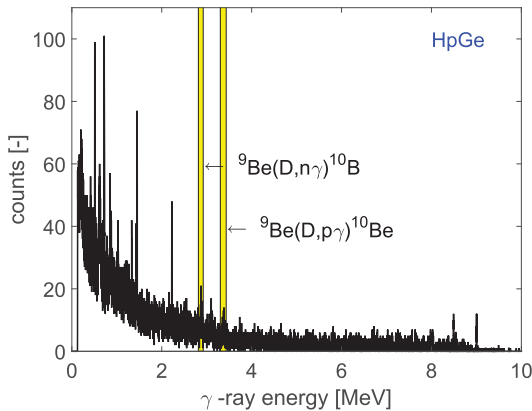


Figure 3. High-resolution GRS measurements showing the full γ -ray energy range of the HpGe detector. We use the high-resolution measurements of the two highlighted peaks. The spectral shapes of these two peaks are shown in figure 4.

exploited for tomographic inversion. We use the ${}^9\text{Be}(\text{D},\text{n}\gamma){}^{10}\text{B}$ and ${}^9\text{Be}(\text{D},\text{p}\gamma){}^{10}\text{Be}$ reaction peaks as they are powerful and good cross section data are available. High-resolution views of these peaks near 2868 keV and 3367 keV are presented in figure 4. Even though the two peaks are recorded with the same detector, the velocity-space observation regions of these two spectra are different as we will discuss in the next section.

Generally the agreement between the measurements and the simulations is good as noted previously [20]. The slight disagreement between the measurements and the simulations, most notably in figure 4, is likely caused by the large Larmor

radius of MeV-range deuterons compared with the width of the line-of-sight [13, 60]. These spatial effects are presently not accounted for in the weight function formalism.

3. Instrumental weight functions

Weight functions describe the velocity-space sensitivity of fast-ion diagnostics and have been calculated for FIDA [50, 61], NPA [50], CTS [29], NES [25, 26, 59] and GRS [27, 28]. NES and GRS weight functions including the instrumental response functions allow an efficient inversion of the measurements by velocity-space tomography. Weight functions w connect the velocity distribution function f to the measurement S by

$$S = \int \int w f dv_{\parallel} dv_{\perp}. \quad (3)$$

In this section we emphasize two basic assumptions of the NES and GRS weight function formalism and illustrate the velocity-space interrogation regions of the various spectral measurements.

First, NES and GRS weight functions rely on the assumption that most neutrons or γ 's originate from a reaction between a fast ion and a thermal ion rather than between two thermal ions or two fast ions. These three basic types of reactions based on the reactant speeds are referred to as beam-beam, beam-thermal and thermal reactions. In JET discharge #86459, beam-thermal reactions dominate (figure 5) as they often do. Beam-beam reactions are usually fairly unlikely due to the small number densities of fast particles whereas thermal reactions are usually fairly unlikely due to the small reaction

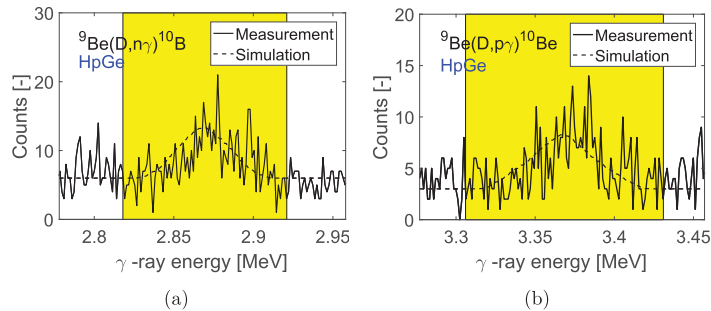


Figure 4. High-resolution GRS measurements of the spectral shapes of the two peaks used for the inversion together with synthetic measurements based on the ASCOT-RFOF code. The data used for the inversion is highlighted in yellow. (a) The peak at 2868 keV originates from the ${}^9\text{Be}(\text{D},n\gamma){}^{10}\text{B}$ reaction. (b) The peak at 3367 keV originates from the ${}^9\text{Be}(\text{D},p\gamma){}^{10}\text{Be}$ reaction.

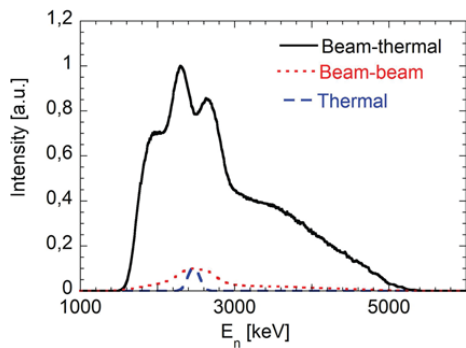


Figure 5. Relative contributions to the neutron energy spectra from beam-thermal, beam-beam and thermal reactions according to a GENESIS simulation of discharge #86459. Beam-thermal reactions dominate over the other contributions.

cross sections at low energies. The beam-thermal assumption is always fulfilled for GRS involving ${}^9\text{Be}$ because the impurity is thermal and the reaction cross sections hence require large ion energies to allow reactions.

Second, here we neglect that the measurements are made in spatially different observation volumes. In principle, the neutrons and γ 's can originate from anywhere along the line-of-sight. However, most neutrons and γ 's originate from the hot plasma core where the fusion reaction rates are largest as the inversion of neutron camera data shows (figure 6) [62]. Here we assume that all neutrons and γ 's originate from the plasma core and neglect emissions from the periphery.

We now turn to the velocity-space interrogation regions of the measured data based on these assumptions. Figure 7 illustrates 5×3 weight functions representing the five detectors and three typical data points in the spectra for each detector. The amplitude of the weight functions is the measurable signal per ion in the relevant detector units (equation (3)). Consequently, the white regions are not observable. The velocity-space sensitivity (amplitudes) of the weight functions of the different spectral data points are rather different which suggests that the measurements complement each other well. In each case the weight function in the left column is sensitive to large portions of our target velocity space, i.e. the part of velocity

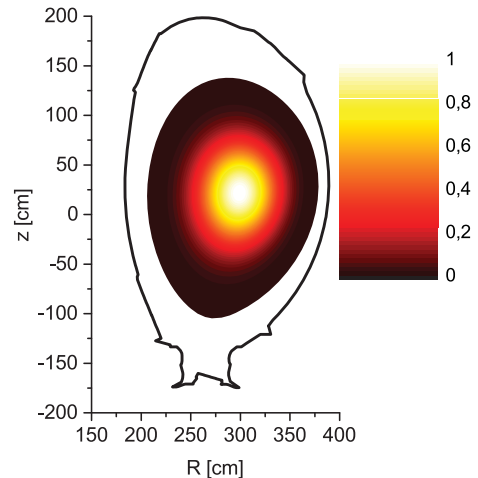


Figure 6. Measured neutron production rates [a.u.] obtained by inversion of neutron camera measurements (in position space) in discharge #86459. Most neutrons are produced in the plasma core.

space shown in figure 7 in which we seek to reconstruct the 2D velocity distribution function. The weight functions in the center column are sensitive to ions at intermediate and high energies but not to low-energy ions, and the weight functions in the right column are sensitive to high-energy ions only.

The data points for the inversion are selected using their associated weight functions. Here we do not seek to reconstruct the part of velocity space below 120 keV since this low-energy region of velocity space is densely populated due to the NBI ions. The inclusion of this densely populated low-energy velocity-space region would make the inference of the relatively sparsely populated high-energy velocity-space region difficult. Hence we reject all data points associated with weight functions with significant values below 120 keV. In figure 7 the 120 keV line is shown in blue. This method to reject the parts of the spectra that are sensitive to densely populated low-energy parts of velocity space is analogous to the rejection of the likewise very bright thermal halo feature originating from thermal ions in FIDA velocity-space tomography [61].

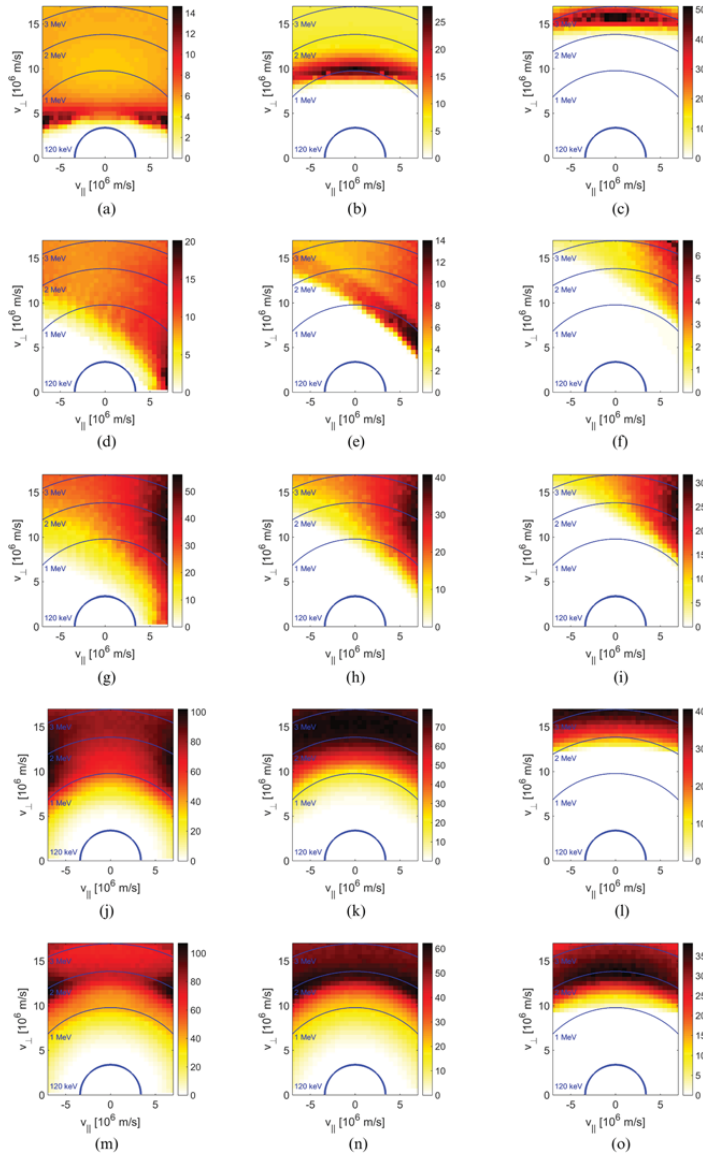


Figure 7. Typical weight functions for the five spectra for low (left column), intermediate (center column), and high (right column) neutron or γ -ray energy shifts expressed in the particular diagnostic units. (a)–(c) TOFOR. (d)–(f) Diamond. (g)–(i) NE213. (j)–(l) HpGe γ -ray peak at 2868 keV. (m)–(o) HpGe γ -ray peak at 3367 keV. The blue dashed lines show 1 MeV, 2 MeV and 3 MeV, and the full blue line shows 120 keV. (a) $t_{\text{tof}} = 58$ ns. (b) $t_{\text{tof}} = 50$ ns. (c) $t_{\text{tof}} = 42$ ns. (d) $E_{\text{dep}} = 813$ keV. (e) $E_{\text{dep}} = 1016$ keV. (f) $E_{\text{dep}} = 1191$ keV. (g) $E_{\text{ph}} = 0.9$ MeVee. (h) $E_{\text{ph}} = 1.2$ MeVee. (i) $E_{\text{ph}} = 1.5$ MeVee. (j) $E_{\gamma} = 2868$ keV. (k) $E_{\gamma} = 2848$ keV. (l) $E_{\gamma} = 2828$ keV. (m) $E_{\gamma} = 3367$ keV. (n) $E_{\gamma} = 3347$ keV. (o) $E_{\gamma} = 3327$ keV.

The weight functions covering only very high ion energies tend to be beneficial since the measured absence of signal for these weight functions helps finding empty regions of velocity space. Hence we use all weight functions reaching into the target velocity space. The rejected data at the high-energy end of the spectra are associated with weight functions that do not cover our target velocity space.

4. MeV-range velocity-space tomography

The NES and GRS weight functions allow us to pose the forward model for the computation of synthetic GRS and NES spectra efficiently as the matrix equation [30, 31]

$$S = WF \quad (4)$$

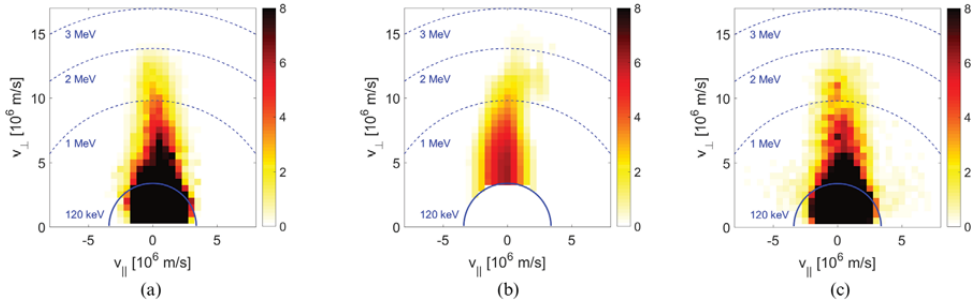


Figure 8. Simulations with the ASCOT-RFOF and SPOT-RFOF codes and measurement of an MeV-range ion velocity distribution function for third harmonic ICRF heating by velocity-space tomography. The dashed lines mark 1 MeV, 2 MeV and 3 MeV. The blue line marks 120 keV which is the lower limit of our target velocity space. (a) ASCOT-RFOF. (b) Measurement. (c) SPOT-RFOF.

which is a discretization of equation (3). Here S is a vector holding the measurements normalized by their uncertainties, F is a vector holding the fast-ion velocity distribution function, and W is a matrix composed of weight functions normalized by the uncertainty of the corresponding measurement [31]. As mentioned in section 2, the absolute scaling of the measured spectra is fairly uncertain. This uncertainty of the absolute scaling means that we will not compute absolutely scaled fast-ion velocity distribution functions. Here we calculate a constant scaling factor for each spectrum by fitting the synthetic spectra to the measured spectra and then scale all weight functions corresponding to a spectrum by this factor. This method provides a relative calibration of the five spectra, but does not change the spectral shapes.

The goal of velocity-space tomography is now to find F (in a.u.), given S and W . The matrix W is ill-conditioned such that a useful and stable solution in F cannot be computed without additional requirements on the solution. This is called regularization. Here we require that the gradients in F are small and that F is non-negative. Hence we pose the inverse problem using first-order Tikhonov regularization as the minimization problem [38]

$$\text{minimize } \left\| \begin{pmatrix} W \\ \lambda L \end{pmatrix} F - \begin{pmatrix} S \\ 0 \end{pmatrix} \right\|_2 \quad \text{subject to } F \geq 0 \quad (5)$$

which we solve using a standard non-negative least-squares algorithm [63]. The problem shown in expression (5) minimizes the sum of the two-norm of the residual (upper row) and the two-norm of the additional constraint on the solution (lower row). Left-multiplication with the penalty matrix L effects a finite difference approximation of a gradient [36]. The free regularization parameter λ balances the smoothness requirement and the goodness-of-fit to the data. As consequence of the normalization, the measurements with the highest signal-to-noise ratio are weighted most heavily in the least-square fit.

5. Benchmark of MeV-range velocity-space tomography and ASCOT-RFOF and SPOT-RFOF simulations

This section demonstrates that measurements of MeV-range 2D velocity distribution functions using velocity-space

tomography are feasible and benchmarks the approach against numerical simulations with the ASCOT-RFOF [20] and SPOT-RFOF [22] codes. The simulated 2D velocity distribution functions averaged over the plasma core are presented in figures 8(a) and 8(c). The simulations of the formation of the fast-ion tail due to ICRF heating from the NBI seed population have been discussed previously [20, 22]. The 2D velocity distribution functions show several expected features. The NBI population has energies below 120 keV. The ICRF waves draw a fast-ion tail in the v_{\perp} -direction (>120 keV) since the wave electric field couples to this velocity component. The tail is close to symmetric about the v_{\perp} -axis. For third harmonic ICRF heating, the tail is expected to terminate at energies of about 2 MeV since the wave-particle interaction becomes very weak above this energy. This strong decrease in the wave-particle interaction is also referred to as the barrier region [22]. The simulations predict that very few ions can be accelerated across the barrier region. Another feature of the simulations is that the tail width increases as v_{\perp} decreases which is explained by collisions driving the distribution towards an isotropic distribution.

Figure 8(b) shows the measurement of the core-averaged MeV-range 2D velocity distribution function based on the three NES spectra and the two GRS spectra. Several features of the inversion are in excellent agreement with the simulations. The measured fast-ion tail is close to symmetric about the v_{\perp} -axis as are the simulations. The predicted and measured tail lengths are very similar which confirms the presence of the barrier region at the predicted location. The measured width of the fast-ion tail including the widening for lower v_{\perp} also follows the predictions very closely. Since the measurements are not absolutely calibrated, we can make no statement about the amplitudes. By construction the amplitudes of the simulation and the measurement are similar in arbitrary units.

The tomographic inversion allows the computation of derived quantities that are not experimentally accessible by other means. Here we integrate the 2D velocity distribution function over v_{\parallel} :

$$f^{1D}(v_{\perp}) = \int f(v_{\parallel}, v_{\perp}) dv_{\parallel}. \quad (6)$$

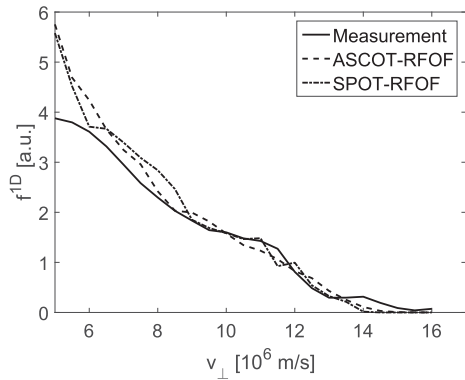


Figure 9. Comparison of measured and simulated 1D velocity distribution functions $f^{1D}(v_{\perp})$ illustrating the tail length in v_{\perp} space.

Figure 9 shows a comparison of the measured and simulated 1D velocity distribution functions $f^{1D}(v_{\perp})$. As in figure 8, the agreement is excellent for $v_{\perp} > 6 \times 10^6 \text{ m s}^{-1}$. The inversion becomes uncertain for lower v_{\perp} because the GRS weight functions do not reach into this region so that this low energy region is not well diagnosed.

Lastly, we note that the obtained results require the use of both NES and GRS diagnostics. We have computed inversions based on the three NES spectra alone and have not been able to find useful solutions. Figure 7 illustrates that the GRS measurements and TOFOR observe similar regions in velocity space whereas the oblique sightlines (i.e. the diamond and the liquid scintillator NES detectors) interrogate mostly $v_{\parallel} > 0$. Hence the GRS measurements are essential to provide the necessary extra views for the region with $v_{\parallel} < 0$. Further, the GRS weight functions have isolevels roughly following lines of constant energy whereas the weight functions of TOFOR have isolevels roughly following lines of constant v_{\perp} . This curvature of the GRS weight functions means that only GRS measurements observe the lower left corner of our target velocity space (low v_{\perp} and $v_{\parallel} < 0$). Thus the GRS diagnostic substantially improves the conditioning of the inverse problem, such that we can only obtain useful results by velocity-space tomography relying both on NES and GRS.

6. Discussion

In this section we discuss the potential and limitations of MeV-range velocity-space tomography. One limitation of our present method is that we do not have a standard candle to cross-calibrate the spectra without reference to a simulated fast-ion distribution function. This is different from FIDA velocity-space tomography since FIDA spectra are absolutely calibrated. Further, very strong direct beam emission is present in all FIDA spectra and can act as standard candle in each spectrum. Here we use a numerical simulation to cross-calibrate the measured spectra. An improvement could be to use an iterative procedure calibrating one spectrum against a synthetic spectrum calculated from a tomographic inversion

based on the other four spectra. This would have the advantage that it does not rely on a simulation. An absolute scaling could be estimated after the inversion using the total neutron count rate. However, this is not attempted here.

A second limitation is that we neglect the spatial dimension of the problem. This limitation also appears to some extent in FIDA tomography as the measurement volumes of the different views are not exactly the same. A possible solution could be to formulate the NES and GRS weight functions with a spatial dimension along the line-of-sight which has already been done [26]. The downside of this idea for velocity-space tomography is that the spatial dimension increases the number of unknowns substantially. Thus more detectors providing more measurement data would be required. The γ -ray tomography provides spatial information, and it could be possible to combine the position-space and velocity-space tomography methods.

Possible applications of velocity-space tomography based on NES and GRS are not limited to JET, ITER and DEMO but include several present machines. Concerning ITER, our results hold promise that measurements of α -particle 2D velocity distribution functions could be feasible. The ITER measurement requirements entail measurements of the α -particle density and the α -particle energy spectrum [64] which can actually not be determined using traditional data analysis procedures. Velocity-space tomography allows core-averaged measurements of these parameters by integration of the measured 2D velocity-distribution function, provided that at least one diagnostic is absolutely calibrated. The α -particles can be directly measured by CTS [65–67] and GRS [68, 69], and CTS measurements at ITER are being designed to be absolutely calibrated. ITER is also equipped with NES [64]. Deuterium and tritium 2D velocity distribution functions, as well as the derived fast-ion density and energy spectra, could also be determined by velocity-space tomography in ITER by CTS, NES and GRS.

The demonstration of a tomographic inversion of NES and GRS data will further be useful in many present tokamaks with NES and GRS diagnostics. For example, EAST has neutron spectrometers [70, 71] as well as two FIDA views [72]. LHD is equipped with CTS [73, 74], fast-ion charge-exchange recombination spectroscopy [75, 76] and a neutron spectrometer [77]. ASDEX Upgrade [43] has five FIDA views [33, 35, 48], two CTS views [44–47] as well as NES [78, 79] and GRS [80]. These various combinations of diagnostics on the various machines provide a rich test bed to develop the velocity-space tomography method for ITER.

7. Conclusions

So far velocity-space tomography has focussed on FIDA data and been limited to energies below 120 keV due to the low FIDA signal levels for more energetic ions. However, with burning plasmas on the horizon, the 2D velocity-space diagnostic of MeV-range particles becomes essential to confront theories describing energetic particles. In this paper we extend the applicability of the velocity-space tomography method

into the MeV-range and demonstrate the measurement of a 2D velocity distribution function in a third harmonic ICRF heating scenario at JET. The tomographic inversion in the MeV-range velocity space requires that we base the inversion on NES and GRS measurements rather than on FIDA. The NES measurements are made with the time-of-flight detector TOFOR, a single-crystal diamond detector and a liquid scintillator detector based on the organic material NE213. The GRS measurements are made with a high-resolution high-bandwidth HpGe detector of which we use spectrally resolved data for two reaction peaks.

The tomographic inversion based on these five spectra is in excellent agreement with SPOT-RFOF and ASCOT-RFOF simulations which validates not only the velocity-space tomography approach but also the simulations. The measurement by velocity-space tomography confirms the predicted length and width of the fast-ion tail in velocity space. The measured tail length is consistent with the presence of the predicted barrier region in velocity space in which the wave-particle interaction is very weak. The measurement of an MeV-range 2D velocity distribution function based on GRS and NES at JET paves the way for measurements of 2D α -particle velocity distribution functions in the upcoming DT campaign at JET and at ITER. Finally, the ITER measurement requirements entail measurements of the α -particle density and energy spectra. However, diagnostic weight functions suggest that these top-level measurement requirements are out of reach for individual diagnostics. Combined velocity-space tomography will allow measurements of these important parameters and is thus a promising diagnostic analysis tool for ITER.

Acknowledgments

We thank the ITPA Energetic Particle Physics Topical Group for its support. This work has been carried out within the framework of the EUROfusion Consortium and has received funding from the Euratom research and training programme 2014–2018 under grant agreement No 633053. The views and opinions expressed herein do not necessarily reflect those of the European Commission.

References

- [1] Litaudon X. *et al* 2016 Overview of the JET results in support to ITER *Nucl. Fusion* (<https://doi.org/10.1088/1741-4326/aa5e28>)
- [2] Heidbrink W. and Sadler G. 1994 *Nucl. Fusion* **34** 535–615
- [3] Jacquinet J. *et al* 1999 ITER physics basis chapter 5: physics of energetic ions *Nucl. Fusion* **39** 2471–95
- [4] Fasoli A. *et al* 2007 Progress in the ITER physics basis chapter 5: physics of energetic ions *Nucl. Fusion* **47** S264–84
- [5] Sharapov S. *et al* 2013 *Nucl. Fusion* **53** 104022
- [6] Gorelenkov N., Pinches S. and Toi K. 2014 *Nucl. Fusion* **54** 125001
- [7] Pinches S.D. *et al* 2015 *Phys. Plasmas* **22** 021807
- [8] Chen L. and Zonca F. 2016 *Rev. Mod. Phys.* **88** 015008
- [9] Romanelli F. 2015 *Nucl. Fusion* **55** 104001
- [10] Kiptily V.G. *et al* 2010 *Nucl. Fusion* **50** 084001
- [11] Murari A. *et al* 2010 *Rev. Sci. Instrum.* **81** 10E136
- [12] Nocente M. *et al* 2010 *Rev. Sci. Instrum.* **81** 10D321
- [13] Nocente M. *et al* 2012 *Nucl. Fusion* **52** 063009
- [14] Tardocchi M. *et al* 2011 *Phys. Rev. Lett.* **107** 205002
- [15] Hellesen C. *et al* 2010 *Nucl. Fusion* **50** 084006
- [16] Gassner T. *et al* 2012 *Phys. Plasmas* **19** 032115
- [17] Hellesen C. *et al* 2013 *Nucl. Fusion* **53** 113009
- [18] Shevelev A.E. *et al* 2013 *Nucl. Fusion* **53** 123004
- [19] Eriksson L.G. *et al* 1998 *Nucl. Fusion* **38** 265–78
- [20] Eriksson J. *et al* 2015 *Nucl. Fusion* **55** 123026
- [21] Nocente M. *et al* 2015 *Nucl. Fusion* **55** 123009
- [22] Schneider M. *et al* 2016 *Nucl. Fusion* **56** 112022
- [23] Salmi A. *et al* 2006 *Plasma Phys. Control. Fusion* **48** 717–26
- [24] van Eester D. *et al* Recent ion cyclotron resonance heating experiments in JET in preparation of a DT campaign in preparation
- [25] Jacobsen A.S. *et al* 2014 *Rev. Sci. Instrum.* **85** 11E103
- [26] Jacobsen A.S. *et al* 2015 *Nucl. Fusion* **55** 053013
- [27] Salewski M. *et al* 2015 *Nucl. Fusion* **55** 093029
- [28] Salewski M. *et al* 2016 *Nucl. Fusion* **56** 046009
- [29] Salewski M. *et al* 2011 *Nucl. Fusion* **51** 083014
- [30] Salewski M. *et al* 2012 *Nucl. Fusion* **52** 103008
- [31] Salewski M. *et al* 2013 *Nucl. Fusion* **53** 063019
- [32] Salewski M. *et al* 2014 *Nucl. Fusion* **54** 023005
- [33] Geiger B. *et al* 2015 *Nucl. Fusion* **55** 083001
- [34] Salewski M. *et al* 2015 *Plasma Phys. Control. Fusion* **57** 014021
- [35] Weiland M. *et al* 2016 *Plasma Phys. Control. Fusion* **58** 025012
- [36] Jacobsen A.S. *et al* 2016 *Plasma Phys. Control. Fusion* **58** 045016
- [37] Jacobsen A.S. *et al* 2016 *Plasma Phys. Control. Fusion* **58** 042002
- [38] Salewski M. *et al* 2016 *Nucl. Fusion* **56** 106024
- [39] Rasmussen J. *et al* 2016 *Nucl. Fusion* **56** 112014
- [40] Jaulmes F. *et al* 2016 *Nucl. Fusion* **56** 112012
- [41] Weiland M. *et al* Phase-space resolved measurement of 2nd harmonic ion cyclotron heating using FIDA tomography at the ASDEX Upgrade tokamak in preparation
- [42] Geiger B. *et al* Study of the fast-ion distribution function in the TCX tokamak based on FIDA spectroscopy and the TRANSP code in preparation
- [43] Stroth U. *et al* 2013 *Nucl. Fusion* **53** 104003
- [44] Salewski M. *et al* 2010 *Nucl. Fusion* **50** 035012
- [45] Furtula V. *et al* 2012 *Rev. Sci. Instrum.* **83** 013507
- [46] Nielsen S.K. *et al* 2015 *Plasma Phys. Control. Fusion* **57** 035009
- [47] Rasmussen J. *et al* 2015 *Plasma Phys. Control. Fusion* **57** 075014
- [48] Geiger B. *et al* 2015 *Plasma Phys. Control. Fusion* **57** 014018
- [49] Heidbrink W.W. *et al* 2004 *Plasma Phys. Control. Fusion* **46** 1855–75
- [50] Heidbrink W.W. *et al* 2007 *Plasma Phys. Control. Fusion* **49** 1457–75
- [51] Heidbrink W.W. 2010 *Rev. Sci. Instrum.* **81** 10D727
- [52] Hirvijoki E. *et al* 2014 *Comput. Phys. Commun.* **185** 1310–21
- [53] Gatu Johnson M. *et al* 2008 *Nucl. Instrum. Methods Phys. Res. A* **591** 417–30
- [54] Cazzaniga C. *et al* 2014 *Rev. Sci. Instrum.* **85** 043506
- [55] Nocente M. *et al* 2015 *Rev. Sci. Instrum.* **86** 103501
- [56] Muraro A. *et al* 2016 *Rev. Sci. Instrum.* **87** 11D833
- [57] Binda F. *et al* 2014 *Rev. Sci. Instrum.* **85** 11E123
- [58] Nocente M. *et al* 2013 *IEEE Trans. Nucl. Sci.* **60** 1408–15
- [59] Jacobsen A.S. *et al* Velocity-space sensitivities of neutron emission spectrometers at JET and ASDEX Upgrade in preparation
- [60] Eriksson J. *et al* 2013 *Plasma Phys. Control. Fusion* **55** 015008
- [61] Salewski M. *et al* 2014 *Plasma Phys. Control. Fusion* **56** 105005

- [62] Nocente M. *et al* 2016 *J. Instrum.* **11** C03001
- [63] Lawson C. and Hanson R. 1974 *Solving Least Squares Problems* (Englewood Cliffs, NJ: Prentice-Hall)
- [64] Donné A.J.H. *et al* 2007 Progress in the ITER Physics Basis Chapter 7: Diagnostics *Nucl. Fusion* **47** S337–84
- [65] Salewski M. *et al* 2008 *Rev. Sci. Instrum.* **79** 10E729
- [66] Salewski M. *et al* 2009 *Plasma Phys. Control. Fusion* **51** 035006
- [67] Salewski M. *et al* 2009 *Nucl. Fusion* **49** 025006
- [68] Chugunov I.N. *et al* 2011 *Nucl. Fusion* **51** 083010
- [69] Nocente M. *et al* Conceptual design of the radial gamma ray spectrometers system for alpha particle and runaway electron measurements at ITER in preparation
- [70] Yuan X. *et al* 2013 *J. Instrum.* **8** P07016
- [71] Zhang X. *et al* 2014 *Nucl. Fusion* **54** 104008
- [72] Huang J. *et al* 2014 *Rev. Sci. Instrum.* **85** 11E407
- [73] Kubo S. *et al* 2010 *Rev. Sci. Instrum.* **81** 10D535
- [74] Nishiura M. *et al* 2014 *Nucl. Fusion* **54** 023006
- [75] Ito T. *et al* 2010 *Rev. Sci. Instrum.* **81** 10D327
- [76] Ito T. *et al* 2012 *Plasma Fusion Res.* **5** S2099
- [77] Tomita H. *et al* 2010 *Rev. Sci. Instrum.* **81** 10D309
- [78] Giacomelli L. *et al* 2011 *Rev. Sci. Instrum.* **82** 123504
- [79] Tardini G. *et al* 2012 *J. Instrum.* **7** C03004
- [80] Nocente M. *et al* 2012 *Nucl. Fusion* **52** 094021

Reference [12]

[12]. M Salewski et al. (2018) *Nuclear Fusion* **58** 036017. Deuterium temperature, drift velocity, and density measurements in non-Maxwellian plasmas at ASDEX Upgrade

Deuterium temperature, drift velocity, and density measurements in non-Maxwellian plasmas at ASDEX Upgrade

M. Salewski¹, B. Geiger², A.S. Jacobsen², I. Abramovic³, S.B. Korsholm¹, F. Leipold¹, B. Madsen¹, J. Madsen¹, R.M. McDermott², D. Moseev³, S.K. Nielsen¹, M. Nocente^{4,5}, J. Rasmussen¹, M. Stejner¹, M. Weiland², The EUROfusion MST1 team^a and The ASDEX Upgrade team^b

¹ Technical University of Denmark, Department of Physics, Kgs. Lyngby, Denmark

² Max-Planck-Institut für Plasmaphysik, Garching, Germany

³ Max-Planck-Institut für Plasmaphysik, Greifswald, Germany

⁴ Department of Physics, University of Milano Bicocca, Milano, Italy

⁵ Istituto di Fisica del Plasma, Consiglio Nazionale delle Ricerche, Milano, Italy

E-mail: msal@fysik.dtu.dk

Received 5 October 2017, revised 5 January 2018

Accepted for publication 11 January 2018

Published 1 February 2018



Abstract

We measure the deuterium density, the parallel drift velocity, and parallel and perpendicular temperatures (T_{\parallel} , T_{\perp}) in non-Maxwellian plasmas at ASDEX Upgrade. This is done by taking moments of the ion velocity distribution function measured by tomographic inversion of five simultaneously acquired spectra of D_{α} -light. Alternatively, we fit the spectra using a bi-Maxwellian distribution function. The measured kinetic temperatures ($T_{\parallel} = 9$ keV, $T_{\perp} = 11$ keV) reveal the anisotropy of the plasma and are substantially higher than the measured boron temperature (7 keV). The Maxwellian deuterium temperature computed with TRANSP (6 keV) is not uniquely measurable due to the fast ions. Nevertheless, simulated kinetic temperatures accounting for fast ions based on TRANSP ($T_{\parallel} = 8.3$ keV, $T_{\perp} = 10.4$ keV) are in excellent agreement with the measurements. Similarly, the Maxwellian deuterium drift velocity computed with TRANSP (300 km s^{-1}) is not uniquely measurable, but the simulated kinetic drift velocity accounting for fast ions agrees with the measurements (400 km s^{-1}) and is substantially larger than the measured boron drift velocity (270 km s^{-1}). We further find that ion cyclotron resonance heating elevates T_{\parallel} and T_{\perp} each by 2 keV without evidence for preferential heating in the D_{α} spectra. Lastly, we derive an expression for the 1D projection of an arbitrarily drifting bi-Maxwellian onto a diagnostic line-of-sight.

Keywords: anisotropic plasma, deuterium density, deuterium rotation, deuterium temperature, bi-Maxwellian, velocity-space tomography

(Some figures may appear in colour only in the online journal)

1. Introduction

Fusion plasmas are often described by just a few parameters summarizing their basic properties. The ion populations are described by the lowest moments of their velocity distribution

functions: the density n , the drift velocity v_d (or equivalently the so-called rotation), the temperature T , and the pressure p . Anisotropic plasmas are described by the temperatures T_{\parallel} and T_{\perp} and the pressures p_{\parallel} and p_{\perp} where the indices refer to directions with respect to the magnetic field.

However, the properties of the main-ion species are almost never measured directly, but are estimated from measurements

^a See Meyer H. *et al* [1]

^b See Kallenbach A. *et al* [2]

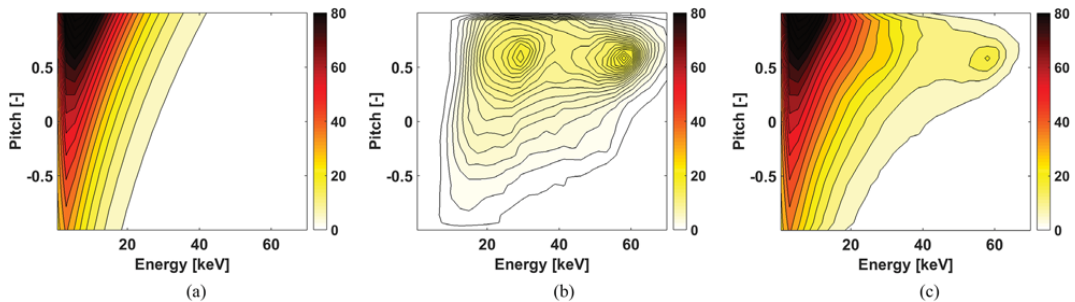


Figure 1. TRANSP splits the deuterium population into (a) a drifting Maxwellian and (b) a fast-ion velocity distribution function computed in the NUBEAM module in $(10^{16} \text{ (keV m}^3\text{)}^{-1})$. (c) The modelled complete deuterium velocity distribution is the sum of both populations. The parameters here are taken from a TRANSP simulation of ASDEX Upgrade [47] discharge #32323 at 1711 ms in the plasma center just before a sawtooth crash. The NBI source is S3. The Maxwellian is described by $T = 6 \text{ keV}$, $n_{\text{th}} = 2 \times 10^{19} \text{ m}^{-3}$ and $v_d = 3 \times 10^5 \text{ m s}^{-1}$. The density of the fast-ion population in (b) is $n_f = 6 \times 10^{18} \text{ m}^{-3}$.

of impurity ions and calculations. For example, deuterium temperatures and drift velocities are routinely estimated from the corresponding impurity parameters which are measured by charge-exchange recombination (CER) spectroscopy. A non-exhaustive list of examples of such measurements on a variety of tokamaks is found in [3–23]. Deuterium temperatures and drift velocities are directly measured by D_α -based CER spectroscopy [24–34] and collective Thomson scattering (CTS) [35–44]. Neutron emission and gamma-ray spectroscopy also allow temperature measurements in high-performance plasmas [45]. A difficulty of main-ion measurements is that the associated distribution function is often highly non-Maxwellian and anisotropic due to the intense auxiliary plasma heating. The non-Maxwellian functional form and the anisotropy has up to now been dealt with by splitting the total population into a thermal, Maxwellian population and an energetic, non-Maxwellian population in analogy to the simulated populations in the widespread TRANSP code [46] (figure 1). In TRANSP fast ions are usually assumed to be part of the energetic population down to energies of $E = 1.5T_i$ where T_i is the Maxwellian ion temperature. The fast ions with higher energies are tracked in the NUBEAM module [46], and when they have slowed down to an energy of $1.5T_i$, they are removed from NUBEAM and added to the thermal population.

If the deviation from a Maxwellian is small, it is argued that the energetic-ion population is negligible [38–41]. In this case the total deuterium population is modelled as a thermal, Maxwellian population which is found as the best-fit Maxwellian to the total distribution function illustrated in figure 1(c). If the deviation from a Maxwellian is large, a common approach is to allow for the existence of an energetic, non-Maxwellian population in addition to a thermal population in analogy to TRANSP [28–31]. In this case one finds the best-fit Maxwellian to the distribution function illustrated in figure 1(a). However, as individual deuterium ions from the ‘thermal’ (figure 1(a)) and the ‘energetic’ (figure 1(b)) populations are indistinguishable, only the total main-ion population (figure 1(c)) can be measured experimentally. We will show that the artificial splitting into thermal and non-thermal populations leads to ambiguity of the inferred bulk ion parameters. We will drop this artificial splitting altogether and consider

one total deuterium ion population, and our goal will be to measure its lowest moments, the density, the drift velocity, and the parallel and perpendicular temperatures and pressures.

Here we demonstrate two new formalisms that accomplish this and account for the anisotropy and the deviation from a Maxwellian of the deuterium population. To this end, we have acquired five spectra of D_α -light originating from the same location simultaneously by active D_α -CER spectroscopy using five different lines-of-sight [48–50]. In our first approach we find the parallel-drifting bi-Maxwellian distribution function that produces the best fit to the five spectra. While this approach in principle allows measurements of the bi-Maxwellian parameters $n, v_{d\parallel}, T_{\parallel}, T_{\perp}, p_{\parallel}, p_{\perp}$ in plasmas that have a bi-Maxwellian distribution function, it is inaccurate for populations that are not Maxwellian or bi-Maxwellian as is often the case at ASDEX Upgrade. Nevertheless, this approach is still worth pursuing as it may be the only option for anisotropic temperature measurements if only two or three simultaneously acquired active CER measurements are available. Further, this approach has advantages compared with traditional CER spectroscopy based on one spectrum since measurements from several detectors are used simultaneously. This approach is hence a form of integrated data analysis [51].

In our second approach, we will not assume any functional form of the distribution function but instead measure the total deuterium distribution function by velocity-space tomography which is becoming an increasingly widespread tool to analyze fast-ion measurements [48–64]. We then calculate $n, v_{d\parallel}, T_{\parallel}, T_{\perp}, p_{\parallel}$ and p_{\perp} as the lowest moments of the total deuterium distribution function. These kinetic parameters are unique and well-defined for any distribution function in tokamak plasmas, and they reduce to the usual Maxwellian parameters if the distribution is Maxwellian.

This paper is organized as follows. Section 2 briefly reviews coordinate systems frequently used to measure drift velocities and ion distribution functions. We calculate the projection of a bi-Maxwellian distribution function onto a diagnostic line-of-sight in section 3, illustrating that perpendicular as well as parallel temperatures can be measured if spectroscopic data from two or more intersecting lines-of-sight are available. In section 4 we discuss measurements of the kinetic parallel

and perpendicular temperatures and pressures, drift velocities and densities as moments of the velocity distribution function using velocity-space tomography. Section 5 gives an overview of the two discharges that we analyze. Sections 6 and 7 discuss difficulties one encounters when trying to fit non-Maxwellian distribution functions with Maxwellians and bi-Maxwellians in 1D and 2D, respectively. Section 8 presents measurement results obtained by fitting spectra with bi-Maxwellians and by velocity-space tomography. Finally, in section 9 conclusions are drawn.

2. Bi-Maxwellians and drift velocities in common coordinate systems

In this section we briefly define the various coordinate systems that are customary in descriptions of distribution functions and drift velocities in a tokamak. The drift velocities are often split into components in the toroidal and poloidal directions referring to a drift parallel to the magnetic axis and a drift azimuthally around it, respectively. As we analyze measurements in the plasma center in a high-power, high-torque plasma, the poloidal drift is not important compared with the toroidal drift. Often these drift velocities are presented in terms of so-called toroidal and poloidal rotations in units of (Hz) or (rad s)⁻¹. However, our formalism to calculate drift velocities and distribution functions is simplest in coordinates referring to parallel and perpendicular directions with respect to the local magnetic field vector due to the rotational symmetry associated with the rapid gyration of the ions. Vectors in these directions can easily be transformed to vectors in toroidal and poloidal directions since the local magnetic field vectors are known.

The anisotropic temperatures and pressures are most easily understood in (v_{||}, v_⊥)-space which can be represented as a slice through the full 3D function $f_v^{3D}(v_{||}, v_{\perp})$ with implied rotational symmetry or as a true 2D function $f_v^{2D}(v_{||}, v_{\perp})$ with no implied third direction. These two functions are related by [52]

$$f_v^{2D}(v_{||}, v_{\perp}) = 2\pi v_{\perp} f_v^{3D}(v_{||}, v_{\perp}) \quad (1)$$

where the factor v_{\perp} is the Jacobian of the transformation from Cartesian to cylindrical coordinates and 2π is the integral over the ignorable gyroangle. The energy E and pitch ξ of a particle are another customary set of 2D coordinates. The 2D coordinate transformations between $f_v^{2D}(v_{||}, v_{\perp})$ and $f(E, \xi)$ are

$$\begin{aligned} E &= \frac{1}{2}m(v_{||}^2 + v_{\perp}^2) & v_{||} &= \xi\sqrt{\frac{2E}{m}} \\ \xi &= \frac{v_{||}}{\sqrt{v_{||}^2 + v_{\perp}^2}} & v_{\perp} &= \sqrt{1 - \xi^2}\sqrt{\frac{2E}{m}} \end{aligned} \quad (2)$$

with the Jacobians

$$J_{v \rightarrow E, \xi} = \frac{1}{m\sqrt{1 - \xi^2}} \quad J_{E, \xi \rightarrow v} = \frac{mv_{\perp}}{\sqrt{v_{||}^2 + v_{\perp}^2}}. \quad (3)$$

A parallel-drifting bi-Maxwellian velocity distribution function in a magnetized plasma with the ignorable gyroangle γ in 3D (v_{||}, v_⊥)-space is

$$f_v^{3D}(v_{||}, v_{\perp}) = n \left(\frac{m}{2\pi}\right)^{3/2} \frac{1}{T_{\perp} T_{||}^{1/2}} \exp\left(-\frac{m(v_{||} - v_{d||})^2}{2T_{||}} - \frac{mv_{\perp}^2}{2T_{\perp}}\right). \quad (4)$$

A Maxwellian with perpendicular drift cannot be represented using the two coordinates (v_{||}, v_⊥) due to the rotational symmetry. A perpendicular drift velocity term of the form (v_⊥ - v_{d⊥})² would represent a ring distribution rather than a drifting Maxwellian due to the rotational symmetry. Therefore such a term is not included. It is possible to allow perpendicular drifts using the formalism shown in section 3 where one describes the rotation symmetric bi-Maxwellian in a coordinate system with a relative perpendicular velocity. In high-power, high-torque plasmas in ASDEX Upgrade, the perpendicular drift can be assumed to be small compared with the parallel drift in the plasma center where the pitch of the magnetic field lines is small. Therefore the 2D bi-Maxwellian is a good model that is often used. In 2D (v_{||}, v_⊥)-space it becomes according to equation (1)

$$f_v^{2D}(v_{||}, v_{\perp}) = n \frac{m^{3/2}}{(2\pi)^{1/2}} \frac{v_{\perp}}{T_{\perp} T_{||}^{1/2}} \exp\left(-\frac{m(v_{||} - v_{d||})^2}{2T_{||}} - \frac{mv_{\perp}^2}{2T_{\perp}}\right), \quad (5)$$

and in 2D (E, ξ)-space according to equations (2) and (3)

$$\begin{aligned} f(E, \xi) &= n \left(\frac{E}{\pi T_{\perp}^2 T_{||}}\right)^{1/2} \\ &\times \exp\left(-\frac{\xi^2 E + \frac{1}{2}mv_{d||}^2 - v_{d||}\xi\sqrt{2mE}}{T_{||}} - \frac{(1 - \xi^2)E}{T_{\perp}}\right). \end{aligned} \quad (6)$$

The standard drifting isotropic Maxwellians in these coordinate systems are obtained by setting $T_{||} = T_{\perp} = T$ in equations (4) to (6).

3. Projection of a bi-Maxwellian with arbitrary drift

For many diagnostics the projection of the distribution function onto a particular direction plays a special role. For example, the Doppler shift $\Delta\lambda$ in CER spectroscopy measurements is given by

$$\Delta\lambda = \lambda_0 \frac{u}{c} \quad (7)$$

where λ_0 is the rest frame wavelength of the emitted light, u is the velocity component along the line-of-sight and c is the speed of light [65]. Blue- and red-shift correspond to negative and positive u , respectively. Similarly, the frequency shift of scattered radiation ω^{δ} in CTS measurements is

$$\omega^{\delta} = u|\mathbf{k}^{\delta}| \quad (8)$$

where \mathbf{k}^{δ} is the difference between the wave vectors of received and incident radiation [66]. The velocity distribution function projected onto the line-of-sight for CER spectroscopy and onto

\mathbf{k}^δ for CTS, $g(u)$, strongly influences the widths of the measured spectra. Here we derive an expression for the 1D projection of a bi-Maxwellian with arbitrary parallel and perpendicular drifts. This expression provides insight into temperature and drift velocity measurements in idealized bi-Maxwellian plasmas. The line-of-sight velocity component of a particle with velocities (v_{\parallel} , v_{\perp}) and a perpendicular drift velocity $v_{d\perp}$ is

$$u = v_{d\perp} \cos \beta + v_{\parallel} \cos \phi + v_{\perp} \sin \phi \cos \gamma \quad (9)$$

where ϕ is the angle between the magnetic field and the line-of-sight and β is the angle between the perpendicular drift velocity and the line-of-sight. Compared with the previously used projection equation [52], we here allow for a perpendicular drift velocity in analogy to the treatment of systematic Doppler shifts due to relative drifts of astrophysical rotating accretion discs to Earth [57]. v_{\parallel} is the parallel drift which is already handled by the existing formalism [52, 67]. The projection of the 3D function onto the line-of-sight can be written using the Dirac δ -function

$$g(u, \phi) = \iiint f^{3D}(v_{\parallel}, v_{\perp}) \delta(v_{\parallel} \cos \phi + v_{\perp} \sin \phi \cos \gamma - (u - v_{d\perp} \cos \beta)) v_{\perp} dv_{\parallel} dv_{\perp} d\gamma \quad (10)$$

which can be interpreted as the projection onto the transformed coordinate

$$u' = u - v_{d\perp} \cos \beta. \quad (11)$$

Integration over γ gives for $\phi \neq 0$ [52]

$$g(u, \phi) = \int_{-\infty}^{\infty} \int_{(u' - v_{\parallel} \cos \phi) / \sin \phi}^{\infty} \frac{2f^{3D}(v_{\parallel}, v_{\perp})}{\sin \phi \sqrt{1 - \left(\frac{u' - v_{\parallel} \cos \phi}{v_{\perp} \sin \phi}\right)^2}} dv_{\perp} dv_{\parallel}. \quad (12)$$

The lower integration limit $(u' - v_{\parallel} \cos \phi) / \sin \phi$ in v_{\perp} describes the border between the observable and unobservable velocity-space regions [52, 67]. Unobservable regions can be identified here by a negative radicant in equation (12). After substituting equation (4) and expanding the fraction by v_{\perp} , we get

$$g(u, \phi) = \frac{2n}{\sin \phi} \left(\frac{m}{2\pi}\right)^{3/2} \frac{1}{T_{\perp} T_{\parallel}^{1/2}} \times \int_{-\infty}^{\infty} \int_{u' / \sin \phi - v_{\parallel} \cot \phi}^{\infty} \frac{v_{\perp} \exp\left(-\frac{mv_{\perp}^2}{2T_{\perp}}\right)}{\sqrt{v_{\perp}^2 - \left(\frac{u' - v_{\parallel} \cos \phi}{\sin \phi}\right)^2}} dv_{\perp} \times \exp\left(-\frac{m(v_{\parallel} - v_{d\parallel})^2}{2T_{\parallel}}\right) dv_{\parallel}. \quad (13)$$

After integration over v_{\perp} ,

$$g(u, \phi) = \frac{n}{\sin \phi} \left(\frac{m}{2\pi}\right) \frac{1}{(T_{\perp} T_{\parallel})^{1/2}} \int_{-\infty}^{\infty} \exp\left(-\frac{m\left(\frac{u' - v_{\parallel} \cos \phi}{\sin \phi}\right)^2}{2T_{\perp}} - \frac{m(v_{\parallel} - v_{d\parallel})^2}{2T_{\parallel}}\right) dv_{\parallel}, \quad (14)$$

and over v_{\parallel} ,

$$g(u, \phi) = \frac{n}{\sin \phi} \left(\frac{m}{2\pi}\right) \frac{1}{(T_{\perp} T_{\parallel})^{1/2}} \left(\frac{2\pi}{m\left(\frac{1}{T_{\parallel}} + \frac{1}{T_{\perp}} \cot^2 \phi\right)}\right)^{1/2} \times \exp\left(-\frac{2m^2(u' - v_{d\parallel} \cos \phi)^2}{4T_{\perp} T_{\parallel} m/2(1/T_{\perp} + 1/T_{\parallel} + (1/T_{\perp} - 1/T_{\parallel}) \cos(2\phi))}\right), \quad (15)$$

and after straightforward simplification and transformation back to u , we find an intuitive equation for the projection of the arbitrarily drifting bi-Maxwellian distribution function onto the line-of-sight:

$$g(u, \phi) = n \left(\frac{m}{2\pi(T_{\perp} \sin^2 \phi + T_{\parallel} \cos^2 \phi)}\right)^{1/2} \times \exp\left(-\frac{m(u - v_{d\parallel} \cos \phi - v_{d\perp} \cos \beta)^2}{2(T_{\parallel} \cos^2 \phi + T_{\perp} \sin^2 \phi)}\right). \quad (16)$$

Equation (16) is a 1D Maxwellian with the effective temperature in the u -coordinate along the line-of-sight

$$T_u = T_{\perp} \sin^2 \phi + T_{\parallel} \cos^2 \phi \quad (17)$$

and the u -drift

$$u_d = v_{d\parallel} \cos \phi + v_{d\perp} \cos \beta. \quad (18)$$

It connects the drifting 1D Maxwellian often used in temperature measurements to an underlying group of 2D arbitrarily drifting bi-Maxwellians with the same 1D projection. The angle between the line-of-sight and the magnetic field is always known. If the direction of the perpendicular drift velocity is known, we also know β for each view. If at least two simultaneous measurements at different viewing angles on the same measurement volume are available and the perpendicular drift direction is known, we could find all parameters of a drifting bi-Maxwellian, assuming that the velocity distribution function has a bi-Maxwellian shape. This is accomplished by measuring T_u and u_d for each view (at least two views) and inverting equation (17) to obtain T_{\parallel} and T_{\perp} and equation (18) to obtain $v_{d\parallel}$ and $v_{d\perp}$. We illustrate this possibility by considering the two extreme angles $\phi = 0^\circ$ and $\phi = 90^\circ$ leading to a particularly simple inversion. For $\phi = 90^\circ$ the parallel temperature and the parallel drift velocity drop out. The width of the Maxwellian is then given by the perpendicular temperature and the drift is the projected perpendicular drift:

$$g(u, \phi = 90^\circ) = n \left(\frac{m}{2\pi T_{\perp}}\right)^{1/2} \exp\left(-\frac{m(u - v_{d\perp} \cos \beta)^2}{2T_{\perp}}\right). \quad (19)$$

For $\phi \rightarrow 0$ the perpendicular temperature and the perpendicular drift velocity drop out (as $\beta \rightarrow 90^\circ$). The width is given by the parallel temperature. The observed u -drift is $v_{d\parallel}$. The special case $\phi = 0$ gives the same results as the limit $\phi \rightarrow 0$ of equation (16) (we omit the analogous derivation for brevity):

$$g(u, \phi = 0^\circ) = n \left(\frac{m}{2\pi T_{\parallel}}\right)^{1/2} \exp\left(-\frac{m(u - v_{d\parallel})^2}{2T_{\parallel}}\right). \quad (20)$$

For $T_{\parallel} = T_{\perp} \equiv T$, ϕ drops out of the temperature terms, and we obtain a standard drifting Maxwellian with the same temperature for any ϕ , but with u -drift velocities that do depend on the direction of the line-of-sight:

$$g(u, \phi) = n \left(\frac{m}{2\pi T} \right)^{1/2} \exp \left(- \frac{m(u - v_{d\parallel} \cos \phi - v_{d\perp} \cos \beta)^2}{2T} \right). \quad (21)$$

4. Kinetic temperatures, drift velocities and densities for arbitrary distribution functions

This section provides definitions of the kinetic parallel and perpendicular temperatures, drift velocities and densities and briefly defines how to compute them from an arbitrary distribution function. At ASDEX Upgrade five active D_{α} -CER spectra are simultaneously measured using five different lines-of-sight [48]. These intersect the beam path of NBI source S3 in the same region in the plasma. Each line-of-sight forms a different angle with the local magnetic field vector, so that different parts of velocity space are observed [67]. For such a setup we can drop the assumption that the 1D projections of the distribution function are Maxwellian. Instead we can find the complete distribution function by velocity-space tomography which provides the best regularized fit to the measurement data. We can then summarize some of the rich information contained in the fitted distribution function by computing its lowest moments. In this section we briefly define these. The zeroth moment is the density:

$$\begin{aligned} n &= \int_{-\infty}^{\infty} f(\mathbf{v}) d\mathbf{v} = \int_0^{\infty} \int_{-\infty}^{\infty} f(v_{\parallel}, v_{\perp}) dv_{\parallel} dv_{\perp} \\ &= \int_{-1}^1 \int_0^{\infty} f(E, \xi) dE d\xi. \end{aligned} \quad (22)$$

The first moment is the drift velocity:

$$\mathbf{v}_d = \frac{1}{n} \int_{-\infty}^{\infty} \mathbf{v} f(\mathbf{v}) d\mathbf{v}. \quad (23)$$

The perpendicular drift is presently neglected in the tomographic inversion. The parallel drift velocity is

$$\begin{aligned} v_{d\parallel} &= \frac{1}{n} \int_0^{\infty} \int_{-\infty}^{\infty} v_{\parallel} f(v_{\parallel}, v_{\perp}) dv_{\parallel} dv_{\perp} \\ &= \frac{1}{n} \int_{-1}^1 \int_0^{\infty} \xi \sqrt{\frac{2E}{m}} f(E, \xi) dE d\xi. \end{aligned} \quad (24)$$

The second moment is known as the pressure tensor

$$\mathbf{P} = m \int_{-\infty}^{\infty} (\mathbf{v} - \mathbf{v}_d)(\mathbf{v} - \mathbf{v}_d) f(\mathbf{v}) d\mathbf{v} \quad (25)$$

which can, for rotational symmetry about the magnetic field, be written as

$$\mathbf{P} = \begin{pmatrix} p_{\parallel} & 0 & 0 \\ 0 & p_{\perp} & 0 \\ 0 & 0 & p_{\parallel} \end{pmatrix} \quad (26)$$

where the parallel and perpendicular kinetic pressures are

$$\begin{aligned} p_{\parallel} &= m \int_0^{\infty} \int_{-\infty}^{\infty} (v_{\parallel} - v_{d\parallel})^2 f(v_{\parallel}, v_{\perp}) dv_{\parallel} dv_{\perp} \\ &= m \int_{-1}^1 \int_0^{\infty} \left(\xi \sqrt{\frac{2E}{m}} - v_{d\parallel} \right)^2 f(E, \xi) dE d\xi, \end{aligned} \quad (27)$$

$$\begin{aligned} p_{\perp} &= \frac{m}{2} \int_0^{\infty} \int_{-\infty}^{\infty} v_{\perp}^2 f(v_{\parallel}, v_{\perp}) dv_{\parallel} dv_{\perp} \\ &= \int_{-1}^1 \int_0^{\infty} (1 - \xi^2) E f(E, \xi) dE d\xi. \end{aligned} \quad (28)$$

The total kinetic pressure is defined as one third of the trace of \mathbf{P} :

$$\begin{aligned} p &= \frac{1}{3} \text{tr}(\mathbf{P}) = \frac{1}{3} (p_{\parallel} + 2p_{\perp}) \\ &= \frac{2}{3} \int_0^{\infty} \int_{-\infty}^{\infty} \left(\frac{1}{2} m (v_{\parallel} - v_{d\parallel})^2 + \frac{1}{2} m v_{\perp}^2 \right) f(v_{\parallel}, v_{\perp}) dv_{\parallel} dv_{\perp} \\ &= \frac{2}{3} \int_{-1}^1 \int_0^{\infty} \left(E - v_{d\parallel} \xi \sqrt{2mE} + \frac{1}{2} m v_{d\parallel}^2 \right) f(E, \xi) dE d\xi. \end{aligned} \quad (29)$$

The corresponding kinetic temperatures are

$$T_{\parallel} = \frac{p_{\parallel}}{n}, \quad (30)$$

$$T_{\perp} = \frac{p_{\perp}}{n}, \quad (31)$$

$$T = \frac{p}{n} = \frac{1}{3} (T_{\parallel} + 2T_{\perp}). \quad (32)$$

If the distribution is Maxwellian, these definitions for kinetic pressures and temperatures reduce to our thermodynamic notions.

5. Overview of discharges #32323 and #33178

In sections 6 and 7 we will investigate discharge #32323 theoretically, and in section 8 we will present measurements in discharges #32323 and #33178. Here we give a brief overview of these discharges. Figure 2 presents time traces of the auxiliary heating power and the plasma stored energy W_{MHD} as well as the impurity (boron) and electron temperatures in the plasma center and the line-integrated electron density. The auxiliary heating was by neutral beam injection (NBI) and electromagnetic wave heating in the electron cyclotron range of frequencies (ECRF) and in the ion cyclotron range of frequencies (ICRF). The measurement times are highlighted in grey. Discharge #32323 has a very low density ($2 \times 10^{19} \text{ m}^{-3}$) and 2.5 MW of NBI heating power (by NBI source S3) which leads to a high impurity temperature (7 keV). We will show that the deuterium population in this discharge is non-Maxwellian and substantially hotter. Discharge #33178 had a higher density ($(6-7 \times 10^{19} \text{ m}^{-3})$) and 3.5 MW NBI heating. We will compare the anisotropic deuterium temperatures with and without additional 4 MW ICRF heating at 5.5 s and 7 s, respectively.

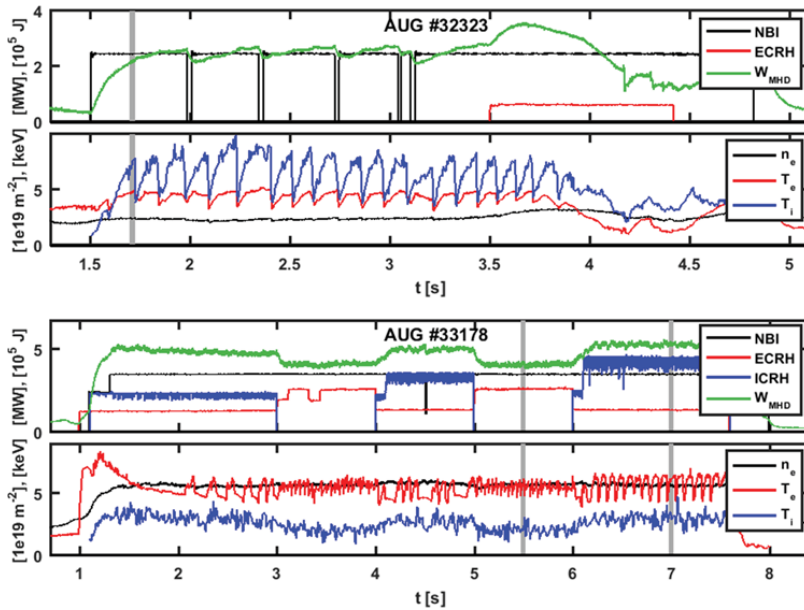


Figure 2. Overview of discharges #32323 and #33178. Time traces of NBI, ECRH and ICRH power and the plasma stored energy W_{MHD} as well as the impurity and electron temperatures in the plasma center and the line-integrated electron density. The time points used in the analysis are highlighted in grey: 1.711 s in discharge #32323 and 5.5 s and 7 s in discharge #33178.

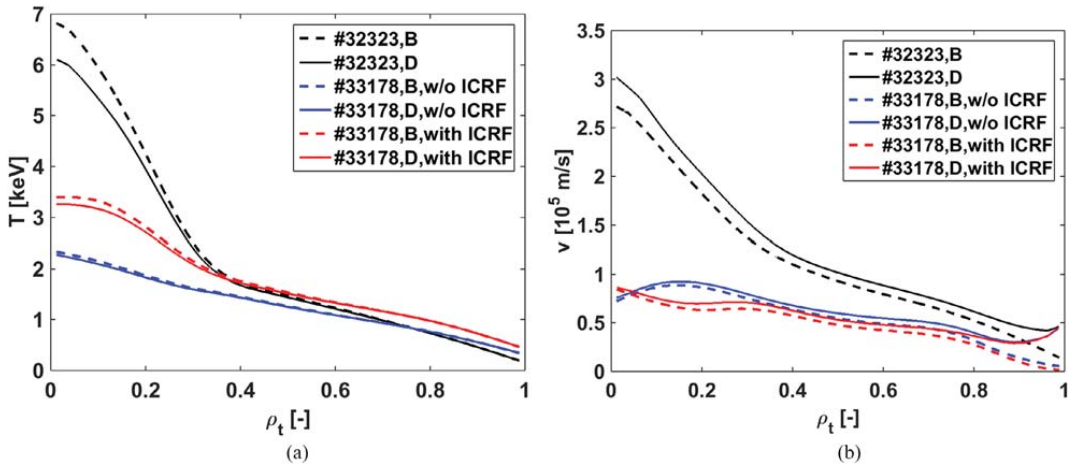


Figure 3. Profiles of measured boron (B) temperatures and toroidal drift velocities with corresponding neoclassical predictions for deuterium (D) according to TRANSP for the three measurements we will discuss. ρ_t is the normalized toroidal magnetic flux.

Profiles of the temperatures and the toroidal drift velocities as function of the normalized toroidal magnetic flux ρ_t for the three analyzed time points are presented in figure 3. The measured boron impurity temperatures and toroidal drift velocities are fairly close to corresponding neoclassical predictions for deuterium according to TRANSP in discharge #33178 whereas they differ by up to about 10–15% in discharge #32323. These neoclassical predictions assume Maxwellian distributions for deuterium and boron. In the next section we will show that such neoclassical predictions are not uniquely

measurable quantities in non-Maxwellian plasmas due to the presence of fast ions.

6. 1D fits of Maxwellians to non-Maxwellian distribution functions

In this section we discuss difficulties in fitting 1D Maxwellians to non-Maxwellian deuterium populations as an underlying model for typical data analysis in D_α -based CER spectroscopy [24–34] and CTS [38–41]. Otherwise this section makes no

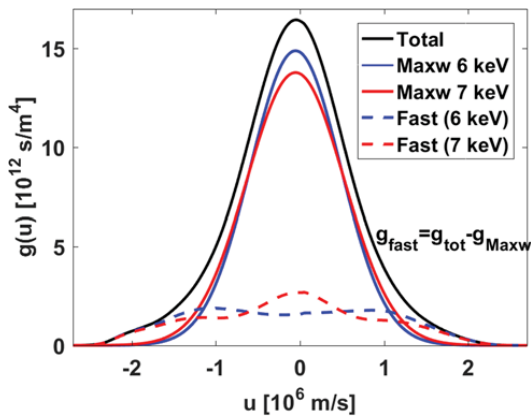


Figure 4. Projection of the velocity distribution functions simulated by TRANSP from figure 1 onto the line-of-sight ($\phi = 80^\circ$). The nominal temperature is 6 keV. Given only the total velocity distribution function (black), the splitting into thermal and fast-ion parts is not unique. This is illustrated by splitting the total distribution into two parts using Maxwellians with temperatures of 6 keV and 7 keV and their respective fast-ion distribution adding to the same total distribution.

reference to any particular diagnostic to gain insight into the basic difficulty. Whereas the Maxwellian velocity distribution function could be a good model for impurity species in the plasma, TRANSP simulations suggest that it can be a poor model for the main-ion species deuterium. The reason is that auxiliary heating selectively populates particular regions in velocity space. Deuterium ICRF and NBI heating therefore generate non-Maxwellian populations of deuterium ions.

Simulation codes such as the widely used TRANSP code deal with the non-Maxwellian ion population by artificially splitting the actual ion population into a thermal, Maxwellian ion population and an energetic ($E > 1.5T_i$), non-Maxwellian population. In TRANSP the deuterium temperature, drift velocity and density of the introduced Maxwellian ion population are calculated based on other measurements, e.g. impurity temperatures and drift velocities. The fast-ion population is calculated by the NUBEAM module. The actual ion population is then modelled as the sum of the Maxwellian and the fast-ion population (figure 1).

However, the splitting of the total deuterium population into two artificial parts based on experimental data is ambiguous. Figure 4 illustrates this dilemma in a 1D example. We project the 2D velocity distribution functions from figure 1 onto a diagnostic line-of-sight at $\phi = 80^\circ$ as discussed in section 3. The contributions from the Maxwellian population and the fast-ion population are plotted in blue as well as the total population (the sum) in black. However, in an experiment we can only measure the total population. The temperature of the Maxwellian according to TRANSP is 6 keV which is the deuterium temperature neoclassically calculated from the impurity temperature. We also show an alternative Maxwellian at 7 keV with the same density and its non-Maxwellian fast-ion complement summing up to the same total distribution. As there is no way to decide which splitting is best, the temperature,

drift velocity and densities are ambiguous if a significant non-Maxwellian population is present. The same dilemma occurs for 2D velocity distribution functions.

An approach to bypass this dilemma is to assume that the energetic, non-Maxwellian population is negligible. Then the total deuterium population reduces to the Maxwellian part. In figure 5 we show temperatures and drift velocities found by fitting 1D Maxwellians to the total projected velocity distribution function from figure 4. The x -axis shows the interval in the projected velocity u which is a proxy for the frequency or wavelength range of CTS or CER spectra used in the fit (equations (7) and (8)). In CTS measurements, only measurement data at small projected velocities u (or Doppler shifts) typical for thermal ions are used to measure temperatures [38–41]. However, figure 5 illustrates that the fitted temperature depends on the range of projected velocities used in the fit, in particular if this range is small. It appears to be best to use wide ranges so that the fitted temperature does not strongly depend on the projected velocity range.

We further vary the adopted ratio of the densities of fast-ion and thermal populations, n_f/n_{th} , which can be computed from the TRANSP simulation. The fitted temperatures and drift velocities depend on both parameters. The nominal density ratio according to TRANSP for the distributions shown in figure 1 is $n_f/n_{th} = 0.3$. For ASDEX Upgrade discharge #32323, the fitted temperature obtained from the total distribution according to TRANSP is about 9 keV which is substantially higher than the nominal temperature according to TRANSP (6 keV). The lower the density of fast ions, the more the fitted temperature to the total population approaches the nominal temperature.

Similar trends are observed for the drift velocity. Figure 5 suggests that we should expect to see differences between the fitted main-ion temperature and the corresponding nominal value from TRANSP due to the deviation from a Maxwellian. The density ratio n_f/n_{th} can be used to estimate how large this effect is for the discharge under consideration. This effect might partly explain the sometimes observed higher fitted temperatures and drift velocities of deuterium compared with the corresponding TRANSP estimates [41].

7. 2D fits of Maxwellians and bi-Maxwellians to non-Maxwellian distribution functions

The 1D examples hinted that the fitted temperatures and drift velocities depend on the fast ion population which is strongly non-Maxwellian. In figure 6 we consider an analogous 2D example, focusing just on the 2D velocity distribution function underlying the measurements but without reference to any particular diagnostic or line-of-sight. We consider again the TRANSP simulation illustrated in figure 1 where the total deuterium population is modelled to consist of a thermal, Maxwellian part and an energetic ion part computed by NUBEAM. Here we compute the kinetic drift velocities and temperatures of the total velocity distribution function according to section 4 and compare these with the corresponding parameters obtained by fitting bi-Maxwellians and

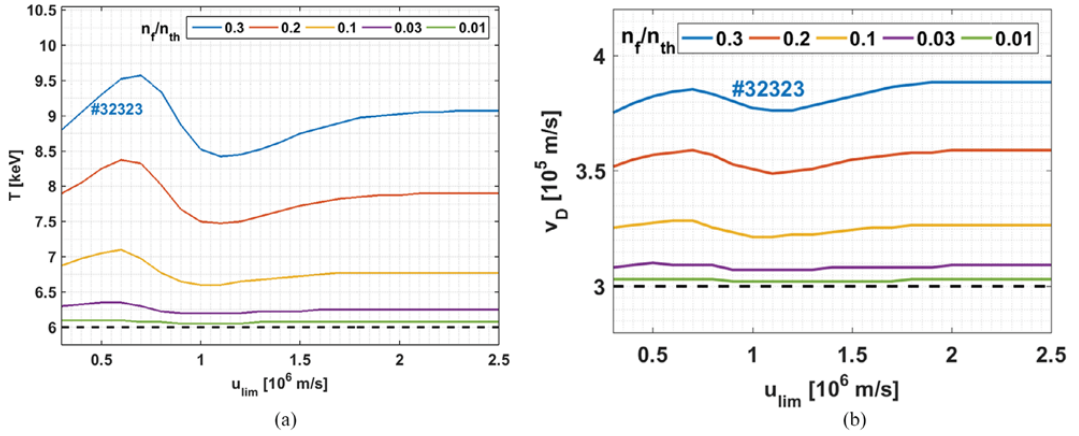


Figure 5. (a) Fitted temperatures ($\phi = 80^\circ$) and (b) parallel drift velocities ($\phi = 10^\circ$) assuming that the total velocity distribution function is Maxwellian. The x-axes show the fitting interval in u which is $[-u_{\text{lim}}; u_{\text{lim}}]$ excluding the interval $[-2; 2] \times 10^5 \text{ m s}^{-1}$ which is typically not experimentally accessible due to the need for a notch filter blocking e.g. the gyrotron radiation or the cold D_α -line. The angles ϕ are judiciously selected to illustrate large temperature and drift velocity changes.

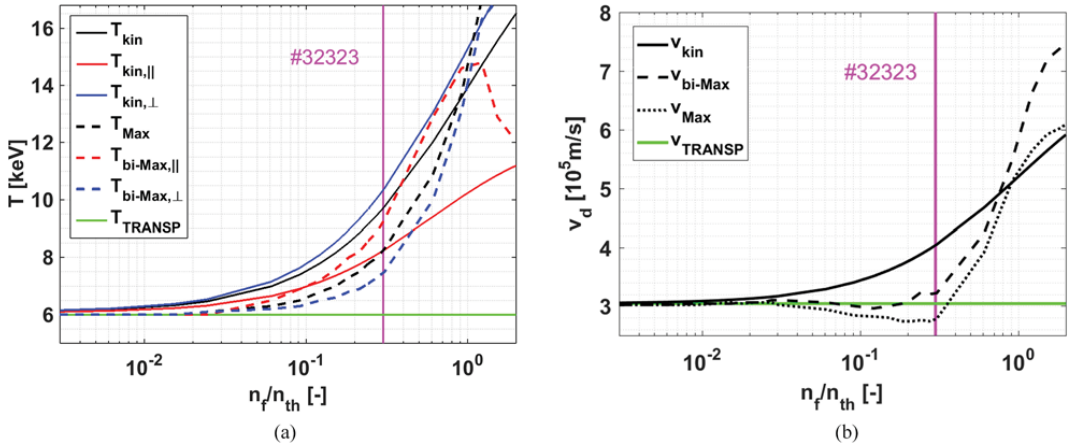


Figure 6. Kinetic temperatures and drift velocities as function of the adopted density ratio of the fast ions and thermal ions in the TRANSP picture. The nominal TRANSP deuterium values are $T = 6 \text{ keV}$ and $v_d = 300 \text{ km s}^{-1}$. Results from fits of Maxwellians and bi-Maxwellians to the total distribution are also shown.

Maxwellians to the total (non-Maxwellian) velocity distribution function. This modelled total distribution is illustrated in figure 1(c). Mathematically, we find the fitted parallel and perpendicular temperatures and parallel drift velocities by solving the minimization problem

$$\text{minimize}_{v_d, T_{\parallel}, T_{\perp}} \left(f_{\text{Maxw}}(E, \xi, n_{\text{tot}}, v_d, T_{\parallel}, T_{\perp}) - f_{\text{tot}}(E, \xi) \right) \quad (33)$$

where $f_{\text{tot}}(E, \xi)$ is the total distribution in figure 1(c). This non-weighted minimization is done for the velocity-space up to 70 keV as illustrated in figure 1. The best-fitting single temperature Maxwellian is obtained with the same formalism and the constraint $T = T_{\parallel} = T_{\perp}$.

We again vary the ratio n_f/n_{th} . In the case of bi-Maxwellian populations, the kinetic parameters are the same as the fitted bi-Maxwellian parameters. If $T_{\parallel} = T_{\perp}$, the bi-Maxwellian

further reduces to the Maxwellian. This limit is approached for $n_f/n_{\text{th}} \ll 1$ where all temperatures approach 6 keV (figure 6(a)) and the parallel drift velocity $3 \times 10^5 \text{ m s}^{-1}$ (figure 6(b)). For larger n_f/n_{th} the kinetic temperatures and the drift velocity increase due to the presence of fast ions. The perpendicular kinetic temperature is larger than the parallel kinetic temperature for NBI source S3 at ASDEX Upgrade due to the beam geometry (injection pitch $p \sim 0.6$ in the plasma center as illustrated in figure 1(b)). The total kinetic temperature is a 2:1 weighted average between the perpendicular and parallel kinetic temperatures equation (32). Figure 6(b) shows an analogous comparison of fitted parallel drift velocities and the corresponding kinetic parallel drift velocities computed as moment of the total velocity distribution function. The fitted parallel drift velocities remain fairly constant for $n_f/n_{\text{th}} < 0.3$ and then increase strongly whereas the kinetic parallel drift velocity increases smoothly.

The bi-Maxwellian temperatures also increase with the ratio n_f/n_{th} but for $n_f/n_{th} = 0.3$, as in ASDEX Upgrade discharge #32323, the fitted parallel temperature is larger than the fitted perpendicular temperature in disagreement with the corresponding kinetic temperatures. The difference to the corresponding kinetic values is about 2 keV. The differences in these temperatures and drift velocities suggest that the drifting Maxwellian and the drifting bi-Maxwellian models do not describe typical distribution functions in a low-density, NBI heated ASDEX Upgrade plasma well. The best fits have a too low drift velocity up to well beyond $n_f/n_{th} = 0.3$ which might be related to the too high parallel and too low perpendicular temperatures of the best fit.

8. Measurement results

In previous sections we have studied how energetic ion populations due to auxiliary plasma heating influence measurements of main-ion temperatures based on theoretical considerations. It appeared that unique densities, drift velocities and anisotropic temperatures could be obtained by considering the total ion velocity distribution function, rather than an artificially introduced thermal part. In this section we develop two formalisms based on these findings allowing for possible anisotropy in the plasma, and we demonstrate them using experimental data. We infer temperatures following two new approaches exploiting that the five active D_α -based CER views allow measurements of kinetic anisotropy. Both approaches rely on the weight function formalism [52, 67–72].

8.1. Fits to the D_α spectra using bi-Maxwellians

In previous applications of weight functions, the total ion distribution has been split into thermal and non-thermal parts. The weight functions depend only on thermal parameters in this picture, whereas they are applied only to energetic, non-thermal ions. Hence we could relate the measurable signal S to the fast-ion velocity distribution function F by the linear matrix equation

$$S = WF \quad (34)$$

where W is a matrix composed of weight functions [53]. However, as we now seek to infer the total deuterium distribution function, the weight functions now depend on the function that we seek to infer, and we obtain a non-linear problem

$$S = W(F)F. \quad (35)$$

The weight functions $W(F)$ can be computed for arbitrary velocity distribution functions but this is computationally very demanding. Here we seek a computationally faster approach and generate a database of weight functions for bi-Maxwellian parameters. The best fitting bi-Maxwellian is found by solving the minimization problem

$$\text{minimize} \left\| S - W(F_{\text{biMax}})F_{\text{biMax}} \right\|_2 \quad (36)$$

where $W(F_{\text{biMax}})$ is the weight function matrix computed using the bi-Maxwellian test functions. The weight functions have been precomputed for a discretization in the parameters $(n, v_d, T_{\parallel}, T_{\perp})$. This allows us to find the best fitting drifting bi-Maxwellian to the five simultaneously measured spectra given the physics model encoded in the weight functions. Traditionally, one 1D Maxwellian is fit to one CER spectrum. Our approach combines measurements from various detectors allowing integrated data analysis. Furthermore, the weight function formalism accounts for the effect of the halo and the variable charge-exchange probabilities for different energies, pitches, and gyro-angles [67, 73]. As consequence we do not obtain any apparent temperatures and apparent drift velocities that need to be corrected [74]. If the velocity distribution function is close to bi-Maxwellian, all parameters can be found rapidly by matrix multiplication.

We applied this formalism to the five simultaneously measured D_α -based CER spectra in ASDEX Upgrade discharge #32323 obtained for the plasma described in figure 1 [50]. With this approach we find parallel and perpendicular temperatures that are consistently higher than the deuterium temperature of 6 keV neoclassically determined by TRANSP based on the measured boron temperature. However, the values vary substantially in the range 7 keV to about 13 keV (depending on used data ranges) and either the parallel or perpendicular temperature of the fitted bi-Maxwellian is higher. This behavior is consistent with the difficulty of fitting a Maxwellian or bi-Maxwellian to a realistic total distribution function as these are not good models in this case (section 7). While this approach works very well using synthetic data and presumably also in bi-Maxwellian plasma, we do not obtain unique results in the strongly non-Maxwellian plasma in discharge #32323 investigated here.

8.2. Temperature and drift velocity measurements by velocity-space tomography

Our second new approach to measure bulk plasma parameters is to find the best fitting smooth velocity distribution function by velocity-space tomography based on the five spectra of D_α -light. In this approach no specific functional form of the ion velocity distribution function is assumed, such as a Maxwellian or bi-Maxwellian, which in turn makes regularization necessary to obtain useful solutions. In previous work velocity-space tomography has been restricted to analysis of D_α -light with large Doppler shifts, so-called fast-ion D_α -light (FIDA [65, 75]), and to the part of velocity space with energies larger than 15–20 keV. Here we include the thermal feature in the fit and infer the complete velocity distribution function of the deuterium population. The basic plasma parameters $n, v_{d,\parallel}, T_{\parallel}, T_{\perp}, p_{\parallel}$ and p_{\perp} can be calculated by taking appropriate zeroth to second moments of the resulting distribution function (section 4). Due to the non-linear nature of the problem (section 8.1), we calculate the solution iteratively. The minimization problem in iteration step i now becomes

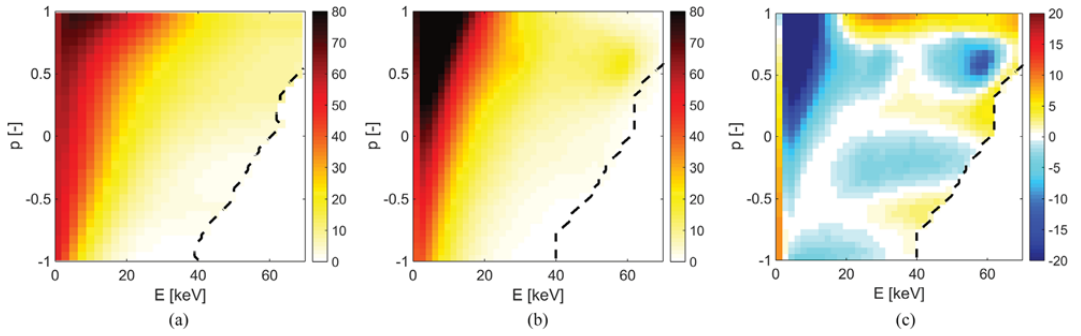


Figure 7. Comparison of a (a) measurement of $f(E, p)$ (10^{16} (keV m^3) $^{-1}$) by velocity-space tomography and a (b) TRANSP simulation for discharge #32323 at 1711 ms before a sawtooth crash in the plasma center. The simulation is the sum of a Maxwellian at 6 keV and the fast-ion velocity distribution function computed with NUBEAM. (c) Difference between (a) and (b).

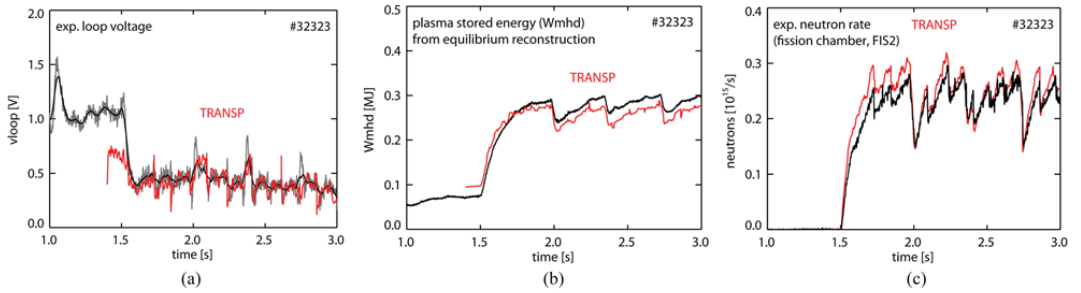


Figure 8. Comparison of the TRANSP simulation in 32323 and measurements. (a) Loop voltage. (b) Plasma stored energy. (c) Neutron rate.

$$\begin{aligned} & \text{minimize} \left\| \left(\begin{array}{c} W(F_{\text{biMax}}(n_{i-1}, v_{d||,i-1}, T_{||,i-1}, T_{\perp,i-1})) \\ \lambda L \end{array} \right) F_i \right\| \\ & - \left(\begin{array}{c} S \\ 0 \end{array} \right) \Bigg\|_2 \text{ subject to } F_i \geq 0 \end{aligned} \quad (37)$$

where the bi-Maxwellian parameters n_{i-1} , $v_{d||,i-1}$, $T_{||,i-1}$ and $T_{\perp,i-1}$ are found as the lowest moments of F_{i-1} according to section 4. The results are not sensitive to the start guess. L is a matrix operator effecting a numerical approximation to a gradient [58]. In this is so-called first-order Tikhonov regularization the parameter λ balances the requirements to fit the data and smoothness [50].

In figure 7, the measured total distribution function in discharge #32323 is compared with the corresponding TRANSP simulation, which is the sum of fast-ion and thermal contributions. The tomography problem was solved for energies to the left of the dashed line. The phase-space densities to the right of the dashed line are assumed to be small since no FIDA light above the noise level is observed in the part of the spectra probing only these velocity-space regions [50]. Overall, the measurement and the simulation are in excellent agreement. Figure 8 demonstrates that the simulated and measured loop voltages, the plasma stored energies, and the neutron rates also agree well, indicating that the TRANSP simulation is a good model for this discharge. The observed differences between

the tomographic inversion and the simulated ion distribution function in figure 7 partly originate from reconstruction uncertainties and could also partly originate from anomalous effects not caught in the TRANSP simulation.

However, the inference of the low-energy part of velocity space hampers the inference of the high-energy part of velocity space due to the much larger phase-space densities in the low-energy part. For example, the peaks at the NBI injection energies are not found whereas they are routinely found in fast-ion velocity-space tomography studies [50]. It will therefore still be advantageous to introduce a lower energy limit in velocity-space tomography studies that are focused on fast ions.

Our goal here is to calculate the lowest moments of the velocity distribution function (section 4). We find that the total density is $2.3 \times 10^{19} \text{ m}^{-3}$ which is comparable to the total density in TRANSP/NUBEAM ($2.6 \times 10^{19} \text{ m}^{-3}$). The measured drift velocity is 400 km s^{-1} and the measured temperatures are $T_{||} = 9 \text{ keV}$ and $T_{\perp} = 11 \text{ keV}$. The corresponding values obtained with TRANSP/NUBEAM when the simulated fast-ion distribution from NUBEAM is accounted for by computing the moments of the total ion distribution function (figure 1(c)) are $T_{||} = 8.3 \text{ keV}$, $T_{\perp} = 10.4 \text{ keV}$, $v_d = 400 \text{ km s}^{-1}$. The agreement between measurements and simulation accounting for fast-ions is excellent. The nominal TRANSP deuterium density ($2 \times 10^{19} \text{ m}^{-3}$), temperature (6 keV) and drift velocity (300 km s^{-1}) are not uniquely measurable quantities. The agreement corroborates our new

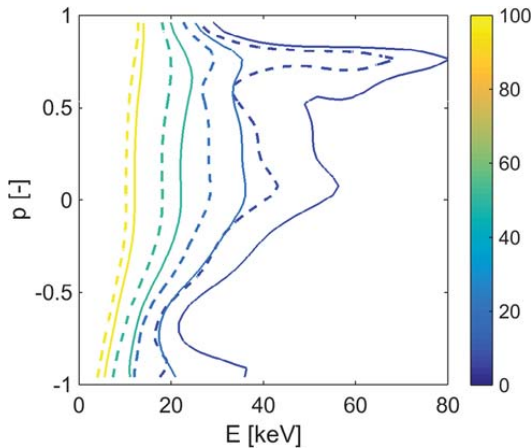


Figure 9. Comparison of measurements of $f(E, p)$ (10^{16} (keV m^3) $^{-1}$) in the plasma center without ICRF heating (dashed lines) and with ICRF heating (full lines) in discharge #33178.

approach to temperature measurements, and it suggests that the nominal temperatures given by TRANSP need to be regarded as lower bounds. We note that this discharge has a very high n_f/n_{th} . In more conventional discharges these differences are smaller according to figure 6.

As a second example of temperature measurements by velocity-space tomography, we study the impact of electromagnetic wave heating in the ion cyclotron range of frequencies (ICRF). Discharge #33178 was heated by NBI and ECRH at 5.5 s and by NBI, ECRH and 2nd harmonic ICRF heating at 7 s (figure 2). The plasma was at steady-state at both times. The core electron density was $6\text{--}7 \times 10^{19} \text{ m}^{-3}$ which is higher than in previous applications of velocity-space tomography. The inversions for both heating schemes are compared in figure 9. The ICRF heating populates the high-energy space such that the distribution function becomes broader. We find evidence for acceleration above the full NBI energy of 60 keV as expected for the 2nd harmonic ICRF heating scenario which accelerates fast ions from NBI. These results are consistent with recent measurements of the fast-ion velocity distribution function in a comparable plasma scenario [62]. The central boron temperature and the neoclassically computed central deuterium temperature according to TRANSP in the NBI-only phase were about 2.3 keV. In the ICRF-heating phase both temperatures are about 1 keV higher according to TRANSP.

From the inversion, we find deuterium temperatures of $T_{\parallel} = 5$ keV and $T_{\perp} = 6$ keV for the NBI-only phase. The ICRF heating increased both T_{\parallel} and T_{\perp} by 2 keV. We find no evidence for preferential heating in the perpendicular direction. The expected tail in the perpendicular direction is likely below the detection limit of FIDA, in particular at high energies exceeding about 150 keV. This is in contrast to the strong fast-ion tail in the perpendicular direction observed at JET above 150 keV [61, 76–78] as γ -ray and neutron emission spectroscopy used for the inversion are much more sensitive at very high energies [57, 69, 71, 72]. At ASDEX Upgrade

such an ICRF heating tail could not be detected by FIDA. Nevertheless, effects of the heating are observed. Fast ions above the critical energy heat preferentially the electrons which in turn quickly approach equilibrium and heat the ions without preferred direction as we observe. At JET, energies below 150 keV were not studied as the γ -ray measurements have little sensitivity at such energies.

Lastly, we note that a substantial fraction of the ICRF heating accelerates hydrogen [62]. H_{α} -light is therefore also detected by FIDA. According to calculations the hydrogen ions become strongly anisotropic with a long high-energy tail. However, this happens at energies outside the FIDA detection range [62]. As the hydrogen is an impurity species with low concentration, we here neglect the presence of hydrogen.

9. Conclusions

We propose two new approaches to measure deuterium densities, drift velocities and parallel and perpendicular temperatures. We further derive an expression for the projection of an arbitrarily drifting bi-Maxwellian distribution function onto the line-of-sight of ion diagnostics, e.g. a CER spectrometer. This projection suggests that measurements of any anisotropy are feasible if simultaneous measurements using different lines-of-sight are made. We measured five active spectra of Doppler-shifted D_{α} -light with the five-view FIDA system at ASDEX Upgrade usually used for fast-ion velocity-space tomography.

In our first approach, we fit a bi-Maxwellian to the five simultaneously acquired spectra to obtain the density, the parallel drift velocity and the parallel and perpendicular temperature. Whereas this approach should work well for plasmas that have a bi-Maxwellian distribution function, we demonstrate that it is less reliable in strongly heated, low-density plasmas in fusion devices due to the non-Maxwellian and non-bi-Maxwellian nature of the plasma.

In our second approach, the full velocity distribution function is measured using velocity-space tomography. Here the bulk plasma parameters are obtained as the lowest moments of the measured velocity distribution function. For a Maxwellian distribution these kinetic parameters reduce to the usual Maxwellian parameters. Firstly, we find that the kinetic temperatures are substantially higher than the usual thermal temperatures calculated from impurity temperatures using TRANSP. This is explained by the impact of fast ions. We stress that the kinetic temperatures are experimentally accessible parameters in any plasma whereas the nominal Maxwellian deuterium temperature according to TRANSP is not a uniquely measurable quantity in the presence of an even moderate fast ion population. Secondly, in a plasma heated by NBI at ASDEX Upgrade, we find substantial anisotropy in the plasma. The measured perpendicular temperature is $T_{\perp} = 11$ keV whereas the parallel temperature is $T_{\parallel} = 9$ keV. The measured boron temperature is 7 keV, and TRANSP determines the single deuterium temperature of 6 keV neoclassically from this boron measurement. However, the parallel and

perpendicular temperatures computed as second moments of the sum of the Maxwellian and the fast-ion population from NUBEAM give $T_{\perp} = 10.4$ keV and $T_{\parallel} = 8.3$ keV which are in excellent agreement with the measurement. Similarly, the measured parallel drift velocity of 400 km s^{-1} is in excellent agreement with TRANSP, if corrected for the impact of fast ions, whereas the nominal deuterium drift velocity computed with TRANSP without any fast-ion correction is 300 km s^{-1} . The measured boron drift velocity in the plasma center is 270 km s^{-1} . As second example, we studied an ICRF heated plasma. Any preferential heating due to ICRF could not be detected using D_{α} -based CER spectroscopy. ICRF elevated the measured parallel and perpendicular temperatures by similar amounts (2 keV).

Acknowledgments

We thank the ITPA energetic particle physics topical group for its support. This work has been carried out within the framework of the EUROfusion Consortium and has received funding from the Euratom research and training programme 2014–2018 under grant agreement No 633053. The views and opinions expressed herein do not necessarily reflect those of the European Commission.

ORCID iDs

M. Salewski  <https://orcid.org/0000-0002-3699-679X>

M. Nocente  <https://orcid.org/0000-0003-0170-5275>

References

- [1] Meyer H. *et al* 2017 *Nucl. Fusion* **57** 102014
- [2] Kallenbach A. *et al* 2017 *Nucl. Fusion* **57** 102015
- [3] Fonck R., Darrow D. and Jaehnig K. 1984 *Phys. Rev. A* **29** 3288–309
- [4] Isler R.C. 1994 *Plasma Phys. Control. Fusion* **36** 171–208
- [5] Stratton B. *et al* 1991 *Nucl. Fusion* **31** 171–5
- [6] Bell R. *et al* 1999 *Rev. Sci. Instrum.* **70** 821
- [7] von Hellerman M. *et al* 1993 *Plasma Phys. Control. Fusion* **35** 799–824
- [8] Bernardo J. *et al* 2016 *Rev. Sci. Instrum.* **87** 11E557
- [9] McDermott R. *et al* 2009 *Phys. Plasmas* **16** 056103
- [10] Pütterich T. *et al* 2012 *Nucl. Fusion* **52** 083013
- [11] Viezzer E. *et al* 2012 *Rev. Sci. Instrum.* **83** 103501
- [12] McDermott R.M. *et al* 2017 *Rev. Sci. Instrum.* **88** 073508
- [13] Bortolon A. *et al* 2013 *Nucl. Fusion* **53** 023002
- [14] Chrystal C. *et al* 2014 *Rev. Sci. Instrum.* **85** 11E302
- [15] Chrystal C. *et al* 2016 *Rev. Sci. Instrum.* **87** 11E512
- [16] Li Y.Y. *et al* 2014 *Rev. Sci. Instrum.* **85** 11E428
- [17] Li Y.Y. *et al* 2016 *Rev. Sci. Instrum.* **87** 11E501
- [18] Field A. *et al* 2009 *Plasma Phys. Control. Fusion* **51** 105002
- [19] Bell R. *et al* 2010 *Phys. Plasmas* **17** 082507
- [20] Brau K. *et al* 1983 *Nucl. Fusion* **23** 1643–55
- [21] Jing W. *et al* 2012 *Plasma Sci. Tech.* **14** 953
- [22] Klyuchnikov L. *et al* 2016 *Rev. Sci. Instrum.* **87** 053506
- [23] Koide Y. *et al* 2001 *Rev. Sci. Instrum.* **72** 119
- [24] Berezovskij E. *et al* 1985 *Nucl. Fusion* **25** 1495–8
- [25] Busche E., Euringer H. and Jaspers R. 1997 *Plasma Phys. Control. Fusion* **39** 1327–38
- [26] Svensson J. *et al* 2001 *Plasma Phys. Control. Fusion* **43** 389–403
- [27] Pütterich T., Wolfrum E., Dux R. and Maggi C. 2009 *Phys. Rev. Lett.* **102** 025001
- [28] Grierson B.A. *et al* 2010 *Rev. Sci. Instrum.* **81** 10D735
- [29] Grierson B.A. *et al* 2012 *Phys. Plasmas* **19** 056107
- [30] Grierson B.A. *et al* 2012 *Rev. Sci. Instrum.* **83** 10D529
- [31] Grierson B.A. *et al* 2013 *Nucl. Fusion* **53** 063010
- [32] Krukin V. *et al* 2013 *Plasma Phys. Rep.* **39** 632–43
- [33] Haskey S. *et al* 2016 *Rev. Sci. Instrum.* **87** 11E553
- [34] Haskey S. *et al* 2017 *J. Instrum.* **12** C10013
- [35] Wurden G. *et al* 1982 *Phys. Rev. A* **26** 2297–300
- [36] Behn R. *et al* 1989 *Phys. Rev. Lett.* **62** 2833–6
- [37] Suvorov E. *et al* 1995 *Plasma Phys. Control. Fusion* **37** 1207–13
- [38] Stejner M. *et al* 2012 *Plasma Phys. Control. Fusion* **54** 015008
- [39] Stejner M. *et al* 2013 *Plasma Phys. Control. Fusion* **55** 085002
- [40] Stejner M. *et al* 2015 *Plasma Phys. Control. Fusion* **57** 062001
- [41] Stejner M. *et al* 2017 *Plasma Phys. Control. Fusion* **59** 075009
- [42] Nishiura M. *et al* 2014 *Nucl. Fusion* **54** 023006
- [43] Abramovic I. *et al* 2017 *J. Instrum.* **12** C08015
- [44] Abramovic I. *et al* Forward modelling of collective thomson scattering for Wendelstein 7—X plasmas: electrostatic approximation (submitted)
- [45] Nocente M. *et al* 2015 *Nucl. Fusion* **55** 123009
- [46] Pankin A. *et al* 2004 *Comput. Phys. Commun.* **159** 157–84
- [47] Stroth U. *et al* 2013 *Nucl. Fusion* **53** 104003
- [48] Weiland M. *et al* 2016 *Plasma Phys. Control. Fusion* **58** 025012
- [49] Jacobsen A.S. *et al* 2016 *Plasma Phys. Control. Fusion* **58** 045016
- [50] Salewski M. *et al* 2016 *Nucl. Fusion* **56** 106024
- [51] Salewski M. *et al* Bayesian integrated data analysis of fast-ion measurements by velocity-space tomography *Fusion Sci. Tech.* accepted
- [52] Salewski M. *et al* 2011 *Nucl. Fusion* **51** 083014
- [53] Salewski M. *et al* 2012 *Nucl. Fusion* **52** 103008
- [54] Salewski M. *et al* 2013 *Nucl. Fusion* **53** 063019
- [55] Salewski M. *et al* 2014 *Nucl. Fusion* **54** 023005
- [56] Geiger B. *et al* 2015 *Nucl. Fusion* **55** 083001
- [57] Salewski M. *et al* 2015 *Plasma Phys. Control. Fusion* **57** 014021
- [58] Jacobsen A.S. *et al* 2016 *Plasma Phys. Control. Fusion* **58** 042002
- [59] Rasmussen J. *et al* 2016 *Nucl. Fusion* **56** 112014
- [60] Jaulmes F. *et al* 2016 *Nucl. Fusion* **56** 112012
- [61] Salewski M. *et al* 2017 *Nucl. Fusion* **57** 056001
- [62] Weiland M. *et al* 2017 *Nucl. Fusion* **57** 116058
- [63] Geiger B. *et al* 2017 *Plasma Phys. Control. Fusion* **59** 115002
- [64] Moseev D. *et al* Fast ion diagnostics in magnetically confined plasmas (submitted)
- [65] Heidbrink W.W. *et al* 2004 *Plasma Phys. Control. Fusion* **46** 1855–75
- [66] Salewski M. *et al* 2010 *Nucl. Fusion* **50** 035012
- [67] Salewski M. *et al* 2014 *Plasma Phys. Control. Fusion* **56** 105005
- [68] Heidbrink W.W. *et al* 2007 *Plasma Phys. Control. Fusion* **49** 1457–75
- [69] Jacobsen A.S. *et al* 2015 *Nucl. Fusion* **55** 053013
- [70] Salewski M. *et al* 2015 *Nucl. Fusion* **55** 093029
- [71] Salewski M. *et al* 2016 *Nucl. Fusion* **56** 046009
- [72] Jacobsen A.S. *et al* 2017 *Rev. Sci. Instrum.* **88** 073506
- [73] Heidbrink W.W. *et al* 2011 *Commun. Comput. Phys.* **10** 716–41
- [74] von Hellermann M. *et al* 1995 *Plasma Phys. Control. Fusion* **37** 71–94
- [75] Heidbrink W.W. 2010 *Rev. Sci. Instrum.* **81** 10D727
- [76] Litaudon X. *et al* 2017 *Nucl. Fusion* **57** 102001
- [77] Eriksson J. *et al* 2015 *Nucl. Fusion* **55** 123026
- [78] Schneider M. *et al* 2016 *Nucl. Fusion* **56** 112022

Reference [13]

[13]. M Salewski et al. (2018) *Fusion Science and Technology* **74**(1-2) 23-36. Bayesian integrated data analysis of fast-ion measurements by velocity-space tomography



Bayesian Integrated Data Analysis of Fast-Ion Measurements by Velocity-Space Tomography

M. Salewski,^{a*} M. Nocente,^{b,c} A. S. Jacobsen,^d F. Binda,^e C. Cazzaniga,^f J. Eriksson,^e B. Geiger,^d G. Gorini,^{b,c} C. Hellesen,^e V. G. Kiptily,^g T. Koskela,^{h,i} S. B. Korsholm,^a T. Kurki-Suonio,^h F. Leipold,^a D. Moseev,^j S. K. Nielsen,^a J. Rasmussen,^a P. A. Schneider,^d S. E. Sharapov,^g M. Stejner,^a M. Tardocchi,^c JET Contributors,[†] ASDEX Upgrade Team,[‡] and EUROfusion MST1 Team[§]

^aTechnical University of Denmark, Department of Physics, Kgs. Lyngby, Denmark

^bUniversity of Milano Bicocca, Department of Physics, Milano, Italy

^cIstituto di Fisica del Plasma, Consiglio Nazionale delle Ricerche, Milano, Italy

^dMax-Planck-Institut für Plasmaphysik, Garching, Germany

^eUppsala University, Department of Physics and Astronomy, Uppsala, Sweden

^fISIS Facility, Science and Technology Facilities Council, Rutherford Appleton Laboratory, Didcot, United Kingdom

^gCCFE, Culham Science Centre, Abingdon, Oxon, United Kingdom

^hAalto University, Department of Applied Physics, Aalto, Finland

ⁱNERSC, Lawrence Berkeley National Laboratory, Berkeley, California

^jMax-Planck-Institut für Plasmaphysik, Greifswald, Germany

Received July 5, 2017

Accepted for Publication August 22, 2017

Abstract — Bayesian integrated data analysis combines measurements from different diagnostics to jointly measure plasma parameters of interest such as temperatures, densities, and drift velocities. Integrated data analysis of fast-ion measurements has long been hampered by the complexity of the strongly non-Maxwellian fast-ion distribution functions. This has recently been overcome by velocity-space tomography. In this method two-dimensional images of the velocity distribution functions consisting of a few hundreds or thousands of pixels are reconstructed using the available fast-ion measurements. Here we present an overview and current status of this emerging technique at the ASDEX Upgrade tokamak and the JET tokamak based on fast-ion D-alpha spectroscopy, collective Thomson scattering, gamma-ray and neutron emission spectrometry, and neutral particle analyzers. We discuss Tikhonov regularization within the Bayesian framework. The implementation for different types of diagnostics as well as the uncertainties are discussed, and we highlight the importance of integrated data analysis of all available detectors.

Keywords — Tokamaks, fast ions, velocity-space tomography.

Note — Some figures may be in color only in the electronic version.

I. INTRODUCTION

Integrated data analysis refers to the combined analysis of measurements from several different

detectors or diagnostics to jointly infer parameters of interest.^{4,5} The inference of the plasma temperature, densities, or drift velocities by integrated data analysis relies on the assumption of Maxwellian distributions of the particles. However, the ion distributions in fusion plasmas are usually not in thermal equilibrium but are non-Maxwellian due to the intense plasma heating. For example, velocity distribution functions in plasmas heated by neutral beam injection (NBI) can have

*E-mail: msal@fysik.dtu.dk

[†]See Ref. 1.

[‡]See Ref. 2.

[§]See Ref. 3.

peaks due to energetic ion sources at full, half, and one-third NBI energy at a pitch determined by the geometry. The pitch is defined as $p = v_{\parallel}/v$ where v_{\parallel} is the velocity component parallel to the magnetic field and v is the velocity magnitude. Electromagnetic wave heating in the ion cyclotron range of frequencies (ICRF) causes anisotropy because ICRF heating increases the velocity components perpendicular to the magnetic field, often into the mega-electron-volt range. Early modelling assumed bi-Maxwellian distribution functions with different temperatures parallel and perpendicular to the magnetic field, but modern ICRF codes predict features that are not well described by bi-Maxwellians in many heating scenarios. For example, a cut-off energy of the velocity distribution function is predicted in deuterium ICRF heating at the third harmonic.⁶ It would often be an oversimplification to model such velocity distribution functions by analytic formulas. The lack of simple models has hampered integrated data analysis of fast-ion measurements in the past.

Integrated data analysis of fast-ion measurements from at least two detectors has recently become possible by velocity-space tomography.^{7–20} The fast-ion velocity distribution function is described by a two-dimensional (2-D) image consisting of a few hundreds or thousands of pixels. The amplitudes in these pixels are then determined by the available measurement data and any prior information one might have by a regularized least-squares fit.

Experimentally, the method was introduced based on Axially Symmetric Divertor Experiment (ASDEX) Upgrade²¹ data first using three simultaneously measured spectra from fast-ion D_{α} (FIDA) spectroscopy in three different views observing the plasma center.^{10,11} Now four to five simultaneously measured FIDA spectra are routinely used.^{12–19} NBI (Refs. 10–18) as well as ICRF heated plasmas¹⁹ have been studied, including sawtooth plasmas^{12–18} and NBI startup scenarios.¹⁸ The first movies of fast-ion velocity distribution functions at ASDEX Upgrade have been presented.¹⁸ Integrated data analysis by combining different fast-ion diagnostics⁹ has been experimentally demonstrated for FIDA and collective Thomson scattering (CTS) measurements at ASDEX Upgrade^{15,17} and very recently for gamma-ray spectrometry (GRS) and neutron emission spectrometry (NES) at the Joint European Torus (JET) (Refs. 3 and 20).

This paper is organized as follows. In Sec. II we describe the velocity-space tomography method using Tikhonov regularization with prior information, and in Sec. III this approach is related to the Bayesian

framework. In Sec. IV we discuss so-called weight functions, which are analogous to lines of sight in position-space tomography, of the most common fast-ion diagnostics. Section V deals with uncertainties. Section VI highlights the importance of integrated data analysis of the available measurements. An outlook is presented in Sec. VII, and Sec. VIII concludes the paper.

II. HIGH-DEFINITION VELOCITY-SPACE TOMOGRAPHY

In analogy to position-space tomography, the forward model to compute synthetic fast-ion measurements from a fast-ion velocity distribution function is cast as the matrix in Eq. (1) (Ref. 8):

$$\tilde{S} = \tilde{W}F, \quad (1)$$

where F is the fast-ion velocity distribution function written as a vector, \tilde{S} contains the measurements written as another vector, and \tilde{W} is a matrix holding the forward model. The calculation of \tilde{W} is discussed in Sec. IV. To take measurement uncertainty $\tilde{\sigma}_s$ into account, each entry in \tilde{S} is normalized with its associated uncertainty, and so is the corresponding line in \tilde{W} (Ref. 9). Hence we obtain the normalized matrix in Eq. (2),

$$S = WF, \quad (2)$$

in the normalized quantities S and W . The tomography problem now is to find a stable and useful solution for F , given S and W . As the signal-to-noise ratio S is on the same order of magnitude for most diagnostics, whereas the measured signal \tilde{S} can differ by orders of magnitude depending on the units, the normalization by $\tilde{\sigma}_s$ substantially improves the conditioning of the tomography problem and allows integrated data analysis of measurements from different diagnostics.

Equation (2) has no exact solution due to noise in the measurements, and hence we instead seek to find a best estimate. However, as in most tomography problems, it turns out that W is ill-conditioned so that small changes in S result in large changes in F in a standard least-squares fit. The measurement noise therefore generates random jitter in the inversion and no stable inversion can be found. To date velocity-space tomography has relied on standard inversion methods: truncated singular value decomposition, the maximum entropy method, and a few variants of the Tikhonov regularization.^{10–12,14,18} We here

discuss Tikhonov's regularization method and solve the minimization problem

$$F^* = \arg \min_F \left\| \begin{pmatrix} W \\ \lambda L \end{pmatrix} F - \begin{pmatrix} S \\ 0 \end{pmatrix} \right\|_2 \text{ subject to } F^* \geq 0, \quad (3)$$

where we also demand the solution to be nonnegative.¹⁸ The upper row minimizes the two-norm of the residual of Eq. (2). Tikhonov's formulation adds the lower row to the least-squares fit which penalizes large values of the two-norm of λLF . L is a matrix representing an operator on F such that LF quantifies an undesired property of the solution. If L is the identity matrix, λLF penalizes large amplitudes of F . If L is a numerical gradient operator, λLF penalizes large gradients and hence seeks out smooth solutions. The regularization parameter λ balances the goodness-of-fit and the regularization requirements and must be found as part of the solution.

Compared with many other tomography applications, the amount of measured fast-ion diagnostic data is small due to the limited optical access to the plasma and the often comparatively low signal-to-noise ratio. Therefore, inversions often have so-called artifacts which are spurious features of the inversion. Artifacts can be reduced by installing additional fast-ion diagnostics^{8,14} and by optimizing the discharges for signal-to-noise ratio. For example, FIDA works very well in L-mode plasmas with low density and few impurities.^{10,12-14}

High-definition tomography techniques additionally make use of prior information to remedy artifacts and to improve the inversions.¹⁸ Besides the usual demand on smoothness, cogent prior information is the nonnegativity of the velocity distribution function, the measured absence of evidence for fast ions within the detection limit, and the position of the injection sources in velocity space for NBI scenarios. Further, a numerical simulation can be used as prior knowledge of the velocity distribution function. With these types of prior information, Eq. (3) is written in extended form as¹⁸

$$F^* = \arg \min_F \left\| \begin{pmatrix} W \\ \lambda \kappa L \end{pmatrix} F - \begin{pmatrix} S \\ \lambda \kappa L F_{sim} \end{pmatrix} \right\|_2$$

$$\text{subject to } \begin{cases} F^* \geq 0 \\ F^*(v_{\parallel 0}, v_{\perp 0}) = 0 \end{cases}, \quad (4)$$

where $\kappa = \kappa(v_{\parallel}, v_{\perp})$ encodes the velocity-space positions of the particle sources of the NBI at the full, half, and one-third NBI injection energies, $F^*(v_{\parallel 0}, v_{\perp 0}) = 0$ is the

velocity-space region with negligible fast-ion densities according to null measurements, and F_{sim} is a numerical simulation used as prior information. These high-definition tomography techniques improved results for the five-view FIDA diagnostic at the tokamak ASDEX Upgrade and further allow the use of inversion techniques for more common FIDA systems with two or three views. The nonnegativity constraint is also essential for tomographic inversion at JET (Ref. 20).

III. BAYESIAN FRAMEWORK FOR VELOCITY-SPACE TOMOGRAPHY WITH TIKHONOV REGULARIZATION

This section justifies the velocity-space tomography formalism using Tikhonov regularization in the Bayesian picture and clarifies the connection between the regularization and the prior information. Bayes' theorem links the posterior distribution function with the likelihood function and the prior distribution function:

$$\text{prob}(F|S) = \frac{\text{prob}(S|F) \times \text{prob}(F)}{\text{prob}(S)}, \quad (5)$$

where

posterior $\text{prob}(F|S)$ = probability of the amplitudes of the pixel values describing the distribution function, given the normalized data

prior $\text{prob}(F)$ = probability of the distribution function before considering the normalized data

likelihood function $\text{prob}(S|F)$ = probability of the normalized data, given the distribution function

$\text{prob}(S)$ = probability of the normalized data, often called the evidence.

Using the forward model, we can assign probabilities to the likelihood function:

$$\text{prob}(S|F) \propto \exp\left(-\frac{1}{2}\left(\tilde{W}F - \tilde{S}\right)^T \tilde{\Sigma}_S \left(\tilde{W}F - \tilde{S}\right)\right), \quad (6)$$

where $\tilde{\Sigma}_S$ is the covariance matrix for the data \tilde{S} . Assuming the noise to be independent and normally distributed, the likelihood function reduces to

$$\text{prob}(S|F) \propto \exp\left(-\frac{1}{2}\left\|\tilde{W}F - \tilde{S}\right\|_2^2\right). \quad (7)$$

Recall that W and S are normalized by the uncertainties. We further assume the prior distribution to be a multivariate Gaussian:

$$\text{prob}(F) \propto \exp\left(-\frac{1}{2}(F - F_0)^T C^{-1}(F - F_0)\right), \quad (8)$$

where F_0 is the estimate of the velocity distribution function before considering the data and C is the covariance matrix for F_0 . If a numerical simulation F_{sim} is available, we may set $F_0 = F_{sim}$. Since the covariance matrix is positive semidefinite, so is its inverse C^{-1} . Hence we can introduce the symmetric decomposition

$$C^{-1} = \lambda^2 L^T L, \quad (9)$$

where λ^2 is a positive free parameter setting a width-scaling for the multivariate Gaussian. The inverse of the covariance matrix C^{-1} is often called the Fisher information matrix. Equation (9) allows us to write Eq. (8) as

$$\text{prob}(F) \propto \exp\left(-\frac{1}{2}\lambda^2\left\|L(F - F_0)\right\|_2^2\right). \quad (10)$$

According to Bayes' theorem [Eq. (5)], the posterior becomes

$$\text{prob}(F|S) \propto \exp\left(-\frac{1}{2}\left\|\tilde{W}F - \tilde{S}\right\|_2^2 - \frac{1}{2}\lambda^2\left\|L(F - F_0)\right\|_2^2\right), \quad (11)$$

where we dropped the evidence term since it just scales the results which does not change the proportionality relation. Maximizing the posterior probability is equivalent to solving the minimization problem:

$$\text{minimize} \left(\left\|\tilde{W}F - \tilde{S}\right\|_2^2 + \lambda^2\left\|L(F - F_0)\right\|_2^2 \right). \quad (12)$$

We prefer the equivalent formulation as

$$\text{minimize} \left\| \begin{pmatrix} W \\ \lambda L \end{pmatrix} F - \begin{pmatrix} S \\ \lambda L F_0 \end{pmatrix} \right\|_2, \quad (13)$$

as it is a stable and convenient form for numeric computation. We have hence recovered the Tikhonov problem from the Bayesian formulation. Equation (9) shows how to obtain a Fisher information matrix or its inverse, the covariance matrix C , from the penalty matrix L in Tikhonov's problem. Conversely, given C , we can find L to within a factor λ by symmetric matrix decomposition. Perhaps the simplest example is the zeroth-order Tikhonov problem where L is the identity matrix. Then C is a diagonal matrix with $1/\lambda^2$ on the diagonal, so that the entries in F are uncorrelated. For first-order or higher-order Tikhonov regularization, we can likewise use Eq. (9) to calculate C . The detailed mathematical form of C depends on how the penalizing derivative is implemented as finite differences.

The complete Bayesian prior corresponding to the Tikhonov problem in Eq. (4) is

$$\begin{aligned} \text{prob}(F) &\propto \exp\left(-\frac{1}{2}\lambda^2(F - F_0)^T (\kappa L)^T (\kappa L)(F - F_0)\right) \\ &\text{subject to} \quad \begin{cases} F^* \geq 0 \\ F^*(v_{\parallel 0}, v_{\perp 0}) = 0 \end{cases} \end{aligned} \quad (14)$$

IV. WEIGHT FUNCTIONS

Weight functions enter the rows of the matrix \tilde{W} in Eq. (1) and are analogous to lines of sight in standard position-space tomography. They quantify how much signal per ion is measured and are hence a convenient formulation of the forward model for velocity-space tomography. The phase space is described by the velocity coordinates $(v_{\parallel}, v_{\perp})$ or (E, p) and the position coordinates \mathbf{x} . $(v_{\parallel}, v_{\perp})$ are the velocities parallel and perpendicular to the magnetic field, and (E, p) are the energy and pitch of the particle, respectively. Here pitch is defined as $p = \frac{v_{\parallel}}{v}$, where v is the magnitude of the ion velocity. The measurable signal s can be found by integration of the weight function w times the fast-ion velocity distribution function f over phase space^{7,22–28}:

$$\begin{aligned} s(m_1, m_2, \phi) &= \int_{vol} \int_0^{\infty} \int_{-\infty}^{\infty} w(m_1, m_2, \phi, v_{\parallel}, v_{\perp}, \mathbf{x}) \\ &\quad \times f(v_{\parallel}, v_{\perp}, \mathbf{x}) dv_{\parallel} dv_{\perp} d\mathbf{x}, \end{aligned} \quad (15)$$

where $s(m_1, m_2, \phi)$ is the integrated measured signal in the interval $m_1 < m < m_2$ where ϕ is the angle between the line of sight and the magnetic field, and m represents the units on the abscissa of the fast-ion measurements, e.g., the energy in GRS measurements or the wavelength in FIDA measurements. The units of the integrated measured signal depend on the diagnostic units. The units of f in Eq. (15) are seconds squared divided by meters to the fifth (s^2/m^5). The weight functions thus show the signal per fast ion as a function of the velocity coordinates in units (signal/fast ion). They can be calculated using a forward model of a given fast-ion diagnostic. One defines a phase-space distribution function consisting of a single pixel and computes the signal as a function of the phase-space coordinates of the pixel. Formally, we can substitute a δ function describing the position of N_f fast ions,

$$f_\delta(v_{\parallel}, v_{\perp}, \mathbf{x}) = N_f \delta(v_{\parallel} - v_{\parallel 0}) \delta(v_{\perp} - v_{\perp 0}) \delta(\mathbf{x} - \mathbf{x}_0), \quad (16)$$

into Eq. (15) and effect the integration. The amplitudes of weight functions at phase-space position $(x_0, v_{\parallel 0}, v_{\perp 0})$ are then

$$w(m_1, m_2, \phi, v_{\parallel 0}, v_{\perp 0}, \mathbf{x}_0) = \frac{s(m_1, m_2, \phi)}{N_f}. \quad (17)$$

The weight functions computed with this formalism account for any physics included in the forward model. However, they neglect any spatial variations within the measurement volume. Further, the weight functions do not account for any background noise which will therefore need to be subtracted, e.g., passive FIDA light. Uncertainties of this type are discussed in Sec. V.

Equation (17) does not provide any insight into the peculiar shapes of the weight functions for each diagnostic. Examples of weight functions for FIDA, CTS, a neutral particle analyzer (NPA), NES, and GRS are presented in Figs. 1 through 6. The basic shapes of the weight functions are explained for each diagnostic by considering the underlying physics processes.^{7,24–27}

The FIDA weight functions²⁴ in Fig. 1 illustrate the excellent coverage of velocity space by the five-view FIDA diagnostic installed at ASDEX Upgrade when the measurements are analyzed together.^{10,14} Each FIDA view individually misses a portion of velocity space, but integrated data analysis of all five detectors together provides excellent coverage of 2-D velocity space allowing the measurement of velocity distribution functions. Nevertheless, the integrated data analysis can further be

improved by adding additional diagnostics. In particular, the velocity-space sensitivity of FIDA drops above the beam injection energy because the charge-exchange probabilities of very highly energetic particles with beam neutrals drop for increasing particle energy. Therefore, the measurements of the high-energy velocity space could likely be substantially improved by adding CTS and NES diagnostics to the FIDA tomography.

Figure 2 illustrates typical CTS weight functions for observation perpendicular to the magnetic field.⁷ If the geometry of CTS experiments is flexible (as often), the weight functions can take very different shapes similar to the FIDA weight functions. The overall shapes of CTS weight functions are similar to those of FIDA weight functions because both are largely determined by the Doppler shift.

Figure 3 shows weight functions for the NPA at ASDEX Upgrade. NPAs measure the energies of fast neutrals generated in charge-exchange reactions between fast ions and neutrals. The measured energy of the neutral in the detector is the same as that of the fast ion in the plasma. Ions in very small pitch and gyroangle ranges can generate a detectable neutral which is reflected in the narrow pitch range of the weight function. The width of the energy interval is the same as the chosen energy bin width in the measurement. NPA weight functions have not yet been used in velocity-space tomography.

Figure 4 illustrates typical weight functions for the time-of-flight neutron emission spectrometer TOFOR at JET (Refs. 25 and 28). The line-of-sight of TOFOR is approximately perpendicular to the central magnetic field at JET (Ref. 29). The weight functions are calculated for the $D(D,n)^3\text{He}$ reaction. The mega-electron-volt-range ions are well diagnosed by TOFOR or other NES instruments in contrast to FIDA. The low time-of-flight signals in TOFOR are not sensitive to high-energy ions with pitches close to ± 1 (Fig. 4). However, NES detectors installed on oblique lines of sight can be sensitive to either $p \sim 1$ or $p \sim -1$.

Figure 5 shows typical weight functions for two-step reaction GRS with a HpGe detector,²⁶ here for the ${}^9\text{Be}(D,n\gamma){}^{10}\text{B}$ reaction. An interesting feature is that at low Doppler-shift the HpGe detector is most sensitive to high-energy ions with pitches close to ± 1 . However, at high Doppler-shift these regions do not contribute any signal whereas the ions with pitches close to 0 contribute the most signal. The velocity-space sensitivities of the NES and GRS detectors at JET (similar to Fig. 1 for FIDA) have been presented elsewhere.^{20,28}

Last, Fig. 6 illustrates typical weight functions for one-step reaction GRS, here for the reaction $D(p,\gamma)^3\text{He}$ (Refs. 27 and 30). The ITER measurement requirements entail resolution of the energy spectra and densities of

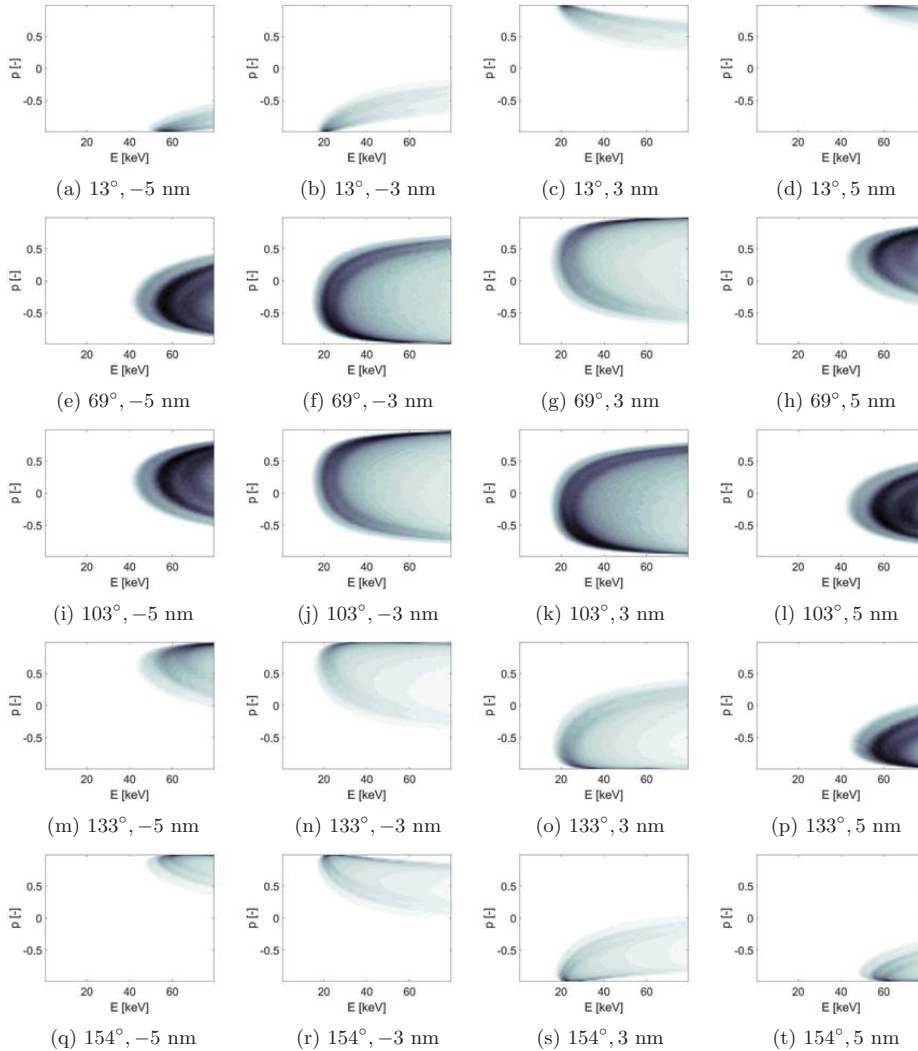


Fig. 1. Typical weight functions (a.u.) for the five FIDA spectra for five different viewing angles for strong and moderate blueshifts (first and second columns) and redshifts (third and fourth columns). The angles describe the angle between the line of sight of the view and the local magnetic field. The wavelengths are relative to the unshifted D_α radiation wavelength of 656.1 nm.

fusion alphas and other fast ions.³¹ Figure 6 illustrates that one-step reaction GRS could in principle provide direct energy resolution of the fast ions without the need for tomographic inversion,²⁷ similar to the NPAs. The other fast-ion diagnostics have weight functions covering very broad energy ranges hampering a direct energy resolution of the individual diagnostics in principle. Tomographic inversion of all available fast-ion measurements at ITER is currently the only known way to

obtain measurements of the alpha-particle energy spectra and other fast-ion energy spectra to fulfill the ITER measurement requirements.³¹

V. UNCERTAINTIES

The uncertainties of velocity-space tomography are conceptually the same as for standard position-space

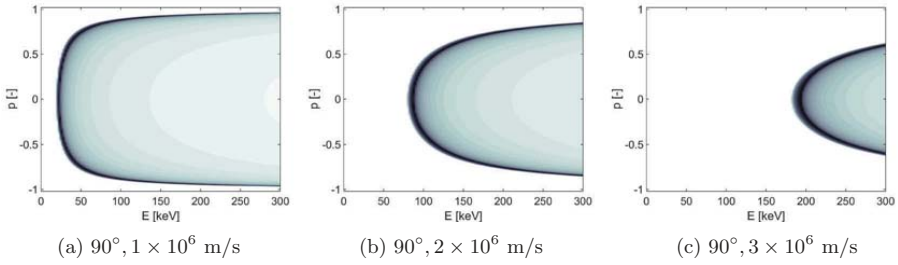


Fig. 2. Typical CTS weight functions (a.u.) for a viewing angle of 90 deg for three projected velocities.

tomography which is unfortunately not straightforward. We may divide the uncertainties into three main categories:

1. uncertainties in the fast-ion measurements S (Ref. 9)
2. uncertainties in the weight matrix W due to uncertainties in nuisance parameters¹²
3. bias uncertainties due to the regularization.¹²

The nature of the uncertainties in the fast-ion measurements depends on the diagnostic. Usually apparently random fluctuations in the signal (so-called noise) are one contribution to the uncertainty. There can also be systematic uncertainties. An example is the passive FIDA light originating from the plasma edge rather than from the measurement volume. The passive FIDA light can be subtracted by beam modulation or passive lines of sight.²³ Whereas uncertainties due to measurement noise are controlled to be small in tomography, any systematic measurement error such as in the background subtraction will propagate into the inversion. Discussions of uncertainties for various fast-ion diagnostics are found in a recent review.³² Uncertainties in the nuisance parameters cover the uncertainties in other parameters needed in the forward model. For example, often the densities and

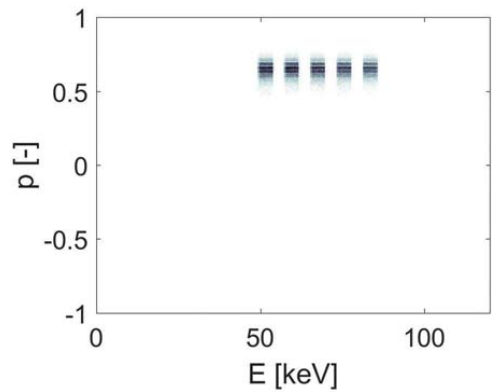


Fig. 3. Typical NPA weight functions (a.u.) for the NPA at ASDEX Upgrade for five different energy ranges of the observed neutrals which are identical to the energy ranges of the fast ions: 50 to 54 keV, 58 to 62 keV, 66 to 70 keV, 74 to 78 keV, and 82 to 86 keV. Only narrow pitch and gyroangle ranges are accepted by the instrument.

temperatures of ions or electrons influence the amplitude of the measured fast-ion signals. Such parameters and their uncertainties are usually measured by other

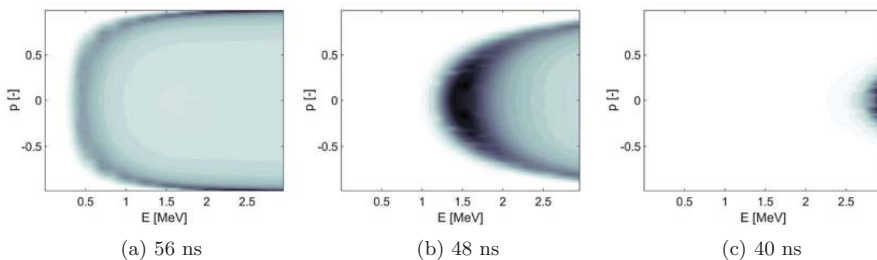


Fig. 4. Typical weight functions (a.u.) for TOFOR for three times of flight.

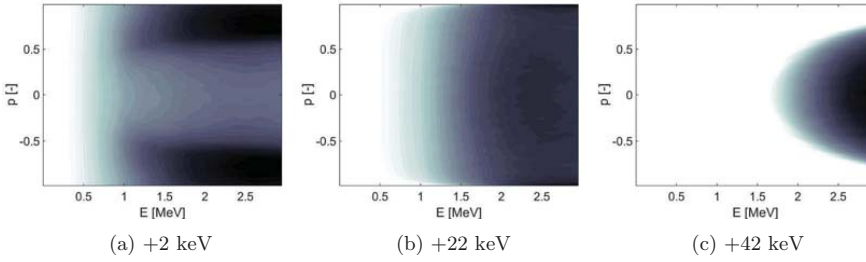


Fig. 5. Typical weight functions (a.u.) for two-step reaction gamma-ray spectrometry using a high-purity Germanium detector resolving the nominal peak energy of 2868 keV. The shifts in (a) to (c) are relative to the nominal peak energy.

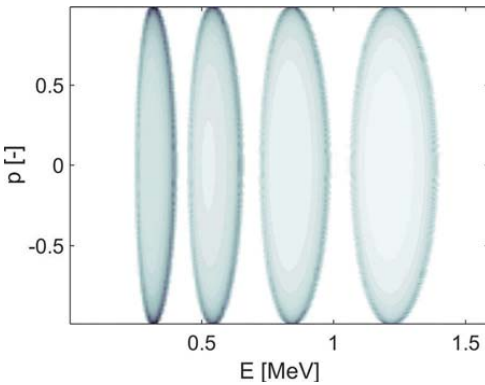


Fig. 6. Typical weight functions (a.u.) for one-step reaction gamma-ray spectrometry using a high-purity Germanium detector resolving the nominal peak energy of 5500 keV. From left to right relative to the nominal peak energy: +200 keV, +350 keV, +550 keV, and +800 keV.

diagnostics. Last, the bias uncertainties cover systematic errors introduced by the regularization which is needed to obtain stable solutions to the tomography problem.

Equation (3) shows that the solution in F depends on the regularization parameter λ , and so do the uncertainties. For very small λ , the lower part of Eq. (3) becomes negligible, and one approaches the original least-squares problem. Even though the fit to the measurement data is very good, the solution is unstable and is completely dominated by measurement noise. The bias due to the regularization is in this case small. For very large λ , the upper part of Eq. (3) becomes negligible and one approaches a very smooth function, but the fit to the measurement data is poor. In this case the uncertainty due to measurement noise is small, but the bias due to regularization is large. A trade-off must be made in the choice of λ to balance the propagation of measurement noise into the inversion against systematic bias

introduced by the regularization itself. Various strategies to choose λ automatically exist, such as the L-curve¹² or generalized cross validation.¹⁸ Assuming that we have chosen λ or choose it automatically, we can quantify the uncertainties in the inversion due to uncertainties in the fast-ion measurements and due to uncertainties in the nuisance parameters. We sample the fast-ion measurements and nuisance parameters from their probability distribution functions and compute a population of inversions:

$$F_i^* = \arg \min_F \left\| \begin{pmatrix} W_i \\ \lambda L \end{pmatrix} F - \begin{pmatrix} S_i \\ 0 \end{pmatrix} \right\|_2 \text{ subject to } F \geq 0.$$

The mean of the N inversions is the best estimate of the velocity-distribution function

$$\langle F^* \rangle = \frac{1}{N} \sum_i F_i^*, \quad (18)$$

and the uncertainty of the inversion is the corresponding standard deviation

$$\delta F^* = \sqrt{\frac{1}{N-1} \sum_i (F_i - \langle F^* \rangle)^2}, \quad (19)$$

which accounts for uncertainties in the signal and the nuisance parameters.

Each pixel of the inversion has its own uncertainty so that we can assess which parts of velocity space can be reliably inferred.^{12,15} If required, we can assess the individual contributions of the measurement noise and the nuisance parameter uncertainty by fixing the other value. The quantification of the systematic regularization bias is an open problem because we would need to know the true distribution function. If it was known, we could substitute and find the regularization bias according to

$$\delta F_{bias} = \arg \min_F \left\| \begin{pmatrix} W \\ \lambda L \end{pmatrix} F - \begin{pmatrix} WF_{true} \\ 0 \end{pmatrix} \right\|_2 - F_{true}$$

subject to $F \geq 0$.

(20)

One may use a numerical simulation or the tomographic inversion to estimate the bias uncertainty.¹²

VI. RECONSTRUCTIONS OF A PHANTOM USING INTEGRATED DATA ANALYSIS

In this section we demonstrate the benefits of integrated data analysis of all available fast-ion measurements at JET. JET discharge #86459 was heated by 4.5-MW NBI and 3-MW ICRF heating at the third harmonic of deuterium.³³ In this scenario a strong fast-ion tail is accelerated above the NBI injection energies of 120 keV. Deuterium ions are accelerated up to energies of about 2 MeV until they encounter the so-called barrier region in velocity space where the coupling between the wave electric field and the ions becomes very weak.⁶ Therefore

only small populations at energies above about 2 MeV are expected. This is shown in the ASCOT simulation in Fig. 7a where the tail terminates at about 2 MeV. The simulation also shows that the tail becomes broader toward lower energies due to collisions. A corresponding tomographic inversion of NES and GRS measurements was in excellent agreement with the simulation.²⁰

In Fig. 7 we demonstrate the importance of integrated data analysis to achieve this result. The three inversions in Figs. 7b, 7c, and 7d are computed using first-order Tikhonov regularization with nonnegativity constraint according to Eq. (3). Figure 7b shows an inversion from noisy, synthetic measurements using all available detectors based on the simulation in Fig. 7a. The detectors are one HpGe GRS detector^{34,35} and three NES detectors: the time-of-flight spectrometer TOFOR (Refs. 29, 36, 37) the liquid scintillator,³⁸ and the single crystal–diamond detector.^{39–41} If the NES and GRS measurements are combined (Fig. 7b), the shape of the fast-ion tail is in excellent agreement with the simulation as also the inversion of actual measurements showed.¹⁷

In Fig. 7c we use only the three NES detectors. We have not been able to obtain inversions resembling the

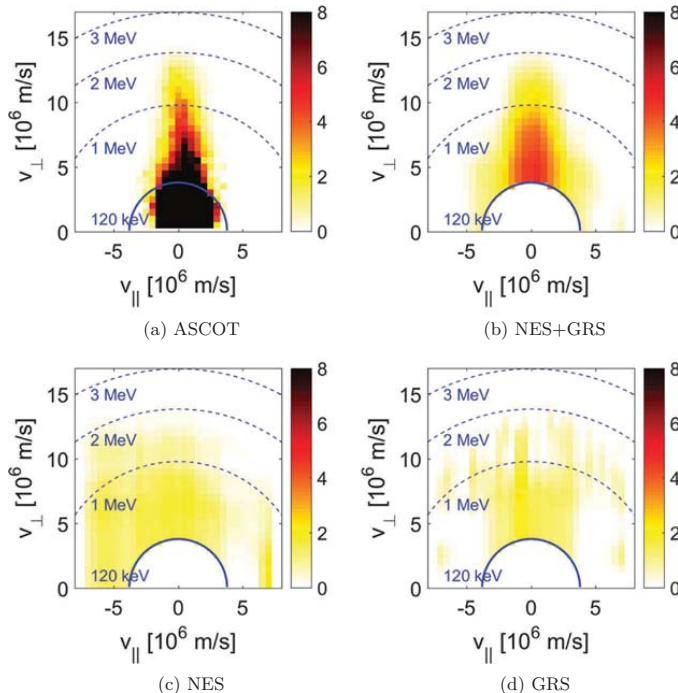


Fig. 7. (a) Simulation. Inversions based on noisy synthetic measurements from the ASCOT simulation: (b) NES and GRS measurements, (c) only NES measurements, and (d) only GRS measurements.

known solution from Fig. 7a for this case. A likely reason is that two of the three NES detectors are on an oblique line of sight. Detectors on this oblique line of sight cover only positive parallel velocities.^{20,25,28} The half-plane with positive parallel velocities is therefore well covered by three sets of weight functions. However, the half-plane with negative parallel velocities is only covered by the weight functions from TOFOR, i.e., by just one view, which is not enough for inversion.

The GRS instrument observes two gamma-ray reaction peaks in high resolution, such that two sets of weight functions and independent measurements are available. These two sets cover the entire velocity space.^{20,26} Roughly, it is possible to localize the position of the tail, but the tail shape cannot be recovered (Fig. 7d).

While TOFOR is the workhorse of this integrated data analysis, it is noteworthy that the 2-D inversion at JET is not successful without the gamma-ray measurements. With TOFOR and the HpGe detector, most of the velocity space shown in Fig. 7b is covered by three sets of weight functions. We conclude that an essential ingredient for the velocity-space tomography method to work is that the relevant parts of velocity space are covered by more than one set of weight functions. Apparently the two sets of weight functions available from the HpGe detector are not sufficient, either.

Currently a second set of GRS instruments is being installed at JET which will have an oblique view ($\phi = 30$ deg). In Fig. 8 we show an inversion based on four GRS spectra observed with two HpGe detectors

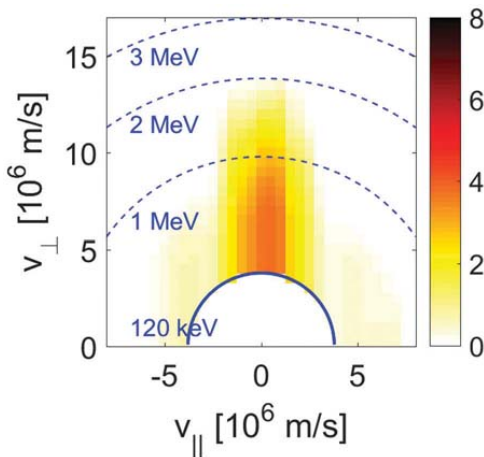


Fig. 8. Inversions based on noisy synthetic measurements from the ASCOT simulation. Here two simultaneous GRS measurements were assumed: $\phi_1 = 90$ deg and $\phi_2 = 30$ deg.

whereas the NES detectors are not used. This type of all-GRS inversion is relevant for alpha-particle diagnostic in the upcoming deuterium-tritium campaign as fast alpha particles do not produce neutrons directly. The reconstruction of the ASCOT simulation based on the noisy synthetic measurements (Fig. 8) is much improved compared with the single GRS detector measurements (Fig. 7d).

VII. OUTLOOK

A near-term goal of velocity-space tomography at JET and ASDEX Upgrade is to include further detectors in the integrated data analysis. The ASDEX Upgrade has up to six FIDA views,^{13,42,43} two CTS views,^{44–46} one NES view,^{47,48} one GRS view,⁴⁹ and one NPA (Ref. 50), as well as five fast-ion loss detectors.^{51,52} Until now only five detectors have been used in the integrated data analysis. At JET, further detectors should become available in the near future to allow measurements in the upcoming deuterium-tritium campaign.^{1,20,53} In particular, an oblique GRS view and an upgraded gamma-ray camera could contribute significantly to the integrated data analysis.

Integrated data analysis based on high-definition velocity-space tomography should now be demonstrated on other machines than ASDEX Upgrade and JET. Good candidates are machines with FIDA views and additional diagnostics, such as DIII-D (Refs. 54 and 55), EAST (Refs. 56, 57, and 58), TCV (Ref. 59), NSTX (Ref. 60), MAST (Refs. 61 and 62), or LHD (Refs. 63 through 66).

An important long-term goal is to measure alpha-particle 2-D velocity distribution functions at ITER. This would allow us to measure the alpha-particle density and the alpha-particle energy spectrum which are part of the ITER measurement requirements.³¹ The core-averaged values of these parameters can be measured by integration of the measured 2-D velocity-distribution function, if at least one diagnostic is absolutely calibrated. The alpha particles at ITER can be directly measured by CTS (Refs. 67, 68, and 69), GRS (Refs. 70 and 71), and possibly charge-exchange recombination spectroscopy.⁷² CTS measurements at ITER are being designed to be absolutely calibrated. ITER is also going to be equipped with NES (Ref. 31). Deuterium and tritium 2-D velocity distribution functions, as well as the derived fast-ion density and energy spectra, could also be determined by velocity-space tomography in ITER by CTS, NES, and GRS. The various combinations of fast-ion diagnostics on the various machines provide a rich test bed to develop the velocity-space tomography method for ITER.

VIII. CONCLUSIONS

We presented an overview and current status of velocity-space tomography as an integrated data analysis tool for fast-ion measurements. As an example of an inversion method, we discussed the Tikhonov regularization and how to use various forms of prior information in the Bayesian framework. Further, we discussed weight functions and uncertainties in the inversions. The recent combined inversion of GRS and NES at JET highlights the need for integrated data analysis. Useful inversions could only be obtained by combined measurements of NES and GRS, not from NES or GRS alone. NES-only or GRS-only inversions do not even work well using synthetic data which are substantially easier than using experimental data. However, if another HpGe GRS detector with an oblique line of sight becomes available at JET, it could be possible to base inversions on GRS data alone. Integrated data analysis of all available fast-ion measurements by tomographic inversion appears to be a promising route to fulfil the ITER measurement requirements on the densities and energy spectra of alpha particles and other fast ions.

Acknowledgements

We thank the ITPA Energetic Particle Physics Topical Group for its support. This work has been carried out within the framework of the EUROfusion Consortium and has received funding from the Euratom research and training programme 2014 through 2018 under grant agreement 633053. The views and opinions expressed herein do not necessarily reflect those of the European Commission.

References

1. X. LITAUDON et al., “Overview of the JET Results in Support to ITER,” *Nucl. Fusion*, **57**, 102001 (2017); <https://doi.org/10.1088/1741-4326/aa5e28>.
2. A. KALLENBACH et al., “Overview of ASDEX Upgrade Results,” *Nucl. Fusion*, **57**, 102015 (2017); <https://doi.org/10.1088/1741-4326/aa64f6>.
3. H. MEYER et al., “Overview of Progress in European Medium Sized Tokamaks Towards an Integrated Plasma-Edge/Wall Solution,” *Nucl. Fusion*, **57**, 102014 (2017); <https://doi.org/10.1088/1741-4326/aa6084>.
4. R. FISCHER, A. DINKLAGE, and E. PASCH, “Bayesian Modelling of Fusion Diagnostics,” *Plasma Phys. Control. Fusion*, **45**, 7, 1095 (2003); <https://doi.org/10.1088/0741-3335/45/7/304>.
5. J. SVENSSON et al., “Integrating Diagnostic Data Analysis for W7-AS Using Bayesian Graphical Models,” *Rev. Sci. Instrum.*, **75**, 10, 4219 (2004); <https://doi.org/10.1063/1.1789611>.
6. M. SCHNEIDER et al., “Modelling Third Harmonic Ion Cyclotron Acceleration of Deuterium Beams for JET Fusion Product Studies Experiments,” *Nucl. Fusion*, **56**, 11, 112022 (2016); <https://doi.org/10.1088/0029-5515/56/11/112022>.
7. M. SALEWSKI et al., “On Velocity Space Interrogation Regions of Fast-Ion Collective Thomson Scattering at ITER,” *Nucl. Fusion*, **51**, 8, 083014 (2011); <https://doi.org/10.1088/0029-5515/51/8/083014>.
8. M. SALEWSKI et al., “Tomography of Fast-Ion Velocity-Space Distributions from Synthetic CTS and FIDA Measurements,” *Nucl. Fusion*, **52**, 10, 103008 (2012); <https://doi.org/10.1088/0029-5515/52/10/103008>.
9. M. SALEWSKI et al., “Combination of Fast-Ion Diagnostics in Velocity-Space Tomographies,” *Nucl. Fusion*, **53**, 6, 063019 (2013); <https://doi.org/10.1088/0029-5515/53/6/063019>.
10. M. SALEWSKI et al., “Measurement of a 2D Fast-Ion Velocity Distribution Function by Tomographic Inversion of Fast-Ion D-Alpha Spectra,” *Nucl. Fusion*, **54**, 2, 023005 (2014); <https://doi.org/10.1088/0029-5515/54/2/023005>.
11. M. SALEWSKI et al., “Doppler Tomography in Fusion Plasmas and Astrophysics,” *Plasma Phys. Control. Fusion*, **57**, 1, 014021 (2015); <https://doi.org/10.1088/0741-3335/57/1/014021>.
12. A. S. JACOBSEN et al., “Inversion Methods for Fast-Ion Velocity-Space Tomography in Fusion Plasmas,” *Plasma Phys. Control. Fusion*, **58**, 4, 045016 (2016); <https://doi.org/10.1088/0741-3335/58/4/045016>.
13. B. GEIGER et al., “Fast-Ion Transport and Neutral Beam Current Drive in ASDEX Upgrade,” *Nucl. Fusion*, **55**, 8, 083001 (2015); <https://doi.org/10.1088/0029-5515/55/8/083001>.
14. M. WEILAND et al., “Enhancement of the FIDA Diagnostic at ASDEX Upgrade for Velocity Space Tomography,” *Plasma Phys. Control. Fusion*, **58**, 2, 025012 (2016); <https://doi.org/10.1088/0741-3335/58/2/025012>.
15. A. S. JACOBSEN et al., “Benchmark and Combined Velocity-Space Tomography of Fast-Ion D-Alpha Spectroscopy and Collective Thomson Scattering Measurements,” *Plasma Phys. Control. Fusion*, **58**, 4, 042002 (2016); <https://doi.org/10.1088/0741-3335/58/4/042002>.
16. F. JAULMES et al., “Numerical and Experimental Study of the Redistribution of Energetic and Impurity Ions by Sawteeth in ASDEX Upgrade,” *Nucl. Fusion*, **56**, 11, 112012 (2016); <https://doi.org/10.1088/0029-5515/56/11/112012>.
17. J. RASMUSSEN et al., “Collective Thomson Scattering Measurements of Fast-Ion Transport Due to Sawtooth

- Crashes in ASDEX Upgrade,” *Nucl. Fusion*, **56**, 11, 112014 (2016); <https://doi.org/10.1088/0029-5515/56/11/112014>.
18. M. SALEWSKI et al., “High-Definition Velocity-Space Tomography of Fast-Ion Dynamics,” *Nucl. Fusion*, **56**, 10, 106024 (2016); <https://doi.org/10.1088/0029-5515/56/10/106024>.
 19. M. WEILAND et al., “Phase-Space Resolved Measurement of 2nd Harmonic Ion Cyclotron Heating Using FIDA Tomography at the ASDEX Upgrade Tokamak (At Press),” *Nucl. Fusion*, **57**, 11, 116058 (2017); <https://doi.org/10.1088/1741-4326/aa7e0a>.
 20. M. SALEWSKI et al., “MeV-Range Velocity-Space Tomography from Gamma-Ray and Neutron Emission Spectrometry Measurements at JET,” *Nucl. Fusion*, **57**, 5, 056001 (2017); <https://doi.org/10.1088/1741-4326/aa60e9>.
 21. U. STROTH et al., “Overview of ASDEX Upgrade Results,” *Nucl. Fusion*, **53**, 10, 104003 (2013); <https://doi.org/10.1088/0029-5515/53/10/104003>.
 22. W. W. HEIDBRINK et al., “Measurements of Fast-Ion Acceleration at Cyclotron Harmonics Using Balmer-Alpha Spectroscopy,” *Plasma Phys. Control. Fusion*, **49**, 9, 1457 (2007); <https://doi.org/10.1088/0741-3335/49/9/008>.
 23. W. W. HEIDBRINK, “Fast-Ion Da Measurements of the Fast-Ion Distribution (Invited),” *Rev. Sci. Instrum.*, **81**, 10, 10D727 (2010); <https://doi.org/10.1063/1.3478739>.
 24. M. SALEWSKI et al., “On Velocity-Space Sensitivity of Fast-Ion D-Alpha Spectroscopy,” *Plasma Phys. Control. Fusion*, **56**, 10, 105005 (2014); <https://doi.org/10.1088/0741-3335/56/10/105005>.
 25. A. S. JACOBSEN et al., “Velocity-Space Sensitivity of Neutron Spectrometry Measurements,” *Nucl. Fusion*, **55**, 5, 053013 (2015); <https://doi.org/10.1088/0029-5515/55/5/053013>.
 26. M. SALEWSKI et al., “Velocity-Space Observation Regions of High-Resolution Two-Step Reaction Gamma-Ray Spectroscopy,” *Nucl. Fusion*, **55**, 9, 093029 (2015); <https://doi.org/10.1088/0029-5515/55/9/093029>.
 27. M. SALEWSKI et al., “Fast-Ion Energy Resolution by One-Step Reaction Gamma-Ray Spectrometry,” *Nucl. Fusion*, **56**, 4, 046009 (2016); <https://doi.org/10.1088/0029-5515/56/4/046009>.
 28. A. S. JACOBSEN et al., “Velocity-Space Sensitivities of Neutron Emission Spectrometers at the Tokamaks JET and ASDEX Upgrade in Deuterium Plasmas,” *Rev. Sci. Instrum.*, **88**, 7, 073506 (2017); <https://doi.org/10.1063/1.4991651>.
 29. M. G. JOHNSON et al., “The 2.5-MeV Neutron Time-of-Flight Spectrometer TOFOR for Experiments at JET,” *Nucl. Inst. Meth. Phys. Res.*, **591**, 2, 417 (2008); <https://doi.org/10.1016/j.nima.2008.03.010>.
 30. M. NOCENTE et al., “Gamma-Ray Emission Spectrum from Thermonuclear Fusion Reactions without Intrinsic Broadening,” *Nucl. Fusion*, **55**, 12, 123009 (2015); <https://doi.org/10.1088/0029-5515/55/12/123009>.
 31. A. J. H. DONNÉ et al., “Chapter 7: Diagnostics,” *Nucl. Fusion*, **47**, 6, S337 (2007); <https://doi.org/10.1088/0029-5515/47/6/S07>.
 32. D. MOSEEV et al., “Fast Ion Diagnostics for Magnetically Confined Plasmas,” *Rev. Modern Plasma Phys.*, submitted.
 33. J. ERIKSSON et al., “Dual Sightline Measurements of MeV Range Deuterons with Neutron and Gamma-Ray Spectroscopy at JET,” *Nucl. Fusion*, **55**, 12, 123026 (2015); <https://doi.org/10.1088/0029-5515/55/12/123026>.
 34. M. NOCENTE et al., “Energy Resolution of Gamma-Ray Spectroscopy of JET Plasmas with a LaBr₃ Scintillator Detector and Digital Data Acquisition,” *Rev. Sci. Instrum.*, **81**, 10, 10D321 (2010); <https://doi.org/10.1063/1.3501386>.
 35. M. NOCENTE et al., “High Resolution Gamma Ray Spectroscopy at MHz Counting Rates with LaBr₃ Scintillators for Fusion Plasma Applications,” *IEEE Trans. Nucl. Sci.*, **60**, 2, 1408 (2013); <https://doi.org/10.1109/TNS.2013.2252189>.
 36. C. HELLESEN et al., “Measurements of Fast Ions and Their Interactions with MHD Activity Using Neutron Emission Spectroscopy,” *Nucl. Fusion*, **50**, 8, 084006 (2010); <https://doi.org/10.1088/0029-5515/50/8/084006>.
 37. C. HELLESEN et al., “Fast-Ion Distributions from Third Harmonic ICRF Heating Studied with Neutron Emission Spectroscopy,” *Nucl. Fusion*, **53**, 11, 113009 (2013); <https://doi.org/10.1088/0029-5515/53/11/113009>.
 38. F. BINDA et al., “Forward Fitting of Experimental Data from a NE213 Neutron Detector Installed with the Magnetic Proton Recoil Upgraded Spectrometer at JET,” *Rev. Sci. Instrum.*, **85**, 11, 11E123 (2014); <https://doi.org/10.1063/1.4895565>.
 39. C. CAZZANIGA et al., “Single Crystal Diamond Detector Measurements of Deuterium-Deuterium and Deuterium-Tritium Neutrons in Joint European Torus Fusion Plasmas,” *Rev. Sci. Instrum.*, **85**, 4, 043506 (2014); <https://doi.org/10.1063/1.4870584>.
 40. M. NOCENTE et al., “Fast Ion Energy Distribution from Third Harmonic Radio Frequency Heating Measured with a Single Crystal Diamond Detector at the Joint European Torus,” *Rev. Sci. Instrum.*, **86**, 10, 103501 (2015); <https://doi.org/10.1063/1.4931755>.
 41. A. MURARO et al., “First Neutron Spectroscopy Measurements with a Pixelated Diamond Detector at JET,” *Rev. Sci. Instrum.*, **87**, 11, 11D833 (2016); <https://doi.org/10.1063/1.4961557>.
 42. B. GEIGER et al., “Multi-View Fast-Ion D-Alpha Spectroscopy Diagnostic at ASDEX Upgrade,” *Rev. Sci. Instrum.*, **84**, 11, 113502 (2013); <https://doi.org/10.1063/1.4829481>.

43. B. GEIGER et al., “Quantification of the Impact of Large and Small-Scale Instabilities on the Fast-Ion Confinement in ASDEX Upgrade,” *Plasma Phys. Control. Fusion*, **57**, 1, 014018 (2015); <https://doi.org/10.1088/0741-3335/57/1/014018>.
44. M. SALEWSKI et al., “Comparison of Fast Ion Collective Thomson Scattering Measurements at ASDEX Upgrade with Numerical Simulations,” *Nucl. Fusion*, **50**, 3, 035012 (2010); <https://doi.org/10.1088/0029-5515/50/3/035012>.
45. S. K. NIELSEN et al., “Recent development of collective Thomson scattering for magnetically confined fusion plasmas,” *Phys. Scr.*, **92**, 2, 024001 (2017); <https://doi.org/10.1088/1402-4896/92/2/024001>.
46. J. RASMUSSEN et al., “Consistency Between Real and Synthetic Fast-Ion Measurements at ASDEX Upgrade,” *Plasma Phys. Control. Fusion*, **57**, 7, 075014 (2015); <https://doi.org/10.1088/0741-3335/57/7/075014>.
47. G. TARDINI et al., “First Neutron Spectrometry Measurements in the ASDEX Upgrade Tokamak,” *J. Instrum.*, **7**, C03004 (2012); <https://doi.org/10.1088/1748-0221/7/03/C03004>.
48. G. TARDINI et al., “Simulation of the Neutron Rate in ASDEX Upgrade H-Mode Discharges,” *Nucl. Fusion*, **53**, 6, 063027 (2013); <https://doi.org/10.1088/0029-5515/53/6/063027>.
49. M. NOCENTE et al., “Gamma-Ray Spectroscopy Measurements of Confined Fast Ions on ASDEX Upgrade,” *Nucl. Fusion*, **52**, 9, 094021 (2012); <https://doi.org/10.1088/0029-5515/52/9/094021>.
50. P. A. SCHNEIDER et al., “A New Compact Solid-State Neutral Particle Analyser at ASDEX Upgrade: Setup and Physics Modeling,” *Rev. Sci. Instrum.*, **86**, 7, 073508 (2015); <https://doi.org/10.1063/1.4926886>.
51. M. GARCIA-MUNOZ et al., “Fast-Ion Redistribution and Loss Due to Edge Perturbations in the ASDEX Upgrade, DIII-D and KSTAR Tokamaks,” *Nucl. Fusion*, **53**, 12, 123008 (2013); <https://doi.org/10.1088/0029-5515/53/12/123008>.
52. M. GARCIA-MUNOZ et al., “Fast-Ion Losses Induced by ELMs and Externally Applied Magnetic Perturbations in the ASDEX Upgrade Tokamak,” *Plasma Phys. Control. Fusion*, **55**, 12, 124014 (2013); <https://doi.org/10.1088/0741-3335/55/12/124014>.
53. F. ROMANELLI, “Overview of the JET Results,” *Nucl. Fusion*, **55**, 10, 104001 (2015); <https://doi.org/10.1088/0029-5515/55/10/104001>.
54. W. W. HEIDBRINK et al., “Hydrogenic Fast-Ion Diagnostic Using Balmer-Alpha Light,” *Plasma Phys. Control. Fusion*, **46**, 12, 1855 (2004); <https://doi.org/10.1088/0741-3335/46/12/005>.
55. W. W. HEIDBRINK et al., “Confinement Degradation by Alfvén-Eigenmode Induced Fast-Ion Transport in Steady-State Scenario Discharges,” *Plasma Phys. Control. Fusion*, **56**, 9, 095030 (2014); <https://doi.org/10.1088/0741-3335/56/9/095030>.
56. X. YUAN et al., “Neutron Energy Spectrum Measurements with a Compact Liquid Scintillation Detector on EAST,” *J. Instrum.*, **8**, P07016 (2013); <https://doi.org/10.1088/1748-0221/8/07/P07016>.
57. X. ZHANG et al., “Diagnosing NB Plasmas on the EAST Tokamak with New Time-of-Flight Neutron Spectrometer,” *Nucl. Fusion*, **54**, 10, 104008 (2014); <https://doi.org/10.1088/0029-5515/54/10/104008>.
58. J. HUANG et al., “Conceptual Design of a Fast-Ion D-Alpha Diagnostic on Experimental Advanced Superconducting Tokamaka,” *Rev. Sci. Instrum.*, **85**, 11, 11E407 (2014); <https://doi.org/10.1063/1.4887820>.
59. B. GEIGER et al., “Study of the Fast -Ion Distribution Function in the TCV Tokamak Based on FIDA Spectroscopy and the TRANSP Code,” *Plasma Phys. Control. Fusion*, **59**, 11, 115002 (2017); <https://doi.org/10.1088/1361-6587/aa8340>.
60. A. BORTOLON, W. W. HEIDBRINK, and M. PODESTA, “A Tangentially Viewing Fast Ion D-Alpha Diagnostic for NSTX,” *Rev. Sci. Instrum.*, **81**, 10, 10D728 (2010); <https://doi.org/10.1063/1.3495768>.
61. C. A. MICHAEL et al., “Dual View FIDA Measurements on MAST,” *Plasma Phys. Control. Fusion*, **55**, 9, 095007 (2013); <https://doi.org/10.1088/0741-3335/55/9/095007>.
62. O. M. JONES et al., “Fast-Ion Deuterium Alpha Spectroscopic Observations of the Effects of Fishbones in the Mega-Ampere Spherical Tokamak,” *Plasma Phys. Control. Fusion*, **55**, 8, 085009 (2013); <https://doi.org/10.1088/0741-3335/55/8/085009>.
63. M. NISHIURA et al., “Spectrum Response and Analysis of 77 GHz Band Collective Thomson Scattering Diagnostic for Bulk and Fast Ions in LHD Plasmas,” *Nucl. Fusion*, **54**, 2, 023006 (2014); <https://doi.org/10.1088/0029-5515/54/2/023006>.
64. T. ITO et al., “Fast Ion Charge Exchange Spectroscopy Adapted for Tangential Viewing Geometry in LHD,” *Rev. Sci. Instrum.*, **81**, 10, 10D327 (2010); <https://doi.org/10.1063/1.3502331>.
65. T. ITO et al., “Effect of Halo Neutrals on Fast-Ion Charge Exchange Spectroscopy Measurements in LHD,” *Plasma Fusion Res.*, **5**, S2099 (2012); <https://doi.org/10.1585/pfr.5.S2099>.
66. H. TOMITA et al., “Development of Neutron Spectrometer Toward Deuterium Plasma Diagnostics in LHD,” *Rev. Sci. Instrum.*, **81**, 10, 10D309 (2010); <https://doi.org/10.1063/1.3464260>.
67. M. SALEWSKI et al., “Investigation of First Mirror Heating for the Collective Thomson Scattering Diagnostic

- in ITER,” *Rev. Sci. Instrum.*, **79**, 10, 10E729 (2008); <https://doi.org/10.1063/1.2956961>.
68. M. SALEWSKI et al., “Comparison of Collective Thomson Scattering Signals Due to Fast Ions in ITER Scenarios with Fusion and Auxiliary Heating,” *Plasma Phys. Control. Fusion*, **51**, 3, 035006 (2009); <https://doi.org/10.1088/0741-3335/51/3/035006>.
69. M. SALEWSKI et al., “Impact of ICRH on the Measurement of Fusion Alphas by Collective Thomson Scattering in ITER,” *Nucl. Fusion*, **49**, 2, 025006 (2009); <https://doi.org/10.1088/0029-5515/49/2/025006>.
70. I. N. CHUGUNOV et al., “Development of Gamma-Ray Diagnostics for ITER,” *Nucl. Fusion*, **51**, 8, 083010 (2011); <https://doi.org/10.1088/0029-5515/51/8/083010>.
71. M. NOCENTE et al., “Conceptual Design of the Radial Gamma Ray Spectrometers System for α -Particle and Runaway Electron Measurements at ITER,” *Nucl. Fusion*, **57**, 7, 076016 (2017); <https://doi.org/10.1088/1741-4326/aa6f7d>.
72. A. KAPPATOU et al., “Feasibility of Non-Thermal Helium Measurements with Charge Exchange Spectroscopy on ITER,” *Nucl. Fusion*, **52**, 4, 043007 (2012); <https://doi.org/10.1088/0029-5515/52/4/043007>.

Reference [14]

[14]. M Salewski et al. (2018) *Nuclear Fusion* **58** 096019. Alpha-particle velocity-space diagnostic in ITER

Alpha-particle velocity-space diagnostic in ITER

M. Salewski¹, M. Nocente^{2,3}, B. Madsen¹, I. Abramovic⁴, M. Fitzgerald⁵, G. Gorini^{2,3}, P.C. Hansen⁶, W.W. Heidbrink⁷, A.S. Jacobsen⁸, T. Jensen¹, V.G. Kiptily⁵, E.B. Klinkby⁹, S.B. Korsholm¹, T. Kurki-Suonio¹⁰, A.W. Larsen¹, F. Leipold¹, D. Moseev⁴, S.K. Nielsen¹, S.D. Pinches¹¹, J. Rasmussen¹, M. Rebai^{2,3}, M. Schneider¹¹, A. Shevelev¹², S. Sipilä¹⁰, M. Stejner¹ and M. Tardocchi³

¹ Department of Physics, Technical University of Denmark, Kgs. Lyngby, Denmark

² Department of Physics, University of Milano Bicocca, Milano, Italy

³ Istituto di Fisica del Plasma, Consiglio Nazionale delle Ricerche, Milano, Italy

⁴ Max-Planck-Institut für Plasmaphysik, Greifswald, Germany

⁵ CCFE, Culham Science Centre, Abingdon, Oxon, United Kingdom of Great Britain and Northern Ireland

⁶ Department of Applied Mathematics and Computer Science, Technical University of Denmark, Kgs. Lyngby, Denmark

⁷ Department of Physics and Astronomy, University of California Irvine, Irvine, CA, United States of America

⁸ Max-Planck-Institut für Plasmaphysik, Garching, Germany

⁹ Center for Nuclear Technologies, Technical University of Denmark, Roskilde, Denmark

¹⁰ Department of Applied Physics, Aalto University, Aalto, Finland

¹¹ ITER Organization, Route de Vinon-sur-Verdon, CS 90 046, 13067 St. Paul-lez-Durance Cedex, France

¹² Ioffe Institute, Polytekhnicheskaya 26, St Petersburg, 194021, Russian Federation

E-mail: msal@fysik.dtu.dk

Received 9 February 2018, revised 16 May 2018

Accepted for publication 21 June 2018

Published 10 July 2018



Abstract

We discuss α -particle velocity-space diagnostic in ITER based on the planned collective Thomson scattering (CTS) and γ -ray spectrometry (GRS) systems as well as ASCOT simulations of the α -particle distribution function. GRS is sensitive to α -particles with energies $E \gtrsim 1.7$ MeV at all pitches p , and CTS for $E \gtrsim 0.3$ MeV and $|p| \lesssim 0.9$. The remaining velocity space is not observed. GRS and CTS view the plasma (almost) perpendicularly to the magnetic field. Hence we cannot determine the sign of the pitch of the α -particles and cannot distinguish co- and counter-going α -particles with the currently planned α -particle diagnostics. Therefore we can only infer the sign-insensitive 2D distribution function $f(E, |p|)$ by velocity-space tomography for $E \gtrsim 1.7$ MeV. This is a serious limitation, since co- and counter-going α -particle populations are expected to have different birth rates and neoclassical transport as well as different anomalous transport due to interaction with modes such as Alfvén eigenmodes. We propose the installation of an oblique GRS system on ITER to allow us to diagnostically track such anisotropy effects and to infer the full, sign-sensitive $f(E, p)$ for $E \gtrsim 1.7$ MeV. α -particles with $E \lesssim 1.7$ MeV are diagnosed by CTS only, which does not allow velocity-space tomography on its own. Nevertheless, we show that measurements of the α -particle energy spectrum, which is an ITER measurement requirement, are now feasible for $E \gtrsim 0.3$ MeV using a velocity-space tomography formalism assuming isotropy in velocity space.

Keywords: ITER, gamma-ray spectrometry, collective Thomson scattering, velocity-space tomography, alpha-particle diagnostic

(Some figures may appear in colour only in the online journal)

1. Introduction

A new era of burning plasmas is approaching with the planned DT experiments at JET [1, 2] and the construction of the ITER tokamak [3]. The ultimate goal for ITER is a fusion power of $P_{\text{fus}} = 500$ MW for an auxiliary heating power of $P_{\text{aux}} = 50$ MW which gives a power amplification of $Q = P_{\text{fus}}/P_{\text{aux}} = 10$ [4]. Many present designs for the next-step device DEMO hope for $Q = 20$ – 50 [5–7]. Such plasmas are primarily heated by α -particles generated in the fusion reaction $D(T,n)\alpha$. Since the fusion born α -particle power is $P_{\alpha} = P_{\text{fus}}/5$, the plasma self-heating fraction η_{α} for well-confined energetic particles is

$$\eta_{\alpha} = \frac{P_{\alpha}}{P_{\alpha} + P_{\text{aux}}} = \frac{Q}{Q + 5}. \quad (1)$$

The plasma self-heating fraction is an alternative way to state the goal to achieve $Q = 10$ which highlights the prominent role of α -particles for the plasma heating [4]. The importance of plasma self-heating by α -particles increases with Q (figure 1). The fusion power world record discharge at JET in 1997 had $\eta_{\alpha} = 11\%$ ($Q = 0.64$) just below ‘break-even’ at $\eta_{\alpha} = 17\%$ ($Q = 1$) [8]. Burning plasmas are predominantly self-heated by α -particles ($\eta_{\alpha} > 50\%$, $Q > 5$), as in ITER ($\eta_{\alpha} = 67\%$) or DEMO ($\eta_{\alpha} = 80\%$ – 91%). At ‘ignition’ the plasma is completely self-heated ($\eta_{\alpha} = 100\%$, $Q \rightarrow \infty$). Burning plasmas will offer new challenges since the temperature and density profiles are self-consistently determined by α -particle heating rather than controlled by auxiliary heating. Furthermore, MeV-range ions may drive a zoo of instabilities deteriorating the plasma performance [9–19]. Due to the central role of α -particles to achieve $Q = 10$ and the possible anomalous transport due to instabilities, the diagnostic of α -particles in ITER will be essential.

In the most basic modelling, α -particles are assumed to follow a classical, isotropic slowing-down distribution. However, neoclassical transport theory and the anisotropic α -particle birth profiles in ITER suggest that the α -particle distribution will be anisotropic [20]. Furthermore, the basic physics of wave-particle interaction suggests that particles close to resonance conditions interact most strongly with modes. These resonance conditions are different for co- and counter-going α -particles such that the expected anomalous wave-induced transport is thought to be substantially different for co- and counter-going particles. However, these two groups of particles cannot be told apart with the currently planned set of α -particle diagnostics. In this paper we hence propose the installation of an extra fast-ion diagnostic at ITER which would allow us to tell co- and counter-going α -particles apart.

Confined α -particles in ITER are expected to be diagnosed by γ -ray spectrometry (GRS) [21–24] and collective Thomson

scattering (CTS) [25–30]. In GRS measurements, the γ -rays emitted by fusion plasmas are spectrally analyzed [31, 32]. The largest γ -ray fluxes today are achieved at JET. Early GRS measurements at JET had a moderate spectral resolution [33–41]. Developments in detectors now allow a much higher spectral resolution such that the Doppler shapes can be analyzed [22, 42–51]. The high nuclear reaction rates in the upcoming DT campaign at JET [1, 2] and later in burning plasmas at ITER and DEMO will further enhance the γ -ray emission [21, 52].

In CTS measurements, scattered electromagnetic waves are spectrally analyzed. Fast-ion CTS measurements were first done at JET [53], and nowadays on ASDEX Upgrade [54–57] and LHD [58]. Wendelstein 7-X is also equipped with CTS [59, 60]. In this paper we demonstrate various ways to determine α -particle velocity distribution functions by integrated data analysis of the GRS and CTS spectra based on velocity-space tomography [57, 61–76]. The velocity-space tomography technique allows the measurement of α -particle densities and energy spectra, which are ITER measurement requirements [77].

Section 2 gives a brief overview of the planned GRS and CTS systems at ITER. In section 3 we illustrate their velocity-space sensitivities. Section 4 presents expected results of velocity-space tomography at ITER and demonstrates that the sign of the pitch cannot be determined, unless an extra fast-ion diagnostic with an oblique view is added. The pitch is defined as $p = v_{\parallel}/v$ where v_{\parallel} is the velocity component along the magnetic field and v the velocity magnitude. This limitation is explained in section 5. In section 6 we compute reconstructions of α -particle distribution functions simulated by ASCOT for the baseline and the hybrid scenario which do show significant asymmetry in pitch. Section 7 discusses further sources of such anisotropy in the α -particle distribution and highlights the importance of measurements that are sensitive to the sign of the pitch. Section 8 presents a way to measure α -particle energy spectra based on CTS or GRS measurements in one view by assuming isotropy in velocity space as prior information. Conclusions are drawn in section 9.

2. Diagnostics for confined α -particles at ITER

For 2D velocity-space or 3D phase-space studies, spectra are of particular interest [62, 78]. The currently planned GRS and CTS systems for α -particle diagnostic are illustrated in figure 2. The CTS system at ITER has several measurement volumes distributed along the 60 GHz, 1 MW probe beam where it overlaps with the fields of view of highly sensitive radiometers [25–30]. We use the central measurement volume illustrated in figure 2. CTS diagnostics measure spectra of scattered radiation which are sensitive to the projection of

the fast-ion velocity distribution function in the measurement volume along $\mathbf{k}^\delta = \mathbf{k}^s - \mathbf{k}^i$. \mathbf{k}^s and \mathbf{k}^i are the wave vectors of the scattered and incident waves, respectively. In CTS the probing radiation is Doppler-shifted according to $\nu^\delta = u|\mathbf{k}^\delta|/2\pi$ where u is the projected velocity of the fast ion onto \mathbf{k}^δ . The angle ϕ between the magnetic field and \mathbf{k}^δ determines together with the observed Doppler shift the interrogation region of the diagnostic in velocity space (see section 3). The central measurement volume of the ITER CTS system has $\phi = 97^\circ$.

The GRS system has just completed its conceptual design phase and is planned to consist of up to two perpendicular detector arrays, one vertical and one radial, out of which we select the views going through the plasma core. The lines-of-sight of both systems are about perpendicular to the magnetic field in the plasma core. GRS measurements are in principle sensitive along the entire lines-of-sight of the detectors, but the γ -ray production is strongly biased towards the plasma center where most fusion reactions occur. α -particle measurements at ITER are mainly foreseen by GRS measurements of the two-step reaction ${}^9\text{Be}(\alpha, n\gamma){}^{12}\text{C}$ which produces γ -rays at 4.44 MeV and 3.2 MeV [79]. The 4.44 MeV γ -rays originate from the decay of ${}^{12}\text{C}$ from the first excited state, and the 3.2 MeV from the decay from the second to the first excited state. The second excited state is expected to get populated mostly due to α -particles with energies larger than 3.4 MeV. Ideally, high-resolution GRS measurements resolve the spectral shapes of these γ -ray peaks which are sensitive to the velocities of the α -particles. In this paper we do not consider the experimental challenges that must be overcome [24, 45, 80, 81], but we assume that both GRS and CTS deliver optimal measurements according to design.

3. Velocity-space coverage of α -particle diagnostics at ITER

The diagnostic velocity-space coverage can be analyzed using weight functions which have been studied for the major confined fast-ion diagnostics [61, 64, 82–86], recently also in 3D phase-space [78]. A few illustrative examples for GRS and CTS weight functions at ITER [24, 61] are presented in figures 3 and 4. We expect detectable signals for the Doppler shifts chosen in figures 3 and 4. The amplitude in the colored regions shows the detectable signal per ion and is thus a measure of the velocity-space sensitivity of the diagnostic. The white regions are not observed.

GRS weight functions for ITER are up–down symmetric about $p = 0$ (figure 3). As GRS relies on the Doppler shift, it is impossible to tell in perpendicular views, if a given particle traverses the detector along or against the direction of the magnetic field. Therefore an ion with a given pitch p_1 generates the same signal as an ion with pitch $-p_1$ which means that the perpendicular GRS at ITER cannot tell co- and counter-going ions apart. Otherwise, the GRS weight functions actually have considerable selectivity in pitch. At the nominal γ -ray peak energy, the sensitivity of co- and counter-going ions is largest whereas at large Doppler shifts the sensitivity to trapped ions

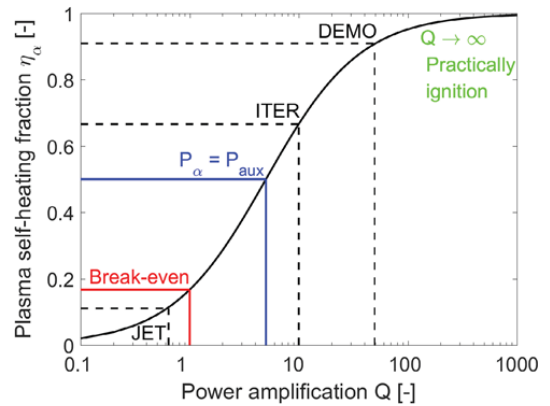


Figure 1. Plasma self-heating fraction η_α as function of the power amplification Q . Plasmas are predominantly heated by MeV-range α -particles for $Q > 5$.

is largest. This pitch selectivity of the two-step reaction GRS weight functions ultimately originates from the conservation of energy and momentum [84].

Figures 3(a)–(c) shows typical GRS weight functions for the γ -ray peak at 3.2 MeV which is most sensitive to α -particles at energies above about 3.4 MeV which is just below the α -particle birth energy. The sensitivity decreases rapidly for lower α -particle energies. α -particles with energies larger than their birth energy at 3.5 MeV, e.g. due to wave heating in the ion cyclotron range of frequencies (ICRF), the Gaussian form of the birth energy distribution or anomalous effects, could easily be detected with this reaction. It will therefore be effective in reconstructions of the velocity-space above the nominal α -particle birth energy.

Weight functions for the 4.44 MeV γ -ray peak (figures 3(d)–(f)) have some similarities with those for the 3.2 MeV peak. However, there are important differences due to the different reaction cross sections of the two reactions. Nuclear resonances boost the sensitivity of the 4.44 MeV γ -ray peak near α -particle energies of 2 MeV and 4 MeV. The sensitivity decreases rapidly for energies below 2 MeV such that this reaction is sensitive down to about 1.7 MeV. The sensitivity in the region between the 2 MeV and 4 MeV resonances should be sufficient for velocity-space tomography.

The viewing angle of CTS is $\phi = 97^\circ$, and hence the ITER CTS system can practically be regarded as a perpendicular system. The difference from a truly perpendicular view is reflected in the slight asymmetry of the CTS weight functions about $p = 0$ (figures 4). The weight functions are slightly lopsided towards negative pitches for positive projected velocities u and towards positive pitches for negative u . This gives us the theoretical possibility to detect asymmetry in the velocity distribution function about $p = 0$. However, the asymmetry in the weight functions is small, and considering realistic noise levels it turns out to be difficult to determine the sign of the pitch of a measured ion.

A measure of the gross velocity-space sensitivity is obtained by computing weight functions covering the entire accessible spectral range. This is equivalent to summing the

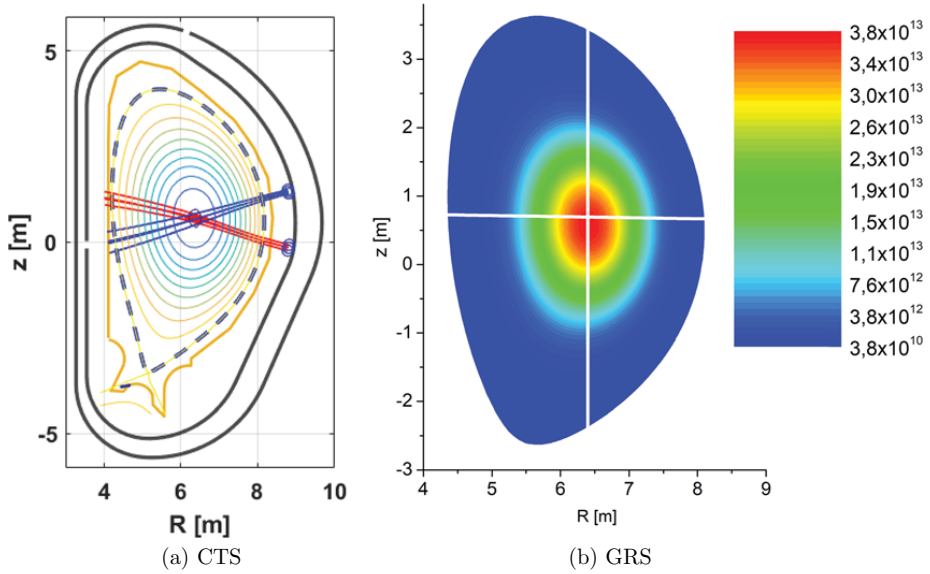


Figure 2. Geometries of the α -particle diagnostic systems planned for ITER in the baseline scenario. (a) Central measurement volume of the CTS system. The probe beam is illustrated in blue, and the central receiver beam is illustrated in red. The measurement volume is located at the intersection of the probe and receiver beams. Magnetic flux surfaces are indicated. (b) Vertical and radial GRS lines-of-sight going through the plasma center. The colours indicate the predicted γ -ray emissivity ($\gamma' \text{ s/m}^3$).

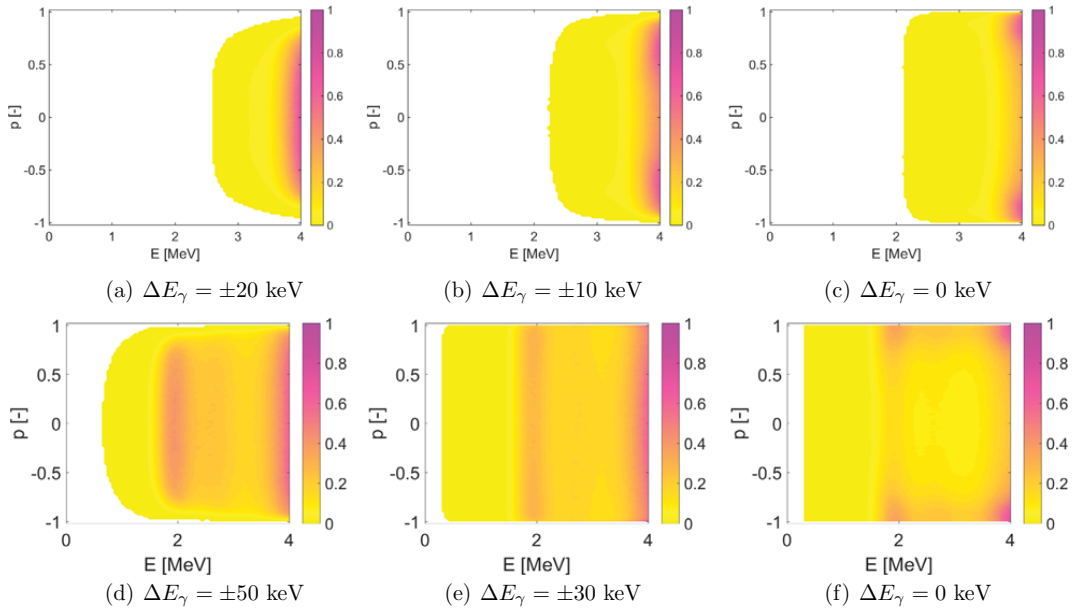


Figure 3. GRS weight functions (a.u.) for $\phi = 90^\circ$ and different Doppler shifts ΔE_γ for the γ -ray peaks at 3.2 MeV (a)–(c) and at 4.44 MeV (d)–(f). (E, p) are the energy and the pitch of the α -particles. The pitch sensitivities change substantially from the wings to the center of the relevant spectral line. All weight functions are up–down symmetric about $p = 0$. The weight functions for positive Doppler shifts are identical to those for the corresponding negative Doppler shifts.

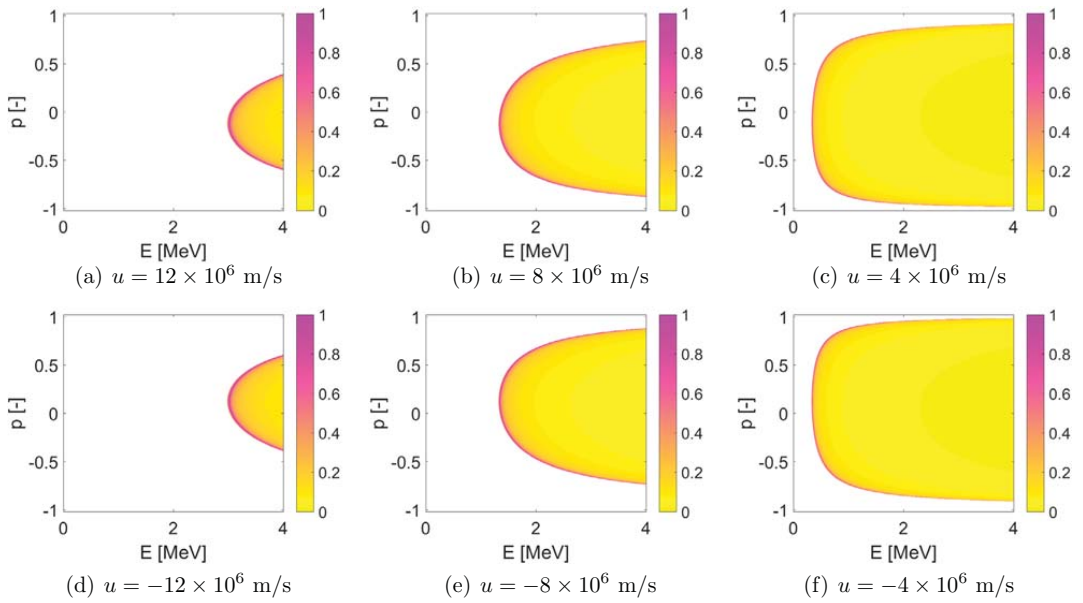


Figure 4. CTS weight functions (a.u.) for $\phi = 97^\circ$ and different projected velocities u . (E, p) are the energy and the pitch of the α -particles. Due to the almost perpendicular observation angle, the weight functions for positive and negative u are very similar but not identical.

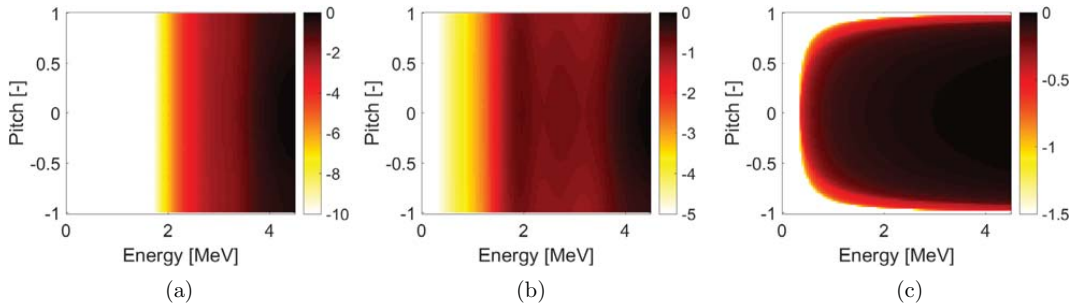


Figure 5. Illustration of gross velocity-space sensitivity of individual fast-ion diagnostics at ITER. (E, p) are the energy and the pitch of the α -particles. (a) GRS at 3.2 MeV. (b) GRS at 4.44 MeV. (c) CTS. The sensitivity functions are normalized. The color scale shows the base ten logarithm.

weight functions associated with each experimentally accessible data point in the spectrum. The weight functions are normalized by the noise levels of their associated measurements before computing the sum which is here assumed to be 10% [63]. Figure 5 illustrates such gross sensitivities for the three spectra (out of which each GRS spectrum will be measured by two detectors simultaneously).

Basic features of the individual weight functions enter the gross velocity-space sensitivity of the γ -ray peaks at 3.2 MeV and 4.44 MeV (figures 5(a) and (b)). The gross velocity-space sensitivities largely resemble what is expected from the energy dependence of the reaction cross sections. The 3.2 MeV peak has little sensitivity at energies below ~ 3.4 MeV and becomes very sensitive above the α -particle birth energy. The 4.44 MeV peak is strongly sensitive at the

resonances at 2 MeV and 4 MeV and has a good sensitivity between the resonances.

The CTS diagnostic (figure 5(c)) can detect α -particles despite the thermal deuterium down to about 0.3 MeV for $p \sim 0$. This energy is based on an assessment of where in the measurable CTS spectrum the α -particles are going to generate most of the scattered radiation [26, 27]. Thermal deuterium (and tritium) ions moving in parallel to \mathbf{k}^δ can have similar projected velocities as MeV-range α -particles moving almost perpendicularly to \mathbf{k}^δ . The projected velocity u is proportional to the Doppler shift in the measured spectrum. The dense thermal bulk population can hence effectively mask the fairly dilute energetic α -particle population at low Doppler shifts. Here we estimate this minimum projected velocity, where the α -particle signal starts to dominate, to be

$u_{\alpha,\min} \sim 3v_{\text{th,D}}$ where $v_{\text{th,D}}$ is the thermal velocity of deuterium. The factor three is not fixed but depends on the relative densities of the α -particles and the bulk ions and how well we know the bulk plasma densities, temperatures, and drifts, in particular for deuterium due to its low mass. On the back-of-the-envelope, this leads to a minimum α -particle energy

$$E_{\alpha,\min} \sim \frac{m_{\alpha}}{m_{\text{D}}} \frac{u_{\alpha,\min}^2}{v_{\text{th,D}}^2} T_{\text{D}} \sim 18T_{\text{D}} \sim 300 \text{ keV}. \quad (2)$$

for one particular pitch. The exact form of the region where we can hope to measure α -particles by CTS is given by weight functions summarized in figure 5(c). For the CTS geometry at ITER, the minimum detectable α -particle energy increases towards extreme pitches, such that α -particles with $|p| \sim 0.9 - 1$ cannot be measured. To detect the α -particles, a CTS with an oblique view would be required ($\phi \sim 0^\circ - 50^\circ$). The region with high gross velocity-space sensitivity is circumscribed by a narrow stripe of intermediate sensitivity where the α -particles produce signals only on one side of the CTS spectrum due to the slight asymmetry of the CTS weight functions about $p = 0$.

We now go one step further and illustrate the gross velocity-space sensitivity of the combined diagnostic set of CTS and GRS. Figure 6 is obtained by summing the weight functions of all spectral points normalized by their associated noise levels. As the noise levels are estimated on theoretical grounds, we should keep in mind that the amplitudes in figure 6 are uncertain. Nevertheless, it is an efficient illustration of the topology of the gross velocity-space sensitivity of the combined diagnostic set at ITER and it provides useful insight into the matrix W required for velocity-space tomography (section 4). Salient features from the individual diagnostics can be recognized in figure 6. α -particles at energies below ~ 0.3 MeV and co- and counter-going α -particles at extreme pitches ($|p| \gtrsim 0.9$) and energies up to ~ 1.7 MeV can hardly be diagnosed by CTS or GRS. The gross velocity-space sensitivity increases substantially from about 1.7 MeV upwards and becomes excellent around the 2 MeV resonance of the 4.44 MeV γ -ray peak. For energies close to this resonance and upwards, the gross velocity-space coverage of the combined diagnostic set at ITER is good. However, CTS is practically the only diagnostic detecting α -particles below ~ 1.7 MeV, covering the pitch range of $|p| \lesssim 0.8 - 0.9$. This causes the protrusion below the 2 MeV resonance of the 4.44 MeV γ -ray peak. Overall, while figure 6 is an illustrative summary of the diagnosed velocity space at ITER, it does not reveal our incapability to determine the sign of the pitch of an ion.

4. Velocity-space tomography based on GRS and CTS at ITER

In this section we analyze the inference of the α -particle distribution at ITER by standard velocity-space tomography using analytic test functions to reveal basic features of the tomography problem. Realistic α -particle distributions computed

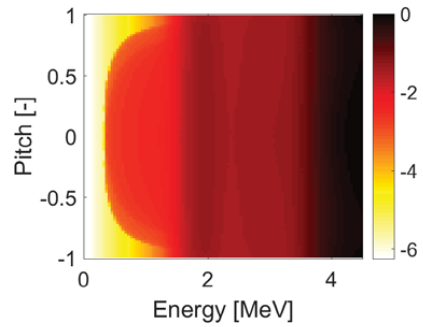


Figure 6. Illustration of the gross velocity-space sensitivity of CTS and GRS together. (E, p) are the energy and the pitch of the α -particles. The sensitivity functions are normalized. The color scale shows the base ten logarithm.

by ASCOT will be studied in section 6. In standard velocity-space tomography, we solve the Tikhonov problem

$$\text{minimize} \left\| \begin{pmatrix} W \\ \lambda L \end{pmatrix} F - \begin{pmatrix} S \\ 0 \end{pmatrix} \right\|_2^2 \text{ subject to } F \geq 0 \quad (3)$$

with the mathematically equivalent formulation

$$\text{minimize} \{ \|WF - S\|_2^2 + \lambda^2 \|LF\|_2^2 \} \text{ subject to } F \geq 0. \quad (4)$$

W is a matrix consisting of normalized weight functions, S is the normalized measured signal written as a vector, L is a penalty matrix, and F is the velocity distribution function rearranged as a vector [70]. In 0th-order Tikhonov regularization L is the identity matrix penalizing large amplitudes of F . In 1st-order Tikhonov regularization L is a numerical gradient operator penalizing large gradients [68]. The regularization parameter λ balances the relative sizes of the data fitting residual $WF - S$ and the penalty term LF and must be determined as part of the solution. An interpretation of what the solution F to the Tikhonov problem represents for almost perpendicular diagnostic systems will be given in section 5. Here we restrict our focus to finding F by standard velocity-space tomography in a few examples.

Figure 7 shows our best attempt to infer the 2D classical α -particle slowing-down distribution function by standard velocity-space tomography for energies down to 300 keV. The classical α -particle slowing-down distribution (figure 7(a)) is given by [87, 88]

$$f(E) = \frac{CE^{1/2}}{E^{3/2} + E_c^{3/2}} \text{erfc} \left(\frac{E - E_b}{\Delta E} \right). \quad (5)$$

Here the birth energy is $E_b = 3.5$ MeV and the crossover energy (where drag on ions equals drag on electrons) is $E_c = 660$ keV, and we use a width of $\Delta E = 100$ keV in the argument of the complementary error function. C is a constant set to obtain the desired total density. The slowing-down distribution is isotropic in velocity space so that it does not depend on the pitch. We calculate synthetic spectra based on this

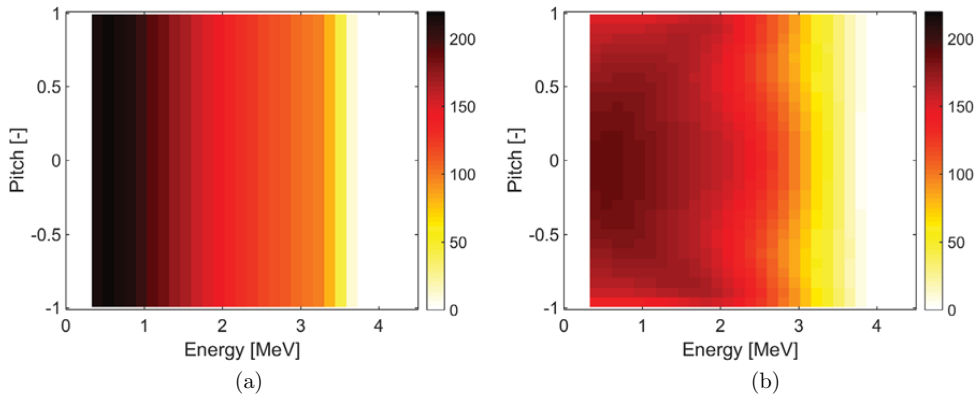


Figure 7. (a) Classical slowing-down distribution in units ($10^{10}/(\text{m}^3\text{eV})$). (b) Tomographic inversion down to 300 keV from noisy, synthetic GRS/CTS measurements based on the distribution in (a). The inversion is plagued by artifacts since CTS is effectively the only available fast-ion diagnostic in the range 300 keV to 1.7 MeV.

distribution function with the combined GRS and CTS diagnostic system, add 10% noise and calculate inversions of the noisy, synthetic spectra. The inversion in figure 7(b) resembles the original function only coarsely. The distribution decreases monotonically for increasing energies at a given pitch, and the phase-space density of ions above the birth energy of 3.5 MeV is practically zero. However, the inversion is plagued by artifacts. The isotropy of the original function is lost in the inversion. The amplitudes of the inversion do depend on the pitch, such that a wave-like pattern is formed. The shape of the CTS weight functions appears to be imprinted in the reconstruction. The artifacts appear because CTS provides practically the only view below about 1.7 MeV where the GRS measurements are only very weakly sensitive. This behaviour relates well to previous findings that inversions based on one view are plagued by artifacts for realistic noise levels [62].

A strategy to circumvent these artifacts is to restrict the velocity-space region to energies larger than 1.7 MeV, so that more than one diagnostic is available everywhere in velocity space. Hence the CTS measurements that have significant sensitivity to α -particles below 1.7 MeV are not used in the tomography problem (see figure 6). The CTS measurements without sensitivity below 1.7 MeV and the GRS measurements can then be used to reconstruct the velocity space above 1.7 MeV.

Reconstructions restricted to energies above 1.7 MeV are presented in figure 8. Figures 8(a) and (b) show the isotropic α -particle slowing-down distribution function and its reconstruction above 1.7 MeV. They are in excellent agreement. The decreasing density towards higher energies is well captured, as is the birth energy at 3.5 MeV. The reconstruction is isotropic to a high degree in agreement with the original function. This demonstrates that the classical, isotropic slowing-down distribution can be reconstructed with the diagnostics currently planned at ITER in the region above 1.7 MeV where both CTS and GRS are sensitive.

In figures 8(c) and (d) we reconstruct an anisotropic function with symmetry about $p = 0$. The anisotropic function has

decreasing phase-space densities towards pitches of $p \sim \pm 1$. This type of distribution function could be a model for the α -particles after a sawtooth crash that has ejected predominantly passing particles rather than trapped particles. This type of anisotropy with symmetry in the co-going and counter-going particles is also captured well in the reconstruction.

However, in figures 8(e) and (f) we attempt to reconstruct a distribution function that is asymmetric about $p = 0$. The original function is lopsided towards negative pitches as a model for ejection of co-going particles from the classical slowing-down distribution. This asymmetry is poorly captured in the reconstruction. The reconstruction is only marginally lopsided towards negative pitches and is almost symmetric such that it erroneously also shows ejection of counter-going particles. The failure to reconstruct the asymmetric distribution function originates from the very poor sensitivity to the sign of the pitch of the current set of diagnostics. We will discuss velocity-space tomography techniques for perpendicular and almost perpendicular systems in section 5.

We could distinguish co- and counter-going ions and the sign of the pitch if ITER had a tangential or oblique fast-ion diagnostic view with respect to the magnetic field. Figure 9 illustrates weight functions for an oblique GRS view with a viewing angle of $\phi = 30^\circ$ which is similar to that currently being installed at JET. Typical weight functions are asymmetric about $p = 0$ allowing the reconstruction of asymmetric functions. At ITER such an oblique GRS instrument could be installed in any port plug from a physics point of view, but this is often challenging from an engineering point of view. One option could be to place it in equatorial port plug 8.

Figure 10 shows reconstructions of the asymmetric α -particle distribution function from figure 8(e) assuming an additional oblique GRS view. The reconstruction captures the asymmetry and shape of the original function. This demonstrates that an oblique GRS view will be required, if we wish to be able to determine the sign of the pitch and tell co- and counter-going ions apart. Close inspection still reveals some

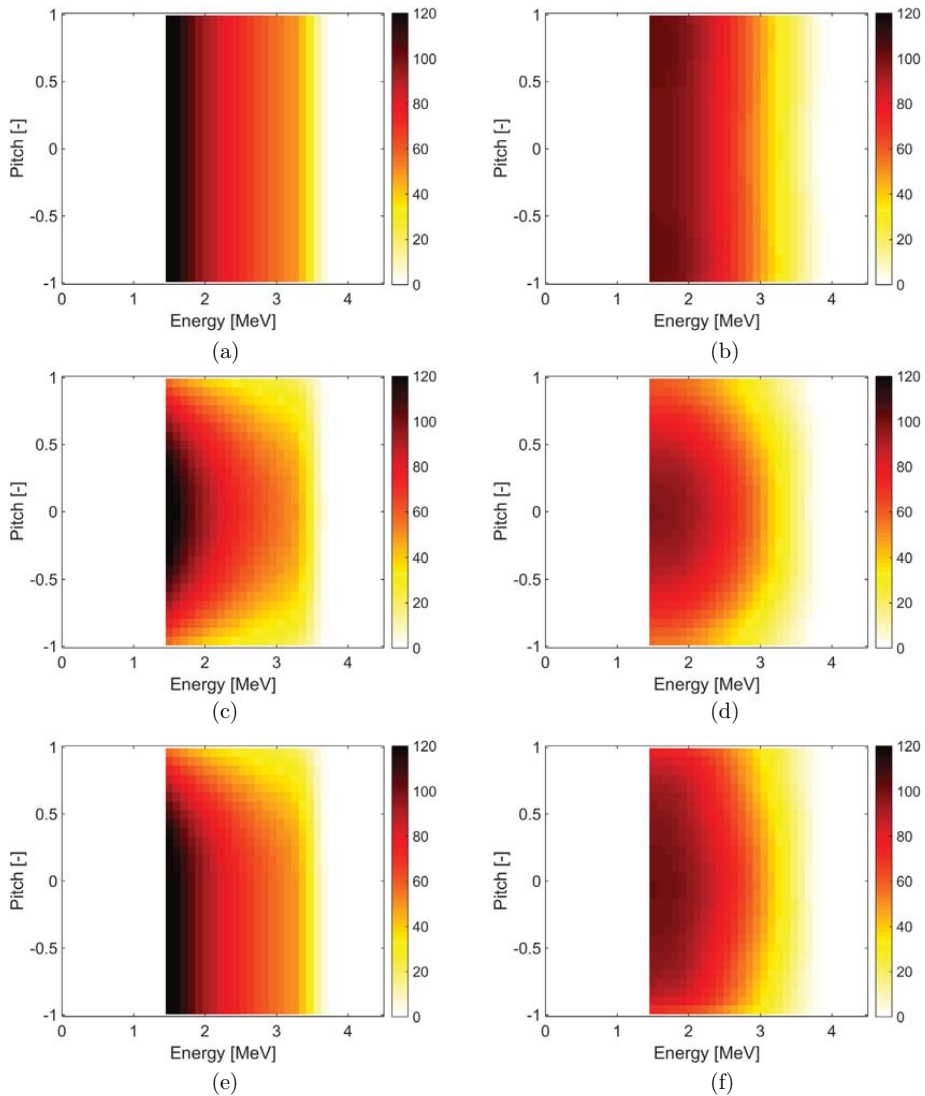


Figure 8. Test distribution functions in units ($10^{10}/(\text{m}^3\text{eV})$) and their respective tomographic inversions down to 1.7 MeV from noisy synthetic data. (a) Isotropic test function. (b) Inversion based on (a). (c) Anisotropic test function with symmetry about $p = 0$. (d) Inversion based on (c). (e) Anisotropic test function with asymmetry about $p = 0$. (f) Inversion based on (e).

erroneous depletion at negative pitches in the inversion, but this artifact is strongly suppressed compared with figure 8(f).

To quantify the improvement due to the additional oblique GRS view, we compute the partial fast-ion densities for ions in the upper and lower (E, p)-halfplanes corresponding to positive and negative pitches for the inversion and the true solution (table 1). The inversions generally have similar α -particle densities as the corresponding true solutions. However, solutions obtained with the currently planned set of GRS/CTS diagnostics always give symmetric distributions of α -particles, despite any asymmetry in the true solution. The asymmetry in the true distribution is captured much better with an additional oblique GRS view.

5. Velocity-space tomography for diagnostics with perpendicular and almost perpendicular views

In this section we discuss the implications of the almost perpendicular viewing directions of the fast-ion diagnostics planned for ITER. Assume first a completely perpendicular system as an idealized model. In this case there is no way to infer the full velocity distribution function F as we never know if a given ion has a pitch of p or $-p$. It is not even possible to infer a pixel function F_i consisting of just one pixel i . The measured signal for the pixel function is as usual

$$S_i = WF_i. \quad (6)$$

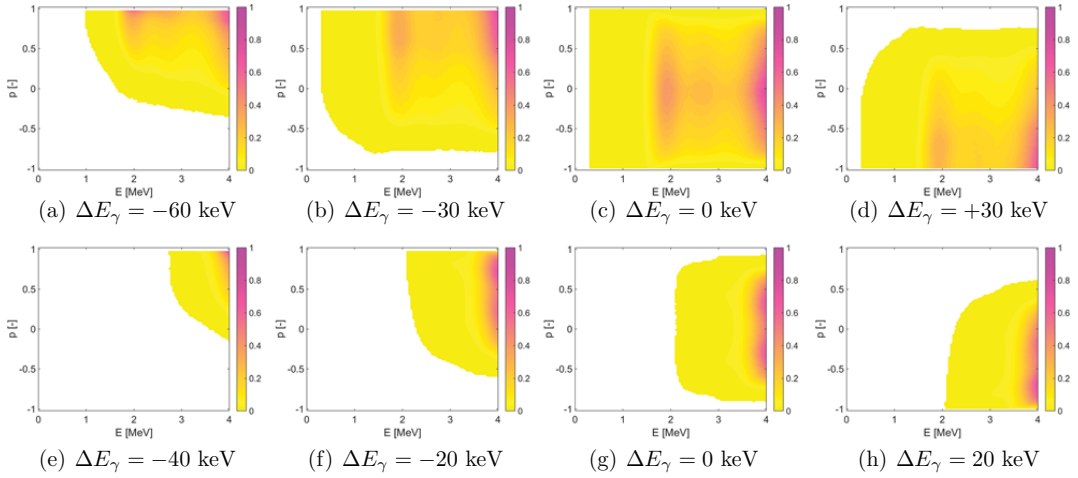


Figure 9. GRS weight functions at various Doppler shifts ΔE_γ for the proposed extra diagnostic view at $\phi = 30^\circ$. Upper row: 4.44 MeV peak. Lower row: 3.2 MeV peak.

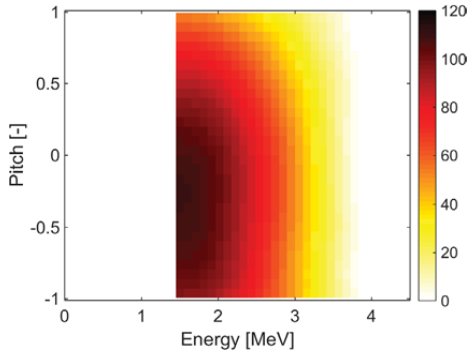


Figure 10. Reconstruction of the asymmetric α -particle distribution function from figure 8(e) with an additional oblique GRS view at $\phi = 30^\circ$.

As we are not sensitive to the sign of the pitch, the mirror image of F_i , \bar{F}_i , produces the same signal as F_i :

$$S_i = W\bar{F}_i. \quad (7)$$

The bar denotes the mirroring operation about $p = 0$. Adding n times equation (6) to m times equation (7) and solving for S gives

$$S_i = \frac{n}{m+n}WF_i + \frac{m}{m+n}W\bar{F}_i. \quad (8)$$

We introduce the function $F_{i,\text{mix}}$ as a mixture of F_i and its mirror image \bar{F}_i :

$$F_{i,\text{mix}} = \frac{n}{m+n}F_i + \frac{m}{m+n}\bar{F}_i. \quad (9)$$

The measurable signal for $F_{i,\text{mix}}$ is

$$S_i = WF_{i,\text{mix}} \quad (10)$$

Table 1. α -particle densities n_α (10^{18} m^{-3}) for $E_\alpha > 1.7 \text{ MeV}$. n_α^+ and n_α^- are the densities for positive and negative pitch, respectively. Their ratio n_α^+/n_α^- measures the asymmetry of the distribution function.

Figure	8(a)	8(b)	8(c)	8(d)	8(e)	8(f)	10
n_α	2.93	2.76	2.39	2.29	2.66	2.57	2.58
n_α^+	1.46	1.37	1.19	1.15	1.19	1.28	1.16
n_α^-	1.46	1.38	1.19	1.14	1.46	1.29	1.43
n_α^+/n_α^-	1.00	0.99	1.00	1.01	0.82	0.99	0.81

which is the same as for \bar{F}_i and F_i . If F_i and \bar{F}_i produce the same signal, then so does any mix of F_i and \bar{F}_i , $F_{i,\text{mix}}$, constructed according to equation (9). This demonstrates our incapability to tell the sign of the pitch apart for entirely perpendicular systems. This result also holds for arbitrary distribution functions since these can be constructed from pixel functions:

$$F = \sum_i F_i. \quad (11)$$

The total signal for an arbitrary distribution function can also be constructed as the sum of signal for pixel functions:

$$S = \sum_i S_i = \sum_i WF_{i,\text{mix}} = W \sum_i F_{i,\text{mix}}. \quad (12)$$

Hence we obtain

$$S = WF_{\text{mix}} \quad (13)$$

showing that any mix of F and \bar{F} gives the same signal. For a completely perpendicular system, we can hence infer F_{mix} from a measured signal by velocity-space tomography. F_{mix} still holds much information about F but we do not make any statement about how the phase-space densities are shared among F and \bar{F} for each pixel according to equation (9).

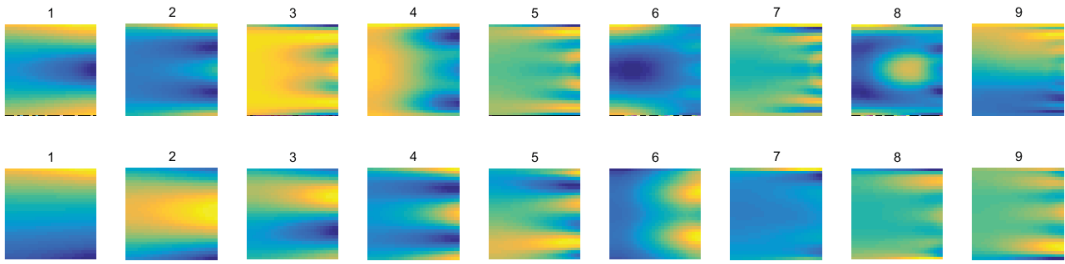


Figure 11. The nine dominant basis functions of a GSVD (yellow: positive, blue: negative). Upper row: the currently planned set of α -particle diagnostics where the first eight basis functions are up–down symmetric. Lower row: the enhanced system with an additional GRS view at $\phi = 30^\circ$. In this cases several of the first nine basis functions are asymmetric and thus allow the construction of asymmetric regularized solutions.

Hence only $f(E, |p|)$ can be inferred by velocity-space tomography for completely perpendicular systems.

Solutions found by Tikhonov regularization tend to be close to up–down symmetric about $p = 0$ for completely perpendicular systems. This is not surprising as all weight functions are up–down symmetric about $p = 0$ in this case. However, it is also instructive to consider the symmetry in terms of the Tikhonov problem. Any mix F_{mix} has the same residual $WF_{\text{mix}} - S$ as F , and hence the least-squares term $\|WF - S\|_2^2$ of Tikhonov’s minimization problem (equation (4)) is not able to separate these. Nevertheless, the Tikhonov penalty term $\|LF_{\text{mix}}\|_2^2 = \|\frac{n}{m+n}LF + \frac{m}{m+n}L\bar{F}\|_2^2$ in equation (4) is smallest for a mix (equation (9)) with $m = n$, i.e. when the mix is symmetric (this follows from a bit of algebra omitted here). Therefore the Tikhonov regularization will select for solutions that are close to up–down symmetric. The up–down symmetric solution is obtained for $m = n = 1$ in equation (9):

$$F_{\text{ud}} = \frac{1}{2}(F + \bar{F}). \quad (14)$$

To directly solve for this up–down symmetric solution and explicitly incorporate our inability to determine the sign of the pitch in the Tikhonov problem, we can pose the problem by computing the up–down symmetric F_{ud} in one halfplane only, e.g. the halfplane with $p > 0$. The signal due to F_{ud} in the full velocity space is

$$S = WF_{\text{ud}}. \quad (15)$$

We introduce the parts of the weight functions with positive pitch, W^+ , and the parts with negative pitch, W^- , and similarly for F_{ud}^+ , F_{ud}^- and \bar{F}_{ud}^- . Then we can write the signal as

$$S = W^+F_{\text{ud}}^+ + W^-F_{\text{ud}}^-. \quad (16)$$

Without changing the result, we can mirror W^- and F_{ud}^- into the upper halfplane and compute the signal as

$$S = W^+F_{\text{ud}}^+ + \bar{W}^-\bar{F}_{\text{ud}}^-. \quad (17)$$

Since we are assuming an up–down symmetric function F_{ud} , we have

$$\bar{F}_{\text{ud}}^- = F_{\text{ud}}^+. \quad (18)$$

Hence

$$S = (W^+ + \bar{W}^-)F_{\text{ud}}^+. \quad (19)$$

For exactly $\phi = 90^\circ$, we also have $W^+ = \bar{W}^-$. For the almost perpendicular system at ITER ($\phi \sim 90^\circ$, but not exactly), F_{ud} is a good approximation to the computed F and illustrates our limitation to infer the pitch. In this case we can simply use equation (19) to infer F_{ud}^+ with the explicit prior information of up–down symmetry. This conveniently uses half the number of grid points but a small error is introduced.

Asymmetries in the original function are not captured by the inversion and are instead redistributed towards a more symmetric inversion as illustrated in figure 8(f). We can still make statements about the 2D velocity distribution function $f(E, |p|)$, just not about the sign of the pitch. We can gain insight into the solution obtained using 1st-order Tikhonov regularization by the generalized singular value decomposition (GSVD) (see [89] and the references therein). It provides the basis of the solutions allowed by the weight matrix W and the regularization matrix L in the Tikhonov problem. As explained in [89], the Tikhonov solution is expressed in terms of the GSVD basis functions, and it can be shown that the Tikhonov solution is dominated by those components that correspond to the largest generalized singular values. The reconstruction of asymmetric Tikhonov solutions from noisy data thus requires that some of the dominant generalized singular values are associated with asymmetric basis functions. Figure 11 illustrates the nine most important basis functions for the currently planned set of α -particle diagnostics and for the enhanced set with an extra GRS view at $\phi = 30^\circ$. The first eight basis functions of the Tikhonov solution for the currently planned set are almost up–down symmetric which results in almost up–down symmetric solutions. On the contrary, several of the nine dominant basis functions for the enhanced set are up–down asymmetric such that it is possible to compute up–down asymmetric solutions.

We can consider the Tikhonov problem to devise a strategy to allow asymmetric regularized solutions. Any asymmetry in the inversion needs to have an incentive in the measurements, which is, however, very hard to deliver with almost

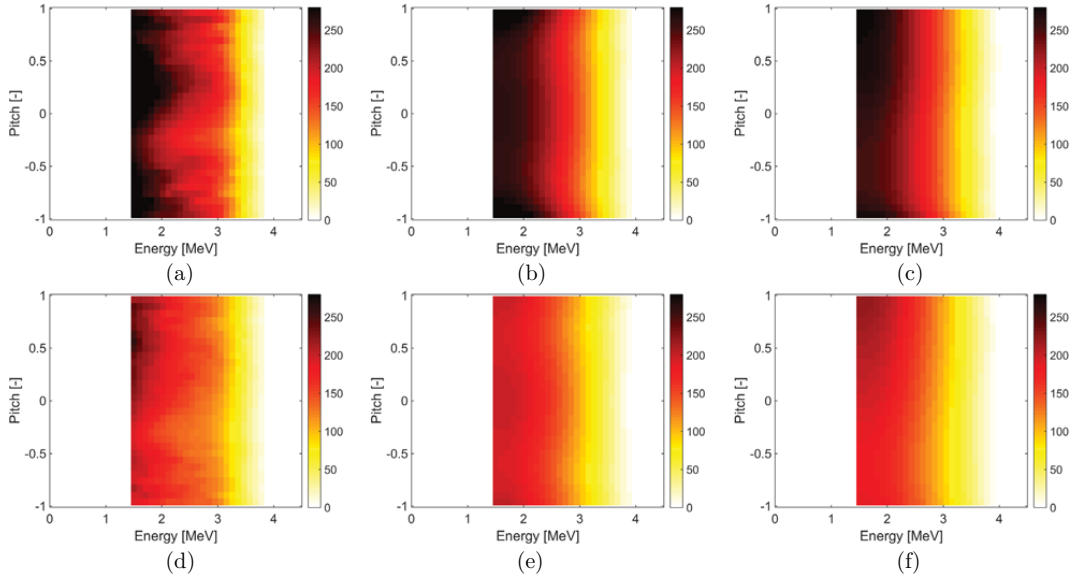


Figure 12. Reconstructions of α -particle distribution functions from ASCOT. (a) ITER baseline scenario. (b) Reconstruction of baseline scenario with planned GRS/CTS diagnostics. (c) As (b) with an extra 30° GRS detector. (d) ITER hybrid scenario with planned GRS/CTS diagnostics. (e) Reconstruction of hybrid scenario with planned GRS/CTS diagnostics. (f) As (e) with an extra 30° GRS detector.

perpendicularly viewing diagnostics. In the Tikhonov problem, the upper row $WF - S$ can introduce asymmetry. The signal is

$$S = WF + \epsilon \quad (20)$$

where ϵ is the noise. Hence the residuals of the true solution F and an erroneous solution F_{mix} , in which the mirror image of the true solution appears, are, respectively,

$$r = |S - WF| = \epsilon \quad (21)$$

$$r_{\text{mix}} = |S - WF_{\text{mix}}| = |W(F - F_{\text{mix}}) + \epsilon|. \quad (22)$$

The three competing terms determining the degree of asymmetry are ϵ , $W(F - F_{\text{mix}})$ and LF_{mix} . The term $W(F - F_{\text{mix}})$ can introduce asymmetry in this case and will effectively prevent the appearance of \bar{F} in the inversion measurements if measurements in tangential or oblique views are made (and if the true F is indeed up-down asymmetric). However, for almost perpendicular views $W(F - F_{\text{mix}})$ is small and it competes with the Tikhonov penalty term λLF_{mix} which will tend to promote evenly distributed or smooth solutions for 0th- and 1st-order Tikhonov regularization, respectively. For almost perpendicular systems this will tend to promote the appearance of \bar{F} in the solution which also explains the data fairly well. We found in section 4 that F_{mix} does not have large enough residuals for the almost perpendicular CTS view (and not at all by GRS) to prevent the appearance of \bar{F} in the solution.

Hence our inversions in section 4 should be understood to represent F_{mix} rather than F , i.e. the amplitude in a given pixel represents a weighted sum of the amplitudes of the pixel and its mirror image. To become more sensitive to the sign of the pitch, the term $W(F - F_{\text{mix}})$ must be increased. This could in principle be done by higher-signal-to-noise ratio measurements but we do not regard this as realistic [62]. The only way

appears to be an extra oblique GRS view which leads to large $W(F - F_{\text{mix}})$ for realistic noise levels.

6. Reconstruction of ASCOT simulations based on GRS and CTS

The classical α -particle slowing-down distribution is symmetric. However, several effects can lead to asymmetry and anisotropy in the α -particle distribution, which we discuss here and in the next section. Here we assess how much anisotropy and asymmetry is expected in ITER based on neoclassical theory. The Monte Carlo orbit-following code ASCOT [90] is used for studies of neoclassical transport of minority particles in toroidal magnetic fusion devices. It follows guiding-center and gyro-orbits of charged particles in realistic geometries. The particles are represented by weighted markers initialized to represent the source population of interest. ASCOT simulates collisional interactions with an assumed Maxwellian background by the Monte Carlo method using given temperature and density profiles.

ASCOT has recently been applied to extensive studies of fusion α -particle wall loads in various ITER scenarios [91, 92] with 3D magnetic background and first wall. The effects of toroidal field ripple, mitigated by ferritic inserts at the toroidal field coils, as well as non-periodic magnetic field perturbations caused by the ferritic test blanket modules and control coils for edge-localized modes were studied. In the simulations, an isotropic α -particle source corresponding to the local DT fusion reaction density of each scenario was assumed, and 100,000 weighted α -markers were followed from their birth energy down to 50 keV.

Table 2. α -particle densities n_α (10^{18} m^{-3}) for $E_\alpha > 1.5 \text{ MeV}$. n_α^+ and n_α^- are the densities for positive and negative pitch, respectively. Their ratio n_α^+/n_α^- measures the asymmetry of the distribution functions.

Scenario	Baseline			Hybrid		
	ASCOT	GRS/CTS	Extra GRS	ASCOT	GRS/CTS	Extra GRS
n_α	7.76	7.55	7.54	5.71	5.58	5.60
n_α^+	4.06	3.78	3.90	3.03	2.80	2.97
n_α^-	3.70	3.77	3.64	2.68	2.78	2.63
n_α^+/n_α^-	1.10	1.00	1.07	1.13	1.01	1.13

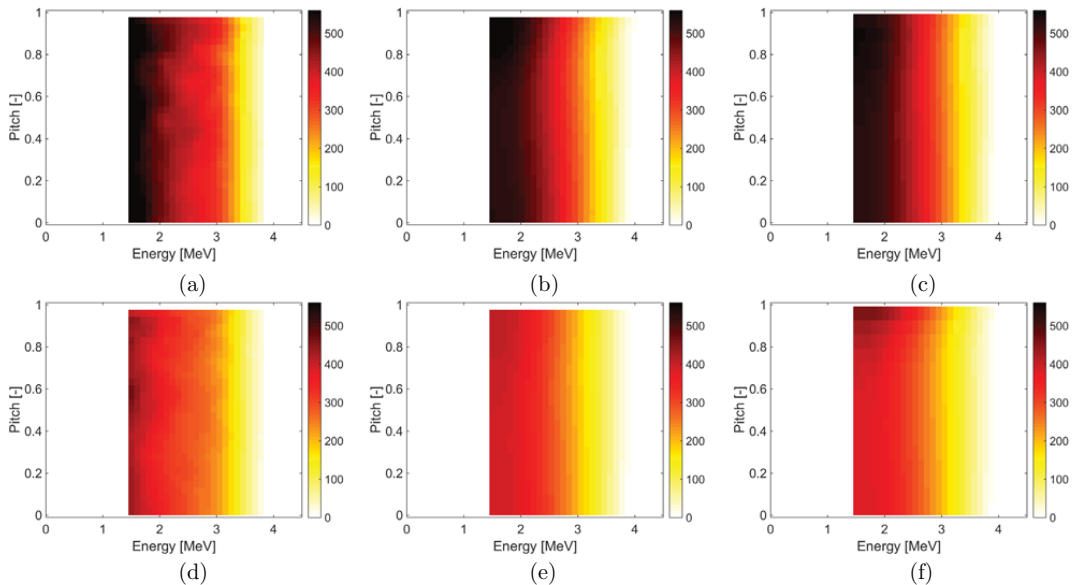


Figure 13. Reconstructions of sign-insensitive α -particle distribution functions $f(E, |p|)$ from ASCOT. (a) ITER baseline scenario represented as $f(E, |p|)$. (b) Full reconstruction of baseline scenario represented as $f(E, |p|)$. (c) Direct reconstruction of $f(E, |p|)$. (d)–(f) As for (a)–(c), but for the ITER hybrid scenario.

In addition to the wall loads that were the primary goal of the simulations previously described [91, 92], the four-dimensional slowing-down distribution $f(R, z, p, E)$ was recorded for the α -population for the ITER baseline (15 MA) and the ITER hybrid (12.5 MA) scenarios in the absence of non-periodic magnetic perturbations. We study these distributions as more realistic models for the α -particles which include anisotropy due to neoclassical transport.

Figure 12 illustrates α -particle distribution functions for the ITER baseline and the ITER hybrid scenarios. Reconstructions from noisy, synthetic measurements based on these are illustrated for the currently planned set of diagnostics and for our proposed extra oblique GRS view at 30° .

Neoclassically, the α -particle distribution is anisotropic even for an isotropic α -particle birth velocity distribution due to the different orbit topologies. Passing particles can either have parallel velocities aligned with the plasma current (positive pitch, co-going), or they have parallel velocities against the current direction (negative pitch, counter-going). There are more particles born on the outboard (low-field) side as compared with the inboard (high-field) side due to the larger

volume. A co-going particle on the outboard midplane drifts first inwards towards the plasma center and then outwards back to its starting flux surface. On the contrary, a counter-going particle drifts first outwards and then inwards back to the starting flux surface. The slowing-down times tend to be larger on the inner flux surfaces traversed by the co-going particles due to the larger temperatures as compared to the outer flux surfaces traversed by the counter-going particles. The steady-state α -particle distribution is therefore expected to be biased towards co-going particles. Similarly, a trapped α -particle with positive pitch on the outboard midplane is on the outer leg of the banana orbit whereas with negative pitch it is on the inner leg. ASCOT simulations contain this type of asymmetry.

As expected, this asymmetry cannot be captured for the currently planned GRS/CTS diagnostic. Our proposed additional 30° GRS view substantially improves the diagnostic of this asymmetry which is only just apparent in figure 12. Nevertheless, the improvement is quantified in table 2 showing the partial α -particle densities with positive and negative pitches and their ratios.

If an additional 30° GRS view cannot be made available, we instead need to be aware that our computed solution is a mix of the solution and its mirror image. In this case it could be misleading to plot the entire function $f(E, p)$. Instead, we propose to present our results in terms of the distribution function $f(E, |p|)$ which is not sensitive to the sign of the pitch. Figure 13 illustrates such halfplane reconstructions for the baseline and the hybrid scenarios without our proposed additional 30° GRS view. We define the function $f(E, |p|) = f(E, p) + \bar{f}(E, p)$ for $p = [0;1]$. The distribution $f(E, |p|)$ is computed in two ways: firstly, we infer the full velocity-space tomography formalism and compute $f(E, |p|)$ afterwards. Secondly, we directly infer $f(E, |p|)$ assuming up-down symmetry. As expected, the two methods give similar results in good agreement with the true solution.

7. Sources of anisotropy in the α -particle distribution

As discussed in section 6, the α -particle distribution is anisotropic even for an isotropic birth velocity distribution in neo-classical transport theory due to the different orbit topologies. This type of asymmetry is reproduced in our ASCOT simulation which showed $n_\alpha^+/n_\alpha^- \sim 1.10$ or larger. In this section we discuss two additional sources of asymmetry.

A second source of asymmetry in the α -distribution is that the birth profile of the α -particles is not isotropic. As α -particles are born in the D(T,n) α reaction, anisotropies in particular in the deuterium velocity distribution due to NBI lead to anisotropies in the α -particle birth profile. The α -distribution will therefore be lopsided towards the direction of the NBI injection, as the suprathermal NBI ions are much more likely to undergo a fusion reaction than the bulk deuterium population. Any rotation induced by the torque of the beam enhances this effect. The ASCOT simulation assumes an isotropic birth profile, and so our simulations do not account for this effect. As the NBI ions are injected with positive pitch, this bias is expected to enhance the asymmetry due to the drift orbits as computed in the ASCOT simulation.

A third source of asymmetry is the physics of wave-particle interaction between energetic particles and Alfvén eigenmodes which is also sensitive to the sign of the pitch of the particle motion. This sensitivity determines the type of instabilities observed and the class of particles which undergo wave-induced transport resulting in anisotropy. To study the drive of eigenmodes, we consider the distribution function $F(E, \mu, P_\zeta)$ in constants-of-motion space. E is the energy, μ the magnetic moment and P_ζ the toroidal canonical angular momentum respectively given by

$$E = \frac{1}{2}mv^2, \mu = \frac{mv_\perp^2}{2B}, P_\zeta = mRv_\zeta - q\Psi \quad (23)$$

where Ψ is the poloidal magnetic flux. When energetic particle velocities are comparable to the phase velocity v_A of the Alfvén wave

$$\frac{\omega}{k} \approx v_A = \frac{B}{\sqrt{\mu_0\rho}}, \quad (24)$$

particles resonantly exchange energy with the waves. ω is the mode frequency, k is the wave number, B is the magnetic field, μ_0 the vacuum permeability, and ρ is the plasma density. Gradients in the distribution function at resonance can provide free energy to drive the modes [93, 94]. The gradient in μ is not relevant as the ion cyclotron frequency exceeds the mode frequency by far so that μ is conserved. For a mode to be unstable, the drive must exceed the damping rate. Gradients in energy are usually negative ($\partial F/\partial E < 0$) whereas the mode frequency ω is positive. Therefore the growth rate associated with gradients in energy is usually negative, which damps the wave:

$$\gamma_L \propto \omega \frac{\partial F}{\partial E}. \quad (25)$$

Spatial radial gradients enter P_ζ , and they can drive an eigenmode given with the growth rate

$$\gamma_L \propto n \frac{\partial F}{\partial P_\zeta} \quad (26)$$

for a given toroidal mode number n (see for example [93] equation (76)). For drive of the mode, the sign of the radial gradient $\partial F/\partial P_\zeta$ matches the sign of the toroidal mode number n . As usually $\partial F/\partial P_\zeta > 0$, positive mode numbers can be driven unstable. (A reversal in sign can suggest that gradients have reversed and that fast particle distributions have become hollow.) The sign of n defines the direction of propagation of the corresponding shear Alfvén wave through the sign of [88]

$$k_\parallel \approx \frac{1}{B} \left(\frac{m}{r} B_\theta + \frac{n}{R} B_\phi \right). \quad (27)$$

k_\parallel is the parallel wave number, m is the poloidal mode number, r and R are the minor and major radii, and B_θ and B_ϕ are the poloidal and toroidal magnetic field. When waves are driven in this manner, they interact most strongly with particles travelling with the same speed and direction given by the resonance condition

$$k_\parallel v_\parallel - \omega = 0. \quad (28)$$

If a single mode interacts with a particle, the quantity $E - (\omega/n)P_\zeta$ is a constant of the motion, and so the particle changes its energy and toroidal canonical angular momentum according to

$$n\Delta E = \omega\Delta P_\zeta \quad (29)$$

which means that loss in energy to the wave leads to outward energetic particle transport towards the edge. The selectivity of the shear Alfvén waves in v_\parallel will thus induce an anisotropy in the α -particle distribution function.

The current set of fast-ion diagnostics is not sensitive to the sign of the pitch, and the consequences of the three sources of asymmetry can therefore not be measured. Given the importance of understanding the α -particle distribution function in

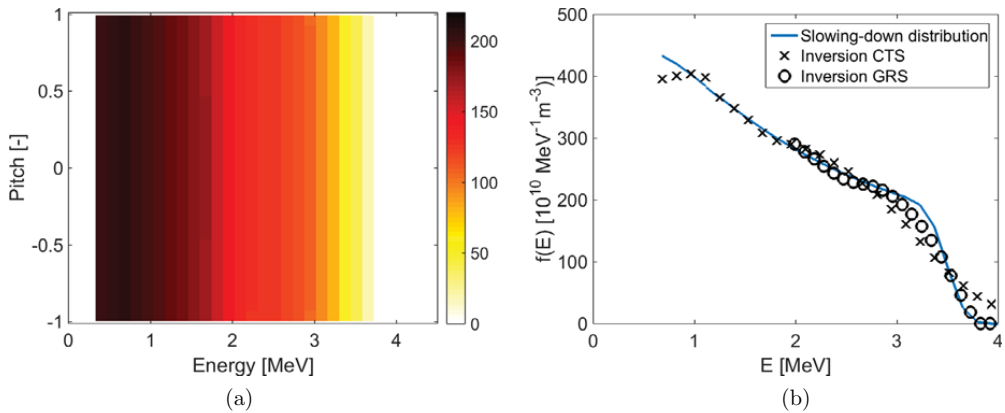


Figure 14. Measurement of energy spectra by velocity-space tomography based on one measured CTS or GRS spectrum and assuming isotropy. (a) The inversion assuming isotropy penalizes gradients in pitch direction strongly and does therefore not depend on the pitch. (b) The inversion effectively constitutes an α -particle energy spectrum which is in excellent agreement with the energy spectrum of the isotropic true solution.

ITER, we therefore propose that an additional GRS detector with an oblique viewing angle should be installed in ITER. With this additional GRS detector, these asymmetries in the α -particle distribution can be tracked. This can give important clues on the physics of wave-particle interaction and the anisotropy of the α -particle distribution function.

8. Measurements of energy spectra for isotropic distributions

Below α -particle energies of 1.7 MeV, CTS is practically the only available diagnostic for confined α -particles. With only one available view, reconstructions of the α -particle distribution function below 1.7 MeV has strong artifacts if standard velocity-space tomography methods are used. The ITER measurement requirements entail measurements of the α -particle energy spectrum and density [77]. The α -particle density could be estimated by assuming a functional form of the α -particle distribution function, e.g. a slowing-down distribution, and fitting the spectra. However, velocity-space tomography is the only known way to measure the energy spectrum.

Here we present a method to nevertheless measure the energy spectrum even if only one view is available. To make up for the lack of measurements, additional prior information is used. We assume the velocity distribution function to be isotropic which is in contrast to the asymmetries observed in sections 6 and 7. A second assumption is that the measurable CTS signal due to NBI ions is negligible compared with measurable CTS signal due to α -particles [26]. If we are prepared to neglect any asymmetry and CTS due to NBI ions, we can encode the isotropy assumption into the first-order Tikhonov regularization which penalizes large gradients in the velocity-distribution function. A solution with a high degree of isotropy can be selected for by penalizing derivatives in pitch direction much more than derivatives in energy direction. Instead of the

standard Tikhonov problem solving for a 2D velocity distribution function, we solve

$$\text{minimize} \left\| \begin{pmatrix} W \\ \lambda_E L_E \\ \lambda_p L_p \end{pmatrix} F - \begin{pmatrix} S \\ 0 \\ 0 \end{pmatrix} \right\|_2 \quad \text{subject to} \quad \begin{matrix} F \geq 0 \\ \lambda_p \gg \lambda_E \end{matrix} \quad (30)$$

which selects for isotropic solutions. Figure 14(a) presents an isotropic inversion where we have chosen $\lambda_p = 100\lambda_E$. The true solution is the α -particle slowing-down distribution function from figure 7(a). The inversion is in excellent agreement with the true solution which is expected since our assumption of isotropy as additional prior information is completely true in this case. However, any anisotropy such as those studied in figure 8 will not be captured with this approach as then the prior information is wrong. In fact, it may not be appropriate to characterize an anisotropic function by an energy spectrum since this parameter disregards any pitch dependence. We compare the energy spectrum of the original function used to compute the synthetic measurements with the energy spectrum of the inversion in figure 14(b). The energy spectrum of the inversion is in good agreement with the energy spectrum of the slowing-down distribution used to compute the synthetic measurements. Hence inversion assuming isotropy now allows us to measure the α -particle energy spectrum down to energies of about 300 keV. The same technique also works for the GRS measurements using one spectrometer for energies close to the 2 MeV resonance and higher (figure 14(b)). In particular the fairly sharp kinks in the energy spectrum in the region around the α -particle birth energy are reconstructed well using GRS.

9. Conclusions

ITER is going to be equipped with collective Thomson scattering (CTS) and γ -ray spectrometry (GRS) systems for

diagnosing α -particles. The velocity space above 1.7 MeV is well diagnosed, but CTS is the only α -particle diagnostic with sensitivity below 1.7 MeV. Due to the perpendicular viewing direction, the extreme pitches $|p| \gtrsim 0.9$ –1 are not observable for $E \lesssim 1.7$ MeV. CTS is sensitive to α -particles down to about 0.3 MeV.

GRS observes the plasma completely perpendicularly and CTS almost perpendicularly to the magnetic field. GRS measurements are hence insensitive, and CTS measurements practically insensitive, to the sign of the pitch of the α -particles. There are three major groups of fast ions: trapped, co-going and counter-going. Since the sign of the pitch cannot be determined with the current set of diagnostics, we cannot tell the groups of co-going and counter-going ions apart. This is a major shortcoming of the fast-ion diagnostic set on ITER, as the physics of fast ions does depend on the sign of the pitch. The α -particle velocity distribution function in the plasma center is neoclassically expected to have more co-passing than counter-passing particles for two reasons: the guiding center drifts of co- and counter-going particles are in opposing directions and the birth profile is biased in the direction of the NBI. The resonance condition with Alfvén waves is also different for co- and counter-going particles. Given the importance of understanding the α -particle distribution function in ITER, we therefore propose that an additional GRS detector with an oblique viewing angle be installed in ITER.

Velocity-space tomography is feasible for energies above 1.7 MeV where GRS and CTS are sensitive. With the currently planned GRS and CTS diagnostics (lacking an oblique view), only the sign-insensitive distribution function $f(E, |p|)$ can be reconstructed from measurements with realistic noise levels. With an extra oblique GRS view, we could also distinguish the sign of the pitch and infer the full distribution function $f(E, p)$. This would substantially improve our diagnostic capabilities to track any anisotropy in the α -particle distribution, for example induced by Alfvén waves.

Below 1.7 MeV velocity-space tomography is not feasible as the GRS is not sensitive so that CTS is practically the only α -particle diagnostic. Nevertheless, we demonstrate that the α -particle energy spectrum, which is an ITER measurement requirement [77], can be inferred for $E \gtrsim 0.3$ MeV based on one CTS spectrum. However, we need to make the approximation that the distribution function is isotropic for measurements of energy spectra based on CTS. The ASCOT code suggests anisotropic α -particle distributions, but the deviation from isotropy is at about 10% acceptable for this measurement.

Acknowledgment

We thank the ITPA Energetic Particle Physics Topical Group for its support. The work leading to this publication has been funded partially by Fusion for Energy under Specific Grant Agreement F4E-393-SG04. This publication reflects the views only of the authors, and Fusion for Energy cannot be held responsible for any use which may be made of the information contained therein. This work has been partially carried out within the framework of the EUROfusion Consortium and

has received funding from the Euratom research and training programme 2014–2018 under grant agreement No 633053. The views and opinions expressed herein do not necessarily reflect those of the ITER Organization, nor the European Commission.

ORCID iDs

M. Salewski  <https://orcid.org/0000-0002-3699-679X>
 M. Nocente  <https://orcid.org/0000-0003-0170-5275>
 A. Shevelev  <https://orcid.org/0000-0001-7227-8448>
 S. Sipilä  <https://orcid.org/0000-0002-2748-0601>

References

- [1] Romanelli F. 2015 *Nucl. Fusion* **55** 104001
- [2] Litaudon X. et al 2017 *Nucl. Fusion* **57** 102001
- [3] Motojima O. et al 2015 *Nucl. Fusion* **55** 104023
- [4] Shimada M. et al 2007 Progress in the ITER physics basis chapter 1: overview and summary *Nucl. Fusion* **47** S1
- [5] Giruzzi G. et al 2015 *Nucl. Fusion* **55** 073002
- [6] Wenninger R. et al 2015 *Nucl. Fusion* **55** 063003
- [7] Wenninger R. et al 2017 *Nucl. Fusion* **57** 016011
- [8] Keilhacker M. et al 1999 *Nucl. Fusion* **39** 209
- [9] Heidbrink W. and Sadler G. 1994 *Nucl. Fusion* **34** 535
- [10] Wong K.L. 1999 *Plasma Phys. Control. Fusion* **41** R1
- [11] Jacquinet J. et al 1999 ITER physics basis chapter 5: physics of energetic ions *Nucl. Fusion* **39** 2471
- [12] Zweben S. et al 2000 *Nucl. Fusion* **40** 91
- [13] Fasoli A. et al 2007 Progress in the ITER physics basis chapter 5: physics of energetic ions *Nucl. Fusion* **47** S264
- [14] Breizman B.N. and Sharapov S.E. 2011 *Plasma Phys. Control. Fusion* **53** 054001
- [15] Sharapov S. et al 2013 *Nucl. Fusion* **53** 104022
- [16] Gorelenkov N., Pinches S. and Toi K. 2014 *Nucl. Fusion* **54** 125001
- [17] Pinches S.D. et al 2015 *Phys. Plasmas* **22** 021807
- [18] Chen L. and Zonca F. 2016 *Rev. Mod. Phys.* **88** 015008
- [19] McClements K.G. and Fredrickson E.D. 2017 *Plasma Phys. Control. Fusion* **59** 053001
- [20] Yavorskij V. et al 2015 *J. Fusion Energy* **34** 774
- [21] Chugunov I.N. et al 2011 *Nucl. Fusion* **51** 083010
- [22] Shevelev A.E. et al 2013 *Nucl. Fusion* **53** 123004
- [23] Gin D. et al 2014 *AIP Conf. Proc.* **1612** 149–52
- [24] Nocente M. et al 2017 *Nucl. Fusion* **57** 076016
- [25] Salewski M. et al 2008 *Rev. Sci. Instrum.* **79** 10E729
- [26] Salewski M. et al 2009 *Plasma Phys. Control. Fusion* **51** 035006
- [27] Salewski M. et al 2009 *Nucl. Fusion* **49** 025006
- [28] Stejner M. et al 2012 *Nucl. Fusion* **52** 023011
- [29] Infante V. 2017 *Fusion Eng. Des.* **123** 663
- [30] Lopes A. 2018 Neutronics analysis of the ITER collective Thomson scattering system submitted *Fusion Eng. Des.* **134** 22–8
- [31] Kiptily V.G., Cecil F.E. and Medley S.S. 2006 *Plasma Phys. Control. Fusion* **48** R59
- [32] Tardocchi M., Nocente M. and Gorini G. 2013 *Plasma Phys. Control. Fusion* **55** 074014
- [33] Boyd D.A. et al 1989 *Nucl. Fusion* **29** 593
- [34] Jarvis O.N. et al 1996 *Nucl. Fusion* **36** 1513
- [35] Kiptily V.G., Cecil F.E., Jarvis O.N. and Mantsinen M.J. 2002 *Nucl. Fusion* **42** 999
- [36] Kiptily V.G. et al 2003 *Rev. Sci. Instrum.* **74** 1753
- [37] Kiptily V.G. et al 2004 *Phys. Rev. Lett.* **93** 115001

- [38] Kiptily V.G. et al 2005 *Nucl. Fusion* **45** L21
- [39] Kiptily V.G. et al 2009 *Nucl. Fusion* **49** 065030
- [40] Kiptily V.G. et al 2012 *Plasma Phys. Control. Fusion* **54** 074010
- [41] Kiptily V.G. et al 2013 *Plasma Fusion Res.* **8** 2502071
- [42] Kiptily V.G. et al 2010 *Nucl. Fusion* **50** 084001
- [43] Murari A. et al 2010 *Rev. Sci. Instrum.* **81** 10E136
- [44] Nocente M. et al 2010 *Rev. Sci. Instrum.* **81** 10D321
- [45] Nocente M. et al 2013 *IEEE Trans. Nucl. Sci.* **60** 1408
- [46] Nocente M. et al 2012 *Nucl. Fusion* **52** 063009
- [47] Tardocchi M. et al 2011 *Phys. Rev. Lett.* **107** 205002
- [48] Eriksson J. et al 2015 *Nucl. Fusion* **55** 123026
- [49] Schneider M. et al 2016 *Nucl. Fusion* **56** 112022
- [50] Nocente M. et al 2015 *Nucl. Fusion* **55** 123009
- [51] Nocente M. et al 2012 *Nucl. Fusion* **52** 094021
- [52] Kiptily V. 2015 *Nucl. Fusion* **55** 023008
- [53] Bindslev H. et al 1999 *Phys. Rev. Lett.* **83** 3206
- [54] Salewski M. et al 2010 *Nucl. Fusion* **50** 035012
- [55] Nielsen S.K. et al 2017 *Phys. Scr.* **92** 024001
- [56] Rasmussen J. et al 2015 *Plasma Phys. Control. Fusion* **57** 075014
- [57] Rasmussen J. et al 2016 *Nucl. Fusion* **56** 112014
- [58] Nishiura M. et al 2014 *Nucl. Fusion* **54** 023006
- [59] Abramovic I. et al 2017 *J. Instrum.* **12** C08015
- [60] Abramovic I. et al Forward modelling of collective Thomson scattering for Wendelstein 7-X plasmas: electrostatic approximation submitted
- [61] Salewski M. et al 2011 *Nucl. Fusion* **51** 083014
- [62] Salewski M. et al 2012 *Nucl. Fusion* **52** 103008
- [63] Salewski M. et al 2013 *Nucl. Fusion* **53** 063019
- [64] Salewski M. et al 2014 *Nucl. Fusion* **54** 023005
- [65] Geiger B. et al 2015 *Nucl. Fusion* **55** 083001
- [66] Salewski M. et al 2015 *Plasma Phys. Control. Fusion* **57** 014021
- [67] Weiland M. et al 2016 *Plasma Phys. Control. Fusion* **58** 025012
- [68] Jacobsen A.S. et al 2016 *Plasma Phys. Control. Fusion* **58** 045016
- [69] Jacobsen A.S. et al 2016 *Plasma Phys. Control. Fusion* **58** 042002
- [70] Salewski M. et al 2016 *Nucl. Fusion* **56** 106024
- [71] Jaulmes F. et al 2016 *Nucl. Fusion* **56** 112012
- [72] Salewski M. et al 2017 *Nucl. Fusion* **57** 056001
- [73] Salewski M. et al 2018 Bayesian integrated data analysis of fast *Fusion Sci. Tech.* **74** 23–36
- [74] Weiland M. et al 2017 *Nucl. Fusion* **57** 116058
- [75] Geiger B. et al 2017 *Plasma Phys. Control. Fusion* **59** 115002
- [76] Moseev D. et al 2018 Recent progress in fast-ion diagnostics for magnetically confined plasmas *Rev. Mod. Plasma Phys.* accepted
- [77] Donn e A.J.H. et al 2007 Progress in the ITER physics basis chapter 7: diagnostics *Nucl. Fusion* **47** S337
- [78] Stagner L. and Heidbrink W. 2017 *Phys. Plasmas* **24** 092505
- [79] Kiptily V.G. 1990 *Fusion Sci. Technol.* **18** 583
- [80] Cazzaniga C. et al 2015 *Nucl. Instrum. Methods A* **778** 20
- [81] Nocente M. et al 2016 *Rev. Sci. Instrum.* **87** 11E714
- [82] Heidbrink W.W. et al 2007 *Plasma Phys. Control. Fusion* **49** 1457
- [83] Jacobsen A.S. et al 2015 *Nucl. Fusion* **55** 053013
- [84] Salewski M. et al 2015 *Nucl. Fusion* **55** 093029
- [85] Salewski M. et al 2016 *Nucl. Fusion* **56** 046009
- [86] Jacobsen A.S. et al 2017 *Rev. Sci. Instrum.* **88** 073506
- [87] Gaffey J.D. 1976 *J. Plasma Phys.* **16** 149
- [88] Pinches S.D. et al 2004 *Plasma Phys. Control. Fusion* **46** B187
- [89] Hansen P.C. 2010 *Discrete Inverse Problems* (Philadelphia: SIAM)
- [90] Hirvijoki E. et al 2014 *Comput. Phys. Commun.* **185** 1310
- [91] Kurki-Suonio T. et al 2016 *Nucl. Fusion* **56** 112024
- [92] Varje J. et al 2016 *Nucl. Fusion* **56** 046014
- [93] Porcelli F. et al 1994 *Phys. Plasmas* **1** 470
- [94] Heidbrink W.W. et al 2008 *Nucl. Fusion* **48** 084001

Reference [15]

[15]. M Salewski et al. (2019) *Journal of Instrumentation* **14** C05019.
Diagnostic of fast-ion energy spectra and densities in magnetized plasmas

5TH INTERNATIONAL CONFERENCE FRONTIERS IN DIAGNOSTICS TECHNOLOGIES
3–5 OCTOBER 2018
INFN FRASCATI, ROME, ITALY

Diagnostic of fast-ion energy spectra and densities in magnetized plasmas

M. Salewski,^{a,1} M. Nocente,^{b,c} B. Madsen,^a I. Abramovic,^d G. Gorini,^{b,c} A.S. Jacobsen,^e V.G. Kiptily,^e S.B. Korsholm,^a D. Moseev,^d S.K. Nielsen,^a A.F.L. Poulsen,^a J. Rasmussen,^a M. Tardocchi,^c B. Geiger,^f J. Eriksson,^g the JET Contributors,² the ASDEX Upgrade Team and the EUROfusion MST1 Team³

^aTechnical University of Denmark, Kgs. Lyngby, Denmark

^bDepartment of Physics, University of Milano Bicocca, Milano, Italy

^cIstituto di Fisica del Plasma, Consiglio Nazionale delle Ricerche, Milano, Italy

^dMax-Planck-Institut für Plasmaphysik, Greifswald, Germany

^eCCFE, Culham Science Centre, Abingdon, Oxon, United Kingdom

^fMax-Planck-Institut für Plasmaphysik, Garching, Germany

^gDepartment of Physics and Astronomy, Uppsala University, Sweden

E-mail: msal@dtu.dk

ABSTRACT: The measurement of the energy spectra and densities of α -particles and other fast ions are part of the ITER measurement requirements, highlighting the importance of energy-resolved energetic-particle measurements for the mission of ITER. However, it has been found in recent years that the velocity-space interrogation regions of the foreseen energetic-particle diagnostics do not allow these measurements directly. We will demonstrate this for γ -ray spectroscopy (GRS), collective Thomson scattering (CTS), neutron emission spectroscopy and fast-ion D_α spectroscopy by invoking energy and momentum conservation in each case, highlighting analogies and differences between the different diagnostic velocity-space sensitivities. Nevertheless, energy spectra and densities can be inferred by velocity-space tomography which we demonstrate using measurements at JET and ASDEX Upgrade. The measured energy spectra agree well with corresponding simulations. At ITER, α -particle energy spectra and densities can be inferred for energies larger than 1.7 MeV by velocity-space tomography based on GRS and CTS. Further, assuming isotropy of the α -particles in velocity space, their energy spectra and densities can be inferred by 1D inversion

¹Corresponding author.

²See author list of [1].

³See author list of [2].

of spectral single-detector measurements down to about 300 keV by CTS. The α -particle density can also be found by fitting a model to the CTS measurements assuming the α -particle distribution to be an isotropic slowing-down distribution.

KEYWORDS: Nuclear instruments and methods for hot plasma diagnostics; Computerized Tomography (CT) and Computed Radiography (CR)

2019 JINST 14 C05019

Contents

1	Introduction	1
2	Velocity-space interrogation regions	2
3	Energy and momentum conservation principles for fast-ion diagnostics	3
4	Generic energy and momentum equations for NES, GRS, CXRS, FIDA, TS and CTS	5
5	Velocity-space tomography and model fitting	7
6	Conclusions	11

1 Introduction

Measurements of the densities and energy spectra of α -particles and other fast ions in ITER are considered highly important and constitute the ITER measurement requirements for energetic particle diagnostics [3]. However, in recent years it was found that the spectra measurable by common fast-ion diagnostics are sensitive to restricted yet rather broad regions in phase space such that densities and energy spectra cannot be directly measured by individual diagnostics. This is illustrated by so-called weight functions [4–14]. Examples of weight functions for neutron emission spectrometry (NES) [15, 16], γ -ray spectrometry (GRS) [17, 18], collective Thomson scattering (CTS) [19–21] and fast-ion D_α (FIDA) spectroscopy [22–25] are presented in figure 1 [14]. The 2D velocity space in figure 1 is described by the energy E and the pitch $p = v_{\parallel}/v$ where v_{\parallel} is the velocity component along the magnetic field and v is the speed. Each point in a measured spectrum is sensitive to a particular region in 2D velocity space such as those illustrated in red in figure 1. We also illustrate a hypothetical weight function which would allow direct energy resolution. One-step reaction GRS [26] is the only diagnostic with some direct energy resolution [9]. The shapes of weight functions for these diagnostics will be explained in this paper by invoking energy and momentum conservation.

Despite the restricted velocity-space coverage of individual measurements, energy spectra and densities can still be found by solving an inverse problem to infer the fast-ion 2D velocity distribution function from the combined set of available measurements. This is referred to as velocity-space tomography [13, 14, 24, 27–41]. Integration over the pitch gives the energy spectrum [33], and subsequent integration over the energy gives the density [31, 35]. If we assume isotropy in velocity space, we can use this approach to also invert measurements from only one detector [40]. Whereas velocity-space tomography is the only known way to measure energetic-particle energy spectra, the energetic-particle density can also be inferred by fitting spectra to the measurements assuming a functional form of the velocity distribution function, e.g. a slowing-down distribution.

This paper consists of two main parts. Firstly, we will show that the velocity-space interrogation regions of fast-ion diagnostics are a consequence of energy and momentum conservation. We will consider one-step reaction GRS, NES, FIDA (or generally charge-exchange recombination spectroscopy (CXRS)) and CTS as well as the analogous electron diagnostic Thomson scattering (TS). Secondly, we will demonstrate techniques to measure energy spectra by velocity-space tomography and related data inversion techniques using measurements at ASDEX Upgrade and JET as well as modelling for ITER.

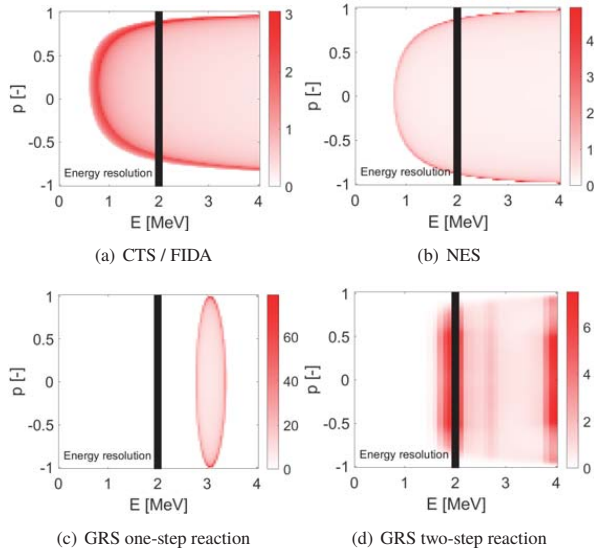


Figure 1. Examples of weight functions [a.u.] of various fast-ion diagnostics illustrated in red as compared to the form required by a weight function to achieve direct energy resolution, marked by a black line at 2 MeV.

2 Velocity-space interrogation regions

Energy and momentum conservation determine to which velocity-space regions energetic-particle diagnostics are sensitive. These conservation principles relate the energy and momentum of the energetic particle in the plasma to the energy and momentum of the detectable particle (including photons). This is well-established for NES and GRS weight functions [7, 9, 10, 30]. FIDA and CTS as well as the related diagnostics CXRS and TS exploit the Doppler shift. The Doppler shift is in turn implied by energy and momentum conservation [42]. Hence we invoke energy and momentum conservation for each diagnostic and derive the shape of weight functions from these principles. This common framework highlights reasons for analogies and differences among the weight functions. To focus on the large-scale shapes of the observable velocity-space regions, we here neglect effects leading to small changes in the observable velocity space, such as non-zero

plasma temperatures, Stark splitting or instrumental broadening [6, 7, 9, 30]. We do not consider any reaction probabilities since they influence only the amplitudes of the weight functions but not the boundaries. [6, 7, 9, 30].

The following sections will show that, for each diagnostic, the fast-ion velocity component u along the line-of-sight appears when the momentum and energy equations are combined. u is related to the energy E_d of the detectable particle (including photons) by these conservation principles. u is also related to the gyroangle Γ of the energetic particle according to [5]

$$u = v_{\parallel} \cos \phi + v_{\perp} \sin \phi \cos \Gamma \quad (2.1)$$

where ϕ is the observation angle between the line-of-sight and the magnetic field and v_{\perp} is the velocity component perpendicular to the magnetic field. Given u , ϕ and $(v_{\parallel}, v_{\perp})$, the corresponding gyroangles can be computed. The resulting probability that the detected particle has energies in the interval $[E_{d,1}, E_{d,2}]$ can be related to the probability that the fast ion has a line-of-sight velocity in the interval $[u_1, u_2]$ (see next section) and to the corresponding fraction of the gyroorbit [6]:

$$\begin{aligned} \text{prob}(E_{d,1} < E_d < E_{d,2} | \phi, v_{\parallel}, v_{\perp}) &= \text{prob}(u_1 < u < u_2 | \phi, v_{\parallel}, v_{\perp}) \\ &= \frac{\Gamma_1 - \Gamma_2}{\pi} = \frac{1}{\pi} \left(\arccos \frac{u_1 - v_{\parallel} \cos \phi}{v_{\perp} \sin \phi} - \arccos \frac{u_2 - v_{\parallel} \cos \phi}{v_{\perp} \sin \phi} \right). \end{aligned} \quad (2.2)$$

The unobserved velocity space corresponds to a probability of zero such that no gyroangle exists allowing a detection in the interval $[E_{d,1}, E_{d,2}]$. The observed velocity space corresponds to probabilities between zero and one. In this case a detection in the interval $[E_{d,1}, E_{d,2}]$ is possible on some parts of the gyroorbit (for prob=1 on the full orbit). Equation 2.2 shows how to find the observable velocity space from the line-of-sight velocity u for the diagnostics that we consider. In the following we will calculate u from the energy E_d and momentum p_d of the detected particle for each diagnostic using energy and momentum conservation.

3 Energy and momentum conservation principles for fast-ion diagnostics

We first formulate the specific non-relativistic energy and momentum conservation equations for NES, GRS, FIDA, CXRS and CTS that connect the projected velocities u with the velocities of the detected particles (including photons). TS will be treated relativistically. In the second step we will solve a set of generic conservation equations modelling all of these fast-ion diagnostics.

GRS and NES:

Consider a generic one-step fusion reaction between a fast particle (f) and a reactant thermal particle (r) to form a reaction product (pr) releasing a detectable photon or a neutron (d). The non-relativistic energy and momentum conservation equations for particles with mass m , velocity \mathbf{v} and $v = |\mathbf{v}|$ are, respectively,

$$\frac{1}{2} m_f v_f^2 + \frac{1}{2} m_r v_r^2 + Q = \frac{1}{2} m_{pr} v_{pr}^2 + E_d, \quad (3.1)$$

$$m_f \mathbf{v}_f + m_r \mathbf{v}_r = m_{pr} \mathbf{v}_{pr} + \mathbf{p}_d. \quad (3.2)$$

Here Q is the released energy, and E_d and \mathbf{p}_d are the energy and momentum of the emitted detected particle (or photon), respectively.

FIDA and CXRS:

Usually FIDA weight functions are calculated invoking the Doppler shift. Here we instead invoke energy and momentum conservation which in turn imply the Doppler shift [42]. In the rest frame of the excited atom, the energy of the released photon, Q , is the difference between the energy levels U and U' before and after the emission, respectively: $Q = U - U' = hf_0$ where h is Planck's constant and f_0 is the frequency. Primes (') mark quantities after the reaction. In the lab frame the total energy is the sum of the kinetic energy and the energy level U . Energy and momentum conservation of the D_α -emission process in the lab frame are then [42]

$$\frac{1}{2}m_f v_f^2 + U = \frac{1}{2}m_f v_f'^2 + U' + E_d, \quad (3.3)$$

$$m_f \mathbf{v}_f = m_f \mathbf{v}_f' + \mathbf{p}_d. \quad (3.4)$$

CTS and TS:

Whereas TS measures the distribution of electrons in the plasma, CTS measures the distribution of ions. Scattering off ions is negligible compared with scattering off electrons due to the large proton-to-electron mass ratio $m_p/m_e = 1836$. The difference between TS and CTS can be illustrated using the dressed particle model which is a simplification of a rigorous kinetic treatment. The dressed particle model is well-suited to highlight the analogy between CTS and TS and, together with energy and momentum conservation, also with other fast-ion diagnostics. A test charge in a plasma is surrounded by other charges that screen the potential of the test charge. The size of this screening cloud is on the order of the Debye length λ_D . A test particle together with its screening cloud is referred to as a dressed particle. For example, the screening cloud of an ion is composed of (a surplus of) electrons and (a lack of) ions. We consider very fast ions so that thermal ions are too slow to participate strongly in the screening, and hence the screening cloud consists mostly of electrons.

In incoherent Thomson scattering, the wavelength of the fluctuation wave field is much smaller than the Debye length, so that scattering occurs incoherently at random phases of the wave electric field. The scattering power due to individual electrons can then be summed to obtain the power due to Thomson scattering from a plasma. Hence we can consider energy and momentum conservation for an individual electron and incident (index i) and scattered (index s) photons,

$$\hbar\omega_i + \frac{1}{2}m_e v^2 = \hbar\omega_s + \frac{1}{2}m_e v'^2, \quad (3.5)$$

$$\hbar\mathbf{k}_i + m_e \mathbf{v} = \hbar\mathbf{k}_s + m_e \mathbf{v}', \quad (3.6)$$

where $\hbar = h/2\pi$, ω is the angular frequency, and \mathbf{k} is the wave vector.

For CTS in the dressed particle model, the radiation is scattered off electrons in the screening cloud surrounding ions. As the wavelength of the mainly ion-induced fluctuation wave field is much larger than the Debye length, the phases of the fluctuation wave field of the test charge and the electrons in the screening cloud are correlated. Scattering from a test electron is therefore balanced by a lack of scattering from its screening cloud, and hence the electron signature in the detectable

spectra is strongly suppressed. This cancellation does not occur for the comparatively immobile ions which are therefore revealed by coherent or collective scattering from their screening clouds. Following the dressed particle model, the energy and momentum equations are identical with those for incoherent Thomson scattering with $m_e \rightarrow m_{di}$, where $m_{di} \approx m_i$ is the dressed ion mass which is about the same as the ion mass.

4 Generic energy and momentum equations for NES, GRS, CXRS, FIDA, TS and CTS

We can now formulate non-relativistic energy and momentum equations which conveniently encompass all of the above emission processes. These energy and momentum equations have in common that the energetic particle with energy $\frac{1}{2}m_f v_f^2$ and momentum $m_f \mathbf{v}_f$ undergoes a process in which a detectable particle with energy E_d and momentum \mathbf{p}_d is formed. The detected particle may be a photon. In NES, GRS and CTS, the process involves another reactant with energy E_r and momentum \mathbf{p}_r , whereas for FIDA we will just set these to zero. Apart from the detectable particle, another particle with mass carries the energy $\frac{1}{2}m_{pr} v_{pr}^2$ and momentum $m_{pr} \mathbf{v}_{pr}$ for all processes. However, for CTS and FIDA $m_{pr} = m_f$ in a non-relativistic treatment. Lastly, there may be a change of the excitation states releasing an energy $Q = U - U'$ in the rest frame. Thus we get the non-relativistic energy and momentum equations in the lab frame:

$$\frac{1}{2}m_f v_f^2 + E_r + U = \frac{1}{2}m_{pr} v_{pr}^2 + U' + E_d, \quad (4.1)$$

$$m_f \mathbf{v}_f + \mathbf{p}_r = m_{pr} \mathbf{v}_{pr} + \mathbf{p}_d. \quad (4.2)$$

To solve these, we eliminate v_{pr} in the energy equation using the momentum equation:

$$\frac{1}{2}m_f v_f^2 + E_r + U = \frac{m_f^2}{2m_{pr}} v_f^2 - \frac{m_f}{m_{pr}} \mathbf{v}_f \cdot (\mathbf{p}_d - \mathbf{p}_r) + \frac{1}{2m_{pr}} (\mathbf{p}_d - \mathbf{p}_r)^2 + U' + E_d. \quad (4.3)$$

The fast-ion velocity appears in direction-independent terms as $v_f^2 = v_{\parallel}^2 + v_{\perp}^2$ and in the direction-dependent dot products including \mathbf{v}_f . The projection of the energetic particle velocity onto the momentum vector of the detectable particle, $\mathbf{v}_f \cdot \mathbf{p}_d$, highlights the selective role of the geometry of the line-of-sight. We solve for $\mathbf{v}_f \cdot (\mathbf{p}_d - \mathbf{p}_r)$ and set the difference in internal energies to $Q = U - U'$:

$$\mathbf{v}_f \cdot (\mathbf{p}_d - \mathbf{p}_r) = \frac{m_f - m_{pr}}{2} (v_{\parallel}^2 + v_{\perp}^2) + \frac{m_{pr}}{m_f} (E_d - E_r - Q) + \frac{(\mathbf{p}_d - \mathbf{p}_r)^2}{2m_f}. \quad (4.4)$$

Equation 4.4 is valid for all diagnostics that we consider. For NES and GRS, we neglect the energy and momentum of the thermal species ($v_f \gg v_r$). They are routinely taken into account in numeric weight function computations using the GENESIS code. For FIDA, these terms are not relevant and we consequently set them to zero.

The projected velocity onto the line-of-sight appears in the dot product $\mathbf{v}_f \cdot \mathbf{p}_d = u p_d$ where p_d is the magnitude of \mathbf{p}_d . Thus we get a simplified equation for the projected velocity u for NES, GRS and FIDA:

$$u = \frac{m_f - m_{pr}}{2p_d} (v_{\parallel}^2 + v_{\perp}^2) + \frac{m_{pr}}{m_f} \frac{E_d - Q}{p_d} + \frac{p_d}{2m_f}. \quad (4.5)$$

For NES, the detected particle is a neutron with $E_d = \frac{1}{2}m_n v_n^2$ and $p_d = m_n v_n$:

$$u_{\text{NES}} = \frac{m_f - m_{pr}}{2m_n v_n} (v_{\parallel}^2 + v_{\perp}^2) + \frac{m_{pr} \frac{1}{2}m_n v_n^2 - Q}{m_f m_n v_n} + \frac{m_n v_n}{2m_f}. \quad (4.6)$$

This is the result obtained in reference [7]. Substitution of equation (4.6) into equation (2.2) reveals the velocity space interrogated by NES.

For GRS, the detected particle is a γ -ray with $E_d = E_\gamma$ and $p_d = E_\gamma/c$ where c is the speed of light:

$$u_{\text{GRS}} = c \left(\frac{m_f - m_{pr}}{2E_\gamma} (v_{\parallel}^2 + v_{\perp}^2) + \frac{m_{pr} E_\gamma - Q}{m_f E_\gamma} + \frac{E_\gamma}{2m_f c^2} \right) \approx c \left(\frac{m_f - m_{pr}}{2E_\gamma} (v_{\parallel}^2 + v_{\perp}^2) + \frac{m_{pr} E_\gamma - Q}{m_f E_\gamma} \right). \quad (4.7)$$

This is the result obtained in reference [9]. Substitution of equation (4.7) into equation (2.2) reveals the velocity space interrogated by GRS. A difference between the neutron and γ -ray spectrometry equations is that the last term is negligible for the γ -ray diagnostic as it is smaller by a factor of the order of the ratio of the energy of the γ and the rest energy of the ion.

Similar to GRS, FIDA relies on the emission of a photon. Hence we obtain basically the same equation for FIDA as for γ -rays. However, for FIDA we can set $m_{pr} = m_f$. We also set $E = hf$, $Q = hf_0$ and $p_d = hf/c$:

$$u_{\text{FIDA}} = c \left(\frac{f - f_0}{f} + \frac{hf}{2m_f c^2} \right) \approx c \left(\frac{f - f_0}{f} \right) = c \left(\frac{\lambda_0 - \lambda}{\lambda_0} \right). \quad (4.8)$$

Neglecting the second term containing the small ratio of the photon energy and the rest energy of the fast ion ($hf/m_f c^2 \sim 10^{-9}$), we obtain the usual Doppler shift formula determining the large-scale shape of FIDA weight functions which can be substituted into equation (2.2) to obtain the interrogated velocity space.

The analogy of the line-of-sight velocities obtained for FIDA (equation (4.8)) and GRS (equation (4.7)) becomes clear. The first term in equation (4.7) is quadratic in v_{\parallel} and v_{\perp} resulting in the circular shapes of one-step reaction GRS weight functions in $(v_{\parallel}, v_{\perp})$ -space. It drops out for $m_{pr} = m_f$ so that no circular shapes appear in Doppler-shift based weight functions (for the classical treatment). The second term in equation (4.7) is related to the Doppler shift. This term has a prefactor m_{pr}/m_f for GRS. For the usual Doppler shift as in FIDA, we have $m_{pr} = m_f$, whereas $m_{pr} \neq m_f$ describes the recoil due to the emission of the energetic γ -ray. The third term in equation (4.6) is important for NES only but is negligible for GRS and FIDA.

For CTS, consider first the generic equation (4.4). Introducing the energies and momenta of the incident photon (i) and the scattered photon (s), we set

$$\mathbf{p}_d = \hbar \mathbf{k}_s, \quad \mathbf{p}_r = \hbar \mathbf{k}_i, \quad E_d = \hbar \omega_s, \quad E_r = \hbar \omega_i. \quad (4.9)$$

As the ion mass and the internal energies are not changed, we have $m_{pr} = m_f$ and $Q = 0$. Equation 4.4 simplifies to

$$\mathbf{v}_f \cdot (\mathbf{k}_s - \mathbf{k}_i) = \omega_s - \omega_i + \frac{\hbar(\mathbf{k}_s - \mathbf{k}_i)^2}{2m_f}. \quad (4.10)$$

We also introduce the differences (δ) of the frequencies and wavevectors of the incident photon (i) and the scattered photon (s),

$$\mathbf{k}_\delta = \mathbf{k}_s - \mathbf{k}_i, \quad \omega_\delta = \omega_s - \omega_i, \quad (4.11)$$

and recover the Doppler shift relation for TS and CTS

$$\omega_\delta = \mathbf{v}_f \cdot \mathbf{k}_\delta - \frac{\hbar k_\delta^2}{2m_f}. \quad (4.12)$$

With $\mathbf{v}_f \cdot \mathbf{k}_\delta = uk_\delta$ we obtain

$$u_{CTS} = \frac{\omega_\delta}{k_\delta} + \frac{\hbar k_\delta}{2m_f}, \quad (4.13)$$

where the second term can be neglected. Equation 4.13 describes two Doppler shifts as apparent from equation (4.10): $\mathbf{v}_f \cdot \mathbf{k}_i$ and $\mathbf{v}_f \cdot \mathbf{k}_s$. The probe radiation has a Doppler shifted frequency in the rest frame of the particle and the emitted radiation from the moving particle has yet another Doppler-shifted frequency in the lab frame. The observable velocity space for a CTS measurement is found by substitution of equation (4.13) into equation (2.2).

Electrons in hot plasmas have large speeds, often a significant fraction of the speed of light, so that a relativistic description may sometimes be necessary. The relativistic energy and momentum equations for CTS are

$$\hbar\omega_i + \gamma_f m_f c^2 = \hbar\omega_s + \gamma'_f m_f c^2, \quad (4.14)$$

$$\hbar\mathbf{k}_i + \gamma_f m_f \mathbf{v}_f = \hbar\mathbf{k}_s + \gamma'_f m_f \mathbf{v}'_f, \quad (4.15)$$

containing the Lorentz factor γ_e with $\gamma_e^2 = 1/(1 - v_e^2/c^2)$. The relativistic solution is

$$\omega_\delta = \mathbf{v}_e \cdot \mathbf{k}_\delta - \frac{\hbar}{2\gamma_e m_e} \left(k_\delta^2 - \frac{\omega_\delta^2}{c^2} \right), \quad (4.16)$$

from which we can recover the non-relativistic equation by setting $\gamma_e \rightarrow 1$ and seeking the solution with $k_\delta^2 \approx \frac{\omega_\delta^2}{u^2} \gg \frac{\omega_\delta^2}{c^2}$.

5 Velocity-space tomography and model fitting

The previous section showed that the principles of energy and momentum conservation suggest that the CTS, FIDA, GRS and NES observe broad regions in velocity space, so that the determination of fast-ion energy spectra from the measurements directly is not possible. Some one-step GRS reactions have direct energy resolution [9], but unfortunately they do not involve α -particles. Further, the diagnostics observe restricted parts of velocity space, so that the direct determination of fast-ion densities is not possible, either. Nevertheless, these important parameters can still be determined by various analysis techniques.

Ideally, the interrogation regions of individual diagnostics can be combined to get a full coverage of the fast-ion phase-space. Integrated data analysis of several diagnostics by velocity-space tomography allows the determination of the 2D velocity distribution function. The integral

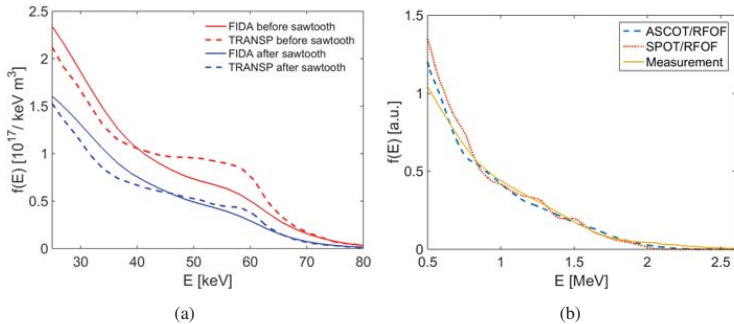


Figure 2. Measurements of fast-ion energy spectra and corresponding simulations. The measurements are obtained by velocity-space tomography and integration over the pitch. (a) FIDA measurement and TRANSP simulation of a fast-ion energy spectrum before and after a sawtooth crash in ASDEX Upgrade discharge #32323 [35]. (b) Combined GRS and NES measurements of an energy spectrum of deuterium ions accelerated by 3rd harmonic ICRF in JET discharge #86459 [36]. The measurements are compared to ASCOT/RFOF and SPOT/RFOF simulations.

over pitch is the energy spectrum [33] and the double integral over energy and pitch gives us the fast-ion density [31, 35]. As the velocity-space tomography problem is ill-posed, we must regularize the solution by prior information. A popular approach is to assume the velocity distribution function to be smooth. As compared to other techniques discussed below, this approach uses the least amount of prior information but requires many measurements.

Energy spectra determined from FIDA measurements in this way appear in figure 2(a) along with a corresponding TRANSP simulation. At ASDEX Upgrade [43], five FIDA spectra can be acquired simultaneously [33]. The energy spectra show the distribution of core fast-ion energies in ASDEX Upgrade discharge #32323 just before and after a sawtooth crash. A velocity-space tomography movie of this event has been published previously [35]. Here we focus on energy spectra. The neutral beam deuterium injection energy is 60 keV so that the energy spectra are expected to have kinks at 60 keV and 30 keV (half injection energy). The inversions from FIDA measurements show weaker kinks at these energies than the TRANSP simulation. This is expected since the measured 2D velocity distribution functions have smaller beam injection peaks than the TRANSP simulations which is explained by the first-order Tikhonov regularization [35].

Figure 2(b) shows measured energy spectra of fast deuterium ions accelerated by 3rd harmonic ICRF heating at JET [1, 44] as compared to ASCOT/RFOR and SPOT/RFOF simulations [46, 47]. A high-resolution GRS detector and three NES detectors acquired spectra simultaneously [15]. Velocity-space tomography based on the GRS and NES measurements gives a 2D velocity distribution function, from which we obtain the energy spectra by integration over pitch. The agreement between theory and experiment is excellent.

Several important points are lost when considering just the energy spectra, which constitute the α -particle ITER measurement requirement [3], instead of 2D velocity distribution functions. Firstly, the strong anisotropy of the 2D velocity distribution function of the NBI ions is lost due to the

integration over pitch. Secondly, the measured and simulated energy distributions are monotonic whereas the measured and simulated 2D velocity distribution functions have peaks at the full and half injection energy such that a bump-on-tail is formed in 2D velocity space. Nevertheless, energy spectra provide an intuitive meeting ground between theory and experiment. The rich information can further be simplified by integration over the energy to obtain the fast-ion density. The agreement of simulated and measured fast-ion densities determined by this approach is good [9, 31].

ITER will be equipped with CTS [5, 40, 48–51] and GRS systems [18, 52, 53]. Velocity-space tomography should be possible for α -particle energies $E_\alpha > 1.7$ MeV [40]. A reconstruction of an energy spectrum computed from synthetic GRS and CTS measurements at ITER [18, 49, 50] appears in figure 3. The α -particle energy spectrum can be reconstructed by integrated data analysis of the GRS and CTS measurements. We stress again that any velocity-space anisotropy of the α -particle distribution function is not reflected in the energy spectra. To study anisotropy, the full 2D distribution function must be measured but this requires an additional detector with an oblique line-of-sight with respect to the magnetic field [40].

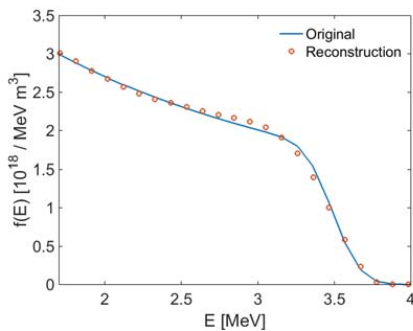


Figure 3. Reconstruction of the energy spectrum for $E > 1.7$ MeV for an isotropic α -particle slowing-down distribution based on synthetic GRS and CTS measurements.

For $0.5 \text{ MeV} < E_\alpha < 1.7 \text{ MeV}$, CTS will be the only direct diagnostic for confined α -particles at ITER since GRS is not sensitive below 1.7 MeV. The lower energy limit arises from the assessment where scattering due to α -particles significantly exceeds scattering due to thermal deuterium and tritium. Depending on assumptions, energies down to about 0.3–0.4 MeV might be accessible. Despite the absence of other diagnostics entering an integrated data analysis, α -particle energy spectra and densities can still be determined using CTS spectra only. To do this we here assume the distribution function to be smooth and isotropic in velocity space [40]. An example of this technique appears in figure 4(a). In particular the region below 1.7 MeV, where GRS is not sensitive, is well reconstructed from the CTS measurements. However, the kink near the α -particle birth energy is not as well reconstructed as is possible in the 2D inversion based on GRS and CTS. The same approach works for single-detector GRS measurements at ITER (figure 4(b)). The GRS inversion does an excellent job at reconstructing the α -particle birth energy due to the very good sensitivity at high energies but GRS becomes insensitive for energies below 1.7 MeV. This 1D inference technique is also useful for runaway electron measurements [54].

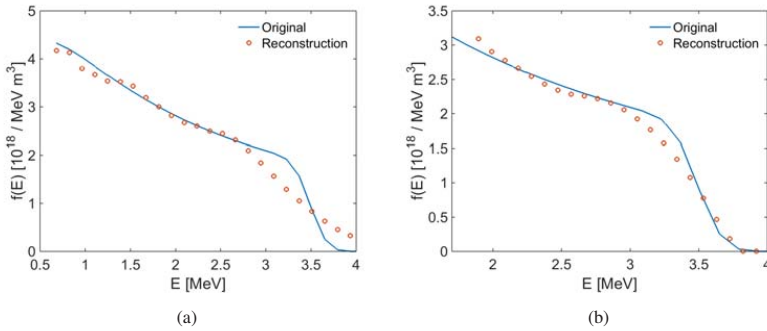


Figure 4. (a) Reconstruction of the energy spectrum for $E > 0.5$ MeV for an isotropic α -particle slowing-down distribution based on single-detector CTS measurements and the prior information that the distribution function is isotropic. (b) As (a), but for GRS for $E > 1.7$ MeV.

A disadvantage of this technique is that the assumption of isotropy precludes the measurement of any anisotropy effects. Nevertheless, the ITER measurement requirement to measure α -particle energy spectra can be met down to 0.5 MeV (optimistically 0.3 MeV) based on the CTS measurements. The assumption of isotropy is perhaps already implied by the requirement to measure energy spectra which ignores any pitch effects. This approach allows the determination of the α -particle density under the assumptions that the α -particle velocity distribution function is smooth and isotropic in velocity space. While smoothness is probably a good assumption, the isotropy assumption is questionable since some anisotropy is expected due to the drift orbit topology, the directional bias of NBI and any anomalous transport due to Alfvénic or other magnetohydrodynamic activity [40].

The last approach that we discuss is to fit a model to the measured spectra by assuming a functional form of the α -particle velocity distribution function, for example a classical slowing-down distribution. The assumption of a functional form of the velocity distribution function is stronger prior information yet than isotropy and smoothness. The slowing-down distribution is both isotropic and smooth, and additionally the spectral shape is given (assuming we know the crossover energy). This approach precludes the measurement of energy spectra as they are assumed in the approach. Nevertheless, the α -particle densities can be inferred by determining the α -particle density that produces the best fit to the measured spectra, for example using a least-square metric accounting for nuisance parameters [55]. Figure 5 illustrates the sensitivity of CTS measurements to the α -particle density for an isotropic slowing-down distribution in a deuterium-tritium plasma. The frequency of the injected electromagnetic waves is 60 GHz. The shapes of the measured spectra depend on the α -particle densities which can hence be determined. In particular the wings of the spectra with Doppler shifts larger than about 1 GHz vary strongly with the α -particle density. The inner part of the spectra with Doppler shifts smaller than about 1 GHz are dominated by scattering from thermal deuterium and tritium. Since the isotropic slowing-down distribution is probably a fairly good model [56], it should allow the determination of α -particle densities with good accuracy.

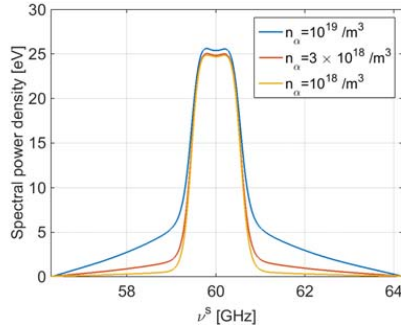


Figure 5. Sensitivity of CTS spectra to the α -particle density for the central CTS measurement volume for the ITER baseline scenario. The α -particle velocity distribution is assumed to be an isotropic slowing-down distribution. The alpha particle density n_α can be inferred by finding the best fit of the model to the measurements.

6 Conclusions

Energy and momentum conservation imply that fast-ion diagnostics observe restricted yet rather broad regions in velocity space. This makes it impossible to directly measure densities and energy spectra of fusion α -particles. The consistent use of energy and momentum conservation stresses the analogies and differences in the velocity-space interrogation regions of NES, GRS, CTS and FIDA. We can nevertheless determine energy spectra and fast-ion densities. Integrated data analysis of the available fast-ion diagnostics allows the tomographic reconstruction of a 2D velocity distribution function which can be integrated to obtain energy spectra and densities. Energy spectra measured in this way at JET and ASDEX Upgrade agree very well with corresponding numerical simulations. This approach will be possible at ITER for α -particles with energies larger than 1.7 MeV based on GRS and CTS. For lower energies down to about 300–500 keV the measurement relies on CTS only, and we need to assume additional prior information on the distribution function to obtain solutions. Energy spectra and densities of the α -particles can be obtained by assuming that their distribution is isotropic in velocity space. Alternatively, fast-ion densities can also be obtained by assuming a functional form of the fast-ion velocity distribution function, such as an isotropic slowing-down distribution, which is stronger prior information yet than smoothness and isotropy.

Acknowledgments

We thank the ITPA Energetic Particle Physics Topical Group for its support. The work leading to this publication has been funded partially by Fusion for Energy under Specific Grant Agreement F4E-FPA-393. This publication reflects the views only of the authors, and Fusion for Energy cannot be held responsible for any use which may be made of the information contained therein. This work has been partially carried out within the framework of the EUROfusion Consortium and has received funding from the Euratom research and training programme 2014–2018 under grant agreement No 633053. The views and opinions expressed herein do not necessarily reflect those of the European Commission.

References

- [1] X. Litaudon, S. Abduallev, M. Abhangi, P. Abreu, M. Afzal, K. Aggarwal et al., *Overview of the JET results in support to ITER*, *Nucl. Fusion* **57** (2017) 102001.
- [2] H. Meyer, T. Eich, M. Beurskens, S. Coda, A. Hakola, P. Martin et al., *Overview of progress in european medium sized tokamaks towards an integrated plasma-edge/wall solution*, *Nucl. Fusion* **57** (2017) 102014.
- [3] A. Donné, A. Costley, R. Barnsley, H. Bindslev, R. Boivin, G. Conway et al., *Progress in the ITER Physics Basis. Chapter 7: Diagnostics*, *Nucl. Fusion* **47** (2007) S337.
- [4] W.W. Heidbrink, Y. Luo, K.H. Burrell, R.W. Harvey, R.I. Pinsky and E. Ruskov, *Measurements of fast-ion acceleration at cyclotron harmonics using balmer-alpha spectroscopy*, *Plasma Phys. Control. Fusion* **49** (2007) 1457.
- [5] M. Salewski, S. Nielsen, H. Bindslev, V. Furtula, N. Gorelenkov, S. Korsholm et al., *On velocity space interrogation regions of fast-ion collective thomson scattering at ITER*, *Nucl. Fusion* **51** (2011) 083014.
- [6] M. Salewski, B. Geiger, D. Moseev, W.W. Heidbrink, A.S. Jacobsen, S.B. Korsholm et al., *On velocity-space sensitivity of fast-ion d-alpha spectroscopy*, *Plasma Phys. Control. Fusion* **56** (2014) 105005.
- [7] A. Jacobsen, M. Salewski, J. Eriksson, G. Ericsson, S. Korsholm, F. Leipold et al., *Velocity-space sensitivity of neutron spectrometry measurements*, *Nucl. Fusion* **55** (2015) 053013.
- [8] M. Salewski, M. Nocente, G. Gorini, A. Jacobsen, V. Kiptily, S. Korsholm et al., *Velocity-space observation regions of high-resolution two-step reaction gamma-ray spectroscopy*, *Nucl. Fusion* **55** (2015) 093029.
- [9] M. Salewski, M. Nocente, G. Gorini, A. Jacobsen, V. Kiptily, S. Korsholm et al., *Fast-ion energy resolution by one-step reaction gamma-ray spectrometry*, *Nucl. Fusion* **56** (2016) 046009.
- [10] A.S. Jacobsen, F. Binda, C. Cazzaniga, J. Eriksson, A. Hjalmarsson, M. Nocente et al., *Velocity-space sensitivities of neutron emission spectrometers at the tokamaks JET and ASDEX upgrade in deuterium plasmas*, *Rev. Sci. Instrum.* **88** (2017) 073506.
- [11] L. Stagner and W.W. Heidbrink, *Action-angle formulation of generalized, orbit-based, fast-ion diagnostic weight functions*, *Phys. Plasmas* **24** (2017) 092505.
- [12] J. Galdon-Quiroga, M. Garcia-Munoz, M. Salewski, A. S. Jacobsen, L. Sanchis-Sanchez, M. Rodriguez-Ramos et al., *Velocity-space sensitivity and tomography of scintillator-based fast-ion loss detectors*, *Plasma Phys. Control. Fusion* **60** (2018) 105005.
- [13] M. Salewski, M. Nocente, A. S. Jacobsen, F. Binda, C. Cazzaniga, J. Eriksson et al., *Bayesian integrated data analysis of fast-ion measurements by velocity-space tomography*, *Fusion Sci. Technol.* **74** (2018) 23.
- [14] D. Moseev, M. Salewski, M. Garcia-Muñoz, B. Geiger and M. Nocente, *Recent progress in fast-ion diagnostics for magnetically confined plasmas*, *Rev. Mod. Plasma Phys.* **2** (2018) 7.
- [15] J. Eriksson, M. Nocente, F. Binda, C. Cazzaniga, S. Conroy, G. Ericsson et al., *Dual sightline measurements of MeV range deuterons with neutron and gamma-ray spectroscopy at JET*, *Nucl. Fusion* **55** (2015) 123026.
- [16] J. Eriksson, C. Hellesen, F. Binda, M. Cecconello, S. Conroy, G. Ericsson et al., *Measuring fast ions in fusion plasmas with neutron diagnostics at JET*, *Plasma Phys. Control. Fusion* **61** (2018) 014027.